Carbonate Platform and Coral Reef Response to Environmental Perturbations: Insights from Scott Reef, North West Shelf, Australia

CARRA GEORGINA WILLIAMS

B.Sc., M.Sc. ORCID: 0000-0002-1312-4438



Supervisor: Professor Jody M. Webster
Associate Supervisor: Associate Professor Tristan Salles
Associate Supervisor: Doctor Victorien Paumard

A thesis submitted in fulfilment of
the requirements for the degree of
Doctor of Philosophy

Geocoastal Research Group
School of Geosciences
Faculty of Science
The University of Sydney
Australia

22 May 2026

Statement of originality

This is to certify that to the best of my knowledge, the content of this thesis is my own work. This thesis has not been submitted for any degree or other purposes. I certify that the intellectual content of this thesis is the product of my own work and that all the assistance received in preparing this thesis and sources have been acknowledged. Where data and interpretations from the unpublished report of (Collins et al., 2009) have been used, any differences between the interpretations presented in this thesis and those in the original report are explicitly identified and discussed.

ChatGPT was used for the purposes of text enhancement in Chapters 1, 4 and 5, to construct the synthetic sea-level curves described in Chapter 4, and to calculate Thompson corrected U-Th open system ages > 300 kyr presented in chapter 5. The use of this generative AI tool includes spelling corrections, minor sentence restructuring, and clarity enhancement. I confirm that where generative AI was used, the content was reviewed for possible errors, inaccuracies, and bias. I take full responsibility for the submitted thesis, confirm the work is my own, and have used generative AI in accordance with University guidelines and policies.

Name: Carra Georgina Williams
Date: 24/07/2026

Authorship attribution statement

This thesis is based on the following original research articles. My own contributions and co-author contributions are detailed on a title page prior to each corresponding chapter.

ARTICLE 1: Williams, C., Paumard, V., Webster, J. M., Leonard, J., Salles, T., O'Leary, M., and Lang, S. (2023). Environmental controls on the resilience of Scott Reefs since the Miocene (North West Shelf, Australia): Insights from 3D seismic data. *Marine and Petroleum Geology*, 151, 106188-. https://doi.org/10.1016/j.marpetgeo.2023.106188

ARTICLE 2: Williams, C., Webster, J. M., Bevitt, J. J., Webb, G. E., Nothdurft, L. D., Paumard, V., ... Murphy, R. J. (2025). Neutron Computed Tomography: A Novel High-Resolution, Non-Destructive Method for Screening Fossil Coral for Diagenetic Alteration for Geochronologic and Paleoclimatic Reconstructions. *Geochemistry, Geophysics, Geosystems*: G3, 26(10). https://doi.org/10.1029/2025GC012439

ARTICLE 3: Williams, C., Webster, J. M., Salles, T., Paumard, V., Grimaldi, C., Lejri, M. (2026). Carbonate platform evolution in response to the Mid - Pleistocene climate transition on the North-West Shelf of Australia: Insights from forward stratigraphic modelling. *Marine Geology*, Article 107716. https://doi.org/10.1016/j.margeo.2026.107716

ARTICLE 4: Williams, C., Webster, J. M., Humblet, M., Braga, J. C., Lowe, A., Murphy, R., Renema, W., Nothdurft, L., Webb, G., Zhao, J., Paumard, V., Lebrec, U., Salles, T., Duyker, S., Wilson, M., and Testa, V. 2025, Chronostratigraphic, paleoecological and paleoenvironmental reconstructions of Scott Reef, Northwest Shelf, Australia: evidence from Pleistocene fossil reef cores.

Carra Georgina Williams
24/07/2026

As supervisor for the candidature upon which this thesis is based, I can confirm that all of the authorship attribution statements listed are correct.

Jody M. Webster
24/07/2026

Abstract

Coral reefs preserve significant archives of past sea-level and associated climatic change due to their depth-dependant growth, generally good preservation potential, and the ability to be precisely dated using radiocarbon and U-series techniques. Coral reefs that develop on isolated carbonate platforms along stable yet rapidly subsiding continental margins have the potential to preserve exceptionally expanded records of past sea-level change. This is because sustained subsidence continuously creates accommodation within the euphotic and mesophotic zones, promoting long-term reef accretion and stratigraphic preservation. Investigation, analyses and interpretation of recovered fossil reef cores from such locations are rare, may be compromised by diagenetic alteration and difficult to resolve due to poor spatial and temporal sampling across the reef. The understanding of the response of coral reefs to environmental changes over millennial timescales is thus limited and requires further investigation. Scott Reef, comprising the isolated North and South Scott carbonate platforms on Australia's North West Shelf (NWS), preserves one of the most continuous and spatially extensive Quaternary reef archives in the Indo-Pacific. Yet, despite its importance for reconstructing regional climate, sea-level change, and carbonate platform evolution, major uncertainties remain regarding the timing of reef initiation and demise, the impact of the Middle Pleistocene Transition (MPT), and the processes governing long-term reef resilience. This thesis aims to advance understanding of the complex interactions between environmental and eustatic controls on carbonate platform evolution and coral reef development through Neogene-Quaternary climate transitions, which also provides valuable insights for predicting coral reef response to future environmental changes. This thesis developed high-resolution qualitative and quantitative geological models of North and South Scott Reef, comparable to similar reef systems worldwide, to assess their response to orbital forcing and associated climate change, including eustacy and environmental perturbations (oceanographic) over a range of spatial and temporal (spatio-temporal) scales. The approach utilises forward stratigraphic modelling to

integrate multi-scale observational data (Ångström to km) to refine lithological interpretations, paleodepositional records and geochronological constraints from fossil reef cores. The data include 3-D seismic, multibeam bathymetry, fossil reef cores, well logs, U-series, and modern ecological records. Our methodological approach integrates detailed logging, high-spatial resolution hyperspectral scanning, neutron computed tomography, petrologic and sedimentary facies analysis, including paleoenvironmental reconstructions using coral and algal assemblages within a chronostratigraphic model spanning 500 kyr.

3-D seismic and well log data are used to establish a new Miocene–Quaternary chronostratigraphic framework for Scott Reef that provides the geological context and long-term evolution of the platform in response to regional controls (tectonics, ocean currents), global forcing (eustasy and climate) and local controls, including platform geomorphology, hydrodynamic energy gradients, and spatial variability in carbonate production across reef-crest, lagoonal, and slope environments. The seismic interpretation workflow used in this study takes advantage of the full 3-D variability of the data to create a high-resolution seismic stratigraphic framework and conduct a detailed seismic geomorphologic analysis that allow the interpretation of four phases of carbonate factory evolution from the Miocene barrier-reef stage through the Pliocene isolated carbonate build-up phase to the modern isolated platforms. The analysis demonstrates that long-term resilience was strongly influenced by antecedent topography, rapid subsidence, and the interaction of regional oceanographic drivers, including the Indonesian Throughflow and the Leeuwin Current, which modulated climate, hydrodynamics, and terrigenous sediment bypass throughout the Cenozoic.

To address the difficulty in dating fossil reef cores that are diagenetically altered and thus compromise chronostratigraphic reconstructions, we apply neutron computed tomography (NCT) as a novel, non-destructive 3-D screening tool for identifying well-preserved aragonitic coral suitable for geochronology and paleoenvironmental reconstructions. Findings from this methodological experiment show that NCT effectively maps carbonate mineral phases and hydrogen-rich organic matter, enabling discrimination between pristine aragonite and low-Mg calcite replacement. Application to Holocene and Pleistocene corals from Papua New Guinea, Ashmore Reef, and Ribbon Reef 5 demonstrates that NCT overcomes limitations of traditional

2-D or destructive methods and is most effective when combined with hyperspectral imaging and SEM analyses.

A forward stratigraphic model is developed to improve the Quaternary sequence stratigraphic framework established in the first case study due to data resolution and to reduce uncertainties around sequence stratigraphic predictions over seismic data gaps. The FSM is then used to investigate the response of Scott Reef to the MPT (1.2–0.7 Ma), a period marked by increased sea-level amplitude fluctuations and monsoonal intensification during ensiung interglacials. Hypotheses applied to the data-calibrated model reveal that platform morphology and growth history can only be reproduced with spatially variable subsidence, increased carbonate production and wave energy, and reduced production on the South Reef leeward margin after ca. 0.5 Ma. The results indicate that major geomorphological reorganisation initiated during the MIS 12 lowstand, with MIS 11 generating an 80-m-thick reef rim and bucket-shaped platform geometry that persists to present. These findings demonstrate the utility of FSM for reducing stratigraphic uncertainty and providing quantitative and qualitative constraints on regionally variable reef responses to eustatic and climatic perturbations.

Finally, detailed geochronologic and paleoenvironmental reconstructions of Quaternary reef development are produced using three boreholes (to 200 m) drilled across the windward and leeward margins of North and South Scott Reef. High-resolution hyperspectral scanning (250 μm), NCT, detailed lithological and sediment facies analysis, coralgal assemblage characterisation, petrography, and new open and closed-system U–Th dating constrains seven reef growth units on North Reef spanning MIS 15 to present, seven units on the South Reef SE margin spanning MIS 11 to present, and four units on the South Reef leeward margin spanning MIS 9 to present. The cores reveal a long-term shallowing-upward trend from deep forereef slope to shallow reef-crest environments, bounded by paleosols. Three identified coralline algal assemblages and four coral assemblages indicate a diverse range of reef settings from shallow reef crest (< 10 m) to deep forereef slope (> 60 m). We present the first detailed documentation of the coral reef communities that developed in Scott Reef from 515 kyr to present. Comparisons with Ribbon Reef 5 highlight the influence of differing subsidence

rates, antecedent seafloor morphology, hydrodynamics, and sediment input on Quaternary reef growth.

Collectively, the chapters comprising this thesis contribute to a significant new understanding of Neogene-Quaternary reef response to eustatic and associated environmental changes and improves the potential accuracy of absolute sea-level reconstructions from diagenetically altered fossil coral reefs. The methods presented in this thesis provide a foundation on which to investigate similar reef systems globally and to predict coral reef response to future environmental changes. However, many more questions and opportunities abound from this thesis that will need to be addressed in future work. For example, the hyperspectral dataset acquired in this study from the fossil reef core drilled on the SE margin of the South Reef reveals a record of extraordinary preservation of aragonitic corals in place. This data provides an incredible opportunity to reconstruct a high resolution absolute sea-level curve, including resolving regional oscillations within the MIS 7 interstadials, and diagenetic history for this region on the NWS.

Acknowledgements

This research was undertaken as part of my doctoral studies within the Geocoastal Research Group, School of Geosciences at The University of Sydney. I am deeply grateful to my supervisor, Professor Jody Webster, for his guidance, encouragement, and unwavering support throughout this project. His energy and enthusiasm for coral reef science is inspiring and contagious. I also thank Associate Professor Tristan Salles, Dr Victorien Paumard, and all co-authors for their collaboration, expertise and contributions to each chapter.

The research reported in this thesis was supported by a Postgraduate Research Scholarship from the School of Geosciences, University of Sydney, and an Australian Government Research Training Program (RTP) Scholarship. Additional funding was provided by the Australian Institute of Nuclear Science and Engineering (AINSE). I am grateful for further financial support through conference and research travel grants, including an International Association of Sedimentologists (IAS) travel grant, a University of Sydney Carers Grant, and support from the University of Western Australia to access core at the Perth Core Library, facilitated by Prof. Simon Lang. I also acknowledge the School of Earth and Oceans at the University of Western Australia for supporting my visitor status and providing access to computing facilities during this research. I gratefully acknowledge the TIDE Research Hub and Prof. Phil Watson for their support of this work, and Woodside Energy for facilitating access to core material and legacy datasets from the North West Shelf. I also thank the instrument scientists at ANSTO - Joseph Bevitt, Jitendra Mata, and Katy Wood, for their assistance with neutron computed tomography and neutron scattering data acquisition, as well as Lawrence Anovitz at Oak Ridge National Laboratory for valuable discussions and expertise related to neutron imaging and porosity data analysis.

My sincere thanks go to the members of the Geocoastal Research Group for their support, knowledge sharing and enthusiasm, and to the School of Geosciences' technical and administrative staff for their assistance during my visits to the university and supporting my remote working environment.

Finally, I wish to express my deepest gratitude to my family and my partners family for their love and support, and for helping make childcare, travel, and attending conferences and fieldwork achievable. To my ineffable partner and son, thank you for your joy, strength, and unconditional support that made every challenge possible. This thesis would not have been possible without your understanding and care.

Contents

Statement of Originality i

Abstract v

Acknowledgements ix

Contents xi

List of Figures xv

List of Tables xix

Definitions and Abbreviations xx

Abbreviations xx

Definitions of Key Terms xx

Chapter 1 Introduction 2

1.1 Understanding Coral Reef Systems 2

1.2 Carbonate Systems Through Time 4

1.2.1 Evolution of Carbonate Platforms and Coral Reefs 4

1.2.2 Coral Reefs as Archives of Sea-level and Environmental Changes 5

1.2.3 Facies Belts and Sequence Stratigraphy 10

1.2.4 Advances in Dating Fossil Corals 13

1.3 Quaternary Fossil Reefs and the Middle Pleistocene Transition 15

1.4 Forward Stratigraphic Modelling in Coral Reef Science 20

1.4.1 FSM Principles and Applications 22

1.4.2 Limitations, Uncertainty and Future Development 27

1.5 Scientific Rationale 28

1.5.1 Scott Reef as a Natural Laboratory 28

1.5.2 The Geological Significance of Scott Reef 32
1.5.2.1 Neogene Foundations 35
1.5.2.2 Quaternary Evolution 38
1.6 Thesis Objectives, Structure and Scope 39

Chapter 2 ARTICLE 1: Environmental Controls on the Resilience of Scott Reefs Since the Miocene (North West Shelf, Australia): Insights from 3D Seismic Data 44

Chapter 3 ARTICLE 2: Neutron Computed Tomography: A Novel High-Resolution, Non-Destructive Method for Screening Fossil Coral for Diagenetic Alteration for Geochronologic and Paleoclimatic Reconstructions 75

Chapter 4 ARTICLE 3: Carbonate Platform Evolution in Response to the Mid - Pleistocene Climate Transition on the North West Shelf of Australia: Insights from Forward Stratigraphic Modelling 100

Chapter 5 ARTICLE 4: Chronostratigraphic, Paleoecological and Paleoenvironmental Reconstructions of Scott Reef, North West Shelf, Australia: Evidence from Pleistocene Fossil Reef Cores 130

Chapter 6 General discussion and synthesis 272

6.1 General Discussion and Synthesis 272
6.1.1 Research question 1: What is the role and nature of eustacy and associated environmental perturbations in shaping carbonate platform development and coral reef evolution at Scott Reef during major Neogene-Quaternary climate transitions? 272
6.1.1.1 Miocene (18–5 Ma): Initiation of Carbonate Build-ups under Eustatic Control 273
6.1.1.2 Pliocene (5–2.5 Ma): Expansion of Isolated Carbonate Buildups 273
6.1.1.3 Pleistocene (2.5 Ma–0 Ma): Increased Eustatic Sea-Level Variability and Platform Resilience 274

6.1.1.4 Holocene (11.7 kyr to present): Catch-up Growth during Rapid Sea-Level Rise 276
6.1.2 Research question 2: How can neutron computed tomography and hyperspectral imaging be used to improve paleoclimatic and geochronologic reconstructions of coral reefs? 277
6.1.3 Research question 3: Can we reconstruct the paleodepositional evolution and chronostratigraphic framework of Scott Reef by synthesising all available legacy data with new sedimentological analyses using innovative screening and dating techniques? 279
6.1.4 Research question 4: What new insights into the main processes controlling reef and carbonate platform evolution emerge through the integration of observational data and synthetic reef growth models? 281
6.1.5 Research question 5: Are the observed differences in reef growth models on the GBR due to eustacy and environmental variances? 283
6.2 Recommendations for future research 284
6.2.1 Expanding and Refining Comparative Reef Datasets 285
6.2.2 Refining Paleowater Depth and Chronologic Reconstructions 287
6.2.3 New Relative Sea Level, Modelling and Measuring Diagenesis 287

Chapter 7 Conclusions and final remarks **289**

Bibliography of Chapters 1 and 6 **291**

Appendix A Chapter 2 Supplementary Data 1 - Results **311**

Appendix B Chapter 2 Supplementary Data 2 - Interpretation **318**

Appendix C Chapter 2 Supplementary Data 3 - Movie of Megator 3-D seismic data **328**

Appendix D Chapter 3 Supplementary Information - Raw NCT data and movie of NCT scans of fossil reef cores **329**

Supplementary Movies 330

Appendix E Chapter 4 Supplement 1 - Details of seismic and well data 333

Appendix F Chapter 4 Supplement 2 - Core interpretation 336

Appendix G Chapter 4 Supplement 3 - Detailed methodology and modelling workflow 348

Appendix H Chapter 4 Supplement 4 - Petrel GPM model parameter files 357

Appendix I Chapter 5 Supplement 1 - Core Interpretation 358

Appendix J Chapter 5 Supplement 2 - Uranium Series Data (Collins et al., 2009) 370

Appendix K Chapter 5 Supplement 3 - Uranium Series Data (This study) 377

Appendix L Chapter 5 Supplement 4 - Raw XRD Data (This study) 379

Appendix M Chapter 5 Supplement 5 - Raw Neutron Computed Tomography Data (This study) 385

Appendix N Chapter 5 Supplement 6 - Hyperspectral Imaging Data (This study) 386

Appendix O Chapter 5 Supplement 7 - Quantitative Hyperspectral Data (This study) 390

Appendix P Chapter 5 Supplement 8 - Thin sections (Collins et al., 2009) 391

Appendix Q Chapter 5 Supplement 9 - Thin sections (This study) 428

Appendix R Chapter 5 Supplement 10 - SEM data (This study) 430

Appendix S Academic conference presentations and awards 434

List of Figures

1.1 Discrete environmental tolerances, such as relative sea-level change, biological and oceanographic factors summarised in (A) from Camoin and Webster (2015), collectively determine architectural geometries and the ability of reefs to 'keep up', 'catch up', or 'give up' (B) (Woodroffe and Webster, 2014). 7

1.2 This study applies the method used at One Tree Reef on the Great Barrier Reef (Dechnik et al., 2017), which interprets distinct coralgal assemblages defined by the distribution and abundance of coral, algal and associated reef biota. 9

1.3 Cross-section of characteristics of carbonate platform facies belts with large-scale sediment geometry and lists of small-scale features, as modified by Schlager (2005) after Wilson (1975). 11

1.4 Sequence stratigraphic controls differ between siliciclastic and carbonate systems (Pomar and Haq, 2016). 12

1.5 The equatorial Pacific curve of Bates et al. (2014) (blue line) spanning the Quaternary period from ca. 2.5 Ma to present, with the envelope of a compilation of other curves in grey from (Gelder et al., 2020). The dotted vertical lines show the period described as the Mid-Pleistocene transition from 41-kyr to 100-kyr oscillations that occurs between ca. 1.2 - 0.7 Ma. 16

1.6 A map plotting sample sites for coral age data, and showing tectonic setting, from Woodroffe and Webster (2014). 17

1.7 Coral reef age data correlated to a eustatic sea-level curve reconstructed from benthic foraminiferal ^{18}O isotope data, showing a spatial and temporal sampling bias to coral reef terraces in tectonically unstable regions and MIS 5e during the Last Interglacial, respectively. The schematics on the right show the expected geomorphic representations of how reefs arrange themselves in response to

different tectonic regimes, over the same sea-level. From Woodroffe and Webster (2014) adapted from Medina-Elizalde (2013). 19

1.8 Schematic representation of a typical carbonate forward stratigraphic modelling workflow. Empirical and analogue data inform the development of a conceptual model. This modelling workflow similar to the one adopted in this study, is iteratively calibrated to observed data through trial-and-error simulation and refinement. From Lanteaume et al. (2018). 21

1.9 The process of sediment diffusion is a function of grain size. Diffusion coefficient multipliers can be used to constrain rates of diffusion through time and space as proxies for climate and oceanographic variations. From Hill et al. (2009). 22

1.10 Forward stratigraphic model of 2-D reef architectures modelled using 1st order eustatic sea-level curve (Waelbroeck et al., 2002) as the primary geological model input. From Pastier et al. (2019). 25

1.11 1-D Forward stratigraphic model of an idealised drill core section demonstrating the importance of integrating high-resolution oceanographic and ecological input data. From Salles et al. (2018). 26

1.12 Geographic location of Scott Reef on the North West Shelf of Australia and Ribbon Reef 5 on the Northeast shelf that was used to establish correlations, connections and details. Triangles indicate IODP Expedition 356 sites (U1461–U1464) that provide critical context on five million years of climate variability and the role of the Indonesian Throughflow along the NWS. This figure was made using GeoMapApp (https://www.geomapapp.org). 30

1.13 (A) Location map of Scott Reef on the North West Shelf of Australia, showing the major oceanographic currents influencing the region. Modified from Gallagher et al. (2014). (B) Modern tidal current flow overlain on North and South Scott (Grimaldi et al., 2024). 35

1.14 Basinward cross-section schematic (A-A') of the Neogene pre and post-rift sediments and structural elements, including the Scott Reef trend (A) and onlapping Pliocene-Quaternary clinoform sediments prograding basinward (B). Scott Reef is located on the Scott Plateau. Adapted from Keep et al. (2007). 37

1.15 Schematic illustrating the thesis design, highlighting the geological time intervals and spatial scales represented by datasets used across the four core research chapters. Seismic stratigraphy, forward stratigraphic modelling, core analyses, and diagenetic screening are integrated to reconstruct carbonate platform evolution at Scott Reef, North West Shelf of Australia. Research objectives and synthesis are presented in Chapters 1 and 6, respectively. 43

6.1 Conceptual sketch of Scott Reef during the MPWP from ca. 2.5 – 5.25 Ma, guided by observational data, including seismic facies and well log data. 274

6.2 Conceptual sketch of Scott Reef during the LGM ca. 18 kyr, guided by observational data, including seismic facies, well log data, thin section data and lithologic interpretation.The thin section illustrates a high-energy depositional environment (rudstone–grainstone) that was subsequently overprinted by subaerial exposure diagenesis during relative sea-level lowstand. The Gamma Ray (GR) log response reflects variations in minor terrigenous input, sediment reworking, and karst-related infill during lowstand conditions, relative to highstand intervals which record elevated GR values due to increased terrigenous influx. This variability is interpreted as a conceptual proxy for reef growth phases and associated shifts in depositional and exposure conditions. 276

6.3 Conceptual model of Scott Reef during the Holocene highstand systems tract (HST), integrating seismic facies, GR well log data, and thin section data. The platform records overall aggradational growth during rapid post-glacial sea-level rise, with reef-margin development, lagoonal sedimentation, and highstand shedding to the basin. Spatial variability between the North and South Reefs are evident due to differential subsidence and platform morphologies. 278

L.1 Stacked powder X-ray diffraction (XRD) diffractograms of selected carbonate core samples. Major reflections of calcite ($\sim$29.4° 2θ), aragonite ($\sim$26–27° 2θ), and dolomite/ankerite ($\sim$30–31° 2θ) are indicated. Individual samples are vertically offset for clarity. Variations in peak intensity and relative phase abundance reflect differences in primary carbonate mineralogy and degrees of diagenetic alteration across the analysed intervals. 380

L.2 Stacked powder X-ray diffraction (XRD) diffractograms of representative carbonate core samples compared with reference patterns for calcite and aragonite. Major diffraction peaks correspond predominantly to calcite, with variable aragonite contributions evident in selected samples. Individual diffractograms are vertically offset for clarity. Differences in peak intensity and phase distribution reflect variability in primary mineralogy and diagenetic alteration across the analysed intervals. 381

L.3 X-ray diffraction (XRD) pattern of a representative carbonate core sample (red trace) with reference peak positions for calcite ($CaCO_3$), aragonite ($CaCO_3$), dolomite ($CaMg(CO_3)_2$), and ankerite ($Ca(Fe^{2+},Mg)(CO_3)_2$) shown below. Vertical bars indicate characteristic diffraction peak positions for each mineral phase. The dominant peak at $\sim$29.4° 2θ corresponds to calcite, with aragonite and minor dolomite/ankerite reflections indicating variable diagenetic overprinting within the sample. 383

L.4 Raw XRD data 384

List of Tables

1.1 Chapter 2: Seismic Stratigraphy and Geomorphology of Scott Reef 41

1.2 Chapter 3: Neutron Computed Tomography for Fossil Coral Screening 41

1.3 Chapter 4: Forward Stratigraphic Modelling of Scott Reef 42

1.4 Chapter 5: Core logging for Chronostratigraphic and Paleoenvironmental Reconstruction 42

2.1 Summary of Chapter 2: Environmental Controls on the Resilience of Scott Reef Since the Miocene. 45

3.1 Summary of Chapter 3: Neutron Computed Tomography as a Non-Destructive Method for Diagenetic Screening of Fossil Corals. 76

4.1 Summary of Chapter 4: Carbonate Platform Evolution in Response to the Mid-Pleistocene Climate Transition. 102

5.1 Summary of chapter 5: Chronostratigraphic, Paleoecological and Paleoenvironmental Reconstructions of Scott Reef Pleistocene Cores. 132

N.1 Drill hole depth intervals scanned with the hyperspectral core imager 389

Definitions and Abbreviations

Abbreviations

NWS Northwest Shelf

GBR Great Barrier Reef

ICB Isolated Carbonate Buildup

NCT Neutron Computed Tomography

FSM Forward Stratigraphic Modelling

MPT Mid-Pleistocene Transition

GIA Glacial Isostatic Adjustment

GR Gamma Ray

ITF Indonesian Throughflow

LC Leeuwin Current

Definitions of Key Terms

Facies	A body of sediment or rock with distinctive depositional characteristics.
Detrital Facies	A sedimentary rock unit composed of fragments (detritus/clasts) derived from the weathering and erosion of pre-existing rocks..

Sequence	A relatively conformable succession of genetically related strata bounded at their upper surface and base by unconformities and their correlative conformities (Vail, et al., 1977) The term is used specifically in a stratigraphic context and should not be used interchangeably with generic sedimentary units or depositional packages.
Package	A descriptive term used in this thesis to refer to distinct sedimentary packages bounded by paleosols that represent discrete sedimentological units within each borehole that lack clear lateral correlation across carbonate platforms. Unlike a sequence, a depositional package does not necessarily imply sequence stratigraphic significance or bounding unconformities.
Cycle	A repetitive stratigraphic or depositional pattern resulting from recurring environmental or sea-level changes across a range of temporal scales. The term is used generically and does not imply formal sequence stratigraphic hierarchy unless explicitly stated.
Carbonate platform	A regionally extensive shallow-marine carbonate depositional system characterised by sustained carbonate production and accumulation across a broad physiographic area.
Isolated carbonate buildup (ICB)	A discrete carbonate accumulation surrounded by deeper-water environments and separated from adjacent carbonate systems. In this thesis, the term encompasses isolated reefs, platforms, pinnacles, and atoll-like carbonate systems of varying size and morphology.
Small isolated carbonate buildup	In this thesis, isolated carbonate buildups with limited lateral extent and relief relative to major platform-scale systems. This term is descriptive and not intended as a formal geomorphic classification.

Large isolated carbonate buildup	In this thesis, isolated carbonate buildups with greater lateral extent, vertical relief, and geomorphic complexity relative to smaller reefal buildups or patch reefs.
Reefal buildup	A general term adopted from the literature referring to a biologically constructed carbonate accumulation formed primarily through *in situ* framework growth by reef-building organisms such as corals and coralline algae.
Atoll	A ring-shaped carbonate platform or reef complex that partially or completely encloses a central lagoon, commonly developed on subsiding volcanic or structural highs.
Patch reef	A relatively small, isolated reef body typically surrounded by lagoonal, platform, or deeper-water sediments and lacking the lateral continuity of larger reef complexes or carbonate platforms.

CHAPTER 1

Introduction

"The whole can only be comprehended by understanding the connections, correlations and details" – Alexander Von Humboldt

1.1 Understanding Coral Reef Systems

Modern reefs are an extraordinary phenomenon (Wood, 1999), although they have not always appeared as they do today. The first evidence of coral-like organisms dates back to the Ediacarian, about 600 Ma (Chen et al., 2002). However, the first reef frameworks built by tabulate and rugose corals emerged during the Ordovician period about 450 Ma (Martin-Garin and Montaggioni, 2023). Modern scleractinian corals that dominate present-day reefs evolved from their predecessors around 240 Ma in the Triassic, making significant evolutionary leaps, including the ability to secrete calcium carbonate skeletons and developing symbiotic relationships with photosynthetic zooxanthellae algae (Woodroffe and Webster, 2014; Martin-Garin and Montaggioni, 2023). During this time, reef building organisms and their associated algae and biota have proliferated and diversified so magnificently in response to ever changing environmental conditions over geological time that new discoveries still reveal themselves today. For example, in 2020, a detached mesophotic reef larger than the Empire State Building was discovered in a water depth of 500 m in the Great Barrier Reef, Australia (Schmidt Ocean Institute, 2020). In 2024, the world's largest singular coral *Pavona clavus*, measuring 34 m wide, 32 m long and 5.5 m high and ca. 300 years old, was discovered in the Solomon Islands (National Geographic Society, 2024). Scientists have been collecting knowledge of coral reefs and their associated carbonate platforms for centuries, and although much has

been learnt, there are still many aspects that we do not understand, particularly the nature of coral reef adaptation to rapidly changing oceanographic conditions and their resilience to unprecedented climatic change. One of the key objectives of modern-day coral reef science is to understand the evolution of coral reefs and their formation histories on a variety of spatial and temporal (spatio-temporal) scales.

Coral reefs also serve as a beacon for the health of our planet and the interconnected web of life in nature. They symbolise intrigue as we seek to know them better to learn about our own history and to contemplate our future and role in nature. They drive us to consider our ethical role and responsibilities towards nature and how we can best preserve these ecosystems for our grandchildren. Importantly, they teach us about the absolute resilience of nature as we learn of their remarkable adaptations through extreme environmental changes that allow them to survive for Millenia. The study of coral reefs, therefore, encompasses scientific inquiry, historical and ecological significance, and philosophical contemplation. Empirical data and theoretical models continue to shape our understanding, while numerical models play an increasingly important role in testing these theories and bridging the gap between realms to understand their nature more precisely. The goal of ongoing and future coral reef and carbonate platform studies is to extract realistic nature-driven models relying on precise field measurements and historical interpretations to better understand, predict and engage management of modern coral reef systems (Greenstein and Pandolfi, 2008), as well as for purely enjoyable scientific curiosity. This research investigates the impact of short (thousands of years: kyr) to long term (millions of years: Ma) changes on coral reef ecosystems to various environmental perturbations, both qualitatively and quantitatively. The introduction reviews the evolution of carbonate systems through time, then discusses the significance of Quaternary fossil coral reefs as archives of past sea-level and environmental changes. We highlight the key climate changes that have occurred in the late Cenozoic because of perturbations in the natural rhythms of the Earth, and the significance of forward stratigraphic modelling and its evolving place in coral reef science. Finally, we outline the scientific rationale and geological context.

1.2 Carbonate Systems Through Time

1.2.1 Evolution of Carbonate Platforms and Coral Reefs

Coral reef science strives to understand the origin, evolution, and long-term history of reef systems, drawing on centuries of scientific inquiry. Historical exploration and navigation of coral reefs includes early observations made by Polynesian seafarers and other indigenous Oceanic cultures (Kirch, 2017), naturalists on exploration voyages, such as Jukes aboard HMS *Fly* (1842-1846; Wilkins, 2001), Darwin aboard HMS *Beagle* (1837-1843; Darwin, 1859) and Humboldt on many of his remarkable expeditions (Wulf, 2015). Expeditions such as the HMS *Challenger* contributed significant data and observations about the topography and character of the seabed and coral reefs, challenging Darwin's theory of coral reefs (Deacon, 2011), but still mainly focusing on reef formation and the role of biological and geological processes. Modern research integrates paleoclimate reconstructions, geochemistry, and tools such as numerical modelling to investigate reef responses to environmental changes. More recently, major scientific achievements of the Integrated Ocean Drilling Program (IODP) (Camoin et al., 2007; Abbey et al., 2011; Rosenthal et al., 2018; Groeneveld et al., 2021; Webster et al., 2025b) have contributed important and high-resolution model reconstructions of key coral reef sites around the world that characterise reef growth history in response to changes in sea-level fluctuations related to ice sheet instability (Camoin and Webster, 2014). The significance of ice sheet dynamics and the associated change in the hydrological cycle is of concern to humanity because of the threat of rising sea-levels and climate change (Woodroffe and Webster, 2014).

Carbonate platforms are large, laterally extensive accumulations of carbonate sediments, primarily composed of calcium carbonate ($CaCO_3$) derived from the skeletal remains of marine organisms such as corals, algae, foraminifera, and molluscs (Pomar and Haq, 2016). They produce a wide range of morphologies that result from the interaction between antecedent topography, tectonic setting, hydrodynamic regime and sea-level history (Burgess et al., 2013). These platforms develop in marine settings where autogenic biological carbonate production exceeds the rate of sediment removal, typically in warm, shallow waters with low

siliciclastic input (Reijmer, 2021), such as the Sahul shelf in North West Australia, and the Great Barrier Reef on North East Australia. Their fossilized counterparts provide evidence that they expanded on Earth during interglacial periods when carbon flux was high in the Ocean basins, often associated with increased weathering of uplifted mountain ranges and modulating Earth's carbon cycle (De Vleeschouwer et al., 2020; Salles et al., 2025). Coral reef communities establish themselves on carbonate platform foundations during marine transgressions and sea-level highstands, preserving detailed records of past sea-level and environmental conditions through their skeletal growth and composition (Camoin and Webster, 2014), while erosional karst surfaces develop during falling sea-level. The reefs' ability to keep pace with relative sea-level change (Figure 1.1) reflects its overall health and long-term stability. Their fossilised skeletons thus preserve information and offer clues about how shallow marine ecosystems might respond to future environmental changes over geologic timescales.

The development of carbonate platforms is also strongly influenced by tectonic setting. Tropical carbonate systems occur in a range of tectonic environments including passive continental margins, active margins, foreland basins, syn-rift basins, and on structural highs such as horst blocks or volcanic edifices. In Southeast Asia in particular, carbonate platforms commonly develop within tectonically complex settings where subsidence, volcanism, and siliciclastic input interact with oceanographic and climatic factors. Studies of Southeast Asian carbonates demonstrate that the interplay between tectonics, nutrient influx, volcanism, and changing oceanographic conditions exert strong controls on carbonate production and reef development over Cenozoic timescales (Wilson, 2011). Establishing the tectonic context of carbonate platform development is therefore critical for interpreting platform morphology and stratigraphic evolution through time.

1.2.2 Coral Reefs as Archives of Sea-level and Environmental Changes

Coral reefs preserve valuable archives of past sea-level changes due to their depth-dependant growth, generally good preservation potential, and the ability to be precisely dated using radiocarbon and U-series techniques (Murray-Wallace and Woodroffe, 2014; Woodroffe and

Webster, 2025). Euphotic reef-building corals, primarily Scleractinia, form large carbonate structures through calcification and support symbiotic zooxanthellae, which generally limits their distribution to the photic zone (0–30 m in clear waters). Their growth depends on specific environmental conditions, including solar radiation, sea surface temperature (SST), water chemistry, and local oceanographic factors such as wave and tide climate, nutrient flux, and salinity (Chappell, 1980; Veron, 1995; Montaggioni and Braithwaite, 2009; Done et al., 2015; Camoin and Webster, 2015). These factors, (Figure 1.1A), along with latitude and substrate composition, control coral and algal assemblages and influence vertical accretion rates and reef development (Done et al., 2015; Woodroffe and Webster, 2014). The distribution of coral morphology and ecological zonation is similarly determined by latitude, water depth, and relative sea-level (eustatic and tectonic), which affects growth rates, reef recruitment, and overall platform morphology (Veron, 2000; Montaggioni, 2005; Grigg, 2006; Scopélitis et al., 2011; Hongo et al., 2012). The interplay between relative sea-level and environmental conditions ultimately determines whether a reef system is in a "keep up," "catch up," or "give up" mode (Figure 1.2B) (Schlager, 2005; Camoin and Webster, 2015; Woodroffe and Webster, 2014). Contrary to Darwin's classical theory of coral reefs, there are numerous morphological types of reefs. Fringing reefs are typically separated from the shore by a lagoon or channel and are highly dependent on antecedent foundations (Kennedy and Woodroffe, 2002). Barrier reefs such as the Great Barrier Reef (GBR), Belize, Maldives and New Caledonia are linear-shaped constructions also separated from the shore by a deep channel but are more heavily controlled by the processes of dissolution during Pleistocene sea-level lowstands (Montaggioni and Braithwaite, 2009). The variability in antecedent topography results in differential growth between the reef front (windward) and reef back (leeward). Atolls, in contrast, are ring-shaped coral reefs encircling a central lagoon and, although traditionally interpreted as the end stage of a subsiding volcanic island (Darwin, 1842), recent work challenges this view. Droxler and Jorry (2021) propose an antecedent karst model in which modern atolls developed on pre-existing flat-topped carbonate banks through repeated glacial–interglacial exposure and karstification, followed by preferential reef accretion along the elevated rims during deglaciations. Numerical forward stratigraphic modelling further supports this reinterpretation, for example, simulations by Liu et al. (2022) demonstrate that atoll formation can be explained

without volcanic subsidence, instead highlighting the importance of antecedent topography, karstification and spatially variable dissolution processes, reef growth dynamics, and Quaternary sea-level oscillations. These models emphasise the importance of geomorphology and hydrodynamic factors in influencing reef architecture. Isolated carbonate platforms, such as the Great Bahama Bank, are generally larger, enclosed or partially enclosed coral reef systems with central lagoons that are commonly occupied by patch reefs. Their morphology is a result of a combination of sea-level change, subsidence and karst erosion that forms suitable limestone substrate for coralgal communities to establish along the reef rim during sea-level rise (Schlager, 2005; Montaggioni and Braithwaite, 2009; Gischler, 2015).

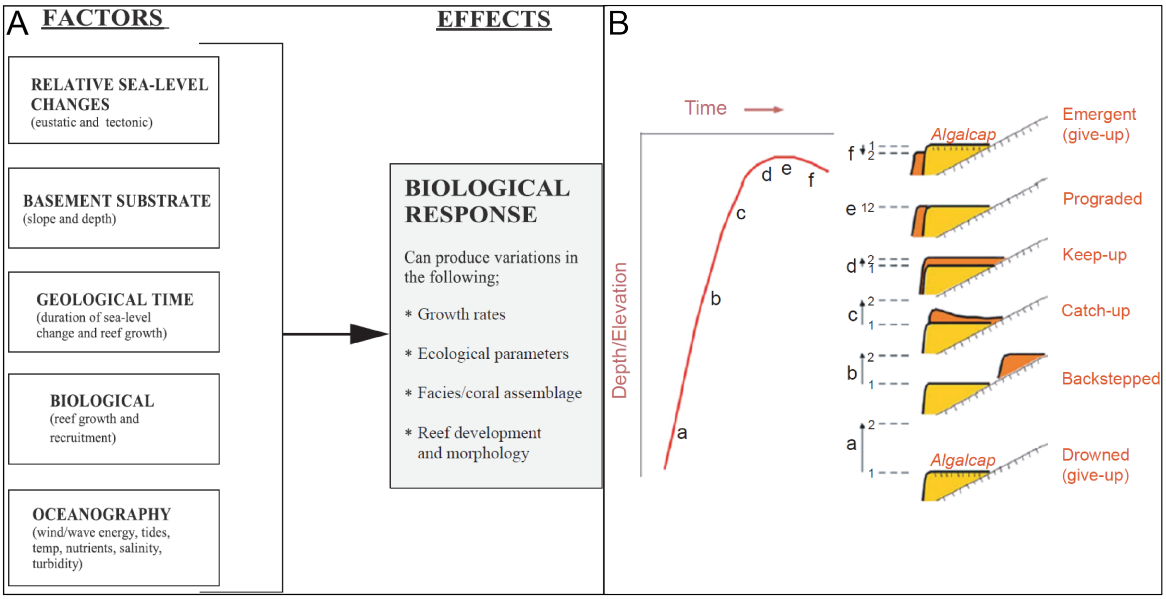


FIGURE 1.1: Discrete environmental tolerances, such as relative sea-level change, biological and oceanographic factors summarised in (A) from Camoin and Webster (2015), collectively determine architectural geometries and the ability of reefs to 'keep up', 'catch up', or 'give up' (B) (Woodroffe and Webster, 2014).

The effects of glacial-isostatic adjustment (GIA) and the poorly constrained habitat depth ranges of species likely affect sea-level reconstructions (Raymo and Mitrovica, 2012; Medina-Elizalde, 2013; Spratt and Lisiecki, 2016; Hibbert et al., 2018). It is therefore imperative for paleo-reef studies in stable continental margins to precisely define paleowater depths from assemblages of reef biota observed in fossil coral cores, typically defined by the

co-occurrence of coral, coralline algae, vermetid gastropods and foraminifera rather than monospecific communities (Abbey et al., 2011; Camoin and Webster, 2015; Braga et al., 2022). Reef building coral communities are reliable sea-level markers and can be used to infer paleoreef biozones and paleowater depths (Davies and Montaggioni, 1985; Cabioch et al., 1999). However, recent studies have demonstrated that many species occur across broader depth ranges than previously recognized, challenging the reliability of such constraints. For example, *Acropora Palmata*, commonly used as a shallow-water relative sea-level indicator (< 5 m) in the Western Atlantic, has been shown to occupy broader depth ranges during periods of rapid sea-level rise, thereby introducing additional uncertainty to reconstructions from Barbados. The magnitude and timing of Meltwater Pulse 1B derived from Barbados (>11 m in <350 years) remain contentious, particularly given contrasting Indo-Pacific records from Tahiti and the GBR that document continuous shallow reef growth and do not support an abrupt step in global sea-level (Murray-Wallace and Woodroffe, 2014; Lambeck et al., 2014; Bard et al., 2016; Mortlock et al., 2016; Hibbert et al., 2018; Webster et al., 2025a). These regional discrepancies highlight the influence of tectonic setting, GIA, environmental conditions, and stratigraphic context when interpreting fossil coral sea-level indicators. Recently, experimental approaches, including the use of microboring (microendolith) trace fossils assemblages have been proposed as more precise depth indicators (< 3 m), though further research is needed to refine their applicability (Chazottes et al., 2009; Nothdurft and Webb, 2009). The most effective method currently known incorporates coral assemblages characterised by coral morphology and taxonomic composition, as well as the depth distributions of associated algal and reef biota into a unified framework, known as coralgal assemblages, providing a more robust approach to paleo-water depth reconstruction (Figure 1.2) (Abbey et al., 2011; Dechnik et al., 2017; Humblet and Webster, 2017; Braga et al., 2022; Webster et al., 2022; Sanborn et al., 2024).

In recent decades, fossil coral reef archives from various localities around the world have been used indirectly to reconstruct past relative sea-levels by providing absolute sea-level positions comparable to isotope analysis of deep-sea sediment cores (Medina-Elizalde, 2013; Camoin

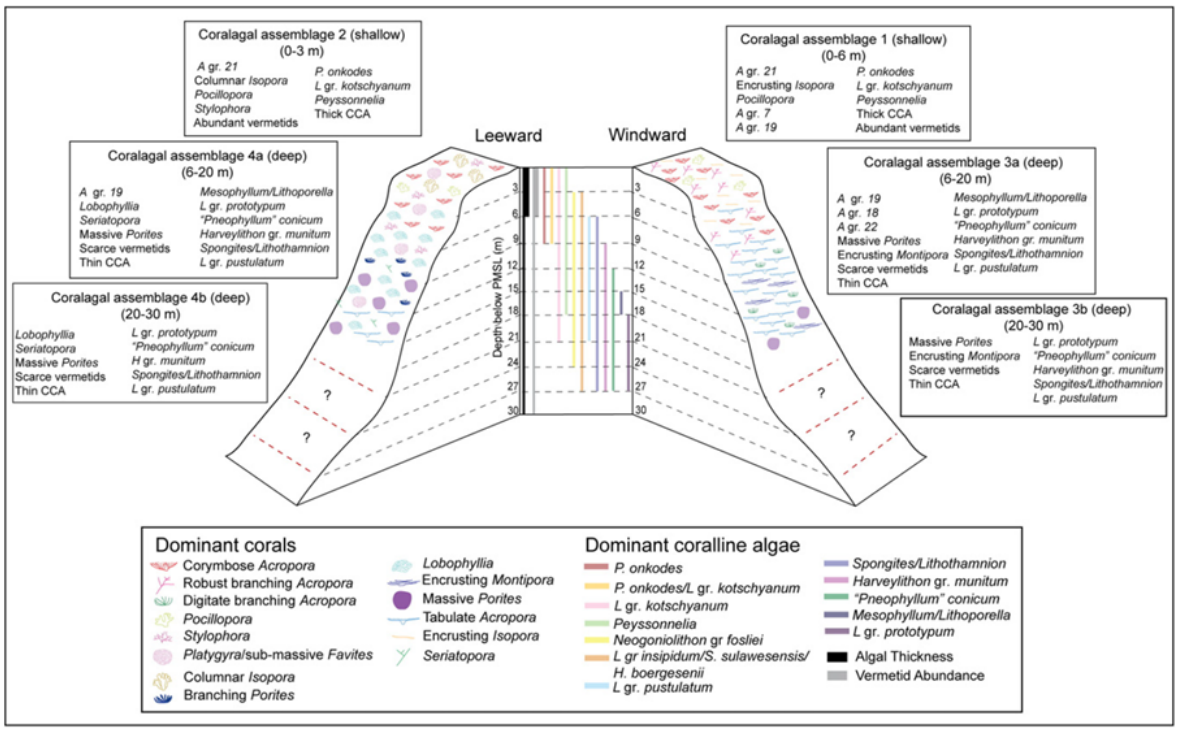


FIGURE 1.2: This study applies the method used at One Tree Reef on the Great Barrier Reef (Dechnik et al., 2017), which interprets distinct coralgal assemblages defined by the distribution and abundance of coral, algal and associated reef biota.

and Webster, 2015; Camoin and Hallmann, 2022). Biological communities preserved in fossil reefs are records of strict ecological niches that occur in specific depth ranges that can be used to reconstruct sea-level position along the core depth (Abbey et al., 2011). This reconstruction also relies on available habitat information of their living counterparts and the accurate identification of fossil corals and coralline algae (Braga et al, 2022). The benefit of using whole reef assemblages (coralgal assemblages), including both corals, and crustose coralline algae, along with associated vermetid gastropods and encrusting foraminifera have been demonstrated in Tahiti, the GBR and other sea-level records (Cabioch et al., 1999; Camoin et al., 2007; Webster et al., 2018; Webster et al., 2025a). These records also demonstrate the usefulness of utilising reef drill cores to understand carbonate platform response to third (millennial scale) and fifth (sub-orbital scale in hundreds of thousands of years) order cycles.

The global distribution of coral reefs, whereby the highest diversity occurs in the Indo-Pacific, provides extensive records of Quaternary sea-level variations (Medina-Elizalde, 2013). By integrating reef morphology, species zonation, and precise geochronological data, coral reef records have become essential for refining models of past and future sea-level changes over different timescales (Murray-Wallace and Woodroffe, 2014; Woodroffe and Webster, 2014).

1.2.3 Facies Belts and Sequence Stratigraphy

Isolated carbonate platforms with significant breaks in slope develop characteristic facies belts that reflect energy gradients and ecological zonation from shallow platform margins to deeper basin settings (Figure 1.3). These depositional gemetries, commonly referred to as undaform (shallow inner platform), clinoform (slope), and fondoform (basin), are associated with variations in water depth, wave and current energy, and light availability, which in turn influence the distribution of distinct sedimentary and ecological assemblages (Figure 1.2) (Rich, 1951; Steel and Olsen, 2002; Schlager, 2005). High-energy grainstone and reefal facies typically occur along platform margins, grading into restricted lagoonal or peritidal interiors and downslope into gravity-transported slope and basinal deposits (e.g., Figure 1.3) (Wilson, 2012). The spatial configuration and temporal evolution of these belts are controlled by accommodation changes and carbonate production, producing characteristic vertical successions widely observed across the Phanerozoic. However, the nature and efficiency of carbonate production has varied through geological time as reef-building organisms have evolved, and therefore modern carbonate systems are not always direct analogues for ancient examples. This uncertainty is less significant for this study, which focuses on Miocene to present-day systems. These well-established facies models provide a foundational framework for stratigraphic interpretation and forward stratigraphic modelling of carbonate platform evolution.

Carbonate sequence stratigraphy is a framework that subdivides carbonate rock records into genetically related depositional cycles, offering a predictive tool to understand the distribution and characteristics of carbonate reservoirs (Vail et al., 1977; Bubb and Hatlelid, 1978; Schlager, 2005; Pomar and Haq, 2016; Van der Looven et al., 2022). Although initially developed

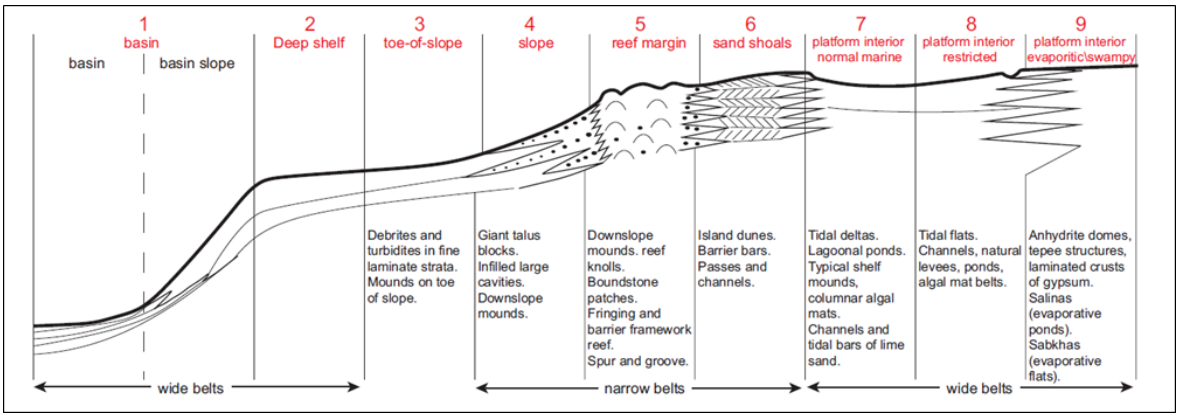


FIGURE 1.3: Cross-section of characteristics of carbonate platform facies belts with large-scale sediment geometry and lists of small-scale features, as modified by Schlager (2005) after Wilson (1975).

for siliciclastic systems, it was later adapted to carbonate environments (Figure 1.4), despite the unique biological and local growth characteristics of carbonates, which differ significantly from clastic systems (Moore and Wade, 2013). Carbonate deposition is autogenic and biologically controlled, with reef and platform growth responding dynamically to environmental factors such as water depth, light availability, and ocean chemistry (Figure 1.1A). Carbonate sequence stratigraphy identifies erosional or depositional stratigraphic surfaces caused by changes in relative sea-level. Major relative sea-level rise floods the continental shelf and results in the formation of a maximum flooding surface, identified on seismic data as downlaps interpreted to represent condensed sections (Schlager, 2005). Major relative sea-level fall exposes sections of the shelf resulting in erosional sequences and unconformities or periods of non-deposition (Sarg, 1988; Loucks and Sarg, 1993). Three main stacking patterns are observed: aggradation, retrogradation and progradation. As such, in siliciclastic systems, the relative sea-level (global eustacy and local tectonics) is considered the main control in determining the amount of accommodation available (Posamentier and Allen, 1999; Catuneanu et al., 2002). However, carbonate systems differ from siliciclastic systems in that sediment production is strongly influenced by biologically mediated *in situ* growth of corals that are bound to distinct environmental thresholds in space and time (Schlager, 2005; Pomar and Haq, 2016). Carbonate production is further characterised by broad latitudinal and environmental trends that influence the type of production system known as carbonate

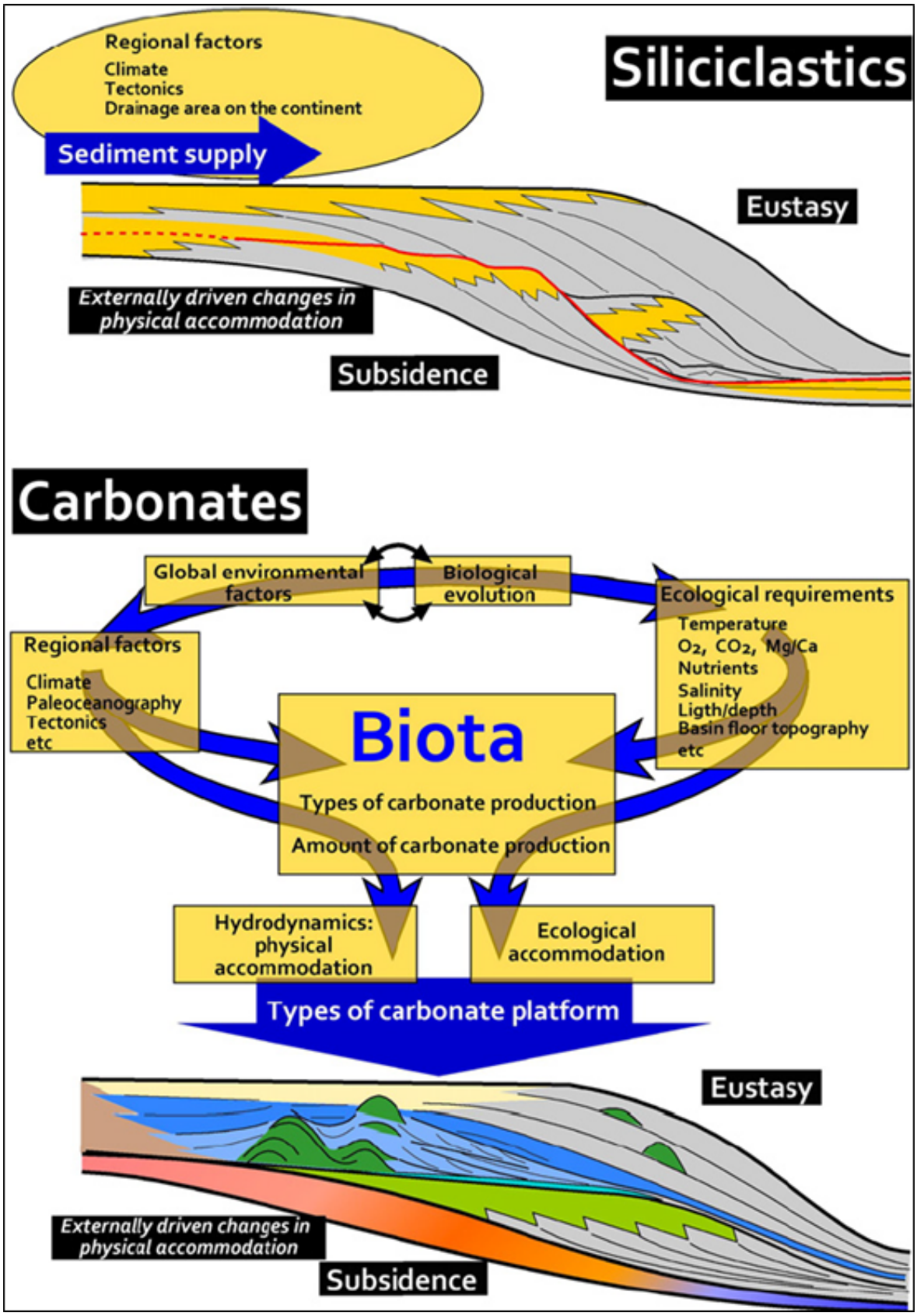


FIGURE 1.4: Sequence stratigraphic controls differ between siliciclastic and carbonate systems (Pomar and Haq, 2016).

factories (Reijmer, 2021). These are categorised into mud mound (M-factory), cool-water (C-factory) and tropical (T-factory) carbonate factories that are a product of the type of marine precipitation and whether the sediment is biotic or abiotic. The production rates of T-factories, which are prevalent along the NWS of Australia are depth controlled, whereby maximum production occurs in the upper euphotic zone (Schlager, 2005) and is an indication of the complex interaction between accommodation space and sediment infilling of that space.

1.2.4 Advances in Dating Fossil Corals

The preferred method for reconstructing paleo-sea-level is to investigate multiple fixed sea-level indicators, with detailed geochronological control (Murray-Wallace and Woodroffe, 2014). Fossil corals are one of the most successful materials for the application of U-series dating in the age range < 600 kyr (Scholz and Hoffmann, 2008), or possibly up to ca. 640 kyr (Cheng et al., 2016), and have been used to demonstrate the timing, duration and amplitude of sea-level change over the late Pleistocene (Medina-Elizalde, 2013; Woodroffe and Webster, 2014).

U–Th dating of fossil corals exploits the radioactive decay of uranium isotopes (^{238}U and ^{234}U) to ^{230}Th within the coral skeleton following skeletal precipitation. Living corals incorporate uranium from seawater during growth but exclude thorium due to its strong particle reactivity and low solubility, resulting in an initial ^{230}Th concentration close to zero at the time of formation. Following coral death, radiogenic ^{230}Th accumulates through the decay of ^{234}U at a known rate, allowing the time elapsed since skeletal formation to be calculated from measured U–Th isotopic ratios, provided the coral has behaved as a closed system with respect to uranium and thorium isotopes (Cheng et al., 2013; Cheng et al., 2016).

The accuracy of coral U–Th ages therefore relies on several key assumptions: preservation of the primary aragonitic mineralogy, minimal detrital ^{232}Th contamination, and the absence of post-depositional uranium gain or loss. Deviations from these conditions, particularly open-system behaviour associated with diagenetic alteration or microbialite development, can lead to age bias or analytical failure. In many fossil corals, coupled anomalies in ^{234}U/^{238}U

and $^{230}Th/^{238}U$ indicate uranium mobility or redistribution of daughter isotopes. Thompson et al. (2003) demonstrated that such open-system behaviour can be quantitatively modelled by incorporating coupled ^{234}U and ^{230}Th addition terms into the U-series decay equations, allowing correction of apparent ages through reconstruction of isotopic evolution trajectories rather than assuming secular isolation. Comparisons of pristine coral ages and open-system age models of Barbados coral reef terraces indicates that open-system corrected ages are as accurate as U-Th ages calculated from pristine corals (Thompson et al., 2003). These models improve the robustness of open-system age interpretations while explicitly accounting for micro-scale diagenetic complexity even after rigorous diagenetic screening of fossil coral samples (Thompson et al., 2003; Scholz and Hoffmann, 2008; Chutcharavan et al., 2018; Hu et al., 2025).

The reliability of U–Th ages based on coral reef records older than the last interglacial (ca. 125 kyr) significantly decreases with age (e.g., Figure 1.7) (Woodroffe and Webster, 2014; Camoin and Webster, 2015; Camoin and Hallmann, 2022) due to post-depositional diagenetic alteration of the primary carbonate mineral aragonite, which is the preferred mineral for dating. Pleistocene highstand reefs in the southern Cook Islands of the South Pacific have been successfully dated to 2.28 Ma using Sr-isotope ratios (Gischler et al., 2022), however, rigorous screening of coral samples and advancements in analytical techniques are essential to mitigate the error of fossil coral-based U-series age reconstructions (Thompson et al., 2003; Hu et al., 2025). A major challenge with using corals for age reconstructions in coral reef science is the diagenetic alteration of fossil corals, which can compromise the accuracy of U-series dating and, consequently, sea-level reconstructions (Montaggioni and Braithwaite, 2009). However, robust age control is also essential for developing chronostratigraphic frameworks needed to investigate the temporal and stratigraphic evolution of reef systems more broadly.

Neutron scattering offers a non-destructive alternative to assess the preservation of original coral skeleton by providing high-resolution (Ångström to nanoscale) 3-D imaging of coral structure, porosity, and carbonate mineral phase (Christe et al., 2007; Ivankina et al., 2020).

Hyperspectral imaging offers a high-resolution quantitative addition to traditional visual core inspection, which is inherently subjective and often insufficient to resolve subtle compositional and textural variations in fossil reef cores. By detecting mineral-specific absorption features in the shortwave infrared (SWIR) spectral range (1000–2500 nm), hyperspectral imagery enables non-destructive identification and spatial mapping of primary and secondary carbonate minerals (e.g., aragonite, calcite, dolomite) and associated clays (Bishop et al., 2021). This approach facilitates accurate screening for well-preserved aragonite suitable for U–Th dating and geochemical analysis, even in cases where diagenetic alteration is spatially heterogeneous and below the detection limits of conventional methods such as X-ray diffraction (Murphy et al., 2017).

Hyperspectral imaging of fossil coral reefs has previously been utilised to screen and map the extent of carbonate mineral diagenetic alteration (Murphy et al., 2017); to produce mineralogical maps of rudist buildups for development of coarse scale digital outcrop models (Krupnik et al., 2016); to evaluate hydrocarbon maturation in shale cores (Rivard et al., 2018) and to delineate laminar fabrics and mineralogical heterogeneity in ancient microbialites (Murphy et al., 2016). However, few studies exist whereby hyperspectral imaging of an entire suite of core samples was used in the full interpretation of fossil reef core for paleoenvironmental and chronological reconstruction, including precise paleowater depth interpretations.

1.3 Quaternary Fossil Reefs and the Middle Pleistocene Transition

Fossil coral reefs are excellent archives of past sea-level and associated environmental changes (Edinger et al., 2007; Cazenave and Remy, 2011; Camoin and Webster, 2015). They therefore represent a unique opportunity, extending beyond instrumental records, to understand how the behaviour of ice sheet decay might affect future sea-level change (Montaggioni and Braithwaite, 2009). By looking at periods of Earth history represented by rapid sea-level rise and associated climate transitions, such as the Mid-Pleistocene Transition (MPT), and how reefs have responded to these changes with respect to reef development, architecture and

composition, we can predict what could be anticipated in the future (Camoin and Webster, 2015). Glacial-interglacial sea-level fluctuations became more apparent in the Quaternary from around 2.7 Ma to present (Montaggioni and Braithwaite, 2009), driven by variations in Earths orbital parameters (Figure 1.5) (Faichney et al., 2011; Petrick et al., 2019). The resulting climate fluctuations have influenced global sea-level oscillations, coupled ocean-atmosphere dynamics, and reef development (Raymo, 1997; Clark et al., 2006; Montaggioni and Braithwaite, 2009; Liautaud and Huybers, 2022). Quaternary fossil reef cores preserved these cyclicities, offering insight into their rate and amplitude, as well as providing relatively unaltered sections of coral from which age reconstructions can be made. The MPT (Figure 1.5; ca. 1.2 to 0.7 Ma) marked a fundamental shift in Earth's climatic cycles, moving from a sea-level rhythm of obliquity-driven high-frequency, 41-kyr oscillations into 100-kyr cycles with ca. 100 m amplitudes (Dwyer et al., 1995). This shift in sea-level pattern had significant implications for carbonate platform and coral reef development and sedimentary processes worldwide because the reef environments are sensitive to bathymetric change (Alonso-Garcia et al., 2023).

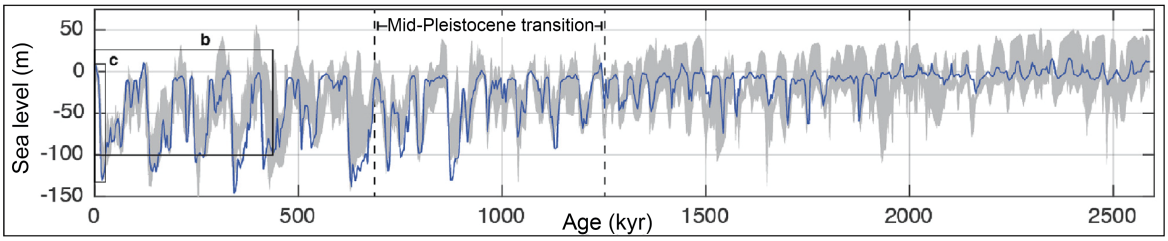


FIGURE 1.5: The equatorial Pacific curve of Bates et al. (2014) (blue line) spanning the Quaternary period from ca. 2.5 Ma to present, with the envelope of a compilation of other curves in grey from (Gelder et al., 2020). The dotted vertical lines show the period described as the Mid-Pleistocene transition from 41-kyr to 100-kyr oscillations that occurs between ca. 1.2 - 0.7 Ma.

Aragonitic scleractinian corals, green algae such as *Halimeda*, and red calcareous algae are the dominant primary carbonate producers in shallow-marine environments. As such, variations in carbonate production are directly correlated to sea-level, with maximum production typically occurring during slow, prolonged highstands (Schlager et al., 1994; Schlager, 2003; Alonso-Garcia et al., 2023). A range of changed modes of sedimentation occurred throughout

reefs worldwide, however, it is generally accepted that the increased amplitude of sea-level oscillations largely induced reef growth and facilitated the expansion of carbonate platforms globally (Montaggioni, 2005). For instance, a study by Yamamoto et al. (2006) found that the MPT triggered coral reef growth in the Ryukyu Group ca. 0.8 Ma, while a review of the Maui Nui Complex in Hawaii by Faichney et al. (2010) found changed modes in sedimentation, including a transition from deep to shallow dominated reef assemblages. Chapter 4 (Figure 2 and Table 1) presents a summary of how some reefs around the world responded to the MPT, demonstrating the complexity and significance that this major shift in Earth's climatic history had on marine systems worldwide. Characterising the response of complex reef systems has significant implications for our understanding of long-term climate dynamics, as well as providing insights into how coral reef eco-geomorphic systems adapted to rapid climate shifts and how future climate change may impact their ability to survive in their current state.

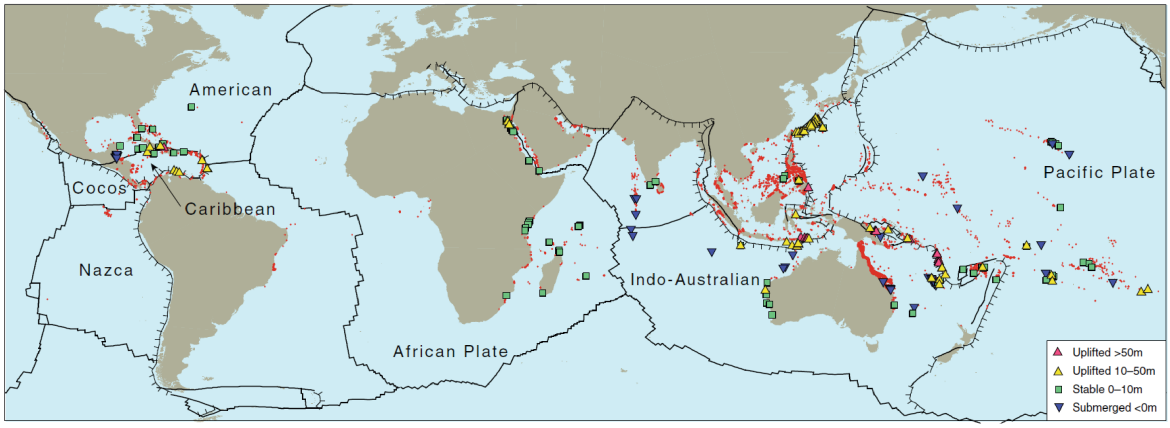


FIGURE 1.6: A map plotting sample sites for coral age data, and showing tectonic setting, from Woodroffe and Webster (2014).

Transgressive and highstand Quaternary coral reefs on relatively stable continental margins (e.g., NWS of Australia, GBR) contain unique and relatively unexplored records of sea-level and climate change (Collins et al., 2011). While extensive work has been undertaken globally, coral reef evolution of the NWS, in particular, remains comparatively less constrained. Ribbon Reef 5 on the GBR provides a well-preserved example of Quaternary reef evolution and serves as an analogue for the NWS as they are both situated in a comparable environmental setting including similar latitude and climate. The timing and amplitude of sea-level fluctuations in

response to ice sheet dynamics over the Quaternary period is essential for understanding their impacts on Earth's climate over millennial scales, orbital Milankovitch cycles, and sub-orbital cycles associated with rapid environmental changes (Camoin et al., 2007). Reef-based sea-level reconstruction relies on the ability to accurately model sea-levels at specific far-field tropical sites (Figure 1.6) (e.g., Hawaii, Tahiti, Barbados, NWS, Great Barrier Reef), with empirical chronologies (Toscano et al., 2011). Despite recent investigations into such far-field sites, there remains a lack of comprehensive spatial and temporal coverage of Quaternary reef development in response to eustatic and environmental change. IODP expedition 310 in Tahiti (Camoin et al., 2007; Iryu et al., 2010; Abbey et al., 2011) and 325 on the GBR (Yokoyama et al., 2011) recovered coral records spanning from 16-10 kyr and 30-10 kyr respectively, focusing on the last glacial maximum (LGM) (Yokoyama et al., 2018), meltwater pulse 1A (Deschamps et al., 2012) and meltwater pulse 1B (Webster et al., 2025a). However, these expeditions also recovered older Pleistocene sequences. In Tahiti, *in situ* coral frameworks have been dated between 132.7 ± 0.8 ka and 118.1 ± 0.6 ka, capturing sea-level fluctuations beyond the Holocene and Marine Isotope Stage (MIS) 3 during MIS 5e (Iryu et al., 2010). Gischler et al. (2013) interpreted stacked reef units ca. 105 m thick from Expedition 325 on the GBR, with evidence of multiple reef growth phases prior to the LGM, potentially extending back to at least MIS 5e. Similarly, IODP expedition 389 (Webster et al., 2025b) expanded the temporal coverage further by drilling into the H8 Hawaiian Pleistocene terrace reefs at ca. 500 kyr (MIS 13), to investigate long-term reef development and the nature of sea-level change that drowned the backstepping reef terraces, with subsidence history forming part of the broader context that facilitated expanded and almost uninterrupted reef growth. Quaternary evolution of Pacific mid-ocean atolls have been investigated using core data at Mururoa atoll (Montaggioni et al., 2015), Funafuti atoll and Caribbean provinces (Montaggioni and Braithwaite, 2009). However, there is a notable data gap in Indo-Pacific Quaternary reef records, specifically along the NWS of Australia. Globally, fossil reef archives are disproportionately concentrated in the Holocene and MIS 5e, with relatively few continuous, well-dated sequences extending beyond MIS 9 (ca. 330 ka) (Figure 1.7) (Medina-Elizalde, 2013; Woodroffe and Webster, 2014; Hibbert et al., 2018). These sparse records bias the Last Interglacial (MIS 5e) (Figure 1.7) because it was the last time that

sea-level was higher than present day and offers a comparison for how reefs might respond to future sea-level rise (Chutcharavan and Dutton, 2021; Dumitru et al., 2023). There is also a bias to tectonically uplifted regions such as the Ryukyus Group (Yamamoto et al., 2006) and the Red Sea (Mansour and Madkour, 2015) (Figure 1.6), which creates challenges with diagenesis (and in turn difficulties reconstructing reliable chronologies), or compressed stratigraphic records. As such, there is a need for fossil coral records from long-lived reef systems with stable tectonism and favourable preservation conditions spanning the Quaternary (Murray-Wallace and Woodroffe, 2014; Woodroffe and Webster, 2014). Additionally, most investigations of coral reef response to the MPT focus on more accessible reef systems in tectonically active regions, including the Maui Nui Complex, Hawaii (Webster et al., 2009), New Caledonia (Montaggioni et al., 2011) and Mururoa (Montaggioni, 2005).

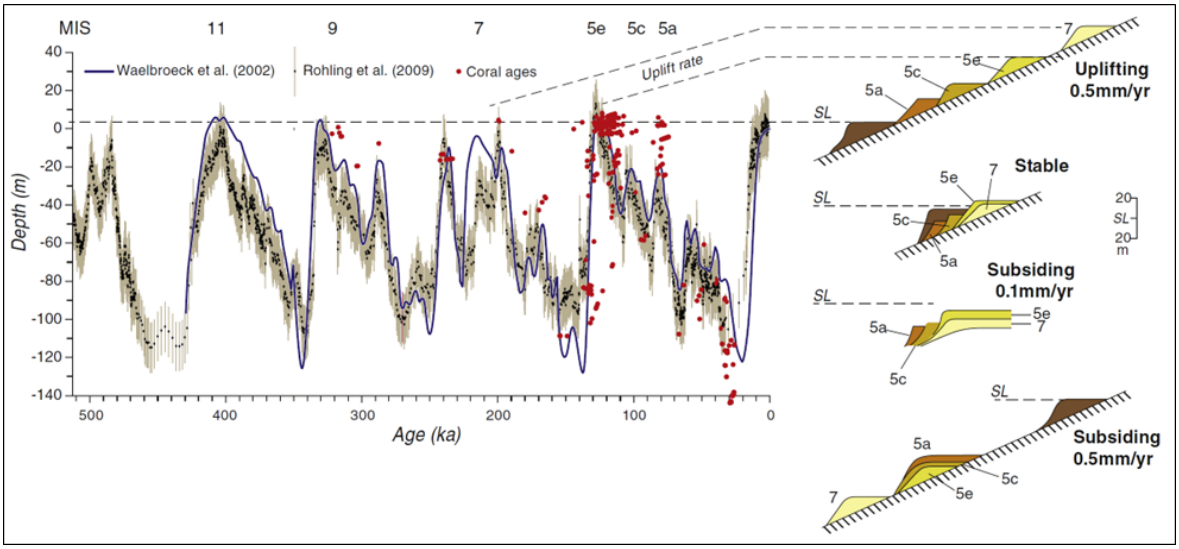


FIGURE 1.7: Coral reef age data correlated to a eustatic sea-level curve reconstructed from benthic foraminiferal ^{18}O isotope data, showing a spatial and temporal sampling bias to coral reef terraces in tectonically unstable regions and MIS 5e during the Last Interglacial, respectively. The schematics on the right show the expected geomorphic representations of how reefs arrange themselves in response to different tectonic regimes, over the same sea-level. From Woodroffe and Webster (2014) adapted from Medina-Elizalde (2013).

Eustacy is the change in global mean sea-level and hydrologic system due to glacial advance and retreat and the associated GIA adjustments to the continental shelves (Thompson et al., 2025). However, regional scale tectonic variations also dictate the rise and fall of sea-level, as well as thermal expansion of seawater, and therefore the preserved stratigraphic record (Figure 1.7). Coral data from subsiding reef sites provide an opportunity to produce more complete sea-level histories because the creation of long term, stable and rapid accommodation facilitated the growth of continuous, expanded reef sequences (Cabioch et al., 1999).

1.4 Forward Stratigraphic Modelling in Coral Reef Science

The forward stratigraphic modelling (FSM) presented in this research was conducted using the Petrel Geologic Process Modelling (GPM) tool. The specific modelling algorithms and parameter configurations used in this study are detailed in Chapter 4. Figure 1.8 provides an overview of the generalised FSM workflow applied, from conceptualisation to calibration. GPM simulates the forward evolution of stratigraphy by applying rules for sediment production, transport, and accumulation within a 3-D time-stepped grid. Input parameters such as relative sea-level fluctuations, carbonate production, and wave energy control spatial and temporal sediment distribution (Hill et al., 2009; Hill et al., 2012). Carbonate growth is constrained by environmental thresholds (e.g., carbonate production rates as a function of energy, depth and sediment suspension), and sediment transport is modelled using diffusion principles, where the diffusion rate is influenced by grain size and distributed according to bathymetric slope. Diffusion coefficient multipliers are user-defined to allow control on spatial and temporal variability due to hypothesised climatic and oceanographic change (Figure 1.9; (Hill et al., 2009)). As the model progresses in time, it dynamically updates bathymetry and builds stratigraphy, producing outputs such as facies distributions, accommodation histories, and stratal geometries that can be compared to empirical datasets for calibration.

GPM was selected for its computational efficiency and integration with subsurface observational datasets (e.g., seismic volumes, well logs, and core data), enabling rapid iteration and

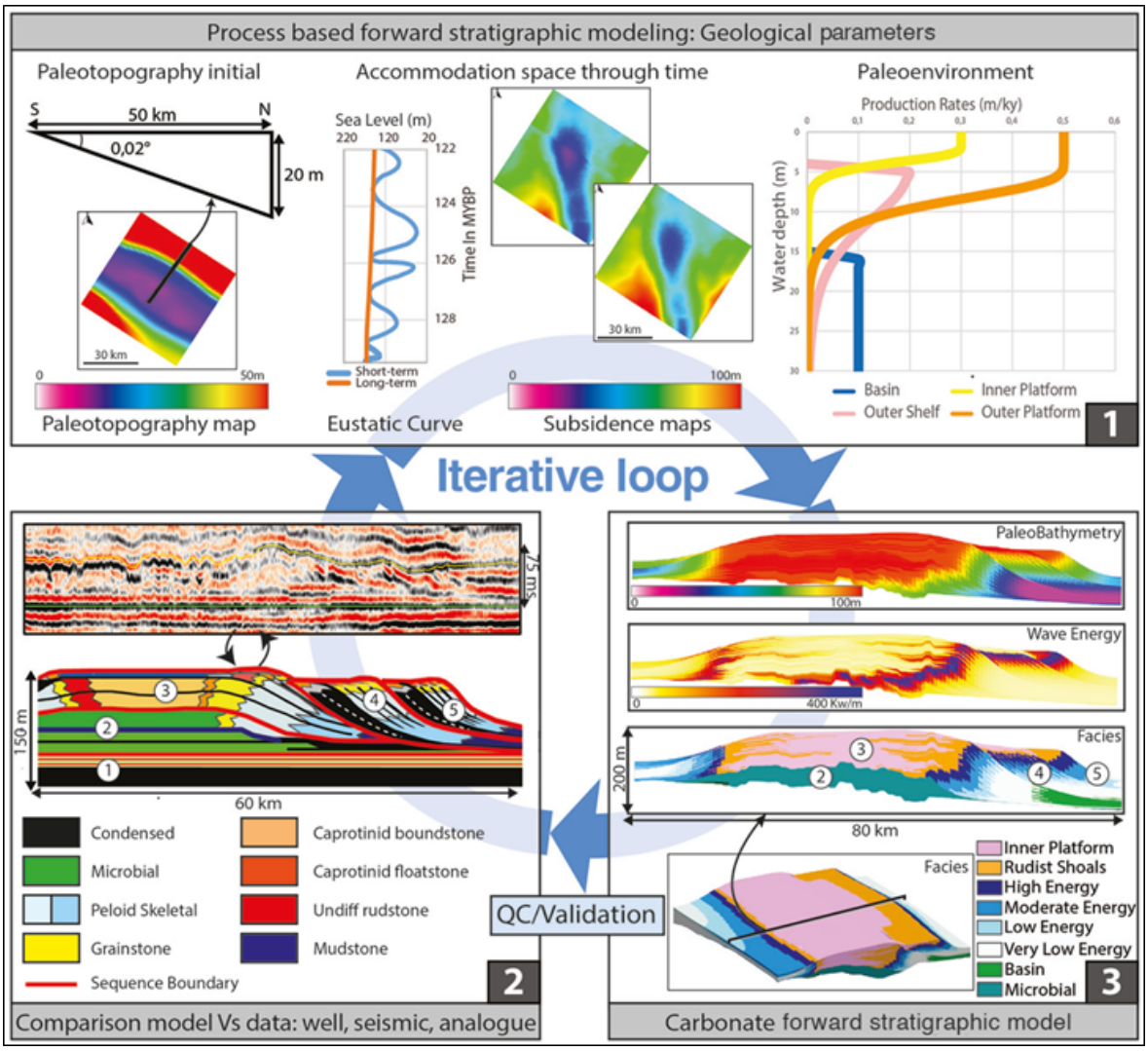


FIGURE 1.8: Schematic representation of a typical carbonate forward stratigraphic modelling workflow. Empirical and analogue data inform the development of a conceptual model. This modelling workflow similar to the one adopted in this study, is iteratively calibrated to observed data through trial-and-error simulation and refinement. From Lanteaume et al. (2018).

direct qualitative and quantitative comparison between model outputs and observations at platform scale. While other FSM tools, such as DionisosFlow (Granjeon and Joseph, 1999; Granjeon, 2014) and pyReef-Core (Salles et al., 2018), are capable of three-dimensional simulations and include more explicit ecological or process-based formulations, GPM is more optimised for rapid scenario testing and large-scale integration with seismic and borehole datasets. GPM provides a practical and effective framework that accounts for all the

processes that drive the evolution of the platform (from carbonate production, wave energy impact, sediment transport, and change in accommodation) at a platform-scale resolution over multiple glacial–interglacial cycles. Its ability to construct fully three-dimensional models while interrogating outputs in one- and two dimensional views facilitates efficient evaluation of platform-scale architecture, margin evolution, and stratigraphic patterns against core and seismic observations.

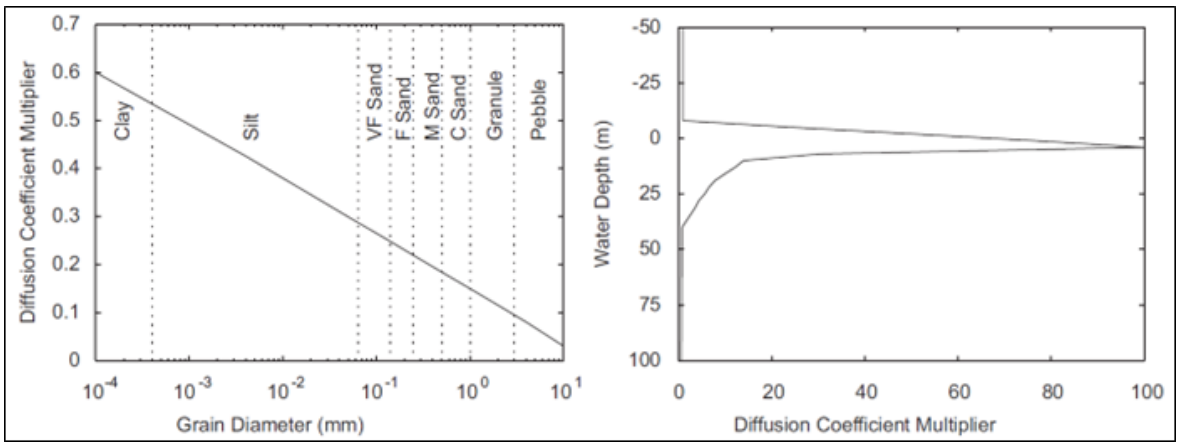


FIGURE 1.9: The process of sediment diffusion is a function of grain size. Diffusion coefficient multipliers can be used to constrain rates of diffusion through time and space as proxies for climate and oceanographic variations. From Hill et al. (2009).

1.4.1 FSM Principles and Applications

Due to the inherent complexity of carbonate depositional systems, understanding their genesis and evolution requires advanced software modelling techniques. FSM has emerged as a key and popular approach for simulating geological processes and reconstructing the depositional geometries of carbonate platforms over geological timescales (Bosence and Waltham, 1990; Paola, 2000; Warrlich et al., 2002; Burgess et al., 2006; Williams et al., 2011; Burgess et al., 2012; Hawie et al., 2015; Kolodka et al., 2016; Busson et al., 2019; Borgomano et al., 2020; Van der Looven et al., 2022; Jiménez et al., 2024). FSM quantifies the interactions between pre-defined forcing parameters on carbonate growth and development, such as sea-level fluctuations, subsidence, carbonate production rates and hydrodynamic processes,

allowing the user to evaluate their relative importance, and offering insights into both the ecological thresholds and geomorphological response of sedimentary systems (Watney et al., 1999). However, numerical reconstructions of nature are inherently imperfect, not only due to uncertainties in the forcing conditions, but also because computational constraints necessitate upscaling. Running models at fine spatial or temporal resolution is often prohibitively expensive, so they inevitably produce a gridded and simplified representation of a continuous and more complex reality. Model scale and resolution, coupled with our current limited understanding of nature, constrain the ability to accurately represent the complexity of carbonate systems. Despite this, FSM's remain useful tools for resource exploration (Bassant and Harris, 2008; Bruneau et al., 2017; John et al., 2021; Jiménez et al., 2024) and scientific enquiry (Bice, 1991; Eberli et al., 1994; Williams et al., 2011; Barrett and Webster, 2012; Montaggioni et al., 2015; Barrett and Webster, 2017; Salles et al., 2018). This technique is particularly useful in carbonate systems where reef growth and sedimentation are governed by interacting biotic and abiotic processes and are highly sensitive to environmental perturbations.

FSM has undergone significant development over the past few decades, evolving from conceptual models of sedimentary processes to sophisticated, data-driven simulations capable of reconstructing high-resolution stratal geometries in response to an increasing number of environmental variables. Initially, early models focused on broad-scale depositional trends to test conceptual ideas of the geologic history, relying on empirical observations to infer stratigraphic architecture (Warrlich et al., 2002), without capacity for data calibration. However, as computational capabilities improved, FSM became increasingly quantitative, integrating process-based approaches to simulate carbonate growth, sediment transport, subsidence, and sea-level fluctuations (Burgess et al., 2012). In the context of carbonate platform and coral reef science, FSM has become a valuable tool for understanding third-order carbonate sequence stratigraphy (Muñoz-López et al., 2025), platform evolution and reef development under varying environmental and eustatic conditions (Warrlich et al., 2002). Early applications of FSM in carbonate geology primarily sought to replicate large-scale platform geometries, which has recently evolved into incorporating more refined ecological (Clavera-Gispert et al., 2017) and sedimentological parameters (Van der Looven et al., 2022), allowing for the simulation of reef accretion, bioerosion, and ecological succession. These advances have

facilitated a deeper understanding of how reefs respond to eustatic and climate variability. More recently, FSM has been employed to test a range of hypotheses regarding reef response to the rapid Holocene sea-level rise (Barrett and Webster, 2012), drowning thresholds of Hawaiian reefs (Webster et al., 2009), and the effects of coral reef terrace morphology and hydrodynamics on the accuracy of past sea-level reconstructions (Chauveau et al., 2026). Its application to Quaternary reef systems, such as Mururoa Atoll (Montaggioni et al., 2015), has provided valuable insights into the interplay of sea-level fluctuations, environmental stresses, and reef-building processes over glacial-interglacial cycles. Similar approaches have recently been applied to atolls in the South China Sea, where numerical modelling has helped disentangle the convolved effects of sea-level change, subsidence, climate and ecological thresholds on reef evolution (Liu et al., 2022).

One body of carbonate FSM research argue that first-second order geological factors explain reef architectures regardless of ecosystemic processes (e.g., Figure 1.10) (Pastier et al., 2019), whilst another body argues that high-resolution geological and ecological processes are important (e.g., Figure 1.11) (Salles et al., 2018; Van der Looven et al., 2022). Whilst first-second order geological processes may offer valuable insights into the broad framework of reef formation, ecosystemic and high-resolution geological factors provide essential information that can significantly influence the systems behaviour. Importantly, no single approach or explanation can fully account for the complexity of reef development, and this is often observed in numerical modelling as 'non-uniqueness' (Posamentier and Allen, 1999; Cross and Lessenger, 1998; Burgess and Wright, 2003; Burgess et al., 2006; Bornholdt et al., 1999; Burgess and Prince, 2015; Busson et al., 2019; Pastier et al., 2019; Van der Looven et al., 2022).

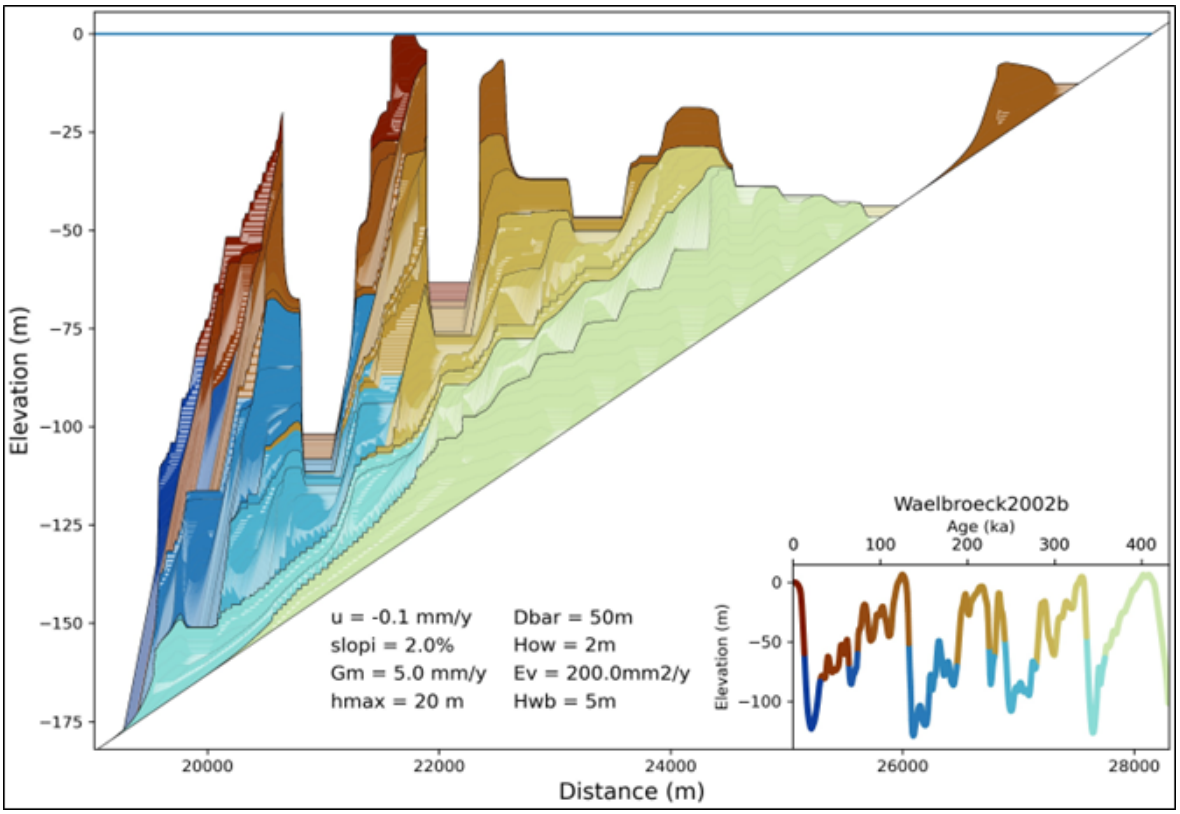


FIGURE 1.10: Forward stratigraphic model of 2-D reef architectures modelled using 1st order eustatic sea-level curve (Waelbroeck et al., 2002) as the primary geological model input. From Pastier et al. (2019).

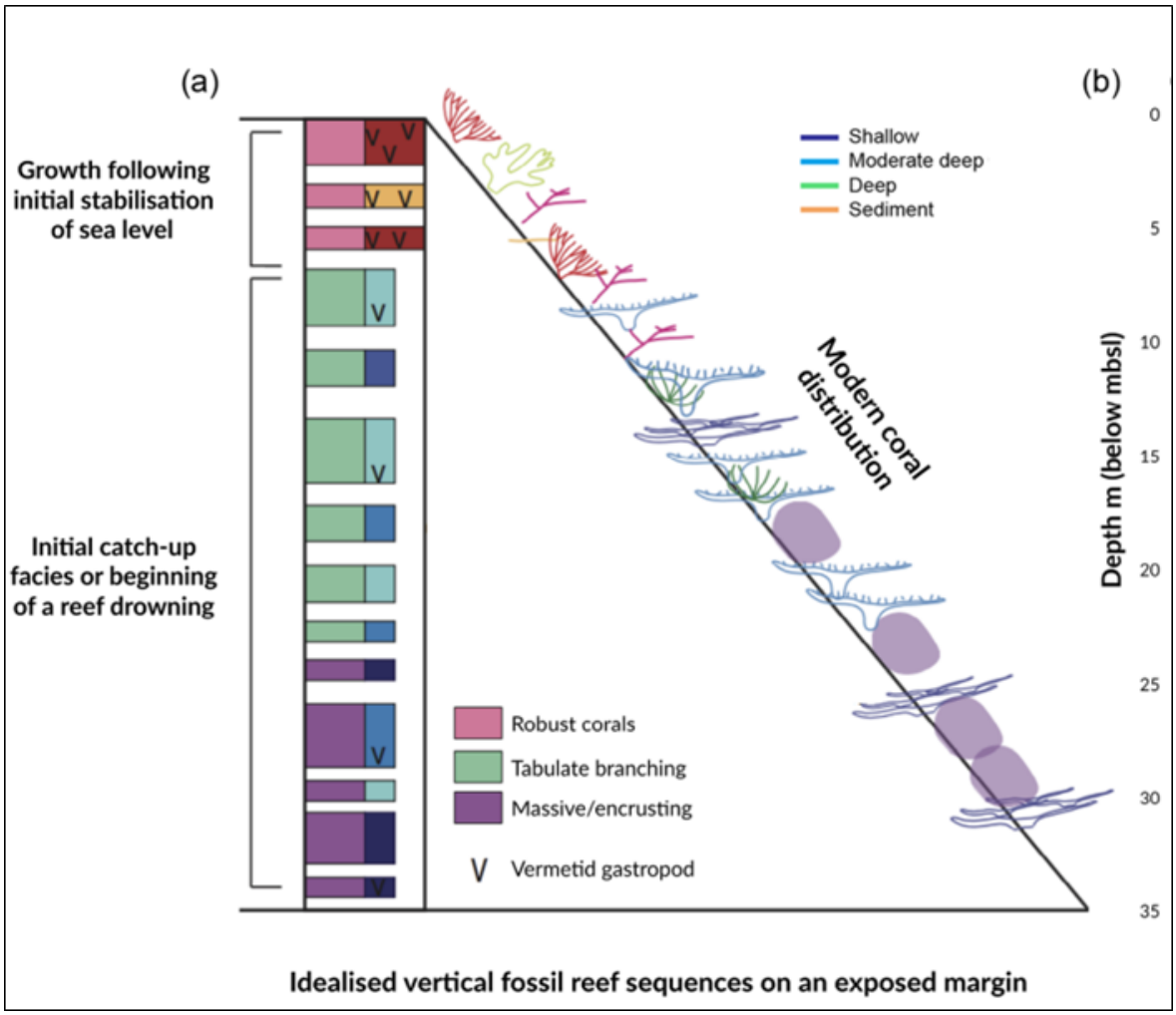


FIGURE 1.11: 1-D Forward stratigraphic model of an idealised drill core section demonstrating the importance of integrating high-resolution oceanographic and ecological input data. From Salles et al. (2018).

1.4.2 Limitations, Uncertainty and Future Development

Our increasing understanding of the natural world through large-scale data acquisition minimises modelling uncertainty and the occurrence of non-uniqueness, yet there remains an ideological approach. Carbonate sedimentation is strongly influenced by biologically mediated processes and environmental thresholds, which introduces additional complexity relative to siliciclastic systems. The approach to carbonate FSM has so far been to quantify input parameters based on sparse empirical data and to fill 'data-gaps' with conceptual ideas based on modern analogues to reduce uncertainties. These models are often founded on analogues that are unrepresentative of realistic sedimentary facies depth ranges and varying biology of carbonate producers through time, leading to under-representation of depositional environments. Small-scale FSMs have previously used ecological restrictions based on paleowater depths obtained from coralgal assemblages, for example the mixed carbonate-siliciclastic platform of the Sorbas Basin (Kolodka et al., 2016), however, wave energy profiles were neglected. Other FSMs assume continuous carbonate production is constrained only by light or wave energy (James et al., 1997; Schlager, 2000; Al-Salmi et al., 2019). Conversely, models that used wave energy to constrain facies, for example, the last deglacial drowning of Tahiti reefs (Seard et al., 2013), failed to use precise paleowater depths. Yet the combination of these conditions significantly determines carbonate sedimentation rate, coral health and the ability to keep pace with sea-level rise, as observed in stratigraphic records of drowning sequences (Hallock and Schlager, 1986; Mutti and Hallock, 2003; Mutti et al., 2005; Beaman et al., 2008; Pomar and Hallock, 2008).

While FSM has been widely applied since the late 20th Century in siliciclastic (Pomar and Haq, 2016) and mixed carbonate-siliciclastic systems (Kendall et al., 1991; Warrlich et al., 2002; Burgess et al., 2006; Hill et al., 2009; Salles et al., 2018), its application to coral reef development, particularly in isolated carbonate platforms, remains underutilized. Additionally, reef growth models rarely incorporate the complex interplay between third order (long-term) and fifth order (short-term) sea-level fluctuations, despite the fundamental need to understand the whole rather than the part. Spatio-temporal analyses of modern and ancient reef systems are often constrained by coarse resolution, limited sampling, and biased site selection, utilising

empirical data from isolated depositional settings (e.g., reef crest, lagoon, or slope) (Webb et al., 2016). Finally, unreliable age estimates undermine chrono-stratigraphic reconstructions, and insufficient integration of multi-scale observed data limits the development of robust models.

While model resolution is not inherently a limitation – it is theoretically possible to simulate carbonate platform evolution at annual timesteps and centimetre-scale grids - such resolutions are not practical nor conceptually appropriate for platforms of this scale (ca. 250 km^2) due to time constraints, computing power and reduced interpretability due to software display performance, which struggles with models > 30 Gb in Petrel. Additional processes, such as grain-to-grain interactions, shear stress and vertical velocity profiles become increasingly important, yet are not explicitly resolved in most FSM frameworks. Arguably, such fine scale resolution is often unwarranted with respect to the temporal and spatial resolution of available input data (e.g., seismic data, sea-level curves, tectonic history) and the research questions invoked. Therefore, a resolution is required that balances computational efficiency with the ability to capture key stratigraphic trends and evaluate the relative influence of different parameters, test key eustatic and environmental sensitivities, and provide a more informed understanding of how individual forcing conditions shape platform evolution.

1.5 Scientific Rationale

1.5.1 Scott Reef as a Natural Laboratory

This thesis focuses on Scott Reef (Figure 1.12), an isolated carbonate platform on the NWS of Australia, because it provides an exceptional natural laboratory to investigate the response of coral reefs to past environmental and eustatic change. Several characteristics make Scott Reef particularly well suited to address the knowledge gaps outlined above and summarised below.

(1) Preliminary reef core studies at Scott Reef (Collins et al., 2009) indicate the presence of prolonged, episodic reef sequences that capture poorly sampled intervals of the Quaternary, including deposits corresponding to MIS 11 (ca. 500 kyr). These interpretations are based

on U–series dating of corals recovered from 17 boreholes drilled during earlier industry exploration campaigns at North and South Scott Reef, including six ocean-facing reef cores. Because these sites are located far from former ice-covered regions (Yokoyama et al., 2001), they preserve well-developed Pleistocene reef sequences that are particularly suitable for reconstructing long-term sea-level and subsidence histories (Collins et al., 2009). These archives provide a rare opportunity to investigate carbonate platform and coral reef responses to both local controls (e.g., environmental and oceanographic variability) and broader eustatic and tectonic influences.

(2) Regional datasets further enhance the value of Scott Reef as a study site. In particular, extensive 3-D seismic data provide evidence for sustained carbonate production on the platform since at least the Miocene (ca. 20 Ma; see seismic depth-slice animation in Appendix C). Many of these datasets were acquired during decades of hydrocarbon exploration on the NWS (Belde et al., 2017), inadvertently creating a unique geological archive that can now be used to investigate long-term (Miocene–Pleistocene) carbonate platform evolution.

(3) The study region is located on a subsiding passive continental margin, which has provided continuous accommodation for reef growth while remaining largely unaffected by GIA, a process known to complicate absolute sea-level reconstructions (Medina-Elizalde, 2013). In addition, nearby sites drilled during IODP Expedition 356 (Gallagher et al., 2014) provide important regional context by documenting the five-million-year history of ITF variability along the NWS. Because the ITF exerts a strong influence on oceanographic conditions that affect coral reef growth, Scott Reef offers an ideal setting to investigate potential links between reef development, long-term oceanographic change, and major climatic transitions such as the MPT. These relationships are explored throughout this thesis, particularly in Chapters 2, 3, and 5.

Understanding complex carbonate systems requires studying their fundamental components in unison and is often an overlooked element of reef studies. The application of carbonate

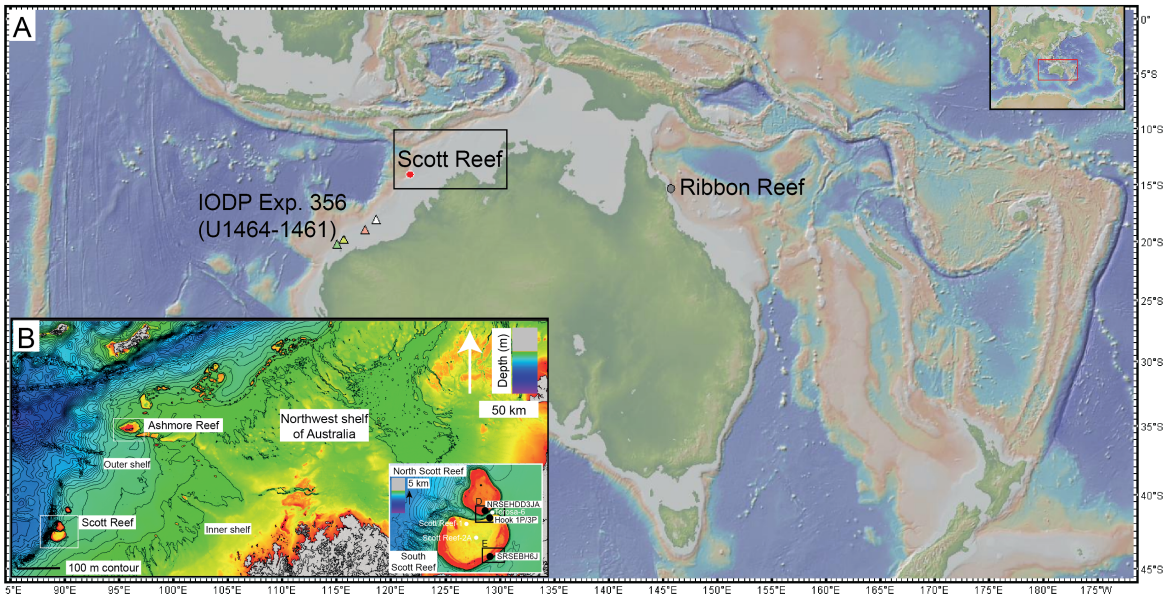


FIGURE 1.12: Geographic location of Scott Reef on the North West Shelf of Australia and Ribbon Reef 5 on the Northeast shelf that was used to establish correlations, connections and details. Triangles indicate IODP Expedition 356 sites (U1461–U1464) that provide critical context on five million years of climate variability and the role of the Indonesian Throughflow along the NWS. This figure was made using GeoMapApp (https://www.geomapapp.org).

sequence stratigraphy lays the foundation of this research by identifying long-term geological patterns in carbonate deposition to provide context and the broader significance of the historical carbonate factory evolution and past eustacy, which is well defined for the regional NWS (Marshall and Lang, 2013) but poorly constrained in the southern Browse Basin. By integrating multi-proxy data including, 3-D seismic data, industry well log data and high-resolution multibeam bathymetry, this study outlines distinct carbonate factories through the identification of seismic stratigraphic surfaces and geomorphological patterns that shaped the platform through time to understand how the Neogene antecedent substrate provided foundations for the Quaternary reefs. By establishing the large-scale stratigraphic framework, this second chapter ensures that finer-scale analyses of reef accretion, coralgal assemblages, and environmental reconstructions in the ensuing chapters are placed within a well-constrained geological context.

A key component of fossil reef based past sea-level reconstruction is obtaining reliable ages from when the reef grew so that the absolute position of past sea-level can be given a temporal reference. This is difficult due to the effects of marine and meteoric diagenesis that alter the primary carbonate mineral phase aragonite to calcite, which is used for dating, often renders radiometric ages and paleoclimate proxy data inaccurate (McGregor and Gagan, 2003). Beyond sea-level reconstructions, providing a robust chronological framework from which to investigate the stratigraphic evolution of the reef system is also critical. A new proof-of-concept technological method using high resolution neutron computed tomographic imaging is utilised in this study to demonstrate how to non-destructively screen whole 3-D fossil reef cores for selecting pristine sections of coral that can be dated.

Hyperspectral imaging is similarly utilised in this study to map the 2-D surfaces of cores to assess diagenetic alterations in sections of *in situ* coral before destructively using SEM for validation prior to conducting U-series dating. It is also used to quantify coralline algal crust thickness, identify coral taxa and growth forms, and locate key stratigraphic surfaces, including unconformities and characteristics of facies boundaries, i.e., type of terrigenous material, in Quaternary reef cores. These capabilities have potential to significantly improve the reproducibility and resolution of facies interpretation, providing new insights into reef evolution, diagenesis, and paleoenvironmental change (Kruse, 2014; Murphy et al., 2017).

These pre-screening methods refine the timing of reef accretion phases and their correlation with broader Quaternary climatic and eustatic events. They provide a methodological bridge between the stratigraphic framework and the lithological and chronological reconstructions developed in this thesis, building on the sequence stratigraphic framework established in Chapter 2. By improving the reliability of U–Th age constraints, they support palaeoenvironmental reconstructions that can be tested using FSM, enabling a more robust interpretation of carbonate platform evolution and its response to past sea-level and climate variability.

The aim of applying FSM in this study is to integrate multi-scale observations (e.g., well logs, cores, and seismic data) to link first- to fifth-order geological processes and bridge spatial data gaps across the reef. Using the sequence stratigraphic framework established in Chapter 2 from 3-D seismic interpretation, FSM simulates platform evolution through the

mid–late Quaternary to test hypotheses regarding carbonate platform and coral reef responses to sea-level oscillations and associated climate change. Model outputs are calibrated against observed datasets, enabling evaluation of alternative evolutionary scenarios and providing insights into the environmental conditions controlling transitions between 'keep-up,' 'catch-up,' and 'give-up' reef growth phases. This approach improves understanding of reef resilience to environmental stress, refines local relative sea-level reconstructions, and contributes to broader predictions of reef response to future climate change.

Finally, detailed fossil reef core interpretations of three boreholes across North and South Scott Reef utilise an integrated methodological approach that combines detailed sedimentological logging, high-spatial-resolution hyperspectral scanning, NCT, petrologic and sedimentary facies analysis, SEM, XRD, and closed-system U–Th dating. Coral and algal assemblages define paleoenvironmental reconstructions within a chronostratigraphic framework spanning the last 500 kyr. This multi-proxy approach builds upon and refines previous interpretations that relied on incomplete lithological descriptions and open-system chronological reconstructions without sufficient diagenetic vetting. By linking small-scale processes such as the destruction of primary coral aragonite and skeletal porosity into the context of large-scale platform evolution, this research aims to advance our understanding of carbonate system dynamics and their sensitivity and resilience to past and future climate variability.

1.5.2 The Geological Significance of Scott Reef

Scott Reef, located on the North West Shelf of Australia, comprised of North Scott, South Scott and Seringapatam (Figure 1.13) (Grimaldi et al., 2024) are significant both as modern coral reef ecosystems and as archives of past sea-level and environmental changes. The extensive scientific investigation of Scott Reef has also been driven by hydrocarbon exploration in the Browse Basin, where large gas accumulations occur in the underlying Mesozoic reservoirs. This industry interest led to the acquisition of extensive seismic datasets and drilling programs, which have provided an exceptional geological framework to study long-term evolution of the carbonate platform. These raised and isolated carbonate platforms provide valuable records of almost uninterrupted, stratigraphically continuous Neogene - Quaternary reef

growth (including the response to the MPT) on a stable far-field site (Collins et al., 2011). They offer insights into the complex interactions between eustatic sea-level fluctuations, oceanographic conditions, and reef growth dynamics that have been difficult to resolve in other reef systems due to rapid uplift or insufficient rates of subsidence and proximity to glaciated regions (Webster et al., 2009; Medina-Elizalde, 2013). The geological history of Scott Reef has been closely bound to the tectonic and climatic evolution of the NWS (James et al., 2004; Gallagher et al., 2014) and is regulated by the Indonesian Throughflow current (Figure 1.13A), which transports warm water from the Western Pacific Ocean and sources the Leeuwin current to the NWS of Australia (He et al., 2021). The reefs developed on the subsiding continental margin overlying Cenozoic carbonate and siliciclastic sediments, with their initiation and growth primarily controlled by changes in relative sea-level, subsidence rates, and regional hydrodynamics (Keep et al., 2007; Collins and Testa, 2010; Palei et al., 2024). Seismic architecture reveals a flat-topped platform characterized by platform margin reefs that border steep marginal slopes mirroring the present-day surface environments. A study in 2006 by Collins et al. (2009) showed there are distinct cycles of upward platform growth forming "stacked saucer" shapes, with each stratigraphic layer closely resembling the previous one. They found that higher energy reef building communities on the South Reef buffer energy from the prevailing SW wave energy from the North Reef – composed of relatively lower-energy reef communities. The study also presented partial lithologic and chronologic interpretations from 17 described boreholes that suggest five sequences of reef growth likely correspond to MIS 1, 5, 7, 9 and 11. However, the descriptions were incomplete, lacking detailed analysis of the coralgal assemblages, which are crucial for reconstructing reliable paleowater depths and therefore sea-level histories. Additionally, the screening process for selecting corals to date was insufficient for establishing a reliable chronological framework.

The NWS is tidally dominated so Scott Reef experiences semi-diurnal tides and a spring tidal range up to 4.1 m (Collins and Testa, 2010; Green et al., 2018). The height of the reef rim above mean sea-level is generally less than the offshore tidal range (4.1 m), meaning that the rim remains submerged at high tide but becomes partially exposed at lower tidal stages. This periodic exposure influences wave energy dissipation across the reef flat and the distribution

of intertidal biota. The seafloor morphologies surrounding Scott Reef include submarine terrace escarpments, fault scarps, valleys, mass wasting deposits, sediment waves, furrows and ridges, all of which requires oceanic currents, gravity-driven processes, and internal waves along the outer shelf and upper continental rise (Belde et al., 2015; Belde et al., 2017; Betzler and Ma, 2024). The high-velocity hydrodynamic environment and strong tidal currents are the dominant forces moving sediments in the region (Wilson, 2013). Internal tidal waves are generated by the interaction of tidal currents that are mostly concentrated on the eastern hook of South Scott Reef (Figure 1.13B) (Green et al., 2018; Rayson et al., 2011). The variation in morphologies between North and South Scott Reef (Figure 1.13B), which likely reflect a combination of underlying basement topography, spatially variable subsidence rates (Collins et al., 2011), and localised hydrodynamic conditions over time, are cited as the trigger for tidal flow separation and the resulting differences in reef development (Wolanski and Deleersnijder, 1998, as cited in Collins et al., 2011). The Browse basin sits on the monsoonal belt with prevailing westerly rains and winds during the summer and dry SE trade winds in the winter (Collins et al., 2011; Palei et al., 2024). The dominant wind and oceanic swell direction is from the West to Southwest (Green et al., 2018; Gilmour et al., 2022). Combined with the unique arcuate to circular reef morphologies (Fig. 1B), this creates a varied range of wave energies along the reef front from high to moderate. The reef front is dominated by primary coral framework (Braithwaite et al., 2000; Montaggioni, 2005; Collins et al., 2011).

The history of Indo-Pacific coral reefs remains poorly resolved, with major gaps in characterisation of the spatial and temporal reef development along the NWS (Collins et al., 2009). Recent studies have investigated reef growth since the last glaciation (MIS3; ca. 60-30 kyr) at Ashmore reefs (Figure 1.13A) (Webster et al., 2022) and since the Miocene at the Rowley shoals (McCaffrey et al., 2025), however reconstruction of the Neogene-Quaternary history of Scott Reef is notably lacking. In addition to their geological significance providing a long-term perspective on reef response to past environmental change, Scott Reef are also critically important ecosystems (McCaffrey et al., 2025). They help inform our understanding of reef resilience to high-frequency (annual, seasonal) modern day climatic perturbations,

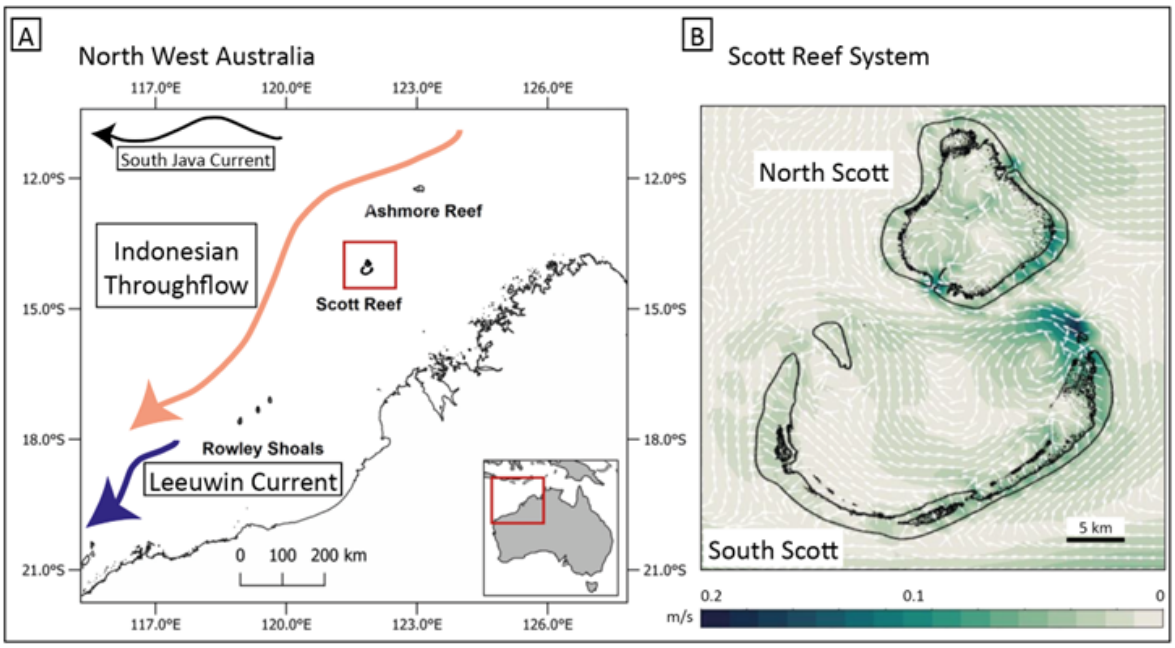


FIGURE 1.13: (A) Location map of Scott Reef on the North West Shelf of Australia, showing the major oceanographic currents influencing the region. Modified from Gallagher et al. (2014). (B) Modern tidal current flow overlain on North and South Scott (Grimaldi et al., 2024).

including sea surface temperature stress and associated coral bleaching events, ocean acidification, and cyclone impacts (Gilmour et al., 2022). Located within a major hydrocarbon province, they also offer valuable insight into the coexistence of sensitive reef ecosystems and offshore resource development, highlighting the importance of integrated environmental and geological research. Ongoing monitoring and research at Scott Reef including geological and ecological modelling, contribute to improving our understanding of reef sensitivity to past and future climate change and informing marine conservation strategies and decision making at global to local scales for modern reef systems (Finnegan et al., 2024).

1.5.2.1 Neogene Foundations

The Browse Basin is a half-graben system running obliquely parallel to the continental margin, bordered by the Scott Reef Trend (i.e., a fault bound structural rise) and the ocean (Keep et al., 2007) (Figure 1.14B). The structural evolution of the NWS consists of two phases of rifting associated with the break-up of the Australian and Indian plates (Rosleff-Soerensen

et al., 2012; Paumard, 2018; Reeve et al., 2022), as well as the Neogene collision between Australia and the Banda Arc (Keep et al., 2007), resulting in far-field inversion of parts of the Carnarvon Basin to the southwest. The final phase of rifting in the Middle Jurassic to Early Cretaceous likely generated the main structural trends identified on seismic data (Figure 1.14C) (Keep et al., 2007; Rosleff-Soerensen et al., 2012). These include a major fault below a thick Cenozoic wedge of carbonate and siliciclastic sediments prograding basinward, and no major overlying structural features. This provided the foundation for reef growth from the Miocene to present (Collins et al., 2011; Riera et al., 2022). Whilst the Browse basin is situated on a passive continental margin, its proximity to major tectonic elements, including the Sunda Trench subduction zone and collisional margin along the Timor Trough strait (Keep and Harrowfield, 2008) *'preclude this part of the Australian plate from being truly classified as a stable continental region'* (Whitney et al., 2016).

Evidence of reefal structures in offshore seismic surveys along the NWS indicate that warm tropical carbonate factories have facilitated carbonate production and coral reef development for ca. 30 Ma (Riera et al., 2022; McCaffrey et al., 2025). These Neogene foundations (spanning from ca. 23.7 to 2.5 million years ago; Berggren et al. (1985)), provided the limestone substrate and topographic highs along the West Australian continental margin (Figure 1.14A) that facilitated the establishment of precursor platforms and reefs along the NWS (Ryan et al., 2009), including Scott Reef (Collins and Testa, 2010), Ashmore Reef (Webster et al., 2022) and the Rowley shoals (James et al., 2004; McCaffrey et al., 2025). During the early to middle Miocene, ongoing subsidence created accommodation for the expansion of extensive shallow-water carbonate systems, facilitated by warm tropical conditions (i.e., the Mid-Miocene Climate Optimum ca. 16 Ma; Müller et al. (2022)) and stable sea-levels (Riera et al., 2022). During this time, the Browse Basin contained a 500 km-long barrier reef system comparable to the modern GBR (Belde et al., 2017). By the late Miocene, falling global sea-levels (Betzler et al., 2018), increased climatic cooling and relatively high subsidence rates restricted reef development (Belde et al., 2017). Through the Pliocene, continued global sea-level lowering (Petrick et al., 2019) and changes in ocean

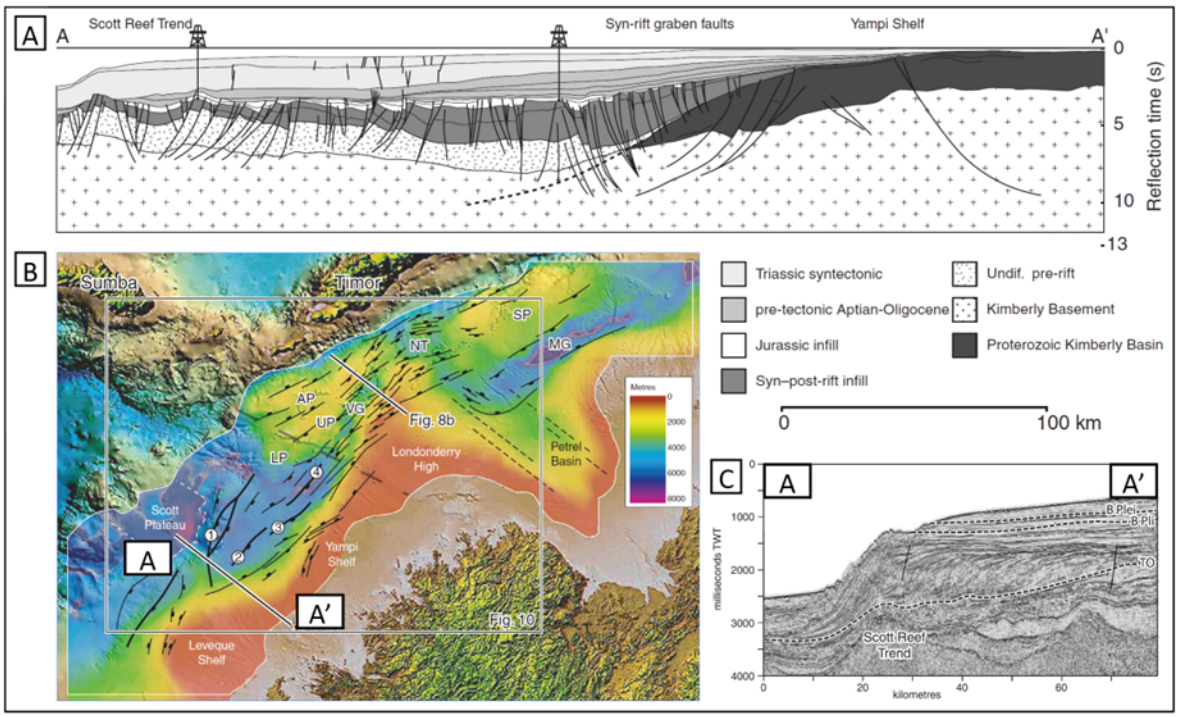


FIGURE 1.14: Basinward cross-section schematic (A-A') of the Neogene pre and post-rift sediments and structural elements, including the Scott Reef trend (A) and onlapping Pliocene-Quaternary clinoform sediments prograding basinward (B). Scott Reef is located on the Scott Plateau. Adapted from Keep et al. (2007).

circulation, linked to the restriction of the ITF, contributed to a long-term cooling and drying out of the NWS. Coinciding with an increase in current-driven drift sedimentation, this affected nutrient availability and upwelling that restricted coral reef distribution and growth rates to the North and South of Scott Reef and the Rowley shoals in this region (Kuhnt et al., 2004; Belde et al., 2017; Christensen et al., 2017; Stuut et al., 2019; He et al., 2021; McCaffrey et al., 2025). Understanding the Neogene geological history of Scott Reef is essential for reconstructing long-term reef evolution and assessing the interplay between tectonic subsidence, sea-level change, and carbonate production. Chapter 2 is designed to develop these insights and provide critical context for interpreting Quaternary reef growth patterns and predicting future reef responses to ongoing environmental change.

1.5.2.2 Quaternary Evolution

The Quaternary geological history of Scott Reef has been largely influenced by the transition from the obliquity-driven 41-kyr world to the 100-kyr world, whereby increased amplitude of glacial-interglacial sea-level fluctuations facilitated increased accommodation for reef growth (Zhang et al., 2023). As global ice sheets expanded and contracted, and subsidence increased (Belde et al., 2017), the NWS experienced significant shifts in relative sea-level, directly influencing the accretion and preservation of reefal carbonates. During interglacial periods, when sea-levels were high, coupled with an aridification of the NWS (Zhang et al., 2023), Scott Reef experienced phases of active reef growth, forming two thick, vertically aggrading platforms (Collins et al., 2009; Belde et al., 2017). Glacial lowstands periodically exposed the platform tops to subaerial erosion and karstification, leading to periods of sedimentation hiatus. The cyclic phases of reef turn on and turn off reflects the complex interaction between eustatic changes and local environmental conditions. Holocene reef development at Scott Reef established during the post-glacial sea-level rise of ca. 10 mm/yr from 11 to ca. 7-6.5 kyr, following the Last Glacial Maximum (20,000 years ago) (Collins et al., 2006; Collins and Testa, 2010). As sea-levels stabilized in the mid-Holocene, coral reef frameworks re-established, forming the modern reef structures observed today. The continued subsidence of the NWS has also contributed to long-term reef preservation and accommodation for further carbonate accumulation.

More work is needed to evaluate the Quaternary geological history of Scott Reef to improve our understanding of their sensitivity to rapid environmental change. Clarifying this past reef response is crucial for predicting future reef resilience under ongoing anthropogenic climate change and sea-level rise. General sedimentological interpretations of carbonate reef core and open system U–Th chronologies through two long boreholes on the SE facing reef crests preliminarily indicate reef growth started at 392 kyr at 200 m depth in MIS 11. However, evidence of pervasive marine and meteoric diagenesis throughout the dated core samples suggests that these dates are uncertain. In Chapter 5, we aim to provide detailed and robust sedimentological descriptions of two previously described and one undescribed reef core from the drowned leeward margin, defining distinct coral-algal assemblages. These data, along

with new closed-system U–Th ages selected from diagenetically screened sections of core that are suitable for dating, enable the reconstruction of precise paleo-depositional environments and chronologies spanning the mid-late Quaternary. We also address the limited comparative studies of isolated reefs (e.g., Scott Reef, NWS) versus barrier reefs (e.g., Ribbon Reef 5, GBR) with similar ages (> 500 kyr), latitudes and climate, in response to Quaternary sea-level oscillations and associated environmental change, by providing a detailed review of their similarities and contrasts.

1.6 Thesis Objectives, Structure and Scope

The overarching theme of this thesis is to advance understanding of the complex interactions between environmental and eustatic controls on carbonate platform evolution and coral reef development through Neogene-Quaternary climate transitions, that also provides valuable insights for predicting coral reef response to future environmental change. This thesis aims to develop high-resolution qualitative and quantitative geological models of North and South Scott Reef, comparable to similar reef systems worldwide, to assess their response to orbital forcing and associated climate change, including eustacy (sea-level change and subsidence) and environmental perturbations (oceanographic) over a range of spatio-temporal scales. The approach (Figure 1.15) utilises forward stratigraphic modelling to integrate multi-scale observational data (Ångström to km) to refine lithological interpretations, paleodepositional records and geochronological constraints from fossil reef cores. The data include 3-D seismic, multibeam bathymetry, fossil reef cores, well logs, U-series, and modern ecological records. The analyses encompass petrology, SEM, XRD, hyperspectral imaging, and neutron computed tomography (NCT).

The objective of this study is to address the following research questions:

(1) What is the role and nature of eustacy and associated environmental perturbations in shaping carbonate platform development and coral reef evolution at Scott Reef during major Neogene-Quaternary climate transitions?

(2) How can neutron computed tomography and hyperspectral imaging be used to improve paleoclimatic and geochronologic reconstructions of coral reefs?
(3) Can we reconstruct the paleodepositional evolution and chronostratigraphic framework of Scott Reef by synthesising all available legacy data with new sedimentological analyses using innovative screening and dating techniques?
(4) What new insights into the main processes controlling reef and carbonate platform evolution emerge through the integration of observational data and synthetic reef growth models?
(5) Are the observed differences in reef growth models on the GBR due to eustacy and environmental variances?

This thesis develops a methodological framework by integrating new observational data with forward stratigraphic modelling to assess key geological controls on carbonate platform and coral reef development across various geological timescales. Structured as four scientific research articles, each chapter explores a specific aspect of this overarching theme while collectively examining eco-geomorphic reef responses to sea-level and climate variability.

Chapter 1 introduces the scientific motivation, overarching research questions, and the broader essential background context.

Chapter 2 examines the long-term evolution of the Scott Reef isolated carbonate platform using high-resolution 3-D seismic, well logs and multibeam bathymetry. It establishes the tectono-stratigraphic framework, identifies key phases of reef initiation and demise, and evaluates the roles of sea-level change, subsidence, carbonate production and oceanography. This chapter establishes the geological context and foundation for subsequent chapters and has been published in *Marine and Petroleum Geology* (https://doi.org/10.1016/j.marpetgeo.2023.106188).

Chapter 3 introduces a new non-destructive method for diagenetic screening of fossil corals using NCT. The technique differentiates primary aragonite from secondary calcite and improves

TABLE 1.1: Chapter 2: Seismic Stratigraphy and Geomorphology of Scott Reef

Analyses	**Key Objectives**
Seismic Sequence Stratigraphy	Interpret 3-D seismic data to define key stratigraphic surfaces, reef and ICB geometries, and platform evolution for the Quaternary-Late Miocene.
Seismic Geomorphology	Map reef facies using seismic attributes such as spectral decomposition to reconstruct platform morphological evolution.
Chronostratigraphic Framework	Integrate seismic stratigraphy and seismic geomorphology with well data and regional age constraints to establish long-term chronostratigraphic framework and carbonate factories.

the reliability of geochronologic and paleoclimatic reconstructions. This methodological advance supports the chronological interpretations developed later in the thesis. This chapter has been published in *Geochemistry, Geophysics, Geosystems* (https://doi.org/10.1029/2025GC012439).

TABLE 1.2: Chapter 3: Neutron Computed Tomography for Fossil Coral Screening

Analyses	**Key Objectives**
Neutron Imaging	Acquire NCT datasets from representative and previously screened modern and fossil coral samples with known diagenetic alteration to visualise coral internal 3-D structure, morphology and mineral phase contrasts.
Diagenetic Screening	Identify aragonite preservation, calcite alteration, and porosity matrix using neutron attenuation contrasts.
Method Validation	Compare neutron results with traditional screening techniques: XRD, SEM, petrology, X-Ray imaging used for U-series screening criteria.

Chapter 4 applies a calibrated forward stratigraphic modelling approach to quantify the response of North and South Scott Reef to sea-level and environmental changes associated with the Mid-Pleistocene Transition. Sensitivity experiments evaluate the relative impacts of subsidence, sea-level amplitude, carbonate production and ecological depth thresholds on platform architecture and margin evolution. This chapter has been published in *Marine Geology* (https://doi.org/10.1016/j.margeo.2026.107716).

Chapter 5 continues to examine the response of the Scott Reef platforms to environmental and eustatic changes since the MPT but focuses on utilising lithologic and chrono-stratigraphic

TABLE 1.3: Chapter 4: Forward Stratigraphic Modelling of Scott Reef

Analyses	**Key Objectives**
Model Construction	Develop base-case FSM scenarios calibrated to core, seismic, and modern multibeam bathymetry data and U-series ages.
Sensitivity Testing	Evaluate platform response to sea-level, subsidence, wave energy and carbonate production changes and compare synthetic stratigraphy with observed platform architecture and facies patterns.
MPT Hypothesis Testing	Extend base-case model to 1.2 Ma and apply hypothesised model assumptions to test platform sensitivity to MPT-associated climate change.

analysis of three long fossil reef core datasets. We integrate the data to reconstruct reef growth and paleodepositional environments across multiple Marine Isotope Stages. The chapter assesses spatial variability in coralgal assemblages, geomorphology and subsidence between the platforms, and compares the findings with regional reef records to refine interpretations of global (eustatic) vs local (environmental) controls. This chapter is intended for submission to *Quaternary Science Reviews*.

TABLE 1.4: Chapter 5: Core logging for Chronostratigraphic and Paleoenvironmental Reconstruction

Analyses	**Key Objectives**
Core Logging	Describe sedimentary lithologies, coral and algal assemblages, and diagenetic features from core logs, hyperspectral and NCT imagery.
Diagenetic screening	Identify carbonate mineral phases and diagenetic alteration using XRD and SEM, supported by petrographic analysis. Select suitable samples for dating.
Chronology	Generate closed system U-series agaes. Integrate U–Th ages with stratigraphic markers to establish a robust chronostratigraphic model.
Paleoenvironmental Reconstruction	Interpret paleowater depth, depositional environment, and exposure events through time within a robust chronostratigraphic framework context.

Chapter 6 synthesises results from all preceding chapters to address the central thesis question concerning the environmental and eustatic drivers of Scott Reef's Neogene–Quaternary

evolution. The chapter discusses implications for understanding future reef behaviour under changing sea-level and climatic conditions and outlines recommendations for further research.

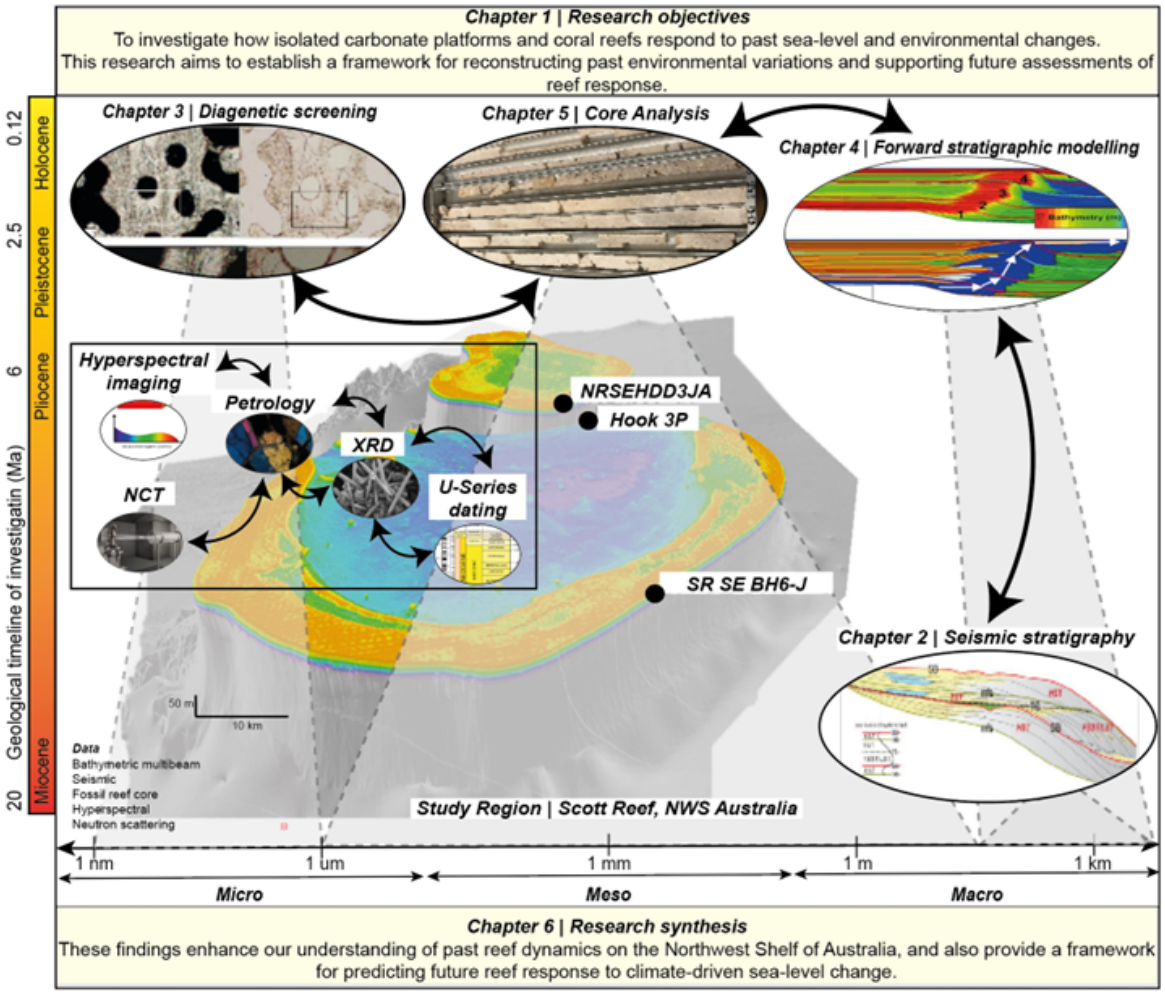


FIGURE 1.15: Schematic illustrating the thesis design, highlighting the geological time intervals and spatial scales represented by datasets used across the four core research chapters. Seismic stratigraphy, forward stratigraphic modelling, core analyses, and diagenetic screening are integrated to reconstruct carbonate platform evolution at Scott Reef, North West Shelf of Australia. Research objectives and synthesis are presented in Chapters 1 and 6, respectively.

CHAPTER 2

ARTICLE 1: Environmental Controls on the Resilience of Scott Reefs Since the Miocene (North West Shelf, Australia): Insights from 3D Seismic Data

---

This chapter presents the following published article:

Williams, C., Paumard, V., Webster, J. M., Leonard, J., Salles, T., O'Leary, M., and Lang, S. (2023). Environmental controls on the resilience of Scott Reefs since the Miocene (North West Shelf, Australia): Insights from 3D seismic data. *Marine and Petroleum Geology*, 151. https://doi.org/10.1016/j.marpetgeo.2023.106188

The paper discusses the carbonate factory evolution of North and South Scott Reef since the Miocene with respect to eustatic and environmental controls. The primary objective is to produce the first chronostratigraphic framework for the platforms, using newly acquired 3-D seismic data. The scope and goal of this paper was to investigate the complex tectono-stratigraphic history of the Browse Basin, NWS, Australia, by proposing four new carbonate factory phases that compliment and build on existing regional stratigraphic frameworks. The paper presents a detailed seismic stratigraphic interpretation of newly reprocessed 3D seismic data, combined with well log data and preliminary core dating that reveals the tectonostratigraphic histories and evolution of North and South Scott Reefs since the Miocene. For the first time, it was possible to reconstruct a chrono-stratigraphic framework, detailing relative sea-level (RSL) changes and the impact of global (e.g., climate, eustasy) and regional (e.g., tectonics) forcing parameters on their development.

TABLE 2.1: Summary of Chapter 2: Environmental Controls on the Resilience of Scott Reef Since the Miocene.

Chapter 2	**Summary**
Scope	Investigation of the long-term evolution and resilience of North and South Scott Reef since the Miocene, using newly reprocessed 3-D seismic data from the Browse Basin, Northwest Shelf of Australia.
Primary Objective	Develop the first comprehensive chronostratigraphic framework for the Scott Reef platforms and surrounding Browse Basin, resolving relative sea-level change and environmental forcing through time.
Data	High-resolution, reprocessed 3-D seismic volume integrated with well log data and preliminary core age constraints.
Methods	Seismic stratigraphic interpretation of reflector geometries, seismic facies, and bounding surfaces, combined with regional correlation to existing stratigraphic frameworks and well control.
Key Results	Identification of four major carbonate factory phases since the Miocene, documenting shifts in platform architecture, depositional environments, and reef persistence through major climatic and eustatic transitions.
Paleogeographic Reconstruction	Reconstruction of nine depositional environments and six paleogeographic maps illustrating platform evolution, margin progradation, backstepping, and drowning phases.
Chronostratigraphic Framework	Establishment of a new Miocene–Quaternary chronostratigraphic framework for Scott Reef, enabling correlation of reef growth phases with relative sea-level fluctuations and regional tectonic events.
Major Insights	Scott Reefs have persisted since the Miocene despite significant eustatic variability, with resilience controlled by a combination of oceanographic conditions, subsidence history, and tectonostratigraphic setting.
Broader Significance	Provides the first basin-scale seismic chronostratigraphic framework for Scott Reef, forming a foundation for subsequent core-based, geochemical, and forward stratigraphic modelling studies presented in later chapters.

Author contributions: I designed the workflow, performed the analysis, interpreted the sequence stratigraphic framework and wrote the manuscript. Victorien Paumard guided the interpretation of the sequence stratigraphic framework, advising on best practise and common standards, as well as providing training for use of Paleoscan software. Jody Webster, Simon Lang, Mick O'Leary and Tristan Salles provided insightful comments and advice on the

structure of the discussion. Jonathon Leanard produced the paleo-climate maps shown in Fig. 20.

Supplementary material: Appendices A and B at the end of this thesis correspond to Supplementary Data 1 (Results) and Supplementary Data 2 (Interpretation), respectively, as cited in the associated published article. Appendix C, not cited in the published article, provides a link to a movie showing the 3-D Megator seismic data depth slices as a visual representation of the carbonate factory evolution since the Miocene.

Marine and Petroleum Geology 151 (2023) 106188

Contents lists available at ScienceDirect

Marine and Petroleum Geology

journal homepage: www.elsevier.com/locate/marpetgeo

Environmental controls on the resilience of Scott Reefs since the Miocene (North West Shelf, Australia): Insights from 3D seismic data

Carra Williams [a,c,*], Victorien Paumard [a,c], Jody M. Webster [a], Jonathon Leonard [b], Tristan Salles [a], Michael O'Leary [c], Simon Lang [c]

[a] Geocoastal Research Group, School of Geosciences, Madsen Building F09, University of Sydney, NSW, 2006, Australia
[b] Earthbyte Group, School of Geosciences, University of Sydney, Madsen Building, NSW, 2006, Australia
[c] Centre for Energy Geoscience, School of Earth Sciences, The University of Western Australia, 35 Stirling Highway, Perth, WA, 6009, Australia

ARTICLE INFO

Keywords:
Seismic stratigraphy
Seismic geomorphology
Carbonate platform
Coral reefs
Tectono-stratigraphy
Paleo-environmental reconstruction
Chrono-stratigraphic framework

ABSTRACT

North and South Scott Reefs are isolated carbonate platforms separated by an inter-reef channel on the NWS, Australia. They evolved from a barrier reef in the Miocene, and into isolated carbonate build-ups (ICB's) during the Pliocene, and finally to the isolated carbonate platforms that continued to present day. However, the timings of coral reef turn on and off are not well constrained with respect to global climatic changes in this region. The North West Shelf (NWS) of Australia recorded marked climatic and oceanographic changes through the Cenozoic. For example: (1) the Mid Miocene Climatic Optimum (MMCO), leading to the onset of ICB's and carbonate platform development; (2) the Mid Pleistocene Transition (MPT) (ca. 0.8–0.6 Ma) and the associated change in regional climate from wet to dry; and (3) glacial-interglacial variability through the Pleistocene until present day. Availability of high resolution and extensive 3D seismic data provides a unique opportunity to investigate the evolution of these reefs using seismic stratigraphy and seismic geomorphology. Four main phases of carbonate factory evolution (Phase I-IV) were identified from the Miocene to present. A chrono-stratigraphic framework is constructed, detailing relative sea-level (RSL) changes and the impact of global (e.g., climate, eustasy) and regional (e.g., tectonics, oceanography) forcing parameters on their development. Seismic stratigraphy reveals that despite rapid accommodation rate changes, the oceanographic setting, antecedent topography and rapid vertical reef accretion played a key role in the persistence of Scott Reefs. It is likely that the Indonesian throughflow (ITF) current has been a critical component in controlling the local climate. The Leeuwin current, tides, swells and wind regimes similarly exert a major influence on the NWS climate, whilst the inter-reef channel likely bypassed terrigenous sediment influx away from the reefs, avoiding periods of inundation during wet climates.

1. Introduction

A 2000 km long Miocene barrier reef that seeded the Scott Reefs on the North West Shelf (NWS), Australia has been described in sections by (Rosleff-Soerensen et al., 2016; Belde et al., 2017; Van Tuyl et al., 2019) and incorporating work on smaller regions by (Rankey, 2020; Thronberens et al., 2022). Overlying Pliocene sediments have been briefly documented for the Browse Basin part of the NWS by McCaffrey et al. (2020). IODP sites nearby (Fig. 1) and to the south of the Scott Reef area core through the upper Tertiary section (Groeneveld et al., 2021). While these wells may be used to tether regional stratigraphic correlations across 100's km, they are however, poorly constrained in the Browse basin where this study is situated. The chronostratigraphic framework is most complete below the Miocene-Pliocene boundary (Thronberens et al., 2022). Above this, the carbonate factories are not well described, despite modern day reefs being evidence of long-term continuation of carbonate platform development and coral reef productivity since the Miocene barrier reef. The Browse basin, which is characterised in detail below the Pliocene, contains three reef successions that have persisted throughout this time, but have yet to be described. This study provides a new tectono-stratigraphic framework for the Browse Basin and describes four carbonate factories that explain how and why Scott Reefs persisted

* Corresponding author. Geocoastal Research Group, School of Geosciences, Madsen Building F09, University of Sydney, NSW, 2006, Australia.
E-mail addresses: carra.williams@sydney.edu.au (C. Williams), victorien.paumard@uwa.edu.au (V. Paumard), jody.webster@sydney.edu.au (J.M. Webster), jonathon.leonard@sydney.edu.au (J. Leonard), tristan.salles@sydney.edu.au (T. Salles), mick.oleary@uwa.edu.au (M. O'Leary), simon.lang@uwa.edu.au (S. Lang).

https://doi.org/10.1016/j.marpetgeo.2023.106188
Received 9 December 2022; Received in revised form 13 February 2023; Accepted 17 February 2023
Available online 24 February 2023
0264-8172/© 2023 Elsevier Ltd. All rights reserved.

for the last 20 million years (Ma).

The position of North and South Scott Reefs on the subsiding NWS of Australia (Collins and Testa, 2009), makes them excellent archives of relative sea level (RSL) change and oceanographic variability over the last 20 Ma. Several other present-day reefs with differing morphologies have persisted along the NWS margin. These include the modern Rowley Shoals, Seringapatam reef, Ashmore Reefs and relict or drowned reefs e.g., Big Bank Shoals (Ryan et al., 2009; Collins and Testa, 2009; Saqab and Bourget, 2015; Rosleff-Soerensen et al., 2016; Van Tuyl et al., 2019; McCaffrey et al., 2020; Thronberens et al., 2022). The presence of these isolated reef systems on the NWS suggests that carbonate production was maintained despite changing paleo-oceanographic and eustatic sea level variations in the relatively recent geologic past, in contrast to the extensive buried Miocene reef systems described by Thronberens et al. (2022). How these isolated carbonate buildups remained locales of coral growth despite the broader regional demise of reef systems across the NW shelf during the Miocene remain unresolved, though a number of studies, including Collins et al. (2011), Webster et al. (2022) and Saqab and Bourget (2015) have attempted to address this question.

Availability of industry 3D seismic data (Fig. 2) provides a unique opportunity to investigate the evolution of the Scott Reef system using seismic stratigraphy and geomorphology, integrated with industry well log and borehole data (Collins and Testa, 2009). The aim of this study is to; (1) using seismic geomorphology and stratigraphy, characterise the history and phases of carbonate factory development of Scott Reefs precursor carbonate platforms and reefs, and (2) constrain the spatio-temporal evolution of Scott Reefs to decipher the relative impact of global (e.g., climate, eustasy) and regional (e.g., tectonics, oceanography) forcing parameters on their development by incorporating paleogeographic reconstructions since the Burdigalian ca.17 Ma. While this study presents an analysis and overview of the carbonate factories since the Miocene, it mainly focuses on the Pliocene-Pleistocene strata of North and South Scott Reefs.

2. Regional setting

2.1. Paleoceanography and climatic evolution of the NWS

The NWS extends for ca. 2400 km from Melville Island in the northeast to the Exmouth Gulf in the southwest, aligning obliquely parallel to the East Timor Trough (Fig. 1). It hosts one of the largest Cenozoic carbonate provinces worldwide (Apthorpe, 1988; Riera et al., 2021, 2022; Webster et al., 2022). The western, passive continental margin of Australia (Rosleff-Soerensen et al., 2016) has preserved most of its stratigraphic record since the Neogene-Pleistocene period. Since ca. 20 Ma, the position of the study site has migrated from about 25°S to 15°S at present (Scotese and Wright, 2018; Müller et al., 2019). The climate regime governing carbonate ramp, platform and reef development on the NWS has changed through time, and is a major factor in controlling the sediment production and depositional environments of this region.

There are four major climate transitions that influenced the development of the Browse Basin; (1) Middle Miocene Climate Optimum (MMCO); (2) Miocene-Pliocene boundary; (3) Pliocene-Pleistocene boundary; (4) Mid Pleistocene Transition (MPT). Presently, the NWS is a carbonate-dominated platform (Jiménez-Moreno et al., 2019; Belde et al., 2017; Lebrec et al., 2022) and the predominant sedimentation is sourced from tropical water carbonates (McCaffrey et al., 2020).

The seasonally wet and warm early Miocene climate (Gallagher et al., 2014; Belde et al., 2017) was optimal for the formation of karst during sea level lowstands and small isolated carbonate build-ups (ICB's) on topographic highs (Gallagher et al., 2014; Christensen et al., 2017) during highstands. However, absence of reefal build-ups in the southern part of the NWS suggests climate was sub-optimal during the deposition of the ramp (Riera et al., 2022). There was a gradual warming up to the MMCO, from ca. 17 to 13.8 Ma and increased intensification of precipitation (Groeneveld et al., 2021) and was associated with a period of reduced ice volume (Miller et al., 2020). It is interpreted to have initiated the growth of larger ICB's and a transition into 'keep-up' sedimentation (Van Tuyl et al., 2018). Facies then transitioned from a prograding shelf in the Langhian to a barrier reef

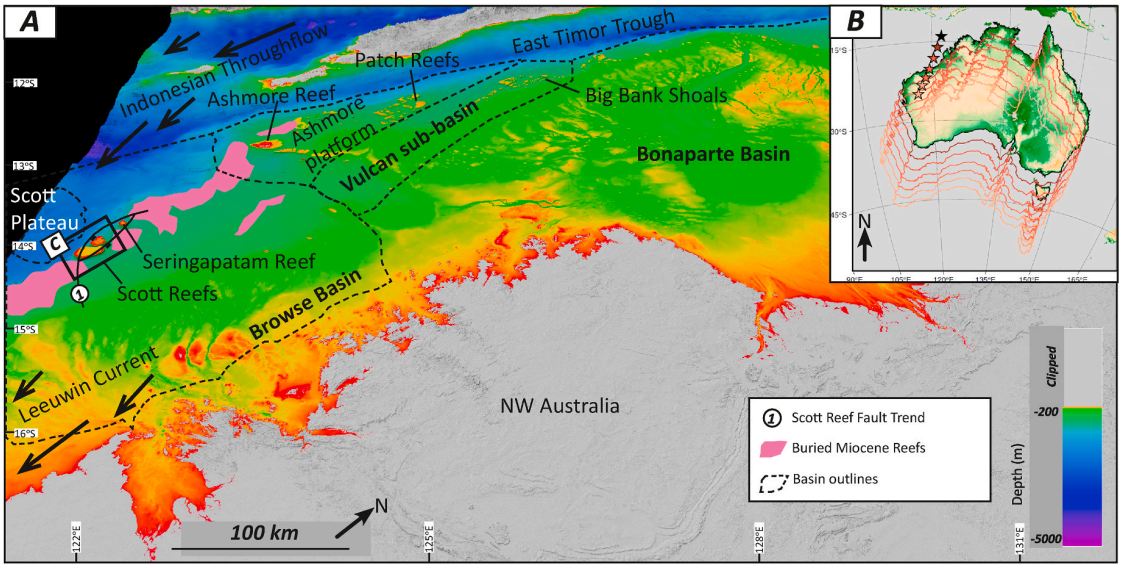


Fig. 1. Location map of North and South Scott Reefs, North West Shelf Australia. (A) Multibeam elevation map of the NW Australian coastline highlighting location of Scott and Seringapatam reefs (adapted from www.deepreef.org, Dr. Robin Beaman). Miocene drowned reefs are shown in pink (adapted from Belde et al., 2017). Browse and Bonaparte basin outlines in dashed line (adapted from Marshall and Lang, 2013). Scott Plateau and Scott Reef Fault Trend are shown (adapted from Keep and Harrowfield, 2008). (B) Plate tectonic motion shown for Australia and its margins since 18.3 Ma in 3 My intervals. Coloured stars correspond to Scott Reefs location relative to each plate tectonic increment. The topography of present-day Australia is shown in colour. Generated with GPlates (http://www.gplates.org) using rotations in Scotese and Wright, 2018).

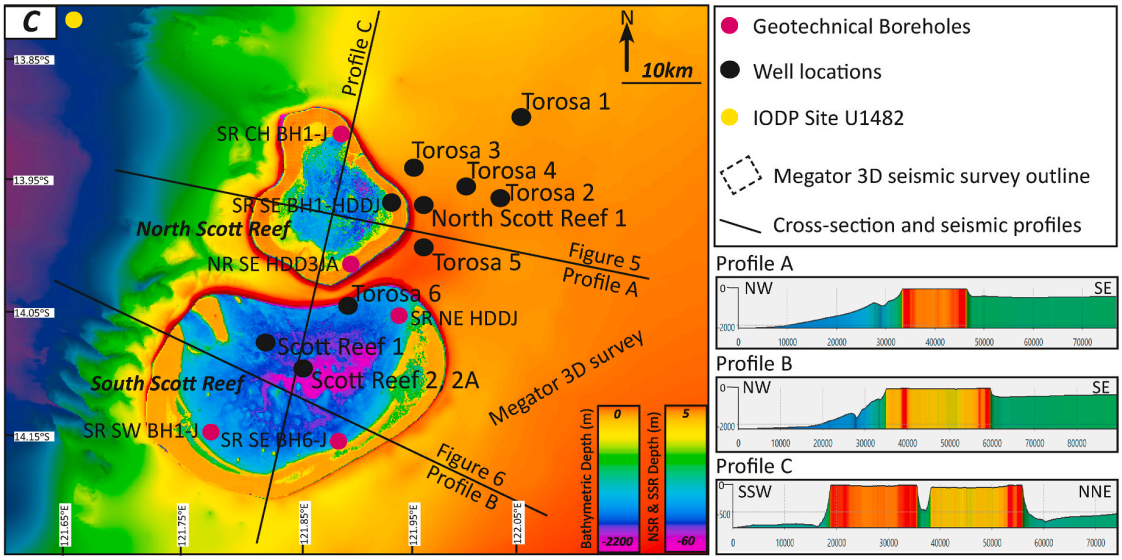


Fig. 2. (C) Bathymetric map of Scott Reefs (data source: AusSeabed 2020 Australia 30 m Multibeam sonar) showing geotechnical boreholes, well locations, approximate location of IODP site 363 U1482 (Rosenthal et al., 2018), and outline of the Megator 3D seismic survey. This survey is a reprocessed composition of six vintage surveys used in the merge, covering the Torosa field, Browse Basin (Source: Woodside processing and interpretation reports). Data Quality: Good to poor. ***Top right:*** Figure symbol key. ***Bottom right:*** Cross sectional profiles A, B, C showing elevation change across North and South Scott reefs. Profile A and B correspond to Figs. 5 and 6 respectively.

complex (McCaffrey et al., 2020), with scattered platforms in the Tortonian and aggrading and prograding isolated platforms up to the Messinian (Rankey, 2020). The Miocene-Pliocene boundary saw an abrupt transition from a dry to humid and more variable climate (He et al., 2021) and high global sea level (Miller et al., 2020). This is documented as the Pliocene climate optimum ca. 4.35 Ma (Christensen et al., 2017; Jiménez-Marino et al., 2019; He et al., 2021). This warm period resulted in a predominantly wet Pliocene epoch and then to an oscillating glacial (cool-dry)-interglacial (warm-wet) climate variability throughout the Pleistocene until present day (Gallagher et al., 2014; Christensen et al., 2017). The Indonesian throughflow (ITF) has been a critical component in controlling the local climate by transporting warm waters from the Indo-Pacific warm pool to the Indian Ocean extending down to the NWS (Gallagher et al., 2014; Auer et al., 2019; Gallagher and Wagstaff, 2021). The Leeuwin current (LC), which increased in strength after ca. 1.2 Ma - triggered by enhanced atmospheric circulation, also transports warm tropical water southwards (He et al., 2021). Coastal upwelling, equatorward wind stress and the northward flowing West Australia Current similarly exert a major influence on NWS climate (Goktas et al., 2016; He et al., 2021).

It is considered that the Pliocene-Pleistocene carbonate platform development on the NWS was controlled by a combination of glacio-eustatic sea level change, subsidence and ocean-current variability (Gallagher et al., 2014; Goktas et al., 2016). The Pliocene-Pleistocene climatic shift is recognised globally as an increase in the frequency of the glacio-eustatic cycles, leading to larger climatic and environmental oscillations (Lisiecki and Raymo, 2005 as cited in Hirase et al., 2016; Goktas et al., 2016; He et al., 2021). Karas et al. (2011) suggested that the Leeuwin Current (LC) was present on the NWS by ca. 2.5 Ma, concomitant with the Pliocene-Pleistocene climatic transition, signalling the importance of fluctuations in ITF intensity and LC strength on ocean circulation since the Pliocene (Tiedemann et al., 2009; Goktas et al., 2016). This coincided with an increase in siliciclastic influx from the continental margin as the environment transitioned into a wetter climate (Christensen et al., 2017; Groeneveld et al., 2021). Additionally, RSL rise (above ca. 10–20 m modern sea level; Burke et al., 2018) in the Late Pliocene at 2.85 Ma and global temperatures >2 °C warmer than today, are recorded at this boundary.

The NWS region underwent dramatic climatic and oceanographic changes throughout the Quaternary period. Many of the inter-related oceanographic conditions, such as the: LC, carbonate supersaturation, aridity and enhanced middle Pleistocene sea level variability, controlled carbonate platform and coral reef development (Gallagher et al., 2014, 2017; Collins et al., 2006). Perhaps most influential, was the rise in amplitude of sea level changes during the MPT, between ca. 1–0.6 Ma, when large ice sheets began to display stronger quasi-100ka cyclicity (Miller et al., 2020), and the associated change in climate from wet to dry (Gallagher et al., 2014, 2017; Yamamoto et al., 2006). The MPT was a period of where Earth climate transitioned from an obliquity driven frequency operating on 41kyr cycles, to a 100kyr eccentricity driven orbital cycles (Milankovitch, 1941; Montaggioni and Braithwaite, 2009), which remains the dominant frequency today. This shifted the Earth into a dry and arid climate and eventually into a period of glacial-interglacial cycles. The timings of coral reef turn on and off are insufficiently understood with respect to these changes, but the MPT is thought to have activated reef growth on the NWS and other regions around the globe: e.g., Ribbon Reef 5, GBR (Webster and Davies, 2003); Ryukyus Islands, Japan (Yamamoto et al., 2006); Seychelles (Braithwaite, 2016; Vyverberg et al., 2018), Maldives (Betzler et al., 2016) and the Gulf of Papua (Mallarino et al., 2021).

2.2. Geological and environmental setting: Scott Reefs

North and South Scott Reef (NSR and SSR) are two raised isolated carbonate build-ups, located in the Browse Basin ca. 270 km offshore on the edge of the Australian continental margin (Fig. 1). The ITF current flows East-West bringing warm, low salinity waters (Collins, 2002; Collins et al., 2011; Gallagher et al., 2017; Green, 2018; Van Tuyl et al., 2018; Auer et al., 2019). They established above thick basinward prograding sediment wedges, comprised of both terrigenous and carbonate sediments (Collins et al., 2011). The current stratigraphic succession for the Scott plateau evolved from a carbonate platform, around 18 Ma (Van Tuyl et al., 2018; Rosleff-Soerensen et al., 2016; McCaffrey et al., 2020). Isolated Carbonate Build-ups (ICB's) established up to around 5 Ma, then to atolls in the Pliocene (McCaffrey et al., 2020) and finally to the reefal build-ups that persisted right through to present day. As such, the

Miocene reefs and build-ups formed the antecedent topographic highs for the present-day reefs (Ryan et al., 2009; McCaffrey et al., 2020; Thronberens et al., 2022). Drawing on similarities to the Maldives platform (Belopolsky and Droxler, 2003; Betzler et al., 2016; Paumard et al., 2017), these modern-day reefs have been separated from the continental landmass throughout its entire 20 Ma history and removed from terrigenous input, being composed of almost entirely carbonate sediments (Collins and Testa, 2009).

The present-day reefs sit above the major Torosa gas field, discovered in the 1970's, with the main reservoir consisting of fluvial and coastal-deltaic siliciclastic sediments from the Earlier-Mid Jurassic Plover formation (Seggie et al., 2019; Collins, 2002). Consequently, the vast majority of data acquisition comes from below the pre-Cenozoic with main reservoirs targeted at around 3600–4400 mTVDss (True Vertical Depth sub surface).

Modern Scott reefs are oceanic atolls that are exposed to a predominant South West wave direction. They are exposed to large semi-diurnal tides that control the sediment transport regime within the atolls and surrounding flanks and channels, as well as regulating nutrients and temperature (Green, 2018). NSR is a pear-shaped enclosed reef-lagoon system (Fig. 2) around 162 km^2, with two channels connecting it to the open ocean. The geomorphology of SSR differs to NSR, being larger, ca. 494 km^2, and characterised by an open lagoon to the North due to the lack of reef crest-flat development. This exposes the windward margin to oceanic conditions. The deep inner lagoon is at ca. 60 mbsl and is filled with patch reefs, channels and show evidence of strong inflowing bottom currents, such as ripples and scours on the seafloor that reworked sediment lagoonwards (Fig. 2C).

Present day coralgal communities have been described in detail for NSR and SSR (Collins, 2002; Collins et al., 2011; Green, 2018; Gilmour et al., 2016) and have been compared to the Houtman-Abrolhos Reef (Collins, 2002). Geomorphic interpretations derived from satellite imagery show oceanographic and environmental differences between NSR and SSR. For example, the shallower North Reef lagoon is fully enclosed (aside from two small channels) by a wider reef crest protecting it from storms. This suggests there is less sediment reworking, however, consequently may be more susceptible to high temperatures, disease outbreaks (Gilmour et al., 2013a,b) coral bleaching and drowning from its own lagoonal sediment.

3. Data and methods

The Browse Basin is a mature petroleum province, resulting in significant data acquisition since the 1970's. Varying data quality is available; however, the majority of interest lies in deep Jurassic age reservoirs, hence there has been little investigation into the overlying Quaternary sediments. IODP expeditions 356 (Groeneveld et al., 2021) and 363 (Rosenthal et al., 2018) coring sites are located proximal to the Scott Plateau, but biostratigraphic data is not sufficient to characterise the Quaternary. Consequently, well data acquisition has been predominantly focused on deeper strata with an absence of interpretations or age control above the 4.0 Ma marker (U7) (Rankey, 2020; Thronberens et al., 2022).

3.1. Well data

A total of 9 wells and 17 boreholes (Fig. 2) have investigated the subsurface of NSR and SSR since 1971 for resource exploration and scientific investigation. Wireline data, specifically Gamma Ray (GR), density and sonic logs are available in the shallow sections for all wells and are used in this study in conjunction with sequence stratigraphy to infer sediment facies. Constrained U/Th ages are taken from NSR reef crest at 201.5 m (NR SE HDD3-JA) and 200.5 m (NR SE BH1 HDD-J) and SSR reef crest at 201.7 m (SR NE HDD1-J) and SSR lagoon at 180 m depth (SR SE BH6-J) (Fig. 2C). However, only SR SE BH6-J and NR SE HDD3-JA boreholes intersect seismic data and could be used to complement seismic stratigraphy interpretations and infer ages (i.e., Table 1).

3.2. Seismic data

The depth seismic data Megator 3D (Fig. 4) covers an area of ca. 1500 km^2. The mega-survey is a reprocessed (2014) and merged volume of six adjacent separate surveys acquired over several years. The Torosa 3D MSS and Dacey 3D MSS cover the deep, ocean waters to the North-east and West of Scott Reefs. The Maxima 3D MSS covers the south reef lagoon and inter-reef channel. The North reef is covered by the Gigas 2D MSS, Tridacna 3D OBC survey and Rosebud 3D MSS survey. The six separate surveys were combined into one contiguous, well imaged, easily interpreted structurally and amplitude reliable 3D dataset, named Megator 3D. Spectral content, phase and amplitude levels were matched to the Tridacna survey, which was shot on a 25 m × 25 m bin spacing.

3.3. Seismic interpretation

A standard model independent, seismic stratigraphic approach was applied to interpret key seismic unconformities bounding seismic sequences (sensu Mitchum and Vail, 1977; Vail et al., 1977; Emery et al., 1996; Paumard et al., 2017; Paumard et al., 2019a; Paumard et al., 2019b; Posamentier et al., 2022). Seismic interpretation of the 3D Megator depth converted volume was conducted in Petrel™ and Paleoscan™ software. Key reflectors were identified and mapped on the seismic data (Fig. 3A), based on reflector discontinuity, geometry, amplitude and frequency. This was done initially in 2D on four main master inlines and crosslines separately for NSR and SSR. Firstly, in Petrel™, the major unconformities were interpreted on one primary inline and one primary crossline for NSR and SSR, then correlated in 3D every 10th crossline/inline and finally auto-tracked throughout the volume. The key seismic horizons were then gridded in depth and depth structure and depth thickness maps (isopach's) were created. Sediment preservation rates were then calculated by dividing 3D unit thickness (U1–U14) by time (Ma). The isopach maps were also used to identify paleo highs for nucleation sites of *in situ* carbonate production. Seismic facies analysis was conducted based on the reflection properties; seismic amplitude, internal configuration, external geometry, reflection continuity and reflection terminations, as well as associations with other seismic facies.

A full volume 3D seismic interpretation of Megator 3D was then conducted in Paleoscan ™ software via a three-step process as outlined in detail by Paumard et al. (2019a) and Saqab (2016). A 3D model grid was generated using algorithms that semi-automatically track adjacent similar seismic traces (Fig. 3B) to generate a continuous relative geological time model, also referred to as a 3D Geomodel (Fig. 4). This model was then checked and any issues identified were resolved by manually refining key surfaces within the model-grid, before generating a new 3D geomodel. This iterative loop was repeated until the best solution was achieved. From the 3D Geomodel, hundreds of 3D seismic horizons were extracted within horizon stacks allowing the user to pan through vertically (i.e., depth domain) the entire stratigraphy of the depositional system. Several attributes were calculated along each horizon, allowing a multi-attribute analysis (sensu Posamentier et al., 2022): variance attribute, high pass frequency filter, RMS amplitude and spectral decomposition. Thus, using the principles of seismic geomorphology, the distribution of seismic amplitudes and depositional geometries are interpreted in plan-view throughout the 3D volume.

4. Results

4.1. Seismic stratigraphic framework

A total of 14 seismic unconformities (H1–H14) bounding 14 seismic

Table 1
Table showing ages of stratigraphic events.

Stratigraphic event*	Period	Name	Dating method	87 Sr/86SR	Age (Ma)*	Depth (mbRT)	Well/Borehole*	Reference/Comment
H14	**L. Pleistocene-3**	**LPl-3**	**U/Th**	/	**0.098 MIS1 (?)**	/	**SR SE BH6-J**	**Collins and Testa (2009)**
H13	**L. Pleistocene-2**	**LPl-2**	**U/Th**	/	**0.392 MIS11(?)**	/	**SR SE BH6-J**	**Collins and Testa (2009)**
H12	**L. Pleistocene-1**	**LPl-1**	**U/Th**	/	**0.578 MIS13(?)**	/	**NR SE HDD3-JA**	**Collins and Testa (2009)**
H11	M. Pleistocene-2	MPl-2	SS	/	ca.0.6	/	SR-1	This study
H10	M. Pleistocene-1	MPl-1	SS	/	ca.0.8	/	SR-1	This study
H9	L. Pliocene	BQua	SS	/	ca.1–.0.8	/	SR-1	This study
H8	M. Pliocene	MPlio	SS- Regional picks	/	ca.3.5	/	SR-1	This study; Gradstein et al. (2020); Powell (2020)
H7	E. Pliocene	BPlio	SS	/	ca.4.08	/	SR-1	This study
			Biostratigraphy	/	**3.7–4.37**	**790**	**NSR-1**	**Thronberens et al. (2022)**
H6	**L. Messinian**	**LMio**	**Sr-age/SS-Regional picks**	**0.709003**	**5.8**	**910**	**NSR-1**	**Thronberens et al. (2022)**; Gradstein et al. (2020); **Powell (2020)**
H5	L. Tortonian	LTor	SS	/	ca.7.2	1032	NSR-1	This study
H4a	M. Tortonian	MTor	SS	/	ca.9.7	1228	NSR-1	This study
H4	**M. Tortonian**	**MTor**	**Sr-age**	**0.708861**	**10.8**	**1305**	**NSR-1**	**Thronberens et al. (2022)**
H3a	L. Serravallian	MMio	SS- Regional picks	/	ca.11.63	1492	NSR-1	This study; Gradstein et al. (2020); Powell (2020)
H3	**Serravallian**	**MMio**	**Sr-age**	**0.708816**	**12.9**	**1565**	**NSR-1**	**Thronberens et al. (2022)**
H2	Langhian	EMio	SS/SS- Regional picks	/	ca.15.9	1686	NSR-1	This study; Gradstein et al. (2020); Powell (2020)
			Sr-age	**0.708616**	**17.7**	**1830**	**NSR-1**	**Thronberens et al. (2022)**
H1	**Burdigalian**	**BMio**	**Sr-age**	**0.708567**	**18.3**	**1940**	**NSR-1**	**Thronberens et al. (2022)**
Biostratigraphy								
N19 S. dehiscens-G. altispira			Biostratigraphy		3.7–4.37	790	NSR-1	Heath (1982)
X Pulleniatina sinis. -random.	E. Pliocene	LMio	Biostratigraphy		4.08	802.5 +- 12.5	NSR-1	Belde et al. (2017)
LO Globoturborotalita nepenthes	L. Messinian	LMio	Biostratigraphy		4.37	867.5 +- 7.5	NSR-1	Belde et al. (2017)
FO Globorotalia tumida	L. Messinian	LMio	Biostratigraphy		5.57	912.5 +- 7.5	NSR-1	Belde et al. (2017) Pacific Calibration
LO Globorotalia lenguaensis	L. Messinian	LMio	Biostratigraphy		6.14	942.5 +- 7.5	NSR-1	Belde et al. (2017) Pacific Calibration
FO Pulleniatina primalis	L. Messinian	LMio	Biostratigraphy		6.60	957.5 +- 7.5	NSR-1	Belde et al. (2017)
Flosculinella bontangensis	Langhian	EMio	Biostratigraphy		14.24–15.1	1600–1960	NSR-1	Belde et al. (2017)
LO Lepidocyclina (Eulepidina) badjirraensis	Burdigalian	BMio	Biostratigraphy		17.54	2298.0 +- 4.0	NSR-1	Chaproniere et al. (1996), core reports assumed LO in the Late Aquitanian

Inferred stratigraphic ages from seismic stratigraphy study. In bold are ages from biostratigraphy data taken from literature and well data (NOPIMS) and well completion reports (Geoscience Australia). Uncertain U/Th ages are taken with permission (WEL) from grey literature (Collins & Testa, 2009) and are from boreholes positioned on the platform margin, suggesting large error and uncertainty. Note: For the strontium isotope dating, sidewall cores of North Scott Reef-1 (NSR-1) were sampled at the Geoscience Australia Core Repository in Perth, Australia. *Sr-ages analysed for this study are presented based on the work of Thronberens et al. (2022) which uses work from Gradstein et al. (2004) and are normalized to the NBS987 standard 87Sr/86Sr = 0.710248. †For the whole-rock–based Sr-ages, the uncertainty is estimated at ±1 Ma. Biostratigraphic data for North Scott Reef-1 (NSR-1) documented in the well completion reports is taken from Heath (1982) via Thronberens et al. (2022), Belde et al, (2017) and this study. All samples were taken from sidewall cores with the exception of No. 21 in NSR-1, which was taken from ditch cuttings. All datums are given in mbRT/mbKB, and all reported absolute ages are based on the Gradstein et al. (2012) timescale. For stratigraphic events the datum has been averaged over the interval in which the event is present. LO, last occurrence.

sequences (U1–U14) have been mapped across the 3D seismic survey (Table 1, Figs. 5 and 6). Identification of these unconformities is based on geomorphologic (i.e., plan view) and cross section (i.e., vertical domain) interpretations, including, amplitude strength, stratal stacking patterns (progradational, aggradational and retrogradational), and reflection terminations.

The water bottom reflector of the Megator 3D seismic survey (Fig. 2) was also mapped. In combination with other data (multibeam, AUV, satellite, Allen Coral Atlas), the seafloor reveals that the modern benthic habitat around Scott Reefs is characterised by an inter-reef channel, a large debris fan, moats, sediment drifts and deep-sea feeder canyons that are present throughout the Plio-Quaternary. A large debris fan sits at the NE margin of SSR (U11, Fig. 9) approximately 10 km in length. The seafloor to the East of the reefs is characterised by carbonaceous sediment drifts, including sediment waves and moats surrounding the NSR and SSR base of slopes.

This study builds upon the established Browse Basin stratigraphic framework for the Miocene (Table 1) (Hull, 1998; Hull and Griffiths, 2002; Rosleff-Soerensen et al., 2012, 2016; Marshall and Lang, 2013; Belde et al., 2015; Saqab and Bourget, 2015; Belde et al., 2017; Van Tuyl et al., 2019; McCaffrey et al., 2020; Rankey, 2020; Thronberens et al., 2022). Nomenclature is adopted from Thronberens et al. (2022) for the Miocene, and from Saqab (2016) for the Quaternary. The same nomenclature pattern is adopted for new seismic sequences identified in

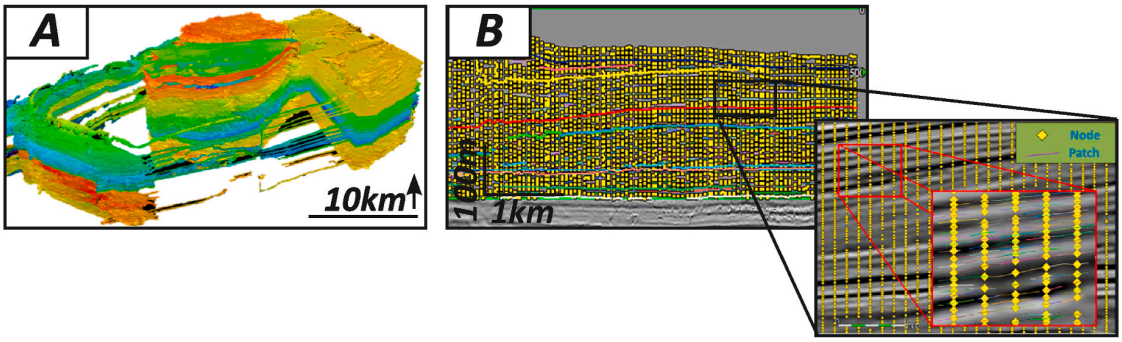


Fig. 3. (A) 14 seismic unconformities interpreted in Petrel based on identification of onlap, downlap, toplap and erosional truncations. An independent depth colour scale applies to each horizon. Model grid computation process: initial model grid (B) showing nodes and patches that are computed based on similarity of wavelets and their relative distances. Each node in the grid represents an elementary horizon patch. A dense node grid was selected for this study to compensate for regions of significant local thickening.

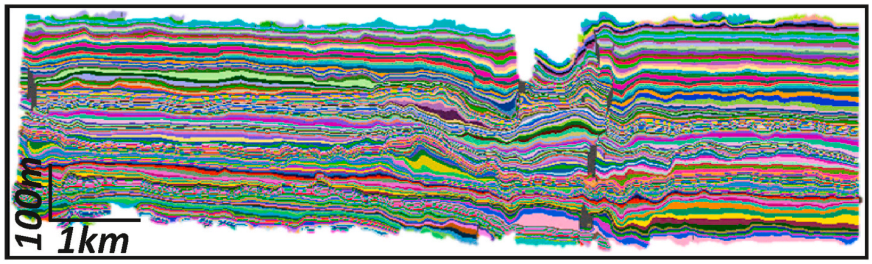


Fig. 4. Preview of final model grid for Plio-Quaternary sequence over NSR and SSR, represented by a multi-colour scale to demonstrate time correlative surfaces (Saqab, 2016).

the Quaternary, (i.e., H1–H14 and U1–U14). H1–H14 are defined based on identification of seismic unconformities. H1–H7 are then calibrated to well 'North Scott Reef-1 (NSR-1)' using Gamma Ray (GR) logs and depths of bounding surfaces taken from literature to determine age (Table 1). No depths or ages have been interpreted thus far for H8–H14; therefore, new interpretations have been made based on seismic reflectivity character and GR well log data responses (sensu Gallagher et al., 2014; Saqab and Bourget, 2015) calibrated to well Scott Reef-1 (SR-1). H12–H14 are further calibrated to uncertain U/Th ages (Collins and Testa, 2009). Detailed descriptions and thicknesses of U1–U14 can be found in *Supplementary data 1_Results*.

4.1.1. Seismic unit 1

(U1 Burdigalian – BMio) Seismic unit U1 (ca. 18.3–15.6 Ma) is bounded by H1 at the base (1940 mbRT) and H2 at the top (1720 mbRT) (Figs. 5 and 6). H1 is a regional high amplitude reflector associated with onlap and downlap reflection terminations above.

4.1.2. Seismic unit 2

(U2 Langhian – EMio) Seismic unit U2 (ca. 15.6–12.9 Ma) is bounded by H2 at the base (1720 mbRT) and H3 at the top (1565 mbRT) (Figs. 5 and 6). H2 is a very high amplitude continuous reflector, truncating underlying strata, with some apparent downlap from overlying strata.

4.1.3. Seismic unit 3

(U3 Serravallian – MMio) Seismic unit U3 (ca. 12.9–10.8 Ma) is bound by H3 at the base and H4 at the top (1305 mbRT) (Figs. 5 and 6). H3 is a very high amplitude, continuous reflector throughout the area and is associated with onlap in the slope margin and occasional toplap in the inner slope.

4.1.4. Seismic unit 4

(U4 E-M. Tortonian – ETor) H4 is very high amplitude, continuous reflector and constitutes a major downlap surface, though some onlaps are seen along the slope margin.

4.1.5. Seismic unit 5

(U5 Late Tortonian – LTor) Seismic unit U5 (ca. 980 mbRT) is bounded by H5 at the base and H6 at the top (910 mbRT) (Table 1, Figs. 5 and 6). H5 is a high amplitude continuous reflector associated with downlapping sediments above and some apparent truncation of strata below, including draping over prograding sigmoidal clinoforms.

4.1.6. Seismic unit 6

(U6 L. Messinian – LMio) Seismic unit U6 (ca. 5.5–4.37 Ma) is bounded by seismic unconformity H6 at the base (ca. 940 mbRT), which marks the maximum lowstand of the Late Messinian and H7 at the top (ca. 790 mbRT). H6 is a very high amplitude reflector and constitutes a toplap surface of reflectors below. It is a major downlap surface to the North of SSR.

4.1.7. Seismic unit 7

(U7 E.Pliocene – BPlio) Seismic unit U7 is bound by H7 at the base (ca. 3.7–4.37 Ma) and H8 at the top (ca. 2.5 Ma). H7 is a weak to medium amplitude, highly continuous, parallel reflector with onlapping sediments.

4.1.8. Seismic unit 8

(U8 M. Pliocene – MPlio) Seismic unit U8 (ca. 3.5 Ma) is bounded by H8 at the base and H9 at the top (ca. 1–0.8 Ma). H8 is a weak to medium amplitude, continuous reflector with onlapping sediments away from modern day Scott Reefs, and a low-medium, semi-continuous reflector beneath SSR and a very high amplitude, continuous reflector below NSR.

4.1.9. Seismic unit 9

(U9 L. Pliocene-E. Pleistocene – BQua) Seismic unit 9 (ca. 1–0.8 Ma)

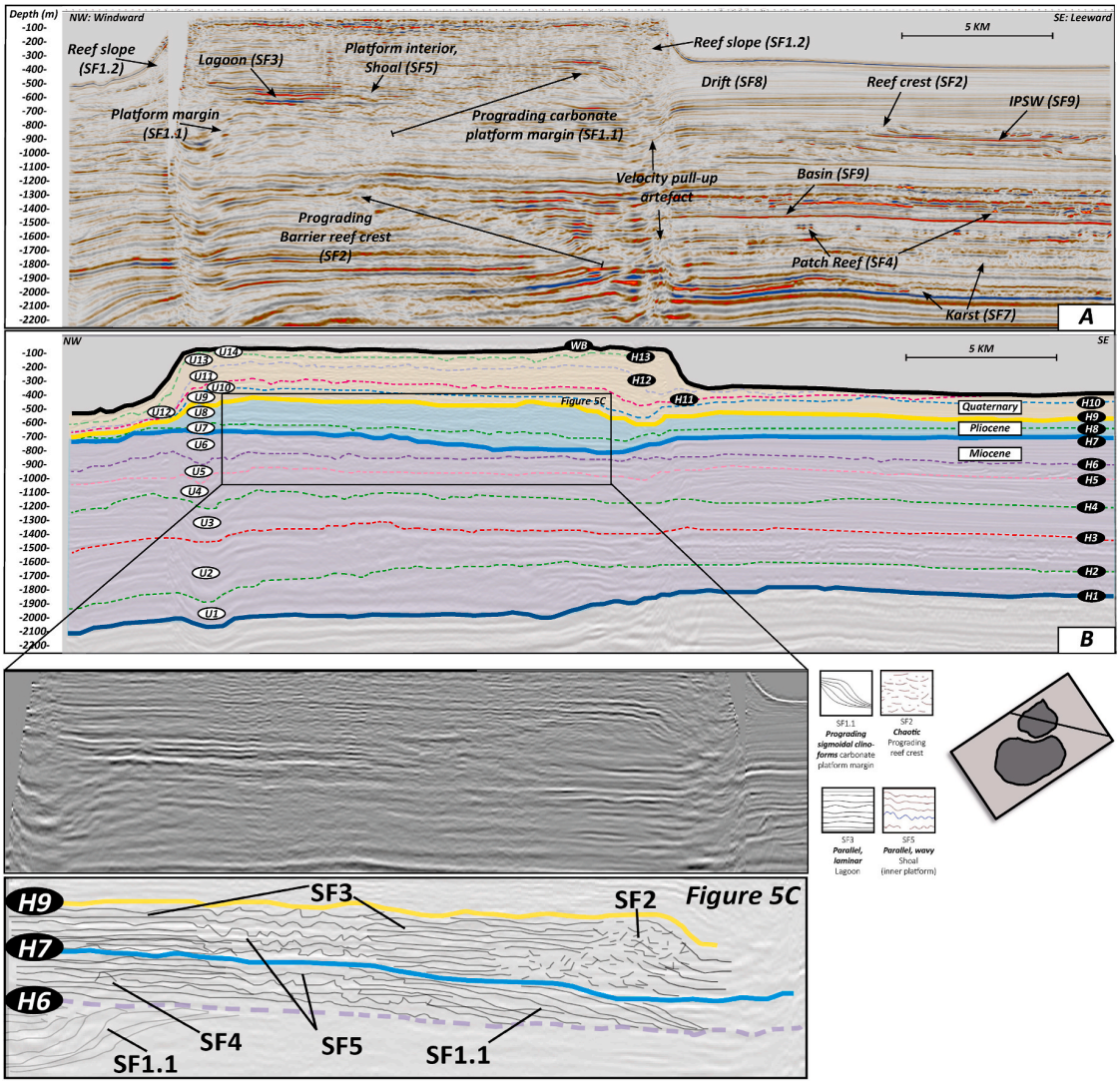


Fig. 5. Uninterpreted cross section sketch of South Scott Reef along Profile B in Fig. 2. Top figure shows seismic facies on original seismic reflectivity data. Middle figure shows sketch of picked horizons H1–H14 and seismic units U1–U14 with Miocene, Pliocene, Quaternary strata in colour overlaid on grey scale seismic reflectivity section corresponding to top profile. Fig. 5C below shows zoomed in section of interpreted seismic facies and corresponding depositional environments.

is bound by H9 at the base and H10 at the top. H9 is a medium to high amplitude semi continuous reflector with some onlap above.

4.1.10. Seismic unit 10

(U10 Mid Pleistocene – MPl-1) Seismic unit U10 (ca 0.0.8–0.6 Ma) is bound by H10 at the base and H11 at the top. H10 NSR is a high amplitude, continuous, reflector with onlap above and toplap below (Table 2). H10 SSR is a continuous weak to medium amplitude reflector with wavy undulating topography.

4.1.11. Seismic unit 11

(U11 Mid Pleistocene – MPl-2) Seismic unit U11 is bound by H11 at the base and H12 at the top. H11 NSR is a medium to high amplitude, continuous surface that sits topographically lower than H11 SSR. H11 SSR is a medium to high amplitude, wavy, semi-continuous surface with onlap above and toplap below.

4.1.12. Seismic unit 12

(U12 Late Pleistocene-2 – LPl-2) Seismic unit 12 is bound by H12 at the base and H11 at the top. It is a medium to high amplitude semi-continuous reflector that varies laterally across NSR and is disturbed in the centre by high amplitude, wavy, discontinuous reflectors.

4.1.13. Seismic unit 13

(U13 Late Pleistocene-2 – LPl-2) Seismic unit 13 is bound by H13 at the base and H14 at the top. H13 NSR is a high amplitude, moderately continuous reflector, characterised by a bucket shape morphology, including raised margins (Harris et al., 2015). H13 SSR is a very high amplitude reflector truncating toplap sediments below (Table 2).

4.1.14. Seismic unit 14

(U14 Late Pleistocene-3 – LPl-3) Seismic unit U14 (ca. 115 mbRT) is bounded by H13 at the base and water bottom at the top (present day seafloor, ca. 41 mbRT NSR and ca. 61 mbRT SSR). H14 NSR is a very high amplitude, semi-continuous reflector, up to 20 m thick and occasionally disrupted by the above water bottom due to velocity pull-ups. H14 SSR is a high amplitude continuous reflector truncating below strata and lies parallel to the seabed.

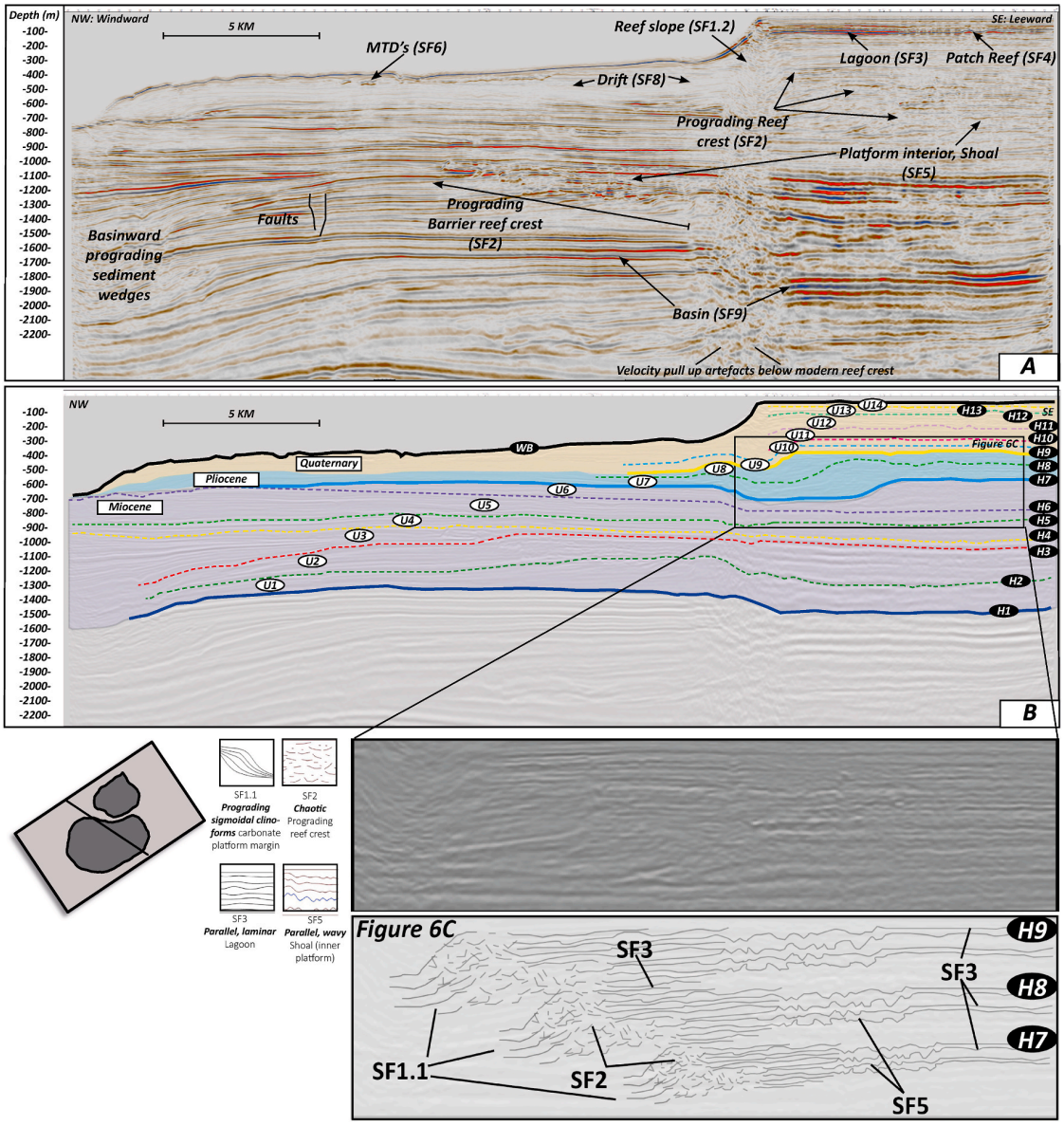


Fig. 6. Uninterpreted cross section sketch of South Scott Reef along Profile B in Fig. 2. Top figure shows seismic facies on original seismic reflectivity data, middle figure shows sketch of picked horizons H1–H14 and seismic units U1–U14 with Miocene, Pliocene, Quaternary strata in colour overlaid on grey scale seismic reflectivity section corresponding to top profile. Fig. 6C below shows zoomed in section of interpreted seismic facies and corresponding depositional environments.

4.2. Seismic facies analysis

Nine main seismic facies were identified and described (Fig. 7; Table 3) based on the reflection properties, including (1) amplitude; (2) internal configuration; (3) external geometry; (4) continuity; and (5) associations with other adjacent seismic facies. Due to significant differences in seismic quality over NSR and SSR, in some cases, a separate description is required for the same seismic facies' interpretation below each reef. (See *Supplementary data 1_Results* for full interpretations.)

4.2.1. Seismic facies 1 (SF1): clinoforms with sigmoidal (SF1.1) and parallel (SF1.2) configuration

Seismic facies SF1 is composed of medium amplitude seismic reflectors, with mounded sigmoidal clinoform external geometries, and high-angle inclined prograding strata reflectors downlapping underlying strata. SF1.1 displays sigmoidal internal configurations of lower amplitude and transition to SF3 or SF5 towards the platform interior. SF1.2 shows parallel clinoform patterns that develop basinward into SF6, SF8 or SF9.

4.2.2. Seismic facies 2 (SF2): mounded seismic reflectors (platform margin)

Seismic facies SF2 represents mounded seismic reflectors that occur specifically along a platform margin.

4.2.3. Seismic facies 3 (SF3): horizontal parallel seismic reflectors (platform interior)

Seismic facies SF3 constitutes sub-parallel to parallel, continuous, and high amplitude seismic reflectors that occur in the platform interior associated with SF4.

Table 2
Descriptions and justification for stratigraphic events.

Stratigraphic event	Seismic unit	Amplitude	Polarity	*Reflection terminations*	Dip	Thickness (NSR-1)	Continuity	Regional correlations & surface type
H14	U14	V.high (NSR), high (SSR)	Peak	Truncation below (NSR, SSR)	/	Variable, ca.20–80 m	Semi-continuous (NSR), continuous (SSR)	***Erosional unconformity***
H13	U13	Variable weak-high (NSR), variable weak-v. high (SSR)	Peak	Onlap above, toplap below (NSR), occasional toplap truncation (SSR), occasionally incoherent	/	Variable	Moderately continuous away from noise	***Erosional unconformity***
H12	U12	Variable medium-high (NSR, SSR)	Peak	Onlap above, toplap below (NSR, SSR)	/	Highly variable	Variable Semi-continuous-discontinuous (NSR, SSR)	***Sequence Boundary***
H11	U11	Medium-high (NSR, SSR)	Peak	Onlap above, toplap below (NSR, SSR)	SE dip	Highly variable	Continuous (NSR), semi-continuous (SSR)	***Maximum flooding surface, Mid Pleistocene Transition***
H10	U10	High (NSR), weak-medium (SSR)	Peak	Onlap above, toplap truncation below	/	Highly variable, topographic variation	Continuous	***Erosional unconformity***
H9	U9	Medium-high	Peak	Onlap above	/	Variable	Semi-continuous	***Sequence Boundary, Pliocene-Pleistocene boundary***
H8	U8	Weak-medium (East), low-medium (SSR), v. high (NSR)	Peak	Onlap above (East), onlap above, toplap below (NSR), uncertain (SSR)	/	Variable	Continuous (East), semi-continuous (SSR), very continuous (NSR)	***Maximum flooding surface, major regional unconformity, T45.2 MFS (TPL)***
H7	U7	Weak-medium	Peak	Draping onlap	/	Highly variable below NSR, SSR	Highly continuous	***Sequence Boundary, Miocene-Pliocene boundary***
H6	U6	Very high	Trough	Toplap below, onlap above (regional highs), Major downlap surface (N SSR)	/	940-790mbRT	Continuous	***Sequence Boundary, T40.0 SB (TM1), SB/TS-LST, Top of Cartier/ Oliver fm or base Barracouta***
H5	U5	High	Peak	Downlap above, truncation below	Basinward prograding	980-910mbRT	Continuous	***Sequence Boundary***
H4	U4	Very high	Trough	Major downlap surface	Basinward	1405-980mbRT	Continuous	***Maximum flooding surface***
H3	U3	Very high	Peak	Onlap (slope margin), toplap (inner slope)	Basinward	1565-1405mbRT	Continuous	***Sequence Boundary***
H2	U2	Very high	Peak	Truncation below, downlap above	Basinward	1720-1565mbRT	Continuous	***Sequence Boundary, T35.0 SB (TM2), BB2***
H1	U1	High	Peak	Toplap (Slope margin), truncation (inner shelf)	Basinward	1940-1720mbRT	High (Slope), medium-Low (inner platform)	***Sequence Boundary, BB1***

Details outlining the stratigraphic significance and justification for interpreting horizons H1-H14. This includes amplitude strength, seismic polarity, reflection termination relationships between above and below strata, general observed regional or local dip of the horizon, approximate thickness observed in NSR-1 for H1-H6 and general comments for H7-H14. Seismic reflection continuity and the general surface type is given, (i.e., unconformity, sequence boundary, maximum flooding surface), and if the interpreted horizons correlate to known regional stratigraphic events.

4.2.4. Seismic facies 4 (SF4): mounded seismic reflectors (platform interior)

Seismic facies SF4 corresponds to mounded seismic reflectors interpreted in the platform interior.

4.2.5. Seismic facies 5 (SF5): chaotic seismic reflectors (platform interior)

Seismic facies SF5 is a semi-discontinuous chaotic, wavy, medium to low amplitude facies that is regarded here as transitional.

4.2.6. Seismic facies 6 (SF6): chaotic seismic reflectors (platform slope)

Seismic facies SF6 is a very chaotic, seismic facies that is seen occasionally on both the proximal and distal platform slope.

4.2.7. Seismic facies 7 (SF7): concave-up seismic reflector

Seismic facies SF7 are sub-circular concave-down seismic reflectors that are easily identified by negative V-shaped depressions and occasionally chimney-like features.

4.2.8. Seismic facies 8 (SF8): double dipping seismic reflector

Seismic facies SF8 is composed of weak reflectors that are identified by double onlapping terminations.

4.2.9. Seismic facies 9 (SF9): parallel seismic reflectors surrounding platform

Seismic facies SF9 includes parallel seismic reflectors surrounding the platforms in a deep-sea setting.

4.3. Seismic geomorphology

Nine main seismic geomorphologic patterns (GP1-10) were identified (Fig. 8; Table 4), based on seismic attributes (e.g., variance, spectral decomposition, RMS amplitude and high pass frequency filters). GP1-GP9 are described with respect to their position basinward or landward of identified carbonate platforms. (See *Supplementary data 1_Results* for full interpretations.)

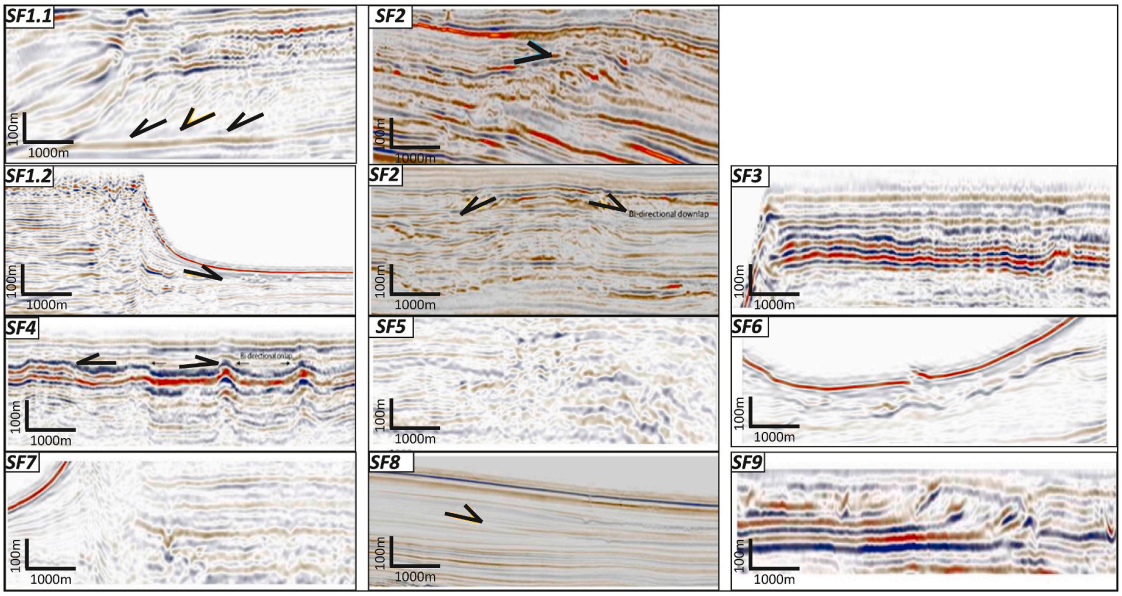


Fig. 7. Figures of various seismic sections summarising seismic facies 1 (SF1) to seismic facies 9 (SF9) observations, seismic character and depositional environment. Arrows indicate onlap (SF2, SF4) and downlap (SF1.1, SF1.2, SF2, SF8).

4.3.1. Geomorphologic pattern 1 (GP1.1 and GP1.2) – medium to steep gradient feature

Geomorphologic pattern GP1.1 occurs basinward along a continuous margin identified on variance attribute. In plan view, a linear, sinuous edge can often be detected.

4.3.2. Geomorphologic pattern 2 (GP2) – curvi-linear feature (platform margin)

Geomorphologic pattern GP2 is interpreted along the platform margin as a continuous sinuous to linear pattern or as a curved, stepped morphology with occasional concentric growth rings.

4.3.3. Geomorphologic pattern 3 (GP3) – sub-circular to elongate feature (platform interior)

Geomorphologic pattern GP3 displays a very high amplitude and frequency and no character in variance attribute. The plan view feature displays little character variation and is associated with a sinuous, irregular circumference with only a gentle change in gradient on high pass filters.

4.3.4. Geomorphologic pattern 4 (GP4) – circular to sub-circular feature (platform interior)

Geomorphologic pattern GP4 is identified by general circular to sub-circular features with locally steep gradients and sub-circular discrete features on variance attribute plan view.

4.3.5. Geomorphologic pattern 5 (GP5) – discrete, patchy, grouped features (platform interior)

Geomorphologic pattern GP5 displays low to medium amplitude and frequency and occasional significant gradient variation.

4.3.6. Geomorphologic pattern 6 (GP6) – chaotic feature (platform margin)

Geomorphologic pattern GP6 is characterised by irregular low to high amplitude and frequency, identified in plan view by chaotic disturbed regions.

4.3.7. Geomorphologic pattern 7 (GP7) – sub-circular to linear features (platform interior)

Geomorphologic pattern GP7 is identifiable by sub-circular discontinuities, and occasional sinuous features in plan view.

4.3.8. Geomorphologic pattern 8 (GP8) – uniform, sinuous feature

Geomorphologic pattern GP8 occurs as a weak to medium amplitude and low frequency, uniform geomorphologic pattern, with an unidentifiable gradient in plan view.

4.3.9. Geomorphologic pattern 9 (GP9) – uniform feature surrounding platform

Geomorphologic pattern GP9 is a high amplitude, low frequency feature with uniform, homogeneous geometry in plan view surrounding the carbonate platforms.

5. Interpretation

Table 5 provides a summary of 9 depositional environments interpreted from analysis of 9 seismic facies (SF1 – SF9) and 9 geomorphologic patterns (GP1-GP9). These environments have been defined from seismic attribute analysis and relevant ancient and modern analogues, giving context and support to proposed interpretations. The recognition of geologically significant patterns is made in section view (depth domain), i.e., stratigraphic analysis; SF1-SF9, and plan (map) view, (spatial domain), i.e., geomorphological analysis; GP1-GP9. Combinations of SF and GP are used to provide interpretations of the depositional environment. The paleogeography is identified throughout 14 main paleogeographical units, separated into Miocene, Pliocene and Quaternary sequences that are bounded by the major identified unconformities.

5.1. Interpretation of depositional environments

SF1.1 and GP1.1 are interpreted as prograding carbonate platform margins. Similar scales and morphology of these environments are made in the Browse basin (i.e., Table 5; Rosleff-Soerensen et al., 2012). SF1.2 and GP1.2 are interpreted to be reef slope facies based on the context of their geomorphology and associated facies (Table 4). The map view is

Table 3
Description of seismic facies SF1-SF9 and interpreted depositional environment.

Seismic Facies	Reflection Characteristics (a) External geometry (b) Internal configuration (c) Amplitude strength (d) Continuity (e) SF Associations	Depositional Environment
SF1: clinoforms; SF1.1: sigmoidal, ***SF1.2***: parallel	(a) Sigmoidal (b) High angle prograding (c) Medium (d) Semi-continuous (e) SF3, SF5, SF8(?), SF9	***SF1.1: Prograding carbonate platform margin; SF1.2: Reef slope***
SF2: mounded seismic reflectors (platform margin)	(a) Mounded, positive topographic relief (b) Parallel to chaotic (c) Weak - high (d) Semi-continuous (e) SF1.2, SF3, SF9	***Barrier Reef or Reef crest***
SF3: horizontal parallel seismic reflectors (platform interior)	(a) Sheet to wavy (b) Horizontal parallel to sub-parallel (c) Very high (d) Continuous (e) SF1.1, SF2, SF4, SF5, SF7	***Lagoon***
SF4: mounded seismic reflectors (platform interior)	(a) High relief, double downlap (b) Mounded, convex-up (c) Medium - high (d) Continuous (e) SF3, SF5, SF7	***Patch Reef***
SF5: chaotic seismic reflectors (platform interior)	(a) Chaotic (b) Wavy (c) Medium - low (d) Semi- continuous (e) SF2, SF3, SF4, SF9	***Back Reef Shoal (transitional facies)***
SF6: chaotic seismic reflectors (platform slope)	(a) Very chaotic, disturbed to irregular (b) high-angle, occasionally sigmoidal downlap, truncations (c) Moderate (d) Chaotic to semi-continuous (e) SF1, SF8, SF9	***Mass Transport Deposits (MTD)***
SF7: concave-down seismic reflector	(a) Sub-circular to negative V-shaped depression, chimney-like, concave down (b) chaotic, patchy (c) medium (d) semi-continuous (e) SF3, SF4	***Karst***
SF8: double dipping seismic reflector	(a) Parallel downlapping (b) Dipping (c) Continuous (d) Weak - medium (e) SF6, SF1.2	***Drift***
SF9: parallel seismic reflectors surrounding platform	(a) Horizontal, parallel to sub-parallel, concave up (b) Sheet, some dip (c) High (d) High continuity (e) SF2	***Basin or Inter-platform Seaways (IPSW)***

Table of seismic facies descriptions and interpretations corresponding to Fig. 7.

represented by steep contours and relief change on high pass seismic attribute. Dark shading, which represents steeper relief, is immediately adjacent to light shading, which represents shallow relief. This is interpreted as a visible gradient change (GP1.2, Fig. 8).

SF2 and GP2 represents a barrier reef crest or isolated reef crest, i.e., *in situ* reef building facies as opposed to lagoon infilling, that commonly occur on topographic highs, either aggrading, prograding or backstepping. Seismic attributes show that GP2 can be either linear in plan view (i.e., barrier reef front), or sub-circular and/or elongate, (i.e., ICB development). GP2 occurs as high amplitude on envelope seismic attribute (GP2, Fig. 8; Table 4). This interpretation is consistent with other reefal carbonates interpreted along the NWS (Burgess et al., 2013; McCaffrey et al., 2020) that display typical reefal stacking patterns or mound shapes that are prominent seismic reflectors, either prograding, aggrading or backstepping. SF2 (barrier reef) initiates above or prior to H1 as an aggradational sequence with small patch reefs and subsequently progrades basinward in a keep up phase.

SF3 and GP3 are identified as a lagoon depositional environment and corresponds to interpretations made by Rosleff-Soerensen et al. (2012) in the Browse Basin. SF3 is consistently associated with mound shaped patch reefs throughout the Miocene and the larger ICB development in the Plio-Quaternary. Seismic facies SF3 can be difficult to distinguish from SF8 (basin), however, correctly recognising adjacent facies associations allows for consistent interpretations. The seismic character does indicate a relatively lower energy sedimentary environment, perhaps due to enclosed reef crests protecting the inner lagoons from heavy swells and tides. Interestingly, SF3 facies can be interpreted as less 'wavy' in NSR Plio-Quaternary than SSR, perhaps due to the lack of recent reef crest in SSR, exposing it to the open ocean.

SF4 and GP4 are interpreted as patch reefs and since the early Miocene exhibit a diverse range of size (<20 m wide to >500 m wide), morphology and orientation as well as a range of seismic reflectivity characteristics, in part due to poor data quality. These facies can be misinterpreted as SF7/GP7 due to geomorphologic similarities in plan view and section view. The key differentiator however, is the sub-circular convex-up shape (SF4/GP4) rather than convex down (SF7/GP7). Pattern and size are the two criteria that help to interpret these correctly.

SF5 and GP5 are key transitional facies and is taken to represent back reef shoals where sediment is reworked (Fig. 8, GP5). Precise lateral and vertical transition of this facies is difficult to infer below SSR due to seismic noise. SF5 occurs in U3–U7 as reworked sediments below SSR where two large ICB's coalesce and the IPSW becomes isolated and more akin to lagoonal environments. The variation in reflectivity character is likely a result of varying currents and interaction with different ICB morphologies and orientations. The prevalence of SF5 below SSR and its relative lack below NSR suggest that throughout their evolutions, SSR has been exposed to open ocean conditions and sediment reworking more than NSR. NSR is protected by a topographically high, relatively wide reef crest. SF5 occurs around 1–2 km landward of the platform margins and is prevalent throughout the late Miocene to early Pleistocene, especially below SSR.

SF6 and GP6 are used to describe gravity-driven flows, such as MTD (mass transport deposits) and offbank sediment transport that are frequent throughout the stratigraphic succession. They most commonly occur at the base of toe of reef slope (Fig. 8, GP6; Table 4) reaching up to 10 km of run out distance, (e.g., modern day inter-reef debris fan (U11, Fig. 9)).

SF7 and GP7 are interpreted to be karst, e.g., Fig. 8, GP7; Table 4. They are easily mis-identified in the Miocene as SF4 (patch reefs), but in-context interpretation and identification of negative rather than positive relief structures differentiate them.

SF8 and GP8 surrounds carbonate platforms and are strongly controlled by ocean currents and associated with moats. They are present primarily to the east of SR's and extend for tens of kilometres and are interpreted to be hemipelagic carbonate, current-controlled drift sedimentation. There is a clear surface expression on modern bathymetric data of surface sediment waves, oriented in various directions indicating the presence of strong, dynamic bottom currents (Betzler et al., 2009) operating around Scott Reefs today.

SF9 and GP9 occurs predominantly basinward of all identified carbonate platforms and intermittently throughout the Miocene and Pliocene on the inner shelf during periods of continental flooding during highstands. They are interpreted to be low energy deep-water sediments deposited in a basin setting or deep seafloor environment.

5.2. Paleogeographic evolution of Scott Reefs

Six interpretative maps were designed (Fig. 9) to describe the evolution of Scott Reefs from the Burdigalian to the Middle Pleistocene. *Supplementary data 2_Interpretation* is available to provide a more complete and detailed interpretation of the Carbonate factory Phases I-IV below.

5.2.1. Miocene (U1–U6)

The Miocene seismic sequence consists of U1–U6 and is characterised

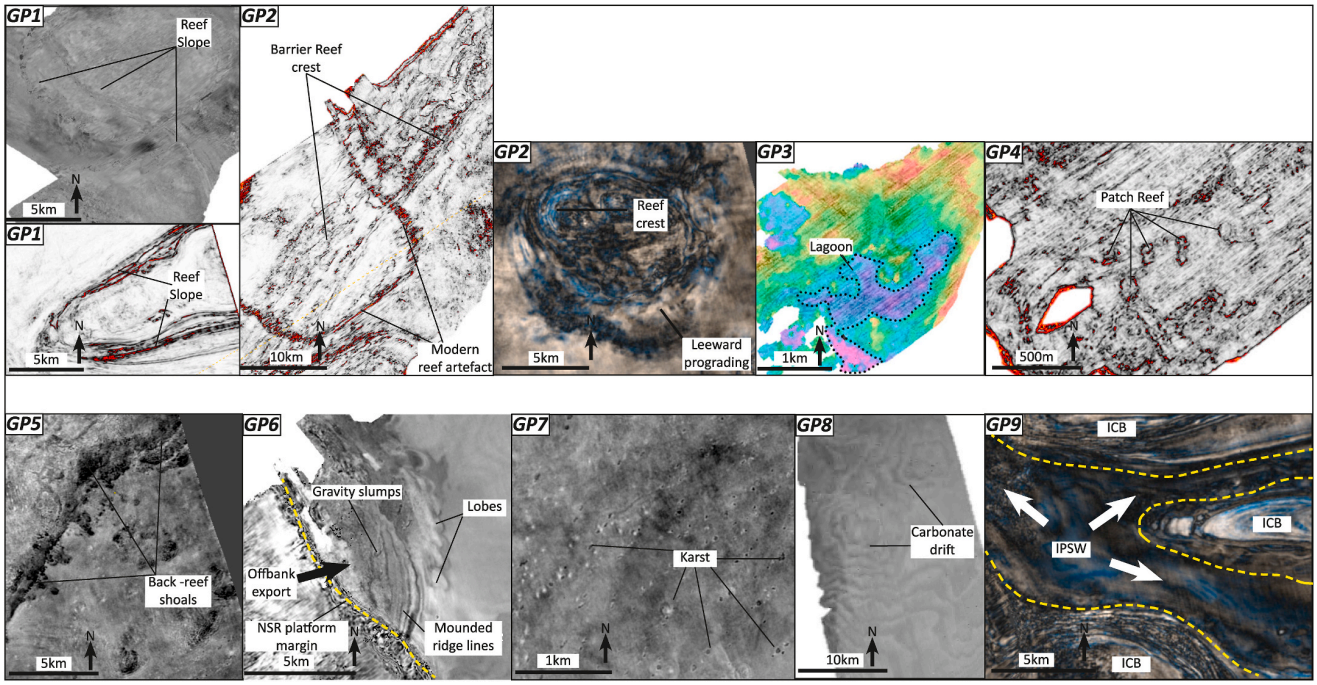


Fig. 8. Figures of various seismic attributes in plan view summarising Geomorphologic pattern 1 (GP1) to Geomorphologic pattern 9 (GP9). GP1 are interpreted as prograding carbonate platform margins, GP2 represents a barrier reef crest or isolated reef crest, GP3 are identified as a lagoon depositional environment, GP4 are interpreted as patch reefs. GP5 represent back reef shoals, GP6 are used to describe gravity-driven flows, such as MTD's, GP7 are interpreted to be karst, GP8 are interpreted to be hemipelagic carbonate drift sediments, GP9 are basin sediments.

by a prograding barrier reef system. There is an apparent inner platform reef evolution from; small patch reefs, to small ICB's, and to larger ICB's that eventually coalesce in the mid to late Miocene, and finally to larger carbonate reef platforms. This is consistent with Browse Basin literature (Rosleff-Soerensen et al., 2012; Van Tuyl et al., 2019; McCaffrey et al., 2020; Riera et al., 2022). Preceding the Miocene (not investigated in this study) is the development from a ramp-type to a rimmed platform, which has prepared the shelf for tropical reef growth by stabilization and formation of hardgrounds. This is regarded as a common pattern for carbonate shelf evolution (Schlager, 2005; Rosleff-Soerensen et al., 2012; Saqab and Bourget, 2015; Paumard et al., 2019b; Riera et al., 2019).

Carbonate factory phase I

5.2.1.1. Seismic unit U1. Burdigalian (B. Mio) H1 is interpreted as a sequence boundary that marks a regional transition from a carbonate ramp setting to an aggradational phase. This transition is associated with coralgal community growth and isolated carbonate build-up development on the inner platform (Saqab, 2016). Seismic Unit U1 (U1, Fig. 9) represents a range of carbonate depositional environments, including a barrier reef crest (GP2) >25 km in length, channels on the outer slope, and small patch reefs (SF4 and GP4) associated with lagoon facies (SF3 and GP3) and shoals (SF5 and GP5) in the inner carbonate platform.

5.2.1.2. Seismic unit U2. Langhian (E. Mio) (ca. 15.9 Ma, correlated to *T35.0 SB TM2*, Fig. 20). H2 is regional sequence boundary marking the base Langhian. It is conformable to the overlying strata and is part of a series of basinward (West) prograding, dipping packages. Seismic Unit U2 continues as a basinward prograding barrier reef system, leaving a stepped pattern of reef crest migration (Fig. 8, GP2; Table 4).

An increase in lagoonal sediment deposition is interpreted as evidenced by high amplitude reflectors in plan view attribute maps (Fig. 8, GP3, Table 5) and section view (SF3, Table 5). This suggests that the barrier reef crest is sufficiently linear and consolidated at this time to create a more closed marine environment in the platform interior. Rosleff-Soerensen et al. (2012) also find a distinct relationship between the demise of the barrier reef and subsequent control on the patch reef distribution. Patch reefs in the Browse Basin are limited to areas exposed to open marine conditions where the reef crest is broken or discontinuous along BR1 (Rosleff-Soerensen et al., 2012), which corresponds in depth to H2.

5.2.1.3. Seismic unit U3. Serravallian (M. Mio) (ca. 12.9 Ma *SB*). Sequence boundary H3 corresponds to an exposure event during a RSL fall. A resulting karst sequence (SF7 and GP7, Fig. 2) is interpreted with collapsed dolines (sinkholes), infilled karst valleys/streams and vertically continuous karst caves that are directly above smaller ICB's in seismic unit 2, (U3 of Fig. 9). The sinuous carbonate platform margin trending E-W across the survey is also interpreted here as a karstified platform edge (Figs. 12 and 13). This karst horizon coincides with a global (eustatic) RSL fall recorded in the Browse basin before the Serravallian-Tortonian boundary by Rosleff-Soerensen et al. (2012). They also observe similar karst trough and doline features during two phases of barrier reef exposure in the Miocene.

Carbonate factory phase II

5.2.1.4. Seismic unit U4. Middle Tortonian (M. Tor) U4 is a period of continued reef expansion with larger isolated carbonate platforms interpreted on the inner platform to the centre and north of the survey and to the south west (U4–U5, Fig. 9). H4 is a prominent downlap surface and marks the maximum transgression and is thus interpreted as a maximum flooding surface. H4 marks the reflooding of the shelf and the re-establishment of reef growth after U3. It is interpreted that the H3 karst event preceded the demise of the barrier reef, or at least is not visible in the survey at this time. Rosleff-Soerensen et al. (2012) also

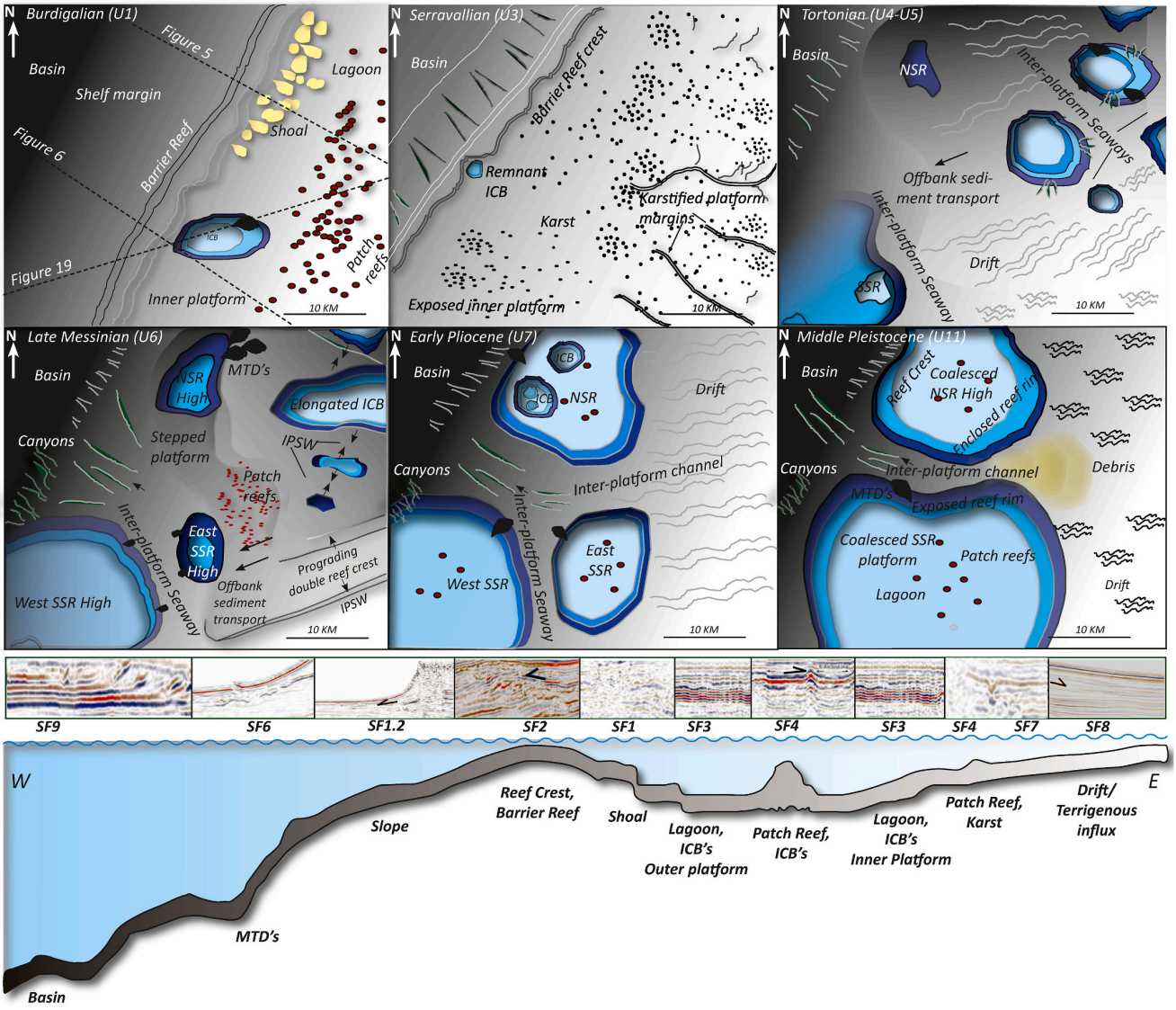


Fig. 9. Six paleogeographic maps are presented as conceptual models to demonstrate the interpreted evolution of Scott Reefs since the Burdigalian. Seismic units: U1, U3, U4-5, U6, U7, U11 were selected as the most representative examples. Dotted lines show approximate locations of seismic lines in Figs. 5, 6 and 19. Corresponding platform elevation is shown below with seismic facies and depositional environment represented across the shelf.

interpret the demise of the barrier reef after this karst event, as well as a eustatic RSL rise.

Plan view geomorphologic patterns and section view stratal relationships (Fig. 10C) agree with the Van Tuyl et al. (2019) interpretation of ICB leeward progradation and windward shedding from westerly winds in the Poseidon 3D survey to the NE. This contrasts the Rankey (2020) interpretation in Torosa field to the south, which shows the opposite, with windward progradation directed by easterly trade winds. Similar interpretations by Rosleff-Soerensen et al. (2012) lead to the conclusion of reef detritus on the leeward side of the ICB's due to unidirectional currents. So, at this time (U4, ca. 10.8 Ma), evidence of increasing current strength is interpreted in the Torosa field, however, this is usually associated with drift deposits (SF8) (Betzler et al., 2009). No evidence of SF8 or GP8 is interpreted in the area. Instead, IPSW sediments (SF9) are interpreted as onlapping the ICB's.

Sub-sequences are identified by rapid aggradational geometries locally within the ICB's in U4, as reefs keep up with sea level rise. They are interpreted as high level (4th/5th order) exposure events seen as high amplitude reflectors. They are confined to the East of the survey and do not extend laterally throughout the survey (Fig. 8).

5.2.1.5. Seismic unit U5. Early Messinian (E. Mes). Seismic unit U5 demonstrates a sharp transition from large isolated carbonate buildups ca. 10 km in length with well-established inter-platform seaways, to coalescing carbonate platforms with double reef crests in H5. A North-South oriented sinuous carbonate platform margin is also interpreted. H5 is interpreted as a sequence boundary associated with increasing outer shelf subsidence >150 m/Ma (McCaffrey et al., 2020). This resulted in increasing sediment influx and basinward prograding clinoforms. The modern day SSR is an example in scale and morphology for the double reef crest (Fig. 11) seen to the SE of the survey, and is an indication of both margins being exposed to wave energy. Both crests prograde outward leading to an increase in carbonate platform extent. An elevated platform below modern NSR is interpreted as the foundations for the first stage of the modern-day isolated carbonate platform. Gravity slumps are interpreted to the NW of NSR that suggests high

Table 4
Table summarising Geomorphic patterns (GP1 - GP9) observations, seismic attributes character and depositional environment.

Geomorphologic pattern (Map view)	Attribute Characteristics (a) map view pattern (b) gradient (c) frequency (d) continuity (e) amplitude strength (f) GP associations	Depositional environment
GP1: medium to steep gradient feature	(a) linear, sinuous edge (b) steep, stepped (c) Low to medium (d) continuous margin (e) medium (f) GP1.2, GP3, GP6, GP9	***Reef slope***
GP2: curvi-linear feature (platform margin)	(a) linear or curved (b) gradual (c) low (d) high (e) low (f) GP1.2, GP3, GP5, GP9	***Barrier Reef or Reef crest***
GP3: sub-circular to elongate feature (platform interior)	(a) sub-circular to irregular (b) gentle (c) Very high (d) Continuous (e) high (f) GP1.1, GP2, GP4, GP5, GP7	***Lagoon***
GP4: circular to sub-circular feature (platform interior)	(a) sub-circular to linear (b) locally steep (c) low (d) discrete (e) low to medium (f) GP3, GP5, GP7	***Patch Reef***
GP5: discrete patchy, grouped features (platform interior)	(a) small patchy, grouped (b) low to high (c) low to medium (d) discrete (e) low to medium (f) GP2, GP3, GP4, GP9	***Back Reef Shoal (Transitional facies)***
GP6: chaotic feature (platform margin)	(a) irregular, disturbed (b) high to variable (c) low to high (d) variable (e) low to high (f) GP1, GP8, GP9	***Mass Transport Deposits (MTD)/ gravity slumps (Distal reef slope)***
GP7: sub-circular to linear features (platform interior)	(a) small sub-circular to linear (b) apparent topographic variation, deep centre, high circumference (c) medium to high (d) discrete (e) medium (f) GP3, GP5	***Karst***
GP8: uniform, sinuous morphology	(a) Parallel, onlapping (b) slight (c) low (d) high, continuous (e) weak to medium (f) GP6, GP1.2	***Drift***
GP9: uniform, homogenous morphology surrounding platform	(a) uniform, homogeneous (b) slight to high (c) low (d) continuous (e) high (f) GP2	***Basin or Inter-platform Seaways (IPSW)***

Table of geomorphologic patterns descriptions and interpretations corresponding to Fig. 8.

volumes of carbonate material is being shed off the platform during this highstand (highstand shedding). This is interpreted as early contouring of the platforms with moats identified around the margin (e.g., Fig. 14) (*sensu* Betzler and Eberli, 2019). Small patch reefs (SF4) can be seen behind the double reef crest in the SE in a lagoon setting (U6, Fig. 9), suggesting that there is continued reef growth on topographic highs during this sea level rise.

5.2.1.6. Seismic unit U6. Late Messinian (L. Mes) (ca. 5.9 Ma, correlated to *T40.0 SB TM1*, Fig. 20) H6 corresponds to the late Miocene and is interpreted as a major regional sequence boundary that marks the top of an aggradational package. The isolated buildups identified in U5 show complex episodes of aggradation, progradation and backstepping (e.g., Fig. 10C). They subsequently merge with adjacent platforms in U6 to form composite systems (U6, Fig. 9; Table 5; Rankey, 2020). This composite system is a vertically aggrading, elongated platform that extends to an elbow shape platform into the adjoining Poseidon 3D survey.

Fig. 14 shows the stepped platform profile transitioning from the eastern topographic high to the western low where the N–S trending IPSW (SF9) separates the eastern platform from a large ICB or isolated carbonate platform in the South-West, extending 7–10 km in length (that is not fully resolvable on seismic due to a data gap) (U6, Fig. 9). These two platforms subsequently expand and merge (from U6 to U14), with transitional shoal facies (SF5) and downlapping reef apron deposits indicating leeward progradation. They are interfingered by deposition of IPSW (SF9) sediments. Thus, it is interpreted that SSR initiates on the offbank prograding clinoforms of the platform margin during a marine transgression.

5.2.2. Pliocene (U7–U8)

The Pliocene sequence is bounded by H7 and H8 and is characterised by a significant reduction in the size of the carbonate factory. The Pliocene seismic facies are homogeneous. The sequence consists of thick, high amplitude conformable and continuous reflectors consistent with lagoon facies along the inner platform. Basin sediments are interpreted on the basinward outer platform margin. Despite a eustatic highstands in the Pliocene, evidence of karst is interpreted throughout U7 and U8 on the Eastern half of the survey as well as on the NSR and SSR platforms. This is evidence of higher order sequences and possibly lower sea level on the inner shelf than previously described for the Pliocene (Qin et al., 2022). However, the resolution of the seismic is insufficient to interpret them in this study. Nevertheless, this seismic unit defines the key shift from ICB's drowning on the inner platform – where suspended sediment reduced light penetration and thus inhibiting carbonate growth (Van Tuyl et al., 2018) - to the onset of the pre-cursor Scott Reef ICB's on the outer shelf margins.

Carbonate factory phase III

5.2.2.1. Seismic unit U7: Early Pliocene (E. Plio). H7 is interpreted as the base Pliocene 'drowning' unconformity and is the most recent horizon (ca. 4.8 Ma) constrained by biostratigraphic data (Table 1) in the Megator seismic dataset. Unconformity H7 follows an aggradational sequence (U6, Fig. 16) and is consistently documented (Van Tuyl et al., 2019; Belde et al., 2015) as the demise of the carbonate factory in the Browse basin. However, several characteristics, including a major transition in seismic facies, suggest this reflector is, instead, a transition to a reduced carbonate production factory, localised to topographic highs (Fig. 16).

Downlap and mound shaped, positive relief features (SF4 – patch reef) continue above H7 below North SSR and is interpreted as continuation of *in situ* carbonate reef growth despite a highstand/flooding event. Concave down V-shaped depressions, interpreted as karst (SF7) are identified on the South-West isolated high - suggesting the platform was periodically exposed during U7. MTD's (SF6 and GP6) are identified along the platform margins (e.g., U7, Fig. 9).

The platform margin to the North of NSR remains a topographic high and sediments, including gravity slumps downlap onto the slope and basinward where erosion has transported large volumes of sediment off the platform (highstand shedding) (Fig. 8, GP6; Table 4). It is noted that this topographic high is directly above the Tertiary rifted Scott Reef trend, implying that tectonic reactivation may have controlled the continuous development of this reef sequence.

Most notably, there is no evidence along this reflector of *in situ* carbonate production in the East of the survey, (i.e., GP1 and SF1 or GP2 and SF2). Elongate sediment drift bodies (SF8) downlap onto the H7 reflector along the eastern half of the survey, blanketing the preceding carbonate platforms (U7, Fig. 9; Fig. 8, GP8; Table 4). This is consistent with a partial drowning interpreted elsewhere in the Browse basin (Rosleff-Soerensen et al., 2012; Rankey, 2020).

5.2.2.2. Seismic unit U8. Middle Pliocene (M. Plio) H8 (ca. 3.5 Ma, correlated to *T45.2 MFS TPL*, Fig. 20) truncates underlying strata and is interpreted to be a maximum flooding surface across the entire survey (U7). Carbonate drift sedimentation, characterised by double downlap (Fig. 8, GP8 and Fig. 7, SF8; Tables 3 and 4) continues to be deposited in the eastern half of the survey. However, negative depressions indicative

Table 5
Geomorphic patterns identified in plan view using seismic attributes.

GP	Continuity (Variance)	Amplitude (RMS)	Frequency (Spectral decomposition)	Map view pattern	Gradient (High pass)	Associated Seismic facies	Interpretation	Ancient or modern Analogue
1.1	Continuous (basinward)	M	L-M	Linear, sinuous edge	Steep to gradual	SF1.1	***Prograding carbonate platform margin***	Browse Basin; Rosleff-Soerensen et al., 2012
1.2	Continuous (basinward or platform interior)	M	L-M	Rounded, stepped	Occasionally steep	SF1.2	***Reef slope***	NWS, Australia; Rosleff-Soerensen et al., 2012; Burgess et al. (2013), Various; Betzler and Eberli, 2019
2	Continuous (along platform margin, platform interior)	L	L	Linear stepped edge	Gradual, sinuous to linear	SF2	***Barrier reef or reef crest***	Present day South Scott Reef, NWS, Australia; McCaffrey et al. (2020); Rankey, 2020
3	Continuous	V.H	H	Homogenous sparse	Gentle	SF3	***Lagoon***	NWS, Australia; Rosleff-Soerensen et al., 2012
4	Discrete	L-M	L	Circular to sub-circular	Locally steep	SF4	***Patch reef***	Browse Basin; Van Tuyl et al., 2019, Scott Reefs; Collins et al. (2014)
5	Discrete	L-M	L-M	Patchy, small sub-circular	Locally minor to variable	SF5	***Shoal (sand apron)***	Great Bahama Bank; Harris et al., 2015, Maldives Archipelago
6	Discrete to continuous, disrupted	L-H	L	Disturbed surface, often linear	Variable	SF6	***Mass transport deposit (gravity slumps)***	Browse Basin; Van Tuyl et al., 2019, Santaren channel; Betzler and Eberli, 2019
7	Discrete	M	M-H	Sub-circular	Locally steep to variable	SF7	***Karst***	Browse Basin; Rosleff-Soerensen et al., 2012
8	Continuous	Weak-M	L	Uniform, homogenous	Gentle, low	SF8	***Drift***	Maldives, Various; Betzler and Eberli, 2019; Saqab and Bourget (2015)
9	Continuous	H	L	Uniform, homogenous	Very low	SF9	***Basin or IPSW***	NWS, Australia; Rankey, 2020

Summary table of 9 geomorphologic patterns identified in plan view using seismic attributes; Variance, RMS amplitude, Spectral decomposition (at 20, 40 and 60Hz). Seismic facies and modern and ancient analogues were used to interpret the depositional environment along major unconformities.

of karst (SF7) below both NSR and SSR suggest topographic highs remained periodically exposed during this maximum marine transgression.

H8 is characterised by two main isolated topographic highs and a steep descent basinward with canyons and a well-established inter-reef channel. Established lagoon facies (SF3) and associated patch reefs and shoal are identified on the inner NSR platform (Fig. 15). The reef slope (SF1.2) of both NSR and SSR is steep with respect to the surrounding seafloor, becoming raised isolated carbonate platforms.

5.2.3. Quaternary (U9-WB)

The Quaternary sequence is bounded by H9 and WB. No biostratigraphic markers are available for the Pliocene-Pleistocene boundary and are inferred from seismic and well log data, and regional Quaternary literature (Table 1). The Quaternary geomorphology is dominated by episodic, aggradational reef turn on events and variable lateral facies distributions. Poor seismic quality beneath NSR makes it difficult to trace unconformities across the steep flanks and between both reefs. It is inferred that major unconformities H10–H14 correlate; however, it is possible that higher order unconformities are locally specific to each reef system. A change in seismic facies from chaotic, mound shape to more continuous, parallel to sub-parallel seismic facies implies a change in depositional processes. A regional transgression marking the Plio-Pleistocene boundary (H9) suggests a change from ICB and reef crest aggradation on topographic highs in 'catch up' phase, to larger isolated carbonate platforms in 'keep up' phase, with consistent and established lateral facies hierarchy. This also suggests a transition to a more stable tectonic setting, (reduced or steady subsidence) and a decrease in the supply of allogenic clastic detritus. This resulted in a shift from siliciclastic and carbonate hemipelagic deposition to a more restricted and protected shallow marine environment, with local uninterrupted carbonate production.

5.2.3.1. Seismic unit U9 (L. Pliocene - E. Pleistocene) and seismic unit 10 (Middle Pleistocene MPl-1). U9 is interpreted to be Late Pliocene – Early Pleistocene and is inferred as the base Quaternary (B. Qua), ca. 1–0.8 Ma. Several reflectors throughout U9 and U10 are interpreted as sub-aerially exposed due to evidence of karst features, (i.e., V-shaped depressions on section view (SF7) and high amplitude sparse, small circular patterns on plan view (GP7)). This suggests, it is a lagoonal environment below SSR with periods of RSL fall and exposure. Significant gravity slope deposits to the east of NSR seen in cross section (chaotic high amplitude reflectors – SF6) and plan view (high amplitude, chaotic reflectors on RMS amplitude and variance attribute maps – GP6) (Fig. 15), suggests the raised reef rims are exposed to high wave energy and offbank transport. Mounded, chaotic reflectors are seen downlapping onto H9 over NSR and suggests there may have been continued carbonate production on regional highs. The cross-sectional geomorphology of SSR draws comparisons to the 'unbalanced aggrading/onlapping' reef anatomy model proposed by Kennedy and Woodroffe (2002) and described for Indo-Pacific reefs by Montaggioni (2005). This model suggested vertical accretion rates of coral frameworks was highly variable. This could suggest there is higher variability of coral framework facies in SSR than NSR. This concurs with the present-day facies' distribution and diversity across NSR and SSR (Green, 2018; Collins, 2002; Collins and Testa, 2009).

Carbonate factory phase IV

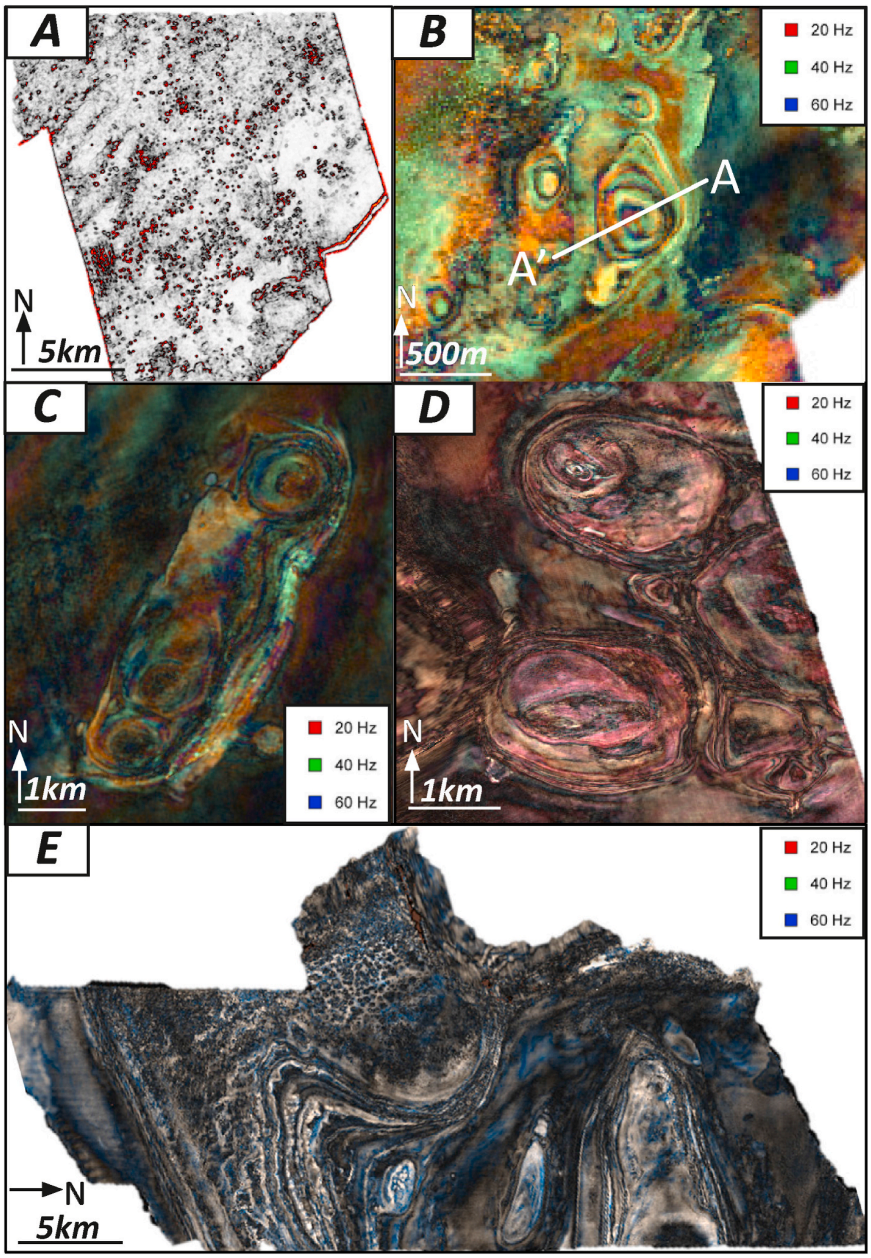


Fig. 10. Seismic unit 1–7, Miocene carbonate factory development: Geomorphologic patterns identified in plan view using seismic attributes; Coherency, RMS amplitude, Spectral decomposition (at 20, 40 and 60 Hz) and cross-referenced with seismic facies to interpret the depositional environment along major unconformities. (A) small patch reefs form in U1, (B) small ICB's develop along U2, (C) larger ICB's build up and out through U4–U7, (D) the larger ICB's coalesce and merge with significant development of moats and current winnowing, and (E) a series of large carbonate platform margins develop, contoured by strong ocean currents.

5.2.3.2. Seismic unit U11: Middle Pleistocene (MPl-2). The geomorphology of seismic unit U11 reflects a key change in seismic facies. Mounded seismic features (patch reefs) are evident along H11. Larger patch reefs are interpreted below SSR, whilst reef crest (GP2) is widest and more complete around NSR. Drift sedimentation persists along the eastern section of the survey and is interrupted by a large debris fan (ca. 10 km in length) between NSR and SSR flowing landward (U11, Fig. 9)

H11 is interpreted as the mid-Pleistocene climate transition, where sea level amplitudes changed to high amplitude, low frequency with rapid deglacial RSL rise and slow falls. It is apparent that this MPT triggered reef growth on both NSR and SSR during a general eustatic sea level fall.This is contrary to general thought that reefs grow preferentially during a marine transgression (Burgess et al., 2013). However, the new locale of reef growth remains in the lagoonal depocenters. By this time, NSR and SSR are developed as isolated platforms on the distal carbonate ramp margin (i.e., U11, Fig. 9).

5.2.3.3. Seismic unit U12 (Late Pleistocene (LPl-1) and seismic unit 13 (Late Pleistocene LPl-2). H13 truncates underlying strata that aggraded in a previous depression over present day central lagoon, and so it is determined to be a truncation unconformity with onlapping strata. Seismic units 12 and 13 are interpreted to be a continuation of phases of rapid reef crest growth (GP2 and SF2) separated by thin weak chaotic reflections of SF5 (i.e., shoal). The shoal represents sediment reworking and lagoon infilling and onlapping the relict reef crest during periods of slow RSL fall. Enhanced subsidence and recurring sea level highstands (Collins et al., 2014) clearly results in a pattern of repetitive reef stacking that is aggradational on seismic data. GR log data shows high amplitude cycles throughout U12 and U13, and overall decreasing GR values that are interpreted as more homogeneous, cleaner carbonate deposits towards the top of the unit (Fig. 17). Some peaks may correlate to fluctuating sea levels of the late Quaternary (e.g., Saqab and Bourget, 2016).

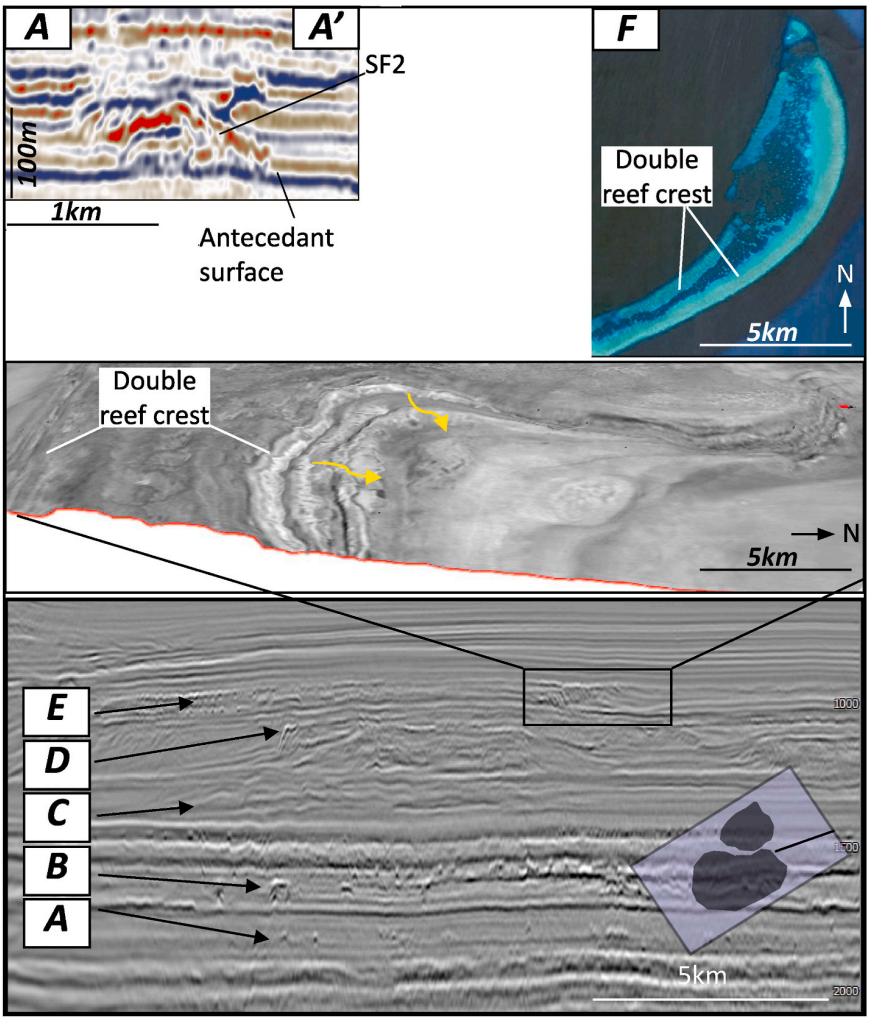


Fig. 11. Cross section A′-A shows the seismic reef crest facies (SF2) in section view corresponding to the plan view cross section A′-A in Fig. 10B. Fig. 11F: Satellite view of a double reef crest on South Scott Reef, NWS, Australia. This is a modern-day analogue of the double reef crest seen in the Miocene. This pattern of reef geomorphologic evolution and inter-platform seaway development is interpreted elsewhere in the Browse basin (Rankey, 2020). Bottom cross section figure location shown in Fig. 5. Panels A–E correspond to Fig. 10 panels A–E comparing section view with map view. A sketch map bottom right shows the location of seismic profile to the East of the survey. (A) small patch reefs form in U1, (B) small ICB's develop along U2, (C) larger ICB's build up and out through U4–U7, (D) the larger ICB's coalesce and merge with significant development of moats and current winnowing, and (E) a series of large carbonate platform margins develop, contoured by strong ocean currents. The zoomed in panel of the double reef crest is taken from E, which corresponds to U7.

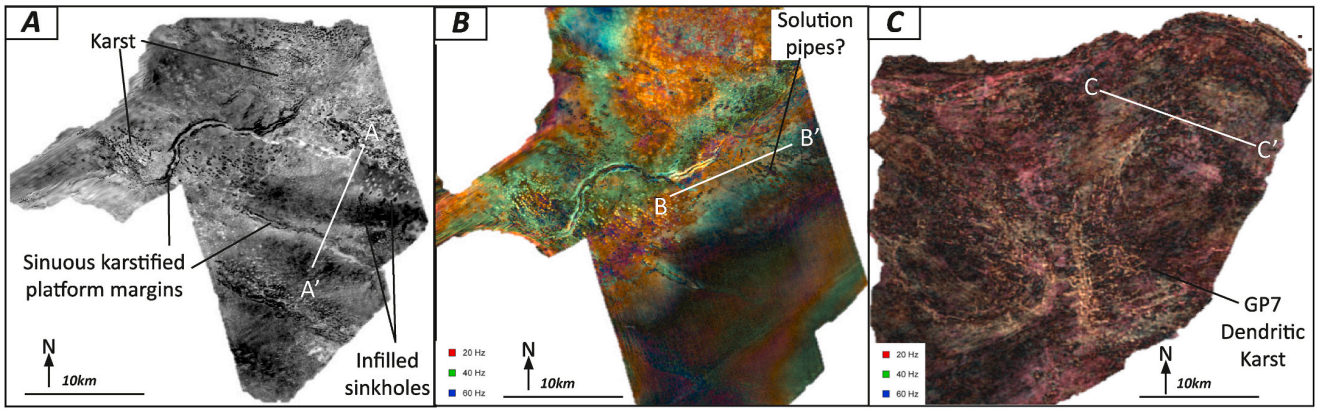


Fig. 12. Karst features visible throughout the survey. Depositional environments identified with use of seismic attributes; (A) High Pass, (B and C) Spectral decomposition at (20, 40 and 60 Hz) and (20, 40 and 60 Hz) respectively and variance.

5.2.3.4. Seismic unit U14: Late Pleistocene (LPl-3). H14 SSR and H14 NSR are identified as erosional unconformities. Seismic unit U14 constitutes an isolated, raised carbonate platform environment, with a significant expanse of lagoonal facies, patch reefs, reef crest, shoals, sand aprons and channels on the inner platform (Fig. 2). The lateral facies distribution is similar to the modern benthic environment, e.g., Fig. 1C. Collins & Testa (2009) provide U/Th ages from core samples, which can be correlated to U14 NSR. This provides an estimated age of ca. 0.098 Ma, which pre-dates the onset of the Last Glacial Maximum ca. 23,000 years ago (Camoin and Webster, 2015; Webster et al., 2022; O'Leary

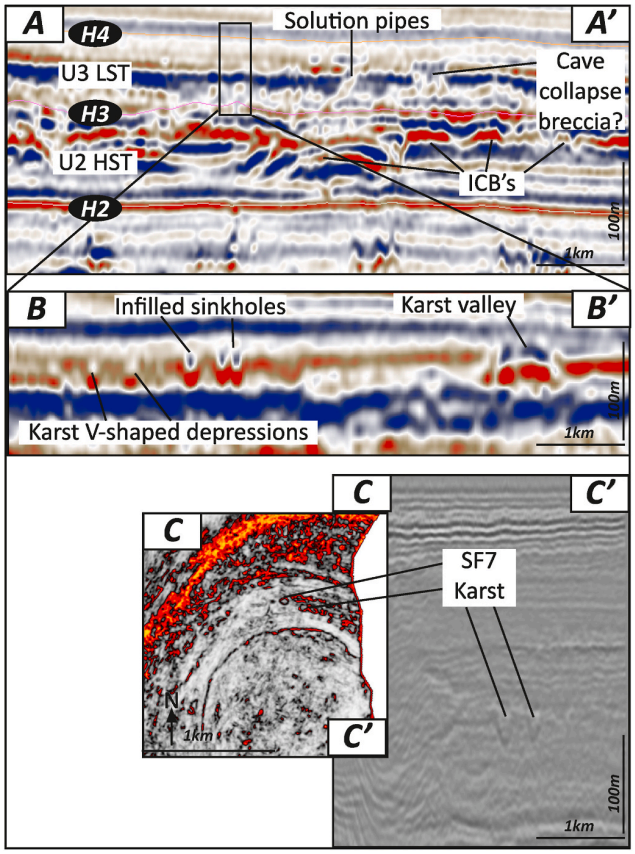


Fig. 13. (A and cross-section A-A′) interpreted plan view and section view of H3. (B and cross-section B′-B) showing interpreted section for H2–H4. (C and cross-section C–C′) Large ca.70 m karst features identified along U8 as concave up V-shaped depressions below modern day SSR. Dendritic patterns observed in plan view. (D) This interpretation concurs with observations made in the Browse Basin by Van Tuyl et al. (2018). Dendritic karst patterns and elongate platform morphologies draw comparisons to the Miocene carbonate platform, Luconia, South China Sea (Hendry et al., 2021).

et al., 2020). This suggests that seismic unit 14 extends from ca. MIS 5 to MIS 1. Scott Reefs would have been exposed as steep-sided rocky islands during lowstands such as the Last Glacial Maximum. Subsequently, during Holocene time (MIS1, 10,000 years ago), around 40 m of rapid vertical accretion occurred during post glacial sea level rise (ca. 0.019 to 0.007 Ma, Collins and Testa, 2009). Evidence of this can be seen above SSR U14 with sediments onlapping the reef crests, although, this episodic reef growth, including drowning events (e.g., Meltwater pulse 1 B; Collins and Testa, 2009) is sub-seismic resolution and is not characterised in this study.

6. Discussion

6.1. Tectono-stratigraphic framework of Scott Reefs

The Neogene and Quaternary tectono-stratigraphic framework of Scott Reef can be described by four main carbonate factories; Phases I-IV (i.e., Figs. 19 and 20). 2nd and 3rd order sequence boundaries are interpreted throughout the Miocene and Pliocene, and up to 3rd and 4th order sequence boundaries are identified for the Quaternary.

The carbonate platforms and barrier reef of Phase I preserve evidence of two large scale marine transgressions that broadly reflects the overall global sea level rise from U1 to U3. Sequence boundary H2 marks the peak of the MMCO at ca. 15.6 Ma (Figs. 19 and 20). Carbonate factory Phase I establishes on an arid, deep marine ramp setting. The reactivation of the Scott Reef trend fault-crest (Fig. 1) creates a topographic high for barrier reef initiation and basinward reef crest migration, with subsequent development of inner platform shoals and small patch reefs. The transition to carbonate factory Phase II is marked by the maximum flooding surface H4 and encompasses seismic units U4 to U7. Phase II, (U4 to U6) is characterised by increased outer shelf subsidence (Rankey, 2020) and two eustatic marine regressions (Fig. 20). This net increase in accommodation space results in complex platform architectures on the inner shelf. The result is the disintegration of the barrier reef into smaller elevated isolated carbonate platforms that eventually aggrade and the development of IPSW's that ultimately coalesce. Phase III, (U7 to U11) documents a significant RSL rise that is associated with a wet, humid interval and reduced carbonate factory. The demise of reefs is interpreted in shallow inner platform settings. However, carbonate reef production continues along the distal, shelf margin highs., i.e., NSR, SSR and Seringapatam Reef. This is likely due to increased subsidence as a result of more crustal extension on the shelf edge (Huang et al., 2020). The transition between Phase III and Phase IV, marked by H11, is characterised by an increase in global sea level amplitude and frequency, but an overall fall in eustatic global sea level (Fig. 20). Phase IV includes U11–U14 and describes a reactivation or initiation of carbonate production at H11 and subsequent 'keep-up' to present day. It is characterised by higher order events that describe the complex interplay of aggradation and exposure.

6.1.1. The role of tectonics and slope instability on Scott Reef evolution

Modern day reefs sit above the Scott Reef Fault Trend (Fig. 1, Keep and Harrowfield, 2008), which likely provided favourable bathymetric and subsidence conditions with periodic reactivation throughout the late Miocene-Pliocene. Thus, placing the sites of carbonate production topographically higher than surrounding regions that were experiencing inundation by terrigenous sediment influx (Burgess et al., 2013). The inter-reef channel (Fig. 2) bypasses sediment away from NSR and SSR directly into the feeder canyons, transporting large volumes of local carbonate and distal terrigenous sediment into the basin. This is contrary to the direction of transport of the modern-day fan, which trends to the East. This suggests that overtime, sediments have been transported in both directions, and indicates that tectonics may have been a contributing factor. Nevertheless, minimal evidence of structural lineaments exists within the Cenozoic strata. Keep and Harrowfield (2005) suggest that recent (Neogene) faulting caused by Cenozoic inversion tectonics is confined to the centre of the Browse basin, landward of this study. Tectono-stratigraphic interpretation of the 3D Megator survey concurs with this, as no significant stratal displacement within the conformable stratigraphic units H1–H14 is interpreted. Two E-W trending faults, ca. 500 m in length are identified to the NW of the survey during U2 and U3 and is coincident with faulting interpreted at this time in the Poseidon survey to the NE (Van Tuyl et al., 2019). However, no obvious structural control is interpreted to influence reef growth (including locally within sub-sequences) other than the Scott Reef Fault Trend. The Plio-Quaternary development of NSR and SSR is interpreted to have initiated on the carbonate platform margins. Isopach data shows a clear topographic high for the nuclei of NSR initiation, but a topographic low for SSR initiation. This contrast suggests the role of tectonics on Scott Reefs' evolution was inconsequential in influencing reef growth.

Evidence of neotectonics along the NWS (Keep et al., 2000, 2002; Keep and Harrowfield, 2008; Hengesh and Whitney, 2016) may have influenced the steepening of NSR and SSR slopes. Indeterminate faulting and collapse of unstable growing carbonate margins and slopes, particularly in greenhouse climates (Liu & Liu, 2021), possibly resulted in regular mass transport deposits (SF6) throughout the Cenozoic history. Finally, small scale, continuous vertical offsets are interpreted to the East of NSR and interpreted as hydrothermal fluid escape or hydrocarbon migration pathways, as per interpretations in the Poseidon

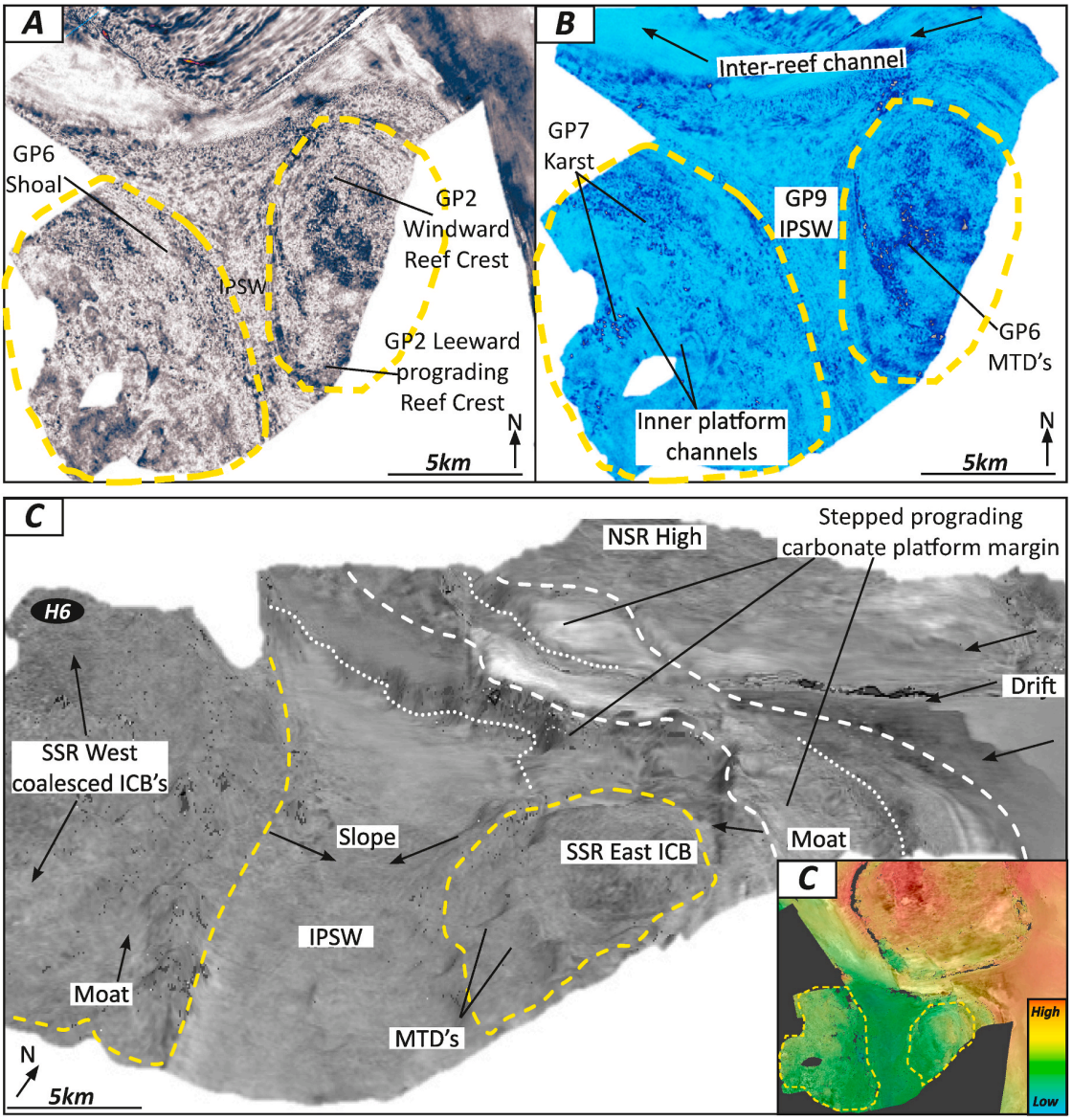


Fig. 14. Unconformity H6 interpreted as a low stands event corresponding to the Messinian RSL fall. Interpretations using evidence from seismic attributes (A) spectral decomposition (at 20 Hz), (B) RMS amplitude and (C) High Pass frequency filter. (A and B) Geomorphologic patterns identified in plan view with dashed outline (yellow) highlighting East and West ICB's over modern SSR. (C) Structured surface of H6 giving 3D perspective of the stepped prograding Miocene carbonate platform showing the East SSR ICB initiating on the offbank downslope deposits. Analogous leeward prograding ICB's are observed in the Browse basin by Van Tuyl et al. (2019). Similar modern seaway straights (IPSW) are identified between reefs in the Maldives archipelago by Paumard et al. (2017).

3D survey to the North East Browse Basin (e.g., Van Tuyl et al., 2019).

6.2. Timing and development of Scott Reef precursor ICB's

6.2.1. North Scott Reef (NSR)

ICB's are interpreted below modern day NSR throughout the Miocene and Pliocene, however, development into a large isolated carbonate platform takes place throughout the Plio-Quaternary (Phase III and IV). Precursor NSR is interpreted to have initiated at the Miocene-Pliocene erosional unconformity (H7) as three small ICB's on the N–S trending carbonate platform margin, eventually building out into one larger ICB on the NW platform margin (i.e., Fig. 16; Fig. 9). Along H7, the leeward reef crest progrades until becoming a topographic isolated high, with an established inner platform lagoon environment (Fig. 16). This pattern of platform development is consistent with models of reef initiation and the key controls and pre-requisites for coral reef establishment (Schlager, 2005), e.g., the Maldives platform (Belopolsky and Droxler, 2003; Paumard et al., 2017) and in particular, along the NWS (Belde et al., 2017; McCaffrey et al., 2020). For example, McCaffrey et al. (2020) hypothesise that the Pliocene drowning event restricted reef growth to seven shelf edge reefs north of 18°S (i.e., Ashmore Reef, Seringapatam Reef, Scott Reef, Rowley Shoals and an atoll ca. 60 km SW of the Rowley Shoals). The authors also comment that increasing aragonite saturation within seawater and variable nutrient upwelling since the mid-Miocene, contributed to the increased and persistent reef growth in these regions.

From our analysis, the geometry and composition of the substrate also had an influence on the establishment and development of the precursor NSR reefs (i.e., Magalhães, 2021; Burgess et al., 2013). Exposure events seen in U3, created rough karst surfaces, which are

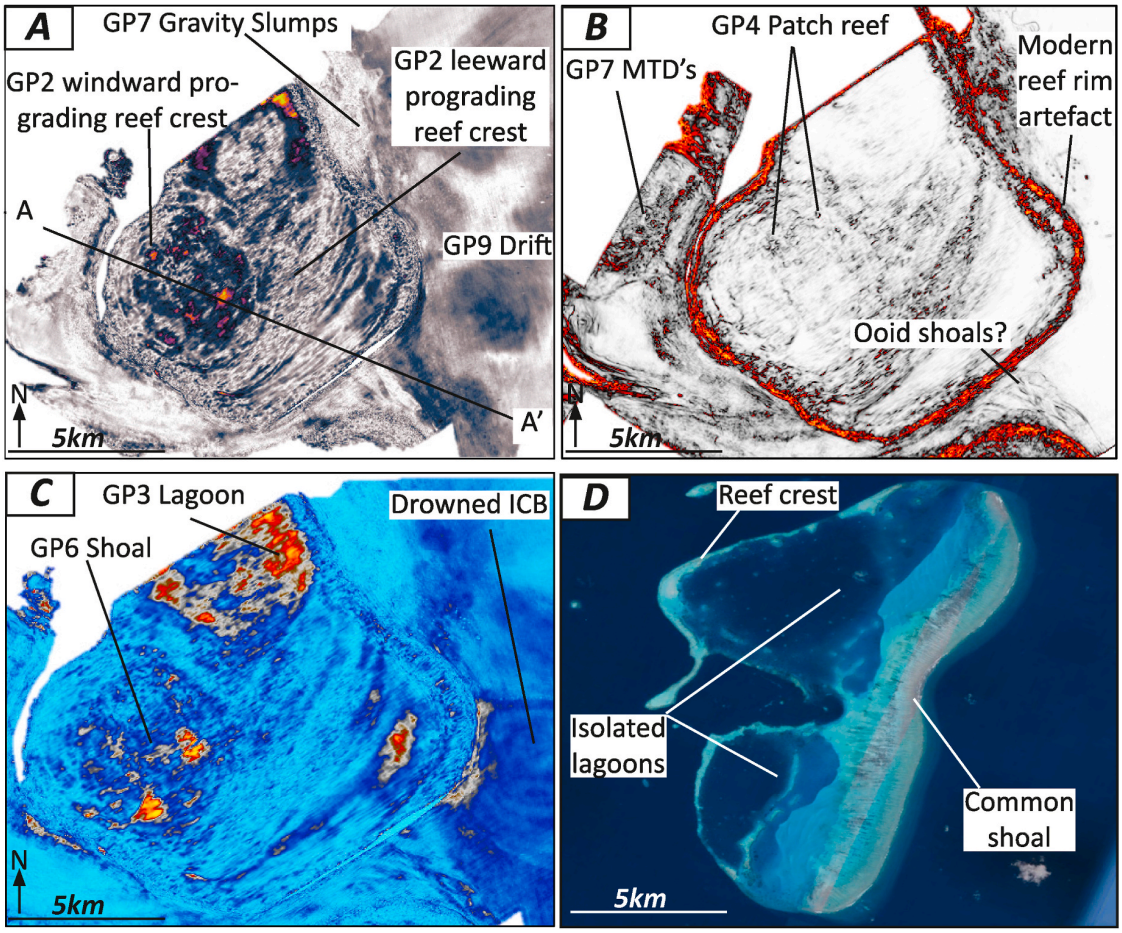


Fig. 15. Geomorphologic patterns along NSR H6 identified in plan view (A, B, C) using seismic attributes; Spectral decomposition (at 20 Hz), Variance and RMS amplitude respectively. (D) Satellite view of two isolated platforms with ocean facing reef crest merging with a common shoal & sand apron in Maldives archipelago.

known to facilitate coral settlement (Burgess et al., 2013; Sanborn et al., 2020). Although, it is argued that controls on geomorphology arise from larger scale tectono-oceanographic factors rather than substrate topography and composition (Montaggioni, 2005). The sustained level slope of the NSR substrate may also have accommodated faster growing pioneer coral assemblages that prefer flat or gentle slopes (Webster, 1999). This suggests the distal platform margin was likely influenced by tectonic flexing, maintaining a flat slope. This influence of the antecedent morphology was important in localizing facies establishment, but became increasingly independent of antecedent control during highstands progradation (Purdy and Gischler, 2005), as we note an increase in lateral topographic variation and geometries during highstands. Fig. 16 shows the initial 'empty-bucket' morphology (Purdy and Gischler, 2005) of NSR during rapid aggradation in the early Pliocene shelf flooding.

The most significant development of NSR is the onset of Quaternary ICB growth. Seismic facies and geomorphologic patterns (Figs. 7 and 8; Tables 3 and 4), suggests that the re-initiation of reef growth for NSR started during U11 (ca. 0.8–0.6 Ma) and corresponds to the MPT. The pattern of the onset and 'keep up' of successive vertical reef sequences is consistent with other Pleistocene reefs that have developed during highstands, e.g., Mururoa Atoll (Montaggioni et al., 2015), the Ryukyu Islands (Yamamoto et al., 2006) and Belize (Humblet and Webster, 2017) as well as carbonate factory and ICB growth on both the NW shelf (i.e., Buffalo ICB; Saqab and Bourget, 2015) and NE shelf of Australia (i.e., Ribbon Reef 5; Webster and Davies, 2003). Isopach thickness maps show gross distribution of sediments focused within the ICB's Quaternary strata.

The sequence stratigraphy and geomorphologic evolution of NSR draws similarities to the Yongle Atoll in the South China Sea. Wu et al. (2022) interpret four stages of carbonate platform development from the Miocene to present (Early Miocene initiation, Middle Miocene flourishing, Late Miocene-Pliocene partial drowning and modern Quaternary Atoll). Yongle atoll and NSR persevered due to favourable oceanographic factors and the bathyal troughs that may have blocked terrigenous clastic material from interfering with the growth of the reefs during wet climes.

6.2.2. *South Scott Reef (SSR)*

SSR initiates as two or three separate ICB's in the late Miocene-Pliocene, divided by an IPSW. The westernmost (larger) ICB initiates in the mid-late Miocene as three smaller ICBs (U4–U5, Figs. 9 and 19). These then merge on the edge of the platform margin and remain after the demise of the barrier reef in U3, leaving carbonate platform remnants. This makes it the first major established carbonate structure below the modern reefs. Though, the precise extent of its development remains unresolvable due to a seismic data gap. The easternmost ICB subsequently establishes in the downslope off bank carbonate deposits along H7 (U6, Fig. 9). It establishes as a prograding mound (prograding reef facies) on top of the N–S trending carbonate platform edge (Fig. 14). This eastern ICB location is reminiscent of the ICB seen in the Miocene (U1, Fig. 9), however, with an elongate morphology that is perpendicular to the original. This could indicate evidence of reactivation of basement faults that were originally responsible for confining carbonate

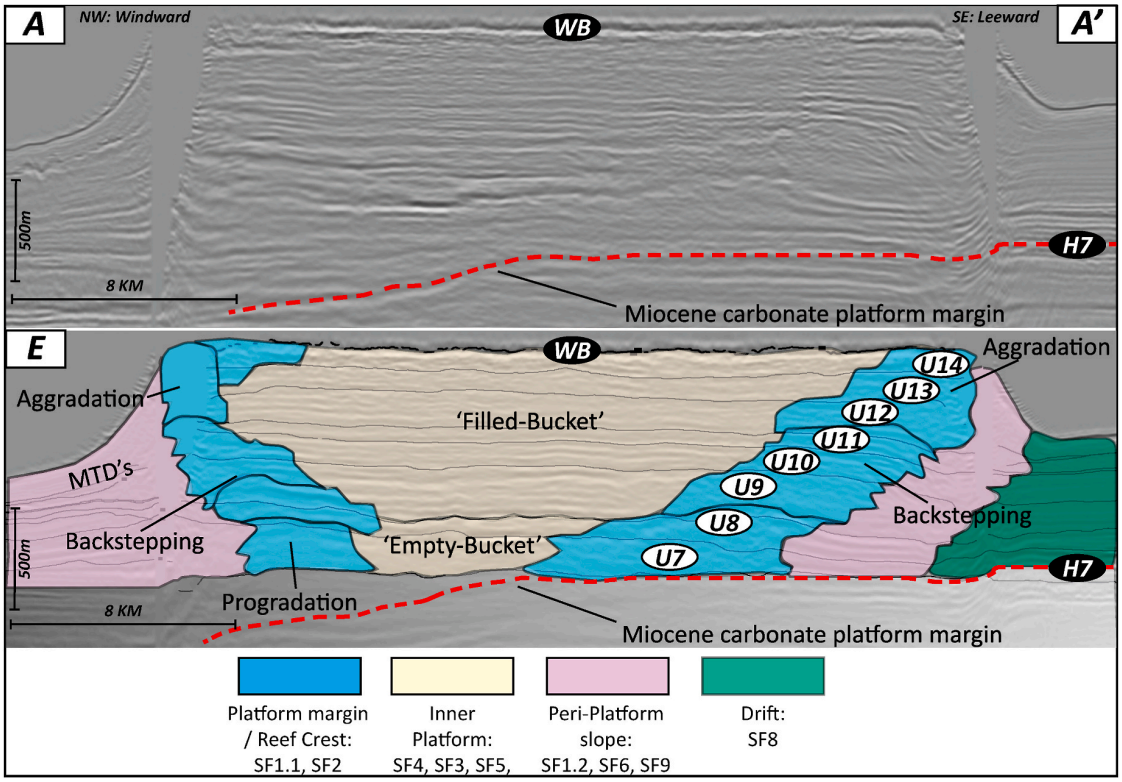


Fig. 16. (E) Interpretive schematic sketch of seismic cross section A-A' (Fig. 15A) of depositional environments and their cross-sectional geometry and relationships. The Maldives platform (Belopolsky and Droxler, 2003) draws parallels to this interpretation of the NSR platform. Similar backstepping patterns are also identified by Qin et al. (2022) in the Xuande platform, Northern South China Sea.

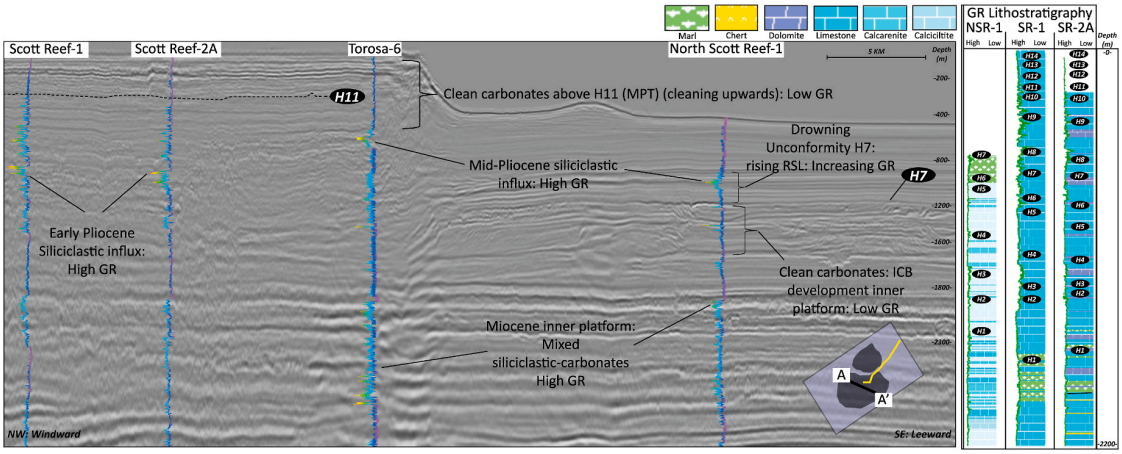


Fig. 17. 3D Seismic transect through wells NSR-1, SR-1, SR-2A and Torosa-6. Transect and cross-section A-A' (Fig. 18) shown in bottom right sketch map. GR logs are displayed showing key signals that correspond to the Pliocene Sea level rise and the Mid-Pleistocene Transition (H11). ***Right***: Lithostratigraphic columns interpreted from GR API values for NSR-1, SR-1 and SR-2A (Source: WEL) with H1–H14 shown corresponding to depth. Colour and pattern descriptions above. The interpretation of more intermittent dolomite sections in well SR2A than SR1 and NSR1 (WEL and WCR) suggest that the inner platform of SSR was more frequently exposed to the complex interplay of multiple meteoric hydrozones (vadose zone, freshwater-lens, mixing zone) (Paterson et al., 2008) on more occasions than NSR.

accumulation to this isolated topographic high (i.e., Burgess et al., 2013). However, isopach maps demonstrate that this site is a topographic low in the early Pliocene. The initiation of this eastern ICB in the early Pliocene therefore appears to be on a topographically deeper setting than would be expected of ICB nucleation (Schlager, 2005). And since development of ICB's are often characterised by periods of rapid aggradation, sediment shedding from the existing carbonate platform margin combined with basinal siliciclastic infill at the toe of slope, could have generated flanking slope deposits that may have formed the substrate for *in situ* carbonate production. This would have reduced the accommodation space required to be filled to subsequently allow progradation (Burgess et al., 2013).

The windward reef crest remained semi-closed throughout SSR platform development, explaining why the modern-day lagoon is only

partially enclosed. The morphology of the ancient and modern open lagoon differs to NSR, which developed an enclosed lagoon with raised rims since initiation.

The variety of evolutionary patterns of two adjacent raised carbonate buildups draws comparisons to the variety seen in the big bank shoals in the Vulcan sub-basin (Fig. 1). The Big Bank ICB, is one of around 150 individual carbonate build-ups located 2–85 km off the shelf edge and 300–600 km from the modern shoreline on the NWS, Australia. Similarities can be drawn between the Big Bank ICB and SSR, with respect to their seismic geomorphology. Both exhibit profiles of vertically aggrading, saucer-shaped reefs above steep slopes, with evidence of 'start up', 'keep-up' and 'out-building' phases that survives to present day on the NWS. Saqab and Bourget (2015) similarly use GR (gamma ray), sonic logs, seismic and regional biostratigraphic data from Well Completion Reports to reveal a comparable Mid Pleistocene age for initiation of the Big Bank ICB Quaternary reef initiation.

6.3. Environmental controls and major climate forcings on carbonate growth and geomorphology

6.3.1. Miocene and the MMCO

Around 35 Ma, major uplift of the Himalayan-Tibetan plateau exposed massive volumes of the crust to weathering and $C0_2$ scrubbing (Berner et al., 1983; Ruddiman and William, 2008), sequestering carbon from the atmosphere and increasing alkalinity of the ocean basins (Raymo et al., 1988). This triggered ideal conditions for the production of carbonate sedimentation in warm, shallow, tropical ocean reservoirs around the world throughout the Miocene, peaking around the MMCO.

The MMCO was a period of quiescence with respect to sea level fluctuations, and climate variability, lending to sustained carbonate production and coral reef growth on the NWS and globally. This allowed lateral expansion to form coalesced platforms, eliminating the pattern of closely spaced, smaller isolated carbonate build-ups (<5 km) in the early to mid-Miocene. The modern Bahamas island chain exemplifies this evolutionary pattern, whereby, smaller ICB's trend along upthrown margins of fault blocks, until subsidence and fault reactivation confines carbonate production to topographic highs (Burgess et al., 2013).

Fig. 10 shows the evolution of carbonate factory phases I and II throughout the Miocene as a transition from barrier reef to reef growth then shifting to the platform interior. Here, the development of small patch reefs (older) to small isolated carbonate build-ups that merged and coalesced to form larger elongate, structures that are mapped laterally into the Poseidon 3D survey to the NE. Reduced subsidence in the late Miocene, may have been the cause of this lateral expansion of the carbonate factory, with a euphotic zone suited for more uniform carbonate production that was unbiased by topographic variability. The large scale morphological trend of the NWS coastline remains relatively unchanged since the Miocene. Large-scale distal to proximal carbonate platform facies successions are similar to modern day, with intermittent siliciclastic input. Episodic prograding lowstand siliciclastic wedges deposited since the Oligocene along the NWS coastline provided a continuous substratum for reef establishment during successive transgressions and highstands (Gallagher et al., 2017; Goktas et al., 2016). This pattern is also seen in the morphologies of the Great Barrier Reef, Belize Barrier Reef and Gulf of Papua, which show similarities to their respective paleo-coastlines (Droxler and Jorry, 2013; Mallarino et al., 2021).

Canyons likely formed in the late Miocene as increasing topographic relief from the aggrading platforms in the NW and SW of the area led to slumping and gravity deposits from erosion by turbidity currents and large swells (U4–U5, Fig. 9). Since their formation, intermittent highstands further developed their steep profiles and likely created hydrodynamic conditions that promote nutrient upwelling and reef growth (Huang et al., 2020). Thus, creating positive feedback for reef perseverance for both the NSR and SSR during marine transgressions and cooling following the MMCO (Belde et al., 2017).

6.3.2. Pliocene and the demise of contemporaneous reefs

41 kyr cycles of obliquity driven orbital precession increased solar maxima in the equatorial and tropic regions, increasing monsoonal activity (Wan et al., 2007) and terrigenous weathering in the Pliocene (Ruddiman and William, 2008). The effect of this climate forcing resulted in massive terrigenous influx to the ocean basins, significant global warming, melting of ice sheets and rapid RSL rise up to 22 m (Miller et al., 2012). This likely drowned many coral reef sites in carbonate factories globally (e.g., QLD and Marion Plateaus (Belde et al., 2017)). Nevertheless, Gallagher et al. (2017) infer that carbonate production in the NWS region began in the Pliocene, and photozoan carbonate platform development began in the late Pliocene. Carbonate sediment was then deposited on paleo highs of basinward prograding non-tropical ramps (Goktas et al., 2016). A similar evolutionary history is interpreted on the GBR by Daniell et al. (2020). Gallagher et al. (2014) links the initiation of this platform development to the intensification of the warm LC, which is stronger during warmer interglacial periods. This concurs with interpretations in this study area. The influx of terrigenous siliciclastic sediment and rapid RSL rise throughout the Pliocene that led to the partial drowning of reefs in the late Miocene, did not end the carbonate factory. Rather, it reduced and limited platform development to topographic highs and marginal settings. This essentially, converted it into a mixed siliciclastic-carbonate setting. Similarities can therefore be drawn to the modern Gulf of Papua system, which demonstrated only partial drowning of distal reefs in the late Miocene (Tcherepanov et al., 2008) and that survive today, e.g., the Ashmore atoll and surrounding trough. Buildups within the proximal platform to the East of the survey were likely unable to keep pace with rapid increase in rates of accommodation creation as well as increasing ocean current strength (e.g., Betzler and Eberli, 2019). It is likely they 'gave-up' due to regressive sediment wedges deposited during subsequent periods with lower rates of accommodation space in the late Pliocene. This pattern of demise is common in the carbonate build-up stratigraphic records (Greenlee et al., 1993). This drowning unconformity in the East of the study area (H7), is subsequently buried by hemi-pelagic sediments, as is typical of drowning carbonate systems (Godet et al., 2013). However, our interpretations instead show rapid vertical aggradation of the precursor NSR and SSR. This suggests that their location, antecedent substrate, reef growth rates and local oceanographic factors played a key role in outpacing dramatic changes in accommodation space, increasing ocean current strength and avoiding sediment influx. Many present-day reef species have growth rates that outpace historic sea level rises. For example, the Acropora sp. was a dominant reef builder around the MPT on the Great Barrier Reef, because of its ability to keep pace with rapid and high amplitude sea level rises (Humblet and Webster, 2017).

Further, drowning unconformities in carbonate platforms are a result of a complex interplay of abrupt RSL rise and paleo-oceanic events (Schlager, 1981, 2005; Zeng and Kerans, 2003; Godet et al., 2013; Catuneanu, 2020). For example, in southern France, early Aptian carbonate platform drowning was triggered by an oceanic anoxic event that weakened rudist-dominated ecosystems that subsequently failed to keep pace with tectonic movements (Godet et al., 2013). Evidence of historic channels and open reef rim margins implies that NSR and SSR were connected and exposed to ocean currents, swells and tides, since the Miocene. This suggests that temperature, salinity and importantly, sediment flux have been regulated in the recent geologic past. Thus, it is imperative to consider that during this time, changing accommodation space and sediment flux was not the sole driver of carbonate platform and reef perseverance. Instead, oceanographic factors held perhaps a more significant influence.

6.3.3. Quaternary and the Mid Pleistocene transition

Quaternary sea level variations were the largest in the Cenozoic due to northern hemisphere glacial advance and retreat (Miller et al., 2020). As such, many Pleistocene reefs exhibit episodic 'turn on' and 'turn off' events of reef growth (Gallagher et al., 2014), e.g., Ribbon Reef 5, GBR

(Webster and Davies, 2003), Hawaii (Webster et al., 2004) and the Ryukyus Islands, Japan (Yamamoto et al., 2006). In stable tectonic environments, such as the NWS, the growth of reef sequences is optimised during sea level highstands, where the resulting geomorphologic characteristics are typified by vertical successions of stacked reefs bounded by episodic erosion surfaces formed during sea level lowstands (Humblet and Webster, 2017).

Continued monsoonal activity and changing ocean-circulation systems introduced new currents to the NWS in the early Quaternary (Saqab and Bourget., 2015), including the LC. However, the ITF continued since the Pliocene and is regarded as a major oceanographic influence on Quaternary development of Scott Reefs (Gallagher et al., 2014, 2017).

The MPT is documented by coral reef initiation along shelf margin carbonate build-ups and barrier reefs throughout the world (Saqab and Bourget., 2015; Yamamoto et al., 2006; Droxler and Jorry, 2013; Berends et al., 2021; Yamamoto et al., 2006). Gallagher et al. (2014) determines the onset of NWS coral and ooid deposition to be after the MPT, ca. 0.5 Ma, activated by higher amplitude glacio-eustatic reef cycles. This initiation resulted from a shift to higher amplitude, lower frequency sea level oscillations. This triggered rapid sea level rises due to fast deglaciations that were likely on-off switches to global reef growth episodes. Droxler and Jorry (2013) discuss the importance of the MPT on coral reef communities that initiate at this time on topographic siliciclastic highs. Yamamoto et al. (2006) similarly discuss the response and onset of coral-gal communities in the Ryukyus Islands to increased sea level amplitude from 41 ka cycles in the early Quaternary to 100 ka in the late Quaternary.

Fig. 18 shows the same reef growth initiation and subsequent cyclic growth phases interpreted at Scott Reefs that likely correspond to the onset of these 100kyr climate cycles. However, it is acknowledged that the link between physical changes of reef expansion and sea level amplitude and frequency changes is uncertain. Particularly since reef expansion at this time also coincided with increasing sea surface temperatures documented around the globe (Ryukyus Islands: Yamamoto et al., 2006; GBR: Droxler and Jorry, 2013; New Caledonia; Montaggioni et al., 2011). Therefore, it is likely that the post-MPT reef expansion was a global event 'responding to tropical climatic and/or oceanographic changes' (Yamamoto et al., 2006). Several authors also draw a link between carbonate growth initiation and the 'orbital-scale variability' of

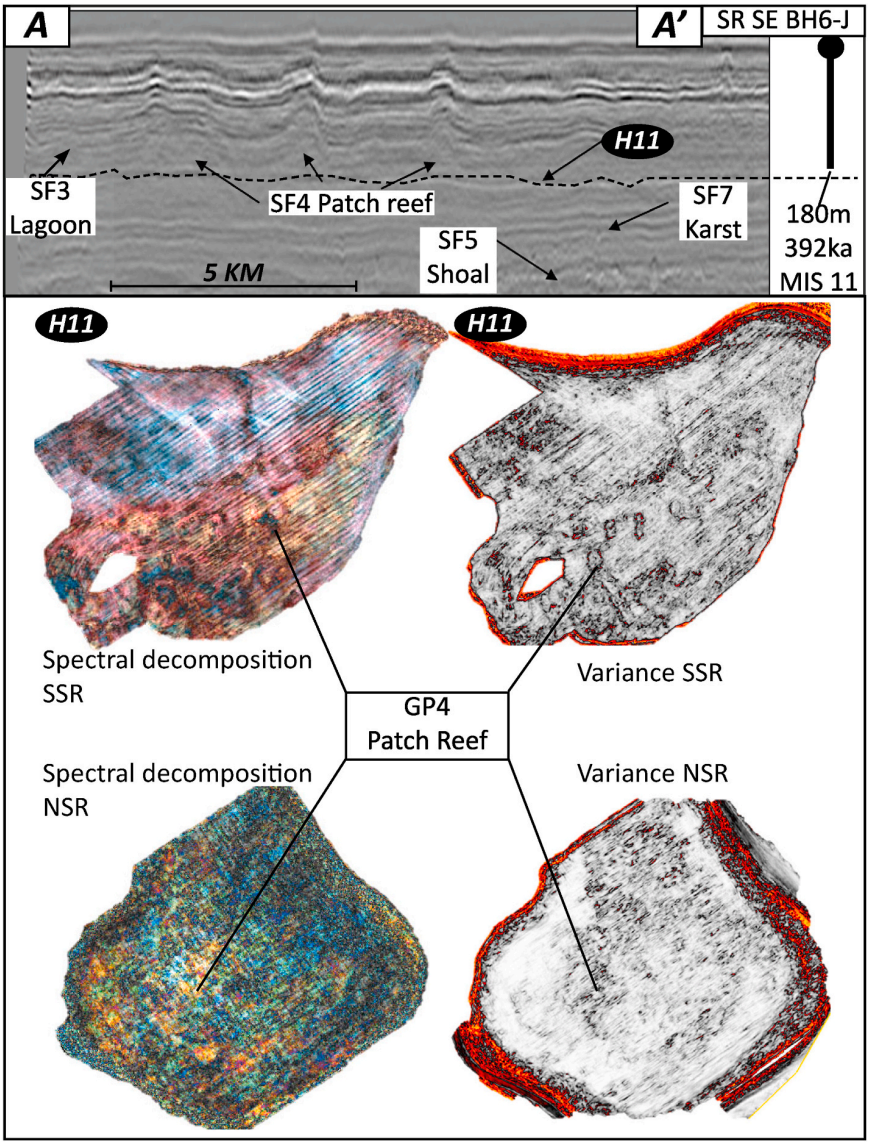


Fig. 18. Section A-A′ is a zoomed in panel over SSR showing seismic facies interpretations and borehole SR SE BH6-J and corresponding U/Th age and depth above H11 (N.B. borehole is located over a seismic data gap). Patch Reefs (GP4) identified along H11 in plan view using spectral decomposition (at 20, 40 and 60 Hz) and variance attribute for NSR and SSR. A major change in seismic facies is observed from parallel, horizontal moderate to high amplitude reflections to variable reflection character, including chaotic transparent, mound shaped facies, indicative of SF4 and GP4 – patch reef. This MPT (MIS15) corresponds to the initiation of the Belize Barrier Reef and the Great Barrier reef and is documented as the initiation of the Buffalo ICB, NWS Australia (Saqab, 2015; Saqab and Bourget, 2016). (N.b., H11 correlates with MIS11 in core section which are rhodolith beds. This indicates the base of reef cycles/reef onset, which are commonly characterised by rhodolith beds, identified in borehole SRSEHDD3-JA. This is indicative of wave agitated substrates, which is coincident with an open lagoonal environment in SSR during this time.)

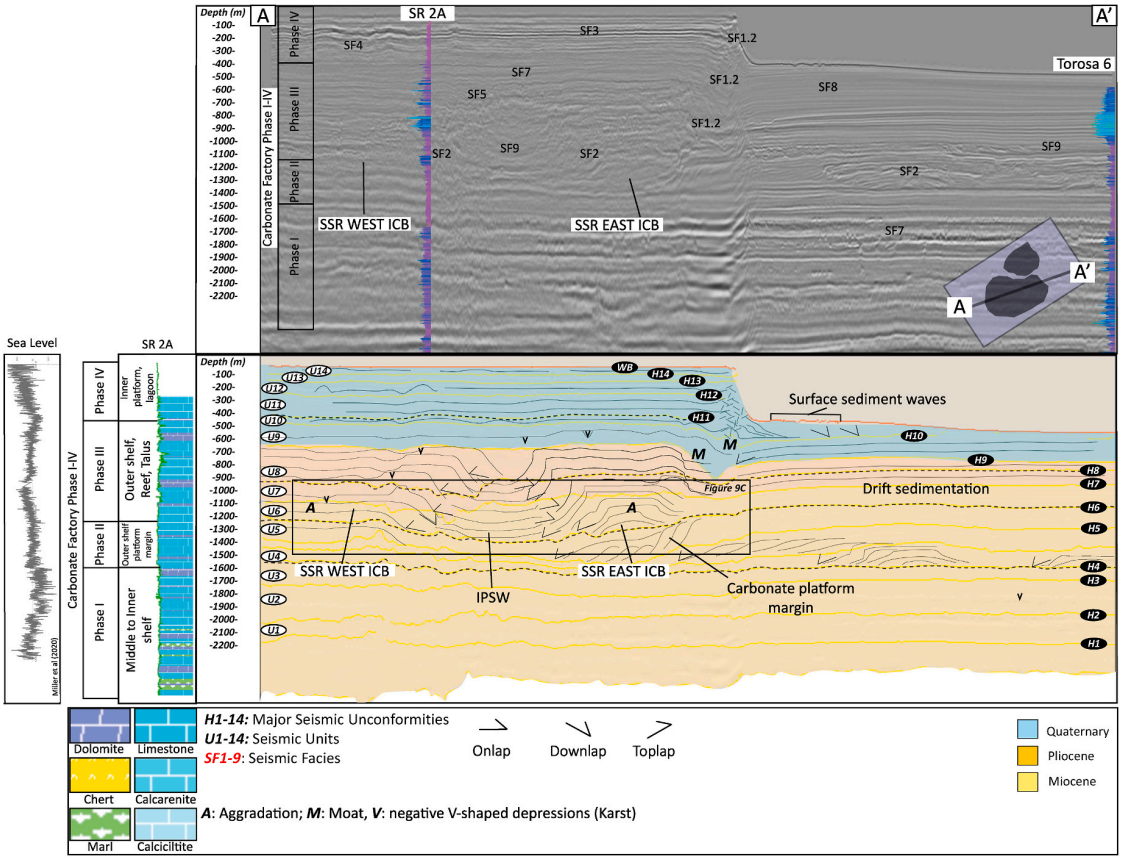


Fig. 19. Tectono-stratigraphic framework of South Scott Reef showing the evolution in seismic section of the two isolated ICB's that eventually coalesce into a raised isolated carbonate platform. Seismic stratigraphic sequence interpreted on sketch (below) and seismic line (above). Bottom left panels show global sea level curve and carbonate factories Phase I-IV that correspond to the facies depositional environments along interpreted GR well log for SR-2A. N.b. When this lithological log is stretched vertically in Petrel, a small marl section is visible, corresponding to high GR values.

the LC activity bringing warm biota rich waters to the NWS (He et al., 2021; Gallagher et al., 2014, 2017 Collins and Testa, 2009). He et al. (2021) suggest that the LC strengthened during the MPT (ca 1.25–0.7 Ma) with progressive warming, in contrast with the long-term global cooling trend. However, increasing ocean current strength is often associated with the decline of isolated carbonate platforms (Betzler and Eberli, 2019). Whilst Scott Reefs were resilient enough to withstand these pressures since the Pliocene, it is interpreted that isolated carbonate platforms around the world (Maldives, Indian Ocean; South China Sea; Marion and Queensland Plateau) have been backstepping significantly through the Neogene and Quaternary as a result of increasing ocean current strength (Qin et al., 2022).

Post-MPT cyclic reef growth at Scott Reefs is constrained through seismic sequence stratigraphy and GR log interpretation, and correlated to uncertain U/Th age data (Collins and Testa, 2009). Fig. 17 highlights the relationship between GR lows corresponding to stratigraphic unconformities that document reef growth. It is interpreted that the onset of high amplitude sea level cycles post-MPT, identified by thick aggrading, conformable stratal sequences, significantly enhanced the vertical aggradation of Scott Reefs. This transformed them from marginal platform reef systems in the Pliocene to large, sub-aerially isolated carbonate build-ups seen today. The interpretation of Scott reef growth initiation at H11 after a period of quiescence, corresponds to an approximate age of ca. 0.6 Ma (Table 1) and is in agreement with the timing of reef onset in other carbonate systems around the world (Big Bank ICB: Saqab and Bourget, 2015).

Interpretations in this study supports the evidence that the Quaternary on the NWS, Australia is characterised by a global sea level fall and the onset (ca. 1 Ma) of increased intensity of the LC (McCaffrey et al., 2020). This is followed by shelf inundation and reflooding of the NW Australian shelf since the last glacial maximum (Webster et al., 2022; O'Leary et al., 2020). This suggests that the onset of the carbonate factory at H11 did not occur during a long-term transgression and was in fact triggered by periods of rapid RSL rise and slow falls, as seen elsewhere during this orbitally driven global climate change, e.g., development of the Vulcan sub-basin ICB's (Saqab and Bourget, 2015).

7. Conclusions

This study integrates detailed seismic geomorphology and seismic stratigraphic interpretations of newly reprocessed 3D seismic data, combined with well log data and preliminary core dating, to reveal the tectono-stratigraphic history of North and South Scott Reefs since the Miocene. The history of carbonate platform evolution is documented through four proposed carbonate factory phases (I-IV) that builds on the existing stratigraphic framework of the NWS. On this basis, we conclude that:

(1) Scott Reefs have persisted through four carbonate factory phases in the form of: small, inner platform isolated reefs and large, raised isolated carbonate platforms, since the Burdigalian. The precursor reefs to the modern-day platforms likely initiated at the Miocene-Pliocene boundary, however, the geomorphologic evolution of NSR and SSR differed.
(2) NSR emerged on the carbonate platform margin above the Scott reef trend topographic high. The reef crest kept pace with rapid

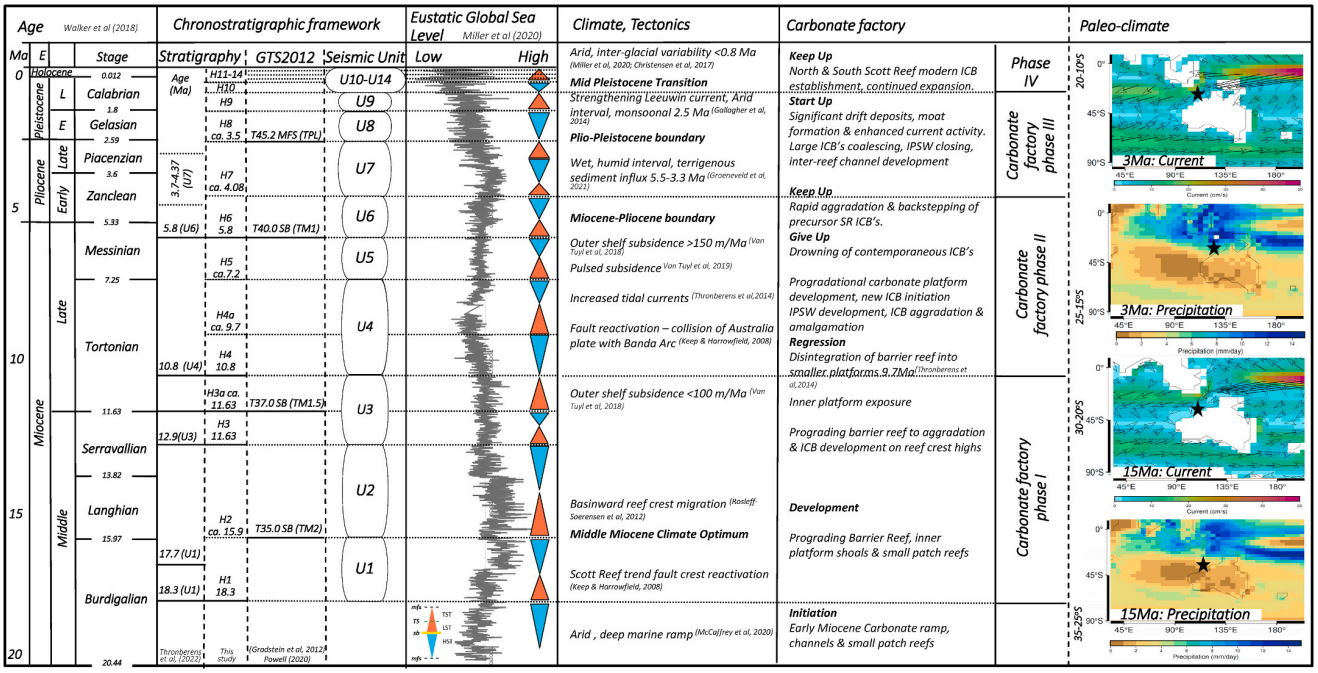


Fig. 20. Chronostratigraphic framework of the Torosa Field, Browse Basin, NWS Australia. Timescale follows Walker et al. (2018). Stratigraphy from Thronberens et al. (2022) and the Neogene regional picks from the Barrow and Exmouth sub-basins and Exmouth Plateau stratigraphy are given (Geological Timescale 2012 (GTS2012); Powell, 2020). Eustatic global sea level from Miller et al. (2020) and interpretive 2nd-4th order stratigraphic sequences are given based on this study's stratigraphic picks. Climate, tectonics, proposed carbonate factories and paleo-climate are also given, corresponding to timescale. Four paleo-climate maps with arrows summarising precipitation and current trends for 15 Ma, and 3 Ma and their corresponding paleo-latitudes. Present day Australian continent outline in black shows relative movement of the continent from 15 Ma to present. Modern day location of Scott Reef is shown by the star. Original data source: Scotese and Wright (2018); Müller et al. (2019)

windward sea level rise, and subsequent development of the leeward reef crest prograded landward. This established a robust inner platform lagoon environment and wide reef crest, subaerially raised and sheltered from the open ocean.

(3) SSR initiated as two or three separate, smaller ICB's, separated by an IPSW that eventually coalesced into a larger, raised platform. The platform failed to develop a windward reef crest, exposing it to high energy ocean conditions and sediment reworking. The open ocean conditions persist to present day leaving an exposed partially closed lagoon. Rapid vertical aggradation of the merged ICB's kept pace with increasing accommodation in the Pliocene and Quaternary, resulting in the isolated carbonate platforms that persisted to present. Uncertain correlations of major unconformities in the late Quaternary suggest there was recent differential subsidence between NSR and SSR, with the proposed correlated unconformities being slightly higher over NSR. This suggests SSR experienced higher subsidence rates.

(4) The evidence for the eustatically driven Miocene-Pliocene carbonate factory demise was not consistent with interpretations in this study. Instead, it is suggested that continued carbonate production was confined to distal topographic highs along the outer platform margin.

(5) The MPT represents a major reef initiation event or reactivation along H11 for both NSR and SSR that were likely in a period of inundation, dormancy or drowned, from between the early Pleistocene to the mid Pleistocene. Despite a long-term cooling trend in the Pleistocene, the change in sea level amplitude and frequency and the onset of inter-glacial variability is considered to be the main driver for this period of cyclic reef growth, seen in other reef systems around the world from around 0.8 Ma.

(6) Carbonate platform production was sustained intermittently at this study site throughout a significant change in latitude (ca. -25-15°S) from ca. 20 Ma to present. This suggests that it was likely the location and oceanographic setting that were the key drivers in determining the resilience and perseverance of this carbonate platform and reef system. Scott Reefs' developed on the distal continental platform where inter-platform seaways, moats and early development of inter-reef channel likely bypassed terrigenous sediment influx away from the reefs basinward via canyons. This avoided periods of inundation during wet, monsoonal climates and periods of strong ocean currents, capitalising on continued accommodation.

(7) In the absence of sufficient biostratigraphic information, this study demonstrates that seismic data and GR logs have proved sufficient to aid in characterising reef development in the context of four carbonate factory phases (I-IV). These phases coincide to eustatic (global) and regional (Australian) climate and environmental forcings. Understanding carbonate platform and coral reef response to the effects of these climatic changes is highly relevant to estimate decadal trends in reefs evolution under predicted future sea level rise trajectories (Miller et al., 2020).

Funding sources

This research was supported by a HDR scholarship from the School of Geosciences, University of Sydney. This research was also funded by a PRSS (post-graduate research support scheme) scholarship, School of Geosciences, University of Sydney, to attend the ICRS conference 2023 to present this work as a poster presentation. This ongoing research continues to be funded by an ANSTO AINSE scholarship. Jonathon Leonard was supported by Australian Research Council grant DE210100084.

Credit author statement

Carra Williams: Conceptualisation, Methodology, Investigation, Visualisation, Data Curation, Writing-Original draft preparation, Software. Victorien Paumard: Supervision, Conceptualisation, Investigation, Methodology, Software, Data Curation, Writing-Reviewing and Editing, Validation, Resources. Jody Webster: Supervision, Conceptualisation, Investigation, Visualisation, Writing-Reviewing and Editing, Resources. Jonathon Leaonard: Visualisation, Data Curation, Writing-Reviewing and Editing, Software, Validation. Tristan Salles: Writing-Reviewing and Editing. Mick O'Leary: Writing-Reviewing and Editing. Simon Lang: Visualisation, Software, Validation, Reviewing and Editing.

Declaration of competing interest

The authors declare that they have no known competing financial interests or personal relationships that could have appeared to influence the work reported in this paper.

Data availability

Details and links of how to source publicly available data included in 'Data availability'

Acknowledgements

Thanks to Stephen Gallagher (University of Melbourne) for support and guidance on biostratigraphic data and well log interpretations. Seismic data is courtesy of Geoscience Australia. We are grateful to Woodside Energy Ltd (WEL) for providing biostratigraphic data and lithostratigraphic interpretations as well as permission to use WEL regional stratigraphy. Thanks to Phil Watson for facilitating the TIDE agreement, which includes permission to use and refence geotechnical data from Collins and Testa (2009). Thanks to Barry Taylor and the Browse team at WEL for providing guidance and feedback on the manuscript draft. Thanks, are also due to the School of Earth Sciences (The University of Western Australia) for providing support and access to a workstation. We are grateful to Eliis and Schlumberger for providing academic licenses to the software Paleoscan™ and Petrel™, respectively.

Appendix A. Supplementary data

Supplementary data to this article can be found online at https://doi.org/10.1016/j.marpetgeo.2023.106188.

References

Apthorpe, M., 1988. Cainozoic depositional history of the North West Shelf. In: Purcell, P.G., Purcell, R.R. (Eds.), The North West Shelf, Australia: Perth, Petroleum Exploration Society of Australia Symposium, pp. 55–84. Proceedings.

Auer, G., et al., 2019. Timing and pacing of Indonesian throughflow restriction and its connection to late Pliocene climate shifts. Paleoceanogr. Paleoclimatol. 34 (4), 635–657.

Belde, J., Back, S., Reuning, L., 2015. Three-dimensional seismic analysis of sediment waves and related geomorphological features on a carbonate shelf exposed to large amplitude internal waves, Browse Basin region, Australia. Sedimentology 62 (1), 87–109. https://doi.org/10.1111/sed.12141.

Belde, J., Back, S., Bourget, J., Reuning, L., 2017. Oligocene and Miocene carbonate platform development in the Browse Basin, Australian northwest shelf. J. Sediment. Res. 87 (8), 795–816. https://doi.org/10.2110/jsr.2017.44.

Belopolsky, A., Droxler, A., 2003. Imaging Tertiary carbonate system, the Maldives, Indian Ocean; insights into carbonate sequence interpretation. Lead. Edge 22 (7), 646–652. https://doi.org/10.1190/1.1599690.

Berends, T., van de Wal, R., Lourens, L., Köhler, P., 2021. On the cause of the mid-pleistocene transition. Rev. Geophys. 59 (2), 1. https://doi.org/10.1029/2020RG000727. Sub Dynamics Meteorology, Sub Algemeen Marine & Atmospheric res, Proceskunde, Stratigraphy and Paleontology, & Marine and Atmospheric Research.

Berner, R.A., Lasaga, A.C., Garrels, R.M., 1983. The carbonate-silicate geochemical cycle and its effect on atmospheric carbon dioxide over the past 100 million years. Am. J. Sci. (1880) 283 (7), 641–683. https://doi.org/10.2475/ajs.283.7.641.

Betzler, C., Eberli, G.P., 2019. Miocene start of modern carbonate platforms. Geology (Boulder) 47 (8), 771–775. https://doi.org/10.1130/G45994.1.

Betzler, C., Hübscher, C., Lindhorst, S., Reijmer, J.J.G., Römer, M., Droxler, A.W., Fürstenau, J., Lüdmann, T., 2009. Monsoon-induced partial carbonate platform drowning (Maldives, Indian Ocean). Geology (Boulder) 37 (10), 867–870. https://doi.org/10.1130/G25702A.1.

Betzler, C., Hübscher, C., Lindhorst, S., Lüdmann, T., Reijmer, J.J.G., Braga, J., 2016. Lowstand wedges in carbonate platform slopes (Quaternary, Maldives, Indian Ocean). Depositional Rec. 2 (2), 196–207. https://doi.org/10.1002/dep2.21.

Braithwaite, C.J.R., 2016. Coral-reef records of Quaternary changes in climate and sea-level. Earth Sci. Rev. 156, 137–154. https://doi.org/10.1016/j.earscirev.2016.03.002.

Burgess, P.M., Winefield, P., Minzoni, M., Elders, C., 2013. Methods for identification of isolated carbonate buildups from seismic reflection data. AAPG (Am. Assoc. Pet. Geol.) Bull. 97 (7), 1071–1098. https://doi.org/10.1306/12051212011.

Burke, K.D., Williams, J.W., Chandler, M.A., Haywood, A.M., Lunt, D.J., Otto-Bliesner, B. L., 2018. Pliocene and Eocene provide best analogs for near-future climates. Proc. Nat. Acad. Sci. - PNAS 115 (52), 13288–13293. https://doi.org/10.1073/pnas.1809600115.

Camoin, G.F., Webster, J.M., 2015. Coral reef response to Quaternary sea-level and environmental changes: state of the science. Sedimentology 62 (2), 401–428. https://doi.org/10.1111/sed.12184.

Catuneanu, O., 2020. Sequence stratigraphy in the context of the "modeling revolution. Mar. Petrol. Geol. 116, 104309 https://doi.org/10.1016/j.marpetgeo.2020.104309.

Christensen, B.A., Renema, W., Henderiks, J., De Vleeschouwer, D., Groeneveld, J., Castañeda, I.S., Reuning, L., Bogus, K., Auer, G., Ishiwa, T., McHugh, C.M., Gallagher, S.J., Fulthorpe, C.S., 2017. Indonesian Throughflow drove Australian climate from humid Pliocene to arid Pleistocene. Geophys. Res. Lett. 44 (13), 6914–6925. https://doi.org/10.1002/2017GL072977.

Collins, L.B., 2002. Tertiary foundations and quaternary evolution of coral reef systems of Australia's North West Shelf. In: Moss, S.J., Keep, M. (Eds.), The Sedimentary Basins of Western Australia 3, October 20-23 2002. Petroleum Exploration Society of Australia, Perth, Western Australia, pp. 129–152.

Collins, L.B., Testa, V., 2009. Quaternary Growth History and Evolution of the Scott Reef Carbonate Platform and Coral Reef: Core Study. Curtin University, 2009. Final Report Prepared for Woodside Energy Limited, March 2009. *Not published, permission and access granted through WEL-UWA TIDE agreement*.

Collins, L.B., Zhao, J.-X., Freeman, H., 2006. A high-precision record of mid–late Holocene sea-level events from emergent coral pavements in the Houtman Abrolhos Islands, southwest Australia. Quat. Int. 145, 78–85. https://doi.org/10.1016/j.quaint.2005.07.006.

Collins, L.B., Testa, V., Zhao, J., Qu, D., 2011. Holocene growth history and evolution of the Scott reef carbonate platform and coral reef. J. Roy. Soc. West Aust. 94 (2), 239, 239.

Collins, L.B., James, N.P., Bone, Y., 2014. Chapter 19 Carbonate shelf sediments of the western continental margin of Australia. Mem. Geol. Soc. Lond. 41 (1), 255–272. https://doi.org/10.1144/M41.19.

Daniell, J., Manoy, T., Beaman, R.J., Webster, J.M., Puga-Bernabéu, Á., 2020. Shelf-edge delta and reef development on a mixed siliciclastic-carbonate margin, central Great Barrier Reef. J. Sediment. Res. 90 (10), 1286–1304. https://doi.org/10.2110/jsr.2020.61.

Droxler, A.W., Jorry, S.J., 2013. Deglacial origin of barrier reefs along low-latitude mixed siliciclastic and carbonate continental shelf edges. Ann. Rev. Mar. Sci 5 (1), 165–190. https://doi.org/10.1146/annurev-marine-121211-172234.

Emery, D., Myers, K., Bertram, G.T., 1996. In: Emery, D., Myers, K., Bertram, G.T. (Eds.), Sequence Stratigraphy. Blackwell Science.

Gallagher, S.J., Wagstaff, B.E., 2021. Quaternary environments and monsoonal climate off northwest Australia: palynological evidence from ocean drilling program site 765. Quat. Sci. Rev. 259, 106917 https://doi.org/10.1016/j.quascirev.2021.106917.

Gallagher, S.J., Wallace, M.W., Hoiles, P.W., Southwood, J.M., 2014. Seismic and stratigraphic evidence for reef expansion and onset of aridity on the Northwest Shelf of Australia during the Pleistocene. Mar. Petrol. Geol. 57, 470–481. https://doi.org/10.1016/j.marpetgeo.2014.06.011.

Gallagher, S.J., Fulthorpe, C.S., Bogus, K., The Expedition 356 Scientists, 2017. Indonesian throughflow. In: Proceedings of the International Ocean Discovery Program, 356: College Station, TX (International Ocean Discovery Program). https://doi.org/10.14379/iodp.proc.356.2017.

Gilmour, J., Smith, L., Cook, K., Pincock, S., 2013a. Discovering Scott Reef: 20 Years of Exploration and Research. © Woodside. Australian Institute of Marine Science. ISBN: 2013 9780642322654 (hbk.) National Library of Australia Cataloguing-in-Publication entry.

Gilmour, J.P., Smith, L.D., Heyward, A.J., Baird, A.H., Pratchett, M.S., 2013b. Recovery of an isolated coral reef system following severe disturbance. Science (Am. Assoc. Adv. Sci.) 340 (6128), 69–71. https://doi.org/10.1126/science.1232310.

Gilmour, J., Speed, C.W., Babcock, R., 2016. Coral reproduction in Western Australia. PeerJ (San Francisco, CA) 4, e2010–e2010. https://doi.org/10.7717/peerj.2010.

Godet, A., Föllmi, K.B., Spangenberg, J.E., Bodin, S., Vermeulen, J., Adatte, T., Bonvallet, L., Arnaud, H., 2013. Deciphering the message of Early Cretaceous drowning surfaces from the Helvetic Alps: what can be learnt from platform to basin correlations? Sedimentology 60 (1), 152–173. https://doi.org/10.1111/sed.12008.

Goktas, P., Austin, J.A., Fulthorpe, C.S., Gallagher, S.J., 2016. Morphologies and depositional/erosional controls on evolution of pliocene-pleistocene carbonate

platforms: northern carnarvon basin, northwest shelf of Australia. Continent. Shelf Res. 124, 63–82. https://doi.org/10.1016/j.csr.2016.05.009.
Gradstein, F.M., Ogg, J.G., Schmitz, M., Ogg, G., 2020. Geologic Time Scale 2020. Elsevier. https://doi.org/10.1016/C2020-1-02369-3.
Gradstein, F.M., Ogg, J.G., Smith, A.G., 2004. A Geologic Time Scale 2004. Cambridge University Press, p. 610.
Gradstein, F.M., Ogg, J.G., Schmitz, M., Ogg, G. (Eds.), 2012. A Geologic Time Scale 2012, Vol. 2. Elsevier, p. 1176.
Green, R., 2018. Hydrodynamics, Thermodynamics and Nutrient Fluxes in a Tide-Dominated Coral Reef Atoll System. Doctoral Thesis. The University of Western Australia.
Greenlee, S.M., Lehman, P.J., Loucks, R.G., Sarg, J.F., 1993. Stratigraphic Framework of Productive Carbonate Buildups Carbonate Sequence Stratigraphy, pp. 43–62, 57AAPG Memoir.
Groeneveld, J., De Vleeschouwer, D., Jackson, C.M., Gallagher, S.J., 2021. Dating the northwest shelf of Australia since the Pliocene. In: Earth and Space Science Open Archive ESSOAr. https://doi.org/10.1002/essoar.10504262.1.
Harris, D.L., Webster, J.M., Vila-Concejo, A., Hua, Q., Yokoyama, Y., Reimer, P.J., 2015. Late Holocene sea-level fall and turn-off of reef flat carbonate production; rethinking bucket fill and coral reef growth models. Geology (Boulder) 43 (2), 175–178. https://doi.org/10.1130/G35977.1.
He, Y., Wang, H., Liu, Z., 2021. Development of the Leeuwin current on the northwest shelf of Australia through the pliocene-pleistocene period. Earth Planet Sci. Lett. 559, 116767 https://doi.org/10.1016/j.epsl.2021.116767.
Hendry, J., et al., 2021. Seismic characterization of carbonate platforms and reservoirs: an introduction and review. Geol. Soc. Lond. Spec. Publ. 509 (1), 1–28.
Hengesh, J.V., Whitney, B.B., 2016. Transcurrent reactivation of Australia's western passive margin: an example of intraplate deformation from the central Indo-Australian plate. Tectonics (Washington, D.C.) 35 (5), 1066–1089. https://doi.org/10.1002/2015TC004103.
Hirase, S., Yokoyama, Y., Lee, C.-T., Iwasaki, W., 2016. The Pliocene-Pleistocene transition had dual effects on North American migratory bird speciation. Palaeogeogr. Palaeoclimatol. Palaeoecol. 462, 85–91. https://doi.org/10.1016/j.palaeo.2016.09.006.
Huang, X., Betzler, C., Wu, S., Bernhardt, A., Eagles, G., Han, X., Hovland, M., 2020. First documentation of seismic stratigraphy and depositional signatures of Zhongsha atoll (Macclesfield Bank), South China Sea. Mar. Petrol. Geol. 117, 104349 https://doi.org/10.1016/j.marpetgeo.2020.104349.
Hull, J.N.F., Smith, S.A., Young, H.C., 1998. Abstract: a model for the sequence stratigraphic interpretation of carbonate wireline log motifs: an example from the North West West Shelf of Australia. AAPG (Am. Assoc. Pet. Geol.) Bull. 82 https://doi.org/10.1306/00AA8ADA-1730-11D7-8645000102C1865D.
Hull, J.N.F., Griffiths, C.M., 2002. Sequence stratigraphic evolution of the Albian to recent section of the Dampier Sub-basin, North West Shelf Australia. In: Keep, M., Moss, S.J. (Eds.), The Sedimentary Basins of Western Australia 3: Proceedings of the Petroleum Exploration Society of Australia Symposium, Perth, Western Australia, 2002, pp. 617–639.
Humblet, M., Webster, J.M., 2017. Coral community changes in the Great Barrier Reef in response to major environmental changes over glacial-interglacial timescales. Palaeogeogr. Palaeoclimatol. Palaeoecol. 472, 216–235. https://doi.org/10.1016/j.palaeo.2017.02.003.
Jiménez-Moreno, G., Pérez-Asensio, J.N., Larrasoaña, J.C., Sierro, F.J., Garcia-Castellanos, D., Salazar, Á., Salvany, J.M., Ledesma, S., Mata, M.P., Mediavilla, C., 2019. Early Pliocene climatic optimum, cooling and early glaciation deduced by terrestrial and marine environmental changes in SW Spain. Global Planet. Change 180, 89–99. https://doi.org/10.1016/j.gloplacha.2019.06.002.
Karas, C., Nürnberg, D., Tiedemann, R., Garbe-Schönberg, D., 2011. Pliocene Indonesian throughflow and Leeuwin current dynamics: implications for Indian ocean polar heat flux. Paleoceanography 26 (2). https://doi.org/10.1029/2010PA001949 np–n/a.
Keep, M., Harrowfield, M., 2005. Basement reactivation and inversion mechanisms in the Timor and Norwegian seas. In: Doré, A.G., Vining, B.A. (Eds.), Petroleum Geology: North-West Europe and Global Perspectives - Proceeding of the 6th Petroleum Geology Conference (London, UK, Vol. 2. The Geological Society Publishing House, pp. 861–872.
Keep, M., Harrowfield, M., 2008. Elastic flexure and distributed deformation along Australia's North West Shelf: Neogene tectonics of the Bonaparte and Browse basins. Geol. Soc. Spec. Publ. 306 (1), 185–200. https://doi.org/10.1144/SP306.9.
Keep, M., Bishop, A., Longley, I., 2000. Neogene wrench reactivation of the Barcoo sub-basin, northwest Australia: implications for Neogene tectonics of the Australian margin. Petrol. Geosci. 6, 211–220.
Keep, M., Clough, M., Langhi, L., 2002. Neogene tectonic and structural evolution of the Timor Sea, NW Australia. In: Keep, M., Moss, S.J. (Eds.), The Sedimentary Basins of Western Australia 3: Proceedings of the Petroleum Exploration Society of Australia Symposium, Perth, pp. 341–355.
Kennedy, D.M., Woodroffe, C.D., 2002. Fringing reef growth and morphology: a review. Earth-Science Reviews 57 (3), 255–277. https://doi.org/10.1016/S0012-8252(01)00077-0.
Lebrec, U., Riera, R., Paumard, V., O'Leary, M.J., Lang, S.C., 2022. Morphology and distribution of submerged palaeoshorelines: insights from the North West West Shelf of Australia. Earth Sci. Rev. 224, 103864 https://doi.org/10.1016/j.earscirev.2021.103864.
Lisiecki, L.E., Raymo, M.E., 2005. A Pliocene-Pleistocene stack of 57 globally distributed benthic δ18O records. Paleoceanography 20 (1), PA1003. https://doi.org/10.1029/2004PA001071 n/a.
Magalhães, A.J.C., et al., 2021. Sequence stratigraphy of clastic and carbonate successions: applications for exploration and production of natural resources. Brazilian Journal of Geology 51 (4).
Mallarino, G., Francis, J.M., Jorry, S.J., Daniell, J.J., Droxler, A.W., Dickens, G.R., Beaufort, L., Bentley, S.J., Opdyke, B.N., Peterson, L.C., Webster, J., 2021. Timescale dependent sedimentary record during the past 130 kyr from a tropical mixed siliciclastic–carbonate shelf edge and slope: Ashmore Trough (southern Gulf of Papua). Sedimentology 68 (6), 2606–2648. https://doi.org/10.1111/sed.12867.
Marshall, N.G., Lang, S.C., 2013. A new sequence stratigraphic framework for the North West West Shelf, Australia. In: Keep, M., Moss, S. (Eds.), The Sedimentary Basins of Western Australia 4: Proceedings of Petroleum Exploration Society of Australia Symposium. Perth: PESA. Petroleum Exploration Society of Australia, pp. 18–21.
McCaffrey, J.C., Wallace, M.W., Gallagher, S.J., 2020. A cenozoic Great barrier reef on Australia's North West Shelf. Global Planet. Change 184, 103048. https://doi.org/10.1016/j.gloplacha.2019.103048.
Milankovitch, M., 1941. Kanon der Erdbestrahlung und seine Andwendung aufdas Eiszeiten-problem. R. Serbian Acad., Belgrade.
Miller, K.G., Wright, J.D., Browning, J.V., Kulpecz, A., Kominz, M., Naish, T.R., Cramer, B.S., Rosenthal, Y., Peltier, W.R., Sosdian, S., 2012. High tide of the warm Pliocene; implications of global sea level for Antarctic deglaciation. Geology (Boulder) 40 (5), 407–410. https://doi.org/10.1130/G32869.1.
Miller, K.G., Browning, J.V., Schmelz, W.J., Kopp, R.E., Mountain, G.S., Wright, J.D., 2020. Cenozoic sea-level and cryospheric evolution from deep-sea geochemical and continental margin records. Sci. Adv. 6 (20) https://doi.org/10.1126/sciadv.aaz1346 eaaz1346–eaaz1346.
Mitchum, R., Vail, P., 1977. Seismic Stratigraphy and Global Changes of Sea Level, Part Seven: Seismic Stratigraphic Interpretation Procedure. https://doi.org/10.1306/M26490C9.
Montaggioni, L.F., 2005. History of Indo-Pacific coral reef systems since the last glaciation: development patterns and controlling factors. Earth Sci. Rev. 71 (1), 1–75. https://doi.org/10.1016/j.earscirev.2005.01.002.
Montaggioni, L.F., Braithwaite, C.J.R., 2009. Quaternary Coral Reef Systems: History, Development Processes and Controlling Factors, first ed. Elsevier.
Montaggioni, L.F., Cabioch, G., Thouveny, N., Frank, N., Sato, T., Sémah, A.-M., 2011. Revisiting the Quaternary development history of the western New Caledonian shelf system: from ramp to barrier reef. Mar. Geol. 280 (1–4), 57–75. https://doi.org/10.1016/j.margeo.2010.12.001.
Montaggioni, L.F., Borgomano, J., Fournier, F., Granjeon, D., 2015. Quaternary atoll development: new insights from the two-dimensional stratigraphic forward modelling of Mururoa Island (Central Pacific Ocean). Sedimentology 62 (2), 466–500. https://doi.org/10.1111/sed.12175.
Müller, R.D., Zahirovic, S., Williams, S.E., Cannon, J., Seton, M., Bower, D.J., Tetley, M.G., Heine, C., Le Breton, E., Liu, S., Russell, S.H.J., Yang, T., Leonard, J., Gurnis, M., 2019. A global plate model including lithospheric deformation along major rifts and orogens since the triassic. Tectonics (Washington, D.C.) 38 (6), 1884–1907. https://doi.org/10.1029/2018TC005462.
O'Leary, M.J., Paumard, V., Ward, I., 2020. Exploring Sea Country through high-resolution 3D seismic imaging of Australia's NW shelf: resolving early coastal landscapes and preservation of underwater cultural heritage. Quat. Sci. Rev. 239, 106353 https://doi.org/10.1016/j.quascirev.2020.106353.
Paterson, R.J., et al., 2008. Controls on early diagenetic overprinting in icehouse carbonates: insights from modeling hydrological zone residence times using CARB3D+. J. Sediment. Res. 78 (4), 258–281.
Paumard, V., Zuckmeyer, E., Boichard, R., Jorry, S.J., Bourget, J., Borgomano, J., Maurin, T., Ferry, J.-N., 2017. Evolution of Late Oligocene - early Miocene attached and isolated carbonate platforms in a volcanic ridge context (Maldives type), Yadana field, offshore Myanmar. Mar. Petrol. Geol. 81, 361–387. https://doi.org/10.1016/j.marpetgeo.2016.12.012.
Paumard, V., Bourget, J., Durot, B., Lacaze, S., Payenberg, T., George, A.D., Lang, S., 2019a. Full-volume 3D seismic interpretation methods: a new step towards high-resolution seismic stratigraphy. Interpretation 7 (3), B33–B47. https://doi.org/10.1190/INT-2018-0184.1.
Paumard, V., Bourget, J., Payenberg, T., George, A.D., Ainsworth, R.B., Lang, S., 2019b. From quantitative 3D seismic stratigraphy to sequence stratigraphy: insights into the vertical and lateral variability of shelf-margin depositional systems at different stratigraphic orders. Mar. Petrol. Geol. 110, 797–831. https://doi.org/10.1016/j.marpetgeo.2019.07.007.
Posamentier, H.W., Paumard, V., Lang, S.C., 2022. Principles of seismic stratigraphy and seismic geomorphology I: extracting geologic insights from seismic data. Earth Sci. Rev. 228, 103963 https://doi.org/10.1016/j.earscirev.2022.103963.
Powell, 2020. Woodside chronostratigraphic chart, NWS, GTS2012. In: Accessed from Swell-1A Interpretative Well Completion Report, NOPIMS well data website: Home. National Offshore Petroleum Information Management System. ga.gov.au.
Purdy, E.G., Gischler, E., 2005. The transient nature of the empty bucket model of reef sedimentation. Sediment. Geol. 175 (1), 35–47. https://doi.org/10.1016/j.sedgeo.2005.01.007.
Qin, Y., Wu, S., Betzler, C., 2022. Backstepping patterns of an isolated carbonate platform in the northern South China Sea and its implication for paleoceanography and paleoclimate. Mar. Petrol. Geol. 146 https://doi.org/10.1016/j.marpetgeo.2022.105927.
Rankey, E.C., 2020. Eustatic, climatic, and oceanographic influences on geomorphology and architecture of isolated carbonate platforms; Miocene, Northwest Shelf, Australia. Lithosphere (1), 2020. https://doi.org/10.2113/2020/8844754.
Raymo, M.E., Ruddiman, W.F., Froelich, P.N., 1988. Influence of late Cenozoic mountain building on ocean geochemical cycles. Geology (Boulder) 16 (7), 649–653. https://doi.org/10.1130/0091-7613(1988)0162.3.CO;2.

Riera, R., Bourget, J., Paumard, V., Wilson, M.E.J., Shragge, J., George, A.D., Borgomano, J., Wilson, T., 2019. Discovery of a 400 km2 honeycomb structure mimicking a regional unconformity on three-dimensional seismic data. Geology (Boulder) 47 (12), 1181–1184. https://doi.org/10.1130/G46484.1. Geological Society of America (GSA).

Riera, R., Bourget, J., Håkansson, E., Paumard, V., Wilson, M.E.J., 2021. Middle Miocene tropical oligotrophic lagoon deposit sheds light on the origin of the Western Australian coral reef province. Palaeogeogr. Palaeoclimatol. Palaeoecol. 576, 110501 https://doi.org/10.1016/j.palaeo.2021.110501.

Riera, R., Bourget, J., Allan, T., Håkansson, E., Wilson, M.E.J., Brandano, M., 2022. Early Miocene carbonate ramp development in a warm ocean, North West Shelf, Australia. Sedimentology 69 (1), 219–253. https://doi.org/10.1111/sed.12917.

Rosenthal, Y., Holbourn, A.E., Kulhanek, D.K., The Expedition 363 Scientists, 2018. In: Proceedings of the International Ocean Discovery Program, Vol. 363. https://doi.org/10.14379/iodp.proc.363.103.2018 publications.iodp.org.

Rosleff-Soerensen, B., Reuning, L., Back, S., Kukla, P., 2012. Seismic geomorphology and growth architecture of a Miocene barrier reef, Browse Basin, NW-Australia. Mar. Petrol. Geol. 29 (1), 233–254. https://doi.org/10.1016/j.marpetgeo.2010.11.001.

Rosleff-Soerensen, B., Reuning, L., Back, S., Kukla, P.A., 2016. The response of a basin-scale Miocene barrier reef system to long-term, strong subsidence on a passive continental margin, Barcoo Sub-basin, Australian North West Shelf. Basin Res. 28 (1), 103–123. https://doi.org/10.1111/bre.12100.

Ruddiman, W.F., William, F., 2008. Earth's Climate: Past and Future, second ed. W.H. Freeman.

Ryan, G., et al., 2009. A pre-cursor extensive Miocene reef system to the Rowley Shoals reefs, Western Australia: evidence for structural control of reef growth or natural hydrocarbon seepage? APPEA J. 49 (1).

Sanborn, K.L., Webster, J.M., Webb, G.E., Braga, J.C., Humblet, M., Nothdurft, L., Patterson, M.A., Dechnik, B., Warner, S., Graham, T., Murphy, R.J., Yokoyama, Y., Obrochta, S.P., Zhao, J., Salas-Saavedra, M., 2020. A new model of Holocene reef initiation and growth in response to sea-level rise on the Southern Great Barrier Reef. Sediment. Geol. 397, 105556 https://doi.org/10.1016/j.sedgeo.2019.105556.

Saqab, M.M., 2016. Stratigraphic and Tectonic Evolution of the Northwestern Bonaparte Basin (North West Shelf of Australia) during the Neogene. Doctoral Thesis. The University of Western Australia.

Saqab, M.M., Bourget, J., 2015. Controls on the distribution and growth of isolated carbonate build-ups in the Timor Sea (NW Australia) during the Quaternary. Mar. Petrol. Geol. 62, 123–143. https://doi.org/10.1016/j.marpetgeo.2015.01.014.

Saqab, M.M., Bourget, J., 2016. Seismic geomorphology and evolution of early–mid Miocene isolated carbonate build-ups in the Timor Sea, North West Shelf of Australia. Mar. Geol. 379, 224–245.

Schlager, W., 1981. The paradox of drowned reefs and carbonate platforms. Geol. Soc. Am. Bull. 92 (4), 197–211. https://doi.org/10.1130/0016-7606(1981)922.0.CO;2.

Schlager, W., 2005. Carbonate Sedimentology and Sequence Stratigraphy. SEPM.

Scotese, C.R., Wright, N., 2018. PALEOMAP Paleodigital Elevation Models (PaleoDEMS) for the Phaerozoic PALEOMAP Project. https://www.earthbyte.org/paleodem-resourcescotese-and-wright-2018/.

Seggie, R., et al., 2019. The geology of the brecknock, calliance and Torosa gas fields, Browse Basin, Western Australia. ASEG Extend. Abstr. 2019 (1), 1, 1.

Tcherepanov, E.N., Droxler, A.W., Lapointe, P., Mohn, K., 2008. Carbonate sequence stratigraphy of the Gulf of Papua mixed depositional system: Neogene stratigraphic signature and eustatic control. Basin Res. 20 (2), 185–209. https://doi.org/10.1111/j.1365–2117.2008.00364.x.

Thronberens, S., Back, S., Bourget, J., Allan, T., Reuning, L., 2022. 3-D seismic chronostratigraphy of reefs and drifts in the Browse Basin, NW Australia. Geol. Soc. Am. Bull. 134 (11–12), 3155–3175. https://doi.org/10.1130/B36286.1.

Tiedemann, R., Mohan, K., Karas, C., Bickert, T., Gupta, A.K., Nürnberg, D., 2009. Mid-Pliocene climate change amplified by a switch in Indonesian subsurface throughflow. Nat. Geosci. 2 (6), 434–438. https://doi.org/10.1038/ngeo520.

Vail, P., Mitchum, R., Thompson, S., 1977. Seismic Stratigraphy and Global Changes of Sea Level, Part 4 Global Cycles of Relative Changes of Sea Level. https://doi.org/10.1306/M26490C6.

Van Tuyl, J., Alves, T.M., Cherns, L., 2018. Geometric and depositional responses of carbonate build-ups to Miocene sea level and regional tectonics offshore northwest Australia. Mar. Petrol. Geol. 94, 144–165. https://doi.org/10.1016/j.marpetgeo.2018.02.034.

Van Tuyl, J., Alves, T., Cherns, L., Antonatos, G., Burgess, P., Masiero, I., 2019. Geomorphological evidence of carbonate build-up demise on equatorial margins: a case study from offshore northwest Australia. Mar. Petrol. Geol. 104, 125–149. https://doi.org/10.1016/j.marpetgeo.2019.03.006.

Vyverberg, K., Dechnik, B., Dutton, A., Webster, J.M., Zwartz, D., Portell, R.W., 2018. Episodic reef growth in the granitic Seychelles during the Last Interglacial: implications for polar ice sheet dynamics. Mar. Geol. 399, 170–187. https://doi.org/10.1016/j.margeo.2018.02.010.

Walker, J.D., Geissman, J.W., Bowring, S.A., Babcock, L.E., compilers, 2018. Geologic Time Scale V. 5.0. Geological Society of America, CHRON. https://doi.org/10.1130/2018.CTS005R3C. ©2018 The Geological Society of America HIST ANOM.

Wan, S., Li, A., Clift, P.D., Stuut, J.-B.W., 2007. Development of the East asian monsoon: mineralogical and sedimentologic records in the Northern South China sea since 20 Ma. Palaeogeogr. Palaeoclimatol. Palaeoecol. 254 (3), 561–582. https://doi.org/10.1016/j.palaeo.2007.07.009.

Webster, J.M., 1999. The Response of Coral Reefs to Sea Level Change: Evidence from the Ryukyu Islands and the Great Barrier Reef. The University of Sydney.

Webster, J.M., Davies, P.J., 2003. Coral variation in two deep drill cores: significance for the Pleistocene development of the Great Barrier Reef. Sediment. Geol. 159 (1), 61–80. https://doi.org/10.1016/S0037-0738(03)00095-2.

Webster, J.M., Clague, D.A., Riker-Coleman, K., Gallup, C., Braga, J.C., Potts, D., Moore, J.G., Winterer, E.L., Paull, C.K., 2004. Drowning of the -150 m reef off Hawaii; a casualty of global meltwater pulse 1A? Geology (Boulder) 32 (3), 249–252. https://doi.org/10.1130/G20170.1.

Webster, J.M., Dechnik, B., Sanborn, K., Yokoyama, Y., Braga, J.C., Willem, R., Humblet, M., Beaman, R.J., Nothdurft, L., Webb, G.E., Jian-xin, Z., Murphy, R.J., Gallagher, Stephen J., O'Leary, M.J., Paumard, V., 2022. Coral reef development and sea-level changes over the past 50,000 years: new evidence from the northwest shelf of Australia. In: Camoin, G.F., Hallmann, N. (Eds.), Coral Reefs and Sea-Level Change: Quaternary Records and Modelling, vol. 49. International Association of Sedimentologists Special Publication, pp. 215–273.

Wu, S., Zhang, H., Qin, Y., Chen, W., Liu, G., Han, X., 2022. Seismic imaging and 3D architecture of Yongle atoll of the xisha archipelago, south China sea. Acta Geol. Sin. (Beijing) 96 (5), 1778–1791. https://doi.org/10.1111/1755-6724.14892.

Yamamoto, K., Iryu, Y., Sato, T., Chiyonobu, S., Sagae, K., Abe, E., 2006. Responses of coral reefs to increased amplitude of sea-level changes at the Mid-Pleistocene Climate Transition. Palaeogeogr. Palaeoclimatol. Palaeoecol. 241 (1), 160–175. https://doi.org/10.1016/j.palaeo.2006.06.014.

Zeng, H., Kerans, C., 2003. Seismic frequency control on carbonate seismic stratigraphy; a case study of the Kingdom Abo sequence, West Texas. AAPG (Am. Assoc. Pet. Geol.) Bull. 87 (2), 273–293. https://doi.org/10.1306/08270201023.

CHAPRONIERE, G.C.H., SHAFIK, S., TRUSWELL, E.M., MACPHAIL, M.K., AND PARTRIDGE, A.D., 1996, Cainozoic (Chart 12), in Young, G.C., and Laurie, J.R., eds., An Australian Phanerozoic Timescale: Melbourne, Oxford University Press, p. 175–186.

CHAPTER 3

ARTICLE 2: Neutron Computed Tomography: A Novel High-Resolution, Non-Destructive Method for Screening Fossil Coral for Diagenetic Alteration for Geochronologic and Paleoclimatic Reconstructions

---

This chapter presents the following published article:

Williams, C., Webster, J. M., Bevitt, J. J., Webb, G. E., Nothdurft, L. D., Paumard, V., ... Murphy, R. J. (2025). Neutron Computed Tomography: A Novel High-Resolution, Non-Destructive Method for Screening Fossil Coral for Diagenetic Alteration for Geochronologic and Paleoclimatic Reconstructions. *Geochemistry, Geophysics, Geosystems*: 26(10). https://doi.org/10.1029/2025GC012439

The work has also been featured in a University of Sydney news story: Neutron scanning of coral fossils reveals climate history

This paper introduces a new method for diagenetic screening of fossil corals. The primary goal is to provide detailed evidence that neutron computed tomography (NCT) can be used as a tool to visualise coral morphology, structure and mineral phase contrasts in 3-D. We explain that fossil corals are important archives of past sea-level and climate, but their diagenetic alteration over time make them unreliable in paleoclimatic and paleochronologic reconstructions. We utilise NCT to find hidden sections of well-preserved aragonite within previously screened fossil coral samples that can be used for dating and paleoclimate studies without destroying the sample. We demonstrate for the first time that a key advantage of NCT is its ability to map hydrogen content, providing a reliable indicator for identifying regions of well-preserved

skeletal aragonite, since aragonite typically retains more water organic-matter than calcite. We also provide recommendations for applying NCT in fossil coral screening workflows.

TABLE 3.1: Summary of Chapter 3: Neutron Computed Tomography as a Non-Destructive Method for Diagenetic Screening of Fossil Corals.

Aspect	**Summary**
Scope	Development and application of neutron computed tomography (NCT) as a high-resolution, non-destructive method for screening fossil corals for diagenetic alteration relevant to geochronologic and paleoclimatic reconstructions.
Primary Objective	Demonstrate that NCT can reliably identify well-preserved skeletal aragonite within diagenetically altered fossil corals, enabling improved sample selection for U–Th dating and paleoclimate analysis.
Data	Three fossil coral samples spanning different ages, genera, and growth morphologies, analysed using NCT and compared with conventional diagenetic screening datasets.
Methods	Neutron computed tomography imaging integrated with petrography, XRD, SEM, hyperspectral imagery, and X-ray CT to characterise mineralogical alteration, skeletal structure, and hydrogen distribution in three dimensions.
Key Results	NCT successfully distinguishes aragonite from calcite by mapping 3-D hydrogen distributions and neutron attenuation, revealing preserved aragonite domains not detected by traditional 2-D or bulk analytical techniques.
Methodological Advances	Demonstrates the unique sensitivity of NCT to hydrogen content, enabling visualisation of coral skeletal architecture, sub-mm growth banding, and internal diagenetic heterogeneity without sample destruction.
Comparative Performance	NCT complements and corroborates established pre-screening methods and, in highly altered samples, identifies remaining aragonite missed by XRD, SEM, thin sections, and hyperspectral approaches.
Practical Implications	As a rapid, non-destructive technique, NCT reduces sampling time and costs, simplifies screening workflows, and improves confidence in selecting pristine coral material for geochronologic and paleoclimatic studies.
Broader Significance	Establishes NCT as a powerful addition to traditional fossil coral screening workflows, providing a methodological foundation for more reliable Quaternary sea-level and climate reconstructions presented in subsequent chapters.

Author contributions: I designed the workflow, performed the analysis, interpreted the data and wrote the manuscript. I wrote the application and research proposal for the ANSTO DINGO beamtime, which was revised and checked by Jody Webster and Gregory Webb. Joseph Bevitt operated the DINGO instrument and data compilation, as well as providing expertise and training in the industry software 3D slicer to visualise the scans. Luke Nothdurft produced SEM images and expertise on diagenetic interpretations. Victorien Paumard and Richard Murphy provided insightful comments and advice on the structure of the discussion.

Supplementary material: Appendix D at the end of this thesis corresponds to Movies S1 to S6 described in the Supporting Information, as cited in the associated published article.

Check for updates

Geochemistry, Geophysics, Geosystems®

RESEARCH ARTICLE
10.1029/2025GC012439

Neutron Computed Tomography: A Novel High-Resolution, Non-Destructive Method for Screening Fossil Coral for Diagenetic Alteration for Geochronologic and Paleoclimatic Reconstructions

Carra Williams[1,2], Jody M. Webster[1], Joseph J. Bevitt[3], Gregory E. Webb[4], Luke D. Nothdurft[5], Victorien Paumard[1,2], Helen McGregor[6,7], and Richard J. Murphy[8]

[1]Geocoastal Research Group, School of Geosciences, Madsen Building F09, University of Sydney, Sydney, NSW, Australia, [2]Centre for Energy and Climate Geoscience, School of Earth and Oceans, The University of Western Australia, Perth, WA, Australia, [3]Australian Nuclear Science and Technology Organisation, Lucas Heights, NSW, Australia, [4]School of the Environment, The University of Queensland, Brisbane, QLD, Australia, [5]School of Earth and Atmospheric Sciences, Queensland University of Technology, Brisbane, QLD, Australia, [6]Securing Antarctica's Environmental Future, University of Wollongong, Wollongong, NSW, Australia, [7]School of Earth, Atmospheric and Life Sciences, University of Wollongong, Wollongong, NSW, Australia, [8]School of Geosciences, Madsen Building F09, University of Sydney, Sydney, NSW, Australia

Abstract A novel high-resolution, non-destructive method for diagenetic screening of fossil corals for geochronologic and paleoclimatic studies using neutron computed tomography (NCT) is proposed. NCT circumvents limitations of traditional techniques, such as destructive sampling and 2-D imaging by providing detailed 3-D visualizations of coral structure and carbonate mineral phases. This method differentiates aragonite and calcite phases in fossil coral, crucial for identifying well-preserved sections suitable for dating and paleoclimatic reconstructions. A key advantage of NCT is its ability to map hydrogen content, providing a reliable indicator for identifying regions of well-preserved skeletal aragonite, since aragonite typically retains more water organic-matter than calcite. NCT scans conducted on a Holocene *Porites* coral (ca. 1.36–1.87 ka BP) from Muschu Island, Papua New Guinea, successfully distinguished between secondary low-magnesium calcite and aragonite skeletal material. This technique was also applied to an *Isopora palifera* fossil coral (ca. 39.4 to 44.8 ka BP) from Ashmore Reef, Northwest Shelf, Australia, which presented a more complex diagenetic history. Comparisons were made with results from hyperspectral imaging, X-Ray CT, scanning electron microscopy, and geochemical and petrological analyses, following calibration using a modern *Porites* coral from One Tree Reef, Southern Great Barrier Reef, Australia. Additionally, NCT was applied to an altered *Acropora humilis* coral (ca. 600 ± 280 ka BP) from Ribbon Reef 5, Great Barrier Reef, revealing small, hidden aragonite sections undetected by surficial hyperspectral imaging. This study demonstrates the advantages of combining NCT with traditional screening methods in identifying well-preserved aragonite for accurate geochronologic and paleoclimatic reconstructions. Recommendations for applying NCT in fossil coral screening are provided.

Plain Language Summary We propose a new method to study fossil coral reef cores to improve our understanding of geological ages and reconstructions of past climate. This method uses neutron computed tomography (NCT) to address challenges with traditional approaches, such as difficulties in observing diagenetic changes caused by freshwater exposure, the destruction of samples during analysis, and visualizing only 2-D structure rather than 3-D structure. For the first time, NCT scans successfully identified pure aragonite mineral in an altered *Porites* coral sample. We compared these NCT results with data from two other samples using more traditional techniques, including hyperspectral imaging and X-Ray CT. In total, we evaluated the strengths and weaknesses of six traditional methods used to assess fossil corals for carbonate mineral alteration. A key advantage of NCT is its ability to map the hydrogen content in 3-D, which provides a reliable indicator for identifying regions of well-preserved skeletal aragonite. By revealing well-preserved aragonite areas in heavily altered fossil corals, NCT has the potential to identify samples for more accurate geological ages and climate information when used alongside other methods. Finally, we provide recommendations for other users applying NCT for fossil coral screening.

Key Points:

- Neutron computed tomographic (NCT) scans reveal 3-D visualizations of spatial carbonate mineral distributions in fossil corals
- NCT scanning is applied to three previously diagenetically screened samples of altered fossil corals and one unaltered modern coral to guide interpretation of NCT data
- NCT complements existing screening methods and the evaluation of geochronology and paleoclimate proxy data

Supporting Information:

Supporting Information may be found in the online version of this article.

Correspondence to:

C. Williams,
carra.williams@sydney.edu.au

Citation:

Williams, C., Webster, J. M., Bevitt, J. J., Webb, G. E., Nothdurft, L. D., Paumard, V., et al. (2025). Neutron computed tomography: A novel high-resolution, non-destructive method for screening fossil coral for diagenetic alteration for geochronologic and paleoclimatic reconstructions. *Geochemistry, Geophysics, Geosystems*, *26*, e2025GC012439. https://doi.org/10.1029/2025GC012439

Received 8 MAY 2025
Accepted 15 SEP 2025

Author Contributions:

Conceptualization: Carra Williams, Jody M. Webster, Joseph J. Bevitt, Gregory E. Webb
Data curation: Carra Williams, Jody M. Webster, Joseph J. Bevitt, Luke D. Nothdurft
Formal analysis: Carra Williams, Luke D. Nothdurft
Funding acquisition: Carra Williams

© 2025 The Author(s). Geochemistry, Geophysics, Geosystems published by Wiley Periodicals LLC on behalf of American Geophysical Union.
This is an open access article under the terms of the Creative Commons Attribution License, which permits use, distribution and reproduction in any medium, provided the original work is properly cited.

Investigation: Carra Williams, Jody M. Webster, Joseph J. Bevitt, Gregory E. Webb, Luke D. Nothdurft
Methodology: Carra Williams, Jody M. Webster, Gregory E. Webb, Luke D. Nothdurft, Richard J. Murphy
Project administration: Carra Williams
Resources: Jody M. Webster, Joseph J. Bevitt, Luke D. Nothdurft, Helen McGregor, Richard J. Murphy
Software: Carra Williams, Jody M. Webster, Joseph J. Bevitt
Supervision: Jody M. Webster, Joseph J. Bevitt
Validation: Jody M. Webster, Gregory E. Webb, Luke D. Nothdurft, Helen McGregor
Visualization: Carra Williams, Joseph J. Bevitt
Writing – original draft: Carra Williams
Writing – review & editing: Jody M. Webster, Joseph J. Bevitt, Gregory E. Webb, Luke D. Nothdurft, Victorien Paumard, Helen McGregor, Richard J. Murphy

1. Introduction

Geochronologic and paleoclimatic reconstructions are critical in their application to modern climate studies and understanding the resilience of reef systems to future change (Sadler et al., 2015; Williams et al., 2023). However, a significant limitation in coral-based reconstructions is the effect of post-depositional alteration (Maliva, 1998; McGregor & Gagan, 2003; Sayani et al., 2011). Diagenesis (i.e., alteration) of fossil coral skeletons is characterized by complex processes of neomorphism, dissolution and reprecipitation, influenced by sea level fluctuation and interactions between water bodies with different chemistries, particularly in undersaturated pore waters (Braithwaite & Montaggioni, 2009). Exposure to meteoric (fresh) water commonly leads to the dissolution or replacement of skeletal aragonite by calcite (Dullo, 1984; James, 1974), while other carbonate minerals (e.g., dolomite) may form in different burial environments (i.e., marine or meteoric). Additionally, secondary aragonite may form after initial biogenic deposition of the coral skeleton, representing diagenetic alteration. Direct contamination from extraneous sediments, such as detrital inputs, can introduce elements that skew environmental proxies and dating results (Strasser et al., 1992; Webb et al., 2009). Terrigenous sediments commonly introduce excess Thorium (Th), complicating radiometric dating (Clark et al., 2014). Movement of different water bodies through coral reef environments creates mixing zones and alters minerals (Paterson et al., 2008), making sea level, climate, and coral diagenesis intimately connected. To ensure the identification of primary aragonite and the integrity of isotopic and elemental tracers, initial screening of samples is crucial (Ma et al., 2021; Smodej et al., 2015; Vyverberg et al., 2018; Woodroffe & Webster, 2014; Zaini et al., 2014).

1.1. Traditional Screening Techniques for Identifying Primary Aragonite

Living and fossil coral reefs (both exposed and those accessible in drill cores) are widely used in geochronologic, paleoclimatic and sea level reconstructions (Thompson, 2022; Vyverberg et al., 2018; Webb, 2024). Traditional methods to identify aragonite in coral include destructive and non-destructive techniques, as summarized below.

Thin section petrography is a destructive method involving cutting a sample for analysis (Bar-Matthews et al., 1993; McGregor & Abram, 2008; McGregor & Gagan, 2003). It provides high-resolution (1–2 μm) textural images of fossil coral under transmitted light but requires substantial preparation time. This method can distinguish between primary and secondary aragonite and other cement phases typical of early marine diagenesis but is best for identifying meteoric calcite (McGregor & Abram, 2008). While it identifies undisturbed skeletal aragonite, it is limited to 2-D structural characteristics with little broader diagenetic context (McGregor & Gagan, 2003). Additionally, thin section analyses may not align exactly with geochemical sampling sites, which can lead to unrepresentative results owing to typical sample heterogeneity.

X-Ray powder diffraction (XRD) is a traditional but destructive technique that provides detailed information on the crystallographic structure by analyzing the diffraction of X-Rays passed through a powdered sample (Ivankina et al., 2020; Kontoyannis & Vagenas, 2000; Raja et al., 2022; Smodej et al., 2015). Calcite and aragonite are easily distinguished by their diffraction peaks (Sayani et al., 2011; Smodej et al., 2015), but sample grinding can cause minor conversion of aragonite to calcite, rendering the results inaccurate (Kontoyannis & Vagenas, 2000). Regardless, XRD remains the most common method for screening fossil corals for low levels of alteration, typically 1%–4% calcite (Dutton et al., 2015; McGregor & Abram, 2008; Raja et al., 2022; Vyverberg et al., 2018). However, as with thin sections, analyzed powders may not be representative of other parts of the sample.

SEM is potentially a destructive technique (non-destructive for small samples) that differentiates the original biogenic microstructure from subtle recrystallization, cements, microbialites, etching and bioerosion products that are otherwise unidentifiable on polished sample surfaces (Nothdurft et al., 2007). It outperforms XRD and petrographic analysis in diagenetic screening (Hibbert et al., 2016; Webb, 2024). Although SEM can detect a wide range of even minor diagenetic textures (Bar-Matthews et al., 1993; Nothdurft & Webb, 2009; Sayani et al., 2011), it is limited to a small area and also may not be representative of larger regions of the core.

X-Rays, X-Ray computed tomography (X-Ray CT) and micro-X-Ray computed tomography (micro-XCT) are non-destructive imaging methods widely used in carbonate and coral reef science (Helmle et al., 2000; Ketcham & Carlson, 2001; Roche et al., 2010). They primarily image X-Ray density contrasts in samples (Koestel et al., 2022) revealing broad internal structures, such as annual density banding (DeCarlo & Cohen, 2017) and differences between regions of aragonite and calcite (McGregor & Gagan, 2003). However, samples commonly

15252027, 2025, 10, Downloaded from https://agupubs.onlinelibrary.wiley.com/doi/10.1029/2025GC012439 by Carra Williams , Wiley Online Library on [02/10/2025]. See the Terms and Conditions (https://onlinelibrary.wiley.com/terms-and-conditions) on Wiley Online Library for rules of use; OA articles are governed by the applicable Creative Commons License

require slicing into equal-thickness slabs to quantify features like density contrasts and annual banding. X-Ray CT scans (i.e., standard medical X-Ray CT) are non-destructive and inexpensive and typically are used to identify growth axes for paleoclimatic and geochemical subsampling from fossil corals, but they reveal only low-resolution skeletal architecture, density changes (Duprey et al., 2012; Helmle et al., 2000; McGregor & Gagan, 2003; Sadler et al., 2015) and dissolution (McGregor & Abram, 2008). Hendy et al. (2007) identified secondary aragonite as high-density anomalies in X-radiographs and bright mottling under UV light in a core from a living massive *Porites* colony, but required confirmation with SEM. Micro-XCT, in contrast, offers much higher spatial resolution of less than 1 μm that captures thin skeletal structures such as dissepiments (Malik et al., 2021). It has also been used in 3-D imaging of carbonate reservoir pore systems, enabling detailed quantification of pore geometry and connectivity. When integrated with petrographic or microfacies analysis, it can help differentiate textural heterogeneity and diagenetic features not resolvable in conventional X-Ray CT scans (Alatrash & Velledits, 2024).

Non-destructive spectroscopic techniques may also identify mineralogy in coral samples. Raman spectroscopy easily distinguishes between aragonite and calcite in corals even at very high resolution (e.g., DeCarlo, 2018; Kontoyannis & Vagenas, 2000; Nothdurft et al., 2007; Stolarski et al., 2021; Webb et al., 2009) and can estimate Mg content in calcites (Boromeo et al., 2017). Hyperspectral imaging allows sub-millimeter 2-D mapping of different mineral phases (Murphy et al., 2017; Schneider et al., 2014; Zaini et al., 2014), distinguishing aragonite, calcite, dolomite and clay minerals, which indicate terrigenous contamination in coral reef environments (Murphy et al., 2017; Webster et al., 2022). For example, hyperspectral scans identified surface distributions of calcite and aragonite in reef cores (Murphy et al., 2017; Webster et al., 2022), but high resolution analysis for identifying small mineral variations is time consuming and still limited to surface 2-D imaging.

Neutron computed tomography (NCT), newly evaluated here, is a non-destructive technique that reveals the detailed 3-D structure, mineral composition and water-organic matter content in fossil corals. Combined this allows identification of the original coral aragonite that is crucial for robust dating and paleoclimatic analyses. Unlike X-rays, which interact with electron density and primarily highlight density contrasts, thermal neutrons interact with atomic nuclei, offering high-resolution contrasts between hydrated and non-hydrated materials (Bevitt, 2018; Williams et al., 2017). Thermal neutrons are strongly attenuated by elements such as hydrogen (H), boron (B), and lithium (Li) (Table 2) making them particularly useful for identifying H-rich materials, such as biomineralized aragonite, organic matter, and hydrated clay minerals (Schwarz, 2005; Williams et al., 2017). These elements are observed on NCT images as the brightest white pixels and have previously been used to interpret clay-enriched fractures in rock cores with relatively high concentrations of H (Williams et al., 2017). Thus, NCT scans can produce high contrast 3-D images that distinguish between aragonite (hydrogenous) and calcite (less hydrogenous) as well as organic matter and clays (Bevitt, 2018; Ivankina et al., 2020; Schwarz, 2005; Williams et al., 2017). A vital difference between biogenic aragonite and calcite that is paramount to this study is that coral aragonite has higher water (Koga et al., 2013; Passe-Coutrin et al., 1995) and organic matter (Cuif & Dauphin, 2005; Cuif et al., 2004; Przeniosło et al., 2008) content compared to calcite. As aragonite transforms into calcite through neomorphism, it loses water and organic matter, reducing its H content (Koga et al., 2013; Webb et al., 2009), which NCT effectively identifies through thermal neutron absorption ratios.

NCT has been applied to the analysis of vertebrate fossil remains (Schwarz, 2005), mineral abundance and distribution in rock - sediment cores (Christie et al., 2007) and fluid inclusions in stalagmites (Wortham et al., 2019). In coral reef science, neutron diffraction and NCT have been used to investigate 3-D structures and seasonal density variations in coral skeletons (Ivankina et al., 2020), but their use in detecting diagenetic changes in fossil corals is unexplored.

The aim of this study is to demonstrate NCT's ability to differentiate aragonite from calcite in fossil corals using a pure aragonite calibration sample and a proof-of-concept sample with mixed aragonite-calcite phases. We demonstrate how this method could be adopted as a pre-requisite for screening samples for geochronologic and paleoclimatic analyses by applying it to two complex diagenetically altered data sets, where the best-preserved material may be "hidden" beneath the surface of a sample. The four data sets (modern *Porites* coral, FM19-1, RR5-70-1, and SWIFT N-1-C-4A2) are qualitatively assessed using NCT data and compared to previous results from hyperspectral analysis, X-Ray CT, thin section microscopy, XRD, Sr/Ca_{atomic} ratios and $\delta^{18}O$ isotope analysis (Sayani et al., 2011). While NCT offers unique capabilities in mapping hydrogen content and differentiating mineral phases, the instrument is not widely available and requires highly trained operators, commercial

15252027, 2025, 10, Downloaded from https://agupubs.onlinelibrary.wiley.com/doi/10.1029/2025GC012439 by Carra Williams , Wiley Online Library on [02/10/2025]. See the Terms and Conditions (https://onlinelibrary.wiley.com/terms-and-conditions) on Wiley Online Library for rules of use; OA articles are governed by the applicable Creative Commons License

15252027, 2025, 10, Downloaded from https://agupubs.onlinelibrary.wiley.com/doi/10.1029/2025GC012439 by Carra Williams , Wiley Online Library on [02/10/2025]. See the Terms and Conditions (https://onlinelibrary.wiley.com/terms-and-conditions) on Wiley Online Library for rules of use; OA articles are governed by the applicable Creative Commons License

rates can be costly, and scanned samples may show temporary residual radioactivity. As such, we evaluate the advantages and limitations of these methods and provide recommendations for independent users applying NCT for fossil coral screening.

1.2. The Effect of Diagenesis on Geochronologic and Paleoclimatic Reconstructions

Biogenic $CaCO_3$ precipitates in two main preservable phases: aragonite and calcite. The preferred precipitate in marine environments depends on the saturation state, Mg^{2+}/Ca^{2+} ratio, pCO_2 and water temperature (e.g., de Choudens-Sánchez et al., 2009; Morse et al., 1997; Morse & Mackenzie, 1990; Sandberg, 1983). While both calcite and aragonite consist of $CaCO_3$, they incorporate different trace elements due to crystallographic differences (Brand & Veizer, 1980; Veizer, 1983). Calcite can contain varying amounts of Mg, and is classified into low-Mg calcite (LMC), high-Mg calcite (HMC) and very high-Mg calcite (VHMC; e.g., Raudsepp et al., 2022). Aragonite, in contrast, tends to incorporate trace metals with larger ions like Sr (Veizer, 1983), and has a denser crystal structure (Nelyubina & Lyssenko, 2012). Among the primary skeletal carbonates, LMC is the least soluble, followed by aragonite, HMC and vaterite (Morse & Mackenzie, 1990). While aragonite and HMC form in modern seawater owing to the high aqueous Mg^{2+}/Ca^{2+} ratio, they are commonly dissolved, replaced or converted to less soluble LMC during meteoric diagenesis. Neomorphism, or in situ replacement of aragonite by calcite, occurs through dissolution and re-precipitation along a thin film and depends on factors such as skeletal structure and distribution of organic matter (Dullo, 1986; Martin et al., 1986; Sorauf & Cuif, 2001; Webb et al., 2009).

Coral reef environments experience complex diagenetic histories due to exposure to meteoric water during sea level falls or tectonic uplift (Braithwaite & Montaggioni, 2009). Exposure can result in karst formation, soil development (preserved as paleosols) and increased terrigenous runoff-groundwater containing non-marine trace elements (e.g., Webster et al., 2022). Subaerial exposure leads to replacement of the original coral aragonite by secondary diagenetic calcite, significantly altering the original trace element and stable isotope ratios, which can compromise geochemical proxies and dating (Brand & Veizer, 1980; Webb et al., 2009). Estimates of aragonite replacement rates range from over months (e.g., Bahama Banks: Grammar et al., 1999; Hendy et al., 2007; Nothdurft & Webb, 2009) to ca.1000s of years (Persian Gulf: Shinn, 1969). Nevertheless, primary aragonite in coral material older than 1,000 years is not uncommon, as observed in Holocene corals (Dechnik et al., 2015; Sanborn et al., 2020; Webster et al., 2022), middle Pleistocene (600 ka) coral reef terraces in Barbados, West Indies (Skinner, 1988; Watanabe et al., 2011), and Pliocene-Pleistocene corals from the Florida platform with preservation suitable for stable isotope proxy analysis (Brachert et al., 2016). However, the detection of aragonite alone does not ensure pristine preservation, since isotopic exchange has recently been demonstrated even in the absence of polymorphic transformation (Stolarski et al., 2025). Similar examples of well-preserved aragonite are found in Miocene reefs in the Caribbean (Denniston et al., 2008), Permian reefs (Wendt, 1977) and many other sites around the world.

2. Geological and Environmental Setting and Samples

Samples used in this study were collected from northern Australia and Papua New Guinea (Figure 1). Three samples are fossil coral specimens extracted from drill cores and one is a modern coral (Table 1).

1. *A modern Porites* sample recovered from the lagoon of One Tree Reef at ca. 0 m below sea-level (mbsl) (Wei et al., 2021) (Figures 1 and 2) was used as a control to provide accurate endmember values of pure aragonite and original porosity. This sample previously provided a reference standard for the aragonite hyperspectral range (Murphy et al., 2017).
2. *FM19-1* is a diagenetically altered *Porites sp*. coral recovered from uplifted Holocene reefs (1.36–1.87 ka BP, where present is 1950 CE) at Rebiew Bay, Muschu Island, Papua New Guinea (PNG) in 1998 (McGregor & Gagan, 2003) (Figures 1 and 3). Core FM19 is well characterized with respect to diagenetic alteration, having undergone vadose zone meteoric diagenesis with variable neomorphism and calcite pore filling (McGregor & Abram, 2008; McGregor & Gagan, 2003; Murphy et al., 2017). It also served as a reference standard for aragonite and calcite in hyperspectral studies (Murphy et al., 2017). FM19-1 is a cut section from the original FM19 core, which was split into two parts: "FM19-1 2nd slice" and "FM19-1 transect seg2." Both sections were scanned in this study, but analyses focus on the "FM19-1 2nd slice" to compare its surface to previous hyperspectral mapping (Murphy et al., 2017) and it is referred to as FM19-1 hereafter.

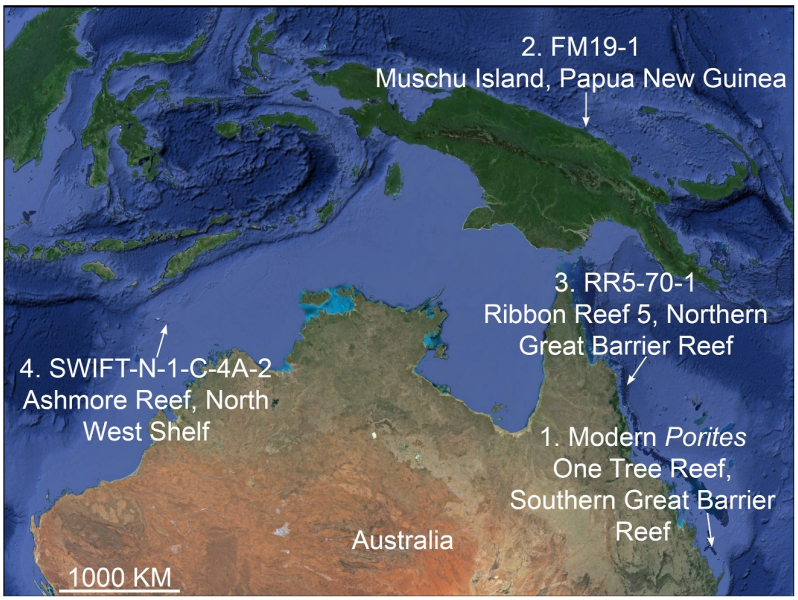


Figure 1. Geographic location of the four samples used in this study, summarized in Table 1.

Previous diagenetic screening of sample FM19-1 includes: (a) XRD, $\delta^{18}O/\delta^{13}C$ and Sr/Ca_{atomic} ratios that were interpreted along diagenetic gradients (McGregor & Gagan, 2003), (b) thin section petrography (McGregor & Abram, 2008), and (c) a study that compared results from (a) and (b) with new hyperspectral data (Murphy et al., 2017). Eleven powder subsamples for XRD, Sr/Ca_{atomic} and $\delta^{18}O$ analyses were collected along the major growth axis of a 7 mm slice of the coral (McGregor & Gagan, 2003). All three studies identified distinct textural (thin section), mineralogical (XRD) and geochemical (decrease in Sr/Ca_{atomic} and variable $\delta^{18}O$) changes, where the shift from aragonite to calcite occurs across a spatially heterogeneous transition zone (Figures 4, 5a, and 5b). Aragonite replacement increased from <1% calcite in subsample 3 to >77% calcite in subsample 11 (McGregor & Abram, 2008; McGregor & Gagan, 2003; Murphy et al., 2017). The diagenetic history can be summarized as an initial leaching of primary aragonite (3%–5% calcite), void filling calcite (10%–30%), fabric selective neomorphic replacement (40%–60%) and complete aragonite replacement (75%–100%) in subsample 11 (Murphy et al., 2017, p. 4).

3. RR5-70-1 is a well described but diagenetically complex section of fossil reef core from the tropical northeast shelf of Australia (Figure 1). This sample underwent diagenetic screening, including hyperspectral analysis. Geochemical analyses (U-series dating, $^{87}Sr/^{86}Sr$ ratios and stable ^{18}O and ^{13}C isotope ratios) and magnetic susceptibility were conducted on select samples for geochronologic reconstruction (Braithwaite et al., 2004). It consists of a neomorphosed *Acropora humilis* coral framework with a matrix composed of $CaCO_3$ with poor preservation of primary aragonite. It was recovered at 125 m below sea floor (mbsf) at Ribbon Reef 5, Great Barrier Reef (GBR) in 1995 (Braithwaite et al., 2004; Braithwaite & Montaggioni, 2009; Humblet & Webster, 2017) and represents one-half of a drill core. It is from the high energy outer shelf reef front (0–10 m original depth) (Webster & Davies, 2003) and belongs to Unit 4 of Braithwaite et al. (2004), characterized by grainstones with scattered coral fragments including, *Acropora*, *faviids*, *Porites* and *Millepora*. $^{87}Sr/^{86}Sr$ ratio

Table 1
Summary of Samples Used in This Study

Sample	Sample name	Data set	Taxa	Age (ka BP)	Location
1	Modern *Porites*	Modern coral	*Porites sp.*	0	One Tree Reef, Southern Great Barrier Reef, Australia
2	FM19-1	Fossil reef core	*Porites sp.*	ca. 1.36–1.87	Muschu Island, Papua New Guinea
3	RR5 70_1	Fossil reef core	*Acropora humilis*	ca. 600 ± 280	Ribbon Reef 5, Northern Great Barrier Reef, Australia
4	SWIFT N1-C-4A2	Fossil reef core	*Isopora palifera*	ca. 13.1 to 44.8	Ashmore Reef, Bonaparte Basin, North West Shelf, Australia

15252027, 2025, 10, Downloaded from https://agupubs.onlinelibrary.wiley.com/doi/10.1029/2025GC012439 by Carra Williams , Wiley Online Library on [02/10/2025]. See the Terms and Conditions (https://onlinelibrary.wiley.com/terms-and-conditions) on Wiley Online Library for rules of use; OA articles are governed by the applicable Creative Commons License

15252027, 2025, 10, Downloaded from https://agupubs.onlinelibrary.wiley.com/doi/10.1029/2025GC012439 by Carra Williams , Wiley Online Library on [02/10/2025]. See the Terms and Conditions (https://onlinelibrary.wiley.com/terms-and-conditions) on Wiley Online Library for rules of use; OA articles are governed by the applicable Creative Commons License

Table 2
Comparison of Elements and Chemical Formulas for Compounds Present in This Study With Additional Compounds Not Present in This Study for Comparison, Showing X-Ray and Neutron Scattering Attenuation Coefficients (Adapted From Christie et al., 2007)

Chemical element	Atomic number	Atomic weight (g mol^{-1})	Density (g cm^{-3})	X-ray mass attenuation coefficient (cm^2 g^{-1}) 120 keV	X-ray attenuation coefficient (cm^{-1}) 120 keV	Neutron scattering cross section (cm^2 g^{-1}) 1.8 Å, 25 meV	Neutrons attenuation coefficient (cm^{-1}) 1.8 Å, 25 meV
H	1	1.0079	0.09	0.282	0.025	49.013	4.411
C	6	12.011	2.26	0.144	0.325	0.278	0.629
O	8	15.999	1.43	0.146	0.209	0.159	0.228
Si	14	28.086	2.33	0.163	0.380	0.046	0.112
Ca	20	40.078	1.55	0.206	0.319	0.043	0.066
Fe	26	55.845	7.87	0.269	2.117	0.125	0.986

Compounds present	Chemical formula	Density	X-ray linear attenuation coefficient (cm^{-1}) 120 keV	Neutron attenuation coefficient (cm^{-1}) 1.8 Å, 25 meV
Air	N_2	0.00	*0.00000*	0.00000
Water	H_2O	1.00	0.16100	5.38000
Kaolinite	$Al_2Si_2O_5(OH)_4$	2.60	0.39780	2.26568
Calcite	$CaCO_3$	2.71	0.46070	0.34373
Aragonite	$CaCO_3$	2.93	?	?
Hematite	Fe_2O_3	5.30	1.22960	0.71837

Note. Note the significantly higher neutron attenuation coefficient for the element hydrogen and for water as compared to X-ray. X-ray mass attenuation coefficients were taken from http://physics.nist.gov/PhysRefData/Xcom/html/xcom1.html and total neutron cross sections calculated for a wavelength of 1.8 A˚ corresponding to a thermal neutron energy of 25 meV from http://www.ncnr.nist.gov/resources/n-lengths/list.html (X-Ray attenuation coefficients for energies of 120 keV, neutron attenuation coefficients for a wavelength of 1.8 A˚ corresponding to a thermal energy of 25 meV).

curve-matching places the age of Unit 4 at ca. 600 ± 280 ka (Marine Isotope Stage 11–17), with high uncertainty due to the low slope of the Sr curve. Radiometric dating was not performed due to substantial diagenetic alteration and detrital contamination. Braithwaite and Montaggioni (2009) previously showed evidence of meteoric diagenesis in the Unit 4 interval, but RR5-70-1 was not analyzed specifically.

4. SWIFT-N-1-C-4A2 is a well characterized and diagenetically complex fossil reef core from the tropical northwest shelf (NWS) of Australia (Figure 1). The core has a multi-generational history of platform exposure due to sea level oscillation, with changing sediment flux and multiple exposure episodes in both marine and meteoric environments (Webster et al., 2022). The sample contains a large portion of submassive *Isopora palifera* coral, encrusted at its base and top by coralline algae and well lithified bioclastic sediments, characteristic of shallow, high energy reef crest-upper slope environments <5 m deep (Webster et al., 2022). It was recovered using a Portable Remotely Operated Drill (PROD; Liu et al., 2025) as part of a seabed drilling campaign ca. 150 km southeast of Ashmore reef in the Bonaparte Basin, NWS, Australia in 2007 (Webster et al., 2022). The sample used in this study was taken from ca. 85 m below seafloor and radiocarbon and U/Th dating place the age of the *Isopora palifera* coral at ca. 39 ka BP (Webster et al., 2022). Significant carbonate mineral alteration was identified proximal to paleosol horizons at major chronostratigraphic boundaries in the broader core (Webster et al., 2022). A suite of screening methods, including hyperspectral, SEM and petrographic thin section analysis, was applied previously to this sample to verify the locations of aragonite and calcite.

3. Methods

3.1. Sample Preparation

Samples used in this study have similar size and composition because high density or large (mass) samples can increase neutron attenuation and absorption, potentially masking internal features and biasing analysis (e.g., Ketcham & Carlson, 2001). For these measurements, neutron beam absorption and scattering did not significantly mask core interiors, so corrections for neutron scattering in high density samples (i.e., Hassanein et al., 2005; Christie et al., 2007) were unnecessary. Samples were placed in an aluminum tube (18 cm inner diameter, 30 cm

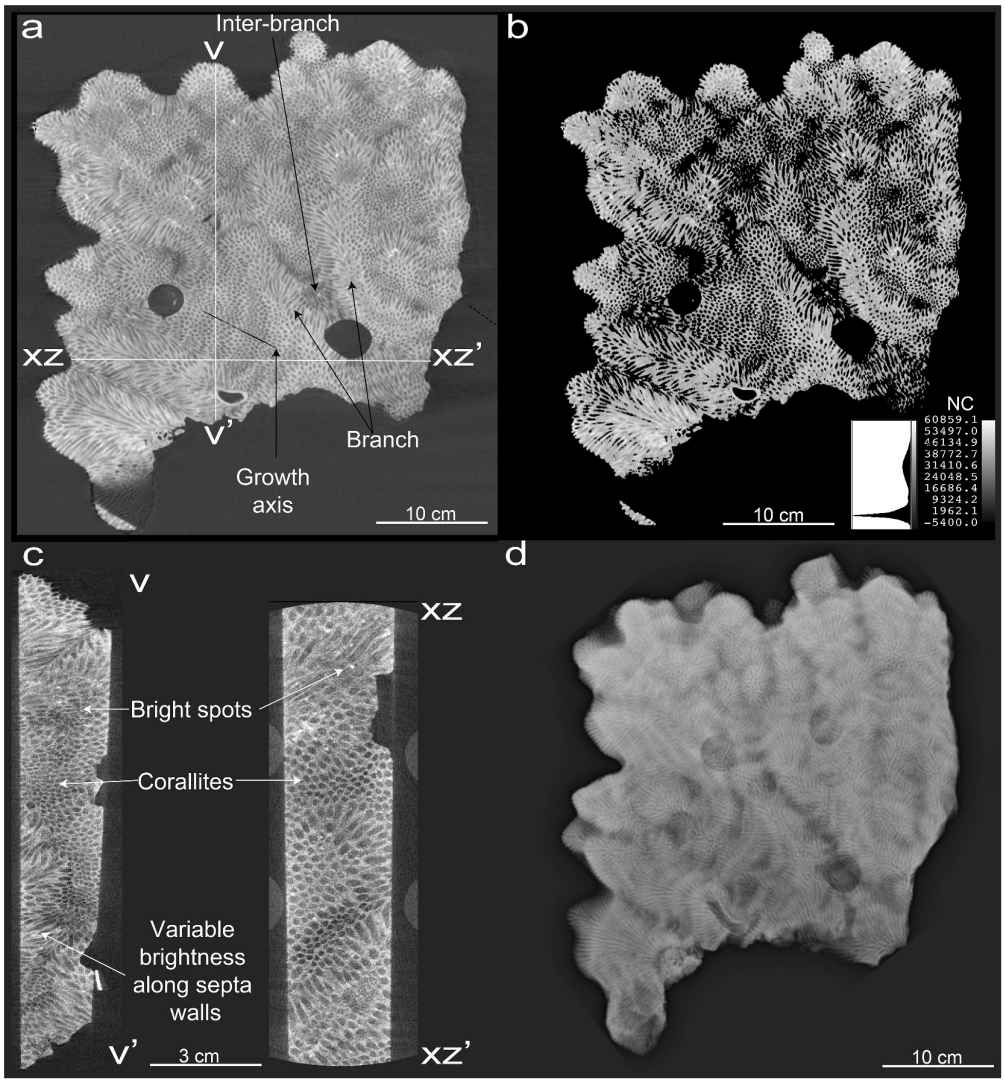


Figure 2. Comparison of neutron computed tomography (NCT) scans (a–c) with traditional X-Ray CT image (d) of the modern unaltered Porites sample from One Tree Reef. 3-D voxels measure 0.0395 mm^3, sample thickness ca. 1 cm (a) 3-D NCT scan showing full neutron count range 0–65,535, (b) 3-D filter applied showing aragonite data range exclusive of porosity (ca. 12,000–65,535 NC). Histogram shows two distinct peaks representing porosity and aragonite ranges. (c) Cross sections V-V′ and XZ-XZ' are 2-D slices of the 3-D NCT slab data (39.5 µm resolution) of V (vertical) and XZ (*x* axis and depth) profiles, respectively. Their positions are indicated by white lines in (a). (d) X-Ray CT image of the same slab used for photos (a, b) showing density variations and blurry low resolution coral morphology.

height, 1.65 mm wall thickness) and wrapped in foil for protection from radiation burn (See Table 3 for sample dimensions). All samples were scanned at low intensity for 2 hr, except for the modern *Porites* sample, which was scanned individually at high intensity, yielding a higher (39.5 µm) resolution to demonstrate NCT's imaging capabilities. After neutron exposure, samples become temporarily radioactive: residual radioactivity decayed to natural levels within 3 days, allowing safe removal from the testing facility.

3.2. NCT Data Acquisition, Calibration and Data Reconnaissance

NCT measurements were conducted at the Australian Nuclear Science and Technology Organisation's (ANSTO) thermal-neutron imaging instrument called "DINGO," located at Lucas Heights, NSW, Australia. DINGO is a pinhole neutron camera that uses an incident beam of thermalized neutrons produced by controlled fission of ^{235}U

15252027, 2025, 10, Downloaded from https://agupubs.onlinelibrary.wiley.com/doi/10.1029/2025GC012439 by Cairn Williams , Wiley Online Library on [02/10/2025]. See the Terms and Conditions (https://onlinelibrary.wiley.com/terms-and-conditions) on Wiley Online Library for rules of use; OA articles are governed by the applicable Creative Commons License

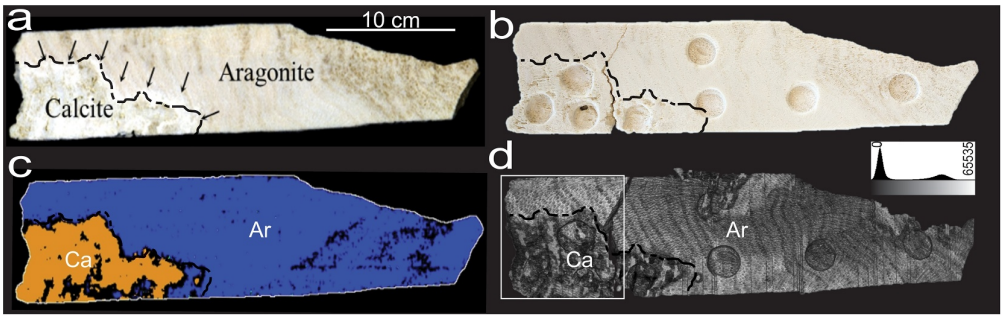


Figure 3. Comparison of images made from FM19-1. (a) Drill core photograph from Murphy et al. (2017) of a cut section of FM19-1 showing calcite and aragonite regions separated by dotted black line boundary. (b) Photograph of the same cut section in (a) after destructive analysis with drill hole samples used for powder XRD analysis, $\delta^{18}O/\delta^{13}C$ and Sr/Ca atomic ratios to detect ca.100% aragonite and ca.100% calcite. (c) Image of the same cut section showing classified carbonate features calcite (Ca—orange) and aragonite (Ar—blue) (Murphy et al., 2017). (d) Neutron computed tomography scan slice near but below the same cut section showing dark (calcite) and lighter (aragonite) sections. Bimodal histogram shows full NC range. 3-D voxels measure 0.0136 mm_3. Note the additional calcite rich region above Ar.

atoms at the 20 MW Open Pool Australian Lightwater (OPAL) multi-purpose research reactor (Garbe et al., 2015; Williams et al., 2017). A collimation ratio (*L*/*D*) of 500 was applied, where *L* is the neutron aperture-to-sample length and *D* is the neutron aperture diameter. The samples were positioned 10 m from the neutron source, and 33 mm from a scintillation detector screen. Attenuated neutrons were recorded on a 0.030 mm terbium-doped gadolinium scintillation screen (Gd_2O_2S: Tb, RC Tritec AG) and the projected light was imaged with a 6,248 × 4176-pixel ZWO ASI2600MM Pro CMOS camera. Acquisition times varied from 1.5 hr (300 angular projections over 0.6° increments, 18 s illuminations for each view) to 17.5 hr (1,000 angular projections over 0.18° increments, 60 s illuminations for each view) depending on instrument availability rather than desired resolution. Additional exposures were taken without samples to measure transmission and background values. In the L/D = 500 configuration, the neutron flux is 4.75×10^7 $ncm^{-2}s^{-1}$. Raw radiographic data were normalized

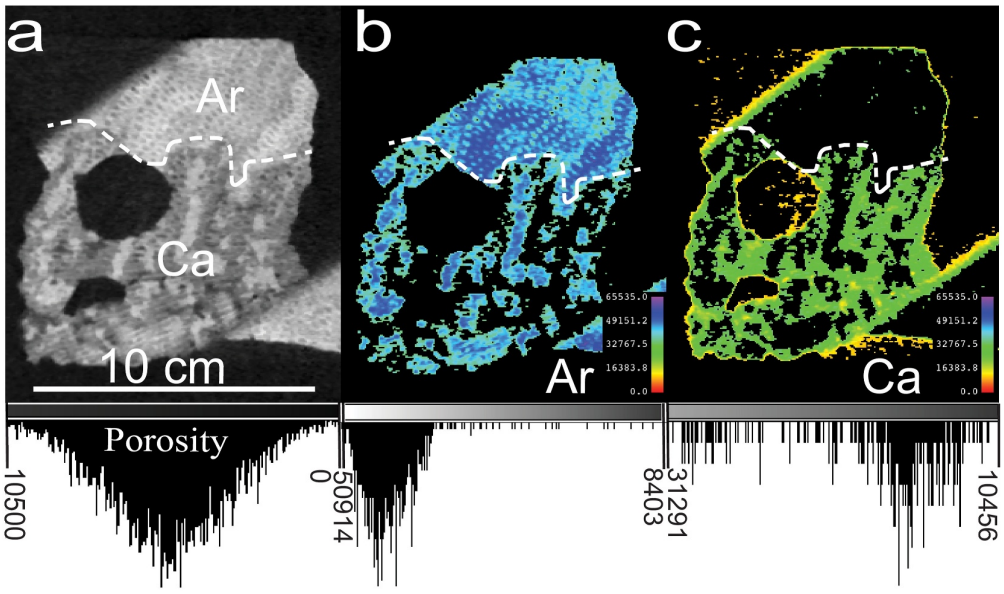


Figure 4. Enlarged Neutron computed tomography scan of the base of FM19-1 (indicated by white box in Figure 3d). (a) Scan with full NC range shown on histogram in Figure 3d. (b) Aragonite (Ar) histogram values (40,000–56,000 NC) displayed in rainbow colors. (c) Calcite (Ca) histogram values (15,000–40,000 NC). Histograms for each material phase are plotted below each scan.

15252027, 2025, 10, Downloaded from https://agupubs.onlinelibrary.wiley.com/doi/10.1029/2025GC012439 by Carra Williams , Wiley Online Library on [02/10/2025]. See the Terms and Conditions (https://onlinelibrary.wiley.com/terms-and-conditions) on Wiley Online Library for rules of use; OA articles are governed by the applicable Creative Commons License

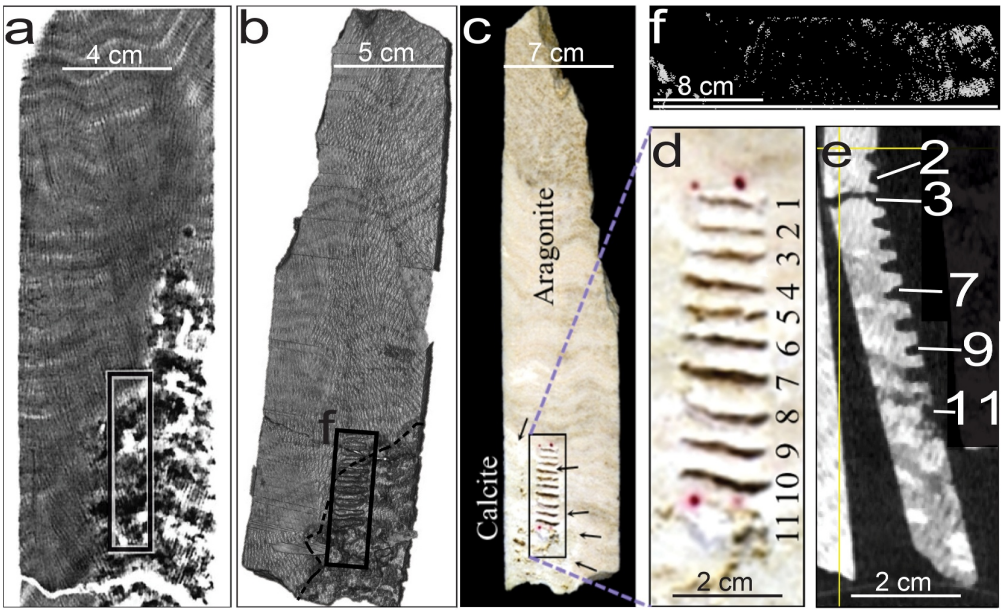


Figure 5. The patchy aragonite-calcite transect in FM19-1 shown on X-Ray positive image and 3-D neutron computed tomographic (NCT) scan. (a) X-Ray positive image of FM19 coral core prior to sampling (McGregor & Gagan, 2003). Black rectangle indicates the region selected for geochemical and thin section sampling and corresponds to the same rectangle in (b–d). (b) Similarly positioned slice of FM19-1 imaged with NCT. (c) Photograph of FM19 slab (Murphy et al., 2017) showing geochemical/XRD sample pits. Thin sections were sampled from the mirror image face on the off cut of the core to allow geochemical and XRD results to be compared as closely as possible to petrography. (d) Enlarged view of sample numbers used in the original study (McGregor & Abram, 2008). (e) XZ profile from the NCT scan of FM19-1 in b, showing locations where samples were collected at sites 3, 2, 9, 7, and 11 corresponding to thin sections and XRD percent calcite in Figure 6. (f) 3-D image of a NCT scan of FM19-1 with a filter applied showing only the highest pixel values (highlighted) corresponding to aragonite, based on interpretations shown in Figure 10.

relative to flat field and dark field images to ensure that the images reflect only the attenuation caused by the sample. Flat field images (taken without samples) were used to correct for beam intensity variations, while dark field images (taken without neutron exposure) accounted for background detector noise (Strobl et al., 2009). 16-bit greyscale tomographic images were reconstructed using Octopus Reconstruction v.8.8© (Heidelberg Engineering GmbH).

2-D visualizations of individual tomographic "slices" were performed using ImageJ™ software (rsb.info.nih.gov/ij) (Schneider et al., 2012), which was used to render raw neutron tomographic data, evaluate histograms and pixel values and enable image selection for comparison with original core data. ImageJ™ provided cross-sectional displays of the core in three perpendicular orientations. The 2-D images form a stack where each pixel in the 2-D bitmap image becomes a voxel (volumetric pixel) in the 3-D space (Schneider et al., 2012). For 3-D reconstruction and visualization, 3-D Slicer 5.2.2 software (Fedorov et al., 2012) was used, including the production of 3-D videos of modern *Porites* and core samples FM19-1 and RR5-70-1 (supplementary data). Table 3 lists the attenuation coefficients for thermal neutrons for mineral species found and assumed in the core samples. Viewing the sequence of 2-D images in 3-D visualization software may result in some data averaging, which is reduced with higher resolution NCT scans, resulting in more precise mineral mapping.

Prior analysis of FM19-1 (X-Ray positive image, thin sections, XRD, geochemical and hyperspectral data), RR5-70-1 (hyperspectral, SEM) and SWIFT-N-1-C-4A2 (hyperspectral data, X-Ray CT, SEM, XRD, thin sections) were used to guide and validate the interpretation of greyscale value ranges between known proportions and distributions of calcite, aragonite and porosity. NCT scans uniquely visualize material composition through NC, where higher NC values correspond to greater attenuation (Table 3). Pixel color or brightness correlates with neutron attenuation, enabling the identification and characterization of materials and their densities. 3-D reconstructions were performed using greyscale and high spectral range color bar data. Pixels selected for data

15252027, 2025, 10, Downloaded from https://agupubs.onlinelibrary.wiley.com/doi/10.1029/2025GC012439 by Carra Williams , Wiley Online Library on [02/10/2025]. See the Terms and Conditions (https://onlinelibrary.wiley.com/terms-and-conditions) on Wiley Online Library for rules of use; OA articles are governed by the applicable Creative Commons License

Table 3
Summary of DINGO Acquisition Parameters and Data Value and Modal Ranges (Most Common) for NCT Scans Performed on Samples FM19-1, RR5-70-1, SWIFT-N-1-C-4A2 and the Modern Porites Coral at ANSTO, Lucas Heights, NSW, Australia

Scan	Sample a	Sample b	Sample c	Resolution (mm)	Intensity	Images	Exposure (s) scanned (cm)	Core dimensions w × h × l (cm)	Min data values	Max data values
1	FM19-1 2nd slice	FM19-1 transect seg2		0.0136	Low	721	20	7w × 0.5 h × 24l	0	65,535
2	RR5 70_1	Scan 1 (top of core)	Scan 2 (base of core)	0.136	Low	520	20	7w × 3h × 3l	600	65,535
3	SWIFT N1-C-4A2			0.0356	Low	2,921	20	4w × 2h × 2l	3,801	49,127
4	Modern Porites			0.0395	High	3,642	20	25w × 3h × 2l	0	65,500

Note. Total neutron cross sections calculated for a wavelength of 1.8 A˚ corresponding to a thermal neutron energy of 25 meV from http://www.ncnr.nist.gov/resources/n-lengths/list.html. Attenuation coefficients include both coherent and incoherent scattering and absorption (i.e., Christie et al., 2007).

analysis were taken from a region similar to previously sampled sites to ensure consistency. However, coarser resolution scans may average across the skeleton and pore spaces, affecting the true data value range. Uncontrollable variations in neutron source intensity also can cause greyscale values to differ between experiments, requiring standardization using reference standards, such as elemental cubes with known material contrasts (e.g., calcite, iron).

3.3. SEM Sample Preparation

Samples (5 × 2.5 cm) from RR5_70_1 and SWIFT-N-1-C-4A2 were examined using SEM to produce 25 images of the microstructure.

4. Calibration of NCT Data

4.1. NCT Imaging of Aragonite and Porosity Using the Modern *Porites* Sample

Calibration of NCT for imaging aragonite and porosity was performed using the modern unaltered *Porites* sample (Figure 2) to establish baseline values for fossil coral analyses. The sample was scanned at the highest resolution (39.5 µm per cubic voxel) in this study (Table 3). The scan clearly defines recognizable skeletal morphology in 2- and 3-D images and serves as a reference for aragonite and pore space neutron attenuation values. 3-D pixel filtering was used to scan through the volumetric data to isolate the composition (aragonite) and density (porosity) characteristics of the sample, represented by two peaks on the data histogram (Figure 2b). The NC data range for each material is defined in Figure 10a. The pore space was guided by the range and distribution of the first peak. The second material phase, aragonite, was interpreted by isolating the pixels that corresponded to the second peak. It is clear from histogram data that no other distinct mineral phase is present, which is consistent with the known composition of the sample. Complex 3-D architecture (see supplementary data), including branch morphology, detailed corallite structure, corallite walls and annual density banding where appropriately oriented (Figure 2a). Small circular bright spots throughout the sample (Figure 2c) that are not characteristic of the coral skeleton may represent allochthonous materials such as organic matter (e.g., endoliths), clay, or other neutron attenuating elements embedded in the skeleton.

4.2. Proof-of-Concept—*FM19-1*: NCT Imaging of Mixtures of Porosity, Aragonite and Calcite

FM19-1 serves as a proof-of-concept for using NCT to image mixtures of aragonite, porosity, and calcite in fossil coral samples, with results constrained and validated by other analytical techniques. FM19-1 contains porosity, original *Porites* aragonite skeleton and diagenetic calcite (Figure 3), introducing a third variable into the NCT imaging outputs and new greyscale thresholds. The neutron scan again shows well-defined corallites and annual density bands in the aragonite portion of the core (Figure 3d). Patches previously determined to be calcite by hyperspectral imaging (Figure 3c) show a more irregular mottled appearance with lower neutron attenuation than skeletal aragonite (Figure 4). A contrast between lighter and darker gray reflects variation in H (volatile) content as well as density variations due to annual changes in skeletal structure associated with growth rates (i.e., density reflects calcification rates vs. linear extension; Anderson et al., 2017). Seasonal growth banding is well developed

15252027, 2025, 10, Downloaded from https://agupubs.onlinelibrary.wiley.com/doi/10.1029/2025GC012439 by Carra Williams , Wiley Online Library on [02/10/2025]. See the Terms and Conditions (https://onlinelibrary.wiley.com/terms-and-conditions) on Wiley Online Library for rules of use; OA articles are governed by the applicable Creative Commons License

15252027, 2025, 10, Downloaded from https://agupubs.onlinelibrary.wiley.com/doi/10.1029/2025GC012439 by Carra Williams , Wiley Online Library on [02/10/2025]. See the Terms and Conditions (https://onlinelibrary.wiley.com/terms-and-conditions) on Wiley Online Library for rules of use; OA articles are governed by the applicable Creative Commons License

in aragonite and poorly in calcite sections, but based on histogram values (0–15,000 NC) these density differences primarily represent the amount of pore space (porosity) in the aragonite part of the core. In the calcite section, lighter patches with well imaged corallites are remnant aragonite and darker patches represent the bulk differences in greyscale between calcite (darker) and aragonite (lighter) and porosity (darkest); corallites are less easily discerned. Thus, although the imaged planes are not identical, the NCT scan may better indicate the spatial heterogeneity of primary aragonite than the classification based on hyperspectral analysis alone (Figure 3c) and well-preserved aragonite is easily distinguishable from bulk calcite. The NCT scan also identified a second calcitic region that is just below the surface of the hyperspectral scan and was not identified from the surface alone (Figure 3d).

Based on the neutron attenuation coefficient of H and the elevated H content in pristine aragonite (Figure 4), pixels with the highest NC on the greyscale were selected to represent aragonite and compared with hyperspectral images from Murphy et al. (2017) (Figure 3c). The hyperspectral results, which used wavelength position and asymmetry to differentiate calcite from aragonite, guided the interpretation in this study along with histogram data ranges and distributions (Figure 4). NCT scans of FM19-1 were used to parameterize calcite and aragonite values (displayed as a bimodal distribution on the histogram of Figure 3d) by analyzing pixels from known mineral regions inferred from hyperspectral imaging (Figure 3c).

The NC data for materials in FM19-1 contain no points greater than 56,000 NC, suggesting that neutron attenuation provides no additional information beyond that threshold. Reducing pixel size increased resolution, and comparisons with collocated geochemical assay samples helped refine the results. The porous nature of the coral skeleton skewed averages in some instances, but zooming in and excluding black (porous) background pixels mitigated this. By filtering out the proposed values for each mineral phase (see supplementary data), the sections of core that disappeared first were compared with known calcite-aragonite regions (McGregor & Gagan, 2003), yielding filtered regions corresponding to hyperspectral absorption wavelengths of >2,333 nm for calcite and >2,308 nm for aragonite (Murphy et al., 2017).

Five thin sections produced by McGregor and Abram (2008) from near the 11 geochemically sampled sites across the patchy aragonite-calcite transect of FM19-1 (McGregor & Gagan, 2003) were chosen as representative images of key diagenetic changes for comparisons with NCT images in this study (Figure 5b). The NCT counts were recorded at sites as close as possible to the XRD sample pits of Figure 5e. NC throughout that transect (McGregor & Gagan, 2003) corresponded to heterogeneous variations in calcite content from 0% to 100% and a systematic decrease in Sr/Ca_{atomic} ratios from 0.0088 to 0.0021 as calcite content increased (McGregor & Gagan, 2003). Modal NC values observed at different calcite percentages are: <1% calcite corresponds to 48,876 NC, 5% to 38,313 NC, 13% to 35,316 NC, 53% to 28,200 NC and 77% to 20,886 NC (Figure 6). Whilst thin section petrography does not provide 3-D mineral distribution, it readily demonstrates the degree and texture of diagenetic alteration where it is applied (McGregor & Abram, 2008) and it has proven complementary to NCT scanning, guiding the thresholds of NC values.

5. Application to Other Fossil Coral Samples

To explore the broader application of NCT to other fossil coral samples, the results from the calibration sample (modern *Porites*) and the proof-of-concept sample (FM19-1) were applied to more diagenetically complex samples (SWIFT-N-1-C-4A2 and RR5-70-1). We evaluated the consistency of NCT in detecting diagenetic alterations and distinguishing between primary and secondary mineral phases and its overall potential as a reliable tool for screening fossil corals.

5.1. Trial Case 1—*SWIFT-N-1-C-4A2*: Defined Mixture of Aragonite and Calcite

SWIFT N1-C-4A2 was scanned at the second highest resolution produced in this study (Table 3). The neutron scan (Figure 7d) shows low neutron attenuation (filtered out and black) throughout most of the sample, except for a portion of the *Isopora* coral where higher attenuation occurs (white-gray pixels) but is not easily identified as coral skeletal structure.

Greyscale data ranges in Figure 10c show three distinguishable peaks, representing porosity, calcite, and aragonite. This sample was scanned near others impregnated with epoxy resin, which skewed the neutron attenuation values to a high and narrow multimodal distribution. Data points from resin were identified by

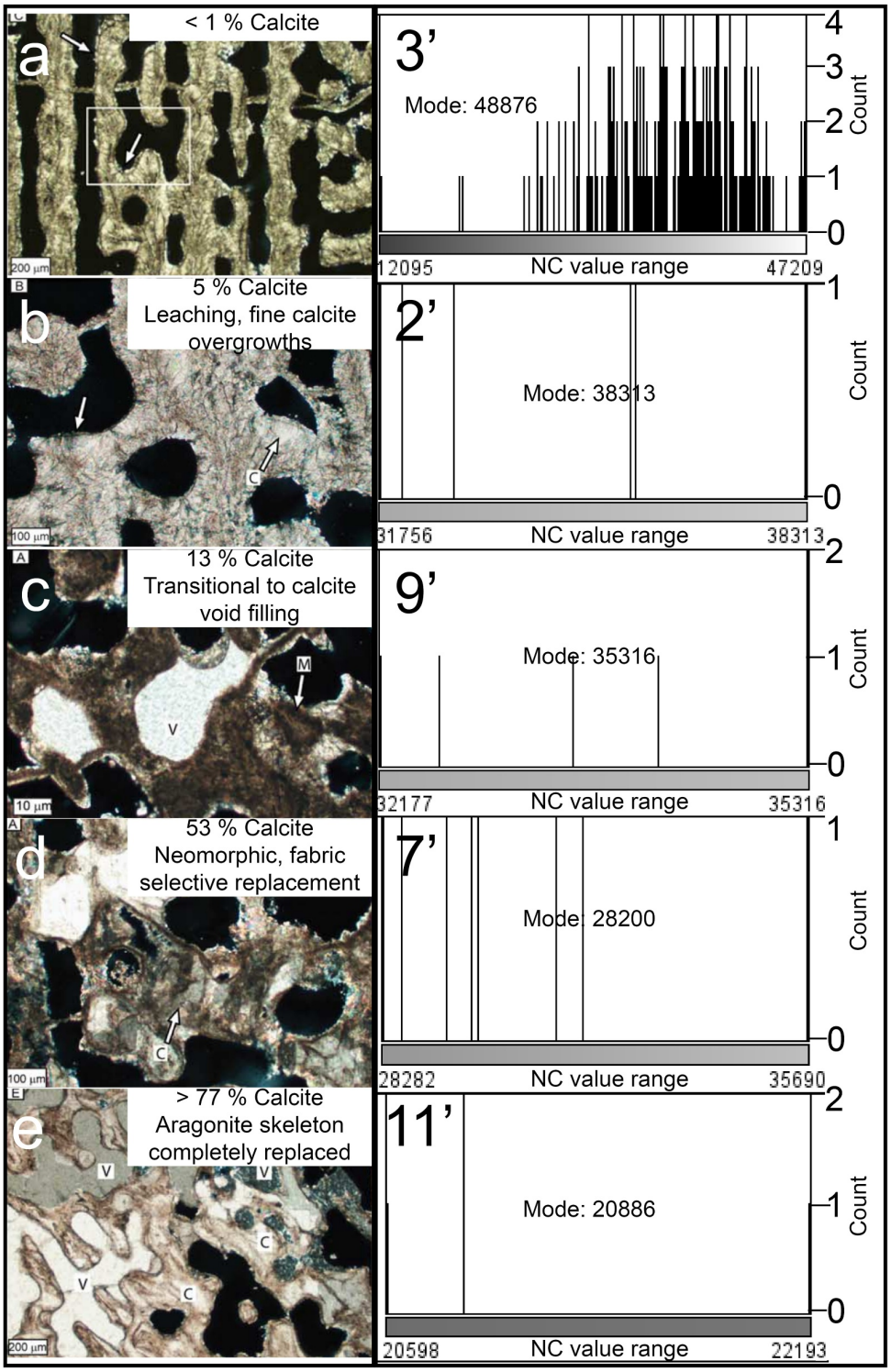


Figure 6.

15252027, 2025, 10, Downloaded from https://agupubs.onlinelibrary.wiley.com/doi/10.1029/2025GC012439 by Carra Williams , Wiley Online Library on [02/10/2025]. See the Terms and Conditions (https://onlinelibrary.wiley.com/terms-and-conditions) on Wiley Online Library for rules of use; OA articles are governed by the applicable Creative Commons License

15252027, 2025, 10, Downloaded from https://agupubs.onlinelibrary.wiley.com/doi/10.1029/2025GC012439 by Carra Williams , Wiley Online Library on [02/10/2025]. See the Terms and Conditions (https://onlinelibrary.wiley.com/terms-and-conditions) on Wiley Online Library for rules of use; OA articles are governed by the applicable Creative Commons License

filtering out values that did not show a change in pixel display in non-resin samples. Aragonite was distinguished by comparison with hyperspectral maps and SEM images (Figure 7e), where high neutron attenuation in NCT scans corresponded to aragonite (Figure 7d). The remaining values were interpreted as calcite or porosity/background noise.

The 3-D distribution of aragonite in the NCT scan of SWIFT-N-1-C-4A2 (Figure 7d) also corresponds to aragonitic regions identified on 2-D hyperspectral maps (Figures 7b and 7c respectively). However, NCT reveals a more extensive 3-D aragonite distribution in the *Isopora palifera* coral, which is confirmed by SEM (Figure 7e). This sample validates the method of distinguishing calcite and aragonite in fossil corals at the centimeter scale using NCT, guided by hyperspectral mapping and confirmed by SEM analyses.

5.2. Trial Case 2—*RR5-70-1*: Sub-Millimeter Scale Mixtures of Aragonite and Calcite

The RR5-70-1 sample was previously considered too altered to provide a reliable date (Braithwaite et al., 2004). Following the successful application of NCT scans in revealing sections of unaltered aragonite in three prior samples of fossil coral, we now apply the method to this more heavily altered fossil coral to identify any small sections of aragonite that might be dateable.

RR5-70-1 consists of relatively poorly preserved *Acropora* with more disseminated calcite (Braithwaite et al., 2004; Braithwaite & Montaggioni, 2009; Humblet & Webster, 2017) than the previous samples. The NCT scan (Figure 8b) shows sub-millimeter scale mixtures of aragonite and calcite throughout the 3-D volume and rather poorly defined skeletal structure. It was scanned at the lowest resolution in this study (Table 3); however, individual branches and corallite orientations are visible but with patchy dark regions. The pattern and intensity of reflectance spectra on hyperspectral maps guide the interpretation of data ranges for aragonite, calcite, and porosity, along with relative greyscale contrasts from previous sample results. The histogram (Figure 10d) shows a higher data volume compared to the modern *Porites* and FM19-1, indicating more diagenetic alteration and/or increased density from reduced porosity. Two distinct peaks represent porosity and mineral phases, with a third, broader region suggesting a transition between calcite and aragonite due to diagenesis. Interpreted aragonite ranges occur within the thresholds defined by the modern *Porites* and FM19-1 (Figure 10). Interpretations of pixel values corresponding to aragonite are distributed in sparse, patchy clumps along denser branch regions (Figure 8d). Calcite replacement appears to be most concentrated within the inner and outer less dense branches (Figure 8c). However, SEM reconnaissance of polished and etched surfaces from several regions found no primary aragonite as the original coral microstructure. The SEM image of the larger scale pattern of coral structure (Figure 8e) shows that the alteration is consistent with blocky diagenetic calcite replacement in a highly porous zone with fluid inclusions. The zoomed in SEM image (Figure 8f) shows rows of remnant "ghost" aragonite fibers (Nothdurft & Webb, 2009) at the micro level trapped between the original growth lines and final blocky calcite fabric (Webb et al., 2009). SEM suggests this sample contains only minor aragonite remnants, which cannot be used for dating.

Thin section petrography confirms SEM interpretations. There is pore filling calcite cement that varies and may be at a later stage than the initial neomorphism as well as dog tooth style cavity filling (Figure 8g). Either of these fabrics could be responsible for the high calcite observed in pores and borings, for example, Figure 8c. There is a ghost overprint of the coral structure (Figure 8g), where tiny aragonite pockets are concentrated in patches (Figure 8h). These tiny patches could be responsible for the sparse patches of high neutron attenuation pixels interpreted as aragonite in the NCT scan (Figure 8d).

No pure aragonite was found on the hyperspectral map (Figure 9f), with black pixels (neither pure aragonite nor pure calcite) suggesting pervasive and transitional diagenesis. 2-D representations of the complex diagenetic alteration also can be seen on the hyperspectral calcite purity map (Figure 9b), OH map (Figure 9c), carbonate

Figure 6. Comparison between representative polarized thin section images, XRD percent calcite, and neutron count values from FM19-1 representing diagenetic alteration across sample sites shown in Figure 5d. Panels (a–e) correspond to thin sections collocated to XRD samples, XRDFM19–3 (<1% calcite), XRDFM19–2 (5% calcite), XRDFM19–9 (13% calcite), XRDFM19–7 (53% calcite) and XRDFM19–11 (77% calcite) respectively (McGregor & Abram, 2008). Panels 3′, 2′, 9′, 7′ and 11′ are NCT histogram plots of the modal (most common) NC values taken from a location similar to the thin section and XRD sample locations 3, 2, 9, 7, and 11, respectively (Figure 5e). The NC value range is given on the *x* axis and the bin count is given on the *y* axis. The height of each bin (count) reflects the number of data points associated with a single pixel value, allowing for a visual representation of data density and variation. NC mode given in Figures 3′, 2′, 9′, 7′ and 11′ decreases with increasing mineral alteration within the aragonite—calcite transect, which is patchy and non-linear, as shown in Figures 5a and 5b.

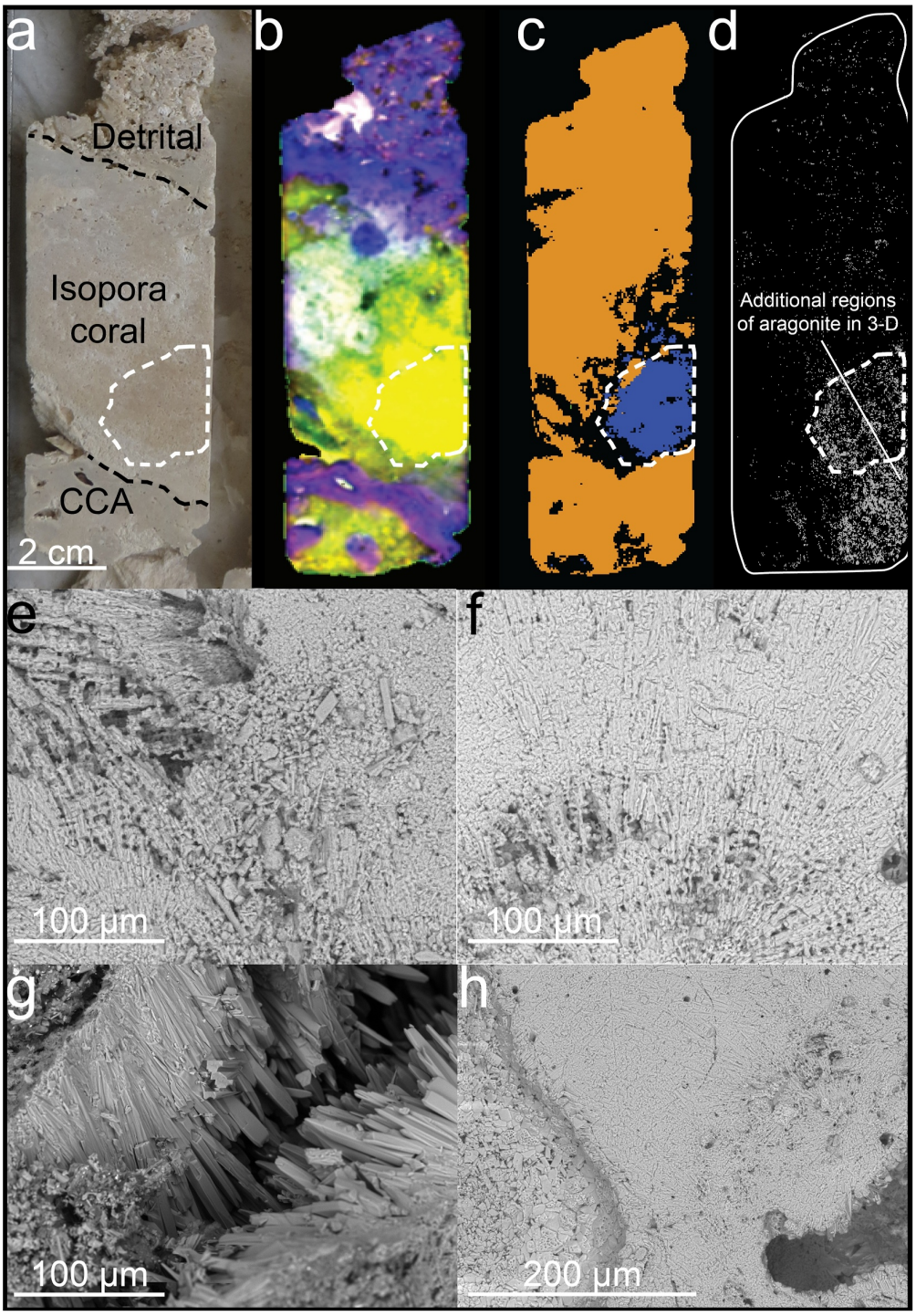


Figure 7. Comparison of different images of SWIFT N1-C-4A2. (a) Photograph showing interpreted sedimentary components (CCA: crustose coralline algae). (b) Water absorption/OH image (Webster et al., 2022). Yellow tones show aragonitic phases and blue tones show crystalline calcite phases. White and reddish tones show transitional carbonate phases. (c) Hyperspectral scan (Webster et al., 2022) showing calcite in orange and aragonite in blue. (d) 3-D neutron computed tomographic scan showing only high neutron attenuation values corresponding to aragonite phases identified in (b, c). (e, f) Are SEM images taken within the coral skeleton, showing original aragonite mineral corresponding to high NC pixels in the NCT scan. (g) SEM image showing abundant secondary aragonite needles, and (h) SEM image showing dissolution and neomorphic calcite.

15252027, 2025, 10, Downloaded from https://agupubs.onlinelibrary.wiley.com/doi/10.1029/2025GC012439 by Carra Williams , Wiley Online Library on [02/10/2025]. See the Terms and Conditions (https://onlinelibrary.wiley.com/terms-and-conditions) on Wiley Online Library for rules of use; OA articles are governed by the applicable Creative Commons License

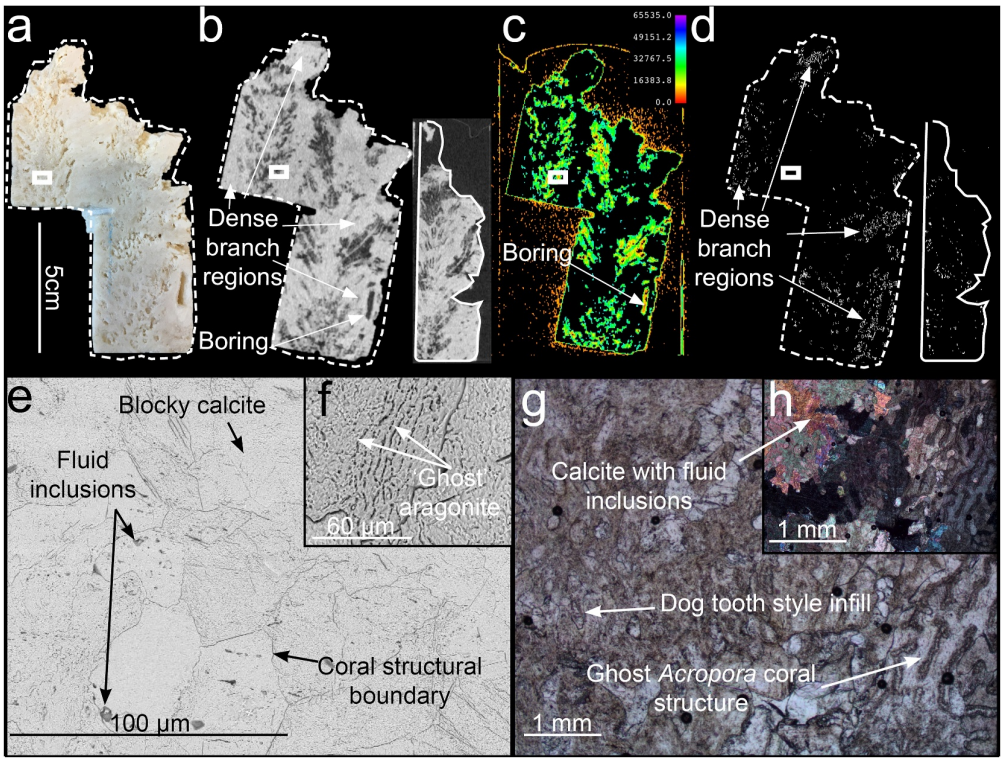


Figure 8. Images of neutron computed tomographic (NCT) scans of RR5-70-1 and SEM images showing micro scale mineral and structural features. (a) Photograph of original core. (b) Image of greyscale 2-D NCT scan showing coral structure and neutron attenuation. 2-D vertical profile is shown in the solid white outline. (c) 3-D pixel filter applied to blended rainbow color scale highlighting calcite, exclusive of porosity. (d) Regions of aragonite shown in 3-D of the NCT scan highlighting highest neutron attenuation pixels guided by regions and patterns of aragonite identified in Figures 9b–9e. 2-D vertical profile of NCT scan is shown in the solid white outline, corresponding to the same profile shown in (b). (e) SEM image showing extensive calcite alteration. (f) SEM scan showing remnant "ghost" aragonite. (g) Plane polarized light thin section showing variable pore filling calcite cement and (h) cross-polarized light thin section of the same view showing calcite with fluid inclusions (cloudy brown). White squares in figures (a–e) show approximate SEM and thin section sample location.

composition map (Figure 9d) and the mixed water and carbonate mineralogy map (Figure 9e). Aragonite is present in the denser branch regions and along the top edge of the sample, where the coral branch extends. These correlate with the NCT results that show brightest pixels with highest neutron attenuation along the same dense branch regions highlighted in Figure 8e. The hydroxyl map (Figure 9c) indicates strong neutron interaction with water, although it is unclear whether this reflects water in aragonite biocrystals or calcite fluid inclusions (Figure 9f). However, because this sample had the lowest resolution in the study, there was more data averaging, which likely skewed the range and distribution of data, complicating greyscale interpretation. Further characterization is needed to account for the potential effects of other H sources including, neomorphic calcite with fluid inclusions (Figure 8e), organic matter around aragonite remains, or leaching of H or mass from the surrounds (Webb et al., 2009), and highly attenuating trace elements and compounds such as clay, magnesium, and iron (Table 2). Additionally, variations in water content across the coral skeleton, influenced by the original organic matter and skeleton thickness, may impact H distribution and neutron attenuation.

5.3. Aragonite-Calcite Calibrations

NCT scan interpretations, supported by previous studies (Ivankina et al., 2020), show that brighter pixels represent aragonite, while darker grays correspond to calcite or aragonite and pore space. Using the modern *Porites* sample (pure aragonite) and the FM19-1 sample (containing both aragonite and calcite), a basic greyscale ratio was established to differentiate between these phases. Despite significant diagenetic alteration in the RR5-70-1 and SWIFT N1-C-4A2 samples, both uncalibrated (Figure 10c) and normalized (Figure 10d) greyscale data

15252027, 2025, 10, Downloaded from https://agupubs.onlinelibrary.wiley.com/doi/10.1029/2025GC012439 by Carra Williams , Wiley Online Library on [02/10/2025]. See the Terms and Conditions (https://onlinelibrary.wiley.com/terms-and-conditions) on Wiley Online Library for rules of use; OA articles are governed by the applicable Creative Commons License

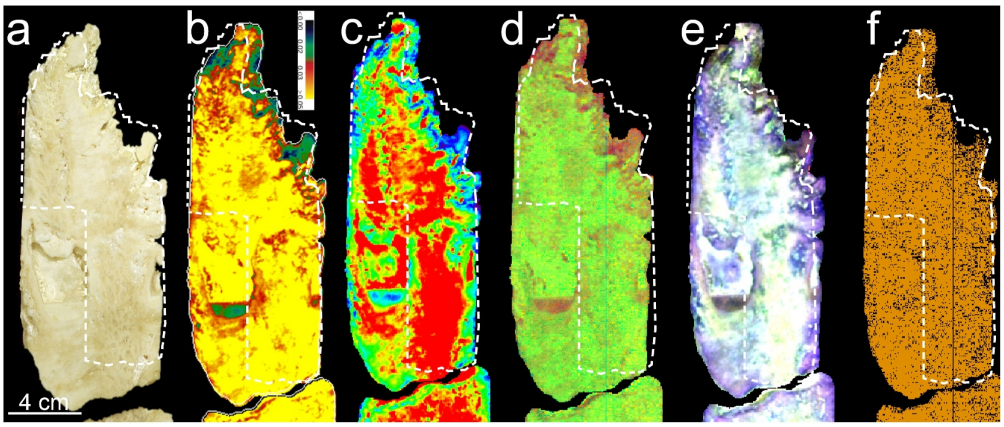


Figure 9. Hyperspectral maps of RR5-70-1. (a) Photograph of the RR5-70-1 original core. Dotted white outline shows cut sample region used for neutron computed tomographic scan (i.e., Figure 8a). (b) Hyperspectral image showing calcite purity index (Webster et al., 2022). (c) Hydroxyl (OH) Map showing regions with lower water content (blue) and higher water content (red). (d) Wavelet intensity and asymmetry map describing changes in the composition of the carbonates. Green relates to calcite and blue relates to aragonite. Intermediate tones are a combination of these phases. (e) Map showing the depth of the OH feature. Yellow indicates aragonitic phases and blue tones represent secondary calcite. White and red tones signify transitional mineral phases. (f) A classified image of the carbonate phase. Pure aragonite appears blue and pure calcite as orange. Black areas are not classified. Further details of the methodology used to produce images b-f can be found in Murphy et al. (2017) and Webster et al. (2022).

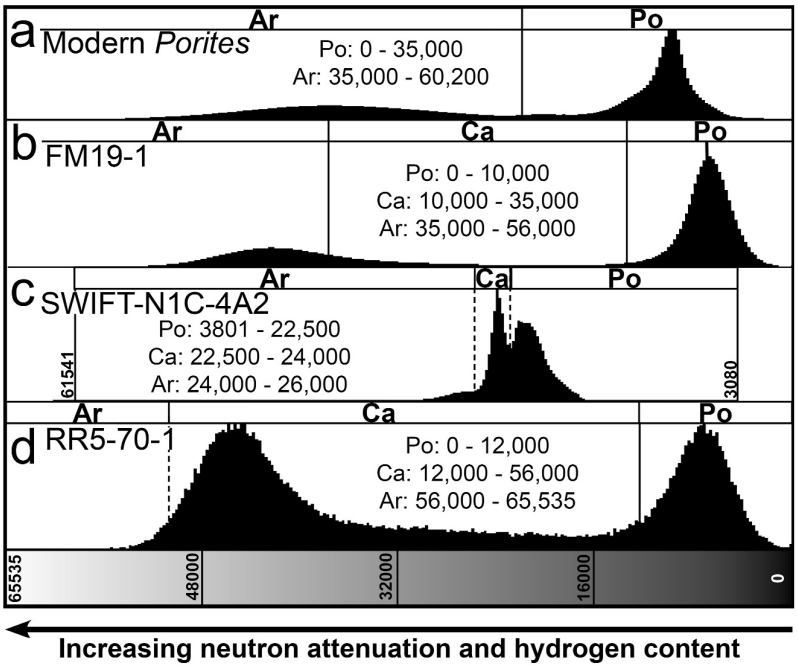


Figure 10. Histogram data of neutron computed tomographic scans of the four data sets evaluated in this study: (a) modern Porites sample, (b) FM19-1 sample, (c) SWIFT-N1C-4A2 sample and (d) RR5-70-1 sample. The range, distribution and frequency of three distinct material characteristics, porosity (Po), calcite (Ca) and aragonite (Ar) are shown with neutron count value ranges included in each panel a–d. The greyscale at the bottom shows the maximum range of neutron counts from 0–65,535, where neutron attenuation increases relative to increasing hydrogen content. Number of bins: 256, bin width: 254.633. Solid black line shows known boundary between mineral phases, dotted lines indicate interpreted and uncertain boundaries.

15252027, 2025, 10, Downloaded from https://agupubs.onlinelibrary.wiley.com/doi/10.1029/2025GC012439 by Carra Williams , Wiley Online Library on [02/10/2025]. See the Terms and Conditions (https://onlinelibrary.wiley.com/terms-and-conditions) on Wiley Online Library for rules of use; OA articles are governed by the applicable Creative Commons License

reveal distinct histogram characteristics for porosity, calcite, and aragonite, aiding the interpretation of alteration in fossil coral samples.

5.4. Secondary Aragonite

SEM images captured both primary and secondary aragonite in areas corresponding to high NC in NCT scans. Primary aragonite is identified on SEM images as needle-like crystals arranged in a radial or fibrous pattern along the original boundaries of coral structures, such as corallites (e.g., Figure 8e), where it was initially deposited during growth. Secondary aragonite appears as coarser pore filling material within the coral skeleton (e.g., Figure 8g). While NCT distinguishes between calcite and aragonite, it may be less effective at differentiating primary from secondary aragonite. However, the broad range of NC values for aragonite in the unaltered modern *Porites* sample (Figure 10a) provides constraints for aragonite's maximum values but also reveals significant H content variation across the sample. This heterogeneity is observed in the broad reflectance spectra of aragonite seen in Murphy et al. (2017), suggesting an opportunity for future studies to evaluate the attenuation range and microstructural differences between primary and secondary aragonite (McGregor & Abram, 2008). Such studies could utilize additional altered coral samples and SEM analyses to confirm sections of pure skeletal aragonite and sections with significant aragonite cement filling. Secondary aragonite can increase bulk density by 10% (Hendy et al., 2007), which may contribute to the higher neutron attenuation values observed and interpreted as aragonite. These values likely represent a combination of primary and secondary aragonite. Optimizing the high filter range during 3-D filtering in ultra-high-resolution scans, along with identifying anomalies in skeletal density, could help isolate primary aragonite while avoiding denser regions of secondary aragonite to mitigate risk associated with geochemical reconstruction artifacts (McGregor & Abram, 2008). Additional analyses, such as XRD, could identify other highly attenuating minerals, such as clay or silicates, that may interfere with interpretations.

However, NCT scanning, as demonstrated in this study, is effective for identifying aragonite in fossil corals without the need to differentiate between primary and secondary aragonite. The technique's main advantage lies in its ability to non-destructively distinguish aragonite from calcite and generate high-resolution 3-D images, allowing precise subsampling for SEM verification.

5.5. Distinguishing Coral Density Variations From Diagenesis

The greyscale graphs of Figures 10a and 10b illustrate the range and distribution of porosity, calcite and aragonite interpreted in the context of coral skeleton structure and previous geochemical screening results for the modern *Porites* and FM19-1 samples, respectively. It represents both mineral hydration and density variations associated with the pore spaces of the coral skeleton growth bands. To clarify the greyscale interpretation and disentangle coral density variations from diagenesis, two factors were assessed. (a) The mineral density difference between pure calcite (2.711 g/cm^3) and aragonite (2.83 g/cm^3) is insignificant relative to neutron passage and is thus ruled out as an explanation for the greyscale contrasts. Coral skeletal density is much lower (1–1.4 g/cm^3) (Barnes & Lough, 1993) and would show a variable neutron response to mineral content. Visual and neutron attenuation contrasts would therefore more likely be a product of variation in H content observable along the coral skeletal structure. (b) Thicker samples contain more material for neutron interaction, which may skew the data frequency, as observed in the RR5-70-1 histogram (Figure 10c), but does not affect the data range or distribution. This is visually evident in the modern *Porites* sample (Figure 2c), where the intensity of NC (brightness) varies significantly across the fixed width of coral branches without any significant variation in branch density, orientation, or structure. Studies have shown that X-Ray beams and photographic density can be influenced by coral structure (Le Tissier et al., 1994), but this is not the case here, implying that neutron attenuation is a representation of H content rather than density alone. Furthermore, pixels selected within the same cross-sectional position (orientation, width and depth) of corallite structure within the modern *Porites* sample were shown to vary NC. This variation in neutron attenuation is clearly not a product of density, coral structure, orientation, or shape. Instead, variations in production of aragonite in the coral skeleton as a product of three mechanisms of coral growth - extension, thickening and tissue uplift (Barnes & Lough, 1993) may be represented in NCT scans as a proxy of 3-D H extent and distribution.

15252027, 2025, 10, Downloaded from https://agupubs.onlinelibrary.wiley.com/doi/10.1029/2025GC012439 by Carra Williams , Wiley Online Library on [02/10/2025]. See the Terms and Conditions (https://onlinelibrary.wiley.com/terms-and-conditions) on Wiley Online Library for rules of use; OA articles are governed by the applicable Creative Commons License

15252027, 2025, 10, Downloaded from https://agupubs.onlinelibrary.wiley.com/doi/10.1029/2025GC012439 by Carra Williams , Wiley Online Library on [02/10/2025]. See the Terms and Conditions (https://onlinelibrary.wiley.com/terms-and-conditions) on Wiley Online Library for rules of use; OA articles are governed by the applicable Creative Commons License

5.6. The Advantage of NCT Over Other Whole Sample Screening Techniques

Previous studies using X-Ray CT on coral samples (Helmle et al., 2000; Ketcham & Carlson, 2001) were compared to the results of this study. X-Ray CT and X-Ray positive images successfully identified seasonal coral growth banding and density contrasts in the modern and Holocene *Porites* samples respectively (Figures 2a and 5a; Buddemeier & Kinzie, 1976; Pichon, 2011; Brachert et al., 2013), but they could not detect variations in mineral phases or resolve complex 3-D skeletal architecture. In contrast, NCT produced higher-resolution images (Figure 2d), offering more detailed morphology and better differentiation of aragonite and calcite. Unlike X-Ray CT, which is limited to detecting density contrasts, NCT is more effective for distinguishing similar density minerals and for detecting H-rich minerals, such as coral aragonite, due to its sensitivity to neutrons (Christie et al., 2007; Vlassenbroeck et al., 2007). The 3-D capabilities of NCT (Figure 2c) also allow for accurate identification of coral genus, growth form, and growth axis, which X-Ray CT and other 2-D methods may miss. Similar high-resolution 3-D imaging capabilities are also provided by micro-XCT, although typically at smaller sample scales.

Murphy et al. (2017) demonstrated that hyperspectral imaging offers a way to map surface contrasts between aragonite and calcite based on their spectral absorption features in the 2,300–2,350 nm range, at high spatial resolution without physical sampling (Figure 3c). However, it did not detect the extent of heterogeneity across the FM19-1 aragonite-calcite transect in as much detail as the X-Ray positive image (Figure 5a) and NCT scan (Figure 3d) and therefore cannot be precisely compared to XRD and geochemical proxies. The inconsistencies in hyperspectral imaging outputs, such as pure calcite in Figure 9f not corresponding with highest levels of calcite in other maps further highlight its limitations. Additionally, hydroxyl OH maps show water content on a 2-D surface without structural context (i.e., coral skeleton), potentially indicating a range of mineral products such as fluid inclusions, organic content, or clays. Substantial processing efforts of the various hyperspectral maps all fall short of locating aragonite in 3-D. NCT provides the advantage of revealing 3-D diagenetic alterations, extending the range of aragonite identification beyond what is seen in 2-D hyperspectral maps (Figure 7c) as well as the internal structure (Figure 8d). The tiny portion and sparse distribution of aragonite discovered by NCT scans hidden beneath the surface of RR5-70-1 (see side profile in Figure 8d) were confirmed by hyperspectral maps and thin sections but were undetected by SEM and the carbonate classification hyperspectral map because of their 1-D and 2-D analyses (respectively). This clearly outlines the advantage of NCT scans that can image the 3-D water content in fossil corals, allowing for isolation of pixels representative of aragonite in 3-D. Nevertheless, hyperspectral imagery complements NCT by providing 2-D maps of aragonite-calcite zones to guide 3-D interpretations, as shown with SWIFT N-1-C-4A2. Ultimately, each screening technique offers merits and limitations pertaining to the scale of resolution and scientific question at hand. However, this study also highlights the importance of multi-method analyses when searching heavily altered fossil corals for remaining primary aragonite.

5.7. Recommendations for Applying NCT to Fossil Coral Diagenetic Screening

Non-destructive techniques in petrological studies are highly desirable, especially where only a limited amount of material is available, such as rare reef cores. Interpretations in this study are subjective at times and heavily informed by other 2-D and destructive analyses that NCT could potentially replace. To ensure the effective use of NCT as proposed, several considerations must be made regarding sample preparation, data acquisition and interpretation. The following recommendations provide guidelines to aid the future application of this technique to fossil coral samples.

NCT scanning in this study was unaffected by sample size or composition; however, other studies recognized these as limitations (Christie et al., 2007; Williams et al., 2017). More consistent thresholds between minerals could be set if samples were of uniform thickness, and measurements should avoid random sample orientation that might obscure key features. New scanning equipment at ANSTO now achieves whole, uncut core scanning, allowing samples larger than the aluminum tube used in this study (18 cm inner diameter) to be imaged without cutting. Achieving consistent and comparable NCT data across samples requires standardization of acquisition parameters. The recommended settings include a spatial resolution between 30–50 μm with a 3–5-hr acquisition time for detailed imaging of mineral phases and skeletal structures. Thicker samples may require higher intensity neutron flux and smaller rotation steps, although with increased acquisition times. Neutron activation requires

intervals between sample measurements, and adjustments to neutron flux should be made over time, especially for multiple scans. Recent modifications to DINGO allow for harnessing low-, medium-, and high-energy neutron source emissions, providing improved flexibility in sample handling, although a potential limitation in other facilities.

Interpreting NCT data requires segmenting mineral phases based on neutron attenuation observed in scans. Coral structure and mineral distribution were investigated most efficiently using 3-D visualization software with volume rendering. In this study, NC histograms revealed distinct peaks corresponding to aragonite, calcite and porosity. These gray-scale ranges (i.e., Figure 10) provide a general reference for similar samples, although some inconsistencies across samples suggest the need for standardized interpretation. In all cases, the highest NC values corresponded with unaltered aragonite serving as a starting point for identifying diagenetic alterations. Establishing a reliable threshold between aragonite and calcite will require further standardization.

In summary, to improve reproducibility, three recommendations for future users include: (a) using reference standards such as pure element cubes or a pure aragonite sample to calibrate and interpret NCT scans, (b) ensuring consistent acquisition parameters, such as resolution, neutron intensity and rotation steps across samples, and (c) combining NCT with other screening methods to confirm the preservation state, given that NC values and greyscale histograms vary based on sample composition and scanning parameters. When it is critical to find original aragonite for geochemical analysis in high value, but altered samples, NCT provides an important screening tool for 3-D, non-destructive screening.

6. Conclusions

Detailed reconstructions of diagenetic histories in fossil coral reefs are essential for their selection for further geochronologic and paleoclimatic studies. This study shows that NCT scans successfully distinguish between coral aragonite and calcite by mapping their 3-D distributions in diagenetically altered fossil corals. With high sensitivity to H content, NCT is an ideal tool for screening well-preserved coral aragonite and also captures sub-mm core features, such as seasonal growth banding and 3-D structure of coral skeletons, offering detailed insights at representative scales. As a high resolution, non-destructive method, NCT reduces sampling time and potentially costs (commercial rates at $9,299/day, and free for academic, merit-based access), while simplifying screening for secondary carbonate mineral replacement, making it a valuable tool for screening diagenetically complex fossil coral reef samples. NCT scans have been shown to complement and corroborate existing pre-screening methods (XRD, SEM, thin section analysis, hyperspectral imagery and X-Ray CT) based on diagenetic screening of three fossil coral samples of various ages, genera and growth morphologies. In a highly altered fossil coral sample, NCT successfully identified the remaining aragonite that other 2-D and 1-D methods missed. Comparing NCT histogram values with petrographic and geochemical analyses showed that neutron attenuation reflects a range of primary carbonate mineral alteration, thereby providing the potential for improved diagenetic screening. Finally, specific recommendations are provided for future users on how to apply this technique for diagenetic screening of other fossil coral samples, emphasizing the need for standardized acquisition parameters and the integration of complementary screening techniques to improve the reliability of geochronologic and paleoclimatic reconstructions.

Conflict of Interest

The authors declare no conflicts of interest relevant to this study.

Data Availability Statement

The NCT scan data used for imaging fossil coral reef cores to reveal 3-D diagenetic alteration in the study are available via Morphosource DOI's (Williams, 2024a, 2024b, 2024c, 2024d). Data include the reprocessed data that were reconstructed with Octopus Reconstruction version 8.9.4.9© (Heidelberg Engineering GmbH) software. Reconstructed neutron tomographic scans are 16-bit .tiff files that can be visualized in 2-D and 3-D visualization software. This study used public domain software for 2-D (ImageJ™ (Schneider et al., 2012)) and 3-D (Slicer 5.2.2 (Fedorov et al., 2012)). No registration, permission, or licenses are required.

15252027, 2025, 10, Downloaded from https://agupubs.onlinelibrary.wiley.com/doi/10.1029/2025GC012439 by Cairn Williams , Wiley Online Library on [02/10/2025]. See the Terms and Conditions (https://onlinelibrary.wiley.com/terms-and-conditions) on Wiley Online Library for rules of use; OA articles are governed by the applicable Creative Commons License

Acknowledgments
Core data were provided with permission from the Perth Core Library and the Geocoastal Research Group, University of Sydney. We thank Colin Braithwaite for sharing data from RR5 cores and providing insight on the diagenetic alteration of zones of interest. We thank the reviewers for providing guidance and detailed feedback on the manuscript draft. Thanks, are also due to the School of Earth Sciences (The University of Western Australia) for providing support and access to a workstation. JMW acknowledges support from the Hanse-Wissenschaftskolleg Institute for Advanced study (Delmenhorst, Germany). We are grateful to the ANSTO scientists for providing support for instrument operation, data acquisition and processing. We acknowledge Dr. Alisha Thompson and Wenona School (Sydney, NSW) for the use of their SEM facilities. This research was supported by a HDR scholarship from the School of Geosciences, University of Sydney. This research was also funded by a PRSS (post-graduate research support scheme) scholarship, School of Geosciences, University of Sydney, to attend the IAS Conference, Dubrovnik, June 2023 to present this work as a poster presentation. This ongoing research continues to be funded by an AINSE Postgraduate Research Award. HVM was supported by ARC SRIEAS Grant SR200100005 Securing Antarctica's Environmental Future, and access to DINGO was granted via ANSTO access proposal P14248. HVM and JW are supported by ARC DP DP200100206 and JW by ANZIC AILAF2103. Open access publishing facilitated by The University of Sydney, as part of the Wiley - The University of Sydney agreement via the Council of Australian University Librarians.

References

Alatrash, H., & Velledits, F. (2024). Comparing petrophysical properties and pore network characteristics of carbonate reservoir rocks using micro-X-ray tomography imaging and microfacies analyses. *GEM-International Journal on Geomathematics*, *15*(1), 1. https://doi.org/10.1007/s13137-023-00243-8

Anderson, K. D., Cantin, N. E., Heron, S. F., Pisapia, C., & Pratchett, M. S. (2017). Variation in growth rates of branching corals along Australia's Great Barrier Reef. *Scientific Reports*, *7*(1), 2920. https://doi.org/10.1038/s41598-017-03085-1

Bar-Matthews, M., Wasserburg, G. J., & Chen, J. H. (1993). Diagenesis of fossil coral skeletons: Correlation between trace elements, textures, and $^{234}U^{238}U$. *Geochimica et Cosmochimica Acta*, *57*(2), 257–276. https://doi.org/10.1016/0016-7037(93)90429-Z

Barnes, D. J., & Lough, J. M. (1993). On the nature and causes of density banding in massive coral skeletons. *Journal of Experimental Marine Biology and Ecology*, *167*(1), 91–108. https://doi.org/10.1016/0022-0981(93)90186-R

Bevitt, J. J. (2018). Discovering dinosaurs with neutrons. *Nature Reviews Materials*, *3*(9), 296–298. https://doi.org/10.1038/s41578-018-0049-0

Borromeo, L., Zimmermann, U., Andò, S., Coletti, G., Bersani, D., Basso, D., et al. (2017). Raman spectroscopy as a tool for magnesium estimation in Mg-calcite. *Journal of Raman Spectroscopy*, *48*(7), 983–992. https://doi.org/10.1002/jrs.5156

Brachert, T. C., Reuter, M., Krüger, S., Böcker, A., Lohmann, H., Mertz-Kraus, R., & Fassoulas, C. (2013). Density banding in corals: Barcodes of past and current climate change. *Coral Reefs*, *32*(4), 1013–1023. https://doi.org/10.1007/s00338-013-1056-7

Brachert, T. C., Reuter, M., Krüger, S., Kirkerowicz, J., & Klaus, J. S. (2016). Upwellings mitigated Plio-Pleistocene heat stress for reef corals on the Florida platform (USA). *Biogeosciences*, *13*(5), 1469–1489. https://doi.org/10.5194/bg-13-1469-2016

Braithwaite, C. J., Dalmasso, H., Gilmour, M. A., Harkness, D. D., Henderson, G. M., Kay, R. L. F., et al. (2004). The Great Barrier Reef: The chronological record from a new borehole. *Journal of Sedimentary Research*, *74*(2), 298–310. https://doi.org/10.1306/091603740298

Braithwaite, C. J., & Montaggioni, L. F. (2009). The Great Barrier Reef: A 700 000 year diagenetic history. *Sedimentology*, *56*(6), 1591–1622. https://doi.org/10.1111/j.1365-3091.2008.00982.x

Brand, U., & Veizer, J. (1980). Chemical diagenesis of a multicomponent carbonate system; 1, Trace elements. *Journal of Sedimentary Research*, *50*(4), 1219–1236. https://doi.org/10.1306/212F7BB7-2B24-11D7-8648000102C1865D

Buddemeier, R. W., & Kinzie, R. A. (1976). Coral growth. *Oceanography and Marine Biology an Annual Review*, *14*, 183–225.

Christe, P., Bernasconi, M., Vontobel, P., Turberg, P., & Parriaux, A. (2007). Three-dimensional petrographical investigations on borehole rock samples: A comparison between X-ray computed-and neutron tomography. *Acta Geotechnica*, *2*, 269–279. https://doi.org/10.1007/s11440-007-0045-9v

Clark, T. R., Roff, G., Zhao, J. X., Feng, Y. X., Done, T. J., & Pandolfi, J. M. (2014). Testing the precision and accuracy of the U–Th chronometer for dating coral mortality events in the last 100 years. *Quaternary Geochronology*, *23*, 35–45. https://doi.org/10.1016/j.quageo.2014.05.002

Cuif, J. P., & Dauphin, Y. (2005). The two-step mode of growth in the scleractinian coral skeletons from the micrometre to the overall scale. *Journal of Structural Biology*, *150*(3), 319–331. https://doi.org/10.1016/j.jsb.2005.03.004

Cuif, J. P., Dauphin, Y., Berthet, P., & Jegoudez, J. (2004). Associated water and organic compounds in coral skeletons: Quantitative thermogravimetry coupled to infrared absorption spectrometry. *Geochemistry, Geophysics, Geosystems*, *5*(11). https://doi.org/10.1029/2004gc000783

DeCarlo, T. M. (2018). Characterizing coral skeleton mineralogy with Raman spectroscopy. *Nature Communications*, *9*(1), 5325. https://doi.org/10.1038/s41467-018-07601-3

DeCarlo, T. M., & Cohen, A. L. (2017). Dissepiments, density bands and signatures of thermal stress in Porites skeletons. *Coral Reefs*, *36*(3), 749–761. https://doi.org/10.1007/s00338-017-1566-9

Dechnik, B., Webster, J. M., Davies, P. J., Braga, J.-C., & Reimer, P. J. (2015). Holocene "turn-on" and evolution of the southern Great Barrier reef: Revisiting reef cores from the Capricorn Bunker Group. *Marine Geology*, *363*, 174–190. https://doi.org/10.1016/j.margeo.2015.02.014

De Choudens-Sanchez, V., & Gonzalez, L. A. (2009). Calcite and aragonite precipitation under controlled instantaneous supersaturation: Elucidating the role of CaCO3 saturation state and Mg/Ca ratio on calcium carbonate polymorphism. *Journal of Sedimentary Research*, *79*(6), 363–376. https://doi.org/10.2110/jsr.2009.043

Denniston, R. F., Asmerom, Y., Polyak, V. Y., McNeill, D. F., Klaus, J. S., Cole, P., & Budd, A. F. (2008). Caribbean chronostratigraphy refined with U-Pb dating of a Miocene coral. *Geology*, *36*(2), 151–154. https://doi.org/10.1130/G24280A.1

Dullo, W. C. (1984). Progressive diagenetic sequence of aragonite structures: Pleistocene coral reefs and their modern counterparts on the eastern Red Sea coast, Saudi Arabia. *Palaeontographica Americana*, *54*, 254–260.

Dullo, W. C. (1986). Variation in diagenetic sequences: An example from Pleistocene coral reefs, Red Sea, Saudi Arabia. In *Reef diagenesis* (pp. 77–90). Springer Berlin Heidelberg.

Duprey, N., Boucher, H., & Jiménez, C. (2012). Digital correction of computed X-radiographs for coral densitometry. *Journal of Experimental Marine Biology and Ecology*, *438*, 84–92. https://doi.org/10.1016/j.jembe.2012.09.007

Dutton, A., Webster, J. M., Zwartz, D., Lambeck, K., & Wohlfarth, B. (2015). Tropical tales of polar ice: Evidence of last interglacial polar ice sheet retreat recorded by fossil reefs of the granitic Seychelles islands. *Quaternary Science Reviews*, *107*, 182–196. https://doi.org/10.1016/j.quascirev.2014.10.025

Fedorov, A., Beichel, R., Kalpathy-Cramer, J., Finet, J., Fillion-Robin, J. C., Pujol, S., et al. (2012). 3D slicer as an image computing platform for the quantitative imaging network. *Magnetic resonance imaging*, *30*(9), 1323–1341. https://doi.org/10.1016/j.mri.2012.05.001

Garbe, U., Randall, T., Hughes, C., Davidson, G., Pangelis, S., & Kennedy, S. J. (2015). A new neutron radiography/tomography/imaging station DINGO at OPAL. *Physics Procedia*, *69*, 27–32. https://doi.org/10.1016/j.phpro.2015.07.003

Grammer, G. M., Crescini, C. M., McNeill, D. F., & Taylor, L. H. (1999). Quantifying rates of syndepositional marine cementation in deeper platform environments-new insight into a fundamental process. *Journal of Sedimentary Research*, *69*(1), 202–207. https://doi.org/10.2110/jsr.69.202

Hassanein, R., Lehmann, E., & Vontobel, P. (2005). Methods of scattering corrections for quantitative neutron radiography. *Nuclear Instruments and Methods in Physics Research Section A: Accelerators, Spectrometers, Detectors and Associated Equipment*, *542*(1–3), 353–360. https://doi.org/10.1016/j.nima.2005.01.161

Helmle, K. P., Dodge, R. E., & Ketcham, R. A. (2000). Skeletal architecture and density banding in Diploria strigosa by X-ray computed tomography.

Hendy, E. J., Gagan, M. K., Lough, J. M., McCulloch, M., & DeMenocal, P. B. (2007). Impact of skeletal dissolution and secondary aragonite on trace element and isotopic climate proxies in Porites corals. *Paleoceanography*, *22*(4). https://doi.org/10.1029/2007PA001462

Hibbert, F. D., Rohling, E. J., Dutton, A., Williams, F. H., Chutcharavan, P. M., Zhao, C., & Tamisiea, M. E. (2016). Coral indicators of past sea-level change: A global repository of U-series dated benchmarks. *Quaternary Science Reviews*, *145*, 1–56. https://doi.org/10.1016/j.quascirev.2016.04.019

15252027, 2025, 10, Downloaded from https://agupubs.onlinelibrary.wiley.com/doi/10.1029/2025GC012439 by Carra Williams , Wiley Online Library on [02/10/2025]. See the Terms and Conditions (https://onlinelibrary.wiley.com/terms-and-conditions) on Wiley Online Library for rules of use; OA articles are governed by the applicable Creative Commons License

Humblet, M., & Webster, J. M. (2017). Coral community changes in the Great Barrier Reef in response to major environmental changes over glacial-interglacial timescales. *Palaeogeography, Palaeoclimatology, Palaeoecology*, *472*, 216–235. https://doi.org/10.1016/j.palaeo.2017.02.003

Ivankina, T. I., Kichanov, S. E., Duliu, O. G., Abdo, S. Y., & Sherif, M. M. (2020). The structure of scleractinian coral skeleton analyzed by neutron diffraction and neutron computed tomography. *Scientific Reports*, *10*(1), 12869. https://doi.org/10.1038/s41598-020-69859-2

James, N. P. (1974). Diagenesis of scleractinian corals in the subaerial vadose environment. *Journal of Paleontology*, 785–799.

Ketcham, R. A., & Carlson, W. D. (2001). Acquisition, optimization and interpretation of X-ray computed tomographic imagery: Applications to the geosciences. *Computers & Geosciences*, *27*(4), 381–400. https://doi.org/10.1016/s0098-3004(00)00116-3

Koestel, J., Fukumasu, J., Larsbo, M., Herrmann, A. M., Ariyathilaka, P., Magdysyuk, O. V., & Burca, G. (2022). Potential of combined neutron and X-ray imaging to quantify local carbon contents in soil. *European Journal of Soil Science*, *73*(1), e13178. https://doi.org/10.1111/ejss.13178

Koga, N., Kasahara, D., & Kimura, T. (2013). Aragonite crystal growth and solid-state aragonite–calcite transformation: A physico–geometrical relationship via thermal dehydration of included water. *Crystal Growth & Design*, *13*(5), 2238–2246. https://doi.org/10.1021/cg400350w

Kontoyannis, C. G., & Vagenas, N. V. (2000). Calcium carbonate phase analysis using XRD and FT-Raman spectroscopy. *Analyst*, *125*(2), 251–255. https://doi.org/10.1039/a908609i

Le Tissier, M. D. A., Clayton, B., Brown, B. E., & Davis, P. S. (1994). Skeletal correlates of coral density banding and an evaluation of radiography as used in sclerochronology. *Marine Ecology Progress Series*, *110*(1), 29–44. https://doi.org/10.3354/meps110029

Liu, J., Ye, M., Zhu, H., Guan, Y., & Zhang, T. (2025). Progress and perspective of seafloor Regolith-sampling robots for ocean exploration. *Journal of Field Robotics*, *42*(4), 1012–1036. https://doi.org/10.1002/rob.22433

Ma, Y., Qin, Y., Yu, K., Li, Y., Long, Y., Wang, R., et al. (2021). Holocene coral reef development in Chenhang Island, Northern South China Sea, and its record of sea level changes. *Marine Geology*, *440*, 106593. https://doi.org/10.1016/j.margeo.2021.106593

Malik, A., Einbinder, S., Martinez, S., Tchernov, D., Haviv, S., Almuly, R., et al. (2021). Molecular and skeletal fingerprints of scleractinian coral biomineralization: From the sea surface to mesophotic depths. *Acta Biomaterialia*, *120*, 263–276. https://doi.org/10.1016/j.actbio.2020.01.010

Maliva, R. G. (1998). Skeletal aragonite neomorphism—Quantitative modelling of a two-water diagenetic system. *Sedimentary Geology*, *121*(3–4), 179–190. https://doi.org/10.1016/S0037-0738(98)00080-3

Martin, G. D., Wilkinson, B. H., & Lohmann, K. C. (1986). The role of skeletal porosity in aragonite neomorphism-Strombus and Montastrea from the Pleistocene Key Largo Limestone, Florida. *Journal of Sedimentary Research*, *56*(2), 194–203. https://doi.org/10.1306/212F88B9-2B24-11D7-8648000102C1865D

McGregor, H. V., & Abram, N. J. (2008). Images of diagenetic textures in Porites corals from Papua New Guinea and Indonesia. *Geochemistry, Geophysics, Geosystems*, *9*(10). https://doi.org/10.1029/2008gc002093

McGregor, H. V., & Gagan, M. K. (2003). Diagenesis and geochemistry of Porites corals from Papua New Guinea: Implications for paleoclimate reconstruction. *Geochimica et Cosmochimica Acta*, *67*(12), 2147–2156. https://doi.org/10.1016/S0016-7037(02)01050-5

Morse, J. W., & Mackenzie, F. T. (1990). *Geochemistry of sedimentary carbonates*. Elsevier.

Morse, J. W., Wang, Q., & Tsio, M. Y. (1997). Influences of temperature and Mg: Ca ratio on CaCO3 precipitates from seawater. *Geology*, *25*(1), 85–87. https://doi.org/10.1130/0091-7613(1997)025<0085:iotamc>2.3.co;2

Murphy, R. J., Webster, J. M., Nothdurft, L., Dechnik, B., McGregor, H. V., Patterson, M. A., et al. (2017). High-resolution hyperspectral imaging of diagenesis and clays in fossil coral reef material: A nondestructive tool for improving environmental and climate reconstructions. *Geochemistry, Geophysics, Geosystems*, *18*(8), 3209–3230. https://doi.org/10.1002/2017gc006949

Nelyubina, Y. V., & Lyssenko, K. A. (2012). From "loose" to "dense" crystalline phases of calcium carbonate through "repulsive" interactions: An experimental charge-density study. *Chemistry*, *18*(40), 12633–12636. https://doi.org/10.1002/chem.201201457

Nothdurft, L. D., & Webb, G. E. (2009). Earliest diagenesis in scleractinian coral skeletons: Implications for palaeoclimate-sensitive geochemical archives. *Facies*, *55*(2), 161–201. https://doi.org/10.1007/s10347-008-0167-z

Nothdurft, L. D., Webb, G. E., Bostrom, T., & Rintoul, L. (2007). Calcite-filled borings in the most recently deposited skeleton in live-collected Porites (Scleractinia): Implications for trace element archives. *Geochimica et Cosmochimica Acta*, *71*(22), 5423–5438. https://doi.org/10.1016/j.gca.2007.09.025

Passe-Coutrin, N., N'Guyen, P., Pelmard, R., Ouensanga, A., & Bouchon, C. (1995). Water desorption and aragonite—Calcite phase transition in scleractinian corals skeletons. *Thermochimica Acta*, *265*, 135–140. https://doi.org/10.1016/0040-6031(95)02405-Q

Paterson, R. J., Whitaker, F. F., Smart, P. L., Jones, G. D., & Oldham, D. (2008). Controls on early diagenetic overprinting in icehouse carbonates: Insights from modeling hydrological zone residence times using CARB3D+. *Journal of Sedimentary Research*, *78*(4), 258–281. https://doi.org/10.2110/jsr.2008.029

Pichon, M. (2011). Porites. In *Encyclopedia of modern coral reefs* (pp. 815–821). Springer. https://doi.org/10.1007/978-90-481-2639-2_273

Przeniosło, R., Stolarski, J., Mazur, M., & Brunelli, M. (2008). Hierarchically structured scleractinian coral biocrystals. *Journal of Structural Biology*, *161*(1), 74–82. https://doi.org/10.1016/j.jsb.2007.09.020

Raja, P. B., Munusamy, K. R., Perumal, V., & Ibrahim, M. N. M. (2022). Characterization of nanomaterial used in nanobioremediation. In *Nanobioremediation: Fundamentals and applications* (pp. 57–83). Elsevier. https://doi.org/10.1016/B978-0-12-823962-9.00037-4

Raudsepp, M. J., Wilson, S., Morgan, B., Patel, A., Johnston, S. G., Gagen, E. J., & Fallon, S. J. (2022). Non-classical crystallization of very high magnesium calcite and magnesite in the Coorong Lakes, Australia. *Sedimentology*, *69*(5), 2246–2266. https://doi.org/10.1111/sed.12991

Roche, R. C., Abel, R. A., Johnson, K. G., & Perry, C. T. (2010). Quantification of porosity in Acropora pulchra (Brook 1891) using X-ray micro-computed tomography techniques. *Journal of Experimental Marine Biology and Ecology*, *396*(1), 1–9. https://doi.org/10.1016/j.jembe.2010.10.006

Sadler, J., Webb, G. E., & Nothdurft, L. D. (2015). Structure and palaeoenvironmental implications of inter-branch coenosteum-rich skeleton in corymbose Acropora species. *Coral Reefs*, *34*(1), 201–213. https://doi.org/10.1007/s00338-014-1228-0

Sanborn, K. L., Webster, J. M., Webb, G. E., Braga, J. C., Humblet, M., Nothdurft, L., et al. (2020). A new model of Holocene reef initiation and growth in response to sea-level rise on the Southern Great Barrier Reef. *Sedimentary Geology*, *397*, 105556. https://doi.org/10.1016/j.sedgeo.2019.105556

Sandberg, P. A. (1983). An oscillating trend in Phanerozoic non-skeletal carbonate mineralogy. *Nature*, *305*(5929), 19–22. https://doi.org/10.1038/305019a0

Sayani, H. R., Cobb, K. M., Cohen, A. L., Elliott, W. C., Nurhati, I. S., Dunbar, R. B., et al. (2011). Effects of diagenesis on paleoclimate reconstructions from modern and young fossil corals. *Geochimica et Cosmochimica Acta*, *75*(21), 6361–6373. https://doi.org/10.1016/j.gca.2011.08.026

Schneider, C. A., Rasband, W. S., & Eliceiri, K. W. (2012). NIH image to ImageJ: 25 years of image analysis. *Nature Methods*, *9*(7), 671–675. https://doi.org/10.1038/nmeth.2089

Schneider, S., Murphy, R. J., & Melkumyan, A. (2014). Evaluating the performance of a new classifier–the GP-OAD: A comparison with existing methods for classifying rock type and mineralogy from hyperspectral imagery. *ISPRS Journal of Photogrammetry and Remote Sensing*, *98*, 145–156. https://doi.org/10.1016/j.isprsjprs.2014.09.016

15252027, 2025, 10, Downloaded from https://agupubs.onlinelibrary.wiley.com/doi/10.1029/2025GC012439 by Carra Williams , Wiley Online Library on [02/10/2025]. See the Terms and Conditions (https://onlinelibrary.wiley.com/terms-and-conditions) on Wiley Online Library for rules of use; OA articles are governed by the applicable Creative Commons License

Schwarz, D. (2005). Neutron tomography of internal structures of vertebrate remains: A comparison with X-ray computed tomography. *Palaeontologia Electronica*, *8*(2), 1.

Shinn, E. A. (1969). Submarine Lithification of Holocene carbonate sediments in the Persian Gulf. *Sedimentology*, *12*(1–2), 109–144. https://doi.org/10.1111/j.1365-3091.1969.tb00166.x

Skinner, A. F. (1988). Dating of marine aragonite by electron spin resonance. *Quaternary Science Reviews*, *7*(3–4), 461–464. https://doi.org/10.1016/0277-3791(88)90046-7

Smodej, J., Reuning, L., Wollenberg, U., Zinke, J., Pfeiffer, M., & Kukla, P. A. (2015). Two-dimensional X-ray diffraction as a tool for the rapid, nondestructive detection of low calcite quantities in aragonitic corals. *Geochemistry, Geophysics, Geosystems*, *16*(10), 3778–3788. https://doi.org/10.1002/2015gc006009

Sorauf, J. E., & Cuif, J. P. (2001). *Biomineralization and diagenesis in the Scleractinia: Part 2, diagenesis* (Vol. 1, pp. 152–163). Bulletin of the Tohoku University Museum.

Stolarski, J., Cisneros-Lazaro, D., Adams, A., Janiszewska, K., & Meibom, A. (2025). Rapid isotopic exchange in mineralogically unaltered coral skeletons. *Scientific Reports*, *15*(1), 20986. https://doi.org/10.1038/s41598-025-06327-9

Stolarski, J., Coronado, I., Murphy, J. G., Kitahara, M. V., Janiszewska, K., Mazur, M., et al. (2021). A modern scleractinian coral with a two-component calcite–aragonite skeleton. *Proceedings of the National Academy of Sciences of the United States of America*, *118*(3), e2013316117. https://doi.org/10.1073/pnas.2013316117

Strasser, A., Strohmenger, C., Davaud, E., & Bach, A. (1992). Sequential evolution and diagenesis of Pleistocene coral reefs (South Sinai, Egypt). *Sedimentary Geology*, *78*(1–2), 59–79. https://doi.org/10.1016/0037-0738(92)90113-6

Strobl, M., Hilger, A., Kardjilov, N., Ebrahimi, O., Keil, S., & Manke, I. (2009). Differential phase contrast and dark field neutron imaging. *Nuclear Instruments and Methods in Physics Research Section A: Accelerators, Spectrometers, Detectors and Associated Equipment*, *605*(1), 9–12. https://doi.org/10.1016/j.nima.2009.01.224

Thompson, D. M. (2022). Environmental records from coral skeletons: A decade of novel insights and innovation. *Wiley Interdisciplinary Reviews: Climate Change*, *13*(1), e745. https://doi.org/10.1002/wcc.745

Veizer, J. (1983). Trace elements and isotopes in sedimentary carbonates. *Reviews in Mineralogy*, *11*, 265–300. https://doi.org/10.1515/9781501508134-012

Vlassenbroeck, J., Cnudde, V., Masschaele, B., Dierick, M., Van Hoorebeke, L., & Jacobs, P. (2007). A comparative and critical study of X-ray CT and neutron CT as non-destructive material evaluation techniques. *Geological Society, London, Special Publications*, *271*(1), 277–285. https://doi.org/10.1144/GSL.SP.2007.271.01.26

Vyverberg, K. L., Jaeger, J. M., & Dutton, A. (2018). Quantifying detection limits and uncertainty in X-ray diffraction mineralogical assessments of biogenic carbonates. *Journal of Sedimentary Research*, *88*(11), 1261–1275. https://doi.org/10.2110/jsr.2018.63

Watanabe, T., Suzuki, A., Minobe, S., Kawashima, T., Kameo, K., Minoshima, K., et al. (2011). Permanent El Niño during the Pliocene warm period not supported by coral evidence. *Nature*, *471*(7337), 209–211. https://doi.org/10.1038/nature09777

Webb, G. E. (2024). Advances in understanding climate change on the Great Barrier Reef using coral-based proxies. *Oceanographic Processes of Coral Reefs*, 62–85. https://doi.org/10.1201/9781003320425-6

Webb, G. E., Nothdurft, L. D., Kamber, B. S., Kloprogge, J. T., & Zhao, J. X. (2009). Rare earth element geochemistry of scleractinian coral skeleton during meteoric diagenesis: A sequence through neomorphism of aragonite to calcite. *Sedimentology*, *56*(5), 1433–1463. https://doi.org/10.1111/j.1365-3091.2008.01041.x

Webster, J. M., & Davies, P. J. (2003). Coral variation in two deep drill cores: Significance for the Pleistocene development of the Great Barrier Reef. *Sedimentary Geology*, *159*(1–2), 61–80. https://doi.org/10.1016/S0037-0738(03)00095-2

Webster, J. M., Dechnik, B., Sanborn, K., Yokoyama, Y., Braga, J. C., Willem, R., et al. (2022). Coral reef development and sea-level changes over the past 50,000 years: New evidence from the northwest shelf of Australia. In G. F. Camoin, & N. Hallmann (Eds.), *Coral Reefs and Sea-Level Change: Quaternary Records and Modelling* (Vol. 49, pp. 215–273). International Association of Sedimentologists Special Publication. https://doi.org/10.54780/iassp49/08

Wei, J. (2021). Reconstruction of palaeoenvironmental changes and the response of the Great Barrier Reef (GBR) ecosystem since 30,000 BP: Implications from REY (rare earth elements and yttrium) and element ratios of reef-building carbonates (Doctoral dissertation).

Wendt, J. (1977). Aragonite in Permian reefs. *Nature*, *267*(5609), 335–337. https://doi.org/10.1038/267335b0

Williams, C. (2024a). Neutron computed tomography: A novel high-resolution, non-destructive method for screening fossil coral for diagenetic alteration for geochronologic and paleoclimate reconstructions [Dataset 1: Media 000646660: Holocene Porites Fossil Coral]. *Morphosource*. https://doi.org/10.17602/M2/M646660

Williams, C. (2024b). Neutron computed tomography: A novel high-resolution, non-destructive method for screening fossil coral for diagenetic alteration for geochronologic and paleoclimate reconstructions [Dataset 2: Media 000645633: Modern Porites Coral Slab]. *Morphosource*. https://doi.org/10.17602/M2/M645633

Williams, C. (2024c). Neutron computed tomography: A novel high-resolution, non-destructive method for screening fossil coral for diagenetic alteration for geochronologic and paleoclimate reconstructions [Dataset 3: Media 000645639: Acropora Fossil Coral]. *Morphosource*. https://doi.org/10.17602/M2/M645639

Williams, C. (2024d). Neutron computed tomography: A novel high-resolution, non-destructive method for screening fossil coral for diagenetic alteration for geochronologic and paleoclimate reconstructions [Dataset 4: Media 000647218: Isopora Palifera Fossil Coral]. *Morphosource*. https://doi.org/10.17602/M2/M647218

Williams, C., Paumard, V., Webster, J. M., Leonard, J., Salles, T., O'Leary, M., & Lang, S. (2023). Environmental controls on the resilience of Scott reefs since the Miocene (North West shelf, Australia): Insights from 3D seismic data. *Marine and Petroleum Geology*, *151*, 106188. https://doi.org/10.1016/j.marpetgeo.2023.106188

Williams, J. N., Bevitt, J. J., & Toy, V. G. (2017). A comparison of the use of X-ray and neutron tomographic core scanning techniques for drilling projects: Insights from scanning core recovered during the Alpine fault deep fault drilling Project. *Scientific Drilling*, *22*, 35–42. https://doi.org/10.5194/sd-22-35-2017

Woodroffe, C. D., & Webster, J. M. (2014). Coral reefs and sea-level change. *Marine Geology*, *352*, 248–267. https://doi.org/10.1016/j.margeo.2013.12.006

Wortham, B. E., Montañez, I. P., Rowland, D. J., Lerche, M., & Browning, A. (2019). Mapping fluid-filled inclusions in stalagmites using coupled X-ray and neutron computed tomography: Potential as a water excess proxy. *Geochemistry, Geophysics, Geosystems*, *20*(6), 2647–2656. https://doi.org/10.1029/2018gc008140

Zaini, N., Van der Meer, F., & Van der Werff, H. (2014). Determination of carbonate rock chemistry using laboratory-based hyperspectral imagery. *Remote Sensing*, *6*(5), 4149–4172. https://doi.org/10.3390/rs6054149

15252027, 2025, 10, Downloaded from https://agupubs.onlinelibrary.wiley.com/doi/10.1029/2025GC012439 by Carra Williams , Wiley Online Library on [02/10/2025]. See the Terms and Conditions (https://onlinelibrary.wiley.com/terms-and-conditions) on Wiley Online Library for rules of use; OA articles are governed by the applicable Creative Commons License

CHAPTER 4

ARTICLE 3: Carbonate Platform Evolution in Response to the Mid - Pleistocene Climate Transition on the North West Shelf of Australia: Insights from Forward Stratigraphic Modelling

---

This chapter presents the following article published in *Marine Geology*:

Williams, C., Webster, J. M., Salles, T., Paumard, V., Grimaldi, C., Lejri, M. (2026). Carbonate platform evolution in response to the Mid - Pleistocene climate transition on the North-West Shelf of Australia: Insights from forward stratigraphic modelling. *Marine Geology*, Article 107716. https://doi.org/10.1016/j.margeo.2026.107716

This paper reconstructs the Quaternary evolution of North and South Scott Reef using a data-calibrated forward stratigraphic modelling (FSM) approach. The primary objective is to quantify the response of these isolated carbonate platforms to increased sea-level amplitude and reduced periodicity associated with the Mid-Pleistocene Transition (MPT), and to evaluate mechanisms driving the partial drowning of the South Scott Reef leeward margin. The study integrates multibeam bathymetry, 3-D seismic data, sedimentary facies, U/Th chronology, and coralgal assemblages to calibrate a 3-D Petrel GPM model spanning 1.2 Ma to present. Sensitivity tests investigate the relative roles of subsidence, sea-level forcing, carbonate production, ecological depth thresholds, and wave energy in controlling platform architecture and facies patterns. A calibrated base-case model (392 kyr to present) reproduces the large-scale geomorphology of both platforms and is extended to 1.2 Ma to test the influence of hypothesised MPT-related environmental change. Trial-and-error style FSM is used to refine parameters controlling accommodation, sediment transport, carbonate production,

and coralgal facies zonation. The resulting synthetic stratigraphy provides new quantitative insights into reef sequence development, lagoonal infilling, margin evolution, and facies variability across multiple glacial–interglacial cycles. We also produced a diagenesis model to support our findings.

Author contributions: I designed the study, conducted the forward stratigraphic modelling, analysed the results, and wrote the manuscript. Jody M. Webster and Tristan Salles provided guidance on geological interpretation, carbonate stratigraphy, and modelling methodology. Victorien Paumard contributed expertise in seismic stratigraphy and assisted with data integration. Camille Grimaldi supplied the modern wave energy data, ecological and oceanographic context, and Mostfa Lejri provided technical advice on Petrel GPM workflows. All authors reviewed and contributed to the final manuscript.

Supplementary material: Appendix E at the end of this thesis corresponds to Supplement 1, Appendix F corresponds to Supplement 2, and Appendix G corresponds to Supplement 3, as cited in the associated published article.

TABLE 4.1: Summary of Chapter 4: Carbonate Platform Evolution in Response to the Mid-Pleistocene Climate Transition.

Aspect	**Summary**
Scope	Quantitative reconstruction of the Quaternary evolution of the North and South Scott Reef carbonate platforms using data-calibrated forward stratigraphic modelling (FSM), spanning 1.2 Ma to present.
Primary Objective	Quantify platform response to increased sea-level amplitude and reduced periodicity associated with the Mid-Pleistocene Transition (MPT), and evaluate mechanisms driving partial drowning of the South Scott Reef leeward margin.
Data Integration	Multibeam bathymetry, 3-D seismic interpretation, sedimentary facies, U–Th chronology, coral and coralline algal assemblages, and modern wave-energy and oceanographic datasets.
Modelling Approach	Three-dimensional carbonate Geologic Process Modelling (GPM) in Petrel, calibrated using a base-case model (392 ka to present) and extended to 1.2 Ma; trial-and-error parameter refinement combined with systematic sensitivity testing.
Key Results	Model results indicate that reef response to the MPT initiates during the MIS 12 lowstand, producing prolonged subaerial exposure and karstification, followed by rapid aggradation during MIS 11 that establishes the persistent bucket-shaped platform morphology.
Sensitivity Tests	Experiments demonstrate that increased sea-level amplitude, wave energy, and time-variable carbonate production are required to reproduce observed stratigraphy, while antecedent topography and subsidence exert first-order controls on platform architecture.
Platform Drowning Mechanism	Partial drowning of the South Scott Reef leeward margin is best explained by a reduction in carbonate production from ca. 0.5 Ma onward, likely linked to increased environmental stress associated with monsoonal intensification and episodic upwelling.
Synthetic Stratigraphy	FSM outputs provide quantitative constraints on sequence development, lagoonal infilling, margin evolution, and facies variability across multiple glacial–interglacial cycles.
Broader Significance	Demonstrates the utility of forward stratigraphic modelling for reducing uncertainty in seismic interpretation and for quantifying carbonate platform response to long-term climatic and eustatic forcing during the Quaternary.

Marine Geology 493 (2026) 107716

Contents lists available at ScienceDirect

Marine Geology

journal homepage: www.elsevier.com/locate/margo

Research Article

Carbonate platform evolution in response to the Mid - Pleistocene climate transition on the North-West Shelf of Australia: Insights from forward stratigraphic modelling

Carra Williams [a,b,*], Jody M. Webster [a], Tristan Salles [a], Victorien Paumard [a,b], Camille Grimaldi [c], Mostfa Lejri [d]

[a] Geocoastal Research Group, School of Geosciences, Madsen Building F09, University of Sydney, NSW 2006, Australia
[b] Centre for Energy and Climate Geoscience, School of Earth and Oceans, The University of Western Australia, 35 Stirling Highway, Perth, WA 6009, Australia
[c] University of Western Australia, Indian Ocean Marine Research Centre, Crawley, Western Australia, Australia
[d] Schlumberger, Oslo, Norway

ARTICLE INFO

Editor: Michele Rebesco

Keywords:
Carbonate platform evolution
Middle Pleistocene transition
Coral Reef
Sea-level change
Paleoclimate
Forward stratigraphic modelling

ABSTRACT

This study presents the first forward stratigraphic model of Scott Reef - two isolated carbonate platforms on the Northwest Shelf (NWS) of Australia, spanning the Middle Pleistocene Transition (MPT; ca. 1.2–0.7 Ma). Scott Reef preserves a unique archive of reef growth sequences paced by millennial (10^3-year) to orbital (10^4–10^5-year) scale sea-level variability under continuous high subsidence, providing valuable analogues for Quaternary reef dynamics and potential future reef responses to accelerated climatic change. We apply forward stratigraphic modelling (FSM) to reduce uncertainty in the existing chronostratigraphic models of Scott Reef, generate synthetic data to improve seismic interpretation, and to test how changing eustatic and environmental conditions during and after the MPT influenced carbonate production, facies distributions, and platform morphology. The model is calibrated using modern bathymetry, seismic sequence stratigraphy, sedimentary facies, coralgal assemblages, U/Th ages, and temporal changes in carbonate production and wave energy. The best fit simulations require increased carbonate production and wave energy after ca. 0.5 Ma, coupled with reduced carbonate production on the South Reef leeward margin. Model results indicate that the first high-amplitude lowstand of MIS 12 initiated prolonged subaerial exposure, karstification, and the development of a bucket-shaped platform morphology, coincident with increased monsoonal intensification after ca. 0.5 Ma. Subsequent reef expansion during the long-duration MIS 11 highstand produced an 80 m thick aggradational reef rim and is consistent with timings of reef growth elsewhere along the NWS, although there are differences to timing and style of reef response to the MPT globally. Synthetic stratigraphy indicates a transition from thin (10–30 m), low-relief progradational-aggradational sequences prior to 0.5 Ma, to thicker (20–50 m) aggradational sequences in the post-MPT 100-kyr world. Constant subsidence rates used in the model (0.29 mm/yr at South Scott Reef and 0.45 mm/yr at North Scott Reef) indicate that increasing sea-level amplitude and reduced periodicity associated with the MPT modulated sequence thickness, resulting in changes in platform morphology and facies patterns after ca. 0.5 Ma. Coupled with continuous high subsidence and increasing monsoonal intensity, these changes indicate that both environmental and eustatic processes were major controls on Scott Reef evolution. Our model has broader implications for understanding the MPT globally, including timing and stratigraphic expression of carbonate platform responses. Trial-and-error style FSM, when ground-truthed to multi-scale observational data, remains a powerful tool to test hypotheses about carbonate platform and coral reef response to rapid environmental changes.

* Corresponding author at: Geocoastal Research Group, School of Geosciences, Madsen Building F09, University of Sydney, NSW 2006, Australia.
E-mail addresses: carra.williams@sydney.edu.au (C. Williams), victorien.paumard@uwa.edu.au (V. Paumard), c.grimaldi@aims.gov.au (C. Grimaldi), mlejri@slb.com (M. Lejri).

https://doi.org/10.1016/j.margeo.2026.107716
Received 23 November 2025; Received in revised form 13 January 2026; Accepted 15 January 2026
Available online 20 January 2026
0025-3227/© 2026 The Authors. Published by Elsevier B.V. This is an open access article under the CC BY license (http://creativecommons.org/licenses/by/4.0/).

1. Introduction

The evolution of carbonate factories along the NWS of Australia is controlled by the interaction between accommodation, carbonate production and environmental forcing (Schlager, 2000; Reijmer, 2021). Previous studies of the NWS demonstrate that platform architecture and facies distributions are sensitive to climatic and oceanographic changes, which regulate carbonate production, sediment transport, and wave energy (e.g., Greenstein and Pandolfi, 2008; Gallagher et al., 2014; Gallagher et al., 2024; Saqab and Bourget, 2015). Superimposed on these controls, glacio-eustatic sea-level change has been shown to exert a first-order control on platform evolution, including exposure history

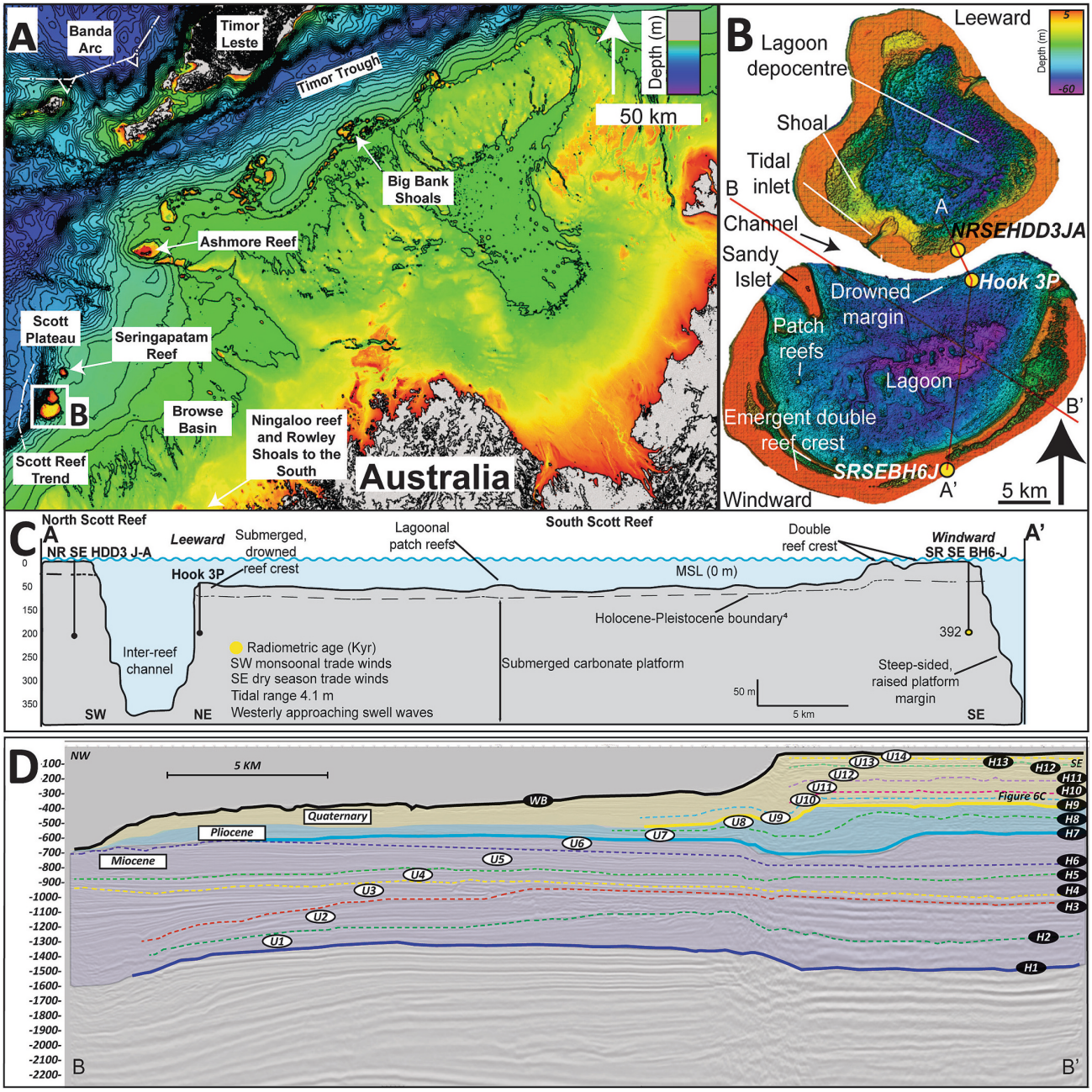


Fig. 1. Regional and local setting of Scott Reef on the Northwest Shelf (NWS) of Australia.
(A) Regional bathymetric multibeam map showing the position of Scott Reef within the Browse Basin, relative to surrounding features including Ashmore and Seringapatam Reefs, Rowley and Big Bank Shoals, and key tectonic elements. Bathymetry is shown using the original rendered RGB colour scale from the DeepReef.org compilation; terrestrial areas are clipped and displayed in greyscale for context, while colours represent offshore bathymetric depth range. (B) High-resolution multibeam bathymetric elevation map of North and South Scott Reef illustrating geomorphological. The cross-section and boreholes used to calibrate the model are indicated (NRSEHDD3JA, Hook 1P/3P, SRSEBH6J). (C) Cross-section (A–A′) through North and South Scott Reef showing borehole positions, radiometric ages (kyr), reef crest elevation, Holocene–Pleistocene boundary, and submerged carbonate platform architecture. Modern environmental conditions including tidal range, trade winds, and prevailing swell are noted. (D) Cross-section (B-B′) through South Scott Reef showing the current knowledge of the third order chronostratigraphic framework defined in Williams et al. (2023) from Miocene to present. H1–14 show interpreted sequence boundaries. U1 – U14 indicate sequence units. The high-resolution Quaternary stratigraphic architecture remains an uncertainty due to low quality seismic and data gaps over the reef crest.

and sequence stratigraphic patterns (Webster et al., 2022; Williams et al., 2023), while tectonic subsidence has governed accommodation and preservation potential (Struckmeyer et al., 1998; Keep et al., 2007; Belde et al., 2017; McCaffrey et al., 2020). The ecological composition of carbonate-producing communities further modulates reef accretion rates and facies patterns as coral and algal assemblages respond to environmental perturbations (Collins, 2002; Green et al., 2019; Rankey, 2020; Gilmour et al., 2022) in response to eustatic variability and associated environmental changes. Despite the progress in understanding NWS carbonate factories, significant knowledge gaps remain concerning the response of carbonate platforms and coral reefs to the Mid Pleistocene Transition (MPT; ca. 1.2–0.7 Ma). The MPT is a period characterised by a fundamental shift in glacial-eustatic cycles from approximately 41 kyr obliquity-driven cycles to 100 kyr eccentricity-paced variability and associated climatic reorganisation (Herbert, 2023; Watanabe et al., 2023). Along the NWS, the onset of monsoonal intensification around 0.5 Ma (Gallagher et al., 2014) occurred as a consequence of the broader climatic and oceanographic reorganisation initiated during the MPT. This monsoonal intensification coincided with increased rainfall, higher sea-surface temperatures, enhanced primary productivity and nutrient upwelling (Auer et al., 2021). These changes were driven by a weakened Leeuwin Current and a strengthened West Australian current (Palei et al., 2024), together with changes in the circulation of the Indonesian Throughflow (Clark et al., 2006; Petrick et al., 2019; He et al., 2021) that delivered nutrient dense cold-water upwelling. Collectively, these oceanographic and climatic changes likely had a profound impact on coral reefs in the region. The response of carbonate platforms to monsoonal intensification has previously been explored, for example in the Maldives (Betzler et al., 2009; Alonso-Garcia et al., 2023) and the Xisha Islands in the South China Sea (Wu et al., 2021) that were strongly influenced by the upwelling regime but remains unconstrained for reefs along the NWS with respect to the MPT.

North and South Scott Reefs are isolated carbonate platforms on the NWS that are uniquely positioned to address these questions. Williams et al. (2023) define the third order (ca. 0.5–3 million years; Haq et al., 1987) chronostratigraphic evolution of Scott Reef, since the Miocene, based on seismic and well core correlation, producing a conceptual evolution of the carbonate factories spanning the last 20 Ma (Fig. 1D). However, the Quaternary stratigraphic architecture and sedimentary response of the system remain an uncertainty due to limitations in seismic data quality and continuity with vast data gaps. The available data are used in this study to inform forward stratigraphic models (FSM), which are calibrated using the modern bathymetry, coralgal assemblages and facies, seismic sequence stratigraphy and U/Th age data. Our method of constraining facies depth-production curves using coralgal assemblages represents a key strength of this modelling approach. By incorporating these constraints within the FSM framework, we provide means to correlate the data and quantify eustatic and environmental changes related to the MPT, to fill data gaps and to improve understanding of the a priori conceptual chronostratigraphic framework by creating new synthetic quantitative information for improving seismic interpretations and predictions. The models may offer broader significance and valuable insights into the response of carbonate platforms to climatic and eustatic changes, and potentially a more comprehensive and complete record of continued reef growth than other Quaternary reef systems in the region.

1.1. Coral reef response to the Mid Pleistocene climate transition

The MPT was a major reorganisation of Earth's climate system (Petrick et al., 2019) and therefore a crucial period to study the response of coral reefs to rapid sea-level and climate change (Montaggioni and Martin-Garin, 2020). During the MPT, (ca. 1.2 to 0.7 Ma), the Earth shifted from an obliquity driven frequency operating on 41 kyr cycles with amplitudes of sea-level fluctuations of 60–70 m to a 100 kyr eccentricity driven orbital cycle with amplitudes of up to 120 m (Dwyer et al., 1995; Clark et al., 2006; Berends et al., 2021; Herbert, 2023), which remains the dominant frequency today. Although this transition represents a third order change in orbital forcing, the associated spectral series reconstructions (i.e., the distribution of frequency and amplitude of orbital scale variability) are complex and unreliable, reflecting interactions between Earth's obliquity, precession, ice-sheet dynamics and internal feedbacks that are not fully understood. This period triggered a climatic shift from a predominantly wet, monsoonal regime on the NWS into a dry-arid period (Gallagher et al., 2014, 2024; Zhao et al., 2024) with enhanced sea surface temperatures at ca. 0.65 Ma (Petrick et al., 2019). This eventually changed into a period of glacial-interglacial cycles with intensified monsoonal variability that were key to the onset of tropical shallow water coral reef development (Webster and Davies, 2003; Yamamoto et al., 2006; Faichney et al., 2011).

Globally, it is generally accepted that the increased amplitude of sea-level cycles facilitated opportunity for reef growth and expansion of carbonate platforms (Belopolsky and Droxler, 2003; Montaggioni, 2005; Davies and Montaggioni, 1985; Gischler and Hudson, 2019; De Gelder et al., 2022). However, as summarised in Fig. 2 and Table 1, the unique environmental settings of individual reef systems resulted in a broad variety of responses and timing that demonstrates the complexity and significance of the MPT on marine systems worldwide. For instance, in the Ryukyu Group (Japan), reef initiation occurred at ca. 0.8 Ma (Yamamoto et al., 2006), and sedimentation patterns in the Maui Nui Complex (Hawaii) transitioned from shallow to mesophotic reef assemblages before eventual drowning (Faichney et al., 2011). On the NWS, mid-late Pleistocene reef development has been characterised at Big Bank Shoals in the Vulcan sub-basin to the North of Scott Reef (Saqab and Bourget, 2016), however, detailed coral reef responses to the MPT in the Browse Basin, including the rate and magnitude of relative sea-level change have not been documented.

1.2. Carbonate forward stratigraphic modelling

While much has been learned about the genesis and evolution of carbonate depositional systems from field (Bathurst, 1975) and laboratory studies (Reijmer et al., 2025), their inherent complexity means advanced modelling techniques now provide an additional tool for integrating diverse datasets and testing process-based hypothesis. FSM has emerged as a key approach for simulating geological processes and reconstructing the depositional geometries of carbonate platforms over geological timescales (Bosence and Waltham, 1990; Harbaugh et al., 1999; Warrlich et al., 2002; Burgess, 2006; Masiero et al., 2020; Borgomano et al., 2020; Tella et al., 2022; Van der Looven et al., 2022). FSM quantifies the interactions between pre-defined forcing parameters on carbonate growth and development. This allows the user to evaluate their relative importance, offering insights into for example, environmental thresholds for coral population dynamics (Pall et al., 2020) and geomorphological response of sedimentary systems (Watney et al., 1999).

While the carbonate depth-production relationship is well constrained mostly for shallow reefs (Bosscher and Schlager, 1993), and widely used in carbonate FSM's, this study aims to apply more precisely constrained paleowater depths, including for mesophotic reefs, based on the habitat tolerances of reef-building organisms – using paleowater depth ranges inferred from coralgal assemblages. Distinguishing between niche ecological communities with distinct habitat depth ranges adds useful insight into the evolution of reef growth during sea-level transgression and highstand by quantifying the change of water depth during sea-level rise. These constraints are derived from detailed coralgal assemblage interpretations, supported by chronostratigraphic control, allowing us to assign narrower and more ecologically realistic depth ranges for each assemblage observed in core. While previous work, for example the 1D FSM studies by Pall et al. (2020), Salles et al. (2018) and others (Kolodka et al., 2016) have demonstrated the theoretical basis for using coralgal assemblages to infer depth limits, our

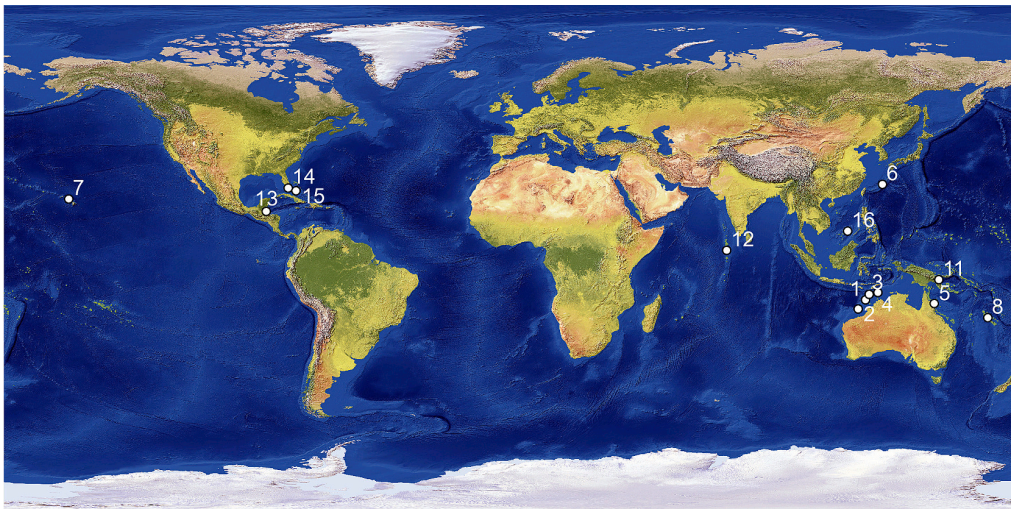


Fig. 2. World map showing the distribution of reef sites around the world, with reef ID numbers corresponding to Table 1. The location of Scott Reef is highlighted as ID 1. Reefs are outlined in pink lines, and the Antarctic Ice Sheet is shown as a pink polygon. Map produced using Natural Earth 10 m elevation data. (For interpretation of the references to colour in this figure legend, the reader is referred to the web version of this article.)

approach integrates this methodology into a full 3-D platform-scale model, thereby reducing uncertainty in the input data and improving the accuracy of simulated facies distributions through time.

In this study, we use FSM to test the hypothesis that the MPT imposed changes in the amplitude and pacing of sea-level cycles, together with intensified monsoonal conditions after ca. 0.5 Ma, that fundamentally altered carbonate production, facies distribution, and platform morphology at Scott Reef under continuous high subsidence.

2. Regional setting

2.1. Tectonics and sedimentology

Scott Reef is situated in a distal down-ramp setting on a far-field tectonically stable continental margin relative to active plate boundaries, however it is not entirely quiescent. Over million-year timescales, geoid and dynamic topography effects have driven significant relative sea-level variation (Whitney et al., 2016). Its relatively high subsidence rate of up to 0.45 mm/yr (with some estimates up to 0.5 mm/yr; Gurnis et al., 2020) has preserved a detailed sedimentological record of Quaternary sea-level and their records of past environmental and climatic change (Collins, 2011). Two characterised (SRSEBH6J, NRSEHDD3JA) and one undescribed (Hook 3P) fossil reef cores from the fore-reef and back reef margins of North and South Scott Reef (Fig. 1C) were recently acquired. Along with available 3-D seismic data (Williams et al., 2023), modern ecological (Done et al., 1994; Green et al., 2019; Gilmour et al., 2022) and bathymetric data (Beaman, 2017), provide an opportunity to develop a large-scale, unified chronostratigraphic model from the MPT (ca. 1.2 Ma) to present.

The North-West Shelf (NWS) is a passive continental margin ranging from ca. 21° S to 13 ° S (Rosleff-Soerensen et al., 2012), although its proximity to major tectonic elements, including the Sunda Trench subduction zone and collisional margin along the Timor Trough strait (Keep et al., 2018) '*preclude this part of the Australian plate from being truly classified as a stable continental region*' (Whitney et al., 2016). The study area is located in the Browse Basin on the NWS (Fig. 1A) and is structurally complex with ongoing subsidence and downwarping of the continental margin (Wilson, 2013) and far field inversion of parts of the Carnarvon Basin to the southwest (Keep and Harrowfield, 2008). North Scott Reef and South Scott Reef are two isolated carbonate platforms that developed on anticlinal trends situated in the south-eastern margin of the Timor Sea. Their evolution from precursor Miocene Reefs (Riera et al., 2021, 2023) and resilience to intermittent environmental stressors are a result of complex interactions between oceanographic, tectonic and ecological factors (Collins, 2002; Williams et al., 2023). Rapid and spatially variable tectonic subsidence (ca. 0.29 mm/yr for North Scott Reef and 0.45 mm/yr for South Scott Reef (Collins et al., 2011) since ca. 13.5 Ma (Riera et al., 2021) coupled with eustatic sea-level change, has determined the episodic reef growth phases over the last ca. 500 Kyr (Collins, 2011). The broader NWS reef system includes Ashmore Reef, Seringapatam Reef, Ningaloo Reef, Rowley Shoals and Big Bank Shoals (Fig. 1A) that are under the influence of the Indonesian Throughflow. The Indonesian Throughflow is a significant exchange of waters and heat between the Pacific and East Indian Oceans (Gallagher et al., 2014) that flows east to west through Scott Reef (Pandey et al., 2007).

2.2. Modern facies and coral reef communities

Scott Reef is a tropical Indo-Pacific reef, heavily influenced by cyclone activity and wave energy, impacting coral reef assemblages and species distributions (Done et al., 1994; Green et al., 2018; Puotinen et al., 2020; Gilmour et al., 2022). Coral coverage is dense and diverse, with a total of 56 genera and 258 species of scleractinian corals recorded in 1994 (Done et al., 1994) and 233 in 2022 (Gilmour et al., 2022). Hard coralline red algal pavements and stunted corals tend to dominate high energy environments, and high coral cover and diverse species are more developed in protected low energy settings (Collins and Testa, 2010). Common hard coral species include *Millepora, Isopora, Echinopora,* massive *Porites, Diploastrea, Acropora, Montipora, Pavona,* Pocilloporidae and Merulinidae (Gilmour et al., 2022). Soft corals dominate the channel region between both reefs, and the South lagoon is heavily populated by robust branching *Acropora*. Branching and massive corals are identified at the SRSEBH6J borehole location, while platy corals are observed below 15 m on the Western South Scott Reef margin, based on site survey observations (Grimaldi et al., 2024). *Acropora* constitutes the highest proportion of total coral coverage, reflecting the overall high energy and turbid environments (Gilmour et al., 2019; Gilmour et al., 2022). A fully enclosed rim on North Scott Reef, except for two tidal channels (Fig. 1B) protects coral assemblages from prevailing swells. While coral growth occurs in various environments, the majority of coral assemblages are concentrated on the eastern outer reef slopes, with bulk sediment transport migrating towards the lagoon (Done et al., 1994), which likely filled the empty bucket over time to become a flat top aggrading platform. The U-shaped open South Reef (Fig. 1B) is exposed

Table 1
A summary of the response of carbonate platforms and coral reefs around the world to the Middle Pleistocene Climate Transition. Reef ID corresponds to ID's shown on the map in Fig. 2.

Reef ID	Location	Reef type	Timing and Response to the MPT	Reference
1	Scott Reef, Browse Basin, NWS, Australia	Isolated carbonate platforms	Continued episodic, vertical reef development.	Williams et al., 2023; Collins et al., 2011
2	Rowley Shoals, Carnarvon Basin, NWS, Australia	Isolated carbonate platforms	Reef growth initiated ca. 1.0–0.5 Ma, coinciding with the shift to larger-amplitude sea-level fluctuations of MPT. 1 platform drowned, 3 continued reef production.	McCaffrey et al., 2025
3	Ashmore Reef, Bonaparte Basin, NWS, Australia	Isolated carbonate platforms	Platform and reef 'turn-on' ca.400 kyr due to limited accommodation in shallow antecedent bank; reef initiation delayed until onset of large-amplitude (100 kyr, ~120 m) glacio-eustatic sea-level cycles created sufficient accommodation for sustained reef growth.	Webster et al., 2022
4	Big Bank Shoals, Vulcan sub-basin, NWS, Australia	Isolated carbonate platforms	Reactivated primary production on topographic highs from ca. 0.8 to 0.58 Ma due to onset of repeated, high-amplitude (~120 m) glacio-eustatic cycles during MPT created necessary conditions for reef development	Saqab and Bourget, 2015
	Various reefs NWS	Isolated platforms	Expansion around 0.5 Ma	Gallagher et al., 2014
5	Ribbon Reef 5, Great Barrier Reef	Ribbon Reef	Large-scale reef accretion and framework development 'turn on' ca. 0.7 Ma in response to the onset of higher-amplitude glacio-eustatic sea-level cycles of the MPT.	Davies and Montaggioni, 1985; Humblet and Webster, 2017
6	Ryukyus Group, Japan	Barrier-fringing reef complex	Early reef growth from 1.45 to 1.65 Ma, with extensive reef-complex development onto karstified limestone substrate.and change in sedimentation mode at ca. 0.8 Ma linked to higher-amplitude sea-level cycles. Condensed quaternary reef section due to uplift.	Yamamoto et al., 2006; Feuillaret et al., 2023
7	Maui Nui Complex, Hawaii	Drowned, terrace-fringing reef complex	Transition from coral-dominated shallow to algal-dominated deeper reef communities post-MPT.	Webster et al., 2009; Faichney et al., 2011
8	New Caledonia	Barrier Reef	Developed ca. 0.4 Ma from a carbonate platform.	Cabioch et al., 2008; Montaggioni et al., 2011
9	Mururoa	Atoll	Changed mode of sedimentation – evolution from lower foreslope reef to reef rimmed carbonate platform. Initiation of sustained reef development occurred after the MPT, between ca. ~0.9 and 0.5 Ma, when the shift to higher-amplitude, 100 kyr sea-level cycles provided repeated accommodation space	Montaggioni et al., 2015
10	Huon Peninsula, Papua New Guinea	Fringing to barrier	Reef expansion. The reef sequence shows that large-scale terrace formation began around 1 Ma, coinciding with the shift from 41 kyr to 100 kyr glacial cycles.	De Gelder et al., 2022
11	Huon Gulf, Papua New Guinea	Fringing/ platform margin reefs	The Huon platforms initiated ca. 0.45 Ma and are products of the post-MPT regime	Webster et al., 2004
12	Maldives Archipelago, Indian Ocean	Isolated tropical carbonate edifice with Atolls	Enhanced carbonate primary production at platform tops.	Belopolsky and Droxler, 2003; Gischler et al., 2008; Droxler and Jorry, 2013; Van der Looven et al., 2022; Alonso-Garcia et al., 2023
13	Belize Barrier Reef	Barrier Reef	Initiated before the MPT and continued through it, showing sustained aggradational reef growth.	Gischler et al., 2010; Gischler, 2015; Gischler and Hudson, 2019
14	Florida Reef Tract	Barrier Reef	Initiated only after the MPT ca. 0.4 Ma, showing a delayed, discontinuous response to MPT.	Gischler, 2015
15	Bahamas Bank	Series of reef-fringed carbonate platforms	Major reef building episode associated with long and high MIS 11 interglacial.	Gischler, 2015

(continued on next page)

Table 1 (*continued*)

Reef ID	Location	Reef type	Timing and Response to the MPT	Reference
16	Meiji Atoll, Xisha Atoll, South China Sea	Low-lying atoll	Thickest reef development after ca. 0.8 Ma	Liu et al., 2022; Wu et al., 2021; Wilson, 2013

to high energy ocean waves and swells and has a submerged northern leeward margin at high tide to a depth of ca. 40 m (Collins et al., 2011). The distinct U shape refracts oceanic swells around the eastern and western hooks, which attenuates wave energy into the inner platform, resulting in coral communities of varying wave energy resistance (Done et al., 1994).

3. Material and methods

3.1. Available data

Since the 1970's, Scott Reef platforms have been studied for oil and gas exploration and broader scientific investigations (Williams et al., 2023), resulting in the accumulation of a wealth of data including reprocessed and depth converted 3-D seismic data, industry well log data and 17 geotechnical boreholes (Supplement 1). The Megator 3-D seismic data and three geotechnical boreholes along with oceanographic data, including very high-resolution multibeam bathymetry (Beaman, 2017), seafloor facies mapping (Allen Coral Atlas, 2022) and modern coralgal assemblage data (Done et al., 1994; Collins et al., 2011; Green et al., 2019; Gilmour et al., 2022) are also utilised in this study. Three geotechnical boreholes with two radiometric ages (Fig. 1C; Table 2; Williams et al., 2023) are used to calibrate the experimental stratigraphic models.

3.2. Petrel Geologic Process Modelling (GPM)

This study uses the deterministic, process-based forward stratigraphic modelling software Petrel Geologic Process Modelling (GPM). GPM is derived from the model SEDSIM, which is a computer model that simulates erosion, transport, and deposition of clastic sediments by free-surface flow in a natural environment (Tetzlaff, 1986; Tetzlaff et al., 2001; Hill et al., 2009; Acevedo-Ramirez et al., 2021). GPM simulates and reproduces the geological evolution of sedimentary processes for North and South Scott Reef. A model grid resolution of 500 × 500 m (0.25 km^2) and temporal resolution of 700 years sufficiently sampled the eustatic sea-level curve to reproduce depositional cycles, whilst considering scale contrasts between the available observed data (3-D seismic, geotechnical borehole data, modern bathymetry). Details of the parameter ranges used in the model design are shown in Table 2. Full methodological details, including equations, the GPM workflow, and the complete model design are provided in section 1.1 of Supplement 3. A brief summary is outlined below.

3.3. Modelling workflow and design

Prior to developing a best case model, an uncalibrated, high-resolution (10-year timesteps) synthetic model was developed using known parameters (Tables 1 and 2; e.g., Belde et al., 2017; Van Tuyl et al., 2019; Green et al., 2019; Williams et al., 2023), paleobathymetry, modern seabed geometry, and carbonate facies observed in core data. This test ensured the modelling framework was functional and capable of producing realistic stratigraphic outcomes before calibration.

Model scenario 1 (Fig. 4A) is the base case 3-D forward model. Input parameters (Fig. 3) including subsidence rates and wave energy were considered well-constrained, reducing the need to vary them across multiple runs and simplifying the experimental process. Key parameters with greater associated uncertainty, for example carbonate production rates through time, were tested through sensitivity experiments to evaluate their effect on model outputs and minimise misfit to hard data, such as the modern multibeam bathymetry. Model scenario 1 prioritised matching simulated sediment thickness to the interpreted thickness from seismic sequence stratigraphy, as well as seismic geomorphology to constrain the spatial extent of depositional environments (Williams et al., 2023), and using the radiometric dates to constrain the start and end of the model. The secondary priority was to replicate the present-day platform bathymetry (Figs. 2 and 4D), including accurate positioning of the parts of the reef crest relative to modern sea-level and and facies maps (Allen Coral Atlas, 2022). Model Scenario 2 uses exactly the same input parameters to extend model scenario 1 further back in time (1.2 Ma to present) to test reef response to MPT-associated environmental change as outlined in the hypotheses. Finally, a high-resolution model (50-year timestep) simulating the Holocene transgression was run in parallel to assess whether simulation resolution influenced facies patterns and sequence thickness relative to the coarse-resolution base

Table 2
Summary of modelled sedimentary facies characteristics and their modelled sensitivity ranges.

Sedimentary facies	Coralgal 1	Coralgal 2	Coralgal 3	Carb 1	Carb 2	Carb 3	Carb 4
Depositional environment	Shallow reef & patch reef	Intermediate reef & patch reef	Deep reef & patch reef	Reworked reef	Lagoon, shoal	Slope talus debris	Basin
Defined facies	Boundstone	Boundstone	Boundstone	Rudstone, packstone	Grainstone - mudstone	Bioclasts – Floatstone, wackestone	Mudstone
Grain size	1 mm	1 mm	1 mm	1 mm	0.04 mm	1 mm	3 mm
Diffusion multiplier							
Transportability (0–1)	0.1	0.1	0.1	2	0.5	0.8	3.2
Erodibility (0–1)	0.1	0.1	0.1	0.1	0.2	0.9	1
Growth dependant factor	Additive: Wave power (increasing), depth	Multiplicative: Wave power (decreasing), depth	Multiplicative: Wave power (decreasing), depth	in situ decay from all coralgal facies every 1 kyr when exposed above sea-level	Wave power (decreasing), depth	in situ decay from Carb 1 facies every 1 kyr when exposed above sea-level	Depth
Production mode	in situ growth	in situ growth	in situ growth	reworked	in situ sediment accumulation	reworked	in situ sediment accumulation
Production depth	0–10 m	10–30 m	30–60 m	n/a	20–60 m	n/a	> 80 m
Carbonate growth rate	2–4 mm/yr	2–3.5 mm/yr	1.7–3 mm/yr	n/a	0.5–2 mm/yr	n/a	0.1 mm/yr
Wave Power	0.5 W/m^2	0.3 W/m^2	0.2 W/m^2	n/a	0.05 W/m^2	n/a	n/a

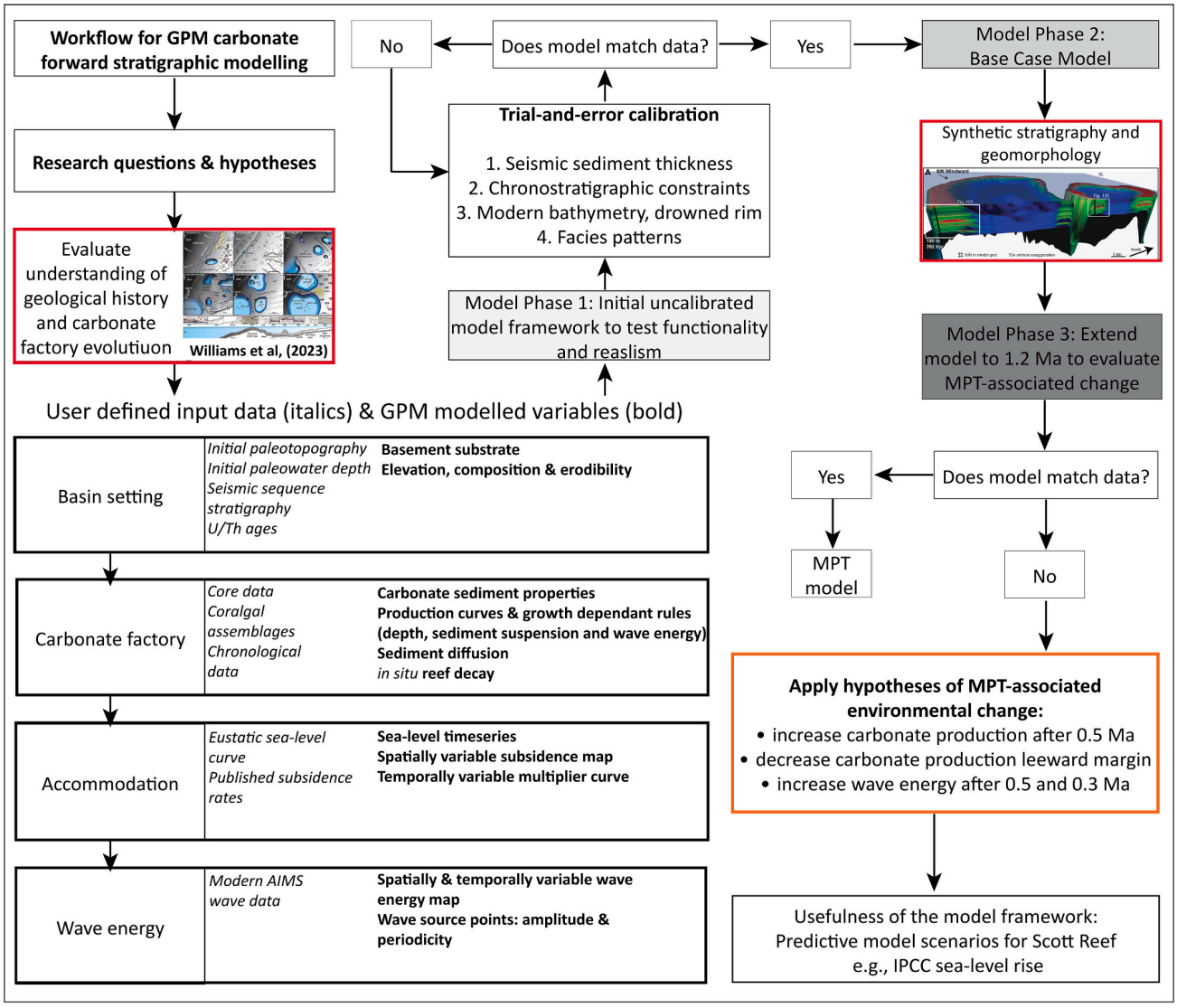


Fig. 3. Workflow for the GPM carbonate forward stratigraphic modelling workflow designed for this study, showing input parameters, calibration steps, and application to research questions. User-defined input data (italics) and GPM modelled variables (bold) include basin setting, carbonate factory, accommodation, and wave energy. The modelling approach begins with uncalibrated trial runs (Model Phase 1) used to test functionality and realism of the model framework, followed by iterative trial-and-error calibration of seismic sequence thickness, chronostratigraphic constraints, modern bathymetry, and facies patterns to establish a base case model (Model Phase 2). The synthetic stratigraphy of Model Phase 2 is then extended to 1.2 Ma (Model Phase 3) to evaluate MPT-associated change. Hypotheses tested include increased carbonate production and wave energy after 0.5 Ma due to increased primary productivity and monsoonal intensification after 0.5 Ma, and decreased carbonate production at the leeward margin due to nutrient upwelling and oversupply. The model framework is useful for generating predictive scenarios for Scott Reef under past and future sea-level conditions.

case model. The full modelling workflow, including data inputs, sensitivity testing, and calibration steps, is summarised in Fig. 3 and detailed in sections 1 of Supplement 3.

3.3.1. *Paleobathymetry and paleowater depth*

The topographic profile of the initial surface had a profound influence on the structure and facies distribution of the overlying depositional layers, as other studies have shown (Barrett and Webster, 2012; Van Tuyl et al., 2019; Liu et al., 2022; Van der Looven et al., 2022). Therefore, the best-fit input surface, derived from prior sequence stratigraphic interpretations and the modern bathymetry (Williams et al., 2023) was applied consistently across all experiments. The calibration of the model was largely guided by the modern bathymetry. Details of the initial paleobathymetry reconstruction are provided in section 1.1.1 of Supplement 3.

Model scenario 1 initiates at 392 kyr in 58 m water depth during the sea-level fall to the lowstand of MIS 10. The initial paleowater depth (58 m) is selected to represent the deep reef assemblages (between 30 and 60 m mbsl, *see* Fig. 7), corresponding to sediment interpretations at the base of the SRSEBH6J borehole (200 m depth). A paleowater depth of 29 m is selected for model scenario 2 (1.2 Ma to present) to correspond to the Miller et al. (2020) sea-level curve data point at 1.2 Ma.

3.3.2. *Accommodation*

Subsidence rates were calculated from individual geotechnical borehole age/depth plots based on Holocene coral ages across Scott Reef (Collins et al., 2011). Model sensitivity experiments were constrained by Pleistocene subsidence estimates (Table 2; Belde et al., 2015) and

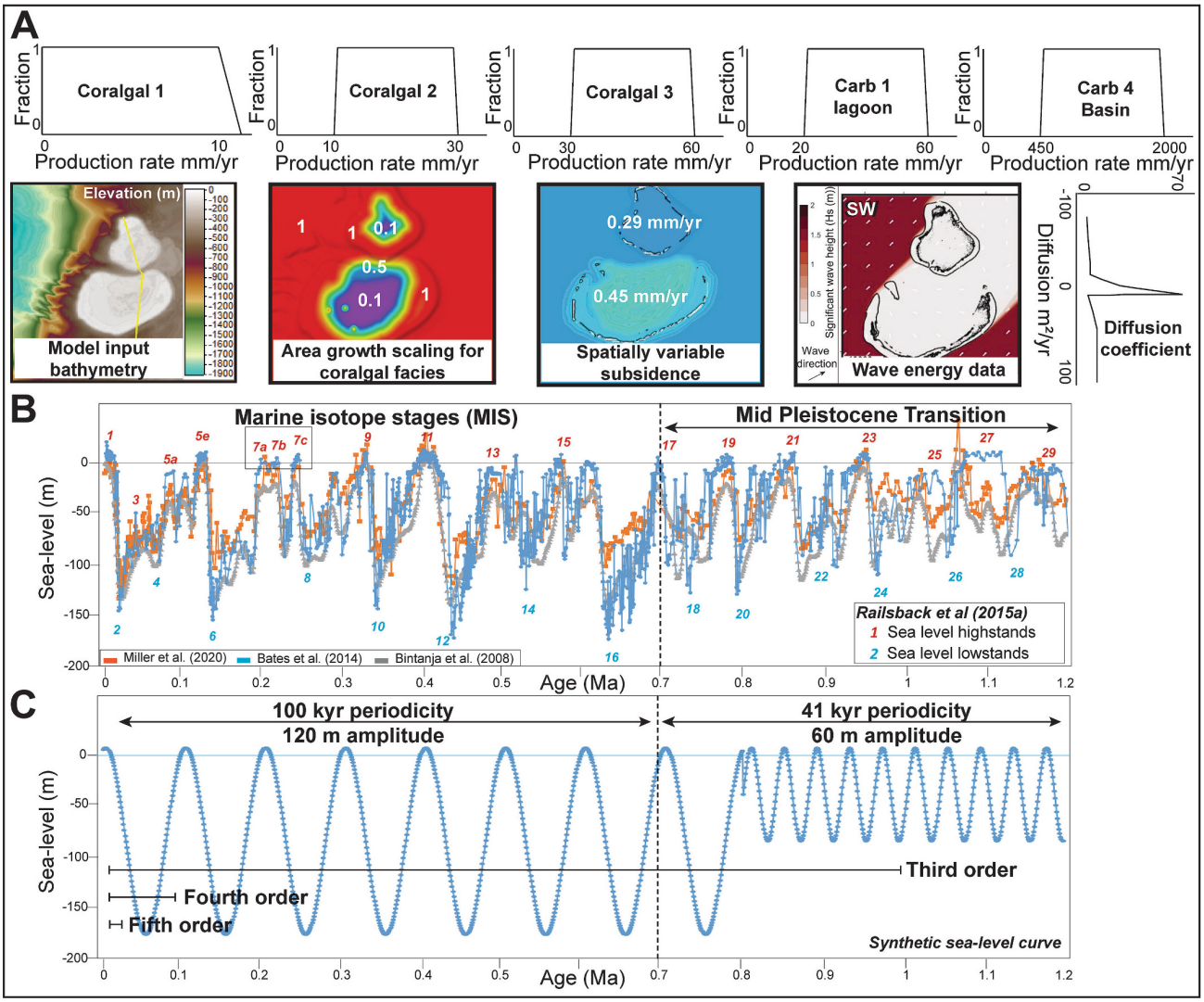


Fig. 4. Model input data and parameters. (A) Production-depth profiles for coralgal and carbonate facies, initial model paleobathymetry, area growth scaling map for coralgal facies, spatially variable subsidence map, and wave energy map provided by AIMS. (B) Eustatic sea-level curves tested in the model (Miller et al., 2020; Bates et al., 2014; Bintanja et al., 2008) plotted against Marine Isotope Stages, with highstands and lowstands following Railsback et al. (2015a). Variation in carbonate production rates through time are shown on the right hand axis. (C) Synthetic sea-level curve incorporating 41 kyr (60 m amplitude) oscillations prior to the Mid-Pleistocene Transition (~0.8 Ma) and 100 kyr (120 m amplitude) oscillations from 0.8 Ma to present. Third, fourth and fifth-order sea-level cyclicity are also shown.

incorporated constant, linearly increasing, and spatially variable and pulsed rates, while calibration was done through systematic trial-and-error to match sediment thickness, facies patterns, and platform morphology on seismic and well data. A stepwise increasing subsidence profile, typically associated with subduction zones but not previously suggested for the NWS, was applied in this study to replicate the successful FSM approach by Van Tuyl et al. (2019) to reproduce carbonate sequences in the Browse Basin at Seringapatam reef, located North of Scott Reef. Further details are given in section 1.1.2 of Supplement 3.

To explicitly evaluate the eustatic impact of the MPT on reef development, we extended the base case model (392 kyr – present) to 1.2 Ma using three eustatic sea-level curves (Table 2). This incorporated the shift from low amplitude 60–70 m, 41 kyr obliquity-driven oscillations to higher amplitude <120 m to 100 kyr eccentricity dominated cycles. All other parameters were held constant, and the role of tectonics was omitted from the model to isolate the effect of changing sea-level amplitude and periodicity on accommodation. As such, the MPT, which occurs over a fifth-order glacio-eustatic cycle (ca. 20–100 kyr period; Van Wagoner et al., 1990) was implemented in the model as a controlled experimental variable, enabling us to assess whether the observed shift in sequence thickness, platform geomorphology and margin drowning could be reproduced under the changing sea-level forcing alone.

The Miller et al. (2020) sea-level curve, sampled every 0.43 kyr produced a good fit to the sedimentary dynamics observed at Scott Reef and was adopted as a constant boundary condition for subsequent experiments. We thus acknowledge that our analysis is biased by the chosen sea-level curve. The sampling rate circumvented the issue of missing data points in the model runs (from 50 to 2000 year timesteps).

3.3.3. *Carbonate factory*

The model considers only tropical carbonate factories (Schlager, 2005; Wright and Burgess, 2005; Pomar and Hallock, 2008) and omits siliciclastic inputs due to the distal setting from terrigenous sources. This is supported by similar reports in regional studies of late Quaternary reefs (Belde et al., 2017; Thronberens et al., 2022) and the observed

absence of high gamma ray peaks in well log data that is used as a proxy for the presence of terrigenous sediment (Šimíček et al., 2012; Marshall and Lang, 2013; Gallagher et al., 2014; Read et al., 2020; Omidpour et al., 2021; Williams et al., 2023). In contrast to many reservoir-focused models, which typically prioritise fluid-flow properties and often simplify ecological controls on carbonate production, our approach explicitly fits the model using paleowater depths constrained by ecologically defined production-depth curves derived from reef biological communities (Pomar, 2001; Abbey et al., 2011; Kolodka et al., 2016) rather than applying generic reef production profiles (Bosscher and Schlager, 1993).

Based on the model's spatial resolution (grid cell of 500 km^2) and timestep (700 kyr), observed carbonate sediments in core, and modern ecological and depositional environments, four in situ carbonate sediments and three reworked detrital sediments were classified and modelled to represent the regional tropical carbonate factory (Table 2) (Michel et al., 2019; Reijmer, 2021). Section 1.1.3 of Supplement 3 details the sediment class control in GPM.

Table 3
Summary of the Geologic Process Model input parameters and sensitivity tests. User-defined input boundary conditions in bold were adjusted through a linear search style trial-and-error (Cross and Lessenger, 1999) to fit the data and produce the initial base case model. Highlight black box indicates five sensitivity tests designed to evaluate reef and platform response to MPT-associated environmental changes, corresponding to the orange coloured box in Fig. 3.

GPM model input parameter	Model scenario 1	Model scenario 2	Holocene Model	Units	Justification and details
Simulation settings					
Run time	0.392 to present	1.2 to present	0.012 to present	Ma	Model 1: time from deepest Quaternary seismic marker with age control to calibrate model. Model 2: Before the onset of the MPT.
Time step	700	2	0.05	kyr	Compromise between model runtime and model size
Grid cell size	500 × 500	500 × 500	500 × 500	m	To capture depositional sequences.
Area of simulation					North and South Scott Reef including deep sea canyons and inter-reef channel.
Initial topography and model start time (age)	H13 at 0.392 (SSR) 0.578 (NSR)	ca. 1.2–0.8	Output surface from model scenario 2 simulated at 0.012	Ma	Model 1: H13 seismic sequence boundary, U/Th age (Williams et al., 2023), constrained by modern multibeam water bottom (Beaman, 2017).
Initial topography water depth	−58 m	−29 m	/		Deep Coralgal assemblage facies identified at base of core corresponding to U/Th age at start of Model scenario 1 (392 kyr). Water depth from Miller et al. (2020) eustatic curves at 1.2 Ma at start of Model scenario 2.
Eustacy					
Subsidence	0.29–0.35 (NSR) 0.45–0.7 (SSR)	0.29–0.35 (NSR) 0.45–0.7 (SSR)	0.29–0.35 (NSR) 0.45–0.7 (SSR)	mm/yr	Published rates and patterns from: Collins et al. (2011); Belde et al. (2015); Van Tuyl et al. (2019) and trial-and-error to fit data. Sensitivity tests to simulate the drowning of the leeward margin of South Scott Reef.
Eustatic sea-level	Miller et al. (2020)	Miller et al. (2020)	Miller et al. (2020)		
Carbonate sedimentary facies					
Maximum carbonate platform margin production rate	1–4 mm/yr	1–4 mm/yr	1–4 mm/yr	mm/yr	Analogues from Indo-Pacific region (Webster et al., 2022), Published rates for category 3 slow growing reefs (Collins et al., 2011; Montaggioni, 2005)
Maximum carbonate platform interior production rate	1	2	1	mm/yr	Analogues from Indo-Pacific (Kennedy and Woodroffe, 2000; Gischler and Hudson, 2019; Webster et al., 2022), and carbonate FSM studies (Burgess, 2013; Liu et al., 2022; Van der Looven et al., 2022)
Maximum basin production rate	0.2	0.2	0.2	mm/yr	Analogues from Indo-Pacific region (Webster et al., 2022), and carbonate FSM studies (Burgess, 2013; Liu et al., 2022; Van der Looven et al., 2022)
Diffusion coefficient	0.1	0.1	0.01	m^2/yr	Values from carbonate FSM studies (Williams et al., 2011) and trial-and-error to fit the data (see Fig. 13 for diffusion curves applied to each facies)
Waves					
Wave amplitude	0.01–0.8	0.01–0.8	0.01–0.8	m	Green et al. (2018); Gilmour et al. (2019, 2022), Modern AIMS data
Wave periodicity	2–13	2–13	2–13	s	Modern AIMS data
MPT sensitivity experiments and assumptions					To test hypotheses of MPT-associated environmental change
1) Eustatic and synthetic sea-level					To evaluate reef and platform response to the MPT-associated increase in sea-level amplitude and reduced periodicity. Miller et al. (2020); Bates et al. (2014); Bintanja and van de Wal (2008); 1.2 Ma to present synthetic sea-level; 41 kyr periodicity 60 m amplitude (1.2–0.8 Ma) and 100 kyr periodicity and 120 m amplitude (0.8–0 Ma).
2) Decreased carbonate production for all coralgal facies >0.5 Ma		0.5 from 1.2 to 0.5 Ma and 1 from 0.5 to 0 Ma	/	Multiplier curve	Hypothesis: increasing nutrient supply around MPT (Petrick et al., 2019; Auer et al., 2021; Palei et al., 2024) to evaluate reef response.
3) Decreased leeward margin carbonate production		0.5 (50% reduction of maximum growth rate		Area growth scaling map	Hypothesis: increasing turbidity, nutrient oversupply, upwelling post- MPT on South-Reef (Petrick et al., 2019; Auer et al., 2021; Palei et al., 2024).
4) Increased wave power		N, S, E, W 8 s periodicity 0.9 m amplitude	/		Hypothesis: monsoonal intensification, changing hydrodynamic regimes post-MPT (Petrick et al., 2019; Auer et al., 2021; Palei et al., 2024):

3.3.4. Sediment characteristics

Borehole NRSEHDD3JA is 200 m deep and was drilled on the fore-reef crest at the present-day sea-level position on the southeast margin of North Scott Reef, with the recovered stratigraphy providing a relative sea-level record through the preserved core, where reef accretion reached sea-level ca. 2.7 kyr ago. SRSEBH6J is 180 m deep and was sampled from 8 mbsl on the fore-reef of the Southeast margin of South Scott Reef (Fig. 1B). It therefore does not record the uppermost reef crest at modern sea-level. Their position on the southeast margins exposes them to moderate to low wave energy environments, where branching and domal coral communities dominate. Hook 1P/3P penetrated 100 m of strata from 40 mbsl on the drowned reef rim of the leeward margin of South Scott Reef, consisting of encrusting and domal coral, coralline algae, microbialites and unconsolidated sand and rubble. Deep-water coral genera are identified at the top of the Hook 3P core (Fig. 3), including *Porites* and thin encrusting algal laminations, indicating that it is incipient rather than completely drowned. Two U/Th ages (Table 3) and sedimentological facies (Supplement 2) provide constraints on the model. The Hook 1P/3P borehole succession on the leeward margin of South Scott Reef is described as a 'give-up' reef, reflecting its present-day morphology where it reef failed to accrete to sea-level (Collins et al., 2011).

Core analyses conducted in this study interpreted two distinct coralgal assemblages identified in SRSEBH6J and NRSEHDD3JA. Coralgal assemblage 1 (Coralgal 1), representing a semi-exposed to sheltered shallow reef slope or reef flats at <10 m water depth, includes encrusting and laminar Merulinidae and *Montipora* corals, crustose coralline algae (*Porolithon*, *Dawsoniolithon*, *Spongites*) (Huisman et al., 2009; Wilson, 2013), and other biota such as planktonic foraminifera from the upper water column and vermetid gastropods. Coralgal 2, which is dominant throughout both cores, represents an intermediate depth range of approximately 10–30 m bridging the zonation between Coralgal 1 and Coralgal 3. Coralgal assemblage 3 (Coralgal 3), associated with middle to deep reef slopes at 30–60 m, includes massive *Porites, Millepora*, *Montipora* and Merulinidae corals, diverse crustose coralline algae (*Peyssonneliacean*, *Lithophyllum gr. pustulatum/prototypum, Lithoporella, Lithothamnion),* planktonic foraminifera as well as *Cycloclypeus, Halimeda*, pelecypods, and soft coral spicules. The depth ranges applied here and explained further in section 1.1.7 of Supplement 3 represent the ecological limits and relative productivity of distinct coralgal communities, as informed by modern ecological observations (Braga et al., 2022) and classic reef accretion models (Bosscher and Schlager, 1993; Schlager, 2005). This assumption is fundamental to the FSM, as reef accretion is constrained by depth, wave energy and sediment suspension and are informed by the interpretation of their ecological zonation.

Four detrital and reworked sediments were incorporated into the model to represent sediment transport and deposition, forming distinct facies belts across the platform. Coarse-grained reworked reef rudstone (Carb 1), which is modelled as a product of in situ boundstone decay from the Coralgal facies on the reef rim (Barrett and Webster, 2012) to the fore-reef slope under high energy conditions, contributes the allochthonous source of lagoonal sediment infill (Kennedy and Woodroffe, 2000). Lagoonal grainstones (Carb 2) were modelled using depth and wave power-dependant growth functions, constrained by FSM studies (Burgess and Pollitt, 2012) with fine grained packstones at depths <60 m observed in the core interpreted as deeper lagoon deposits and contributing the low-energy autochthonous lagoonal infill. Depth dependant growth was applied to settings shallower than 60 m (Table 2), while wave-power dependence (half-growth rate = 0.05 W/m^2) reduced growth under higher energy conditions. Slope facies (Carb 3) representing skeletal grainstones and packstones, were simulated by reworking of Carb 1 facies (reworked reef rudstone). Basin sediments, representing carbonate mud and wackestones, are classified as Carb 4 and were modelled as in situ deposits accumulating below 200 m.

3.3.5. Carbonate production through time

To approximate oceanographic forcing variations as a result of MPT-related environmental change, we incorporated a time-dependent multiplier curve (Table 2) that reduced the production rate by 50% from 1.2 to 0.5 Ma, to approximate nutrient-driven accretion potential, which increased carbonate production after 0.5 Ma, coinciding with increased circulation along the NWS during the MPT (Clark et al., 2006; Petrick et al., 2019; Palei et al., 2024). This approach captures third order effects of post-MPT oceanographic shifts on reef carbonate production, while acknowledging that explicit currents and nutrient dynamics were not modelled. Direct evidence of systematic changes in reef productivity across the MPT is lacking, and the model did not have robust constraints to calibrate production multiplier curves before and after the transition. However, we applied a similar strategy to other carbonate FSM sensitivity experiments, who acknowledge that carbonate production rates through time are variable and poorly constrained (e.g., Van der Looven et al., 2022), by iteratively adjusting multipliers through time to reproduce observed stratigraphic thickness and platform morphological changes governed by reef productivity. Conversely carbonate production is reduced on the South Reef leeward margin after 0.5 Ma to approximate the increased environmental stress in this region due to higher turbidity and nutrient oversupply, primarily linked to suspension of fine carbonate sediments (lime mud). This rule is applied using an area growth scaling map and geotime function detailed below.

3.3.6. Coralgal assemblages and ecological thresholds

Biological communities preserved in fossil reefs are records of strict ecological niches that occur in specific depth ranges that can be used to reconstruct sea-level position along the core depth (e.g., Abbey et al., 2011). In our model framework, these communities are not treated as descriptive paleoecological indicators alone, but as functional constraints on paleowater depth ranges that refine production envelopes for different coralgal assemblages. This approach integrates modern habitat data and the taxonomic identification of fossil corals and coralline algae (coralgal assemblages) (Braga et al., 2022) to constrain depth-production curves (Fig. 7). The benefit of using whole reef assemblages (coralgal assemblages), including corals, coralline algae, vermetid gastropods and encrusting foraminifera, have been shown to yield robust reconstructions of relative sea-level records in Tahiti and the GBR (Cabioch et al., 1999; Camoin and Webster, 2015; Abbey et al., 2011; Webster et al., 2009; Webster et al., 2022), and here these same ecological principles underpin the FSM. This provides a means of linking coralgal assemblage-derived depth constraints to carbonate growth responses across both third order (ca. 0.5–3 Ma period; Haq et al., 1987; Goldhammer and Lehmann, 1993; Hill et al., 2012) and fifth order (sub-orbital scale in hundreds of thousands of years) eustatic cycles, thereby embedding paleoecological evidence directly into the model design. These ranges were applied as ecological restriction functions that limit carbonate production to specific depth windows. For example, shallow coralgal assemblages (0–10 m) were restricted to the upper reef crest, whereas deeper assemblages (30–60 m) were confined to lower fore-reef settings. This approach ensures that simulated facies distributions are ecologically realistic for the study area and directly tied to known environmental tolerances across the platform.

3.3.7. Carbonate sediment transport properties

Diffusion in GPM is a simplified proxy for complex transport processes (waves, currents, gravity flows). It assumes sediment moves downslope at a rate proportional to slope steepness and sediment properties. This allows large-scale platform morphology to be reproduced without explicitly simulating multiple hydrodynamic processes. The diffusion coefficient (Table 2), which is a multiplier of the user-defined sediment erodibility and transportability properties are poorly constrained in forward stratigraphic models that oversimplify the complex web of nature (Sultana et al., 2022). However, studies have shown that flat-topped, steep-sided carbonate platforms form when

sediment diffusional transport rates are low relative to production rates (Sultana et al., 2021; Williams et al., 2011; Williams et al., 2023). As a consequence, reduced and possibly unrealistic volumes of reworked material are produced. In our model, low diffusion coefficients (0.01–0.1 m^2/yr; Table 2) were selected to reproduce the preservation of reef framework on the platform margins rather than to prioritise simulations of slope accumulation.

In GPM, a calculation of the residence time of strata within a user-defined water depth, i.e., the vadose, mixing or phreatic zones, can be used as a proxy to identify periods of possible karstification, cementation or dissolution. However, structural changes incurred due to processes of differential dissolution and fracture karst cannot be implemented (e.g., Badlands; Liu et al., 2022). We run the diagenetic GPM model to simulate duration of subaerial exposure in the vadose zone with a surface coefficient of 0.8 which approximates the position of the surface as a fraction of the distance between the topography and the sea-level. Section 1.1.7 of Supplement 3 provides equations and further details of carbonate sediment transport properties in GPM.

3.4. Wave energy

Regional wave processes are important for reef development (Pastier et al., 2019; Salles et al., 2018). Wave energy influences reef growth, architecture and ecological thresholds by influencing hydrodynamic conditions that control sediment re-distribution, heat exchange and nutrient flux. Although waves alone do not directly transport sediment except in shallow nearshore zones, their interaction with reefal structures can generate wave-induced currents that facilitate sediment movement and influence depositional patterns. As such, wave energy is considered a major forcing condition in forward modelling frameworks for predicting reef response to environmental and climatic changes (Ferreira et al., 2021; Lange et al., 2021). The GPM wave energy rules and their implementation in our models are outlined in section 1.2.1 of Supplement 3, and the wave energy data are described in section 1.2.2.

Tidal processes operate on daily timescales and cannot be explicitly modelled in FSMs spanning millions of years (Burgess, 2001; Hill, 2006). Further, their influence on carbonate systems remains poorly understood, although, they clearly have a large effect on platform interior water-property regulation and fluctuation, including Scott Reefs which have a tidal range of 4.1 m (Grimaldi et al., 2024). Burgess (2001) and others (Read et al., 1991; Bosence et al., 1994) approximate the effect of tides on reefs by reducing carbonate production in the upper 1 m of the water column to account for reduced circulation and frequent subaerial exposure, though was not incorporated in our model.

3.4.1. Wave energy over time

To incorporate the monsoonal intensification during interglacial periods along the NWS from ca. 0.5 Ma (Gallagher et al., 2014; Petrick et al., 2019; Auer et al., 2021; Palei et al., 2024) in our simulations, we varied wave energy direction, amplitude and periodicity using trial-and-error and modern wave data (see supplement 3). From 0.5 Ma - present, wave energy was increased from the SW and North (Table 2) to simulate a more energetic hydrodynamic regime, and to replicate increased storm intensity that is known to approach predominantly from the North in present day (Grimaldi et al., 2024). Although direct constraints on past wave climate at Scott Reef are lacking, this experiment provides a means to evaluate the relative role of wave energy in modulating facies distribution and platform geomorphology during environmental changes associated with the MPT.

4. Results

A calibrated best-case geological model of reef and platform sequences over the Pleistocene was developed for two model scenarios spanning different geological intervals: (1) Model scenario 1 (392 kyr to present), and (2) Model scenario 2 (1.2 Ma – present). Model scenario 1 is calibrated against all available empirical constraints to provide a base case model from which sensitivity tests and extended simulations can be meaningfully evaluated. The extended model (2) tests how the platform responded to the hypothesised environmental changes related to the MPT. For reproducibility, model parameter files and input data can be accessed via Supplement 4.

4.1. Model Scenario 1 – Base case model calibration (392 kyr to present)

Model scenario 1 (Fig. 6A), reproduces the observed platform geomorphology of the North and South Scott Reef platforms in broad terms, generating steep, elevated margins surrounding central lagoons, creating an empty bucket-shape platform for the South Reef and a more flat topped platform for the North Reef that are comparable to the large-scale morphology evident in the seismic data. The South Reef platform interior comprises ca. 254 m of stacked lagoonal grainstones, with three large patch reefs. Along the SE margin, five vertically aggrading reef sequences (red in Fig. 6A) correspond to MIS sea-level highstands and closely match observed sediment thickness and reef facies in the SRSEBH6J borehole (i.e., 180 m). The modelled sediment thickness closely matches observed age data (Fig. 8C, Williams et al., 2023). These successions record repeated intervals of accommodation driven by high continuous subsidence, which enabled reef accretion even during lower amplitude highstands such as MIS 7. The apparent 'layer-cake' stacking of reefs, attributed to sustained long-term subsidence, has also been documented in the Late Pleistocene – Holocene succession (ca. 600 kyr to present) of the Great Barrier Reef Province (Webb, 2025).

The model of South Scott Reef records thicker deposits due to higher subsidence rates and the final model timestep closely resembles the modern seafloor geomorphology, including the drowned leeward margin (Fig. 4C). To match the observed data, the model required reducing carbonate production on the South Reef leeward margin by 50% (Table 3). However, the platform slope fails to simulate sufficient reworked sediment, as a consequence of a low diffusion coefficient (Table 3), and thus fails to capture the extent of highstand shedding. Both platforms are primarily aggradational and the margins are dominated by intermediate reef facies, suggesting they can be primarily characterised as a 'catch up' reef. During sea-level lowstands, subaerial exposure surfaces developed in the model, however, the absence of well-defined reef flat or backstepping terraces suggests that the steep-sided platform margins, coupled with the lack of long-term sea-level stability (Jorry et al., 2016), prevented reef backstepping during glacial lowstands. This is generally consistent with the present-day bathymetry, which shows little evidence of stepped terrace morphology, except for a small uneven terrace at ca. 12–20 m on the eastern margin of the South Reef (Done et al., 1994).

4.1.1. Paleobathymetry

Sensitivity testing of the paleobathymetric input, defined by topographic structure and initial model paleowater depth, was the most influential parameter affecting model outputs. Simulations were highly sensitive to minor variations in the paleobathymetry. For example, a scenario using a smoothed version of the input surface showed progradational to aggradational geometries along the South Scott Reef leeward margin that eventually merged with the North Scott Reef platform (Fig. 9G), likely because the inter-reef channel was insufficiently deep to bypass sediment. Numerous other simulations imposing different initial paleowater depth produced wildly variable morphologies, including barrier reefs. This evolutionary pattern has been observed in the New Caledonia Barrier Reef, which developed around 400 kyr on top of a carbonate platform (Cabioch et al., 2008). This supports the conclusions of other FSM studies that demonstrate initial platform elevation and topographic morphology are major controls on carbonate platform evolution (Van der Looven et al., 2022; Liu et al., 2022).

4.1.2. Sedimentology

Sediment diffusion, which governed the erosion, transport and redeposition of carbonate sediments in our model, had the greatest control on facies patterns and was a major influence on the volume of sediment produced on the platform top and in the basin. We applied a low diffusion coefficient, consistent with the lower range of values tested by Williams et al. (2011), which produced flat-topped, steep-sided platforms with limited sediment transport. As a consequence, slope facies are underrepresented in the model. Each sediment type in GPM was further parameterised with individual erodibility and transportability ranges from 0 to 1 (see Table 3), allowing some in situ reef material to be preferentially eroded and reworked into rudstones (Fig. 6A), though not in volumes sufficient to match core observations. We therefore acknowledge that time-invariant diffusion limits the ability to simulate higher transport of material during events such as highstand shedding or margin collapse.

4.1.2.1. Coralgal assemblages and detrital sediments. The forward stratigraphic model reproduces 9 of the 10 coralgal assemblages identified in core (Fig. 5). This comparison provides a measure of model performance

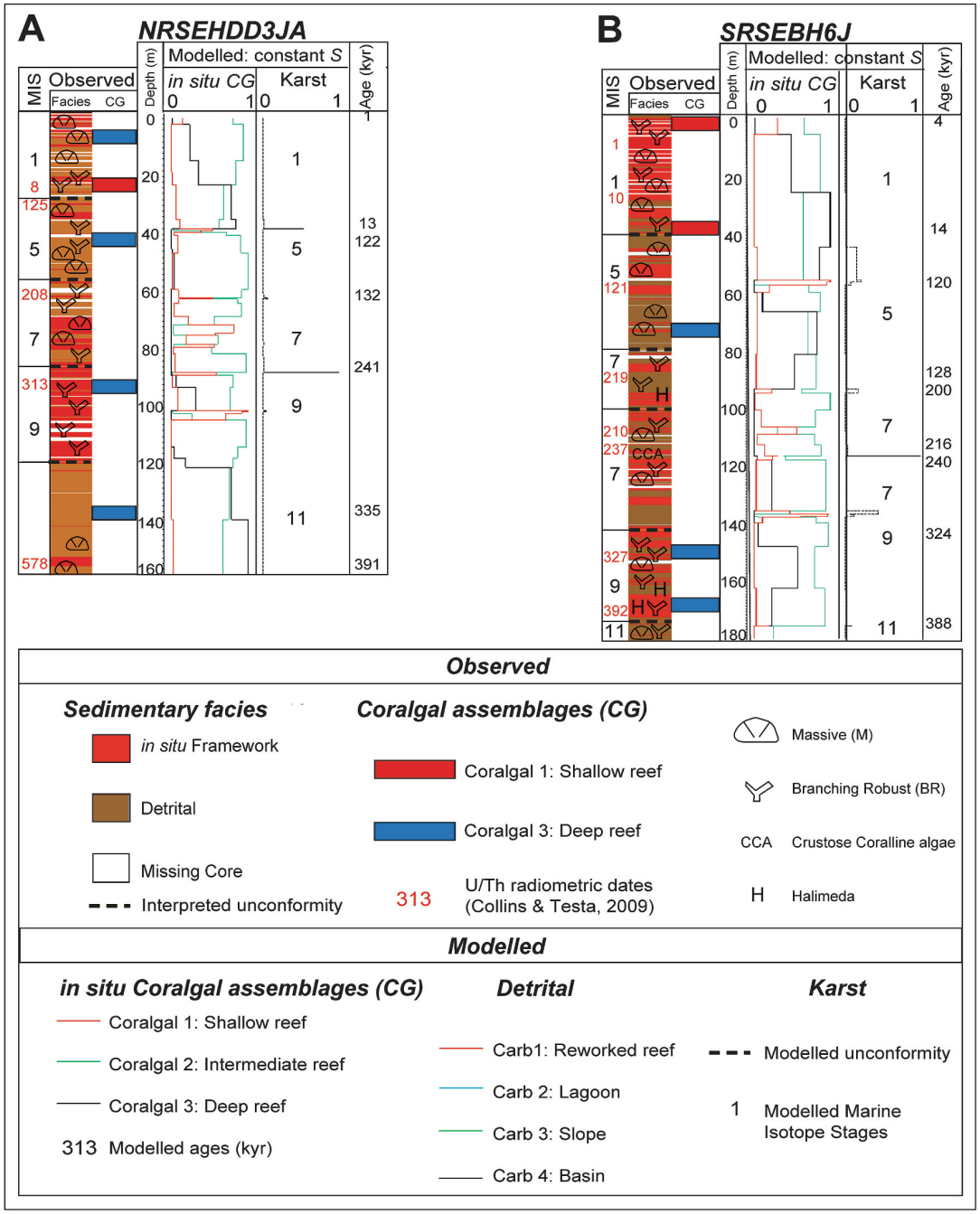


Fig. 5. Comparison of interpreted and simulated carbonate sedimentary facies in boreholes NRSEHDD3JA (North Reef) and SRSEBH6J (South Reef), located on the southern margins of Scott Reef, for Model Scenario 1. The forward stratigraphic model reproduces 9 of the 10 coralgal assemblages identified in core and correlates well with the observed subaerial exposure surfaces, with the notable exception of the Holocene unconformity.

and shows that the base case captures the main trends in platform-wide facies distribution. The observed unconformities in core, correlate well with the modelled subaerial exposure horizons, with the notable exception of the Holocene unconformity, which occurs deeper in SRSEBH6J (45 m) than radiometric ages suggest (35.9 m). This may arise in part due to considerable uncertainty in carbonate production rates through time (Van der Looven et al., 2022) or the meltwater pulses known to have occurred during the Holocene deglaciation. For example, Meltwater Pulse 1B occurred at ca. 11 kyr, followed by Meltwater Pulse 1C at ca. 8 kyr, which is not well constrained but was discussed by Blanchon (2011) as a brief period of rapid sea-level rise, characterised by a jump of 6 m at 7.5 Kyr. These events are well documented from coral reef records in the Caribbean and Indo-Pacific and have been shown to induce short-lived pauses in reef accretion, backstepping and drowning (Collins et al., 2011). Higher proportions of rudstone in NRSEHDD3JA compared to SRSEBH6J indicate increased reef framework erosion of the Coralgal 1 facies on the southeast crest of North Scott Reef. Core observation of NRSEHDD3JA also indicate heavily altered and recrystallised rudstone facies and longer residence time of the platform top in the vadose zone, as indicated by the GPM diagenesis model of Fig. 12C. This is interpreted to reflect increased physical and chemical degradation of original boundstone fabrics during repeated subaerial exposure, dissolution, and reworking, potentially due to lower subsidence rates on the North Reef and prolonged exposure to meteoric waters during lowstands.

Alternating in situ framework and detrital sediments for the MIS 9 reef unit in NRSEHDD3JA correspond with the simulation, including the deep assemblage at 92.15 m and a peak in Carb 2 deposits at ca. 130 m corresponding to grainstone facies observed in core. Shallow reef facies observed at 38.4 m (SRSEBH6J) were absent in both the base case model and the high-resolution Holocene model (Fig. 8D), suggesting differences to observed data are not a result of model resolution. Deep and intermediate reef facies dominate North and South Scott Reef margins and is a consequence of high subsidence and suggests reef builders lagged behind rapid marine transgressions such as the Holocene and MIS 11, which is supported by the abundance of domal *Porites* corals observed in core, typical of moderate to low energy conditions.

The simulation of the South Reef margin produced all major highstands except for MIS 3, while NRSEHDD3JA does not simulate MIS 3 and 7b (Fig. 5B and 8A). Hook 3P simulates MIS 1, 3, 5, 7a-c, 9 and 11 (Fig. 8A) as a result of the lower topographic position relative to the raised South Reef rim. Further, MIS 7, which in most eustatic sea-level reconstructions failed to reach modern sea level and is often associated with limited flooding of shallow-water environments (e.g., Waelbroeck et al., 2002), contributes to thick reefal sequences in North and South Scott Reef (25 m and 39 m respectively) due to continuously high subsidence throughout the Quaternary (Collins et al., 2011).

4.1.3. Subsidence

In our simulations, subsidence modified the accommodation imposed by eustatic control on the model, thereby influencing overall sediment thickness and the capacity for reefs to initiate or keep-up (Seard et al., 2013) through successive MIS cycles. Scott Reef is highly sensitive to both the rates and spatial distribution of subsidence. In our uncalibrated model experiments (model phase 1 of Fig. 3) constant subsidence (Fig, 9C) reproduced observed sediment thickness and facies patterns but produced a flat-topped geometry and failed to replicate the drowned South Scott Reef margin. Linearly increasing subsidence (Fig, 9B), modelled using a gradual multiplier from 392 kyr to present, assumed subsidence increased through time in the Browse basin (Gurnis et al., 2020). This reduced accommodation, yielded insufficient model thickness and unrealistically thick shallow reef facies on the windward margin exposed to prolonged periods of wave energy. Spatially variable and pulsed subsidence (Fig. 9A) incorporating a Holocene rate of 0.7 mm/yr, demonstrates that higher subsidence rates increase accommodation and accelerated earlier drowning of the leeward South Scott Reef margin and successfully reproduced facies patterns and platform geomorphology. Collectively, these experiments show that while orbital-scale sea-level cycles determine the timing of reef development, variable geomorphologies between the North and South Scott Reef can arise from imposed subsidence differences.

4.1.4. Modelled Sequence Stratigraphy

Fig. 8 outlines the chronostratigraphic evolution of the model scenario 1 of Scott Reef and illustrates variations in sedimentation patterns and hiatuses between the North and South Reef.

MIS 11. The model initiates in the MIS 11 transgression at 29 m water depth and thus does not record the full MIS 11 sequence. The simulated MIS 10 unconformity is overlain by a thick 31 m shallowing upwards sequence on the South Scott Reef platform margin. Deep reef facies 'turn on' at 390 kyr succeeded by intermediate reef facies and shallow reef facies at 366 kyr along the platform margin. The staggered MIS 11 transgression forces the reef margin to backstep towards the platform interior (Fig. 8C). Prevailing SW wave energy breaks over the south reef margin promoting both reef crest development and lagoonal patch reef growth on antecedent highs (Fig. 8C thumbnail).

MIS 9. Deep reef facies establish on the simulated South Scott Reef platform margin during the marine sea-level rise of MIS 9 which is re-occupied by intermediate reef at 329 kyr followed by shallow reef at 326 kyr. Rapid sea-level rise forces the reef to backstep towards the platform interior (Fig. 8C), producing a 40 m thick flat topped sequence for the South Reef and 32 m for the North. The modelled sediment thickness is lower than the 30 m observed in the core data for South Scott Reef and 36 m for the North Reef (Collins et al., 2011; Williams et al., 2023). A 2 kyr hiatus in reef sedimentation is observed in the model during the peak of the MIS 9 highstand signalling a brief coral reef drowning event.

MIS 7. A 2 m thick unit of reworked reef rudstones are eroded from coralgal facies and redeposited on the platform margin behind the reef crest prior to the maximum sea-level fall of MIS 8 at 241 kyr. The low amplitude high frequency sea-level cycles of MIS 7 were on the order of 15–30 m and occurred on orbital timescales of ca. 20–40 kyr (Montaggioni, 2005; Camoin and Webster, 2015). MIS 7a, 7b and 7c represent high frequency peaks of the MIS 7 highstand (Fig. 4B) and are simulated in the model as mounded, prograding sequences of intermediate to shallow reef accumulation in South Scott Reef. Only MIS 7c at 236 kyr and 7a at 209 kyr are represented in the North Scott Reef platform (Fig. 5B and 8A) due to lower accommodation. The modelled sediment thickness is 50 m for South Scott Reef and 27 m for North Scott Reef, which is comparable with estimates from observed sequence thickness in the NRSEHDD3JA core but not the SRSEBH6J core (32.65 m and 90.75 m, respectively).

MIS 5. Coral reef turns on in the model at 124 kyr on the Southeast margin of South Scott Reef corresponding to the MIS 5e highstand. Coralgal 1 re-establishes above coralgal 2 at 117 kyr representing MIS 5a, which is consistent with the borehole data. A major hiatus in sedimentation occurs in the model from 114 to 12 kyr on both platforms corresponding to the MIS 2 and MIS 4 unconformities. A 32 m model thickness for South Reef and 22 m for the North Reef corresponds to observed sequence thickness in the cores for MIS 5 (29.35 m and 24.25 m for South and North Reef respectively).

MIS 3. MIS 3 reefs, which are also observed at Ashmore reef ca. 200 km to the North (Webster et al., 2022) are only simulated at Hook 3P (36–56 kyr) (Fig. 8A) on the drowned leeward margin (Fig. 4C) due to higher subsidence rates in this region and deeper paleowater depth.

MIS 1. The rapid Holocene sea-level rise produces a 50 m (South Reef) and 30 m (North Reef) thick shallowing upwards cycle from deep facies on the margin slopes at 14 kyr, to intermediate to shallow reef facies, forming a sigmoidal growth pattern in the high-resolution Holocene model of Fig. 8D, which is typical for the Holocene sea-level rise (Schlager, 2005). Coralgal 1 initiates within the last 1.4 kyr to present day, forming 3 m sediment thickness (Fig. 7A-D). The observed

uppermost section of MIS 1 Holocene sequence in the SRSEBH6J core data is 35.9 m and 26.5 m in NRSEHDD3JA, measured from the MIS 5 drowning surface to the modern water bottom. The modelled MIS 1 reef 'turn on' establishes with intermediate reef facies at 14 kyr, which is 4 kyr earlier than U/Th ages place the Holocene unconformity (10 kyr).

Although these simulated thicknesses are not precisely comparable, they reproduce the overall observed facies successions in the core data. Discrepancies between simulated and observed sequence thicknesses and occurrence of MIS's are likely an artifact of the model timestep resolution (700 years), the sea-level curve sampling rate and unconstrained variations in coral reef growth rates over time due to unresolvable environmental perturbances such as disease and bioerosion.

A high-resolution model of MIS 1 (Holocene) with 50-year timesteps was simulated (Fig. 8D), keeping all other parameters unchanged, to test the variation in facies patterns and sequence sediment thickness compared to the base case model (700 year timestep), as a consequence of model resolution. Shallow coralgal facies turn on at 13 kyr, 1kyr earlier than the coarser base case model and the thickness is 48 m for the South Reef and 36 m for the North reef compared to 51 m and 30 m in the base case model, respectively. There are no apparent variations in the geomorphology and sequence stratigraphy of the Holocene model otherwise.

4.1.5. *Modelled wave energy and transport*

The best simulation output for experimental scenario 2 used modern wave data provided by AIMS with a dominant SW wave propagation, producing reef morphologies that effectively buffered platform interiors (Fig. 10G-K), developed platform interior patch reefs and restricted reef development on the outer ridge of South Scott Reef (Fig. 10A). However, the disparity between leeward and windward margin development and lack of leeward margin progradation (Fig. 6A), was less pronounced than in other reef systems, such as One Tree Reef (Marshall and Davies, 1981) and Ishigaki Island, Ryukyu Group, Japan (Hongo and Kayanne, 2009). This may be due to Scott reef's relatively high subsidence rate limiting opportunity for any significant leeward migration, combined with the large surrounding basin water depths relative to the small size (i.e., carbonate production) of the isolated Scott Reef (Schlager, 2005).

Development of the platform margin was highly dependent on hydrodynamic energy and wave source direction (Montaggioni, 2005; Gischler et al., 2008; Lowe and Falter, 2015) enforced by waves in our model, which increased carbonate production and vertical accretion of coralgal 1 during highstands in our simulation experiments (Fig. 10). Wave energy dissipation controlled coralgal species zonation, including the growth control of deeper water facies due to reduced wave energy through depth (Schlager, 2005). This resulted in euphotic dominated (shallow coralgal) assemblages in high energy zones, i.e., closest to the wave source from the N, S, E and W, and oligotrophic (deep or detrital facies) dominated facies in sheltered areas (Van der Looven et al., 2022), i.e., furthest from the wave source (Fig. 10G-K). Wave energy also played a critical role in sediment transport across the platform. As a

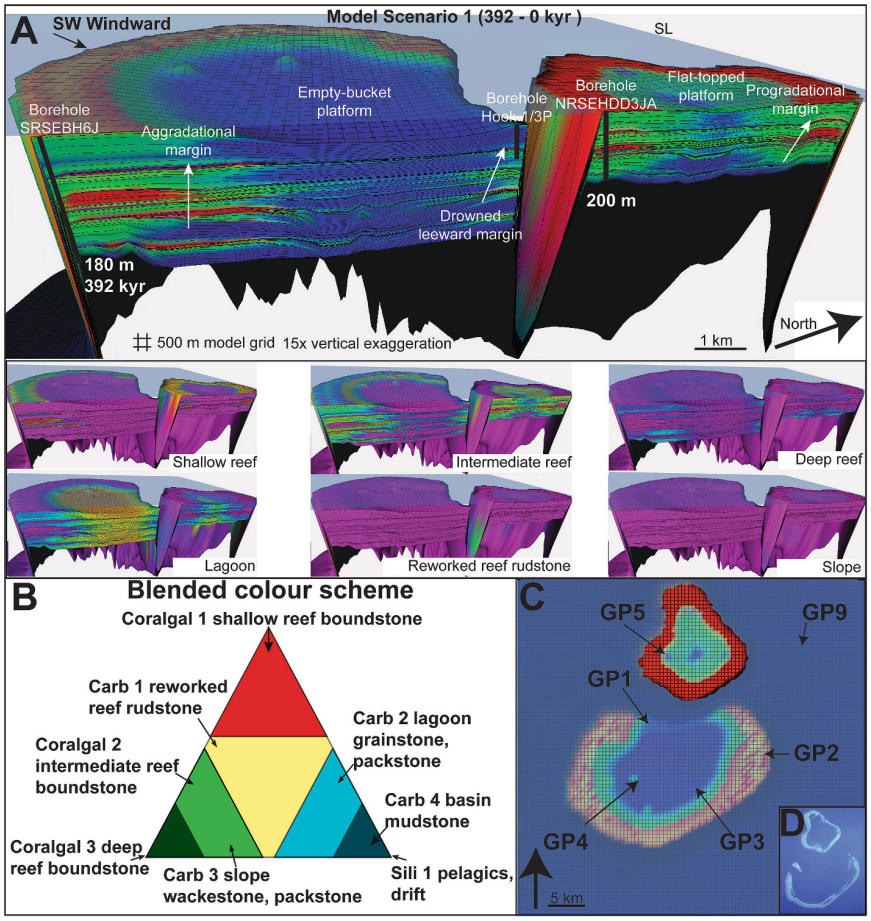


Fig. 6. (A) 3-D simulation output of model scenario 1 (392 kyr to present) with a N-S cross-section cut away corresponding to A-A' profile in Fig. 1. (B) Blended colour scheme indicates modelled facies colours that apply to all figures of simulation outputs unless otherwise indicated. (C) Aerial view of final model timestep representing the modern seafloor. The modelled geomorphologic patterns (GP) indicated corresponding to seismic facies represent: GP1 – reef slope, GP2 – reef crest, GP3 – lagoon, GP4 – patch reef, GP5 – back reef shoal, GP9 – basin. The blended colour scheme in B applies. (D) Modern satellite image of Scott Reef for comparison.

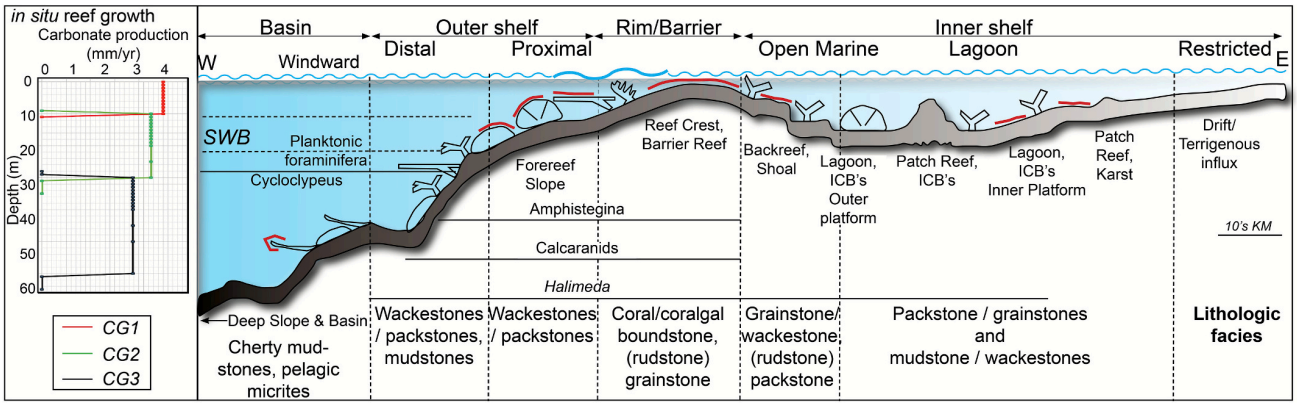


Fig. 7. Schematic showing spatial and depth zonation of coralgal assemblages observed in the modern Scott Reef environment, including distributions of coral morphotypes, Crustose Coralline Algae (CCA), *Halimeda* and foraminifera. The left panel shows carbonate sediment production curves for the three defined coralgal assemblages (CG1: Coralgal 1, CG2: Coralgal 2, CG3: Coralgal 3), which represent distinct ecological depth ranges: CG1 (shallow <10 m)), CG2 (intermediate 10–30 m), and CG3 (deep 30–60 m). These depth-ranges reflect the ecological niches of each assemblage and therefore do not all extend into shallow environments.

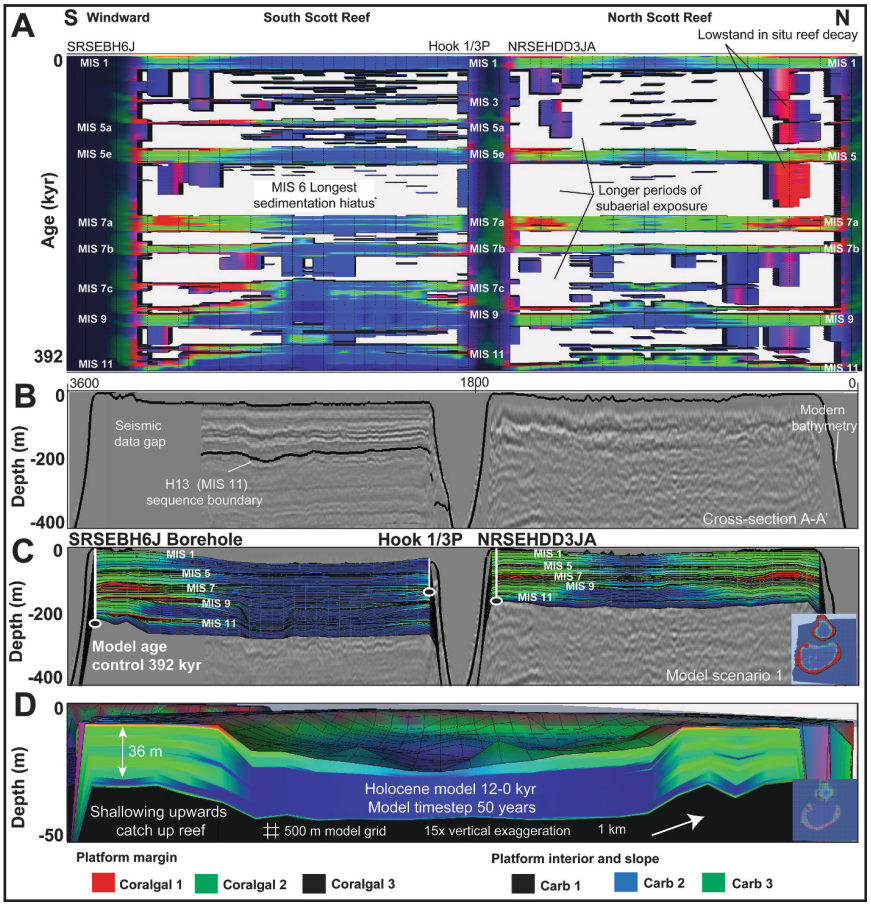


Fig. 8. Model cross-section A-A' of North and South Scott Reef (see Fig. 1 for cross-section location). (A) Wheeler diagram of Model scenario 1 (392–0 kyr) showing periods and duration of platform sedimentation, including sedimentation hiatus during subaerial exposure. (B) Seismic profile A-A' with key features shown, including the modern bathymetry and initial model surface (H13) from Williams et al. (2023). Correlations between seismic facies and modelled facies are indicated. (C) Cross section of simulated model scenario 1 (392–0 kyr) calibrated to the U/Th age of 392 kyr from SRSEBH6J borehole. (D) High resolution model of the Holocene (50-year timestep) for North Scott Reef showing similar facies patterns and model thickness to the coarse resolution model scenario 1 (700 year timestep). Model facies colour scheme is outlined below.

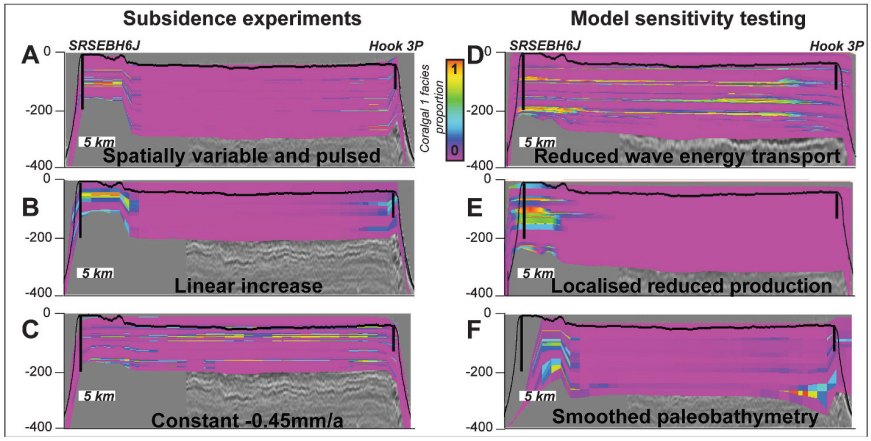


Fig. 9. *E*-W cross-sections (A-C, E-G) and N-S 3-D cross-section (D) through South Scott Reef intersecting boreholes SRSEBH6J on the SE fore-reef margin and Hook 3P on the drowned leeward margin. Four subsidence rates (A-C) and three other parameters (E-G) are varied in model phase 1 to test the functionality and realism of the initial uncalibrated model framework and to explore possible controls on the drowning of the leeward South Reef margin. Coralgal 1 facies are displayed to highlight evolution of the upper euphotic zone.

result, the model demonstrates how wave action facilitates the erosion and redistribution of Carb 1 sediment from in situ boundstone on windward margins to fore-reef, back-reef and slope environments, providing an allochthonous source of coarse lagoon material (Fig. 6A). This outcome is consistent with observations from modern reef systems, where sand aprons and coarse detrital deposits are typically restricted to the reef belt and adjacent aprons, such as those observed across the Iles Éparses carbonate platforms (Jorry et al., 2016) in the Southwest Indian Ocean (Prat et al., 2016), rather than extending across the entire lagoon (Rankey, 2016).

The general model hydrodynamics defined by the wave-sediment interaction is largely successful in the model's ability to replicate observed depositional facies (framework and detrital) from source to sink by differentiating between high and low energy environments due to wave energy, resulting in sufficiently clear lateral and vertical zonation of reef facies (Barrett and Webster, 2012; Montaggioni and Martin-Garin, 2020; Van der Looven et al., 2022). In real reef systems, wave breaking at the reef crest can generate strong cross-reef surge currents, which are capable of mobilising and transporting sediment into back reef and lagoon environments (Yao et al., 2023). Although wave-induced flows alone may be insufficient to transport coarse material, their interaction with tidal currents can significantly amplify sediment flux. A flood tidal delta is well developed on modern North Scott Reef (Fig. 1B). These tidal inlets and associated flood-tidal deltas can migrate through time, influencing the back reef infilling. Field studies have shown that sediment transport rates can increase by up to 40-fold when wave action is combined with strong tidal flows (Yao et al., 2023). However, tidal currents, which are not explicitly modelled in GPM, are typically stronger than wave-induced currents, and more likely to be responsible for transporting coarse material in real reef environments, particularly Scott Reef, which has a large tidal range (4.1 m: Grimaldi et al., 2024). Despite this limitation, the model remains a valuable tool for exploring relative sediment transport patterns and reefal response to varying hydrodynamic energy regimes.

4.2. Model Scenario 2 – Extending the base case model prior to the MPT (1.2 Ma - present)

Model Scenario 2 (1.2 Ma to present; Figs. 11 and 12) and the conceptual sketch in Fig. 14 illustrate the synthetic stratigraphy characterising Scott Reef's response to the MPT, showing that the present platform architecture continues to at least 1.2 Ma.

4.2.1. Platform evolution and sequence stratigraphy

Prior to the MPT (1.2–0.8 Ma), high frequency 41 kyr sea-level cycles with ca. 65 m amplitudes restricted vertical accommodation, producing thin (10–30 m) progradational to aggradational sequences, with the exception of MIS 17, which produced a mounded platform rim (Fig. 12B). Post-MPT, the transition to higher amplitude (up to 130 m) 100 kyr glacial-interglacial cycles, coupled with high subsidence, created greater accommodation. Although subsidence was the primary control on the thickness of stratigraphic sequences, the increased sea-level amplitudes influenced the extent and timing of sedimentation, resulting in thicker (20–80 m) aggradational sequences on the platform margin and interior. Fig. 12 presents the reasonable correlation between the five main stratigraphic unconformities interpreted on the seismic profile of South Scott Reef (Fig. 12B), defined by the continuity of high amplitude reflectors and evidence of onlap of strata above and toplap below (Paumard et al., 2017: Williams et al., 2023) and the synthetic sequence stratigraphic ages separating the highstands of MIS 1–11 (Fig. 12B).

Nine geomorphologic patterns (GP1–GP9) identified by Williams et al. (2023) present similarities with the modelled facies (Fig. 6C). Modelled geomorphology patterns identified based on their basinward or landward positions relative to the carbonate platforms correspond to geomorphologic patterns interpretations. Convex upwards reflectors with positive topographic relief relate to lagoonal patch reefs in map view (Fig. 6C), while medium to steep gradient features (GP1.1) match slope sediments. However, some patterns, such as GP6 (mass transport deposits) and GP7 (karst), were not captured due to software and resolution limitations.

4.2.2. Geomorphological and facies development

During the sea-level rise of MIS 11, the platform is flooded at 416 kyr, and the growth potential of the reef rim consistently outpaced sedimentation in the platform interior, producing bucket shape morphologies that continued to the present (Fig. 6C and 12A). North and South Scott Reef both developed a bucket shaped morphology, though relief differences between the margin and interior of South Scott Reef are more pronounced and characterised by deep water facies and a leeward margin that 'gave-up' (Fig. 12B). Drowning of the South Reef leeward margin in the models occurs gradually from MIS 11 to the Holocene due to a 50% reduction in carbonate production (2 mm/yr, see Table 2 and Fig. 4A). The leeward margin becomes a catch-up reef dominated by deep and intermediate reef facies (Fig. 12B). Coralgal 1 shallow reef facies fail to establish during the Holocene highstand. A starved lagoon

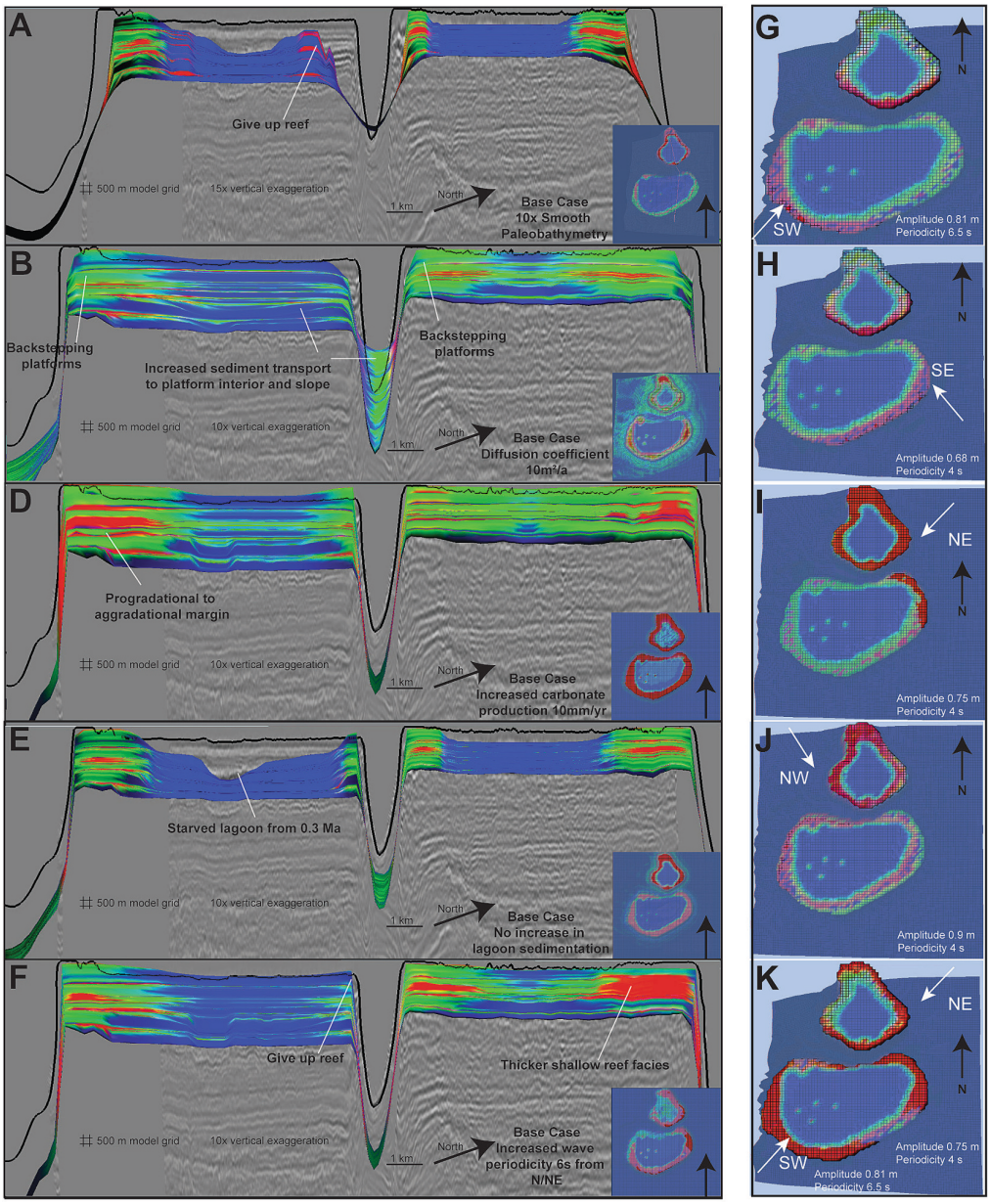


Fig. 10. Sensitivity tests of Model Scenario 1 exploring the impact of environmental and production parameters on Scott Reef platform evolution (392 kyr to present). Panels A–F show model cross-sections through North and South Scott Reef overlain on seismic profile A-A' (see Fig. 1) with corresponding final model timestep in plan-view (bottom right insets). (A) Testing a (10×) smoothed surface of the paleobathymetry produces a give-up reef. (B) Increased sediment transport (diffusion coefficient = 10 m^2/a) results in backstepping platforms and increased slope deposition. (D) Higher carbonate production rates (10 mm/yr) produce progradational to aggradational margin growth. (E) Excluding increased lagoonal sedimentation produces a starved lagoon after 0.3 Ma and is a result of using a trend of the modern bathymetry for the initial model surface. (F) Increased wave periodicity (6 s) from the NNE successfully produces a give-up reef morphology. Panels G–K show plan-view wave energy scenarios with varying amplitude and periodicity from different wave source directions (SW, SE, NE, NW), illustrating the control on reef rim development and facies patterns. Together, these experiments highlight how antecedent bathymetry, sediment transport, carbonate production, and hydrodynamic forcing modulate platform trajectories beyond eustatic control. The colour scheme is defined in Fig. 6B.

in the base case model experiments (Fig. 10E) indicated there were insufficient carbonate sedimentation from both autochthonous and allochthonous sources to fill the South Lagoon, whose volume is nearly three times larger than that of the North Lagoon. A multiplier of both in situ lagoonal sediment production to produce the autochthonous source of material and increased carbonate production to produce the allochthonous material was required.

Increased carbonate production post-MPT (ca. 0.5 Ma) resulted in reef expansion to develop the elevated and wider rims and a bucket-shaped platform consistent with the seismic facies. Increasing carbonate production also produced more Carb 1 rudstone material in the fore-reef and back reef, which increased the lagoonal autochthonous material. The increased wave energy from the SW and NE, which is consistent with the direction of modern-day storm-induced currents, after 0.5 Ma developed the reef rim to reproduce the modern geomorphology. The simulation output of Fig. 11A extended the base case model without applying these environmental assumptions and failed to match the observed facies patterns in core and seismic.

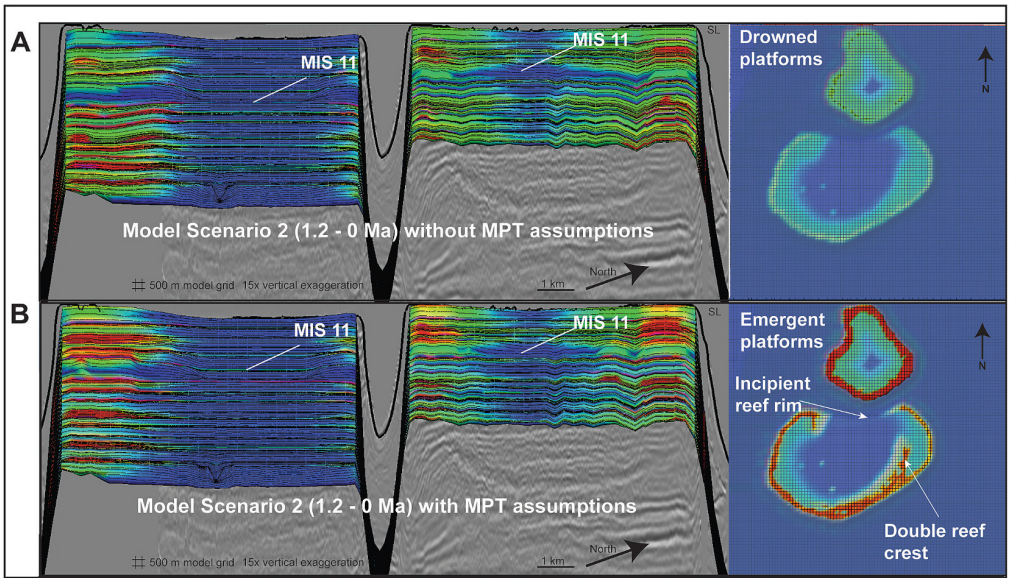


Fig. 11. Model Scenario 2 simulations (1.2–0 Ma) extending the base case model to test the influence of the Mid-Pleistocene Transition (MPT) and environmental assumptions on Scott Reef evolution. Forward stratigraphic model results in panel (A) extends the base case without adjusting parameters, and (B) extends the base case and includes assumptions about environmental changes associated with the MPT (increased carbonate production and wave energy after 0.5 Ma and reduced carbonate production on the leeward margin of the South Reef). The final model timesteps are shown on the right of the corresponding model. Without MPT assumptions (A), Scott Reef becomes a give up reef dominated by intermediate and deep reef facies and develops a submerged South Reef rim but fails to simulate shallow reef in MIS 1. Incorporating MPT assumptions (B) produces shallow reef expansion after MIS 11, an emergent double reef crest in the modern, and thicker aggradational sequences after MIS 11. The colour scheme is defined in Fig. 6B.

Lagoonal infill is known to occur predominantly under storm-driven high-energy conditions (Kennedy and Woodroffe, 2000), and our approach of modelling reworked reef rudstone partly compensates for the absence of Carb 1 within the lagoon, though it remains a limitation of model design. A trade-off was also necessary: low diffusion allowed steep platform margins to develop, but reduced the volume of eroded reef material available to fill the lagoon, failing to match seismic geometries for the South Reef. This suggests the South Reef was exposed to higher-energy conditions under the prevailing SW wave regime. Under higher subsidence conditions, the model produces an "empty bucket" lagoon that can only be infilled by imposing higher energy or increased lagoonal sedimentation rates. Accordingly, we applied a rate of 2 mm/yr to the South Reef lagoon to match the seismic profile, which is double the rate used in other carbonate forward stratigraphic models (Burgess, 2013; Liu et al., 2022; Van der Looven et al., 2022).

4.2.3. *MPT expression and subaerial exposure*

The simulations identify two key stratigraphic patterns that we postulate to have occurred due to the increased amplitude of sea-level cycles and associated environmental change related to the MPT. The first is a prolonged subaerial exposure surface in the synthetic stratigraphy (Fig. 12C), identified on seismic profile as a karst depression (Fig. 12A) and correlating with an abrupt transition to a bucket-shaped platform, coincident with MIS 12, which is the first high-amplitude (ca. 100 m) sea-level lowstand after the MPT. This interpretation is further supported by the occurrence of dolomite observed in the NRSEHDD3JA core at 189 m above a calcrete horizon (see Supplement 2), identified by secondary brown sediment infill of dissolved pores. Dolomite can occur in the mixing zone where pore space contains a mixture of meteoric and seawater (Warren, 2000; Flügel, 2009). The second expression of the MPT in the synthetic model is the ensuing long-lived MIS 11 highstand, which produced an 80 m raised rim and established the bucket-shaped morphology that persists to the present.

4.3. *Testing the influence of increased amplitude and reduced periodicity of sea-level changes*

The unique fingerprints of MISs across different eustatic sea-level curve reconstructions (i.e., rate, amplitude and duration; Pastier et al., 2019), produced variable reef development. To disentangle the influence of the eustatic sea-level forcing from tectonic variations, we tested three different eustatic sea-level curves (Table 3), each based on differing $\delta^{18}O$ records and age models (Clark et al., 2006), and a synthetic curve of the literal interpretation of the MPT eustatic change from 41 kyr to 100 kyr cycles (Miller et al., 2020; Bintanja and van de Wal, 2008; Bates et al., 2014; synthetic; Fig. 4C, Table 2) to address our hypothesis that the change in periodicity and amplitude of sea-level after the MPT influenced the Scott Reef platform development.

The eustatic-only experiments (Miller et al., 2020; Bintanja and van de Wal, 2008; Bates et al., 2014; synthetic) consistently reproduce two distinct stratigraphic signals: (1) reef expansion at ca. 1.1 Ma (MIS 27) and (2) margin progradation during MIS 11. In the eustatic curve reconstructions (A–C), sequence thickness decreases progressively towards the present, which is in contrast to the findings from our base case model, and is caused by reduced accommodation associated with longer lowstands and repeated subaerial exposure. The prolonged lowstands result in the thinner platform interior sequences, which is a fundamental characteristic of shallow-water carbonate factories (Wilkinson et al., 1999; Burgess and Pollitt, 2012). By contrast, the synthetic curve (D) produces an abrupt shift from thick to thin sequences at ca. 0.8 Ma, directly linked to the imposed change from 41 kyr, 60 m cycles to 100 kyr, 120 m cycles.

These initial experiments (Fig. 13) were conducted without applying tectonics and demonstrate that eustacy had a major control on model outcomes, including the timing of reef growth, sequence thickness and the number of reef growth sequences corresponding to MIS highstands preserved in the model. In all experiments, carbonate production rates were sufficient to keep pace with sea-level change, and is consistent with findings that different sea-level histories produce broadly similar reef

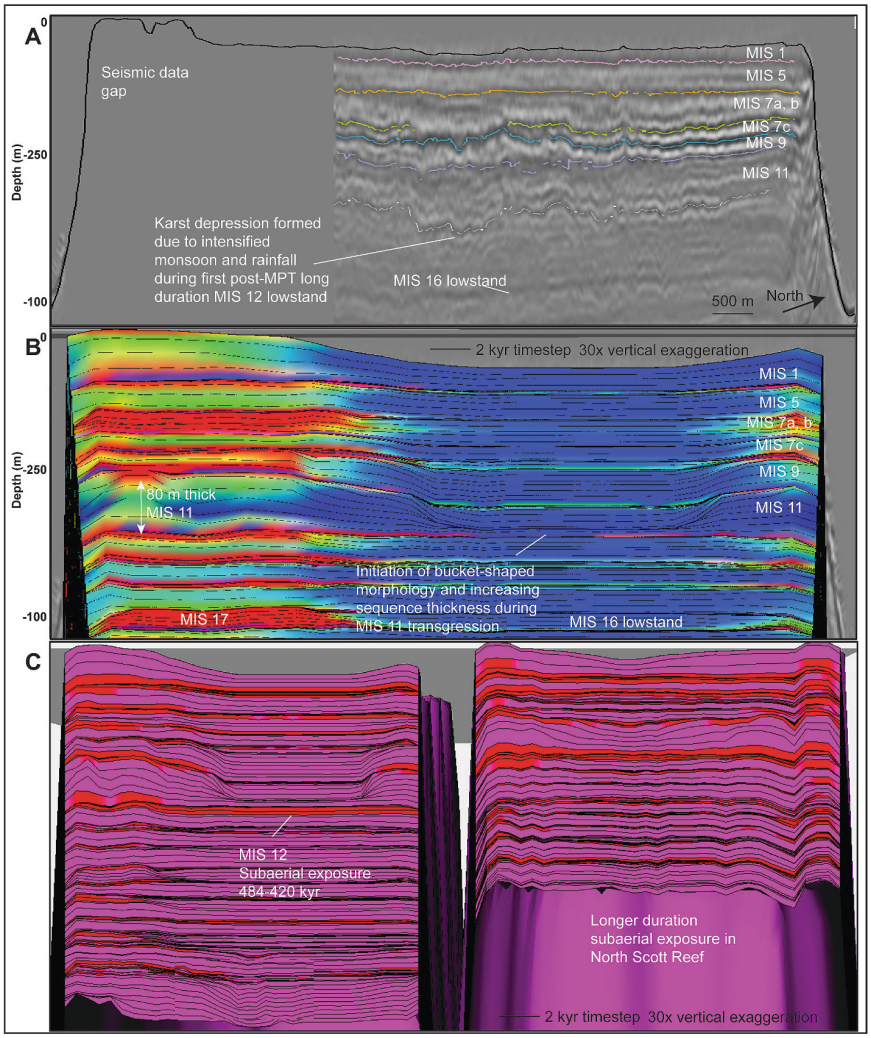


Fig. 12. South Scott Reef platform seismic stratigraphy compared to synthetic stratigraphy and modelled diagenesis. Panel (A) shows interpreted sequences boundaries between sea-level highstands of MIS 1–11 and the initiation of a karst depression in the platform interior interpreted to have occurred during the MIS 12 lowstand. (B) a zoomed in view of the GPM simulation output of model scenario 2 of the South Reef, showing synthetic stratigraphy broadly matching the seismic profile in (C). The model shows a transition to increased sequence thickness and the initiation of a "bucket" morphology during the prolonged MIS 11 highstand. (C) A GPM diagenesis model calculating the residence time of strata within the vadose zone, used as a proxy for development of karst and as supporting evidence for the interpretations of the prolonged MIS 12 lowstand. Red colour shows periods of subaerial exposure; pink is no subaerial exposure. The colour scheme in panel B is defined in Fig. 6B. (For interpretation of the references to colour in this figure legend, the reader is referred to the web version of this article.)

structures (Camoin and Webster, 2015, Woodroffe and Webster, 2014 and the classic interpretation of Schlager (1981), who argued that a healthy reef will likely be able to keep up with even rapid glacio-eustatic sea-level rise. It also suggests that the eustatic changes during the MPT had a significant impact on the carbonate factory, including observed reef expansion during MIS 11 (Fig. 13), which supports the evidence so far that the MIS 11 highstand was as a critical inflection point in the MPT. However, simulation outputs from the subsidence experiments, demonstrate that tectonics modulates this control, exerting a greater influence on sequence thickness and facies patterns.

5. Discussion

This study integrated sedimentological, ecological, and geophysical datasets within a forward stratigraphic modelling framework to address two questions: (1) how did the Mid-Pleistocene Climate Transition influence carbonate platform and coral reef development at Scott Reef, and (2) what mechanisms controlled the drowning of the leeward margin of South Scott Reef? A further consideration is whether these two processes were related. Despite the simplified model framework relative to the complexity of the preserved depositional record, model outputs broadly reproduce observed stratigraphy and facies distributions, providing confidence in the below insights into platform response to sea-level and environmental forcing.

5.1. Carbonate platform and coral reef response to the MPT

The Scott Reef platforms were already established by 1.2 Ma (Williams et al., 2023), indicating that the MPT did not initiate platform development and challenges the prevailing narrative that the MPT acted as a universal 'trigger' for reef initiation. Instead, the MPT resulted in a reorganisation of an existing active isolated carbonate platform, facilitating increasing sequence thickness to present and modifying facies patterns in response to continued accommodation and increased carbonate productivity and wave energy.

Despite the uncertainty surrounding the precise age span of the MPT,

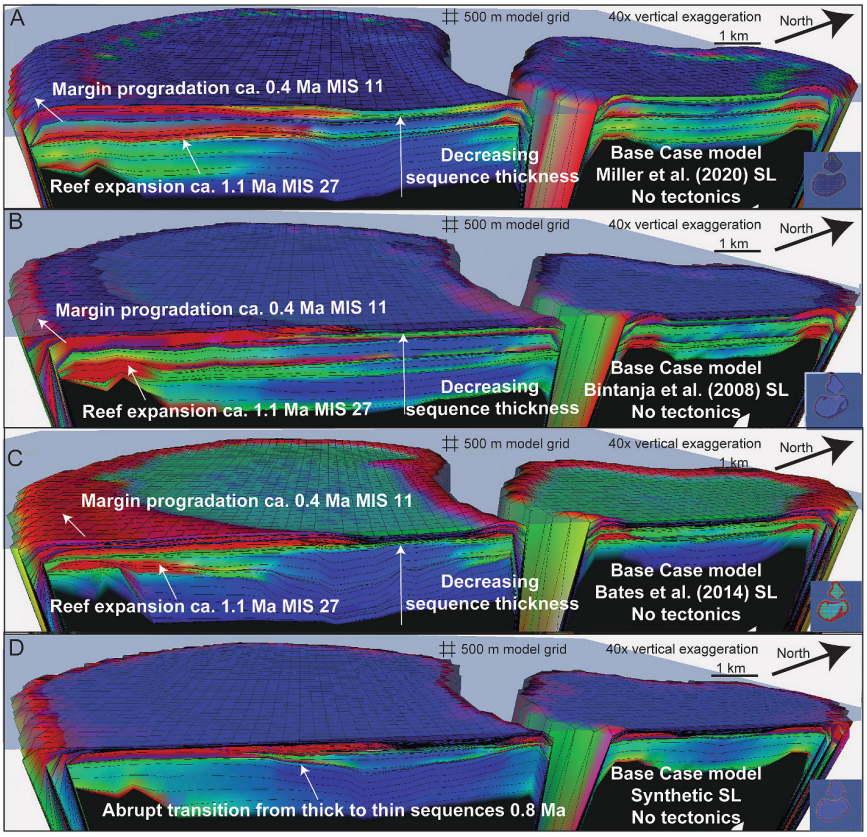


Fig. 13. MPT experiment applying only eustacy with no tectonic subsidence for Model Scenario 2 (1.2–0 Ma) using four sea-level curves. Initial bathymetry and base-case parameters remain constant. (A) Miller et al. (2020), (B) Bintanja et al. (2008), and (C) Bates et al. (2014) eustatic sea-level curves (see Fig. 4) each control variations of a similar pattern – reef expansion ca. 1.1 Ma (MIS 27) and margin progradation from ca. 0.4 Ma (MIS 11) with progressively thinner sequences towards the present due to increasingly prolonged lowstands and subaerial exposure. (D) Synthetic sea-level curve describing literal changes in sea-level amplitude and periodicity during the MPT produces an abrupt transition from thicker to thinner sequences at ca. 0.8 Ma. The colour scheme is defined in Fig. 6B.

the synthetic stratigraphic model suggest that reef expansion and morphological changes occurred during the MIS 12 lowstand and MIS 11 highstand around 0.4 Ma. The exceptionally thick MIS 11 sequence (Fig, 12B) produces a distinct pattern of shallowing upwards and vertical aggradation in our model in a catch up response to a long-duration transgression, which created optimal conditions for reef development (Husson et al., 2018), and back reef infilling, as is typical during still-stands (Davies and Montaggioni, 1985; Camoin and Webster, 2015). This pattern of reef response to increased sea-level amplitude is described for other Indo-Pacific reefs since the last glaciation (Montaggioni, 2005) due to a similarly slow and long-lasting sea-level rise. It is plausible to correlate the possible increase in carbonate production (not the preserved accumulation rate) by coral reefs during this transition in response to specific oceanographic changes such as seawater chemistry or solar irradiance absorbed by the water column, although independent geochemical constraints obtained from the fossil coral skeletons (Webb, 2025; Thompson, 2022) would be required to test specific mechanisms. The timing of initiation of Quaternary isolated carbonate buildups along the NWS also correspond to the initiation of abrupt sea-level rise and the unusually long-duration MIS 11 sea-level highstand, which *reactivated* carbonate primary production on topographic highs (Saqab and Bourget, 2015). Although, complex interactions between subsidence, sea-level and climate variability drowned one of the four Neogene Rowley Shoals to the south (McCaffrey et al., 2025). In contrast, however, many Indo-Pacific reefs, such as the Great Barrier Reef (Webster and Davies, 2003; Braithwaite et al., 2004; Braga and Aguirre, 2004; Humblet and Webster, 2017), Huon Peninsular (Chappell et al., 1996; De Gelder et al., 2022), and the Ryukyus Islands (Yamamoto et al., 2006), describe reef turn on observed after ca. 0.8 Ma and linked to the transition to 100 kyr glacial cycles.

While the long and warm MIS 11 may have facilitated reef development, regions such as the GBR, Belize Barrier Reef and Florida Reef Tract, which are mixed carbonate-siliciclastic systems (Gischler et al., 2010), were possibly dominated by siliciclastic sedimentation, inhibiting earlier Pleistocene reef expansion as observed at Scott Reef (Riera et al., 2021; Williams et al., 2023). Globally, reefs also changed sedimentation patterns in response to MPT-associated sea-level change. For example, Montaggioni et al. (2015) described a transition at Mururoa atoll from low carbonate production restricted to the foreslope during 41-kyr cycles (1.8–0.8 Ma), to an open system platform during the MPT (0.8–0.5 Ma), and finally to reef-rimmed platforms in the 100-kyr world (ca. 0.5 Ma – present). In contrast, continuous subsidence at Scott Reef facilitated continuous vertical accretion from 1.2 Ma to present.

This suggests that reef response to the MPT was neither synchronous nor uniform but mediated by the complex interplay between regional and eustatic conditions. While sea-level frequency and amplitude likely played an important role in shaping reef morphology (Montaggioni, 2005), other factors, such as antecedent topography, hydrodynamic energy regimes, subsidence patterns and ecological successions, also significantly influence reef response to abrupt eustatic and climatic change. For instance, not all offshore atolls in Belize have the same reef-rimmed morphologies despite similar sea-level histories and regional conditions, only Glovers Reef has a well-developed reef rim and deep lagoon (Gischler and Hudson, 2019).

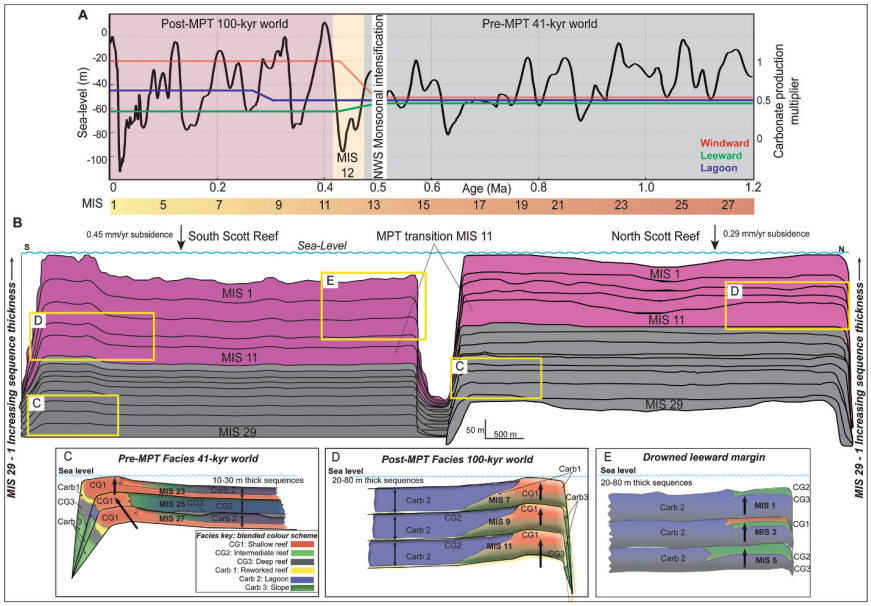


Fig. 14. Conceptual sketch of the Model Scenario 2 (1.2 Ma to present) simulated sequence stratigraphy of North and South Scott Reef, showing the transition from 41 kyr, pre-MPT keep-up reef sequences (10–30 m thick, progradational, shallow reef–dominated margins) (panel C), to 100 kyr post-MPT catch-up sequences (20–50 m thick, aggradational, deeper reef dominated) (panel D). The prolonged MIS 11 highstand is a major step in producing the "empty bucket" morphology and leeward margin drowning of the South Reef that is postulated to have functioned in relation to increased amplitude and reduced periodicity of sea-level cycles and increased monsoonal intensification during interglacials. South Scott Reef records thicker sequences under higher subsidence (0.45 mm/yr) compared to North Scott Reef (0.29 mm/yr). The model illustrates one possible iteration of the transition from a 41 kyr cycle with 60 m amplitude from 1.2 to 0.7 Ma (MIS 29–17), to a longer 100 kyr cycle with 120 m amplitude, which becomes more pronounced after the MPT, primarily as a result of increasing subsidence through time, which is contrary to the forcing of eustacy alone (see Fig. 13). Panels A-D show detailed facies responses to the sea-level oscillations of the pre-MPT and post-MPT world, respectively. Panel E illustrates the give-up reef on the drowned leeward margin of South Scott Reef post-MPT due to decreased carbonate production and increased water depth.

It is more likely that the noisy transition in the spectral series represents a disruption to the climate that was not uniform globally and when comparing the hypothesis model outcomes with the response of reefs globally we find that a large variety of changes occurred. The MPT did not universally turn reefs on, it disrupted long-term patterns to carbonate factories over a variety of timescales. Additionally, most of the spectral series show initiation of this transition beginning around 2.5 Ma, (e.g., De Gelder et al., 2020). The Bates et al. (2014) curve, which is reconstructed using $\delta^{18}O$ stacks from multiple records using coral-based sea-level benchmarks (De Gelder et al., 2020), was applied to our MPT model and resulted in a drowned platform. The most relevant spectral series to apply to models of reefs on the NWS requires further investigation perhaps using objective functions to systematically quantify errors.

5.2. *Mechanisms for the partial drowning of South Scott Reef*

Warrlich et al. (2002) use CARBONATE 3D to quantitively investigate the factors controlling atoll drowning with respect to the theory (e.g., Schlager, 1981). They show how drowning can occur under rapid relative sea-level rise that outpaces vertical accretion, including the rate and pattern of rapid rises and repeated drops, and reduced carbonate production due to environmental stresses.

Experimental simulations of model scenario 1 (392 kyr to present) (Figs. 9 and 10) can reproduce the submergence of the South Scott Reef leeward margin under three different scenarios; (1) applying a spatially variable subsidence rate and stepwise increasing relative sea-level change (Fig. 9A), (2) reduced carbonate production as a proxy for slower growing reefs on the leeward margin (Fig. 8C), and (3) an overly smooth, but unrealistic paleobathymetry (Fig. 10A). In reality, each of these factors are likely interconnected in a complex web of feedback loops. As such, although our base case model applied reduced carbonate production to drown the leeward margin, we acknowledge that aspects of all three scenarios are equally realistic. Below, we review these mechanisms in the context of analogues and modern regional tectono-environmental conditions, considering oceanographic factors and variable long-wavelength warping of the seabed.

5.2.1. *Climate-driven oceanographic mechanisms*

Collins et al. (2011) attribute the drowned leeward margin of South Scott Reef to high sediment supply and high turbidity that limited coral growth. This theory is substantiated by the core evidence which shows the margin is covered in sand and is not recolonised by modern reef, as well as the occurrence of unconsolidated sand and rubble observed in the Hook 3P core, which records low energy reef species mixed with lagoon-derived sediment. Wilson (2013) suggests there is evidence of episodic upwelling over the leeward margin of the South Scott Reef deep lagoon above the edge of the channel where *Halimeda* beds proliferate, outcompeting coral assemblages. A similar mechanism was proposed for the northern GBR during the Last Interglacial (LIG), where De Deckker et al. (2020) attributed extensive *Halimeda* facies and suppressed coral growth to enhanced upwelling linked to intensification of the East Australian Current, a process that almost led to the drowning of the GBR LIG reef regionally. Grimaldi et al. (2024) substantiate this observation by reporting colder temperatures in the open South Reef lagoon, possibly driven by upwelling along the steep continental slope through cold water bores, which alleviates thermal stress and promotes reef resilience during periods of elevated sea surface temperatures. These environmental conditions likely delivered turbulent waters and nutrient oversupply during increased episodic upwelling after onset of the monsoonal intensity along the NWS after 0.5 Ma (Gallagher et al., 2014) (Fig. 14A). This increased environmental stress would have reduced carbonate production, promoting lagoonal sediment deposition and contributed to the drowning of the leeward margin and the survival of the windward reef crest. Our simulations capture this increased environmental stress showing that the leeward margins failure to grow to

present sea-level is best explained by reduced carbonate production (Fig. 4). And so in agreement with the causes of simulations of atoll drowning by Warrlich et al. (2002), modern benthic observations, core evidence (e.g., the occurrence of *Halimeda* and microbialites and deep water coral assemblages - see Supplement 2), and the simulation outputs in this study, we conclude that the partial drowning of the leeward margin of South Scott Reef resulted from reduced carbonate production as a consequence of increased environmental stress. The mechanism was the monsoonal intensification around 0.5 Ma following eustatic changes and climate reorganisation during the MPT.

Incorporating proxies for tidal processes in the model on daily scales was unrealistic, although studies have done this (Burgess et al., 2011). It therefore remains unconstrained that the primary mechanism for the drowning of the leeward margin was amplified by tidally driven short-term sea-level fluctuations combined with intense cyclone exposure, which is evidenced by the boulder fields on the outer reef flat and surrounding fore-reef slope (Collins et al., 2011). Many carbonate platforms with high tidal ranges, including the Campeche Bank (Logan et al., 1969), were outpaced by rapid early Holocene sea-level rise, while others such as the Caribbean platforms (Schlager, 1981) were reduced in size. Our simulation method of applying reduced carbonate production on the leeward margin was sufficient to approximate this stress.

During the MPT, the weakening of the Indonesian Throughflow and Leeuwin Current during glacial periods (Auer et al., 2021) may have modified regional oceanographic conditions. Specifically, the weakened Leeuwin Current (Wijeratne et al., 2018), would have given rise to northward flowing currents such as the Leeuwin undercurrent, propagating wave energy from the South and Southwest at Scott Reef. While ocean currents are primarily generated by wind, not by currents, changes in currents systems can modulate the direction and intensity of wave propagation, refract and scatter surface waves, causing shifts in significant wave heights and direction, as well as influence seasonal regimes (Wang et al., 2025). This reorientation of wave energy would have exposed the leeward margins to increased hydrodynamic stress, potentially restricting coral growth. Further, interglacial periods post-MPT characterised by monsoonal intensification from the North, similar to the modern monsoonal system (Auer et al., 2021; Palei et al., 2024), a stronger Leeuwin Current and warmer sea surface temperatures (Petrick et al., 2019) would have driven wave energy periodically from the North and amplified seasonal variability, particularly during storm events. Incorporating this hypothesised change in hydrodynamic regime in our model demonstrated how these fluctuations contributed to differential preservation of reef structures across the platform, disrupting reef development in the South Reef leeward margin from 0.5 Ma to present (Fig. 11B). Fig. 11A demonstrates the model outcome that did not incorporate these assumptions showing that the reef crest did not reach modern sea-level.

Increased carbonate production during MIS 11 amplified topographic relief across the platform because in tropical systems, shallow reefs track sea-level change and concentrate production along the margins, which subsequently infills the lagoon (Schlager, 2005). Intensified monsoonal activity during this time likely incurred increased rainfall on the emergent platforms resulting in significant dissolution and karstification, which correlates to the occurrence of dolomite and calcrete horizon observed in core. Liu et al. (2022) use forward stratigraphic models of the Meiji Atoll in the South China Sea to suggest that the atoll formed primarily due to spatially differential dissolution across the platform margin and interior. However, we suggest based on our models that the change in amplitude of sea-level coupled with coincident environmental change that resulted in increased rainfall and karst dissolution during MIS 12, were the combined cause for this dramatic change in the South Reef's platform morphology.

5.2.2. Impact of tectonics on accommodation

Collins et al. (2011) report variable subsidence rates for North and South Reef (0.29 mm/yr and 0.45 mm/yr respectively). Given that no evidence of Neogene faulting is observed on seismic profiles (Williams et al., 2023) (although we cannot see below the reef crest), we postulate alternative mechanisms for spatially and temporally variable subsidence across the platforms, which in our model experiments successfully drowned the leeward margin of South Scott Reef (Fig. 9A).

Flexural loading and long-wavelength warping of the seabed (Keep et al., 2007; DiCaprio et al., 2009; Belde et al., 2015; Hengesh and Whitney, 2016; Whitney et al., 2016), provide a plausible geodynamic mechanism for the pulsed subsidence theory. While flexure is fundamentally a response to loading, the Browse Basin is structurally complex, with long-lived basement rift inheritance and fault reactivation producing differential accommodation at short spatial scales (Keep et al., 2007; Belde et al., 2015). Episodic tectonic deformation and distributed strain have been shown to generate stepwise changes in subsidence and relative sea-level (Hengesh and Whitney, 2016; Whitney et al., 2016). These processes are consistent with our pulsed subsidence experiments, where rapid, localised increases in subsidence temporarily submerged the reef margin before recovery during intervals of reduced loading (Schlager, 1981; Warrlich et al., 2002), which also provide a reasonable explanation for the contrasting morphologies of the North and South Reefs. Rather than requiring unrealistically large or instantaneous loads, this interpretation reflects the structural heterogeneity of the basin and supports a tectonic control on the episodic drowning observed at South Scott Reef, as observed in rapidly subsiding regions like the Huon Gulf and Hawaii (Webster et al., 2009). This likely amplified local subsidence rates, periodically driving platforms below the euphotic zone and curbing shallow reef re-establishment (Whitney et al., 2016). Despite evidence of high subsidence rates of up to 0.5 mm/yr (Gurnis et al., 2020) and a pulsed, stepwise subsidence rate within the Browse basin (Van Tuyl et al., 2019), present day reefs along the NWS (i.e., Scott Reef, Seringapatam Reef, Ashmore Reefs) have persisted through time. Although the Browse Basin is often regarded as tectonically stable, the sustained productivity and extensive accommodation facilitated by spatially and temporally variable subsidence suggest a more complex tectonic influence than previously assumed.

Nonetheless, calibrating the exact subsidence profile is a non-trivial task (Bornholdt et al., 1999) and raises concerns about parameter 'non-uniqueness' (Posamentier and Allen, 1999; Cross and Lessenger, 1998; Burgess and Wright, 2003; Burgess, 2006; Burgess and Prince, 2015; Busson et al., 2019; Pastier et al., 2019; Van der Looven et al., 2022), whereby different parameter sets yield similar results. Perhaps a quantitative objective function to calculate an error of uncertainty that can be minimised could further constrain the most appropriate mechanism for drowning the leeward margin. Our modelling approach should therefore be viewed as a simplified approximation of complex relative sea-level histories. Given the inherent uncertainties in timeseries reconstructions, especially the Miller et al. (2020) global sea-level curve, as well as assumptions in spectral analyses and boundary condition, our base case simulation should be viewed as one possible scenario rather than a definitive characterisation of response to the MPT due to change in amplitude of sea-level cycles.

5.2.3. Influence of Paleotopography

Paleobathymetry can influence inherited long-term topography (Barrett and Webster, 2012), and our base case model shows that the long-lived elevation was one possible cause of the drowning of the leeward margin. Establishing a realistic paleobathymetry and paleowater depth for model initiation - informed by the modern bathymetry, seismic stratigraphy, coralgal assemblages and chronological constraints - was critical to building a successful base-case model, enabling meaningful calibration of other parameters and replication of observed stratigraphic and geomorphologic features. This highlights the importance of antecedent platform topography, suggesting that the paleowater depth and elevation of Scott Reef's early Pleistocene substrate above the surrounding seafloor (i.e., a paleotopographic high controlled by Neogene tectonics, Webster et al., 2022) may have been key to its

long-term survival through the Quaternary relative sea-level and associated climatic changes. This finding may also add to the discussion on why only outer shelf reefs along the NWS with sufficient elevations above the seafloor survived since the Miocene, while inner shelf platforms such as Ashmore Reef ultimately drowned due to sustained exposure during lowstands followed by rapid sea-level rise, compounded by proximity to terrigenous influx (Webster et al., 2022). Together, this suggests that while the MPT associated increase of sea-level amplitude is a key trigger for reefs on the NWS, antecedent paleobathymetry was the primary control on whether reefs could take advantage of this accommodation.

5.3. GPM and forward stratigraphic model limitations

Despite the demonstrated relevance and robustness of GPM and its continued application in carbonate platform research (e.g., Ferreira et al., 2021; Jiménez et al., 2024), FSM remains a simplification of natural reef processes and does not fully capture the facies spatial heterogeneity or ecological complexity of carbonate platform evolution. In particular, carbonate production and wave energy multipliers represent a first-order control on simulated accretion rates, platform thickness, and facies distributions, and their application introduces an uncertain empirical component to model outcomes. Although we demonstrated in model scenario 2 that simulations without the imposed multiplier assumptions (Fig. 11A) failed to adequately match the data, the absolute value of the multiplier that was selected to better match the data (Fig. 11B) remains arbitrary and warrants ongoing calibration and experimentation in future studies. Similar limitations are noted in previous FSM studies, for instance, Busson et al. (2019) modelled a reduction in size of the Great Bahama Bank during the Holocene sea-level rise, contradicting sedimentological evidence from (Grammer et al., 1993), who demonstrated there was lateral slope and margin accretion during the Holocene. In this study, our simulations successfully drowned the South Reef leeward margin, which is consistent with observed data, yet the specific mechanisms and timing remain imprecise due to the inability to model tidal currents, turbidity, storm-driven wave processes, and other environmental forcing conditions such as sea surface temperature, pH and salinity, which can affect the reefs overall health and ability to keep pace with relative sea level change (Gischler and Hudson, 2019). However, we acknowledge that no simulation can take all of these processes and environmental variables into account (Montaggioni et al. (2015), much less so perhaps because of our limited understanding of these processes in nature.

6. Conclusions

This study presents the first forward stratigraphic model of Scott Reef, two isolated carbonate platforms on the Northwest Shelf of Australia, spanning the MPT (ca. 1.2 Ma to present). Scott Reef preserves a unique archive of reef growth sequences paced by millennial (10^3-year) to orbital (10^4–10^5-year) scale sea-level rhythms under continuous high subsidence, providing valuable analogues for both Quaternary reef dynamics and future reef responses to accelerated climatic change. The conceptual framework of environmental thresholds was constrained by the modern bathymetry, seismic sequence stratigraphy, sedimentary facies, coralgal assemblages, U/Th ages and temporal changes in carbonate production and wave energy. Using these parameters to calibrate a best-fit scenario to observed data, we conclude that:

1. Coralgal assemblages were essential for defining initial model paleowater depth and carbonate production-depth curves, as their distinct habitat depth ranges adds useful insight into the evolution of reef growth sequences by visually expressing rate of change of water depth during sea-level rise.
2. The bucket shape morphology initiated after the first high amplitude lowstand of MIS 12, during which time the longest period of subaerial exposure is simulated in the GPM diagenesis model (ca. 484–420 kyr). This horizon correlates with the occurrence of the first major karst depression at 316 m below the modern lagoon observed on seismic profiles and is postulated to coincide with increased dissolution due to increased rainfall linked to monsoonal intensification around 0.5 Ma after the MPT.
3. The model simulates an 80 m thick shallowing upwards sequence at 412 kyr during the first high amplitude, long duration highstand in the post-MPT 100-kyr world (MIS 11) that initiates the bucket shape morphology that continues to present. Thus, we conclude that reef expansion occurred during MIS 11, and is consistent with timings of reef growth elsewhere along the NWS, although there are differences to timing and style of reef response to the MPT globally.
4. The synthetic stratigraphy expressed two distinct growth phases: thin (10–30 m), low-relief progradational and aggradational sequences before 0.5 Ma, and thicker (20–50 m) aggradational sequences after 0.5 Ma, corresponding to the shift from 41 kyr to 100 kyr sea-level cycles.
5. The constant subsidence rates (0.29 mm/yr; SSR, 0.45 mm/yr; NSR) used in the model to match observed data suggest that sea-level change related to the MPT modulates the change in sequence thickness. The MPT therefore affects the Scott Reef platform producing a change in platform morphology and facies patterns controlled by increasing amplitude of sea-level cycles at 0.5 Ma, coupled with continuous high subsidence, and increasing monsoonal intensity that amplified processes of dissolution and karstification on the platform tops during prolonged periods of subaerial exposure. Thus, both environmental and eustatic controls were major forcings on Scott Reef evolution.
6. The drowned leeward margin of South Scott Reef is reproduced by decreased carbonate production, increased lagoon sedimentation and wave energy from the North, consistent with modern storm-induced currents. These proxies for environmental stress intensified after ca. 0.5 Ma as monsoonal intensity on the NWS increased ocean upwelling, turbulence and nutrients, enabling stress-tolerant species such as *Halimeda* to outcompete coral framework.

The forward stratigraphic model simulation outputs enable quantification of spatial and temporal facies transitions observed in seismic and core data and provides a robust framework for reconstructing carbonate platform evolution and demonstrates the usefulness of the GPM tool to the coral reef science community. The synthetic stratigraphy fills data gaps, constrains the conceptual chronostratigraphic framework and stratigraphic architecture, and generates new information to improve seismic interpretation and predictions of platform response to the MPT. Trial-and-error style forward stratigraphic modelling remains a powerful and versatile tool, when ground-truthed to multi-scale observational data, to test hypotheses about carbonate platform and coral reef response to rapid environmental change.

Supplementary data to this article can be found online at https://doi.org/10.1016/j.margeo.2026.107716.

Declaration of generative AI and AI-assisted technologies in the manuscript preparation process

During the preparation of this work the author(s) used CoPilot for the purposes of text enhancement. The use of this generative AI tool includes spelling corrections, minor sentence restructuring, and clarity enhancement. I confirm that where text was modified by generative AI, the content was reviewed for possible errors, inaccuracies, and bias. After using this tool/service, the author(s) reviewed and edited the content as needed and take(s) full responsibility for the content of the published article.

CRediT authorship contribution statement

Carra Williams: Writing – original draft, Visualization, Software, Resources, Project administration, Methodology, Investigation, Formal analysis, Data curation, Conceptualization. **Jody M. Webster:** Writing – review & editing, Visualization, Validation, Supervision, Software, Resources. **Tristan Salles:** Writing – review & editing, Visualization, Validation, Supervision, Software, Resources, Project administration, Methodology. **Victorien Paumard:** Writing – review & editing, Visualization, Validation, Supervision, Software, Resources. **Camille Grimaldi:** Writing – review & editing, Resources, Data curation. **Mostfa Lejri:** Writing – review & editing, Validation, Software, Resources.

Declaration of competing interest

The authors declare that they have no known competing financial interests or personal relationships that could have appeared to influence the work reported in this paper.

Acknowledgments

We gratefully acknowledge Marc Humblet and Juan Carlos Braga for their contributions to coral and coralline algae identification used in this study and Willem Renema for taxonomic identification of *Cycloclypeus* foraminifera. Core data were provided with permission from the Perth Core Library and the Geocoastal Research Group, University of Sydney. We thank the reviewers for their guidance and constructive feedback on the manuscript. Support and access to computing facilities were provided by the School of Earth and Oceans, The University of Western Australia. We thank Schlumberger for providing the Petrel™ software license and technical support. This paper is a review of "Coral reef response since the Mid-Pleistocene Climate Transition on the Northwest Shelf, Australia: Insights from fossil coral reef cores." This paper incorporates material that is © Australian Institute of Marine Science and © Woodside Energy Group Ltd. (1994). The Australian Institute of Marine Science and Woodside Energy Group Ltd. do not necessarily endorse any modifications made to that material.

Data availability

Data used in this study and model outputs are available online. The forward stratigraphic model parameter files and output simulations are archived at https://github.com/Carra2023/Scott-Reef-GPM-Base-Case-forward-stratigraphic-model. All core material analysed in this study is archived at the Perth Core Library, Geological Survey of Western Australia (GSWA). The Scott Reef cores are publicly available for research purposes and can be accessed by submitting a formal core viewing and sampling request to the Perth Core Library via the GSWA website (https://www.wa.gov.au/organisation/department-of-mines-petroleum-and-exploration/geological-survey-of-western-australia/core-library-sample-access). Requests are subject to standard GSWA approval procedures and availability. The core interpretations used in this manuscript can be accessed via Supplement 2.

References

Abbey, E., Webster, J.M., Beaman, R.J., 2011. Geomorphology of submerged reefs on the shelf edge of the Great Barrier Reef: the influence of oscillating Pleistocene Sea-levels. Mar. Geol. 288, 61–78.

Acevedo-Ramirez, C.A., Stephenson, W., Wakes, S., Mariño-Tapia, I., 2021. Wave transformation on a fringing reef system with spur and groove structures. J. Geophys. Res. Oceans 126, e2020JC016910.

Allen Coral Atlas, 2022. Imagery, maps, and monitoring of the world's tropical coral reefs. https://doi.org/10.5281/zenodo.3833242.

Alonso-Garcia, M., Reolid, J., Jimenez-Espejo, F.J., Bialik, O.M., Alvarez Zarikian, C.A., Laya, J.C., Carrasquiera, I., Jovane, L., Reijmer, J.J., Betzler, C., Eberli, G.P., 2023. Sea-level and monsoonal control on the Maldives carbonate platform (Indian Ocean) over the last 1.3 million years: climate of the Past Discussions, 2023, pp. 1–44.

Auer, G., Petrick, B., Yoshimura, T., Mamo, B.L., Reuning, L., Takayanagi, H., De Vleeschouwer, D., Martinez-Garcia, A., 2021. Intensified organic carbon burial on the Australian shelf after the Middle Pleistocene transition. Quat. Sci. Rev. 262, 106965.

Barrett, S.J., Webster, J.M., 2012. Holocene evolution of the Great Barrier Reef: Insights from 3D numerical modelling. Sediment. Geol. 265–266, 56–71. https://doi.org/10.1016/j.sedgeo.2012.03.015.

Bates, S.L., Siddall, M., Waelbroeck, C., 2014. Hydrographic variations in deep ocean temperature over the mid-Pleistocene transition. Quat. Sci. Rev. 88, 147–158. https://doi.org/10.1016/j.quascirev.2014.01.020.

Bathurst, R.G.C., 1975. Carbonate Sediments and their Diagenesis. Elsevier, Amsterdam, New York.

Beaman, R.J., 2017. Northern Australia bathymetry compilation: Deepreef Explorer. https://www.deepreef.org/2017/02/28/nthaus-bathy/ (accessed December 2024).

Belde, J., Back, S., Reuning, L., Eberli, G., 2015. Three-dimensional seismic analysis of sediment waves and related geomorphological features on a carbonate shelf exposed to large amplitude internal waves, Browse Basin region, Australia. Sedimentology 62, 87–109. https://doi.org/10.1111/sed.12141.

Belde, J., Back, S., Bourget, J., Reuning, L., 2017. Oligocene and Miocene carbonate platform development in the Browse Basin. Australian Northwest Shelf: J. Sediment. Res. 87, 795–816. https://doi.org/10.2110/jsr.2017.44.

Belopolsky, A., Droxler, A., 2003. Imaging Tertiary carbonate system, the Maldives, Indian Ocean: Insights into carbonate sequence interpretation. Lead. Edge 22, 646–652. https://doi.org/10.1190/1.1599690.

Berends, C.J., Köhler, P., Lourens, L.J., Wal, R.S.W., 2021. On the cause of the Mid-Pleistocene transition. Rev. Geophys. 59 (2). https://doi.org/10.1029/2020RG000727.

Betzler, C., Hübscher, C., Lindhorst, S., Reijmer, J.J.G., Römer, M., Droxler, A.W., Lüdmann, T., 2009. Monsoon-induced partial carbonate platform drowning (Maldives, Indian Ocean). Geology 37 (10), 867–870. https://doi.org/10.1130/G25702A.1.

Bintanja, R., van de Wal, R.S.W., 2008. North American ice-sheet dynamics and the onset of 100,000-year glacial cycles. Nature 454 (7206), 869–872. https://doi.org/10.1038/nature07158.

Blanchon, P., 2011. Meltwater Pulses. In: Hopley, D. (Ed.), Encyclopedia of Earth Sciences Series: Encyclopedia of Modern Coral Reefs. Springer Netherlands, Dordrecht, pp. 683–690. https://doi.org/10.1007/978-90-481-2639-2_232.

Borgomano, J., Lanteaume, C., Léonide, P., Fournier, F., Montaggioni, L.F., Masse, J.-P., 2020. Quantitative carbonate sequence stratigraphy: Insights from stratigraphic forward models. AAPG Bull. 104, 1115–1142. https://doi.org/10.1306/11111917396.

Bosence, D., Waltham, D., 1990. Computer modeling the internal architecture of carbonate platforms. Geology 18, 26–30. https://doi.org/10.1130/0091-7613(1990)018<0026:CMTIAO>2.3.CO;2.

Bornholdt, S., Nordlund, U., Westphal, H., 1999. In: Harbaugh, J.W., et al. (Eds.), Numerical Experiments in Stratigraphy: Recent Advances in Stratigraphic and Sedimentologic Computer Simulations, 62. SEPM Spec. Publ, pp. 85–90.

Bosence, D.W.J., Pomar, L., Waltham, D.A., Lankester, T.H.G., 1994. Computer modeling a Miocene carbonate platform, Mallorca, Spain. AAPG Bull. 78, 247–266.

Bosscher, H., Schlager, W., 1993. Accumulation rates of Carbonate Platforms. J. Geol. 101 (3), 345–355. https://doi.org/10.1086/648228.

Braga, J.C., Aguirre, J., 2004. Coralline algae indicate Pleistocene evolution from deep, open platform to outer barrier reef environments in the northern Great Barrier Reef margin. Coral Reefs 23 (4), 547–558. https://doi.org/10.1007/s00338-004-0414-x.

Braga, J.C., Humblet, M., Ramos, D.A.E., Dechnik, B., Webster, J.M., 2022. Quaternary coral, coralline algal and vermetid assemblages as sea-level indicators: a review. In: IAS Special Publication: Coral Reefs and Sea-Level Change: Quaternary Records and Modelling. A Window Into the Future, 49, pp. 1–38.

Braithwaite, C.J.R., Dalmasso, H., Gilmour, M.A., Harkness, D.D., Henderson, G.M., Kay, R.L.F., Wilson, P.A., 2004. The Great Barrier Reef: the chronological record from a new borehole. J. Sediment. Res. 74 (2), 298–310. https://doi.org/10.1306/091603740298.

Burgess, P.M., 2001. Modeling carbonate sequence development without relative sea-level oscillations. Geology 29, 1127–1130. https://doi.org/10.1130/0091-7613(2001)029.

Burgess, P.M., 2006. The signal and the noise: Forward modeling of allocyclic and autocyclic processes influencing peritidal carbonate stacking patterns. J. Sediment. Res. 76 (7–8), 962–977. https://doi.org/10.2110/jsr.2006.084.

Burgess, P.M., 2013. CarboCAT: A cellular automata model of heterogeneous carbonate strata. Comput. Geosci. 53, 129–140. https://doi.org/10.1016/j.cageo.2011.08.026.

Burgess, P.M., Pollitt, D.A., 2012. The origins of shallow-water carbonate lithofacies thickness distributions: one-dimensional forward modelling of relative sea-level and production rate control. Sedimentology 59 (1), 57–80.

Burgess, P.M., Prince, G.D., 2015. Non-unique stratal geometries: Implications for sequence stratigraphic interpretations. Basin Res. 27 (3), 351–365. https://doi.org/10.1111/bre.12082.

Burgess, P.M., Wright, V.P., 2003. Numerical forward modeling of carbonate platform dynamics: an evaluation of complexity and completeness in carbonate strata. J. Sediment. Res. 73 (5), 637–652. https://doi.org/10.1306/020503730637.

Burgess, P.M., Williams, H.D., Wright, V.P., Della Porta, G., Granjeon, D., 2011. Investigating Carbonate Platform Types: Multiple Controls and a Continuum of Geometries, 30164. Search and Discovery Article.

Busson, J., Joseph, P., Mulder, T., Teles, V., Borgomano, J., Granjeon, D., Wunsch, M., 2019. High-resolution stratigraphic forward modelling of a Quaternary carbonate margin: Controls and dynamics of the progradation. Sediment. Geol. 379, 77–96. https://doi.org/10.1016/j.sedgeo.2018.11.004.

Cabioch, G., Montaggioni, L.F., Faure, G., Ribaud-Laurenti, A., 1999. Reef coralgal assemblages as recorders of paleobathymetry and sea level changes in the Indo-Pacific province. Quat. Sci. Rev. 18 (14), 1681–1695.
Cabioch, G., Montaggioni, L., Thouveny, N., Frank, N., Sato, T., Chazottes, V., Sémah, A. M., 2008. The chronology and structure of the western New Caledonian barrier reef tracts. Palaeogeogr. Palaeoclimatol. Palaeoecol. 268 (1–2), 91–105.
Camoin, G.F., Webster, J.M., 2015. Coral reef response to Quaternary Sea-level and environmental changes: State of the science. Sedimentology 62 (2), 401–428. https://doi.org/10.1111/sed.12184.
Chappell, J., Omura, A., Esat, T., McCulloch, M., Pandolfi, J., Ota, Y., Pillans, B., 1996. Reconciliaion of late Quaternary Sea levels derived from coral terraces at Huon Peninsula with deep sea oxygen isotope records. Earth Planet. Sci. Lett. 141 (1), 227–236. https://doi.org/10.1016/0012-821X(96)00062-3.
Clark, P.U., Archer, D., Pollard, D., Blum, J.D., Rial, J.A., Brovkin, V., Roy, M., 2006. The middle Pleistocene transition: Characteristics, mechanisms, and implications for long-term changes in atmospheric pCO2. Quat. Sci. Rev. 25 (23–24), 3150–3184. https://doi.org/10.1016/j.quascirev.2006.07.008.
Collins, L.B., 2002. Tertiary foundations and quaternary evolution of coral reef systems of Australia's North West Shelf. In: Moss, S.J., Keep, M. (Eds.), The Sedimentary Basins of Western Australia 3, October 20–23 2002. Petroleum Exploration Society of Australia, Perth, Western Australia, pp. 129–152.
Collins, L.B., 2011. Geological setting, marine geomorphology, sediments and oceanic shoals growth history of the Kimberley region. J. R. Soc. West. Aust. 94 (2), 89–105.
Collins, L.B., Testa, V., 2010. Quaternary development of resilient reefs on the subsiding Kimberley continental margin, Northwest Australia. Braz. J. Oceanogr. 58 (spe1), 67–77. https://doi.org/10.1590/S1679-87592010000500007.
Collins, L.B., Testa, V., Zhao, J., Qu, D., 2011. Holocene growth history and evolution of the Scott reef carbonate platform and coral reef. J. R. Soc. West. Aust. 94 (2), 239, 239.
Cross, T.A., Lessenger, M.A., 1998. Sediment volume partitioning: Rationale for stratigraphic model evaluation and high-resolution stratigraphic correlation: Sequence Stratigraphy—Concepts and Application. Norwegian Petroleum Society Special Publication 8, 171–195.
Cross, T.A., Lessenger, M.A., 1999. Construction and application of a stratigraphic inverse model. In: Harbaugh, J.W., Watney, W.L., Rankey, E.C., Slingerland, R., Goldstein, R.H., Franseen, E.K. (Eds.), Numerical Experiments in Stratigraphy: Recent Advances in Stratigraphic and Sedimentologic Computer Simulations. SEPM Special Publication 62. Society for Sedimentary Geology, Tulsa, OK, pp. 69–84.
Davies, P.J., Montaggioni, L., 1985. Reef growth and sea level change: the environmental signature. In: Proceedings of the Fifth International Coral Reef Symposium, Tahiti, 3, pp. 477–515.
De Deckker, P., Moros, M., Perner, K., Blanz, T., Wacker, L., Schneider, R., Jansen, E., 2020. Climatic evolution in the Australian region over the last 94 ka—spanning human occupancy—and unveiling the last Glacial Maximum. Quat. Sci. Rev. 249, 106593. https://doi.org/10.1016/j.quascirev.2020.106593.
De Gelder, G., Jara-Muñoz, J., Melnick, D., Fernández-Blanco, D., Rouby, H., Pedoja, K., Lacassin, R., 2020. How do sea-level curves influence modeled marine terrace sequences? Quat. Sci. Rev. 229, 106132. https://doi.org/10.1016/j.quascirev.2019.106132.
De Gelder, G., Husson, L., Pastier, A.-M., Fernández-Blanco, D., Pico, T., Chauveau, D., Pedoja, K., 2022. High interstadial sea levels over the past 420 ka from the Huon Peninsula, Papua New Guinea. Commun. Earth Environ. 3 (1), 1–12. https://doi.org/10.1038/s43247-022-00583-7.
DiCaprio, L., Gurnis, M., Müller, R.D., 2009. Long-wavelength tilting of the Australian continent since the late cretaceous. Earth Planet. Sci. Lett. 278 (3), 175–185. https://doi.org/10.1016/j.epsl.2008.11.030.
Done, T.J., Williams, D.McB, Speare, P.J., Turak, E.I., Davidson, J., DeVantier, L.M., Newman, S.J., Hutchins, J.B., 1994. Surveys of Coral and Fish Communities at Scott Reef and Rowley Shoals: Produced in Accordance with the Scott Reef Research Services Agreement between Woodside Offshore Petroleum Pty. Ltd. and the Australian Institute of Marine Science.
Droxler, A.W., Jorry, S.J., 2013. Deglacial origin of barrier reefs along low-latitude mixed siliciclastic and carbonate continental shelf edges. Annu. Rev. Mar. Sci. 5 (1), 165–190.
Dwyer, G.S., Cronin, T.M., Baker, P.A., Raymo, M.E., Buzas, J.S., Corrège, T., 1995. North Atlantic Deepwater temperature change during late Pliocene and late Quaternary climatic cycles. Science 270 (5240), 1347–1351. https://doi.org/10.1126/science.270.5240.1347.
Faichney, I.D.E., Webster, J.M., Clague, D.A., Braga, J.C., Renema, W., Potts, D.C., 2011. The impact of the Mid-Pleistocene transition on the composition of submerged reefs of the Maui Nui complex, Hawaii: Palaeogeography. Palaeoclimatol. Palaeoecol. 299 (3–4), 493–506.
Ferreira, L.C.L., Grillo, A.C., Repinaldo Filho, F.P.M., Souza, F.N.R., Longo, G.O., 2021. Different responses of massive and branching corals to a major heatwave at the largest and richest reef complex in South Atlantic. Mar. Biol. v. 168, no. 5. https://doi.org/10.1007/s00227-021-03863-6.
Feuillaret, L., Humblet, M., Iryu, Y., Fujita, K., 2023. Reconstruction of late Middle Pleistocene reef growth history and environmental changes in the Ryukyu Islands, southern Okinawa Island. Proceedings of the JpGU Meeting, 2023. https://doi.org/10.13140/RG.2.2.15997.58084.
Flügel, E., 2009. Diagenesis, Porosity, and Dolomitization, in Microfacies of Carbonate Rocks. Springer, Berlin, pp. 267–338. https://doi.org/10.1007/978-3-642-03796-2_7.
Gallagher, S.J., Wallace, M.W., Hoiles, P.W., Southwood, J.M., 2014. Seismic and stratigraphic evidence for reef expansion and onset of aridity on the Northwest Shelf of Australia during the Pleistocene. Mar. Pet. Geol. 57, 470–481. https://doi.org/10.1016/j.marpetgeo.2014.06.011.
Gallagher, S.J., Auer, G., Brierley, C.M., Fulthorpe, C.S., Hall, R., 2024. Cenozoic history of the Indonesian Gateway. Annu. Rev. Earth Planet. Sci. 52 (1), 581–604. https://doi.org/10.1146/annurev-earth-040722-111322.
Gilmour, J.P., Cook, K.L., Ryan, N.M., Puotinen, M.L., Green, R.H., Shedrawi, G., Oades, D., 2019. The state of Western Australia's coral reefs. Coral Reefs 38 (4), 651–667. https://doi.org/10.1007/s00338-019-01795-8.
Gilmour, J.P., Cook, K.L., Ryan, N.M., Puotinen, M.L., Green, R.H., Heyward, A.J., 2022. A tale of two reef systems: local conditions, disturbances, coral life histories, and the climate catastrophe. Ecol. Appl. 32 (3), e2509. https://doi.org/10.1002/eap.2509.
Gischler, E., 2015. Quaternary reef response to sea-level and environmental change in the western Atlantic. Sedimentology 62, 429–465. https://doi.org/10.1111/sed.12184.
Gischler, E., Hudson, J.H., 2019. Holocene tropical reef accretion and lagoon sedimentation: A quantitative approach to the influence of sea-level rise, climate and subsidence (Belize, Maldives, French Polynesia). Depositional Rec. 5 (3), 515–539. https://doi.org/10.1002/dep2.62.
Gischler, E., Hudson, J.H., Pisera, A., 2008. Late Quaternary reef growth and sea level in the Maldives (Indian Ocean). Mar. Geol. 250 (1), 104–113. https://doi.org/10.1016/j.margeo.2008.01.004.
Gischler, E., Ginsburg, R.N., Herrle, J.O., Prasad, S., 2010. Mixed carbonates and siliciclastics in the Quaternary of southern Belize: Pleistocene turning points in reef development controlled by sea-level change. Sedimentology 57 (4), 1049–1068. https://doi.org/10.1111/j.1365-3091.2009.01133.x.
Goldhammer, R.K., Lehmann, P.J., 1993. The origin of high-frequency platform carbonate cycles and third-order sequences (lower Ordovician El Paso Gp, West Texas): Constraints from outcrop data and stratigraphic modeling. J. Sediment. Res. 63. https://doi.org/10.1306/D4267AFA-2B26-11D7-8648000102C1865D.
Grammer, G.M., Ginsburg, R.N., Harris, P.M., 1993. Timing of deposition, diagenesis, and failure of steep carbonate slopes in response to a high-amplitude/high-frequency fluctuation in sea level, Tongue of the Ocean, Bahamas.
Green, R.H., Lowe, R.J., Buckley, M.L., 2018. Hydrodynamics of a tidally forced coral reef atoll. J. Geophys. Res. Oceans 123 (10), 7084–7101. https://doi.org/10.1029/2018JC013946.
Green, R.H., Lowe, R.J., Buckley, M.L., Foster, T., Gilmour, J.P., 2019. Physical mechanisms influencing localized patterns of temperature variability and coral bleaching within a system of reef atolls. Coral Reefs 38, 759–771.
Greenstein, B.J., Pandolfi, J.M., 2008. Escaping the heat: Range shifts of reef coral taxa in coastal Western Australia. Glob. Chang. Biol. 14 (3), 513–528. https://doi.org/10.1111/j.1365-2486.2007.01506.x.
Grimaldi, C.M., Faubel, C., Thomas, L., Sahin, A.D., Ryan, N.M., Rayson, M., Green, R., Cuttler, M.W., Treml, E.A., Lowe, R.J., Gilmour, J.P., 2024. Local coral connections within an atoll reef system underlie reef resilience and persistence. Limnol. Oceanogr. 69 (12), 3020–3032. https://doi.org/10.1002/LNO.12720.
Gurnis, M., Kominz, M., Gallagher, S.J., 2020. Reversible subsidence on the North West Shelf of Australia. Earth Planet. Sci. Lett. 534, 116070. https://doi.org/10.1016/j.epsl.2020.116070.
Haq, B.U., Hardenbol, J.A.N., Vail, P.R., 1987. Chronology of fluctuating sea levels since the Triassic. Science 235 (4793), 1156–1167.
Harbaugh, J.W., Watney, W.L., Rankey, E.C., Slingerland, R., Goldstein, R.H., Franseen, E.K., 1999. Numerical Experiments in Stratigraphy: Recent Advances in Stratigraphic and Sedimentologic Computer Simulations: Tulsa. SEPM (Society for Sedimentary Geology), Oklahoma, p. 245.
He, Y., Wang, H., Liu, Z., 2021. Development of the Leeuwin current on the northwest shelf of Australia through the pliocene-pleistocene period. Earth Planet. Sci. Lett. 559, 116767. https://doi.org/10.1016/j.epsl.2021.116767.
Hengesh, J.V., Whitney, B.B., 2016. Transcurrent Reactivation of Australia's Western Passive Margin: An Example of Intraplate Deformation from the Central Indo-Australian Plate. Tectonics (Washington, D.C.) vol. 35 (5), 1066–1089. https://doi.org/10.1002/2015TC004103.
Herbert, T.D., 2023. The Mid-Pleistocene climate transition. Annu. Rev. Earth Planet. Sci. 51 (1), 389–418. https://doi.org/10.1146/annurev-earth-032320-104209.
Hill, J., 2006. Modelling of Reefs and Shallow Marine Carbonates. Ph.D. thesis,. University of Edinburgh, p. 210.
Hill, J., Tetzlaff, D., Curtis, A., Wood, R., 2009. Modeling shallow marine carbonate depositional systems. Comput. Geosci. 35 (9), 1862–1874. https://doi.org/10.1016/j.cageo.2008.12.006.
Hill, J., Wood, R., Curtis, A., Tetzlaff, D.M., 2012. Preservation of forcing signals in shallow water carbonate sediments. Sediment. Geol. 275–276, 79–92. https://doi.org/10.1016/j.sedgeo.2012.07.017.
Hongo, C., Kayanne, H., 2009. Holocene coral reef development under windward and leeward locations at Ishigaki Island, Ryukyu Islands, Japan. Sediment. Geol. 214 (1), 62–73. https://doi.org/10.1016/j.sedgeo.2008.01.011.
Huisman, J.M., Leliaert, F., Verbruggen, H., Townsend, R.A., 2009. Marine benthic plants of Western Australia's shelf-edge atolls: Records of the Western Australian Museum. Supplement 77, 50–87.
Humblet, M., Webster, J.M., 2017. Coral community changes in the Great Barrier Reef in response to major environmental changes over glacial-interglacial timescales. Palaeogeogr. Palaeoclimatol. Palaeoecol. 472, 216–235. https://doi.org/10.1016/j.palaeo.2017.02.003.
Husson, L., Pastier, A.M., Pedoja, K., Elliot, M., Paillard, D., Authemayou, C., Sarr, A.C., Schmitt, A., Cahyarini, S.Y., 2018. Reef carbonate productivity during Quaternary Sea level oscillations: Geochemistry. Geophys. Geosyst. 19 (4), 1148–1164.
Jiménez, G., Latiff, A.H.A., Ben Habel, W., Poppelreiter, M., 2024. Effective application of geological process modeling for unraveling carbonate build-up complexity: A case

study from the EX-Carbonate build-up in central Luconia Province, Malaysia. Mar. Pet. Geol. 170, 107117.
Jorry, S.J., Camoin, G.F., Jouet, G., Roy, P.L., Vella, C., Courgeon, S., Borgomano, J., 2016. Modern sediments and Pleistocene reefs from isolated carbonate platforms (Iles Eparses, SW Indian Ocean): A preliminary study. Acta Oecol. (Montrouge) 72, 129–143. https://doi.org/10.1016/j.actao.2015.10.014.
Keep, M., Harrowfield, M., 2008. Elastic flexure and distributed deformation along Australia's North West Shelf: Neogene tectonics of the Bonaparte and Browse basins. Geol. Soc. Lond. Spec. Publ. 306 (1), 185–200. https://doi.org/10.1144/SP306.9.
Keep, M., Harrowfield, M., Crowe, W., 2007. The Neogene tectonic history of the North West Shelf, Australia. Explor. Geophys. 38 (3), 151–174.
Keep, M., Holbourn, A., Kuhnt, W., Gallagher, S., 2018. Progressive Western Australia collision with Asia: Implications for regional orography, oceanography, climate, and marine biota. J. R. Soc. West. Aust. 101, 1–16.
Kennedy, D.M., Woodroffe, C.D., 2000. Holocene lagoonal sedimentation at the latitudinal limits of reef growth, Lord Howe Island, Tasman Sea. Mar. Geol. 169, 287–304. https://doi.org/10.1016/S0025-3227(00)00093-1.
Kolodka, C., Vennin, E., Bourillot, R., Granjeon, D., Desaubliaux, G., 2016. Stratigraphic modelling of platform architecture and carbonate production: A Messinian case study (Sorbas Basin, SE Spain). Basin Res. 28 (5), 658–684.
Lange, I.D., Benkwitt, C.E., McDevitt-Irwin, J.M., Tietjen, K.L., Taylor, B., Chinkin, M., Gunn, R.L., Palmisciano, M., Steyaert, M., Wilson, B., East, H.K., Turner, J., Graham, N.A.J., Perry, C.T., 2021. Wave exposure shapes reef community composition and recovery trajectories at a remote coral atoll. Coral Reefs 40 (6), 1819–1829.
Liu, J., Webster, J.M., Salles, T., Wang, S., Ma, Y., Xu, W., Li, G., Yan, W., 2022. The formation of atolls: New insights from numerical simulations. J. Geophys. Res.: Earth Surf. v. 127, no. 8.
Logan, B.W., Bass, M.N., Cebulski, D.E., 1969. Carbonate sediments and reefs, Yucatan shelf, Mexico. AAPG Mem. 11, 1–128.
Lowe, R.J., Falter, J.L., 2015. Oceanic forcing of coral reefs. Annu. Rev. Mar. Sci. 7 (1), 43–66.
Marshall, J.F., Davies, P.J., 1981. Submarine lithification on windward reef slopes: Capricorn-Bunker Group, southern Great Barrier Reef. J. Sediment. Res. 51. https://doi.org/10.1306/212F7DEC-2B24-11D7-8648000102C1865D.
Marshall, N.G., Lang, S.C., 2013. A new sequence stratigraphic framework for the North West Shelf, Australia. In: Keep, M., Moss, S. (Eds.), The Sedimentary Basins of Western Australia 4: Proceedings of the Petroleum Exploration Society of Australia Symposium: Perth, Petroleum Exploration Society of Australia, pp. 18–21.
Masiero, I., Kozlowski, E., Antonatos, G., Xi, H., Burgess, P., 2020. Numerical stratigraphic forward models as conceptual knowledge repositories and experimental tools: an example using a new enhanced version of CarboCAT. Comput. Geosci. 138, 104453.
McCaffrey, J.C., Wallace, M.W., Gallagher, S.J., 2020. A cenozoic Great barrier reef on Australia's North West Shelf. Glob. Planet. Chang. 184, 103048. https://doi.org/10.1016/j.gloplacha.2019.103048.
McCaffrey, J.C., Gallagher, S.J., Wallace, M.W., Averes, T., Fabian, S.G., Lindhorst, K., Krastel, S., 2025. The Rowley Shoals atolls: Remnants of a Miocene great barrier reef on the north-west Australian margin. Glob. Planet. Chang. 245, 104688. https://doi.org/10.1016/j.gloplacha.2024.104688.
Michel, J., Laugié, M., Pohl, A., Lanteaume, C., Masse, J.-P., Donnadieu, Y., Borgomano, J., 2019. Marine carbonate factories: A global model of carbonate platform distribution. Int. J. Earth Sci. 108 (6), 1773–1792. https://doi.org/10.1007/s00531-019-01742-6.
Miller, K.G., Browning, J.V., Schmelz, W.J., Kopp, R.E., Mountain, G.S., Wright, J.D., 2020. Cenozoic Sea-level and cryospheric evolution from deep-sea geochemical and continental margin records. Sci. Adv. 6 (20), eaaz1346. https://doi.org/10.1126/sciadv.aaz1346.
Montaggioni, L.F., 2005. History of Indo-Pacific coral reef systems since the last glaciation: Development patterns and controlling factors. Earth Sci. Rev. 71 (1), 1–75. https://doi.org/10.1016/j.earscirev.2005.01.002.
Montaggioni, L.F., Martin-Garin, B., 2020. Quaternary development history of coral reefs from West Indian islands: A review. Int. J. Earth Sci. 109 (3), 911–930. https://doi.org/10.1007/s00531-020-01839-3.
Montaggioni, L.F., Cabioch, G., Thouveny, N., Frank, N., Sato, T., S'emah, A.-M., 2011. Revisiting the Quaternary development history of the western New Caledonian shelf system: from ramp to barrier reef. Mar. Geol. 280 (1–4), 57–75. https://doi.org/10.1016/j.margeo.2010.12.001.
Montaggioni, L.F., Borgomano, J., Fournier, F., Granjeon, D., 2015. Quaternary atoll development: new insights from the two-dimensional stratigraphic forward modelling of Mururoa Island (Central Pacific Ocean). Sedimentology 62 (2), 466–500. https://doi.org/10.1111/sed.12175.
Omidpour, A., Moussavi-Harami, R., Mahboubi, A., Rahimpour-Bonab, H., 2021. Application of stable isotopes, trace elements and spectral gamma-ray log in resolving high-frequency stratigraphic sequences of a mixed carbonate-siliciclastic reservoirs. Mar. Pet. Geol. 125, 104854.
Palei, R.R., Gupta, A.K., Sanyal, P., Jaiswal, M.K., 2024. Leeuwin current dynamics in the SE Indian Ocean and implications for regional surface hydrography since the latest Miocene: Results from ODP Site 763A. Glob. Planet. Chang. 237, 104459. https://doi.org/10.1016/j.gloplacha.2024.104459.
Pall, J., Chandra, R., Azam, D., Salles, T., Webster, J.M., Scalzo, R., Cripps, S., 2020. Bayesreef: A Bayesian inference framework for modelling reef growth in response to environmental change and biological dynamics. Environ. Model Softw. 125, 104610. https://doi.org/10.1016/j.envsoft.2019.104610.
Pandey, V.K., Bhatt, V., Pandey, A.C., Das, I.M.L., 2007. Impact of Indonesian throughflow blockage on the southern Indian Ocean. Curr. Sci. 93 (3), 399–406.
Pastier, A.M., Husson, L., Pedoja, K., Bézos, A., Authemayou, C., Arias-Ruiz, C., Cahyarini, S.Y., 2019. Genesis and architecture of sequences of Quaternary coral reef terraces: Insights from numerical models: Geochemistry. Geophys. Geosyst. 20 (8), 4248–4272.
Paumard, V., Zuckmeyer, E., Boichard, R., Jorry, S.J., Bourget, J., Borgomano, J., Maurin, T., Ferry, J.-N., 2017. Evolution of late Oligocene - early Miocene attached and isolated carbonate platforms in a volcanic ridge context (Maldives type), Yadana field, offshore Myanmar. Mar. Pet. Geol. 81, 361–387. https://doi.org/10.1016/j.marpetgeo.2016.12.012.
Petrick, B., Martínez-García, A., Auer, G., Reuning, L., Auderset, A., Deik, H., Takayanagi, H., De Vleeschouwer, D., Iryu, Y., Haug, G.H., 2019. Glacial Indonesian Throughflow weakening across the Mid-Pleistocene Climatic transition. Sci. Rep. 9 (1), 16995. https://doi.org/10.1038/s41598-019-53382-0.
Pomar, L., 2001. Types of carbonate platforms: a genetic approach. Basin Res. 13, 313–334.
Pomar, L., Hallock, P., 2008. Carbonate factories: A conundrum in sedimentary geology. Earth Sci. Rev. 87 (3), 134–169. https://doi.org/10.1016/j.earscirev.2007.12.002.
Posamentier, H.W., Allen, G.P., 1999. Attributes of key surfaces. In: Posamentier, H.W., Allen, G.P. (Eds.), Siliciclastic Sequence Stratigraphy: Concepts and Applications. SEPM (Society for Sedimentary Geology) Concepts in Sedimentology and Paleontology No. 7, pp. 105–119. https://doi.org/10.2110/csp.99.07.0053.
Prat, S., Jorry, S.J., Jouet, G., Camoin, G., Vella, C., Le Roy, P., Pastol, Y., 2016. Geomorphology and sedimentology of a modern isolated carbonate platform: The Glorieuses archipelago, SW Indian Ocean. Mar. Geol. 380, 272–283.
Puotinen, M., Drost, E., Lowe, R., Depczynski, M., Radford, B., Heyward, A., Gilmour, J., 2020. Towards modelling the future risk of cyclone wave damage to the world's coral reefs. Glob. Chang. Biol. 26, 4302–4315. https://doi.org/10.1111/gcb.15136.
Rankey, E.C., 2016. On facies belts and facies mosaics: Holocene isolated platforms, South China Sea. Sedimentology 63 (7), 2190–2216.
Rankey, E.C., 2020. Eustatic, climatic, and oceanographic influences on geomorphology and architecture of isolated carbonate platforms: Miocene, Northwest Shelf, Australia. Lithosphere 2020 (1), 8844754.
Read, J.F., Osleger, D., Elrick, M., 1991. Two-dimensional modeling of carbonate ramp sequences and component cycles: Kansas Geological Survey. Bulletin 233, 473–488.
Read, J.F., Li, M., Hinnov, L.A., Nelson, C.S., Hood, S., 2020. Testing for astronomical forcing of cycles and gamma ray signals in outer shelf/upper slope, mixed siliciclastic-carbonates: upper Oligocene, New Zealand. Palaeogeogr. Palaeoclimatol. Palaeoecol. 555, 109821.
Reijmer, J.J., 2021. Marine carbonate factories: Review and update. Sedimentology 68 (5), 1729–1796.
Reijmer, J.J., De Kruijf, M., Slootman, A., Kranenburg, L.J., De Boer, R.A., 2025. Experiments on the settling of carbonate sand–mud suspensions. J. Sediment. Res. 95 (1), 28–48.
Riera, R., Bourget, J., Håkansson, E., Paumard, V., Wilson, M.E.J., 2021. Middle Miocene tropical oligotrophic lagoon deposit sheds light on the origin of the Western Australian coral reef province. Palaeogeogr. Palaeoclimatol. Palaeoecol. 576, 110501. https://doi.org/10.1016/j.palaeo.2021.110501.
Riera, R., Paumard, V., Bourget, J., Allan, T., Lebrec, U., 2023. Evolution of the Exmouth-Barrow carbonate margin through the Miocene: Insights from 3D seismic data and field investigations (North West Shelf, Australia). Sediment. Geol. 449, 106371.
Rosleff-Soerensen, B., Reuning, L., Back, S., Kukla, P., 2012. Seismic geomorphology and growth architecture of a Miocene barrier reef, Browse Basin, NW-Australia. Mar. Pet. Geol. 29 (1), 233–254. https://doi.org/10.1016/j.marpetgeo.2010.11.001.
Salles, T., Pall, J., Webster, J.M., Dechnik, B., 2018. Exploring coral reef responses to millennial-scale climatic forcings: Insights from the 1-D numerical tool pyReef-Core v1.0. Geosci. Model Dev. 11 (6), 2093–2110. https://doi.org/10.5194/gmd-11-2093-2018.
Saqab, M.M., Bourget, J., 2015. Controls on the distribution and growth of isolated carbonate build-ups in the Timor Sea (NW Australia) during the Quaternary. Mar. Pet. Geol. 62, 123–143. https://doi.org/10.1016/j.marpetgeo.2015.01.014.
Saqab, M.M., Bourget, J., 2016. Seismic geomorphology and evolution of early–mid Miocene isolated carbonate build-ups in the Timor Sea, North West Shelf of Australia. Mar. Geol. 379, 224–245.
Schlager, W., 1981. The paradox of drowned reefs and carbonate platforms. Geol. Soc. Am. Bull. 92 (4), 197–211.
Schlager, W., 2000. Sedimentation rates and growth potential of tropical, cool-water, and mud-mound carbonate systems: carbonate Platform Systems. Component. Interact. 178 (1), 217–227. https://doi.org/10.1144/GSL.SP.2000.178.01.14.
Schlager, W., 2005. Carbonate sedimentology and sequence stratigraphy: SEPM (Society for Sedimentary Geology). Concepts Sedimentol. Paleontol. no. 8.
Seard, C., Borgomano, J., Granjeon, D., Camoin, G., Riegl, B., 2013. Impact of environmental parameters on coral reef development and drowning: Forward modelling of the last deglacial reefs from Tahiti (French Polynesia; IODP Expedition #310). Sedimentology 60 (6), 1357–1388. https://doi.org/10.1111/sed.12030.
Šimíček, D., Bábek, O., Leichmann, J., 2012. Outcrop gamma-ray logging of siliciclastic turbidites: Separating the detrital provenance signal from facies in the foreland-basin turbidites of the Moravo-Silesian Basin, Czech Republic. Sediment. Geol. 261, 50–64.
Struckmeyer, H.I., Blevin, J.E., Sayers, J., Totterdell, J.M., Baxter, K., Cathro, D.L., 1998. Structural evolution of the Browse Basin, North West Shelf: New concepts from deep-seismic data: the Sedimentary Basins of Western Australia II. Petrol. Explorat. Soc. Australia (PESA) 345–367.
Sultana, D., Burgess, P., Bosence, D., 2022. How do carbonate factories influence carbonate platform morphology? Exploring production– transport interactions with numerical forward modelling. Sedimentology 69 (1), 372–393.
Tella, T.O., Winterleitner, G., Morsilli, M., Mutti, M., 2022. Testing Sea-level and carbonate production effects on stratal architecture of a distally steepened carbonate

ramp (Upper Miocene, Menorca): A 3D forward modelling approach. Sediment. Geol. 441, 106267.
Tetzlaff, D.M., 1986. Computer simulation model of clastic sedimentary processes. AAPG Bull. 70. https://doi.org/10.1306/9488621D-1704-11D7-8645000102C1865D.
Tetzlaff, D., Priddy, G., Merriam, D.F., Davis, J.C., 2001. Sedimentary process modeling: From academia to industry. In: Merriam, D.F., Davis, J.C. (Eds.), Geologic Modeling and Simulation. Springer, United States, pp. 45–69. https://doi.org/10.1007/978-1-4615-1359-9_4.
Thompson, D.M., 2022. Environmental records from coral skeletons: A decade of novel insights and innovation. Wiley Interdiscip. Rev. Clim. Chang. 13, e745.
Thronberens, S., Back, S., Bourget, J., Allan, T., Reuning, L., 2022. 3-D seismic chronostratigraphy of reefs and drifts in the Browse Basin, NW Australia. Geol. Soc. Am. Bull. 134 (11–12), 3155–3175. https://doi.org/10.1130/B36286.1.
Van der Looven, T., Winterleitner, G., Betzler, C., Mutti, M., 2022. A biotic perspective on the Oligo-Miocene evolution of the Maldives carbonate platform from forward stratigraphic modelling (Indian Ocean). Mar. Pet. Geol. 145, 105907. https://doi.org/10.1016/j.marpetgeo.2022.105907.
Van Tuyl, J., Alves, T., Cherns, L., Antonatos, G., Burgess, P., Masiero, I., 2019. Geomorphological evidence of carbonate build-up demise on equatorial margins: a case study from offshore Northwest Australia. Mar. Pet. Geol. 104, 125–149. https://doi.org/10.1016/j.marpetgeo.2019.03.006.
Van Wagoner, J.C., Mitchum, R.M., Campion, K.M., Rahmanian, V.D., 1990. Siliciclastic Sequence Stratigraphy in Well Logs, Cores, and Outcrops: Concepts for High-Resolution Correlation of Time and Facies, vol. 7. American Association of Petroleum Geologists, Tulsa, Okla., U.S.A.
Waelbroeck, C., Labeyrie, L., Michel, E., Duplessy, J.C., McManus, J.F., Lambeck, K., Labracherie, M., 2002. Sea-level and deep water temperature changes derived from benthic foraminifera isotopic records. Quat. Sci. Rev. 21 (1), 295–305. https://doi.org/10.1016/S0277-3791(01)00101-9.
Wang, H., Villas Bôas, A.B., Vanneste, J., Young, W.R., 2025. Scattering of surface waves by ocean currents: the U2H map', Journal of fluid mechanics. In: Watanabe, Y., Abe-Ouchi, A., Saito, F., Kino, K., O'ishi, R., Ito, T., Kawamura, K., Chan, W.L. (Eds.), Astronomical forcing shaped the timing of early Pleistocene glacial cycles: Communications Earth & Environment, 1005, p. 113.
Warren, J., 2000. Dolomite: Occurrence, evolution and economically important associations. Earth Sci. Rev. 52, 1–81. https://doi.org/10.1016/S0012-8252(00)00022-2.
Warrlich, G.M.D., Waltham, D.A., Bosence, D.W.J., 2002. Quantifying the sequence stratigraphy and drowning mechanisms of atolls using a new 3-D forward stratigraphic modelling program (CARBONATE 3D). Basin Res. 14 (3), 379–400. https://doi.org/10.1046/j.1365-2117.2002.00181.x.
Watanabe, Y., Abe-Ouchi, A., Saito, F., Kino, K., O'ishi, R., Ito, T., Chan, W.-L., 2023. Astronomical forcing shaped the timing of early Pleistocene glacial cycles. Commun. Earth Environ. 4, 7. https://doi.org/10.1038/s43247-023-00765-x.
Watney, W.L., Rankey, E.C., Harbaugh, J., 1999. Perspectives on stratigraphic simulation models: current approaches and future opportunities. In: Harbaugh, J.H., Watney, W.L., Rankey, E.C., Slingerland, R., Goldstein, R.H., Franseen, E.K. (Eds.), Numerical Experiments in Stratigraphy: SEPM Special Publication, 62, pp. 3–21.
Webb, G.E., 2025. Australia's two Great Barrier Reefs: what can ~360 Million Years of Change Teach Us? J. Mar. Sci. Eng. 13 (8), 1582. https://doi.org/10.3390/jmse13081582.
Webster, J.M., Davies, P.J., 2003. Coral variation in two deep drill cores: significance for the Pleistocene development of the Great Barrier Reef. Sediment. Geol. 159 (1), 61–80. https://doi.org/10.1016/S0037-0738(03)00095-2.
Webster, J.M., Clague, D.A., Riker-Coleman, K., Gallup, C., Braga, J.C., Potts, D., Paull, C. K., 2004. Drowning of the −150 m reef off Hawaii: A casualty of global meltwater pulse 1A? Geology 32 (3), 249–252. https://doi.org/10.1130/G20170.1.
Webster, J.M., Braga, J.C., Clague, D.A., Gallup, C., Hein, J.R., Potts, D.C., Wallace, L.M., 2009. Coral reef evolution on rapidly subsiding margins. Glob. Planet. Chang. 66 (1), 129–148. https://doi.org/10.1016/j.gloplacha.2008.07.010.
Webster, J.M., Dechnik, B., Sanborn, K., Yokoyama, Y., Braga, J.C., Renema, W., Humblet, M., Beaman, R.J., Nothdurft, L.D., Webb, G.E., and Zhao, J.X., 2022, Coral reef development and sea-level changes over the past 50,000 years: New evidence from the North-West Shelf of Australia: in: Camoin, G.F., Hallmann, N. (Eds.), Coral Reefs and Sea-Level Change: Quaternary Records and Modelling, special Publication 49. International Association of Sedimentologists, pp. 215-273.
Whitney, B.B., Hengesh, J.V., Gillam, D., 2016. Styles of neotectonic fault reactivation within a formerly extended continental margin, North West Shelf, Australia. Tectonophysics 686, 1–18. https://doi.org/10.1016/j.tecto.2016.06.008.
Wijeratne, S., Pattiaratchi, C., Proctor, R., 2018. Estimates of surface and subsurface boundary current transport around Australia. J. Geophys. Res. Oceans 123 (5), 3444–3466. https://doi.org/10.1029/2017JC013221.
Wilkinson, B.H., Drummond, C.N., Diedrich, N.W., Rothman, E.D., 1999. Poisson processes of carbonate accumulation on Paleozoic and Holocene platforms. J. Sediment. Res. 69 (2), 338–350.
Williams, H.D., Burgess, P.M., Wright, V.P., Della Porta, G., Granjeon, D., 2011. Investigating carbonate platform types: Multiple controls and a continuum of geometries. J. Sediment. Res. 81 (1), 18–37. https://doi.org/10.2110/jsr.2011.6.
Williams, C., Paumard, V., Webster, J.M., Leonard, J., Salles, T., O'Leary, M., Lang, S., 2023. Environmental controls on the resilience of Scott Reef since the Miocene (North West Shelf, Australia): Insights from 3D seismic data. Mar. Pet. Geol. 151, 106188. https://doi.org/10.1016/j.marpetgeo.2023.106188.
Wilson, B., 2013. The Biogeography of the Australian North West Shelf: Environmental Change and Life's Response, First edition. Elsevier, p. 640. https://doi.org/10.1016/C2012-0-00618-7.
Woodroffe, C.D., Webster, J.M., 2014. Coral reefs and sea-level change. Mar. Geol. 352, 248–267. https://doi.org/10.1016/j.margeo.2013.12.006.
Wright, V.P., Burgess, P.M., 2005. The carbonate factory continuum, facies mosaics, and microfacies: an appraisal of some of the key concepts underpinning carbonate sedimentology. Facies 51 (1–4), 17–23. https://doi.org/10.1007/s10347-005-0049-6.
Wu, F., Xie, X., Zhu, Y., Coletti, G., Betzler, C., Cui, Y., Shang, Z., 2021. Early development of carbonate platform (Xisha Islands) in the northern South China Sea. Mar. Geol. 441, 106629. https://doi.org/10.1016/j.margeo.2021.106629.
Yamamoto, K., Iryu, Y., Sato, T., Chiyonobu, S., Sagae, K., Abe, E., 2006. Responses of coral reefs to increased amplitude of sea-level changes at the Mid-Pleistocene climate transition: Palaeogeography. Palaeoclimatol. Palaeoecol. 241 (1), 160–175.
Yao, Y., Li, Z., Xu, C., Jiang, C., 2023. A study of wave-driven flow characteristics across a reef under the effect of tidal current. Appl. Ocean Res. 130.
Zhao, S., Grant, K.M., Heslop, D., Gallagher, S.J., Bolton, C.T., Auer, G., 2024. Early Pleistocene orbital-scale variability in Australian Northwest Shelf sediments. Paleoceanogr. Paleoclimato. v. 39, no. 10. https://doi.org/10.1029/2024PA005015.

CHAPTER 5

ARTICLE 4: Chronostratigraphic, Paleoecological and Paleoenvironmental Reconstructions of Scott Reef, North West Shelf, Australia: Evidence from Pleistocene Fossil Reef Cores

---

Williams, C., Webster, J. M., Humblet, M., Braga, J. C., Lowe, A., Murphy, R., Renema, W., Nothdurft, L., Webb, G., Zhao, J., Paumard, V., Lebrec, U., Salles, T., Duyker, S., Wilson, M., and Testa, V. 2025, Chronostratigraphic, paleoecological and paleoenvironmental reconstructions of Scott Reef, Northwest Shelf, Australia: evidence from Pleistocene fossil reef cores. (This chapter is intended for submission to *Quaternary Science Reviews*).

This paper presents a detailed, multi-proxy sedimentological, paleoecological, and chronological reconstruction of three high-recovery Pleistocene reef cores from North and South Scott Reef. The resulting chronostratigraphic model resolves seven reef-growth units on the North Reef (MIS 15–present), seven units on the South Reef SE margin (MIS 11–present), and four units on the South Reef leeward margin (MIS 9–present), bounded by regionally correlatable exposure surfaces and paleosols. Coral and coralline algal assemblages provide a robust framework for resolving paleowater depths and defining three depositional environments (reef crest/shallow slope, intermediate slope, and deep slope), revealing an overall shallowing-upwards platform evolution initiating during MIS 9. Preservation contrasts across the platforms demonstrate that closed-system U/Th ages are best supported on the South Reef SE margin, whereas pervasive diagenesis, dolomitisation, and iron-rich alteration—particularly during MIS 7—record complex fluid–rock interaction linked to repeated

exposure and variable subsidence. Comparison with Ribbon Reef 5 indicates some significant lithologic and facies differences but highlights broadly similar long-term reef resilience, despite contrasting subsidence regimes and stratigraphic architectures.

Author contributions: I designed the analytical workflow, conducted core logging and multi-proxy analyses, interpreted the sedimentological, paleoenvironmental, and sequence-stratigraphic framework, and wrote the manuscript. Jody Webster provided guidance on reef stratigraphy, coral reef development, and regional context. Marc Humblet and Juan Carlos Braga contributed expertise in coral and coralline algal taxonomy and paleoecological interpretation. Jianxin Zhao produced the U-Th ages. Alexander Lowe, Richard Murphy, and Samuel Duyker contributed to hyperspectral imaging, mineralogical analyses, and data processing. Willem Renema provided expertise on foraminifera taxonomic identification. Luke Nothdurft and Gregory Webb contributed to petrographic, diagenetic, and SEM interpretations. Victorien Paumard, Ulysse Lebrac and Tristan Salles provided input on seismic stratigraphy, chronostratigraphic integration and modelling concepts. Moyra Wilson provided advice on diagenetic and paleosol interpretations, and Vivienne Testa contributed to the regional geological context and data integration. All authors reviewed and approved the final manuscript.

Supplementary material: Appendices I–R correspond to Supplementary Materials 1–10, as cited in this chapter. High-resolution versions of the images can be accessed by clicking on the figures.

TABLE 5.1: Summary of chapter 5: Chronostratigraphic, Paleoecological and Paleoenvironmental Reconstructions of Scott Reef Pleistocene Cores.

Component	**Summary**
Scope	Multi-proxy reconstruction of Pleistocene reef evolution using three high-recovery cores from North and South Scott Reef, spanning multiple glacial–interglacial cycles (MIS 15–present).
Objectives	Establish a robust Quaternary chronostratigraphic framework; constrain paleowater depths and depositional environments using coral and coralline algal assemblages; assess spatial variability in reef growth and preservation; compare Scott Reef evolution with Ribbon Reef 5.
Data and Methods	Integrated core logging, coral and coralline algal assemblage analysis, hyperspectral imaging, neutron computed tomography, XRD, SEM, thin-section petrography, and rigorously screened closed-system U/Th geochronology.
Key Results	Seven reef-growth units identified on the North Reef (MIS 15–present), seven on the South Reef SE margin (MIS 11–present), and four on the leeward margin (MIS 9–present), bounded by regionally correlatable exposure surfaces and paleosols.
Depositional Environments	Three depth-controlled environments defined: reef crest/shallow slope ($<$10 m), intermediate slope (15–30 m), and deep slope ($>$30–60 m), recording an overall shallowing-upwards platform evolution initiating during MIS 7.
Preservation and Diagenesis	Best-preserved closed-system U/Th ages occur on the South Reef SE margin; pervasive diagenesis, dolomitisation, and iron-rich alteration—particularly during MIS 7—reflect repeated exposure, variable subsidence, and fluid–rock interaction.
Major Insights	Reef inception likely initiated during MIS 15 near the Mid-Pleistocene Climate Transition; reef growth trajectories diverged during the Holocene, ranging from keep-up to give-up behaviour across platform margins.
Regional Context	Comparison with Ribbon Reef 5 indicates some significant lithologic and facies differences, but broadly similar long-term reef resilience despite contrasting subsidence regimes and stratigraphic architectures.
Broader Significance	Provides one of the most continuous far-field tropical Quaternary reef records globally, offering critical constraints on reef response to sea-level change, climate variability, and long-term platform resilience.

Chronostratigraphic, paleoecological and paleoenvironmental reconstructions of Scott Reef, Northwest Shelf, Australia: evidence from Pleistocene fossil reef cores

Author names and affiliations
Carra Williams[1, 7], Jody M. Webster[1], Marc Humblet[1, 2], Juan Carlos Braga[3], Alexander Lowe[4], Richard Murphy[4], Willem Renema[5], Luke Nothdurft[6], Gregory Webb[7], Jianxin Zhao[7], Victorien Paumard[1, 8, 9], Ulysse Lebrec[8], Tristan Salles[1], Samuel Duyker[10], Moyra Wilson[1, 8], Vivian Testa[11]

[1] Geocoastal Research Group, School of Geosciences, Madsen Building F09, University of Sydney, NSW, 2006, Australia
[2] Department of Earth and Planetary Sciences, Nagoya University, Nagoya, Japan
[3] Departamento de Estratigrafía y Paleontología, Universidad de Granada, Granada, Spain
[4] Australian Centre for Field Robotics, Room 310, Sydney Robotics Hub J18, Sydney, Australia
[5] Naturalis Biodiversity Centre, Leiden, The Netherlands & Department of Ecosystem & Landscape Dynamics, Institute for Biodiversity & Ecosystem Dynamics, University of Amsterdam, Amsterdam, The Netherlands
[6] Queensland University of Technology, School of Earth and Atmospheric Sciences, 4000 Brisbane, Australia
[7] University of Queensland, School of the Environment, 4072 Brisbane, Australia
[8] Centre for Energy and Climate Geoscience, School of Earth Sciences, The University of Western Australia, 35 Stirling Highway, Perth WA 6009, Australia
[9] UWA Oceans Institute, The University of Western Australia, 35 Stirling Highway, Perth WA 6009, Australia
[10] Sydney Analytical, University of Sydney, NSW, 2006, Australia
[11] Lesmurdie, Western Australia

carra.williams@sydney.edu.au; jody.webster@sydney.edu.au; humblet.marc.n3@f.mail.nagoya-u.ac.jp; jbraga@ugr.es; alexander.lowe@sydney.edu.au; rjm011@icloud.com; willem.renema@naturalis.nl; l.nothdurft@uq.edu.au; g.webb@uq.edu.au; j.zhao@uq.edu.au; victorien.paumard@uwa.edu.au; ulysse.lebrec@uwa.edu.au; tristan.salles@sydney.edu.au; samuel.duyker@sydney.edu.au; moyra.wilson@uwa.edu.au; testa@westnet.com.au

Keywords: *Fossil coral reef core, Mid Pleistocene Climate Transition, Scott Reefs, Northwest Shelf, Australia, paleoclimate, sedimentological and stratigraphic record*

Abstract

Three Pleistocene fossil reef cores (maximum penetration 200 m and average recovery 88%) were collected in 2006 across the isolated carbonate platforms of North and South Scott Reef, Northwest Shelf, Australia. This high-quality database is perhaps the best-known continuous core data in the region. The cores provide a unique opportunity to document the lithological and coral community changes within a chronological context in response to major

Quaternary sea-level oscillations and associated environmental changes. Although Quaternary reefs are excellent archives of past sea-level and climate, their efficacy for providing reliable paleoclimatic and paleochronological reconstructions relies on empirical chronologies that may be compromised by diagenetic alteration. We incorporate existing open-system U/Th ages presented for the first time in this study as the foundation for the geochronological model and introduce new Thompson-corrected open-system ages and new closed-system ages that, because they are based on detailed diagenetic vetting, improve the chronological resolution. Our approach integrates detailed logging, high-spatial resolution hyperspectral scanning, neutron computed tomography, petrologic and sedimentary facies analysis, to define paleoenvironmental reconstructions using coral and algal assemblages within a new chronostratigraphic model spanning 500 kyr. A diverse range of lithologies occur including *in situ* coralgal boundstone (reef framework facies), rudstone, grainstone, packstone, floatstone and wackestone, as well as microbialites. These lithologies occur in complex transitions, separated by discontinuous paleosol horizons that define key stratigraphic boundaries within each core. Diagenetic overprinting, including dolomitization and cementation, further modifies parts of the successions. Three coralline algal assemblages and four coral assemblages indicate a diverse range of reef settings from shallow reef crest (< 10 m) to deep forereef slope (> 60 m). We present the first detailed documentation of the coral reef communities that developed in Scott Reef from 515 kyr to present. Major reef building coral taxa identified in the fossil record are consistent with those occupying the modern environment including *Porites, Acropora, Montipora, Isopora, Pocillopora,* and *Heliopora*. We resolve seven chronostratigraphic packages on the North Reef (MIS 13 to present), seven on the South Reef SE margin (MIS 11 to present), and four on the South Reef leeward margin (MIS 9 to present). Packages are bounded by paleosols identified by calcrete or reddened soils and generally indicate shallowing upwards trends, with younger packages progressing from deep fore-reef

slope to shallow water reef crest environments. MIS 11–9 packages in the South Reef occurred in a deep reef setting, although transported coral rubble indicates the presence of high-energy shallow reef communities occurred by MIS 11. *In situ* shallow water high-energy assemblages are recorded on the North Reef since MIS 13 and the South Reef since MIS 9. The South Reef leeward margin failed to keep up with the rapid Holocene marine transgression, leading to a give-up reef. This was likely due to changing oceanographic factors, such as enhanced nutrient flux from upwelling associated with intensified monsoonal activity during interglacials, and increased accommodation associated with rapid subsidence. Comparisons with the Quaternary Ribbon Reef 5 (RR5) reef sequences on the NE margin of Australia indicate that despite differences in initial depositional setting – RR5 developing from a mesophotic open-shelf, and Scott Reef from a deeper forereef slope – as well as differences in subsidence regime, shelf geometry and local oceanographic conditions, both systems reveal broadly similar long-term reef development history from ca. MIS 15 to present. This includes broadly comparable coralgal assemblages, a distinct *Halimeda*-grainstone interval during MIS 5, and evidence of persistent ecological resilience and recovery following repeated subaerial exposure events. However, South Scott Reef experienced substantially higher subsidence rates (0.45 mm/yr) than RR5 (0.1 mm/yr), yet both systems exhibit broadly comparable long-term net accumulation rates, with ca. 180 m of reef strata accumulated over ca. 515 kyr at South Scott Reef (ca. 0.35 m/kyr) compared to ca. 210 m over ca. 700 kyr at RR5 (ca. 0.3 m/kyr). This indicates that RR5 records a longer temporal interval within a comparable stratigraphic thickness, resulting in a more condensed stratigraphic succession relative to South Scott Reef.

1. Introduction

Transgressive and highstand Quaternary coral reefs that develop on subsiding, far-field continental margins, such as the Northwest Shelf (NWS) of Australia, Great Barrier Reef

(GBR), and the Belize and New Caledonia Barrier Reefs (Cabioch et al., 2008; Montaggioni et al., 2011; Gischler et al., 2010; 2015; Gallagher et al., 2014; Gischler and Hudson., 2019; Webster et al., 2022) preserve long, stratigraphically continuous records of reef growth and their response to sea-level and associated climate change (Collins et al., 2011; Murray-Wallace and Woodroffe, 2014; Gischler, 2015). Although fossil reef archives have provided valuable insights into the nature of past sea-level and environmental change (Abbey et al., 2011; Yokoyama et al., 2011; 2018; Deschamps et al., 2012; Camoin et al., 2015; Webster et al., 2025), relatively few records preserve long-term sedimentological, chronostratigraphic and paleoecological evolution of reef systems through multiple glacial-interglacial cycles (Medina-Elizalde, 2013; Hibbert et al., 2016).

Quaternary evolution of Indo-Pacific mid-ocean atolls has been investigated using core data from Mururoa atoll (Montaggioni et al., 2015). Comparable Quaternary reef and carbonate platform records from other settings include the Huon Gulf (Webster et al., 2004), Caribbean reef provinces (Montaggioni and Braithwaite, 2009), and the Maldives (Alonso-Garcia et al., 2024). However, there remains a significant data gap in well-dated Indo-Pacific Quaternary reef records along the NWS of Australia beyond the Holocene and Last Interglacial. Fossil reef archives from the NWS, including Ashmore reef (Webster et al., 2022) and the Abrolhos Islands (Eisenhauer et al., 1993), provide important constraints late Quaternary reef development. However, continuous and chronologically robust reef records become increasingly sparse prior MIS 9 (ca. 330 kyr), and high-resolution reconstructions extending beyond MIS 5e remain rare both regionally and globally (Woodroffe and Webster, 2014; Medina-Elizalde, 2013; Hibbert et al., 2016). Available reef records are also biased toward tectonically uplifted regions, where subaerial exposure and accessibility facilitate sampling. However, prolonged exposure creates resulting in extensive diagenetic alteration complicates

reliable chronological reconstruction (Toscano et al., 2011; Medina-Elizalde, 2013; Murray-Wallace and Woodroffe, 2014; Camoin and Webster, 2015; Webster et al., 2022), or compressed stratigraphic records (e.g., Ryukyus Group; Yamamoto et al., 2006), which arguably also occur in relatively stable margins (Webster et al., 2009). Accurately resolving Quaternary sea-level history and the chronostratigraphic succession of distinct reef growth phases requires continuous reef cores with high recovery and reliable chronologies. As such, there is a pressing need for fossil coral records from long-lived reef systems with favourable preservation spanning the Quaternary to resolve earlier Pleistocene sea-level highstands (Murray-Wallace and Woodroffe, 2014; Woodroffe and Webster, 2014). Scott Reef is exceptional in providing three high quality, long cores with up to as much as 96% recovery, including two from the same platform, that offer a uniquely continuous record of Quaternary reef growth from a subsiding passive margin. To our knowledge no comparable data set exists globally.

Coral data from long-lived subsiding reef sites, such as Scott Reef, produce reliable indicators of sea-level variations because the creation of long term, stable and rapid accommodation produces expanded reef successions (Cabioch et al., 1999; Collins, 2002; 2010). Although subsidence rates are lower (ca. 0.3 – 0.45 mm/yr) than in hotspot regions such as Hawaii, (ca. 2–3 mm/yr), which produced significantly expanded stratigraphically continuous reef sections (Webster et al., 2007; 2009), preliminary studies of Scott Reef (Collins et al., 2009) indicate that prolonged, episodic stratigraphic reef sequences are preserved spanning > 500 kyr (MIS 15). These data provide a rare opportunity to investigate carbonate platform and coral reef response to local environmental and oceanographic forcing, in addition to glacio-eustatic change, far from former ice-covered regions (Yokoyama et al., 2001). In particular, sediment cores recovered during IODP expedition 356 (Gallagher et al., 2014; 2017)

document the long-term (5 Ma) variability in the Indonesian throughflow (ITF) along the NWS near Scott Reef, providing an opportunity to evaluate whether changes in ITF strength and associated oceanographic conditions influenced reef development through time.

Building upon earlier interpretations of Scott Reef (Collins, 2002; Collins et al., 2009; Collins, 2010) in this study, we apply a suite of high-resolution screening techniques, including 2-D hyperspectral imaging (Murphy et al., 2017), 3-D neutron computed tomography (NCT) (Christie et al., 2007; Williams et al., 2025), X-Ray diffraction (XRD), scanning electron microscopy (SEM) and thin section petrography (Nothdurft and Webb, 2007; 2009; Webb, 2024) to identify well-preserved *in situ* aragonitic coral suitable for dating. Three of the longest and most continuous Scott Reef cores (NRSEHDD3JA, SRSEBH6J, Hook 1P/3P) were analysed to develop and produce a more detailed and precise Quaternary stratigraphy and chronology of North Scott Reef (NSR) and South Scott Reef (SSR) carbonate platforms. We reassessed existing open-system U/Th ages from Scott Reef and generated new, robust closed-system ages that provide more precise and detailed chronological control. Dates were integrated with new detailed core logging to address three objectives. First, we identified variations in sedimentary facies and coral-algal assemblages to reconstruct their paleoenvironmental changes, relative sea-level fluctuations, and to correlate reef development with MISs during the mid-late Quaternary. Second, we identified broad diagenetic trends and paleosol horizons to reconstruct periods of platform emersion, which together with sedimentological descriptions, paleoenvironmental reconstructions and chronological constraints, were used to correlate sedimentary packages with MISs. These correlations provide a framework for evaluating how Quaternary climatic and environmental change influenced reef growth history and coral-algal assemblages. Finally, we compare Scott Reef on the NWS with Ribbon Reef 5 on the GBR to evaluate how different reef systems have responded to

Pleistocene sea-level and environmental change. They are chosen for comparison because they: (1) represent similar shelf edge environments, latitudes and climate, (2) the Pleistocene-Holocene reef at both sites have been studied, documenting long term evolution of coral assemblages during deglacial sea-level highstands (Collins et al., 2009; Webster and Davies, 2003; Braga and Aguirre, 2004; Braithwaite et al., 2004; Dechnik et al., 2017a; Humblet and Webster, 2017), and (3) they include strata up to 515 and 700 kyr, respectively, and therefore provide context for understanding Pleistocene reef inception and development in response to environmental changes.

2. Regional Setting

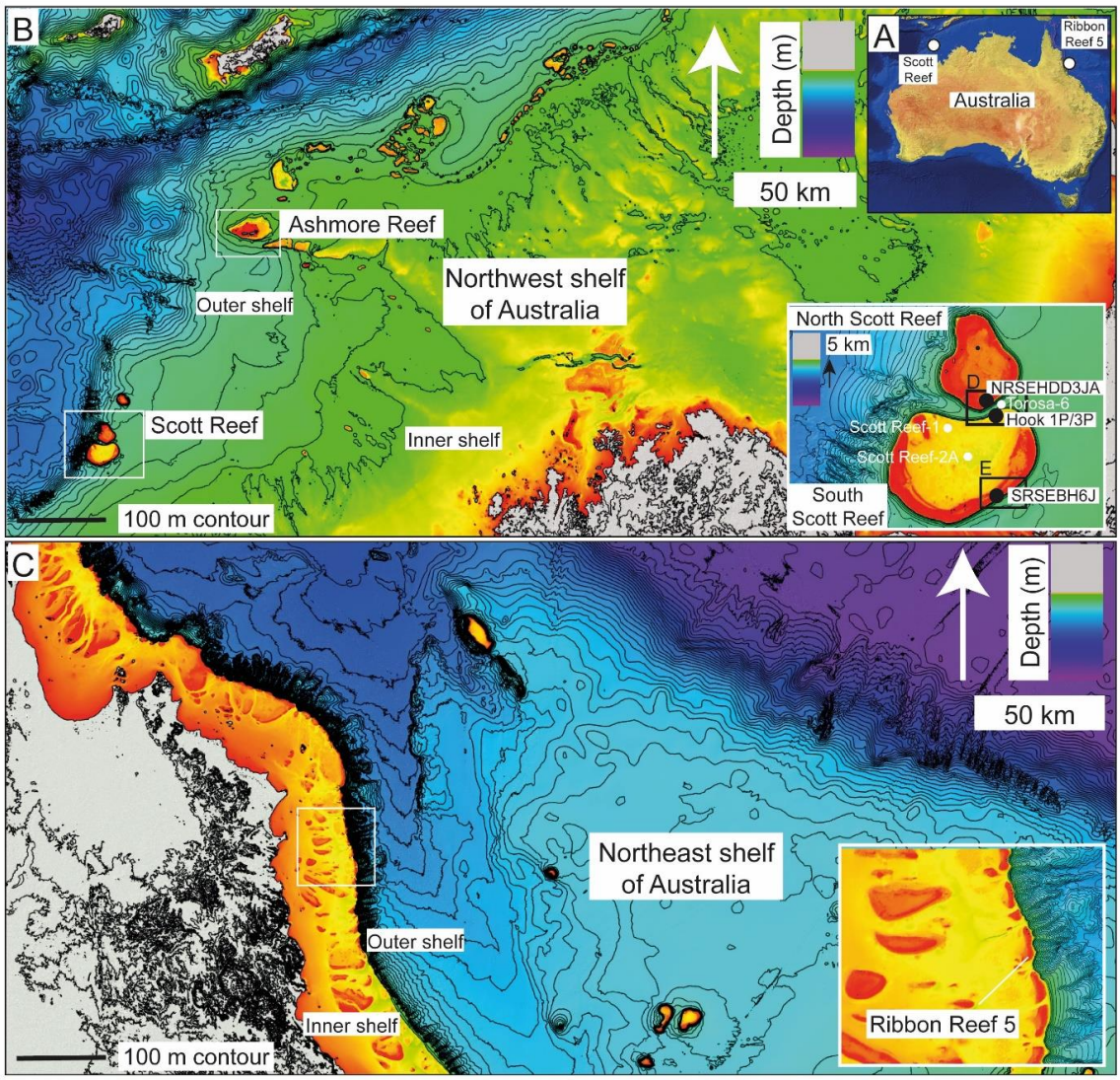


Figure 1. (A) Geographic location of Scott Reef on the Northwest Shelf of Australia and Ribbon Reef 5 in the Northern Great Barrier Reef, produced using Natural Earth 10 m elevation map (https://www.naturalearthdata.com/downloads/10m-raster-data/). (B) Regional map view of the Northwest Shelf of Australia with inset of Scott Reef, comprised of North and South Scott, showing core locations used in this study and Ashmore Reef to the North. Black rectangles indicate map views of the cores displayed in close view in Figure 9. (C) Regional map view of the Northeast shelf of Australia with inset of Ribbon Reef 5.

Scott Reef is an isolated system of two coral reef carbonate platforms that includes North (NSR) and South Scott Reef, (SSR) (Fig 1B; Grimaldi et al., 2024). They are located at 14º S (Scotese and Wright, 2018; Müller et al., 2019) in the Browse Basin on the outer continental margin of the NWS of Australia, approximately 300 km from the Australian coast (Fig. 1A). Water depth surrounding the raised platforms and reefs is ca. 500 m, with a 2 km wide channel separating NSR and SSR. The dominant hydrodynamic energy occurs from the Southwest, with periodic Southern Ocean monsoons and tropical cyclones (Green et al., 2019; Puotinen et al., 2020) controlling the platform geomorphology and facies patterns. They are fully exposed to oceanic wave energy, with average wave height of 1.25 m, a spring tidal range of 4.1 m, and maximum current speeds of 0.4 m/s recorded on the east hook of SSR (Collins and Testa, 2010; Gilmour et al., 2019; Grimaldi et al., 2024). Regional climate is tropical with an average annual sea surface temperature (SST) of 30ºC (Green, 2018). Regional oceanic conditions and climate are heavily modulated by the ITF and the Leeuwin Current, which bring tropical water and warm SSTs (Gordon, 2005; Gallagher et al., 2014; 2024; Petrick et al., 2019; He et al., 2021). Collins (2002; 2010) emphasised that reef biogeography and development along the NWS are influenced not only by the Leeuwin Current, but also broader variability in the ITF, particularly through its role in larval dispersal, water mass structure, and reef ecological differentiation.

North Scott Reef has a pear-shaped, near-fully enclosed reef flat surrounding a central lagoon and two tidal channels that exchange water with the ocean; it has a subsidence rate of ca. 0.29 mm/yr (Collins et al., 2011; Williams et al., 2026). South Scott Reef has a higher subsidence rate of ca. 0.45 mm/yr (Collins et al., 2011) resulting in a half-moon shaped reef flat with a deep (ca. 60 m) central lagoon containing mesophotic (> 30 m) reefs (Wilson, 2013; Heyward and Radford, 2019) that slope down at the northern flank to the inter-reef channel (Fig. 1B). These contrasts in platform morphology and subsidence regime were first recognised

in regional syntheses of the western Australian margin reefs (Collins, 2002; 2010), which emphasised the role of differential subsidence in producing distinct reef geometries and accommodation histories between North and South Scott Reef. Scleractinian corals are prevalent across the reef flat, crest, slope and lagoons, with *Acropora* being the dominant coral genus (Grimaldi et al., 2024) contributing to the robust structural framework. Massive *Porites*, Merulinidae, encrusting *Montipora* and branching *Pocillopora* and *Isopora* constitute the main reef slope coral communities (Gilmour et al., 2022).

3. Material and Methods

Table 1. Summary of Scott Reef core details and core storage information.

Core location	Eastings	Northings	Elevation above seabed (m)	Hole depth (m)	Core recovery (%)	Core missing (%)	Environmental context	Core storage location (2025)	Curated by Core Location	Owned by	Core status
South Scott Reef											
SR SE BH6 J	379501.36	8431040.96	-8.22	180	96.09	70.87	South Scott Reef SE reef crest	Perth Core store, WA, Australia	Geoscience Australia	Geoscience Australia	Cut, missing sections
HOOK 1 P	381301.47	8447540.15	-43.35	37.25	65.8	54.32					Cut, missing sections
HOOK 3 P	381296.6	8447537.4	-43.3	100.53	97.1	34.17	South Scott Reef leeward submerged reef crest	Perth Core store, WA, Australia	Geoscience Australia	Geoscience Australia	Cut, missing sections
North Scott Reef											
NR SE HDD3 - JA	380012.62	8449453.79	0.52	201.5	92.38	81.73	North Scott Reef SE reef crest	Perth Core store, WA, Australia, University of Sydney GRG	Geoscience Australia	Geoscience Australia	Cut, missing sections

3.1 Core datasets and logging

Rotary cores (Fig. 1) were acquired by Woodside Energy Ltd. as part of a 2006 geotechnical site investigation conducted by Worley Parsons (Collins et al., 2010) in water depth from 0 to 41 m across NSR and SSR. Table 1 summarises the datasets investigated in this study, including environmental position on the reef, core recovery and missing samples.

Detailed core logging using established criteria (Abbey et al., 2011; Dechnik et al., 2015; 2017a; Humblet and Webster, 2017; Sanborn et al., 2020; Webster et al., 2022) was conducted using the physical core material, high-resolution (250 microns) hyperspectral images, petrographic thin sections and NCT scans. Distinct sedimentary packages were defined to represent discrete sedimentological units within each core that lack clear lateral correlation across the platform. The sedimentary packages, lithologic facies and coralgal assemblages were identified based on existing (i.e., Collins et al., 2009) and new objective observations, including the identification of paleosols. Paleosols were identified based on horizonation, soil fabric, *in situ* mineral alteration and precipitation (e.g., calcretes, cementation, karstification), and redoximorphic features consistent with subaerial exposure. These attributes are often preserved and therefore provide reliable indicators of pedogenesis and paleoenvironmental conditions, including evidence for subaerial exposure (Carew and Mylroie, 1991; Bain and Foos, 1993; Mack et al., 1993; Boardman et al., 1995; Kraus, 1999; Nettleton et al., 2000; Tabor and Myers, 2017; Huang et al., 2017). Based on classifications of Carew and Mylroie (1991), and in the absence of detailed elemental and isotopic data, we use paleosol as a broad umbrella term to include all subaerial exposure-related features, including intrapaleosol bifurcation, composite paleosols, terra-rossa paleosols and calcarenite protosols.

Biological components, sedimentological features, and sedimentary boundaries, including bedding and exposure surfaces, were identified using criteria developed for Expedition IODP 389 (Webster at al., 2025). Sedimentological descriptions build upon the preliminary work by Collins et al. (2009), and follow the Udden-Wentworth (1922) classification for grain size. Carbonate rock textures were described using the Dunham (1962) classification, as modified by Embry and Klovan (1971), including mudstone, wackestone, packstone, grainstone and boundstone. Paleoenvironmental interpretations of the reef framework are based on Montaggioni (2005).

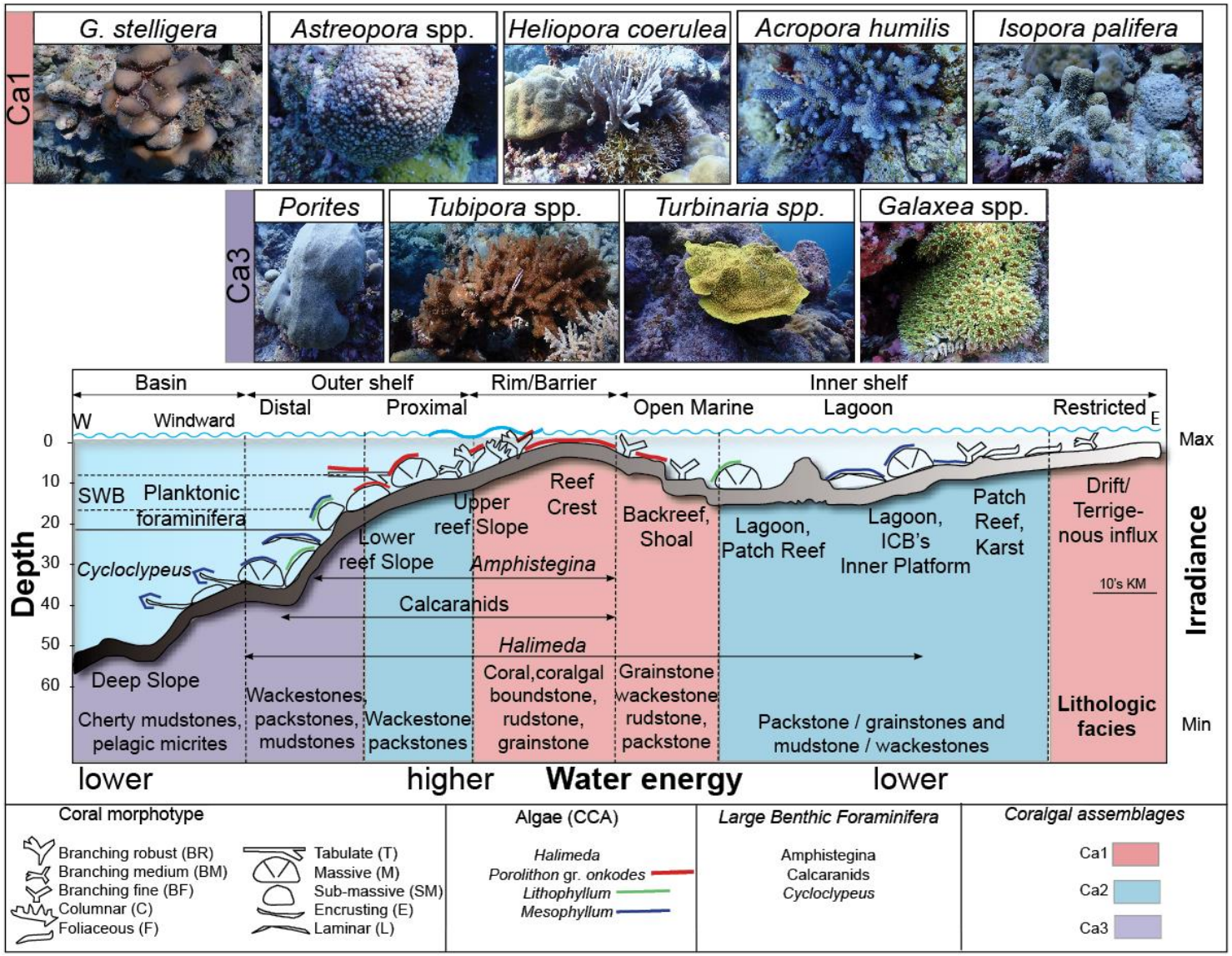

Ca1
G. stelligera
Astreopora spp.
Heliopora coerulea
Acropora humilis
Isopora palifera
Ca3
Porites
Tubipora spp.
Turbinaria spp.
Galaxea spp.
Basin
Outer shelf
Rim/Barrier
Inner shelf
W
Windward
Distal
Proximal
Open Marine
Lagoon
Restricted
E
Depth
0
10
20
30
40
50
60
SWB
Planktonic foraminifera
Cycloclypeus
Upper reef Slope
Reef Crest
Lower reef Slope
Amphistegina
Calcaranids
Halimeda
Backreef, Shoal
Lagoon, Patch Reef
Lagoon, ICB's Inner Platform
Patch Reef, Karst
Drift/ Terrige-nous influx
10's KM
Max
Irradiance
Min
Deep Slope
Cherty mudstones, pelagic micrites
Wackestones, packstones, mudstones
Wackestone packstones
Coral,coralgal boundstone, rudstone, grainstone
Grainstone wackestone rudstone, packstone
Packstone / grainstones and mudstone / wackestones
Lithologic facies
lower
higher
Water energy
lower
Coral morphotype
Branching robust (BR)
Branching medium (BM)
Branching fine (BF)
Columnar (C)
Foliaceous (F)
Tabulate (T)
Massive (M)
Sub-massive (SM)
Encrusting (E)
Laminar (L)
Algae (CCA)
Halimeda
Porolithon gr. onkodes
Lithophyllum
Mesophyllum
Large Benthic Foraminifera
Amphistegina
Calcaranids
Cycloclypeus
Coralgal assemblages
Ca1
Ca2
Ca3

Figure 2. Generalised profile of Scott Reef showing habitats with spatial and depth variations in lithologies, corals, crustose coralline algae and reef biota. Relative irradiance is indicated on the right-hand axis to indicate the decrease in light availability with water depth. Conceptual relative hydrodynamic energy gradient (wave and current energy conditions) across the reef is shown on the bottom axis. Modern corals from Scott Reef representing corals identified in core for coral assemblages 1 (Ca1) and 2 (Ca2) (Photo credit: Camille Grimaldi, Nicole Ryan, and the Australian Institute of Marine Science). Figure modified from Williams et al. (2026).

3.2 Diagenetic screening and hyperspectral mineralogical analysis

To minimise the risk of selecting diagenetically altered fossil coral samples for dating, a multi-method screening approach was employed and is described below. To evaluate the validity of pre-existing chronological ages provided from the cores (Collins et al., 2009), hyperspectral mapping, XRD and SEM was applied.

NCT measurements were conducted on a subset of coral samples from all three cores at the Australian Nuclear Science and Technology Organisation's (ANSTO) thermal neutron imaging instrument called "DINGO," located at Lucas Heights, NSW, Australia to reveal detailed 3-D structure, mineral composition and water-organic matter content in fossil corals (Schwarz et al., 2005; Williams et al., 2017; Bevitt, 2018; Ivankina et al., 2020; Williams et al., 2025). NCT scans use neutron scattering technology that detects the higher hydrogen content in well preserved coral aragonite relative to diagenetic calcite. NCT scans were used in this study to screen samples of *in situ* coral for selecting sections of aragonite most suitable for dating. To our knowledge, this represents the first application of NCT scanning for fossil coral geochronological screening.

Shortwave infrared (SWIR) hyperspectral imaging at 250-micron resolution was conducted on all three cores to map mineralogical and diagenetic variability following the methods of Murphy et al. (2017), Bishop et al., (2021) and Webster et al. (2022). Two datasets were produced to screen samples for suitability for U/Th dating: (1) using the HCI-4 system (Corescan Pty. Ltd.) and (2) using the equipment and code developed in Murphy et al., (2017) *(see supplement 6).* Diagnostic spectral parameters were extracted at key wavelengths to identify variations in carbonate mineralogy, hydroxyl- and iron-bearing phases, allowing

discrimination between aragonite, calcite, dolomite and clay-rich intervals. Diagenetic patterns were primarily assessed using four spectral indices targeting the 900 nm (Fe^{3+}), 1460 nm (OH), 2200 nm (Al-OH) and 2340 nm (CO_3) absorption features. The 2340 nm (CO_3) absorption depth product (e.g., Fig. 7b) was the most effective proxy for aragonite preservation (blue) versus calcite recrystallisation (yellows – reds). The 900 nm feature relates to ferrous iron oxides and sulphates, and the 1400 nm feature is sensitive to hydroxyl-bearing silicates and OH bonding. These features were interpreted together as indicative of subaerial exposure surfaces, as elevated iron and clay-related spectra responses may reflect increased weathering and terrigenous material input associated with exposure and reworking.

Existing petrographic thin sections (Collins et al., 2009) and new thin sections (this study) were used to distinguish between primary and secondary aragonite and other cement phases (McGregor and Abram, 2008) and to identify the presence of micro-borings, staining and sediment infills (Nothdurft and Webb, 2009). Thin sections were selected based on the presence of coral (*in situ* where possible) and coralline algae, and were co-located to XRD samples where possible to allow for close comparison. XRD was conducted on a total of 32 representative powder samples using the Rigaku Smart lab SE powder diffractometer at The University of Sydney Analytical Laboratory, to assess abundances of calcite in the coral skeleton (Table 8) (*see appendix for detailed methodology*).

SEM was used to examine microstructural preservation and secondary mineral phases in representative dated coral samples using a Hitachi Tabletop SEM at Queensland University of Technology (QUT) (TM3000). Sections from 11 samples from three cores (Table 2) were polished and etched in dilute formic acid as per Webb et al., (2009). The samples were then

imaged in high resolution to reveal the microstructure and any calcite filled microborings that are otherwise unidentifiable on polished thin sections (Nothdurft et al., 2007; Nothdurft and Webb, 2009; Hibbert et al., 2016; Salas-Saavedra et al., 2018). The images also revealed the main diagenetic features and environments (e.g., marine, meteoric) interpreted in the cores (Braithwaite & Montaggioni, 2009; Gischler et al., 2013).

The most suitable sections of coral identified by the above screening methods that were free of obvious diagenetic alteration such as dissolution, staining, sediment fill and secondary cement (Webster et al., 2022) were selected from the Scott Reef cores for U/Th dating.

3.3 Chronological framework

Open and closed system radiometric ages constrain the chronological framework developed in this study, based on the sample selection criteria outlined above (Table 2). Previous open system (Collins et al., 2009) U/Th ages were dated as per the U-series dating methods of Zhao et al. (2001) and Yu et al. (2006) using a thermal ionization mass spectrometer (TIMS) at the University of Queensland.

New closed system and Thompson-corrected open system U–Th dating was performed on coral subsamples (Table 2) at the University of Queensland Radiogenic Isotope Facility (RIF), with full isotopic data reported in Table 9. Subsamples (approximately 1 g) were extracted from corals interpreted to represent *in situ* growth. Samples were initially cleaned in an ultrasonic bath, crushed to ca. 1 mm fragments, and subjected to oxidative cleaning in a 15% H_2O_2 solution for 24 hours. Following a further 15 minutes of sonication, samples were rinsed three times with Milli-Q water and dried overnight on a hotplate at 60 °C. After pre-

treatment, approximately 0.15 g of the most pristine aragonitic fragments were hand-picked under an optical microscope for U–Th geochemical analysis. Selected subsamples were dissolved in double-distilled HNO_3, spiked with a mixed ^{229}Th–^{233}U tracer, and analysed in duplicate using a Nu Plasma HR multi-collector inductively coupled plasma mass spectrometer (MC-ICP-MS). Sample screening, analytical procedures, initial ^{230}Th corrections, and age calculations followed established protocols outlined by Zhao et al. (2009), Clark et al. (2014), and Salas-Saavedra et al. (2018).

Measured and decay-corrected initial uranium isotope compositions ($\delta^{234}U_i$) were evaluated as an indicator of closed-system behaviour and preservation of primary marine signatures. Initial $\delta^{234}U$ values ($\delta^{234}U_i$) are calculated from back-calculated initial ($^{234}U/^{238}U$) activity ratios following $\delta^{234}U = [(^{234}U/^{238}U)_a - 1] \times 1000$, consistent with conventions outlined by Chutcharavan et al. (2018). Samples are classified as closed, closed–open (transitional), or open system based on $\delta^{234}U_i$ values relative to modern seawater (145.0 ± 1.5‰; Chutcharavan et al (2018)). Closed-system samples yield ages considered reliable within analytical uncertainty, whereas open-system samples exhibit elevated or depleted $\delta^{234}U_i$ values consistent with post-depositional uranium mobility and require interpretation using open-system corrections using the calculations of Thompson et al. (2013). Thompson-corrected interpreted ages are provided for samples in this study only. For previously published data (Collins et al., 2009), ages and activity ratios are reproduced as originally reported. Samples exhibiting significant U loss or falling within the “forbidden zone” of activity-ratio space (Cheng et al., 2013) (see Figure 10 insert) are identified and excluded from chronological interpretation, following established screening protocols for coral U-series dating (e.g., Chutcharavan et al., 2018; Webster et al., 2022). Modern seawater has a well-constrained $\delta^{234}U$ value of ca. 145‰, and screened modern and late Quaternary corals typically fall within a narrow range around

this value (Chutcharavan et al., 2018). Following their recommendation of a generous tolerance to account for analytical uncertainty and minor natural variability, samples were classified as consistent with seawater values if $\delta^{234}U_i$ fell within 145 ± 8‰ (137–153‰). Samples outside this range were flagged as potentially affected by open-system behaviour and evaluated in conjunction with additional screening parameters (e.g., ^{232}Th concentrations, [$^{230}Th/^{232}Th$], and petrographic observations). Because the Scott Reef dataset includes samples extending beyond 60 ka, we adopt this broader tolerance window to minimise over-rejection of well-preserved material while remaining consistent with the magnitude of seawater variability discussed by Chutcharavan et al. (2018). Samples outside the 137–153‰ range are interpreted cautiously, particularly where deviations coincide with elevated detrital Th or petrographic evidence for diagenetic alteration.

Table 2. Summary of coral samples selected and screened for radiometric dating from the Scott Reef cores analysed in this study. All listed samples were scanned using hyperspectral imaging. Samples in bold were scanned with SEM. Diagenetic characteristics based on XRD and SEM screening results are reported in Table 7. Corrected ^{230}Th ages (kyr) reported in Table 9 are provided together with coral genus and depositional context (IS = *in situ*; IS? = probable *in situ*; ISN = uncertain; ISX = not *in situ*). Paleowater-depth interpretations are inferred from associated coral and CCA assemblages identified in thin section. All Collins et al., (2009) samples have corresponding thin sections (*see Supplement 8*). Samples shown in bold were screened using SEM; samples shown in italics were screened using NCT; samples shown in bold italics were screened using both methods. All samples were screened using hyperspectral to ensure they were aragonitic and free of significant calcite and/or dolomite (see Table 7 for diagenetic details).

Sample name	Core	Core depth (m)	Dated Lithology	Coral genera	CCA and paleowater depth
This study					
628889	SR SE BH6-J	9.3	IS Coral	*Porites*	/
628890	SR SE BH6-J	22.4	IS Coral	*Porites*	Aa1 - shallow < 6 m
628891	SR SE BH6-J	33	IS Coral	*Porites*	/
628892	SR SE BH6-J	45.64	IS? Coral	Merulinidae/ Agariciidae?	Aa1 (< 10 m) fragments at 43.8 m
628893	SR SE BH6-J	51.35	IS Coral	*Porites*	Aa1 (< 10 m) at 50.7 m
628894	SR SE BH6-J	71.9	IS Coral	*Heliopora coerulea*	Aa1 – shallow (< 10 m)?
628895	SR SE BH6-J	81	IS? Coral	*Diploastrea/ Favites?*	/
628896	SR SE BH6-J	81.38	ISN Coral	Poritidae?	encrusted by CCA and thin laminar coral (bioeroded)

628898	SR SE BH6-J	102	IS Coral	*Turbinaria?*	/
628899	SR SE BH6-J	102.58	IS Coral	*Acropora*	/
628897	SR SE BH6-J	106.2	IS Coral	*Goniastrea stelligera*	/
628900	SR SE BH6-J	107.548	IS Coral	*Porites/ Montipora?*	/
628901	SR SE BH6-J	117.276	ISX Coral	*Porites*	*Halimeda*, planktonic foraminifera – pelagic deepwater?
928902	SR SE BH6-J	125.01	IS Coral	*Porites*	Aa3 at 126 m – deep > 30 m
628903	SR SE BH6-J	142.2	IS Coral	Merulinidae	Aa3 at 144 m – deep > 30 m
628904	SR SE BH6-J	171.9	ISN Coral	*Porites*	/
628905	SR SE BH6-J	177.2	IS Coral	*Porites*	Aa3 – deep > 30 m
609964	Hook 3P	20.58	IS? Coral	Laminar coral	*Halimeda*
609971	Hook 3P	61.97	ISX Coral	?	Ca1 coral clasts
609983	Hook 3P	95.3	ISX Coral	*Astreopora*	Aa1 - shallow < 10 m
Collins et al. (2009)					
BH6-J-1.50	SR SE BH6-J	1.5	ISN Coral	Massive framestone	Aa1 - shallow < 6 m
BH6-J-1.80	SR SE BH6-J	1.8	ISN Coral	Massive framestone	No algae/no ID
BH6-J-5.25	SR SE BH6-J	5.25	ISN Coral	Massive framestone	Aa1 - shallow < 6 m
BH6-J-9.45	SR SE BH6-J	9.45	ISN Coral	Branching/massive framestone	No algae/no ID
BH6-J-11.65	SR SE BH6-J	11.65	ISN Coral	Massive framestone	No algae/no ID
BH6-J-15.85	SR SE BH6-J	15.85	ISN Coral	Branching/massive framestone	No algae/no ID
BH6-J-17.55	SR SE BH6-J	17.55	ISN Coral	Tabulate framestone	No algae/no ID

BH6-J-18.65	SR SE BH6-J	18.65	ISN Coral	Massive framestone	Aa1 - shallow < 6 m
BH6-J-23.40	SR SE BH6-J	23.40	ISN Coral	Massive framestone	No algae/no ID
BH6-J-26.60	SR SE BH6-J	26.6	ISN Coral	Massive framestone	Aa1 - shallow < 6 m
BH6-J-27.90	SR SE BH6-J	27.9	ISN Coral	Massive framestone	No algae/no ID
BH6-J-32.20	SR SE BH6-J	32.2	ISN Coral	Branching/massive framestone	No algae/no ID
BH6-J-32.45	SR SE BH6-J	32.45	ISN Coral	Massive framestone	No algae/no ID
BH6-J-32.95	SR SE BH6-J	32.95	ISN Coral	Massive framestone	No algae/no ID
BH6-J-34.60	SR SE BH6-J	34.6	ISN Coral	Massive framestone	No algae/no ID
BH6-J-51.25	SR SE BH6-J	51.25	ISX Coral	Massive coral clast	Aa1 at 50.7 m - shallow < 10 m
BH6-J-85.10	SR SE BH6-J	85.1	ISN Coral	Massive framestone	Aa1 - shallow < 10 m?
BH6-J-177.20	SR SE BH6-J	177.2	ISX Coral	Branching/massive coral clast	Aa3 – deep > 30 m
HDD3-JA-1.10	NR SE HDD3-JA	1.1	IS Coral	*Porites*	Aa1 - shallow < 10 m
HDD3-JA-8.60	NR SE HDD3-JA	8.6	IS Coral	*Porites*	Aa3 – deep > 30 m
HDD3-JA-23.25	NR SE HDD3-JA	23.25	IS Coral	*Porites*	Aa1 - shallow < 6 m
HDD3-JA-23.80	NR SE HDD3-JA	23.8	IS? Coral	*Acropora*	Aa1 - shallow < 6 m
HDD3-JA-27.20	NR SE HDD3-JA	27.2	ISX Coral	Coral branch	Aa3 – deep > 30 m?
HDD3-JA-31.60	NR SE HDD3-JA	31.6	ISN Coral	Sub-massive Merulinidae	No algae/no ID
HDD3-JA-58.00	NR SE HDD3-JA	58	IS Coral	Columnar *Pavona*	No algae/no ID
HDD3-JA-91.40	NR SE HDD3-JA	91.4	IS? Coral	Encrusting *Montipora*	Aa3 at 92 m – deep > 30 m?

HDD3-JA-151.10	NR SE HDD3-JA	151.1	ISN Coral	*Platygyra*	No algae/no ID
1P-02	Hook 1P	11.2	IS Coral	Laminar/encrusting framestone	No algae/no ID
HOOK 1P-03	Hook 1P	14.18	IS Coral	Massive/tabulate framestone	No algae/no ID

3.4 Coralline algae identification

A total of 55 coralline algal samples were selected for identification using methods adapted from prior reef-core studies (Cabioch et al., 1999; Braga and Aguirre, 2004; Webster et al., 2009; Humblet et al., 2019). Sampling was restricted to visible coralline algal crusts primarily from *in situ* framework (i.e. *in situ* encrusting assemblages over corals) to reduce the risk of reworked material and ensure paleoecological-bathymetric integrity (Cabioch et al., 1999). Thin sections (2.3 × 4.0 cm) were prepared from each sample and examined under petrographic microscope and SEM to identify non-geniculate taxa to the lowest feasible taxonomic level, and to measure thallus thickness and total crust thickness (Braga and Aguirre, 2004). Identification of coralline algae was based on the same morpho-anatomic diagnostic criteria to delimit species and species groups that were applied to living coralline algae in the Indo-Pacific areas (Payri et al., 2000; Maneveldt and Keats, 2014; Van der Merwe and Maneveldt, 2016; Rösler et al., 2016; Caragnano et al., 2018). We followed the generic classification scheme proposed by Rösler et al. (2016) and Caragnano et al. (2018) for the family Corallinaceae, order Corallinales. We created species groups for species that share common characters observable in fossil corallines, but which are separated by features that are not preserved in fossil specimens or include cryptic species. The paleodepths inferred from coralline algal assemblages were derived from the distributions of living members of the identified taxa (Adey et al., 1982; Cabioch et al., 1999; Littler and Littler, 2003; Payri et al., 2000; Dechnik et al., 2017a; Braga et al., 2022). These data were integrated with lithofacies context to constrain paleobathymetry and reconstruct reef accretion history across glacio-eustatic cycles.

3.5 Coral identification

In this study, corals were identified to genus or species level where possible, following the taxonomic classification of Veron et al. (2016) with modifications for Merulinidae by

Huang et al. (2014), Lobophylliidae by Huang et al. (2016), and Pachyseridae by Quek et al. (2023), as well as identification criteria presented in Humblet et al. (2015). Species groups were created when multiple species within the same genus and displaying similar growth forms could not be distinguished. *In-situ* reef framework corals were distinguished from detrital material by using established criteria: (1) noting corallite orientation (i.e., right way up), (2) geopetal structures, (3) location of crustose coralline algae (CCA) (i.e., upper surface of coral indicates right way up) or equal encrustation/boring on all sides, (4) the presence of basal encrustation contacts with the underlying substrate, and (5) the absence of physical abrasion and rounding indicative of transport (Camoin et al., 2007; Dechnik et al., 2015; Webb et al., 2016; Webster et al., 2022). Bioeroders, such as boring sponges, bivalves, and microborers, also provided valuable proxies for reconstructing paleo-depth trends across reef frameworks (Weinstein et al., 2019). Their presence and relative abundance were noted in the core logging. Corals were defined as encrusting when they formed thin (< 5 cm), laterally extensive skeletons that grew attached to and covering a substrate, and as massive if more than 5 cm thick. Sub-massive corals were identified as intermediate forms, characterised by thick, mound-like morphologies lacking fully developed massive structure. The term laminar was used for thin, sheet-like colonies where attachment style (attached versus free margins) could not be confidently determined. Branching coral morphotypes are considered to have fine, medium or thick (robust) branches, depending on branch thickness < 1 cm, 1–1.5 cm or >1.5 cm respectively (Humblet et al., 2019). Sedimentary facies and fossil assemblages are interpreted in terms of paleoenvironments based on analogy with distribution of sediments and reef organisms in modern reef systems. These modern environments and depth zonations form the basis for reconstructing depositional environments through time and are summarised in Figure 2.

In situ coral framework facies were used to provide constraints based on known typical modern depositional settings and hydrodynamic energy. Coral-algal assemblages are used to define paleo-water depth interpretations of the broad lithologic facies interpretations. For example, robust branching *Acropora* gr. *humilis* are shallow water coral framework builders that establish in < 10 m water depth. Identifying associated coralline algae can further constrain this depositional environment depth.

4. Results

Distinct chronostratigraphic packages bounded by major unconformities were correlated where possible between all three cores, identified by their lithologic facies (Fig. 3, Table 3), structures, biotic assemblages, diagenetic characteristics (Fig. 4), ages and comparison with modern examples.

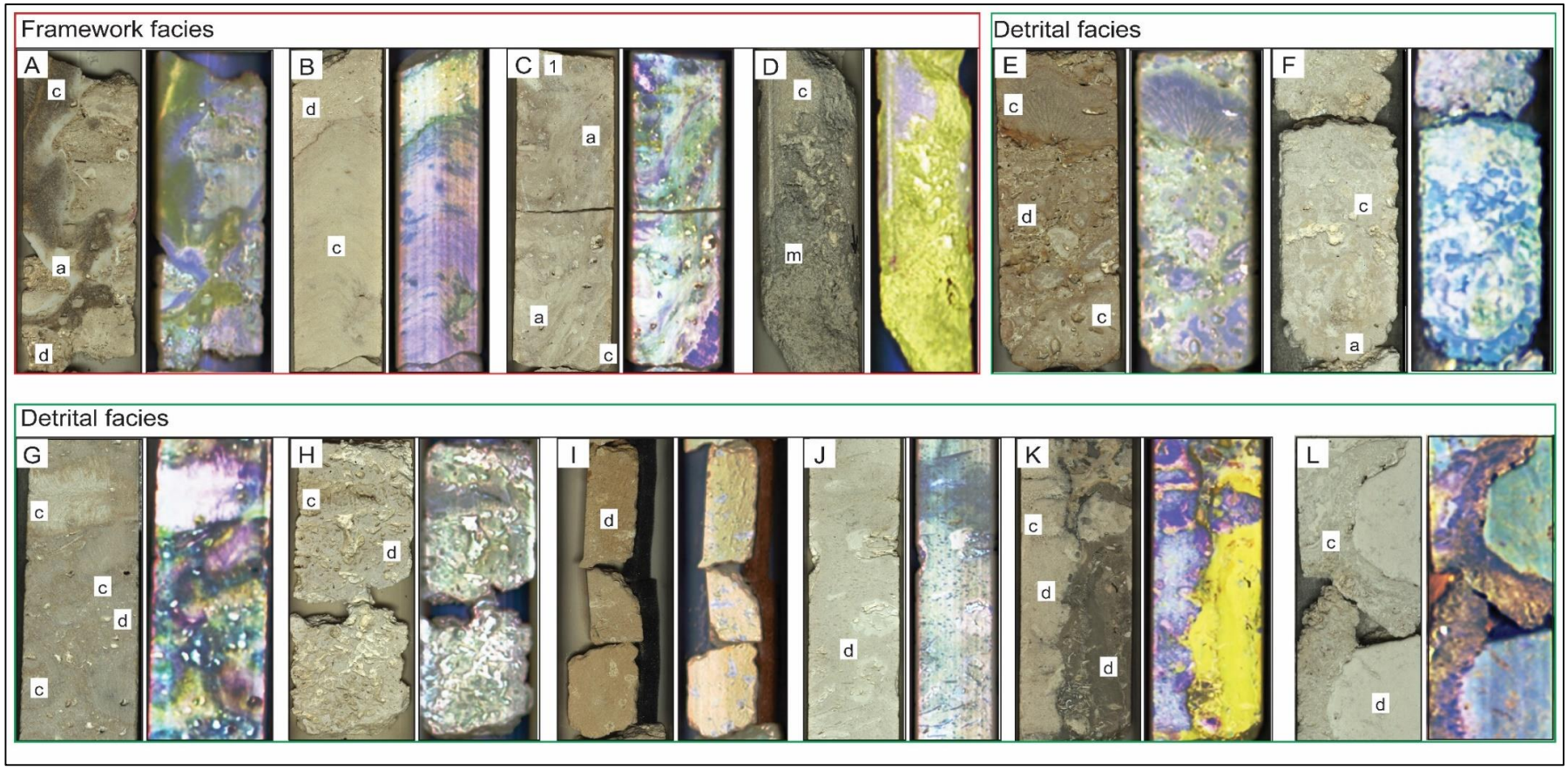


Figure 3. High resolution (250 microns) images of the main lithologies and their corresponding hyperspectral false colour images. Framework facies: (A) *Heliopora coerulea* framestone (SRSEBH6J: 71 m) (B) Massive framestone *Porites* (SRSEBH6J: 85 m) (C) Bindstone facies with thick encrusting coralline algae (SRSEBH6J: 100 m). (D) Microbialite framestone (Hook 1P: 18 m). Detrital facies: (E) Cemented Grainstone-

Rudstone facies (NRSEHDD3JA: 91 m), (F) Rhodolith-rudstone facies (Hook 3P: 48 m), (G) Rudstone facies (Hook 3-P: 69 m). (H) Heavily dissolved *Halimeda*-rich Rudstone facies (NRSEHDD3JA: 100 m?). (I) Floatstone facies (SRSEBH6J: 69 m). (J) Wackestone facies (SRSEBH6J:135.3 m). (K) *Halimeda*-Rudstone facies with grey, brown bioclastic grainstone/packstone matrix (SRSEBH6J: 157 m). (L) Floatstone facies with robust branching coral clasts in very fine, buff, homogeneous chalky bioclastic matrix, interpreted to be deposited in a deep forereef slope setting (Hook 3P: 99 m). Individual components are identified using letter notation, where a = coral, c = coralline algae (including rhodolith algal nodules in panel F), d = detrital material and m = microbialites. Core tray width is 7.5 cm in all images. Hyperspectral false colour composite images are composed of three spectral bands between 440 and 740 nm mapped to RGB that are not visible to the human eye and support identification of compositional and structural variations within the core. For example, purple colours were a useful indicator for coral.

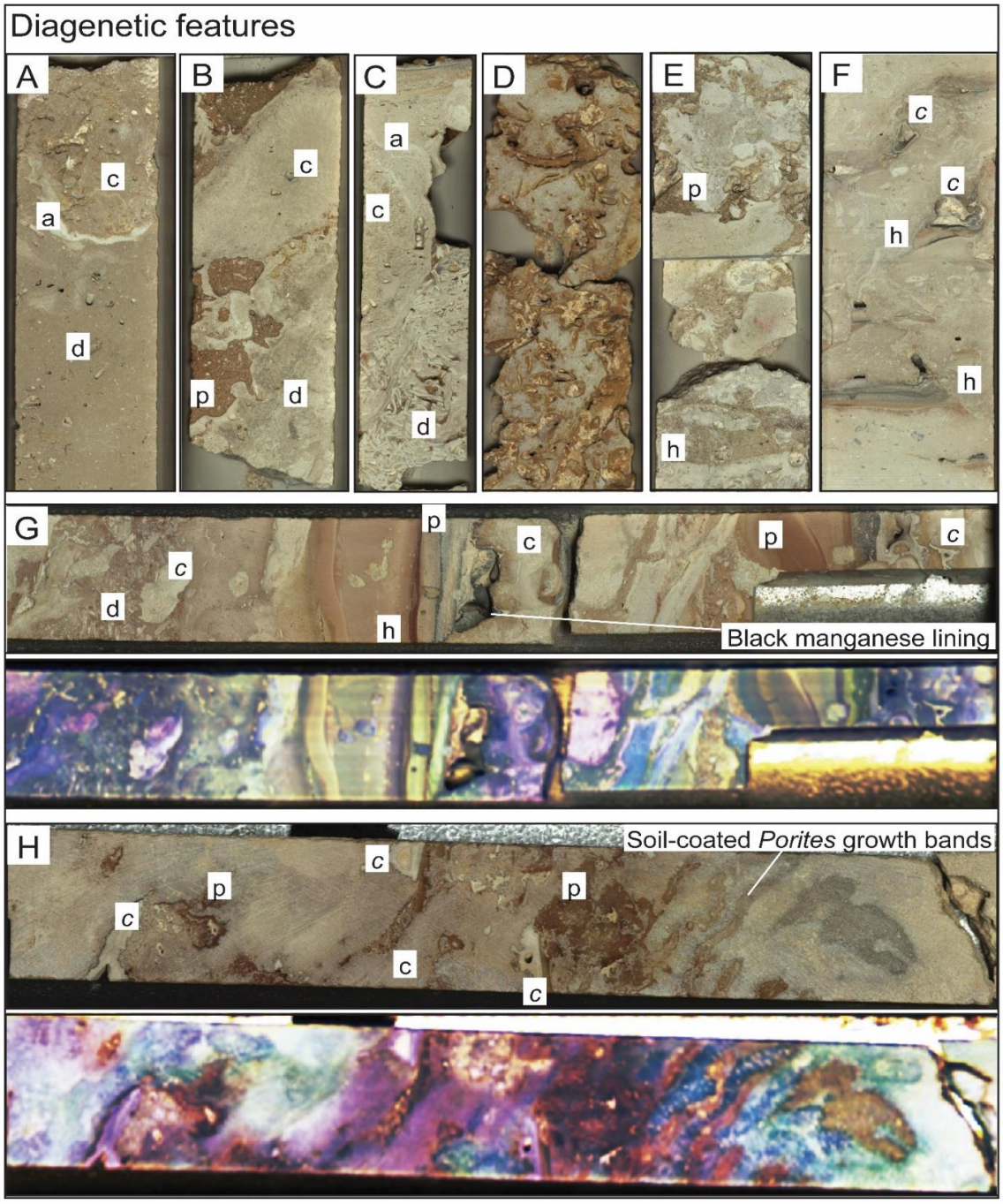


Figure 4. Representative diagenetic features of the Scott Reef cores. (A) Dolomite lithofacies (NRSEHDD3JA: 189 m), (B) sediment infilling cavities in rudstone facies (SRSEBH6J: 72m) as evidence of a subaerial exposure horizon, (C) Horizon with karst features and secondary cements coating dissolved *Halimeda* grains (SRSEBH6J: 81 m). (D) Yellow-brown staining of dissolved bioclasts, with leaching and vugs (NRSEHDD3JA: 118.7 m). (E) Horizonation:

horizontal brown sediment layer, minor leaching (NRSEHDD3JA: 118.7 m). (F) Horizonation: layered sedimentary infill of distinct colours (grey, brown, yellow, and dark grey) within fractures and partially dissolved clasts. Cementation and calcite nodules (SRSEBH6J: 102 m). (G) First sharp unconformable horizon of MIS 9 (Hook 3P: 96 m) with sub-vertical layered seams between coral fragments partially infilled with several generations of carbonate cement and black manganese lining. Deposited during multiple phases of sedimentation during exposure. (H) Paleosol surface (Hook 3P: 71 m: SR-NE-P2) likely deposited during MIS 7d, stratified layering of dark-brown sediment coating growth rings of *Porites* coral. Several generations of cement infill vugs and cavities. Individual components are identified using letter notation, where a = coral, c = coralline algae, *c* = secondary cements, d = detrital material, p = paleosol, H = Horizonation pedogenesis (Huang et al., 2017). Core tray width is 7.5 cm in all images. Hyperspectral false colour composite images are composed of three spectral bands between 440 and 740 nm that are not visible to the human eye and support identification of compositional and structural variations within the core.

Table 3. Summary of the primary sedimentary facies identified in the Scott Reef cores, adapted from Webster et al., (2022).

Sedimentary facies	**Characteristic components**	**Associated biota**	**Taphonomy**	**Depositional environment**
Framestone	*In situ* coral framework with associated crustose coralline algae crusts (CCA), and occasionally *Halimeda*.	Vermetid gastropods, encrusting foraminifera, red algae	Moderately well preserved to complete recrystallisation; some *in situ* growth structures retained; minimal to moderate bioerosion. Variable porosity and infill cement.	Most abundant on fore-reef, channels, lagoon.
Bindstone	*In situ* and non-*in situ* coral bound in place by thick encrusting coralline algae.	Vermetid gastropods, red algae, microbial crusts.	Moderate to high preservation potential; biotic encrustation stabilizes framework.	High energy fore-reef, reef crest.
Rudstone	Redistributed and lithified coral fragments > 30 mm within bioclastic carbonate sand matrix.	Calcifying reef biota, *Halimeda*, molluscs, echinoids, foraminifera	Broken and abraded coral fragments, bioerosion common. Variably cemented and leached; moderate transport.	Reef crest, back reef shoal, lagoon.
Rhodolith-Rudstone	Grainstone/packstone supported matrix with ~20 to 40% composed of coralline algal rhodoliths 2 to 4 cm in diameter.		Fragmented and abraded rhodoliths, micritisation of skeletal components, variable bioerosion, episodic reworking under moderate to high-energy.	

Grainstone	Lithified bioclastic carbonate sand and coral reef organisms in a mud-free matrix.	Foraminifera, *Halimeda*, molluscs, echinoids, red algae	Well-sorted; abrasion and rounding of grains common. Variably cemented and leached.	Back reef shoal, lagoon.
Packstone	Bioclastic carbonate grains and fine mud matrix, often containing coral, mollusc, and foraminiferal components.	Foraminifera, molluscs (bivalves, gastropods), echinoids	Bioerosion and fragmented.	Moderate-energy, fore-reef slope.
Floatstone	Gravel sized bioclasts floating in matrix of fine peloids and skeletal debris.	Foraminifera, peloids, bryozoans, echinoids, *Halimeda*		Low energy 15-60 m depth.
Wackestone	Predominantly carbonate mud with >10 % sparse skeletal grains.	Planktic foraminifera, molluscs (bivalves, gastropods), microbial mats.	Fine-grained, limited transport.	Low-energy, deep-reef slope.
Bioclastic carbonate sand	Sand-sized carbonate fragments from coral reef organisms.	Corals, foraminifera, molluscs (bivalves, gastropods), echinoids, red algae	Unlithified to partially lithified.	High-energy reworking, shoals.

4.1 Lithologic reef facies

Table 3 and Figure 3 summarise the key lithologic facies and diagenetic features used to interpret the depositional environments based on observations from the core dataset, including three coral growth framework facies, seven detrital facies representing transported and reworked sediments and various diagenetic features (Fig. 4), following established criteria (Montaggioni, 2005; Camoin et al., 2007; Dechnik et al., 2015; Webster et al., 2022).

4.1.1 Coralline algal assemblages and paleoenvironmental settings

CCA summarised in Table 5 were identified in the Scott Reef cores and are interpreted to represent three distinct depositional settings: (1) high-energy shallow reef crests (< 10 m), intermediate (< 30 m) and deeper reef slope environments (> 30 m) including deep slope (> 60 m) when associated with *Cycloclypeus* foraminifera. These assemblages were defined based on dominant coralline algal species groups, and associated taxa, and comparison with modern analogues from Scott Reef (Huisman et al., 2009) and the broader Indo-Pacific region (e.g., Braga et al., 2022; Humblet et al., 2019; Webster et al., 2022).

Table 4. Summary of the coral, coralline algae, large and encrusting benthic foraminifera and other reef biota found in the Scott Reef cores.

Scleractinian corals		**Coralline algae**	**Large benthic foraminifera**	**Reef biota**
Family ACROPORIDAE	Family **PORITIDAE**	**Order CORALLINALES**	**Family NUMMULITIDAE**	Vermetid gastropods
Acropora gr. *humilis*	*Goniopora* sp.	*Porolithon* gr. *onkodes*	*Cycloclypeus*	Gastropods
Acropora gr. *muricata?*	*Porites* sp.	*Dawsoniolithon* sp.	*Operculinella?*	Soft coral
Astreopora	Family **LOBOPHYLIIDAE**	*Harveylithon* sp.	*Heterostegina*?	Octocoral spicules
Isopora gr. *palifera*	*Lobophyllia* sp.	*Harveylithon* gr. *munitum*		Bivalves
Montipora sp.	*Echinophyllia*	*Hydrolithon* sp.	Family **CALCARINIDAE**	Molluscs
Family **MERULINIDAE**		*Hydrolithon* gr. *boergesenii*	*Calcarina* sp.	Echinoderm spicules
Goniastrea sp.		*Lithoporella* sp.		
Goniopora	Family **EUPHYLLIIDAE**	*Neogoniolithon* spp.	Family **AMPHISTEGINIDAE**	
Platygyra	*Galaxea*	*Spongites* sp.	*Amphistegina lessonii*	
Favites?	*Euphyllia*	*Lithophyllum* sp.	*Amphistegina radiata*	
Cyphastrea	Family D**ENDROPHYLLIIDAE**	*Lithophyllum* gr. *pustulatum*		
Dipsastraea	*Turbinaria*	*Lithophyllum* gr. *prototypum*	Family **HOMOTREMATIDAE**	
Goniastrea retiformis?	Family **SIDERASTREIDAE**	*Lithophyllum* gr. *kotschyanum*	*Homotrema rubrum*	
Goniastrea stelligera	*Coscinaraea*?	*Amphiroa* sp.		
Family **AGARICIDAE**	Family **FUNGIIDAE**	Order **SPOROLITHALES**	Family **ACERVULINIDAE**	
Pavona?	*Fungia*	*Sporolithon* sp.	*Acervulinids*	
Leptoseris?		Order **HAPALIDIALES**	*Acervulina*	
Coeloseris mayeri	**Non-Scleractinian corals**	*Lithothamnion* spp.		
Leptoseris papyracea?	Family **HELIOPORIDAE**	*Mesophyllum* spp.	Family **TEXTULARIIDAE**	
Family **PACHYSERIDAE**	*Heliopora*	**Other red algae**	*Textulariid*	
Pachyseris rugosa	Family **TUBIPORIDAE**	Order **PEYSSONNELIALES**		

Family **POCILLOPORIDAE**	*Tubipora*	Peyssonneliaceans	Family **PENEROPLIDAE**
Seriatopora sp.	Family **MILLEPORIDAE**	**Calcareous green algae**	*Sphaerogypsina*
Pocillopora	*Milleporid* sp.*?*	*Halimeda*	
	Millepora		

Table 5. Summary of crustose coralline algal assemblages and their paleoenvironmental interpretations. Analogues used to support the interpretations are provided.

Algal assemblage (Aa)	Algal assemblage	Associated reef biota	Distribution	Paleoenvironment and inferred water depth
Aa1	*Porolithon* gr. *onkodes, Lithophyllum* gr. *pustulatum, Lithophyllum* gr. *kotschyanumm Lithophyllum* sp., *Harveylithon?* spp. *Neogoniolithon* spp., *Dawsoniolithon* sp., *Spongites* sp., *Hydrolithon* sp., and Peyssonneliaceans,	Vermetid gastropods, encrusting foraminifera, echinoids, barnacles, serpulids, small benthic foraminifera, gastropods and bivalves.	SRSEBH6J, NRSEHDD3JA	CCA indicate shallow < 10 m, plus vermetids indicate < 6 m.
Aa2	*Harveylithon* gr. *munitum, Dawsoniolithon* sp., *Lithophyllum* gr. *prototypum, Lithophyllum* gr. *pustulatum.*	Encrusting foraminifera, bivalves, foraminifera.	SRSEBH6J, NRSEHDD3JA	Intermediate Reef slope < 30 m
Aa3	*Mesophyllum* spp., *Lithoporella* sp., *Sporolithon* sp., *Lithophyllum* gr. *pustulatum, Spongites* sp., *Lithothamnion* sp., *Lithophyllum* sp., *Amphiroa,* and Peyssonneliaceans	Bioeroders, Gastropods, abundant dissolution of aragonitic components such as *Halimeda,* encrusting foraminifera.	SRSEBH6J, NRSEHDD3JA	Deep forereef slope > 30 m, nodules of CCA with encrusting forams commonly occur in depths of several tens of metres.

Algal assemblage 1 (Aa1) is dominated by *Porolithon* gr. *onkodes* forming thick, crusts commonly associated with *Lithophyllum* spp. (e.g., *Lithophyllum* gr. *pustulatum, Lithophyllum* gr. *kotschyanum* and *Lithophyllum* gr. *prototypum)*, *Spongites* sp., *Hydrolithon* sp., *Harveylithon*? sp., Peyssonneliaceans*,* and in some cases *Mesophyllum* spp. and *Dawsoniolithon* sp. (e.g., *Dawsoniolithon* gr. *conicum). Porolithon* gr. *onkodes* dominates the CCA assemblages at the reef front in Scott Reefs today (Huisman et al., 2009). At Ashmore Reef about 250 km north of Scott Reef, thick crusts of *Porolithon* gr. *onkodes* are abundant and encrust coral colonies in shallow water high-energy reef settings < 10 m (Webster et al., 2022), as they do elsewhere in Indo-Pacific reefs (Cabioch et al., 1999; Littler and Littler, 2003; Braga et al., 2022) and on the GBR (Dechnik et al., 2017a). Some secondary and accessory components of Aa1, such as *Lithophyllum* gr. *pustulatum*, have a wide depth range and taxa typical of poorly illuminated settings, such as *Mesophyllum* spp. are more common in Aa3. Where Aa1 co-occurs with abundant vermetid gastropods, it indicates water depths shallower than 6 m (Cabioch et al., 1999; Braga et al., 2022).

Algal assemblage 2 (Aa2) is characterised by *Harveylithon* gr. *munitum, Dawsoniolithon* sp. and *Lithophyllum* sp*. (e.g., Lithophyllum* gr. *prototypum, Lithophyllum* gr. *pustulatum).* Corals with encrusting *Harveylithon* sp., *Dawsoniolithon* sp. and *Lithophyllum* sp. in the absence of *Porolithon* gr. *onkodes* occur in the GBR in less than 30 m water depths (Dechnik et al., 2017a). Aa2 is therefore interpreted to have been deposited in water depths < 30 m.

Algal assemblage 3 (Aa3) is dominated by *Mesophyllum* spp*.,* with accessory components including *Neogoniolithon* spp., *Lithoporella* sp*., Sporolithon* sp*., Spongites* sp*., Lithothamnion* sp*.,* and *Amphiroa*. Coralline species with a wide depth range can also be found

in Aa3, including *Lithophyllum* spp. *(e.g., Lithophyllum* gr. *pustulatum),* together with Peyssonneliaceans. The dominance of *Mesophyllum* species, the absence of species characteristic of Aa1 and Aa2, and the co-occurrence of calcareous green algae (*Halimeda*) suggests that this assemblage was deposited in a deep, low energy reef slope environment in water depths > 30 m (Dechnik et al., 2017a) and possibly > 60 m when *Cycloclypeus* foraminifera are observed.

4.1.2 Fossil coral assemblages and paleoenvironmental settings

Thirty-five coral species and species groups were identified from twenty-seven genera in the three cores (Table 4). Four coral assemblages were defined based on dominant coral taxa and morphologies. The resulting paleoenvironmental interpretations of each coral assemblage were defined using modern coral assemblage distributions across Scott Reef (Veron, 1986; Green et al., 2019; Gilmour et al., 2019; 2022), the Northwest Shelf (Twiggs and Collins, 2010; Wilson, 2013; Moustaka et al., 2019; Heyward and Radford, 2019; Webster et al., 2022) and the Indo-Pacific (Cabioch et al., 1999b; Abbey et al., 2011; Braga et al., 2022) and along with association with co-occurring CCA assemblages defined above (Fig. 5).

Table 6. Summary of coral assemblages and their paleoenvironmental interpretations. The paleowater depths of the coral assemblages and their associated components are given, Indo-Pacific analogues used to support the interpretations are also provided.

Coral assemblage (Ca)	Key components	Associated components	Distribution	Paleoenvironment and inferred water depth
Ca1	Massive *Porites* and associated branching robust to medium and tabular branching fine *Acropora (e.g., staghorn - A. muricata type),* encrusting and massive *Montipora, massive Isopora, Lobophyllia? Euphyllia? Favites, Agariciidae?* Siderastreidae *(e.g., Coscinarea?),* Merulinidae *(e.g., Cyphastrea?),* associated branching robust *Pocillopora,* branching robust *Heliopora coerula,* massive *Platygyra, Goniastrea stelligera.*	Algae up to 5 cm thick, red coralline algae, encrusting foraminifera, abundant vermetid gastropods	All cores	<10 m (< 6 m where Aa1 is associated with vermetid gastropods), consistent with upper forereef slope to reef-flat settings.
Ca2	Massive *Porites* and associated massive *Platygyra, Goniastrea retiformis?*	Algae up to 5 mm thick.	NRSEHDD3JA	< 15 m, protected back reef environment.
Ca3	Massive *Porites* as long-lived individual colonies or mixed assemblage commonly with encrusting *Montipora*	Algae up to x cm thick, occasionally with vermetid gastropods.	All cores	15–60 m fore-reef slope, or < 30 m when associated with Aa2.
Ca4	Encrusting Merulinids (e.g., *Goniopora*? *Dispsastrea*?), Agaricids (e.g., *Pavona, Coeloseris mayeri, Pachyseris rugosa?, Leptoseris papyracea?*), massive and encrusting *Porites*, massive *Galaxea*, encrusting *Montipora* and Acroporids (e.g., *Astreopora* and *Isopora*?), sub-massive *Goniopora*, laminar *Turbinaria*? Encrusting *Tubipora*? Encrusting Siderastreidae*? Lobophyllia/Symphyllia, Echinophyllia,* Fungiidae*?* Dendrophyllidae	Microbialites and thin or laminated algae up to <10 mm, mostly 1-5 mm, red coralline algae. Rhodoliths common.	All cores	> 20 m, representing deeper-water settings with higher turbidity, lagoons, or submerged reef slopes protected from wave energy. Depths > 30 m are inferred when associated with Aa3, and > 60 m when associated with *Cycloclypeus* foraminifera.

Coral Assemblage 1 (Ca1) is characterised by massive *Porites* and associated with robust to medium branching and tabular fine branching *Acropora (*e.g., staghorn – *A. muricata* type*),* encrusting to massive *Montipora* and massive *Isopora.* Other common taxa include *Lobophyllia? Euphyllia? Favites,* Agariciidae? Siderastreidae *(*e.g., *Coscinaraea?* and Merulinidae *(*e.g., *Cyphastrea?).* This assemblage can also contain robust branching *Pocillopora, Heliopora coerula,* massive *Platygyra,* and *Goniastrea stelligera,* representing a diverse reef community. In the modern Scott Reef environment, similar *Porites/Acropora* assemblages with *Cyphastrea* as minor components are characteristic of deep inner reef flats (Done et al., 1994), while robust branching *Acropora/Isopora/Pocillopora* coral species usually dominate the upper forereef slope and reef flats, in water depths of < 10 m (Cabioch et al., 1999; Gilmour et al., 2022). However, when associated with thick algal crusts of *Porolithon* gr. *onkodes* and vermetid gastropods, *Acropora/Isopora* communities in Tahiti and on the GBR are known to have established in < 6 m water depth (Montaggioni and Camoin, 1993; Dechnik et al., 2017a). Massive *Porites* 'bommies' are common on the windward margin of Ningaloo Reef, ca. 800 km to the south, in water depths of 4–6 m (Twiggs and Collins, 2010). Encrusting to massive *Montipora* occur on the windward margin of One Tree Reef on the GBR in 9–12 m water depth and on the mid-upper reef slopes of Mururoa Atoll in 15–30 m water depth (Dechnik et al., 2017a; Camoin et al., 2001). However, the dominance of robust branching species in this assemblage and the common co-occurrence of thick algal crusts of Aa1 and vermetid gastropods suggests assemblage Ca1 represents deposition in water depths of < 6 m.

Coral Assemblage 2 (Ca2) is primarily composed of massive *Porites* and massive *Platygyra*, and possibly *Goniastrea retiformis*?, occurring only in the North Scott Reef core NRSEHDD3JA. *Platygyra* occurs on OTR from 0–15 m water depth (Dechnik et al., 2017b), while massive *Porites* and *Goniastrea retiformis* are observed as an assemblage in the modern

Scott Reef environment characteristic of sheltered reef flats and lagoon slopes (Done et al., 1994). This assemblage composition and modern analogue is consistent with similar assemblages observed in protected back reef environments in the broader Indo-Pacific region (Veron et al., 2016).

Coral Assemblage 3 (Ca3) is dominated by large, thick, massive *Porites*, occurring as long-lived individual colonies or in mixed association with encrusting *Montipora*. *Porites* can occur in water depths down to 60 m (Veron et al., 2016) and is therefore not, on its own, a precise indicator of paleoenvironment (Braga et al., 2022). However, when associated with encrusting *Montipora* and Aa2, Ca3 can be diagnostic of water depths < 30 m (Camoin et al., 2001).

Coral Assemblage 4 (Ca4) is a diverse coral assemblage occurring predominantly in the Hook cores. It is characterised by encrusting Merulinidae (e.g., *Dispsastrea*?), Agariciidae (e.g., *Pavona, Leptoseris papyracea?*), *Pachyseris rugosa*?, encrusting *Montipora*, and massive to encrusting *Porites*. Other taxa include massive *Galaxea*, Acroporidae such as *Astreopora* and *Isopora*?, sub-massive *Goniopora*, laminar *Turbinaria*?, encrusting *Tubipora*?, encrusting Siderastreidae?, Lobophylliidae, including *Lobophyllia* or *Symphyllia* and *Echinophyllia,* and possible Fungiidae and Dendrophyllidae species. The corals are encrusted by thin, 1–5 mm thick algal crusts and are associated with microbialites in the Holocene of Hook 1P (Fig. 3D). Association with *Halimeda* in all the cores can indicate a deeper reef slope environment in water depths of > 20 m (Webster et al., 2022). *Pavona* species can occur from 0 to mesophotic depths (Veron and Pichon, 1979; CoralTraitDatabase, 2020; OBIS, 2020). *Pachyseris, Leptoseris* and *Echinophyllia* can dominate reef slopes in > 20 m water depth (Braga et al., 2022), while encrusting *Montipora* and *Lobophyllia* were found to extend to 30

m on the leeward and windward margins of OTR (Dechnik et al., 2017a). Sub-massive *Goniopora* and free-living corals such as *Fungia*, can be characteristic of low energy environments and tolerant of turbid settings (Veron, 1986; Dechnik et al., 2017a), and thus distribution of corals in an assemblage can vary independently of depth, because increased turbidity reduces light penetration and can cause deep assemblages to occur at relatively shallower depths (Braithwaite, 2016; Braga et al., 2022). Ca4 is therefore characteristic of a deeper turbid environment protected from wave action such as lagoon or fore-reef slope in water depths > 20 m. Depths > 30 m are inferred when associated with Aa3, and > 60 m when associated with *Cylcoclypeus* foraminifera.

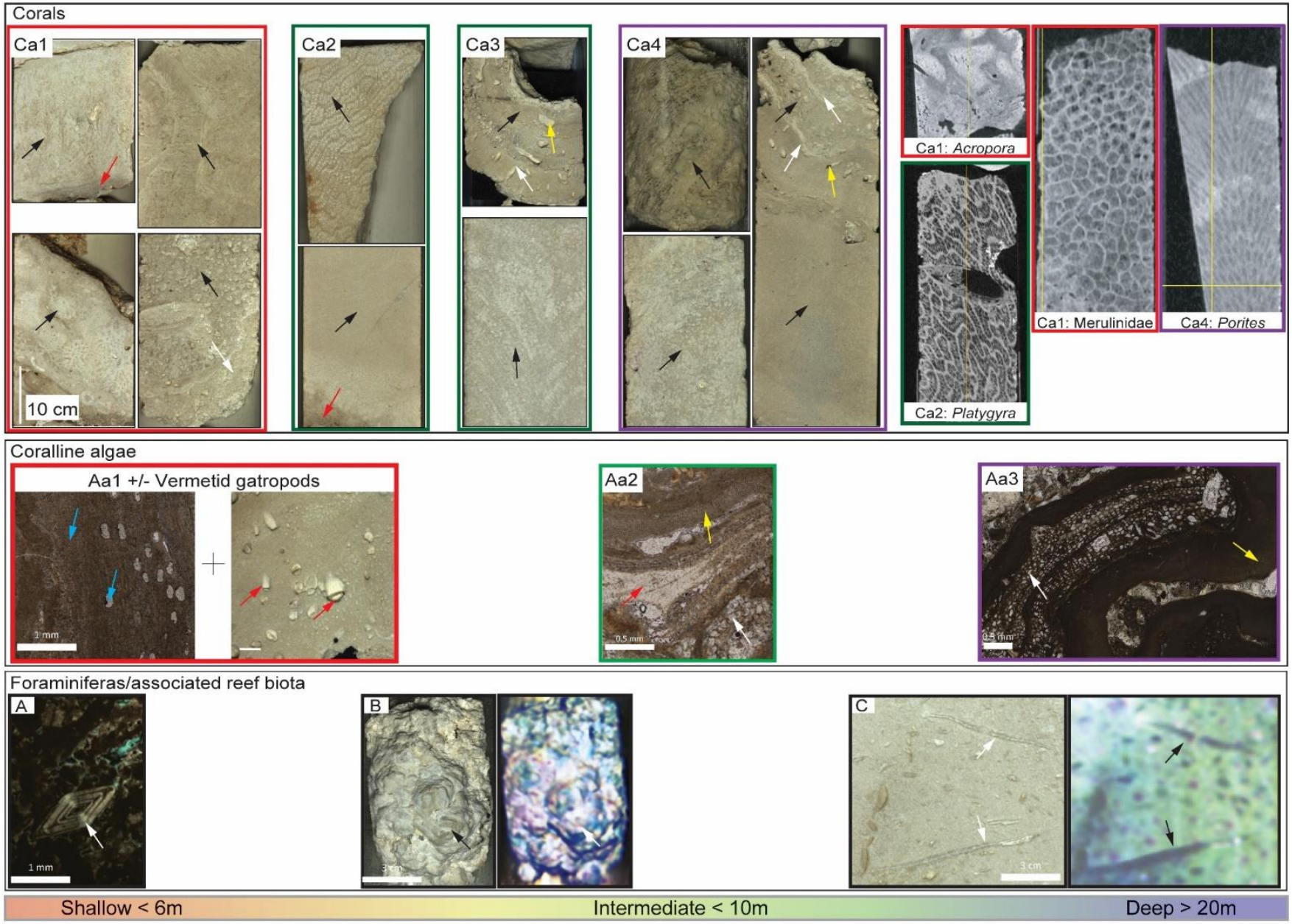

Corals
Ca1
Ca2
Ca3
Ca4
10 cm
Ca1: Acropora
Ca2: Platygyra
Ca1: Merulinidae
Ca4: Porites
Coralline algae
Aa1 +/- Vermetid gatropods
1 mm
Aa2
0.5 mm
Aa3
0.5 mm
Foraminiferas/associated reef biota
A
1 mm
B
C
3 cm
Shallow < 6m
Intermediate < 10m
Deep > 20m

Figure 5. Summary of the coralgal assemblages identified in this study. Top panel shows examples of the four coral assemblages Ca1 – Ca4. Corals in Ca1 are characteristic of shallow, high energy upper reef crest/slope environments. (Ca1) Clockwise from top left: core images of representative corals in Ca1 include, fine branching *Acropora in situ* with encrusting base and corallites right way up (top); Cerioid *Favites*?; massive Merulinidae; robust branching *Acropora.* Black arrows indicate coral, corallite or branch, white arrows indicate CCA, red arrows indicate basal encrustation surface, yellow arrows show bioerosion. (Ca2) core image of *Platygyra* (top) and massive *Porites* (bottom). (Ca3) encrusting *Montipora* (top) and massive *Porites* (bottom). (Ca4) Clockwise from top left: *Dispastraea*, massive *Porites* with encrusting *Montipora* and thin interlaminations of CCA, *Goniopora*. Neutron computed tomographic scans of representative corals that were used to screen sections of coral for dating are shown far right. Brightest whites show highest neutron attenuation and correspond to unaltered aragonite, darker colours correspond to calcite (Williams et al., 2025). Middle panel shows examples of the three algal assemblages identified in this study. Arrows in Aa1 (sample 609949) indicate (blue) *Porolithon* gr. *onkodes* and (red) vermetid gastropods, which together suggest deposition in <6 m water depth. Arrows in Aa2 (sample 609949) indicate (red) bivalve, (yellow) probably *Dawsoniolithon* sp. with (white) encrusting foraminifer, suggest deposition in <30 m water depth. Aa3 (sample 609942) illustrates *Mesophyllum* sp. characteristic of deep-water environments intergrown with encrusting foraminifera. Yellow arrow shows the coaxial ventral core. White arrow indicates encrusting foraminifera. Bottom panel shows various reef biota identified in this study associated with coral and algal assemblages. (A) Large benthic foraminifera *Amphistegina* spp. (*lessonii*?), (B) spheroidal rhodoliths in core (left) and false colour (right), and (C) *Cycloclypeus* foraminifera in core (left) and false colour (right). The lowermost panel indicates water depth corresponding to coralgal assemblages presented above.

4.2 Sedimentary and diagenetic facies analysis

For each core, visual observations of the cores, thin sections, SEM, XRD hyperspectral maps, and core photographs were integrated to characterise the sedimentary (Table 3) and diagenetic facies (Table 7) of each unit. Available U/Th ages were then used to establish a robust chronostratigraphic framework, from which the paleoenvironmental interpretations of each sedimentary package across North and South Scott Reef were reconstructed.

Table 7. Summary of paleosol horizons identified in the Scott Reef cores and their corresponding labels shown on Fig. 12, integrating sedimentological facies transitions, diagenetic and pedogenic features, hyperspectral mineralogical indicators, and available chronological constraints. Hyperspectral colour ranges are given in Figs. 7-9. Where applicable, horizons are compared with exposure surfaces and calcrete intervals previously identified by Collins et al. (2009) to provide contextual correlation. Examples of representative paleosols are shown in Figure 4 and indicated in bold in the table.

Core and depth (m)	Interpretation	Paleosol label	Associated sedimentary facies	Diagenetic and pedogenic evidence	Hyperspectral indicators	Chronological constraint	Correlation to Collins et al. (2009)
NRSEHDD3JA							
26.8 m	Holocene–MIS 5 unconformity	NR–P1	Grainstone/rudstone to framework dominated package (Ca1).	Brown sediment infilling cavities.	Sharp transition from blue to red on 2340 nm absorption feature (**Fig. 7B**). Minor amounts of clay and iron oxides.	U/Th coral ages	26.8 m: R1 thin calcrete, U/Th boundary ages
53.4 m	MIS 5–7 paleosol	NR–P2	Coral framestone (Ca4) to rudstone facies.	Grey-orange-brown sediment infilling bivalve borings and dissolved bioclasts.	Moderate amounts of clay and minor amounts of iron oxides.	U/Th coral ages	51.72 m: R2 calcrete, leached zone
84.05m	MIS 7–9 paleosol	NR–P3	Grainstone/rudstone to rudstone facies.	Yellow-orange sediment coating bioclasts and dissolved coral fragments.	Moderate amounts of clay and iron oxides.	U/Th coral ages	81 m: R3? leached zone
113.2-129 m	MIS 9–11 paleosol, and sub-stages MIS 9a, 9c and 9e?	NR–P4	Grainstone to rudstone facies.	Yellow to dark brown staining of dissolved bivalves and coral clasts and fine sediment infill of	Three very strong 900 nm absorption feature (Fe) events at 113.2 m, 118.7 and 127.1 to 132.7 m. Strong 2200 nm	U/Th coral ages	119 m: R4? calcrete

				cavities, leaching and vugs (**Fig. 4D**).	feature corresponding to 118.7 m.		
158 m	MIS 11–13 paleosol	NR–P5	Packstone with branching fine coral clasts to rudstone facies with branching robust coral clasts. Gradual transition from Ca4 to Ca2.	Horizonation: horizontal brown sediment layer; minor leaching (**Fig. 4E**).	Minor clays and moderate iron oxides in grainstone sample at 156.25 m.	U/Th coral ages	Not defined
190.8 m	MIS 13–15? paleosol	NR–P6	Floatstone to dolomitised floatstone facies.	Yellow staining of dissolved bioclasts, bivalves and coral clasts and fine brown sediment matrix at 190.8 m. Dolomite at 189 m (**Fig. 4A**).	Minor clays evident abundant iron oxides. Distinct 40 cm long dolomite interval.	U/Th coral ages (kyr)	Not defined/possible hiatus?
SRSEBH6J							
36.3 m	Holocene–MIS 5 unconformity	SR–P1	Floatstone to coral framework (Ca3).	Brown coloured secondary sediment infilling of dissolved bioclasts in a floatstone matrix.	Sharp transition from blue to red on 2340 nm absorption feature (**Fig. 8B**). No evidence of clay minerals. Trace amounts of iron oxides (**Fig. 8B and 8F**).	U/Th coral ages	36 m: R1 calcrete
69.45 m	MIS 5–7c drowning unconformity	SR–P2	Packstone/rudstone to floatstone/wackestone (deep facies > 60 m).	Stratified sediment infill.	Moderate increase in iron oxides from ca. 64 m to 76 m. Trace amounts of clays at 69 m.	U/Th coral ages	Not defined
72.7 m	MIS 7c–7e paleosol	SR–P3	*Halimeda*-rudstone to coral framestone (Ca1).	Brown coarse sediment infilling cavities in rudstone facies (**Fig. 4B**).	Moderate increase in iron oxides from ca. 64 m to 76 m. Trace amounts of clays at 73 m.	U/Th coral ages	78 m: R2 calcrete
96-102.3 m	MIS 7e paleosol	SR–P4	Packstone to coral framestone and bindstone (Ca1).	Horizonation: layered sedimentary infill of distinct colours (grey, brown, yellow, and dark grey) within fractures and dissolved clasts, with	Trace amounts of clay at 103 m. Iron oxides abundant from 95 m to 105 m.	U/Th coral ages	95 m: R3 calcrete

				cementation and calcite nodules from ca. 96-102.3 m.			
107-112 m	MIS 7e-9c paleosol	SR–P5	Framestone (Ca4) to floatstone with robust branching coral clasts (Ca1).	Horizonation: layered sedimentary infill of distinct colours (grey, brown, yellow, and dark grey) within fractures and dissolved clasts, with cementation and calcite nodules	No clays observed. Iron oxides abundant from 108 m to 114 m.	U/Th coral ages	
140 m	MIS 9c–9e paleosol	SR–P6	*Halimeda*-grainstone with no coral clasts to rudstone facies with branching fine coral clasts. Change in colour from creamy white to brown.	Heterogeneous brown and grey sedimentary infill of dissolved cavities in a *Halimeda*-grainstone.	Moderate iron-oxides from ca. 143 m to 145 m (**Fig. 8F**) and notable increase at 158 m. Al-rich phyllosilicates evident at 142 m.	U/Th coral ages	140 m: R3a transitional contact
168 m	MIS 9e–11 paleosol	SR–P7	Floatstone facies	Red brown staining around large forams and coral clasts.	Trace amounts of clays ana moderate amounts of iron oxides evident at 172 m.	U/Th coral ages	170m?
Hook 1/3P							
20.5 m	Holocene–MIS 5 unconformity	SR–NE–P1	Altered *Halimeda*-grainstone to coral framework (Ca4).	Slight orange-brown staining in rudstone.	Sharp transition from blue to red on 2340 nm absorption feature (**Fig. 9B**). No evidence of clay minerals. Trace amounts of iron oxides (**Fig. 9F**), becoming abundant for 2 m below.	U/Th coral ages	Not defined
61.89 m	MIS 5–7a? paleosol and sub-stage MIS 7a–7b? paleosol at 67.35 m? Sub-stage MIS 7b–7c? paleosol at 72.05 m?	SR–NE–P2	61.89 m: transition from floatstone to framestone (Ca1), 67.35 m: continuous framestone (Ca1), 72.05 m: framestone (Ca4) to packstone.	Slightly stained dark-grey-brown floatstone at 61.89 m, grey-light brown sediment infill of *Porites* framework at 67.35 m (**Fig. 4H**), irregular mottled fabric, red brown calcarenite matrix with calcite vug-infilling cement at 72.05 m.	Moderate, patchy clays evident from ca. 69 m to 72.7 m. Iron-oxides abundant from ca. 65 m to 73 m.	/	Not defined

94.9 m	MIS 7c–9c? paleosol and sub-stage MIS 9c–9e? paleosol at 96 m	SR–NE–P3	Horizonation: layered sedimentary infill of distinct colours (grey, brown, yellow, and dark grey) within fractures and dissolved clasts. Cementation and black (manganese) deposits coating cavities (**Fig. 4G**) present at 94.9 m and 96 m.	Distinct occurrence of clays at 94.9m and 96 m. Iron oxides abundant from 92 m to 96.5 m.	/	Not defined

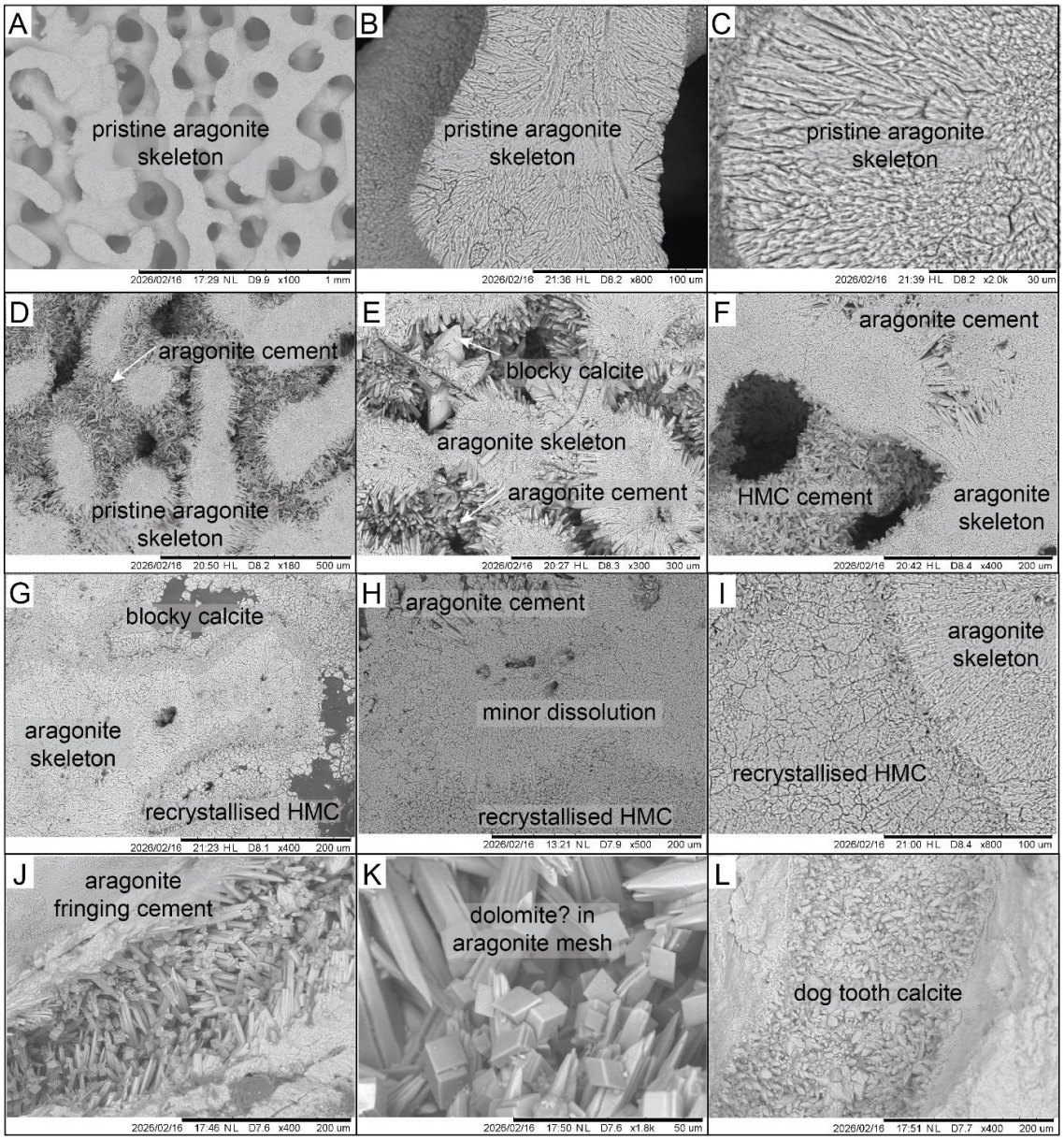


Figure 6. Representative SEM micrographs of skeletal reef framework components and associated marine and meteoric cements from Scott Reef, illustrating a spectrum of diagenesis, used for vetting samples for U/Th dating. (A–C) Pristine aragonite skeletal microstructure. (D) Skeletal aragonite framework with aragonite cement. (E) Aragonitic skeleton partially occluded by blocky calcite cement, suggestive of meteoric diagenesis. (F) High-Mg calcite (HMC) cement replacing skeletal framework. (G) Recrystallised HMC with development of blocky calcite. (H) Minor dissolution features within recrystallised HMC. (I) Transition from

aragonitic skeleton to recrystallised HMC. (J) Dense fringes of acicular aragonite cement lining cavities. (K) Euhedral rhomboids interpreted as possible dolomite within an aragonitic mesh. (L) Dog-tooth calcite cement infilling secondary porosity.

Table 8. Diagenetic characteristics of selected Scott Reef core samples based on hyperspectral, XRD and SEM analyses. Samples shown in **bold** were selected for radiometric dating and are listed in Table 2 and U/Th data in Table 9. All NRSEHDD3JA samples were dated for open-system U/Th ages by Collins et al. (2009). Aragonite % in italics are values determined by XRD; all others are from quantitative hyperspectral data. All samples were screened with hyperspectral.

Sample name	Core	Core depth (m)	Coral assemblage	Aragonite (%)	Calcite (%)	Dolomite (%)	Screening method	Context
609971	Hook 3P	61.97	Ca1	54.2	41.9	0	NCT, Hyperspectral	ISN
609972	Hook 3P	65.92	-	0.1	99.9	0	Hyperspectral	ISX
609973	Hook 3P	68.61	Ca1	1.2	98.7	0.001	NCT, Hyperspectral	IS?
609974	Hook 3P	70.51	-	0	99.9	0	NCT, Hyperspectral	ISX
609980	Hook 3P	87.98	Ca3	2.0	98.0	0	NCT, Hyperspectral	IS?
609981	Hook 3P	93.71	Ca1	7.1	80.6	0	NCT, Hyperspectral	IS?
609982	Hook 3P	94.874	-	0	95.7	0	NCT, Hyperspectral	ISX
609983	Hook 3P	95.3	Ca4	14.6	71.7	0	NCT, Hyperspectral	ISX
609945	SR SE BH6-J	5.25	Ca1	*99.4*	0.6	0	NCT, Hyperspectral	IS
609946	SR SE BH6-J	26.4	Ca4	*100*	0	0	NCT, Hyperspectral	IS
609948	SR SE BH6-J	38.66	Ca1	73.6	26.3	0	NCT, Hyperspectral	IS
609951	SR SE BH6-J	69.25	-	40.9	55.8	0	NCT, Hyperspectral	ISX
609952	SR SE BH6-J	71.4	Ca1	99.3	0.7	0	NCT, Hyperspectral, SEM	IS
609953	SR SE BH6-J	78.1	-	26.9	49.7	0	NCT, Hyperspectral	ISX
609955	SR SE BH6-J	97.2	Ca1	76.3	21.0	0	NCT, Hyperspectral	IS
609958	SR SE BH6-J	149	-	49.4	48.5	0	NCT, Hyperspectral	ISX
8.6	NR SE HDD3-JA	8.6	Ca3	93.8	6.2	0	Hyperspectral	IS
23.25	NR SE HDD3-JA	23.15	-	*82.8*			Hyperspectral	IS
609931	NR SE HDD3-JA	33	-	1.2	98.7	0	NCT, Hyperspectral	ISX
34.05	NR SE HDD3-JA	34.05	-	0.2	99.7	0	Hyperspectral	ISX
36.1	NR SE HDD3-JA	36.1	-	3.1	96.8	0	Hyperspectral	ISX
609932	NR SE HDD3-JA	51.9	-	0.1	99.1	0	NCT, Hyperspectral	ISX

62.5	NR SE HDD3-JA	62.5	-	1.7	98.2	0	Hyperspectral	IS
77	NR SE HDD3-JA	77	-	0.8	99.1	0	Hyperspectral	ISX
84.05	NR SE HDD3-JA	84.05	-	40.8	59.2	0	Hyperspectral	ISX
609934	NR SE HDD3-JA	84.6	-	0.3	99.5	0	NCT, Hyperspectral	ISN
92.15	NR SE HDD3-JA	92.15	-	2.4	97.5	0	Hyperspectral	ISX
113.2	NR SE HDD3-JA	113.2	-	2.1	97.6	0	Hyperspectral	ISX
609937	NR SE HDD3-JA	118.5	-	0.1	99.9	0	NCT, Hyperspectral	ISX
132.7	NR SE HDD3-JA	132.7	-	0.2	99.5	0	Hyperspectral	ISX
140.45	NR SE HDD3-JA	140.45	-	0.6	99.4	0	Hyperspectral	ISX
151	NR SE HDD3-JA	151	Ca4	0.5	99.3	0	Hyperspectral	IS
609941	NR SE HDD3-JA	171.7	Ca2	0.2	99.8	0	NCT, Hyperspectral	IS
609942	NR SE HDD3-JA	189.4	-	0.1	3.5	0.964	NCT, Hyperspectral	IS?
193.5	NR SE HDD3-JA	193.5	-	0.5	99.3	0	Hyperspectral	ISX

4.2.1 North Scott Reef Southeast margin

Core NR SE HDD3-JA (elevation below sea level 0.52 m and hole depth 201.5 m) is close to sea-level and located on the Southeast reef crest of North Scott Reef between the lagoon and steep slope. This core intersects seven sedimentary packages and is situated in a moderate energy hydrodynamic setting associated with a 4.1 m tidal range and average ocean current velocity between 0 and 0.1 m/s (Green et al., 2018). XRD data indicate pervasive recrystallisation below the Holocene, with all Pleistocene samples showing < 40.8 % aragonite and thus no new samples were selected from this core for U-series dating (Table 8).

Table 9. Uranium-series geochemical data, initial uranium isotope compositions, and interpreted ages for fossil coral samples from Scott Reef (this study) and previously published data from Collins et al. (2009). Activity ratios are reported as measured and detrital-corrected values using the decay constants of Cheng et al. (2013). Initial $\delta^{234}U$ values ($\delta^{234}U_i$) are calculated from back-calculated initial ($^{234}U/^{238}U$) activity ratios following $\delta^{234}U = [(^{234}U/^{238}U)_a - 1] \times 1000$, consistent with conventions outlined by Chutcharavan et al. (2018). Samples are classified as closed, closed–open (transitional), or open system based on $\delta^{234}U_i$ values relative to modern seawater (145.0 ± 1.5‰; Chutcharavan et al (2018)). Closed-system samples yield ages considered reliable within analytical uncertainty, whereas open-system samples exhibit elevated or depleted $\delta^{234}U_i$ values consistent with post-depositional uranium mobility and require interpretation using open-system corrections using the calculations of Thompson et al. (2013). Thompson-corrected interpreted ages are provided for samples in this study only. For previously published data (Collins et al., 2009), ages and activity ratios are reproduced as originally reported. Samples exhibiting significant U loss or falling within the "forbidden zone" of activity-ratio space (see Figure 10 insert) are identified and excluded from chronological interpretation, following established screening protocols for coral U-series dating (e.g., Chutcharavan et al., 2018; Webster et al., 2022).

Sample Name (this study)	**Depth (m)**	**^{238}U (ppm) ± 2σ**	**^{232}Th (ppb) ± 2σ**	**[^{230}Th / ^{232}Th] ± 2σ**	**[^{230}Th / ^{238}U] ^{a} ± 2σ**	**[^{234}U / ^{238}U] a ± 2σ**	**Age (ka) ± 2σ**	**$\delta^{234}Ui$ (‰) ± 2σ**	**$\delta^{234}U_i$**	**U-Series isotope system interpretation**	**Thompson-corrected Interpreted Age (ka) ± 2σ**
628889	9.3	3.126 ± 0.0029	1.322 ± 0.004	169.86 ± 2.96	0.0237 ± 0.0004	1.1472 ± 0.0013	2.265 ± 0.04 ka	1.1481 ± 0.0013	148.1382	Closed	**1.9 ± 0.4 ka**
628890	22.4	2.541 ± 0.0026	0.112 ± 0.002	3842.99 ± 79.87	0.0556 ± 0.0006	1.1478 ± 0.0016	5.416 ± 0.058 ka	1.15 ± 0.0016	150.0363	Closed	**4.4 ± 0.5 ka**
628891	33	2.3954 ± 0.0024	0.047 ± 0.002	14703.29 ± 644.42	0.0951 ± 0.0007	1.1451 ± 0.0014	9.455 ± 0.071 ka	1.149 ± 0.0014	149.0491	Closed	**8.8 ± 0.5 ka**
628892	45.64	2.7207 ± 0.0025	0.146 ± 0.003	40768.43 ± 885.63	0.7188 ± 0.0029	1.1114 ± 0.0014	110.8 ± 0.8 ka	1.1523 ± 0.0019	152.3492	Closed-Open	**108.7 ± 1.2 ka**
628893	51.35	2.3313 ± 0.0014	1.978 ± 0.005	2647.83 ± 12.06	0.7404 ± 0.0028	1.1096 ± 0.0015	117 ± 0.9 ka	1.1526 ± 0.002	152.5924	Closed-Open	**114.7 ± 1.3 ka**

628895	81	0.4905 ± 0.0009	1.901 ± 0.005	626.06 ± 3.69	0.7997 ± 0.0045	1.1151 ± 0.002	133.1 ± 1.5 ka	1.1678 ± 0.0028	167.8384	Open	**124.7 ± 2.0 ka**
628894	71.9	1.952 ± 0.0017	4.428 ± 0.013	1286.29 ± 7	0.9617 ± 0.0045	1.0828 ± 0.0015	223.6 ± 3.5 ka	1.1559 ± 0.0027	155.9205	Open	**219.1 ± 3.4 ka**
628896	81.38	3.0713 ± 0.0019	0.317 ± 0.004	28141.59 ± 341.95	0.9562 ± 0.0023	1.0826 ± 0.0016	219.8 ± 2 ka	1.1538 ± 0.0025	153.8376	Closed-Open	**216.3 ± 2.7 ka**
628897	106.2	2.3018 ± 0.0019	0.416 ± 0.003	16153.03 ± 140.42	0.963 ± 0.0033	1.0797 ± 0.0013	227.1 ± 2.7 ka	1.1515 ± 0.0023	151.532	Closed-Open	**224.8 ± 2.9 ka**
628898	102	1.7827 ± 0.0017	4.41 ± 0.011	1175.25 ± 4.61	0.9583 ± 0.0031	1.0827 ± 0.0015	221.2 ± 2.5 ka	1.1546 ± 0.0025	154.5743	Open	**217.4 ± 2.9 ka**
628899	102.58	3.1232 ± 0.0022	0.139 ± 0.003	66878.44 ± 1385.27	0.9822 ± 0.0031	1.1096 ± 0.0009	217.6 ± 2.1 ka	1.2027 ± 0.0018	202.6593	Open	**190.9 ± 1.9 ka**
628900	107.548	2.5833 ± 0.0024	0.451 ± 0.004	17093.08 ± 143.34	0.9833 ± 0.0027	1.0758 ± 0.0012	247.6 ± 2.8 ka	1.1527 ± 0.0022	152.6877	Closed-Open	**244.5 ± 3.0 ka**
628901	117.276	2.5667 ± 0.0026	0.501 ± 0.004	15365.47 ± 130.73	0.989 ± 0.0042	1.0767 ± 0.0014	252 ± 4.2 ka	1.1564 ± 0.0028	156.356	Open	**246.8 ± 4.0 ka**
928902	125.01	1.7531 ± 0.0014	1.417 ± 0.004	3865.47 ± 14.14	1.0294 ± 0.0029	1.0758 ± 0.0016	300.3 ± 5.1 ka	1.1772 ± 0.0031	177.2401	Open	**281.8 ± 5.0 ka**
628903	142.2	1.9499 ± 0.0018	0 ± 0	2044183.58 ± 204614.58	1.0396 ± 0.0022	1.0598 ± 0.0021	357 ± 9 ka	1.1642 ± 0.0036	164.2057	Open	**336.7 ± 8.776 ka**
628904	171.9	2.375 ± 0.0022	0.11 ± 0.004	70862.35 ± 2380.58	1.0609 ± 0.0037	1.0598 ± 0.0018	428 ± 21 ka	1.2005 ± 0.0097	200.5312	Open	**384.3 ± 12.731 ka**
628905	177.2	19.4041 ± 0.0152	6.52 ± 0.038	9502.01 ± 58.38	1.053 ± 0.0022	1.0578 ± 0.0017	406 ± 12 ka	1.1824 ± 0.0044	182.3508	Open	**400.6 ± 13.438 ka**
609964	20.58	3.2914 ± 0.0026	0.148 ± 0.002	3612.38 ± 64.74	0.0536 ± 0.0005	1.1459 ± 0.0014	5.223 ± 0.048 ka	1.148 ± 0.0014	148.0467	Closed	**4.9 ± 0.5 ka**
609971	61.97	1.0064 ± 0.0011	64.45 ± 0.093	54.85 ± 0.19	1.1573 ± 0.004	1.0775 ± 0.0017	Significant U loss, fall into Forbidden Zone				
609983	95.3	1.4874 ± 0.0017	11.97 ± 0.014	413.49 ± 0.97	1.0964 ± 0.0026	1.0405 ± 0.002					

Sample Name (Collins et al., 2009)	**Depth (m)**	**^{238}U (ppm) ± 2σ**	**^{232}Th_nm_g ± 2σ**	**[^{230}Th / ^{232}Th] ± 2σ**	**[^{230}Th / ^{238}U] a ± 2σ**	**[^{234}U / ^{238}U] a ± 2σ**	**Corr_^{230}Th_Age_ka**	**δ^{234}Ui (‰) ± 2σ**	**δ^{234}U$_i$**	**U-Series isotope system interpretation**	**Reported Age (ka) ± 2σ**
BH6-J-1.50	1.5	2.7794 ± 0.051	0.19 ± 0.00574	50.173 ± 0.00505	3.80E-05 ± 1.148	1.148 ± 0.0013	0.741 ± 0.007	1.148 ± 0.0013	148	Closed	**0.741 ± 0.007**
BH6-J-1.80	1.8	2.6066 ± 0.047	0.219 ± 0.00144	201.329 ± 0.00147	5.30E-05 ± 1.148	1.148 ± 0.0012	0.806 ± 0.005	1.149 ± 0.0012	149	Closed	**0.806 ± 0.005**
BH6-J-5.25	5.25	3.468 ± 0.048	0.208 ± 0.00064	1000.246 ± 0.00062	7.10E-05 ± 1.148	1.148 ± 0.0013	1.35 ± 0.007	1.149 ± 0.0013	149	Closed	**1.35 ± 0.007**
BH6-J-9.45	9.45	2.811 ± 0.043	0.236 ± 0.00132	669.143 ± 0.00144	7.30E-05 ± 1.145	1.145 ± 0.0011	2.296 ± 0.008	1.146 ± 0.0011	146	Closed	**2.296 ± 0.008**

BH6-J-11.65	11.65	3.12 ± 0.046	0.34 ± 0.00046	2394.052 ± 0.00073	0.00019 ± 1.147	1.147 ± 0.0014	2.59 ± 0.019	1.149 ± 0.0014	149	Closed	**2.59 ± 0.019**
BH6-J-15.85	15.85	3.4355 ± 0.044	0.279 ± 0.00053	2954.003 ± 0.00069	9.10E-05 ± 1.148	1.148 ± 0.0013	3.356 ± 0.01	1.149 ± 0.0013	149	Closed	**3.356 ± 0.01**
BH6-J-17.55	17.55	2.736 ± 0.042	0.17 ± 0.01286	110.093 ± 0.01014	0.00013 ± 1.149	1.149 ± 0.0011	3.78 ± 0.019	1.151 ± 0.0011	151	Closed-Open	**3.78 ± 0.019**
BH6-J-18.65	18.65	2.833 ± 0.052	0.182 ± 0.00094	1652.136 ± 0.00079	0.00015 ± 1.147	1.147 ± 0.0013	4.033 ± 0.015	1.148 ± 0.0013	148	Closed	**4.033 ± 0.015**
BH6-J-23.40	23.4	2.7723 ± 0.048	0.298 ± 0.00302	709.252 ± 0.00418	0.00018 ± 1.145	1.145 ± 0.0013	5.749 ± 0.019	1.147 ± 0.0013	147	Closed	**5.749 ± 0.019**
BH6-J-26.60	26.6	2.5614 ± 0.036	0.514 ± 0.00294	839.381 ± 0.007	0.00024 ± 1.149	1.149 ± 0.0010	7.175 ± 0.025	1.153 ± 0.0010	153	Closed-Open	**7.175 ± 0.025**
BH6-J-27.90	27.9	2.2999 ± 0.039	0.285 ± 0.00168	1457.548 ± 0.00222	0.00018 ± 1.145	1.145 ± 0.0010	7.983 ± 0.02	1.148 ± 0.0010	148	Closed	**7.983 ± 0.02**
BH6-J-32.20	32.2	2.1313 ± 0.047	0.348 ± 0.00062	4144.208 ± 0.001	0.00024 ± 1.145	1.145 ± 0.0014	9.081 ± 0.028	1.149 ± 0.0015	149	Closed	**9.081 ± 0.028**
BH6-J-32.45	32.45	2.3919 ± 0.037	0.208 ± 0.00317	918.326 ± 0.00306	0.00018 ± 1.145	1.145 ± 0.0011	9.21 ± 0.022	1.148 ± 0.0012	148	Closed	**9.21 ± 0.022**
BH6-J-32.95	32.95	2.5236 ± 0.042	0.211 ± 0.0004	7879.106 ± 0.00039	0.00024 ± 1.145	1.145 ± 0.0012	9.41 ± 0.027	1.148 ± 0.0013	148	Closed	**9.41 ± 0.027**
BH6-J-34.60	34.6	2.3228 ± 0.045	0.229 ± 0.00185	1656.321 ± 0.00196	0.00027 ± 1.145	1.145 ± 0.0013	9.985 ± 0.03	1.149 ± 0.0013	149	Closed	**9.985 ± 0.03**
BH6-J-51.25	51.25	2.6788 ± 0.049	0.336 ± 0.00062	42707.145 ± 0.00096	0.00118 ± 1.111	1.111 ± 0.0013	120.496 ± 0.44	1.156 ± 0.0017	156	Open	**120.496 ± 0.44**
BH6-J-85.10	85.1	2.1202 ± 0.039	0.226 ± 0.00077	34887.642 ± 0.0008	0.00117 ± 1.089	1.089 ± 0.0012	220.459 ± 1.257	1.166 ± 0.0019	166	Open	**220.459 ± 1.257**
BH6-J-177.20	177.2	2.3531 ± 0.045	0.167 ± 0.00302	10704.452 ± 0.00233	0.00168 ± 1.06	1.060 ± 0.0012	386.844 ± 7.602	1.180 ± 0.0030	180	Open	**386.844 ± 7.602**
HDD3-JA-1.10	1.1	2.7744 ± 0.045	0.167 ± 0.00062	0.00048 ± 71.36	0.0281 ± 8.60E-05	1.150 ± 0.0013	2.689 ± 0.009	1.15 ± 0.0013	150	Closed	**2.689 ± 0.009**
HDD3-JA-8.60	8.6	2.8637 ± 0.046	0.121 ± 0.0006	0.00034 ± 29.334	0.0595 ± 0.00017	1.146 ± 0.0012	5.789 ± 0.018	1.146 ± 0.0012	146	Closed	**5.789 ± 0.018**
HDD3-JA-23.25	23.25	2.8703 ± 0.033	0.212 ± 0.00118	0.00117 ± 23.35	0.0874 ± 0.00021	1.145 ± 0.0008	8.624 ± 0.023	1.145 ± 0.0008	145	Closed	**8.624 ± 0.023**
HDD3-JA-23.80	23.8	3.6686 ± 0.037	0.184 ± 0.00295	0.00252 ± 16.797	0.0866 ± 0.00013	1.146 ± 0.0008	8.526 ± 0.015	1.146 ± 0.0008	146	Closed	**8.526 ± 0.015**
HDD3-JA-27.20	27.2	2.4926 ± 0.059	0.16 ± 0.0051	0.00379 ± 2.506	0.782 ± 0.00142	1.108 ± 0.0018	128.939 ± 0.627	1.108 ± 0.0018	108	Open	**128.939 ± 0.627**
HDD3-JA-31.60	31.6	2.1101 ± 0.051	0.228 ± 0.00028	0.00029 ± 3.281	0.8043 ± 0.00153	1.110 ± 0.0013	135.651 ± 0.607	1.11 ± 0.0013	110	Open	**135.651 ± 0.607**
HDD3-JA-58.00	58	2.8925 ± 0.049	0.829 ± 0.00109	0.00419 ± 1.944	0.9496 ± 0.00331	1.085 ± 0.0011	212.283 ± 2.328	1.085 ± 0.0011	85	Open	**212.283 ± 2.328**

HDD3-JA-91.40	91.4	1.9539 ± 0.043	0.184 ± 0.00058	0.00049 ± 2.496	1.0426 ± 0.00182	1.070 ± 0.0012	334.055 ± 4.685	1.07 ± 0.0012	70	Open	**334.055 ± 4.685**
HDD3-JA-151.10	151.1	1.2112 ± 0.038	0.166 ± 0.00631	0.00487 ± 4.204	1.0339 ± 0.00214	1.031 ± 0.0012	514.977 ± 29.864	1.031 ± 0.0012	31	Open	**514.977 ± 29.864**
HOOK 1P-02	11.6	2.4235 ± 0.068	0.329 ± 0.00074	0.00113 ± 14.065	0.1041 ± 0.0004	1.146 ± 0.0016	10.341 ± 0.045	1.146 ± 0.0016	146	Closed	**10.341 ± 0.045**
HOOK 1P-03	14.9	2.5967 ± 0.074	0.242 ± 0.00429	0.00056 ± 12.024	0.1117 ± 0.00053	1.144 ± 0.0018	11.153 ± 0.059	1.144 ± 0.0018	144	Closed	**11.153 ± 0.059**

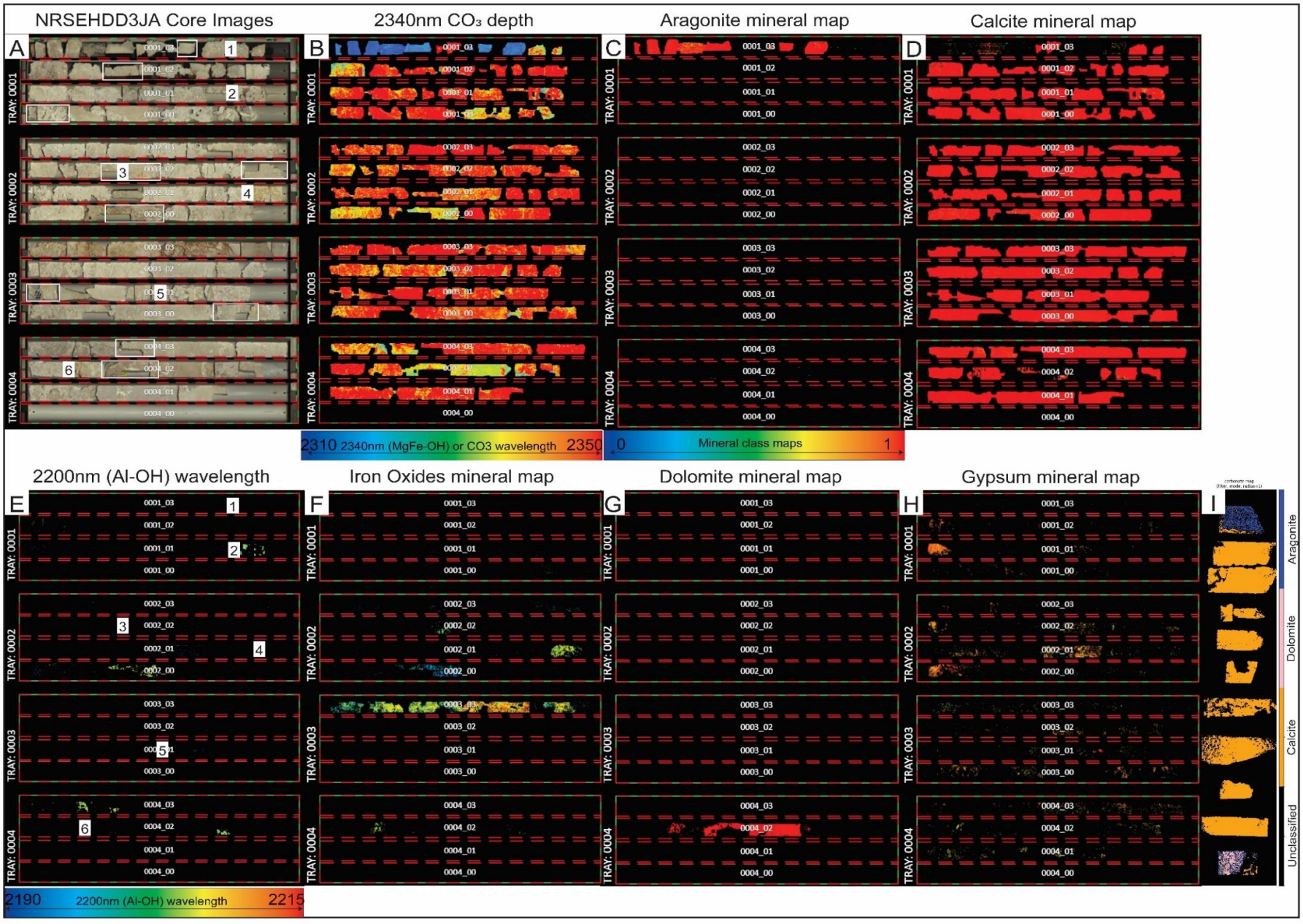

NRSEHDD3JA Core Images
2340nm CO_3 depth
Aragonite mineral map
Calcite mineral map
A
B
C
D
TRAY: 0001
TRAY: 0002
TRAY: 0003
TRAY: 0004
0001_03
0001_02
0001_01
0001_00
0002_03
0002_02
0002_01
0002_00
0003_03
0003_02
0003_01
0003_00
0004_03
0004_02
0004_01
0004_00
1
2
3
4
5
6
2310 2340nm (MgFe-OH) or CO3 wavelength 2350
0 Mineral class maps 1
2200nm (Al-OH) wavelength
Iron Oxides mineral map
Dolomite mineral map
Gypsum mineral map
E
F
G
H
I
2190 2200nm (Al-OH) wavelength 2215
Aragonite
Dolomite
Calcite
Unclassified

Figure 7. Hyperspectral images of Scott Reef core NRSEHDD3JA used to guide lithologic interpretations. (A) High-resolution core images of recovered sections of NRSEHDD3JA core. Numbers 1-6 illustrate interpreted paleosols that correlate with the occurrence of Al-rich phyllosilicates. (B) Carbonate (CO_3) absorption depth at 2340 nm, highlighting variation in carbonate mineral content and diagenetic alteration. Warmer colours indicate higher absorption depths corresponding to higher abundances of calcite mineral. (C) Classified mineral class map showing distributions of Aragonite. (D) Classified mineral class map showing distributions of Calcite. (E) Al–OH absorption at 2200 nm, indicating minor clay or the occurrence of phyllosilicates, used to interpret the paleosols in (A). (F) Classified mineral class map showing distributions of Iron oxides. (G) Classified mineral class map showing distributions of Dolomite. (H) Classified mineral class map showing distributions of Gypsum. (I) Hyperspectral images of 11 NRSEHDD3JA core samples using the equipment and code developed in Murphy et al., (2017) to validate the imaging methods. Spectral ranges defined are 2308 – 2322 nm for aragonite, 2333 – 2345 nm for calcite, and 2320 – 2328 nm for dolomite. The 11 samples correspond to the samples in white boxes in panel A from shallow at the top left to deep at the bottom right. Core tray numbers are indicated and are 1 m long by 12 cm wide. Colour legend in panel C applies to all mineral class maps.

4.2.1.1 **Package 1 –** *Coral framework and rudstone (core depth 0–26.5m; thickness 26.5m thick)*

The 2340 nm (CO_3) hyperspectral absorption feature indicates well-preserved aragonite within Holocene reef framework facies, expressed as blue tones in Figure 7, with the exception of a completely altered sample at 22.9 m, which appears red in Figure 7. Reduced absorption (red to yellow-green tones) represents diagenetically altered zones dominated by calcite, and trace amounts of gypsum and no evidence for dolomite. The sharp spectral transition from blue to red at 26.5 m, corresponds to the Holocene–Pleistocene boundary. The 900 nm and 2200 nm (Al-OH) absorption features indicate slightly elevated absorption at 26.5 m corresponding to Al-rich phyllosilicates and Fe associated with the Holocene–Pleistocene boundary, and elevated Fe levels at 22.9 m. Package 1 extends from the top of the core to 26.5 m and is characterised by *in situ* massive and branching coral framework interbedded with rudstone facies and a grainstone with dissolved *Halimeda* plates at 22.9 m. There is minor diagenetic alteration throughout with minor marine micrite cements. A 1 m thick gradational paleosol occurs at the base of the package (NR–P1: Table 7), marked by dark-brown staining of *Halimeda*-rich grainstone–rudstone facies.

Chronostratigraphic and paleoenvironmental interpretation (MIS 1 ca. 10 kyr)

The uppermost sedimentary package 1 is composed of Holocene reef framework that initiates at 23.8 m, with an *in situ Acropora* colony and a massive *Porites* coral at 23.25 m, encrusted by CCA and vermetid gastropods, characteristic of Ca1 deposited in a shallow water (< 6 m) environment. A U-series age from a pristine coral at 23.15 m indicates reef growth at 8.6 kyr (Table 9). At 22.9 m a calcitic interval associated with minor amounts of Fe could indicate a very brief period of platform exposure. At 8.6 m, a massive *Porites* coral associated with Aa3, overlain by carbonate sand at 8.45 m, marks a transition to a lower energy,

mesophotic fore-reef slope or deep back-reef lagoon environment (> 20 m). This assemblage, dominated by non-geniculate coralline algae tolerant of low light, is typical of lower energy hydrodynamic settings (Adey and Macintyre, 1973; Braga and Aguirre, 2004; Webster et al., 2009). A U-series age of 5.8 kyr at 8.6 m indicates continued reef accretion into the mid-Holocene (Table 9). The presence of the shallow algal assemblage (Aa1), together with a fine-branching *Acropora* colony with encrusting foraminifera and vermetid gastropods at 1.45 m and a *Porites* coral at 1.1 m represent a return to a higher energy, shallow reef environment. This sequence of coralgal assemblages indicate an initial deepening sequence followed by a shallowing upwards trend to present. A major stratigraphic hiatus between packages 1 and 2 is consistent with prolonged subaerial exposure since the Last Interglacial (ca. 120 kyr).

4.2.1.2 **Package 2 –** G*rainstone-rudstone dominated with minor coral framework (core depth 26.5–51.85m; thickness 24.25m)*

Hyperspectral mineral maps indicate that sedimentary package 2 is composed of almost pure calcite with intermittent patches of gypsum, including a 6 cm thick interval at 35 m. Sedimentary package 2 is 24 m thick composed of bioclastic *Halimeda*-rich grainstone to rudstone interval with heavily altered or dissolved branching and massive coral clasts such as submassive Merulinidae, and *in situ* massive *Porites* framework common between 43 and 48 m. There is abundant dissolution of aragonitic components such as *Halimeda* and some algal laminations up to 20 mm thick. Thin section and XRD data confirm that this package is pervasively altered with heavily micritised skeletal grains and secondary voids lined with microspar cement composed of dog-tooth calcite crystals. SEM observations indicate exposure to both marine and meteoric diagenesis. The package is bounded by a subaerial exposure event at 52 m (Fig. 7), characterised by grey-orange-brown sediment infilling bivalve borings and

dissolved bioclasts. Evidence for this pedogenic event extends for 20 cm with no direct evidence of paleosol horizonation (NR–P2: Table 7).

Chronostratigraphic and paleoenvironmental interpretation (MIS 5 ca.120 kyr)

Association with Aa3 and abundant bivalves, indicates deposition in a moderate to low energy reef slope setting (> 30 m), with U/Th coral ages constraining accumulation between < 208.5 kyr and 125.7 kyr (Table 9).

4.2.1.3 **Package 3 –** *Recrystallised rudstone to floatstone, grainstone and coral framework (core depth 51.85–82.5m; thickness 32.65m)*

Calcite is the major component of package 3 with minor volumes of gypsum throughout and no evidence for dolomite. Iron oxides and clays are evident at the base of the package (NR–P3: Table 7). Sedimentary package 3 is 32 m thick and heavily altered, predominantly composed of rudstones to floatstones, grainstones and sections of recrystallised coral framework throughout. The top of package 3 is a grainstone-rudstone facies with light-dark brown secondary sediment infilling consistent with pedogenic processes, including evidence for root structuring (rhizoliths) observed in thin section (Collins et al., 2009). XRD and hyperspectral data confirm that this package is heavily altered with < 1.7 % aragonite (Table 8), indicating that the pre-existing U/Th age is unreliable.

Chronostratigraphic and paleoenvironmental interpretation (MIS 7 ca. 240 kyr)

A completely recrystallised, *in situ* massive *Porites* at 80.5 m, with associated vermetid gastropods and Aa1 at the top of the package, together with evidence of Aa2 at 53.6 m, indicates two distinct phases of shallow water deposition with paleowater depths of < 6 m. Altered branching coral clasts within the grainstone-rudstone facies, including *Seriatopora*, is

indicative of a high energy reef slope environment. Bindstone facies with encrusting coral at 71 m marks a transition to a reef crest or forereef setting. The presence of branching *Montipora* and *Porites* coral clasts and *in situ* columnar *Pavona* coral at 58 m indicates environmental stabilisation within the upper reef slope. This package is characterised by an apparent shallow to deep to shallow trend with an unreliable U/Th coral age of 212 kyr at 58 m (Table 9) likely placing it within MIS 7.

4.2.1.4 Package 4 – *Rudstone and grainstone (core depth 82.5–115m; thickness 32.5m)*

The top of package 4 shows increased absorption in the 900 nm and 2200 nm features and pervasive calcite and gypsum throughout. Three very strong 900 nm absorption feature (Fe) events occur at 113.2 m, 118.7 (Fig. 4D) and 127.1 to 132.7 m as well as a strong 2200 nm feature corresponding to 118.7 m. Sedimentary package 4 is composed almost entirely of detrital material composed of reworked branching-fine coral clasts and bioclastic sediment in grainstone and rudstone facies. The section is heavily leached with dissolution, recrystallisation and borings evident throughout, including marine cements replacing the aragonitic *Halimeda* grains (Fig. 4C). Yellow-orange sediment coatings on bioclasts and dissolved coral fragments are observed at the top of the package, while yellow to dark-brown staining of dissolved bivalves and coral clasts, together with fine-grained sediment infill of cavities, leaching features, and vugs, occurs at the base of the package from 115 m, where brown sediment infills secondary porosity within grainstone facies and is interpreted as a paleosol (NR–P4: Table 7).

Chronostratigraphic and paleoenvironmental interpretation (MIS 9 ca. 334 kyr)

Two *in situ* coral colonies are identified at 91 m (massive Merulinidae and *Montipora*) and 96 m (*Coeloseris mayeri*) (Ca4). *Lithophyllum* gr. *prototypum* and *Lithophyllum* gr. *pustulatum* coralline algae (Aa2) indicate deposition in an intermediate to deep, low energy

setting (< 30 m). *Porolithon* gr. *onkodes* and branching coral clasts at the base of the package indicate provenance from a shallow setting. Well-preserved *Sphaerogypsina* foraminifera at 92.15 m indicate fairly shallow (<10 m), high energy depositional settings. However, *Amphistegina lessonii* foraminifera, typical of low-moderate energy environments such as the fore-reef or reef slope, occur at 113.20 m. Therefore, overall, this package is interpreted to represent two shallowing upwards sequences from lower to upper fore-reef slope that could be correlated to multiple sea-level oscillations associated with MIS 9. A date of 334 kyr at 91.4 m is consistent with deposition during MIS 9e.

4.2.1.5 **Package 5 –** *Grainstone-rudstone dominated (core depth 115–158 m; thickness 43 m)*

A minor increase in the 2200 nm Al-OH absorption feature and a pronounced increase in the 900 nm feature are observed in the grainstone sample at 156.25 m. Elevated 2200 nm absorption indicates high abundance of Al-rich phyllosilicates (Fig. 7). Hyperspectral mineral maps further show continued moderate amounts of gypsum, dominance of calcite, and no detectable aragonite. Package 5 is dominated by grainstone-rudstone facies, with interbedded wackestone between 132 and 137 m containing branching and domal coral clasts. Horizontal brown sediment layering and minor leaching are observed within the package. The top of the package is bounded by a paleosol (NR–P4: Table 7) identified by yellow-orange secondary sediment infill within grainstone facies. The paleosol bounding the base of the package is less clearly expressed in the hyperspectral image but clearly visible in the core as horizontally layered soil horizons (NR–P5: Table 7). Crystalline textures and dissolved *Halimeda* plates occur throughout the sequence, particularly within the upper 10 m, while extensive leaching, dissolution, cementation, and yellow-orange staining between 121 and 129 m indicate significant diagenetic alteration.

Chronostratigraphic and paleoenvironmental interpretation (MIS 13 ca. 515 kyr at 151 m)

In situ Platygyra and *Porites* corals of Ca2 (Table 6) occur near the base of the package and indicate deposition in deeper reef slope settings. An age of 514 kyr at 151 m tentatively places this package within MIS 13 (Table 9), however, complete diagenetic alteration evidenced by XRD analyses (Table 8) precludes reliable age determination.

4.2.1.6 **Package 6 –** *Coral framework and grainstone-rudstone-floatstone dominated (core depth 158–190.8 m; thickness 32.8 m)*

A minor increase in the 2200 nm Al-OH absorption feature and a pronounced increase in the 900 nm feature are observed. Hyperspectral mineral maps indicate the package is dominated by calcite, moderate gypsum occurrences, and no detectable aragonite. A dolomitic interval is identified at 189 m (Fig. 4A) (> 96% dolomite from XRD analysis; Table 8) and is substantiated by spectral anomalies in the 2340 nm (MgFe-CO_3) band in hyperspectral maps (Fig. 7G). The sedimentary package 7 extends from ca. 158 – 190.8 m and consists of grainstone-rudstone and floatstone facies with *in situ* coral framework. Yellow staining is observed on dissolved bioclasts, bivalves and coral clasts within a fine brown sediment matrix at 190.8 m. Increased clay content is associated with the base of the upper bounding paleosol (NR–P6: Table 7), while iron-rich sediment is observed toward the top of the package.

Chronostratigraphic and paleoenvironmental interpretation (MIS 15?)

Between 170 m and 190.8 m the occurrence of Aa3 suggest the base of this package was likely deposited in a deeper (> 30 m), low energy setting. Ca1 coral clasts such as *Seriatopora* branches indicate the euphotic (light-dependant) carbonate factory was active nearby. From 170 m to the top of the package, increasing algal thickness (ca. 5–20 mm) of Aa1

and robust branching coral framework including *Heliopora* sp., *Lobophyllia* and sub-massive Merulinidae, suggests the package transitioned to a shallow (< 10 m) upper forereef slope/reef flat environment and is therefore a shallowing upwards sequence. This package is interpreted to be *in situ* and detrital reef material possibly deposited during MIS 15?

4.2.1.7 **Package 7 –** *Coral framework and floatstone facies (core depth 190.8–200 m; thickness 9.2 m)*

Hyperspectral mineral maps indicate the absence of aragonite, with carbonate mineralogy dominated by calcite and continued occurrences of gypsum. The sedimentary package 7 extends from ca. 190.8 m to the base of the core at 200 m and consists of *in situ* massive *Porites* at the base of the package and crystalline floatstone facies with detrital fine-branching, massive and sub-massive coral clasts. No discernible paleosol is identified at the base of the core, and the package likely extends beyond the cored interval.

Chronostratigraphic and paleoenvironmental interpretation (MIS 15?)

This package, consisting of Ca3 and Aa3 was deposited in a deep (> 30 m) reef slope setting and was possibly deposited during MIS 15, but pervasive diagenesis and recrystallisation prevented reliable dating. Several non-*in situ* clasts of fine-branching corals and thick (> 20 mm) CCA crusts in the floatstone matrix imply the euphotic carbonate factory was operating nearby.

4.3 South Scott Reef Southeast margin

Core SRSEBH6J (elevation below sea level 8.22 m and hole depth 180 m) intersects seven distinct sedimentary packages, spanning MIS 1–11. It is located on the slightly submerged fore reef setting of southeast South Scott Reef (Fig. 1B), and experiences moderate hydrodynamic

energy associated with a 4.1 m tidal range, exposing the crest during low spring tide (Grimaldi et al., 2024). Overall, this fore-reef environment kept pace with the Holocene sea-level rise and largely consists of robust branching, laminar and massive coral morphologies interspersed with detrital facies. Hyperspectral and XRD data indicate high preservation of original aragonite mineral, validating the reliability of pre-existing U/Th ages (Collins et al., 2009) and confidence in selecting new samples for dating in this study. A linear regression through the U–Th age–depth data (Fig. 10) yields an average subsidence rate of ca. 0.37 mm/yr, comparable to previously reported rates for South Scott Reef (Collins et al., 2009).

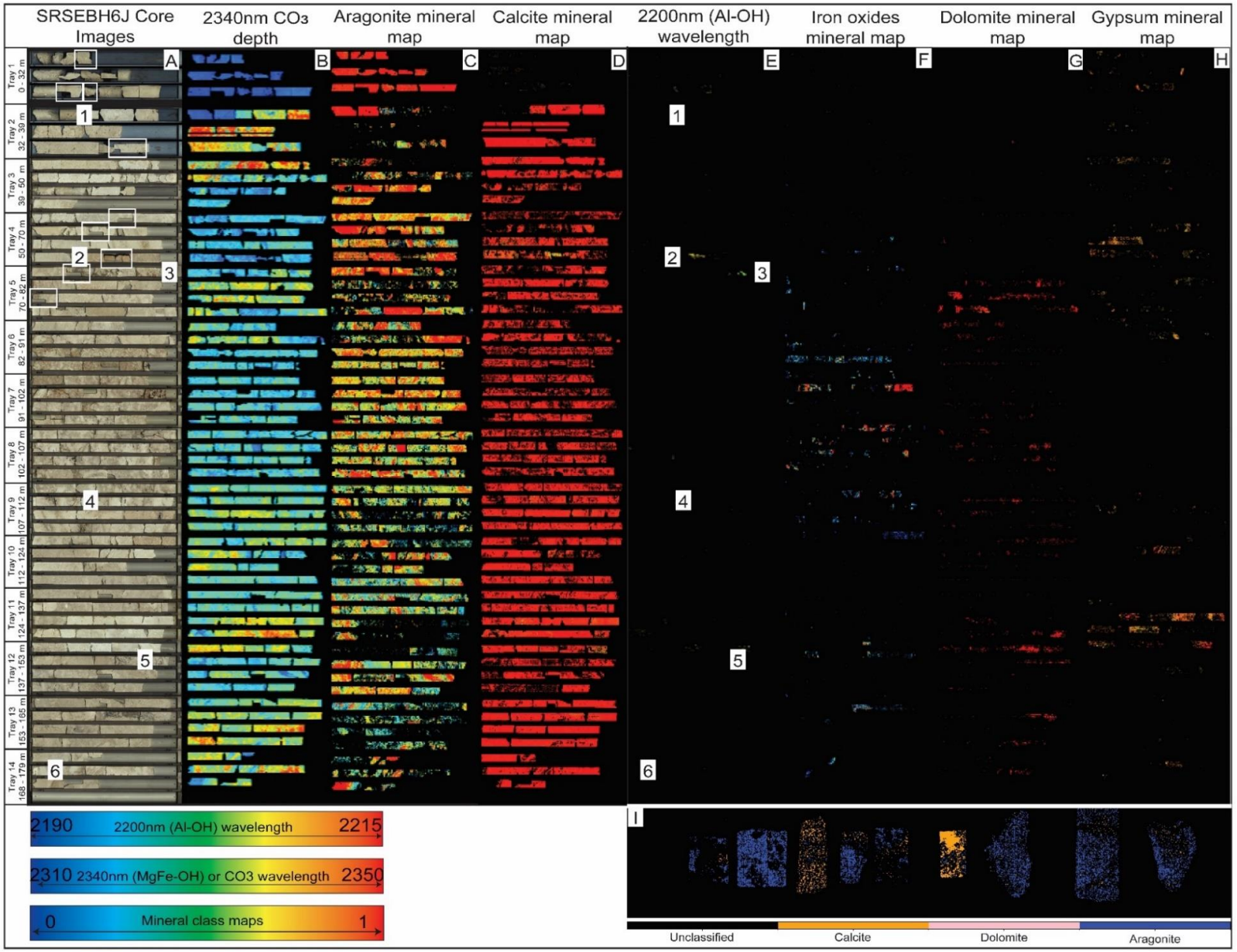

SRSEBH6J Core Images
2340nm CO3 depth
Aragonite mineral map
Calcite mineral map
2200nm (Al-OH) wavelength
Iron oxides mineral map
Dolomite mineral map
Gypsum mineral map
A
B
C
D
E
F
G
H
I
Tray 1 0 - 32 m
Tray 2 32 - 39 m
Tray 3 39 - 50 m
Tray 4 50 - 70 m
Tray 5 70 - 82 m
Tray 6 82 - 91 m
Tray 7 91 - 102 m
Tray 8 102 - 107 m
Tray 9 107 - 112 m
Tray 10 112 - 124 m
Tray 11 124 - 137 m
Tray 12 137 - 153 m
Tray 13 153 - 165 m
Tray 14 168 - 179 m
1
2
3
4
5
6
2190 2200nm (Al-OH) wavelength 2215
2310 2340nm (MgFe-OH) or CO3 wavelength 2350
0 Mineral class maps 1
Unclassified
Calcite
Dolomite
Aragonite

Figure 8. Core images and hyperspectral data of Scott Reef core SRSEBH6. (A) High-resolution core images of recovered sections of NRSEHDD3JA core. Numbers 1-6 illustrate interpreted paleosols that correlate with the occurrence of Al-rich phyllosilicates. (B) Carbonate (CO_3) absorption depth at 2340 nm, highlighting variation in carbonate mineral content and diagenetic alteration. Warmer colours indicate higher absorption depths corresponding to increased carbonate mineral alteration. Extensive blue zones in the 2340 nm carbonate feature throughout the Pleistocene indicate high primary aragonite mineral preservation and are consistent with XRD data. (C) Classified mineral class map of aragonite. (D) Classified mineral class map of calcite. (E) Al–OH absorption at 2200 nm, indicating minor clay or the occurrence of phyllosilicates, used to interpret the paleosols in (A). (F) Classified mineral map of iron oxides. (G) Classified mineral map of dolomite. (H) Classified mineral map of Gypsum. (I) Hyperspectral images of SRSEBH6J core samples using the equipment and code developed in Murphy et al., (2017) to validate the imaging methods. Spectral ranges defined are 2308 – 2322 nm for aragonite, 2333 – 2345 nm for calcite, and 2320 – 2328 nm for dolomite. The 9 samples correspond to the samples in white boxes in panel (A) from shallow at the top, to deep at the bottom. Core tray numbers are indicated and are 1 m long by 12 cm wide.

4.3.1.1 **Package 1 –** *Coral framework and rudstone dominated (core depth 0–36.3 m; thickness 36.3 m)*

Package 1 is composed of aragonite with moderate amounts of gypsum and trace levels of calcite, but no discernible dolomite. Minor Al-rich phyllosilicates on the 2200 nm hyperspectral absorption feature and an abrupt shift from aragonite to calcite observed on the CO_3 hyperspectral map at ca. 36.3 m depth corresponds to the Holocene–Pleistocene boundary (Fig. 8B). The sedimentary package 1 of core SRSEBH6J is predominantly *in situ* coral framework composed of massive, sub-massive and encrusting coral growth forms. Floatstone facies transition to *in situ* coral framework at 35 m. The base of the package is defined by a paleosol (SR_P1: Table 7), indicated by brown coloured secondary sediment infilling of dissolved bioclasts in a floatstone matrix.

Chronostratigraphic and paleoenvironmental interpretation (MIS 1 ca. 10 kyr)

The identification of corals such as isolated massive *Porites* and encrusting Dendrophylliidae characteristics of Ca3 and Ca4 together with Aa3? (*Mesophyllum*?) indicate reef growth initiated at the base of the package (ca. 36–26 m) in a deep (> 30 m) reef slope environment. Ca1 associated with abundant vermetid gastropods (Fig. 5) suggests the uppermost section of the package was deposited in a shallow water reef crest environment within < 6 m water depth. Radiometric ages of 1.35 kyr at 5.25 m and 7.2 kyr at 26.5 m, reported by Collins et al. (2009), were independently validated in this study using XRD and hyperspectral analyses to confirm the unaltered preservation of the *Montipora* corals used for dating. This package is a shallowing upwards sequence deposited during the Holocene, with the Holocene-Pleistocene boundary identified at 36.3 m depth. The initiation of coral reef framework at 35 m indicates that reef accretion initially lagged behind accommodation creation during sea-level rise. This boundary corresponds to an age of ca. 10 kyr (Table 9) and is marked

by a sharp hyperspectral transition and the first appearance of clay minerals (Fig. 8). Three closed system ages (this study: Table 9) confirm this package is Holocene age.

4.3.1.2 Package 2 – *Coral framework (and bindstone), grainstone, rudstone and floatstones (core depth 36.3–69.45 m; thickness 33.15 m)*

Calcite dominates the top of package 2 until ca. 45 m depth, where calcite and aragonite both show strong spectral characteristics on the 2340 nm hyperspectral feature (Fig. 8B). Moderate volumes of gypsum occur throughout the package with trace amounts of dolomite. Iron oxides and clays are evident at the base of the package (SR_P2: Table 7). Sedimentary package 2 is composed of sections of coral framework interbedded with grainstones and rudstones. A diverse suite of i*n situ* coral framework with Ca1 associated with vermetid gastropods establish at 51 m and continue to the top of the package with episodic intervals of floatstone and grainstone facies. Petrologic observations indicate development of vadose silt interpreted as consistent with marine cementation and meteoric diagenesis, but XRD data show generally good preservation of primary aragonite mineral throughout, including 73% aragonite in bindstone facies at 38 m (Table 8, Fig. 3C).

Chronostratigraphic and paleoenvironmental interpretation (MIS 5e–5c ca. 114–108 kyr)

Composed of floatstone to wackestone facies with occurrences of *Cycloclypeus* foraminifera, the bottom 6 m of the package initiates in a low energy reef slope environment > 60 m paleowater depth. Aa1 at the top of the package associated with vermetid gastropods, places deposition within 6 m paleowater depth. A diverse suite of coral morphologies includes branching, massive, sub-massive and encrusting, with *in situ Porites* and *Montipora* and coral clasts of fine-branching *Acropora*, Agariciidae, *Astreopora*, Siderastreidae, and Merulinidae, including *Cyphastrea* and *Favites*. This package is therefore characterised as a shallowing-

upward succession from a deep slope to a shallow reef environment (< 6 m). Two new closed system U/Th ages (this study: Table 9) confirm this package is MIS 5 age. A new closed system age of 108.7 kyr at 45 m places the top of package 2 within MIS 5c and an age of 114.7 kyr at 51.2 m indicates the base of the package initiated in MIS 5e (Fig. 11).

4.3.1.3 Package 3 – *Framestone to rudstone-floatstone dominated (core depth 69.45–72.7 m; thickness 3.25 m)*

Package 3 is composed of mixed calcite and aragonite mineral phases, with aragonite becoming the stronger spectral feature on the 2340 nm hyperspectral map towards the top of the package. Iron oxides and dolomite mineral are prevalent throughout, with gypsum confined to the top of the package, with clays present at the top and base (SR_P3: Table 7). Sedimentary package 3 is a 3.25 m thick sequence composed of rudstone and floatstone facies with interbedded coral framestone and bindstone. Small fine-branching *Acropora* coral fragments are embedded in the floatstone matrix containing encrusting foraminifera, molluscs, *Halimeda* and other aragonitic skeletons. Thin section data (Appendix P - Q) indicate subaerial diagenesis in the vadose zone, but XRD data indicate 93% preservation of aragonitic material from the *in situ Heliopora coerula* coral at 71. 5 m.

Chronostratigraphic and paleoenvironmental interpretation (MIS 7c ca. 224–216 kyr)

Ca1 with associated thick (> 15 mm) CCA crusts establish at 72.7 m in a shallow reef setting (< 10 m) and were succeeded by *Halimeda*-rich rudstone to floatstone facies characterising a deepening upwards succession. Two new closed to open system U/Th ages of 224 kyr at 106 m from an *in situ Goniastrea stelligera* coral, and 216 kyr at 81 m (Table 9) place this package within MIS 7c.

4.3.1.4 **Package 4 –** *Grainstone-rudstone dominated (core depth 72.7–112 m; thickness 29.3 m)*

Package 4 is composed of mixed calcite and aragonite mineral phases, with calcite becoming dominant towards the top. Iron oxides are prevalent throughout, with gypsum and dolomite more common towards the top of the package. Minor traces of clays occur at the base. Sedimentary package 4 comprises thick sections of *Halimeda*-rich rudstone, grainstone-rudstone, intermittent coral framework and a 2 m thick succession of bindstone facies at the base of the package. XRD data indicate 76% preservation of aragonite mineral at 97 m. Petrographic analyses identify two generations of cement at 82 m, including submarine aragonite cement that coats *Halimeda* plates (Fig. 4C). Possible minor paleosol at 92 m (SR_P4) and 112 m (SR_P5) (Table 7) are indicated by layered deposits of dark-brown sediment coating coral clasts, and a section of black-stained (manganese?) cements and significant dissolution of the rudstone components. Between ca. 107–113 m, dark brown sediments coat coral fragments, and a horizontally layered soil horizon is observed at 108 m.

Chronostratigraphic and paleoenvironmental interpretation (MIS 7e ca. 244 kyr)

Package 4 initiates with *in situ* bindstone of Ca1 and thick crusts (>15 mm) of Aa1 indicating deposition in < 10 m water depth. Rhodoliths are common throughout this package and coral framework occur at 81 m and 85 m deposited in a shallow reef environment. From ca. 89 – 85 m grainstone-rudstone facies with large robust branching clasts of Ca1 coated with CCA > 5 mm indicate deposition occurred in a higher energy reef flat or more turbid upper reef slope setting. Algal assemblage Aa3 from 76 m to the top of the package at 72.7 m signals a shift to intermediate to deep (several tens of meters) depositional environment. Package 4 therefore represents a deepening sequence from a high energy fore-reef slope or back reef environment to a deeper fore-reef slope. A paleosol surface interpreted at 108 m (SR_P5: Table

7) is only evident on the 900 nm iron-depth absorption feature (Fig. 8F) suggesting that it was a brief exposure sufficient for the oxidation of iron but too brief for accumulation of clay-rich siliciclastic material. This provides evidence of intermittent subaerial exposure, likely in response to high-frequency, high-amplitude saw-tooth sea-level oscillations during MIS 7, within the sub-stage 7e. A new closed to open system U/Th age of 244.5 kyr sampled at 102 m from an *in situ Porites* coral (this study: Table 9), support the interpretation that this package was deposited during MIS 7e.

4.3.1.5 Package 5 – *Mixed detrital and coral framework (core depth 112 – 140 m; thickness 38 m)*

Hyperspectral mineral maps indicate that package 5 consists of calcite and aragonite, with iron oxides, dolomite and gypsum common predominantly in the upper and lower sections of the package. Clays are evident at the top (SR_P5) and base (SR_P6) of the package. Sedimentary package 5 is composed of variable lithofacies, including coral framestone, grainstone, rudstone and floatstone towards the top of the package and packstone and wackestone facies towards the base. Vadose calcrete alteration is identified in thin section at the top of the package with marine phreatic cementation evident towards the base.

Chronostratigraphic and paleoenvironmental interpretation (MIS 9a ca. 281 kyr)

Petrographic analysis of algal and coral assemblages indicates an overall deep marine environment. *Cycloclypeus* foraminifera in a packstone-rudstone matrix present at 112 and 135 m, associated with rhodoliths, *Halimeda* and hemipelagic sediments, a micritic matrix, and small coral fragments are diagnostic of a pelagic deep-water setting. A corrected open-system U/Th age of 281 kyr at 125 m suggest this package was deposited during MIS 9a.

4.3.1.6 **Package 6 –** *Crystalline rudstones and floatstone with coral framestone (core depth 140–165.4 m; thickness 25.4 m)*

Hyperspectral mineral maps indicate that package 6 is composed of mixed calcite and aragonite, with increasingly more aragonite towards the top of the package. Dolomite and gypsum occur intermittently throughout. Clay minerals and iron oxides are present at the top and base of the package, and a distinct iron-rich interval occurs at 158 m depth. This interval is characterised by a dense yellow hue in false-colour imagery (Fig. 3K), indicating a unique spectral signature relative to surrounding material, and elsewhere in the cores. Sedimentary package 6 is characterised by crystalline rudstones and floatstones, with occasional intervals of carbonate sand. The lithofacies contain diagenetically altered laminar and branching *Acropora* coral clasts, with very small (ca. 10 mm) rhodoliths (Fig. 5B) and *Halimeda* common throughout the package, Package 6 is bounded at its base by an 8 m thick transitional paleosol horizon (SR_P7: Table 7). This interval is characterised by orange to dark brown sediment infill within secondary porosity of a *Halimeda*-rich grainstone–rudstone facies (Fig. 3J). Large cavities within a *Halimeda*-rudstone are filled by fine-grained brown-black sediment at 157.45-157.85 m, with micritised skeletal grains, including foraminifera and bivalve fragments, set in blocky spar/microspar cement.

Chronostratigraphic and paleoenvironmental interpretation (MIS 9e ca. 336 kyr)

Ca4 associated with encrusting morphologies, thick algal laminations, *Halimeda* and rhodoliths support the interpretation of a deep (> 20 m) setting. Diagenetically altered *in situ* laminar *Dipsastraea* coral framestone is identified at 156.530 m and large (2-3 cm long) *Cycloclypeus* foraminifera (Fig. 5C), typical of deep water (>60-120 m) occur in a grain-supported rudstone at 158 m. The thick paleosol at the base of the package (SR_P7: Table 7) could indicate prolonged exposure during the lowstand of MIS 10. The facies at 157 m were

likely deposited in a low energy deep forereef slope environment. A corrected open-system U/Th age of 336 kyr at 142 m (Table 9) indicates this package was likely deposited during MIS 9e.

4.3.1.7 **Package 7 –** *Floatstone dominated with coral framework (core depth 165.4–179.2 m; thickness 14 m)*

Iron oxides are observed at the top of package 7. Calcite dominates the package with notable occurrences of strong spectral features on the 2340 nm depth feature relating to aragonite, particularly at 174 m. Dolomite and gypsum occur at ca. 172 m. Floatstone facies dominate the lowermost sedimentary package 7 with *in situ* coral framework at 177 and 171 m. Large gastropods, *Halimeda* and other reef bioclasts occur in the grainstone matrix. Well-developed marine phreatic cements are observed in thin section at 165 and 177 m.

Chronostratigraphic and paleoenvironmental interpretation (MIS 11a ca. 384 kyr)

Well-developed submarine cements, deep marine foraminifera (e.g., textulariids) and *in situ* massive *Porites* at the base of the core and package are indicative of a deep marine setting. A corrected open-system U/Th age of 384 kyr at 171.9 m indicates this package was deposited during MIS 11a (Table 9).

4.4 South Scott Reef leeward margin

Core Hook 1P was drilled to 37.1 m, plugged and abandoned. Hook 3P was drilled 5 m away (43.3 mbsl and hole depth 100.53 m) (Fig. 1) and collectively they intersect four distinct sedimentary packages. It is located on the submerged leeward fore reef setting above the channel edge between North and South Scott Reef, although experiences high hydrodynamic energy associated with tidal currents through the inter-reef channel, winds and ocean currents

during spring tides (Grimaldi et al., 2024). Overall, this high-energy, deeper fore-reef environment facilitated the accumulation of more bindstone facies, microbialites, and massive domal coral facies with encrusting coralline algal laminations, which collectively can withstand more turbulent wave and current energy.

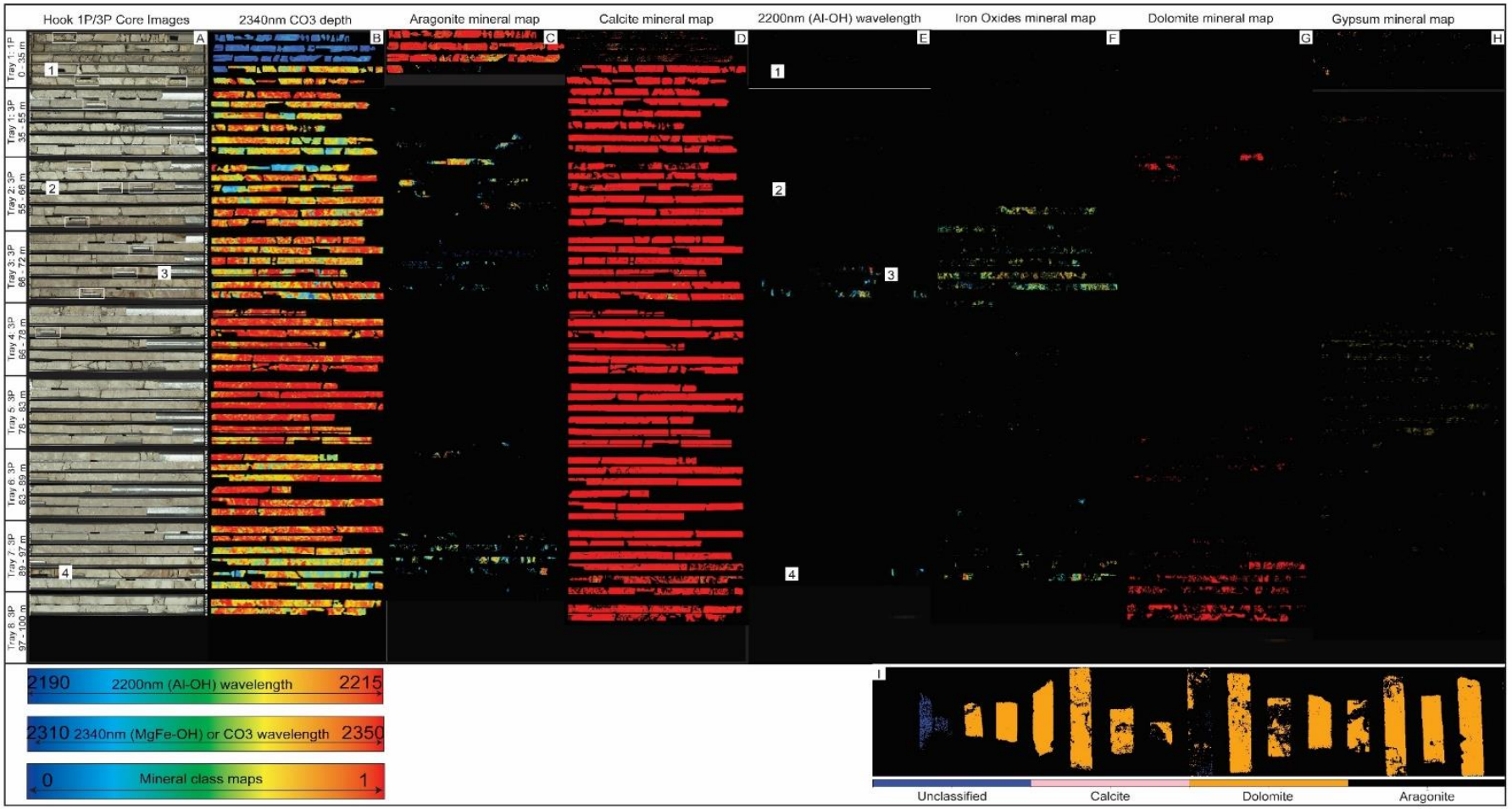


Figure 9. Core images and hyperspectral data of Scott Reef core Hook 1P/3P. (A) High-resolution core images of recovered sections of Hook 1P/3P core. Numbers 1-5 illustrate interpreted paleosols that correlate with the occurrence of Al-rich phyllosilicates shown in E. (B) Carbonate

(CO_3) absorption depth at 2340 nm, highlighting variation in carbonate mineral content and diagenetic alteration. Warmer colours indicate higher absorption depths corresponding to increased carbonate mineral alteration. (C) Classified mineral map of aragonite. (D) Classified mineral map of calcite. (E) Al–OH absorption at 2200 nm, indicating minor clay or the occurrence of phyllosilicates, used to interpret the paleosols in (A). (F) Classified mineral map of iron oxides. (G) Classified mineral map of dolomite. (H) Classified mineral map of Gypsum. (I) Hyperspectral images of Hook 1P/3P core samples using the equipment and code developed in Murphy et al., (2017) to validate the imaging methods. Spectral ranges defined are 2308 – 2322 nm for aragonite, 2333 – 2345 nm for calcite, and 2320 – 2328 nm for dolomite. The 13 samples correspond to the samples in white boxes in panel (A) from shallow at the top, to deep at the bottom. Core tray numbers are indicated and are 1 m long by 12 cm wide.

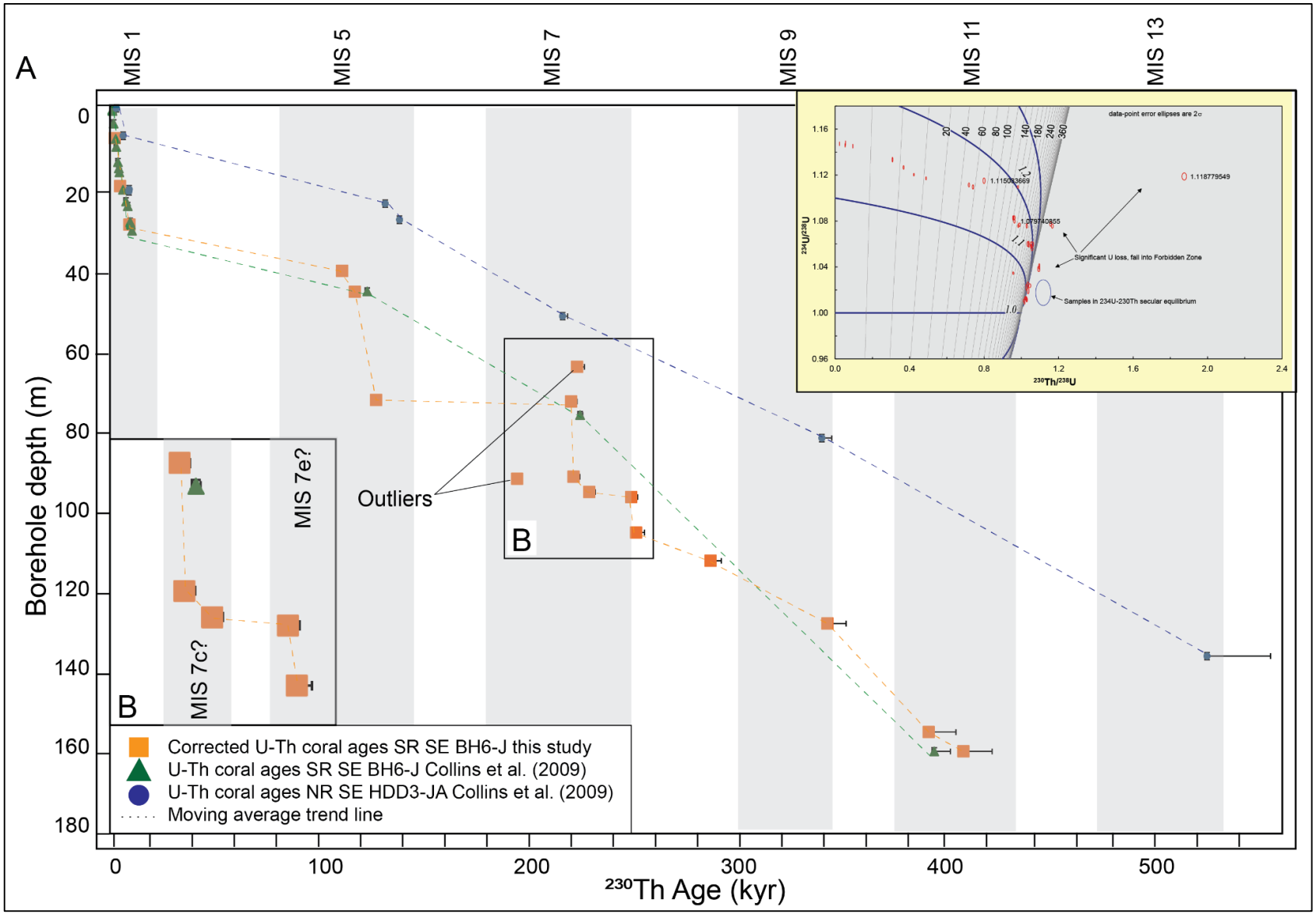

A
MIS 1
MIS 5
MIS 7
MIS 9
MIS 11
MIS 13
Borehole depth (m)
0
20
40
60
80
100
120
140
160
180
0
100
200
300
400
500
230Th Age (kyr)
Outliers
B
MIS 7e?
MIS 7c?
B
Corrected U-Th coral ages SR SE BH6-J this study
U-Th coral ages SR SE BH6-J Collins et al. (2009)
U-Th coral ages NR SE HDD3-JA Collins et al. (2009)
Moving average trend line
data-point error ellipses are 2σ
1.118779549
1.115093669
1.079740855
Significant U loss, fall into Forbidden Zone
Samples in 234U-230Th secular equilibrium
234U/238U
230Th/238U
1.16
1.12
1.08
1.04
1.00
0.96
0.0
0.4
0.8
1.2
1.6
2.0
2.4

Figure 10. Subsidence history of the SRSEBH6J core (South Scott Reef) and NRSEHDD3JA core (North Scott Reef) based on U–Th coral ages from this study and Collins et al. (2009). Age–depth trends derived from both closed- and open-system calculations show broadly coherent stratigraphic superposition between datasets despite diagenetic complexities. Trend lines indicate a long-term subsidence rate of ca. 0.37 mm/yr for South Scott Reef and ca. 0.29 mm/yr for North Scott Reef, consistent with differential subsidence between the two platforms reported in Collins et al. (2009). Panel B highlights high-resolution sampling through MIS 7, illustrating potential substage structure and short-term sea-level oscillations superimposed on the long-term trajectory. However, interpretation of fine-scale (≤5–10 kyr) sea-level variability should be treated cautiously. Evaluation of coral preservation using $\delta^{234}U$ and U concentration indicates that many older samples (>50 ka) likely behaved as open systems and were corrected using Thompson corrected open-system calculations (Thompson et al., 2003). The authors revised seawater $\delta^{234}U$ value (ca. 1.45 rather than ca. 1.47) and evidence for temporal variability in seawater $^{234}U/^{238}U$ through glacial–interglacial cycles introduce additional non-quantifiable uncertainties, particularly for older samples. Analytical 2σ uncertainties are shown as horizontal error bars, but true age uncertainties for open-system corals are likely greater. While ages robustly resolve major isotope stages, detailed intra-stage sea-level reconstructions should be interpreted with caution. Two anomalous MIS 7 samples that are inconsistent with stratigraphic superposition within the core are interpreted as outliers and excluded from chronostratigraphic reconstruction, despite having been selected for U–Th dating following diagenetic screening. Top right insert: U–Th evolution diagram showing measured coral compositions plotted as activity ratios of $^{230}Th/^{238}U$ versus $^{234}U/^{238}U$. Blue curves represent theoretical closed-system decay trajectories through time, and the horizontal line at $^{234}U/^{238}U = 1$ indicates secular equilibrium. Red data points (with 2σ error ellipses) illustrate the distribution of analysed samples. Samples plotting along closed-system

trajectories are consistent with minimal post-depositional alteration, whereas those displaced toward or within the shaded “forbidden zone” reflect open-system behaviour (e.g., U gain or loss) requiring model-based age correction and implying greater age uncertainty.

*4.4.1.1 **Package 1** – Coral framework (core depth 0–20 m; thickness 20 m)*

Package 1 is dominated by aragonite with moderate amounts of calcite and gypsum and moderate amounts of iron oxides at ca. 19 m depth and at the base of the package. An abrupt transition in absorption depth on the 2340 nm hyperspectral map occurs at 20 m (Fig. 9B). The topmost sedimentary package 1 consists of *in situ* coral framestone characterised by Ca 4 including heavily bored laminar Merulinidae, *Porites* and encrusting *Montipora,* with thin, 1–10 mm thick algal crusts. A microbialite is identified at 19 m depth, which appears to be iron-rich on the 900 nm hyperspectral map. The package is bounded at its top and base by unconsolidated carbonate sand composed of large coral clasts, including weakly cemented encrusting and domal coral fragments coated with coralline algae.

Chronostratigraphic and paleoenvironmental interpretation (MIS 1 ca. 11.15 kyr)

The Holocene-Pleistocene boundary is clearly marked by carbonate mineral phase transition in hyperspectral maps from aragonite to calcite (Fig. 9B). Trace amounts of terrigenous clays suggest that the submerged setting during the last glaciation of MIS 2 precluded terrestrial soil deposition in this region. This package, consisting of Ca4 and thin encrusting algal interlaminations was deposited in a deep (> 20 m), turbid, high-energy setting. A closed system age of 5.2 kyr (this study: Fig. 11) and an open system age of 11.1 kyr at 14.86 m places this package in the Holocene.

*4.4.1.2 **Package 2** – Coral framework and rudstone/floatstone dominated (*core depth 20–62 m; thickness 39 m)

Package 2 contains minor amounts of gypsum, no detectable iron oxides, and is dominantly calcitic, with discrete aragonitic zones at 54, 57 and 59 m depth that co-occur with dolomite. A distinct 5 m *Halimeda*-grainstone facies is observed at the top of package 2 (Fig.

3H). An *in situ* massive *Porites* at 57 m with a thick CCA crust (>20 mm) is estimated to be ca. 40–45 years old, based on a count of growth bands (Fig. 3B). The package shows an upward transition from coral framework (Ca4) into floatstone with common rhodolith-rudstone. *In situ* encrusting laminar corals, and large (> 4 cm) fine-branching coral clasts, including *Seriatopora*, Merulinidae and Pocilloporidae constitute the rudstone components. *In situ* massive *Porites,* Agariciidae*,* submassive *Astreopora* and branching *Pocillopora* clasts (Ca1) with thick CCA occur near the base of the package (54–57 m), which is bounded by an Fe and Al-rich transitional paleosol from ca. 62–72 m (SR_NE_P2: Table 7). XRD data indicate < 1.2 % aragonite preservation (Table 8).

Chronostratigraphic and paleoenvironmental interpretation (MIS 5?)

Sedimentary package 2 is a deepening-upwards sequence with Ca1 and Aa1 common from 62 to 51 m deposited in a moderate to high energy reef flat to upper fore-reef slope environment. Significant thorium loss in the screened samples precluded reliable open or closed system U/Th age determinations. This may be associated with the co-occurrence of microbialites, which can scavenge thorium and distort the primary U/Th ratios.

4.4.1.3 Package 3 – *Coral framework, grainstone, rudstone/floatstone and packstones (core depth 62–94 m; thickness 32 m; paleosol ca. 62–72 m and ca. 86–96 m)*

Package 3 is dominated by calcite, with evidence of aragonite locally preserved at the top and base of the package. Iron oxides are abundant from ca. 62-72 m (SR_NE_P2: Table 7), while moderate gypsum concentrations occur from ca. 66 – 80 m. Patches of dolomite are present from the base of the package up to ca. 80 m. Clay deposits are observed from ca. 70-72 m. Packstone and rudstone facies are common from the base of the package to ca. 85 m, above which framestone, rudstone and floatstone become common and often in rapid transition.

Fossil components include rhodoliths and *Halimeda*. The transition between packages 2 and 3 at ca. 62 m depth is identified by a change in lithology, including a colour transition from orange brown (paleosol) to chalky white (detrital coralline rudstone). The paleosol permeates from ca. 67–71 m through altered and crystalline rudstone facies, coating individual coral clasts with brown-orange fine-grained sediment, making it difficult to distinguish framestone from rudstone, as well as the beginning and end of the exposure event. Dissolution, borings, minor karst with cements, and mud/clay infilled cavities (forming geopetal structures) are common features (e.g., Fig. 4D and 4E). XRD data indicate pervasive calcite replacement throughout with < 7.1 % aragonite.

Chronostratigraphic and paleoenvironmental interpretation (MIS 7 including sub-stages?)

The occurrence of *in situ* Ca4 and encrusting foraminifera associated with nodules of CCA are commonly found in water depths of several tens of meters and were likely deposited in a deep water, low energy setting. A transition to robust branching coral clasts, Ca1 and increasing algal thickness indicate a transition to higher energy conditions from 85 m to the top of the unit. The complexity of pedogenic features is interpreted to reflect the saw-tooth high-frequency, low-amplitude oscillations of MIS 7 and likely includes the highstands of MIS 7a, c and e.

4.4.1.4 Package 4 *– Floatstone – rudstone (core depth 94–100 m; thickness 6 m; paleosol ca. 94–100 m)*

Dolomite and calcite are the dominant minerals in this package, with iron oxides concentrated towards the top. Clay is observed at the top (SR_NE_P3: Table 7). Hyperspectral false colour maps show the interval between ca. 100.53–96 m as bright white, a feature not observed in the other cores (Fig. 3L). The lowermost section of the package (ca. 100.53–96 m)

is composed of very fine buff-white chalky sediment with floating and dissolved branching, laminar and encrusting coral clasts with thin (< 2 mm) CCA. XRD data suggest this unique matrix, which consists of CCA fragments, bivalves, echinoids and soft coral spicules preserves 14.6 % of aragonite mineral at 95 m depth. The facies is characterised by mud-coated clasts in which fractures and dissolution cavities are infilled by finely layered sediments of distinct colours (grey, brown, yellow, and dark grey). Localised cementation and black manganese-rich deposits line cavities (Fig. 4G) at 94 m and 96 m.

Chronostratigraphic and paleoenvironmental interpretation (MIS 9 including sub-stages?)

The base of package 4 was likely deposited in a very low energy deep (> 20 m water depth) fore-reef slope environment. Coral clasts within the floatstone matrix are characteristic of Ca4 and are primarily encrusting, laminar and massive forms that were possibly deposited during the sub-stages of MIS 9e. Evidence of Aa1 (*Porolithon* gr. *onkodes*, *Hydrolithon* gr. *boergesenii*) robust branching *in situ*? *Acropora* coral of Ca1 at top of the package (95 m) indicate the reef caught up to sea-level in a shallowing upwards sequence possibly deposited in MIS 9c.

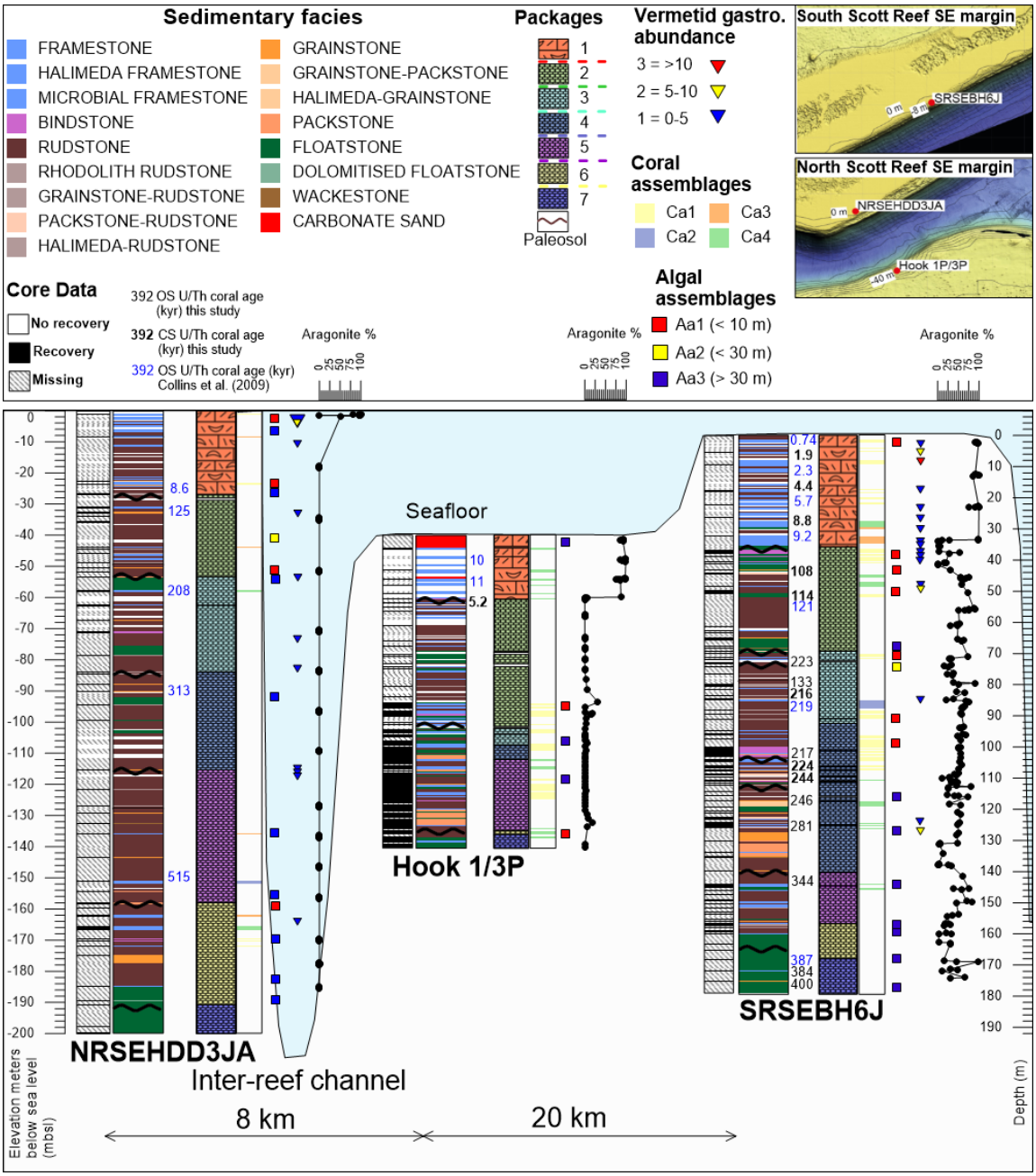


Figure 11. Summary of sedimentary facies, chronostratigraphic packages bounded by paleosols, coralgal assemblages, reef biota, and radiometric ages from this study and Collins et al. (2009). U/Th coral ages include open-system (OS) and closed-system (CS) ages produced in this study, as well as open-system ages reported in Collins et al. (2009) and presented here with permission from Woodside Energy Ltd (see Table 2 and 3). Intervals of no physical core recovery are shown in white, whereas diagonally hatched intervals represent sections not available (missing) for analysis in this study, for which basic lithological interpretations were

inferred from preliminary interpretations reported in Collins et al. (2009), used with permission from Woodside Energy Ltd.

5. Discussion

5.1 Paleoenvironmental evolution and coral-algal community variations through time

Visual observations of the cores, thin sections, SEM, XRD and comparisons with hyperspectral maps and core photographs showed strong correspondence between geochemical and spectral transitions and observed lithological changes, and were used to develop the stratigraphic framework. Previous work on Scott Reef data (Collins et al., 2009; Collins, 2002; 2010) established the presence of stacked Quaternary reef packages and identified subsidence as a primary control on accommodation. The present study builds upon this foundation and defines a new chronostratigraphic model that suggests the start of the major shallow reef building assemblages occurred in the North Reef during MIS 13 and the South Reef during the MIS 9 highstand in < 10 m water depth (Fig. 11-13). This is coincident with the first occurrence of algal assemblage Aa1, which is characteristic of shallow high-energy environments. Deep reef assemblages dominated by massive *Porites* and laminar *Dipsastraea,* encrusting *Montipora* and other encrusting forms of Ca4 (Table. 6), and their association with Aa3 (Table 5) were deposited in a deep reef slope environment during the MIS 11 to MIS 9 highstands in the South Reef and MIS 15 to MIS 13 highstands in the North Reef (Figs. 10-12). However, the morphology and taxonomy of the non *in situ* corals in the MIS 15 to MIS 9 sections of the NRSEHDD3JA and SRSEBH6J cores, include fine-branching taxa (e.g., *Seriatopora)*, taxa with fine- to robust-branching morphologies (e.g., *Heliopora, Acropora, Porites, Pocillopora, Millepora*), and massive Merulinidae, with CCA up to 20 mm thick. This suggests that the majority of coral clasts were derived from nearby shallow euphotic coral reef communities and possibly that shifts in the loci of deposition occurred (Braithwaite, 2016). It primarily indicates

that major reef building processes were already established and possibly initiated during the MIS 15 transition to high-amplitude, low-frequency sea-level oscillations associated with the Middle Pleistocene Transition (Clark et al., 2006). This would be consistent with expansion of carbonate platforms along the NWS during the same period (Gallagher et al., 2014; Saqab and Bourget, 2015; 2016), and elsewhere around the world (Williams et al., 2026).

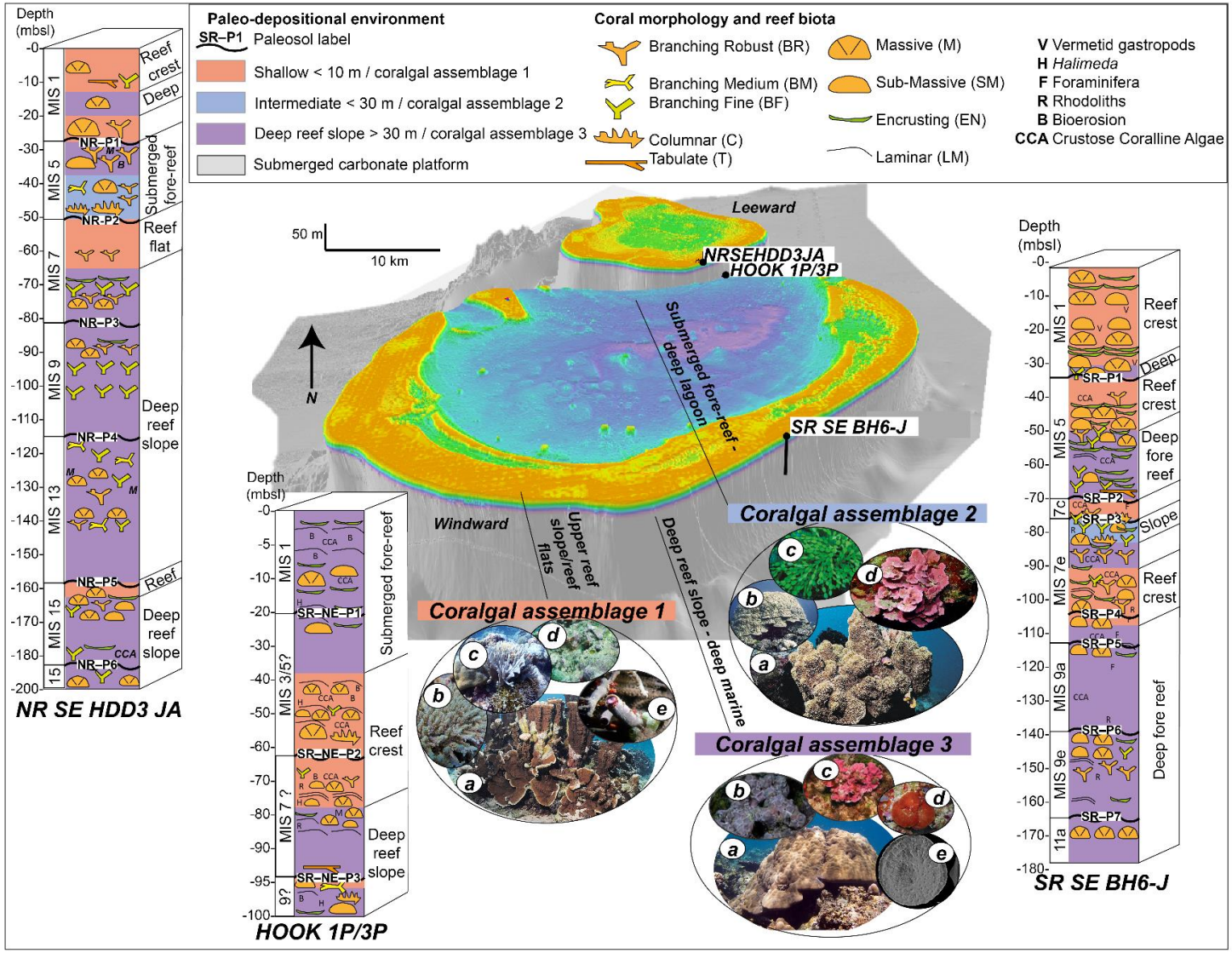

Paleo-depositional environment
SR–P1 Paleosol label
Shallow < 10 m / coralgal assemblage 1
Intermediate < 30 m / coralgal assemblage 2
Deep reef slope > 30 m / coralgal assemblage 3
Submerged carbonate platform
Coral morphology and reef biota
Branching Robust (BR)
Branching Medium (BM)
Branching Fine (BF)
Columnar (C)
Tabulate (T)
Massive (M)
Sub-Massive (SM)
Encrusting (EN)
Laminar (LM)
V Vermetid gastropods
H Halimeda
F Foraminifera
R Rhodoliths
B Bioerosion
CCA Crustose Coralline Algae
Depth (mbsl)
NR SE HDD3 JA
Reef crest
Deep
Submerged fore-reef
Reef flat
Deep reef slope
Reef
Deep reef slope
NR–P1
NR–P2
NR–P3
NR–P4
NR–P5
NR–P6
MIS 1
MIS 5
MIS 7
MIS 9
MIS 13
MIS 15
Leeward
50 m
10 km
NRSEHDD3JA
HOOK 1P/3P
SR SE BH6-J
Submerged fore-reef - deep lagoon
N
Windward
Upper reef slope/reef flats
Deep reef slope - deep marine
Coralgal assemblage 1
Coralgal assemblage 2
Coralgal assemblage 3
HOOK 1P/3P
Submerged fore-reef
Reef crest
Deep reef slope
SR–NE–P1
SR–NE–P2
SR–NE–P3
MIS 1
MIS 3/5?
MIS 7 ?
9?
SR SE BH6-J
Reef crest
Deep
Reef crest
Deep fore reef
Slope
Reef crest
Deep fore reef
SR–P1
SR–P2
SR–P3
SR–P4
SR–P5
SR–P6
SR–P7
MIS 1
MIS 5
7c
MIS 7e
MIS 9a
MIS 9e
11a

Figure 12. Summary of Scott Reef paleodepositional environments during each Marine Isotope Stage based on lithological, chronological and coralgal interpretations. Paleosol horizons are labelled for each core corresponding to Paleosol labels in Table 7. Modern counterparts of the coral and algal assemblages are summarised showing representative habitat locations on a high-resolution bathymetric multibeam map of North and South Scott Reef. In coralgal assemblage 1: (a) encrusting *Montipora*, (b) *Acropora*, (c) *Heliopora*, (d) *Porolithon* gr. *onkodes,* coralgal assemblage 2: (a) Massive *Platygyra*, (b) Massive *Porites*, (c) *Halimeda*, (d) *Lithophyllum*, coralgal assemblage 3: (a) Massive *Porites*, (b) encrusting *Montipora*, (c) *Mesophyllum*, (d) Peyssonneliaceans, (e) *Cycloclypeus* foraminifera.

Despite these differences, coral communities identified in the North and South Reef are broadly similar, with a notable increase in diversity in the South Reef, particularly in the leeward margin. This is consistent with the modern-day environment that also records higher diversity in the South Reef (Gilmour et al., 2022). The mechanisms driving these differences cannot be resolved here but could possibly be a consequence of the open lagoon facilitating coral spawning from the regional NWS reefs such as Seringapatam Reef and Ashmore Reef ca. 250 km to the North (Webster et al., 2022). This may also suggest that the South Reef developed under more dynamic environmental conditions with exposure to the open ocean, winds, tidal regime and currents promoting the development of more robust, tolerant species. The South Reef leeward margin exemplifies the failure of the mesophotic reef communities to outcompete more stress tolerant algae such as *Halimeda* bioherms, which are observed in the modern deep lagoon (Wilson, 2013). The Hook 1/3P core can be characterised as a give up reef based on the vertical transition from deep fore-reef slope to shallow fore-reef/lagoon during MIS 7 to eventually submerged fore-reef slope in the modern. Deep water coral communities of Ca4, dominated by encrusting and laminar *Porites, Montipora, Pavona* and *Goniopora*, associated with deep thin Aa3 crusts are covered by 4 m of carbonate sand to the top of the core, indicating that the reef failed to keep pace with the Holocene sea-level rise, and is supported by findings from Collins et al. (2011). The demise of the leeward South Reef margin might also be attributed to the increased sediment flux during MIS 3, sourced by major paleo-rivers in the region and the resuspension of shelf sediments via large sediment waves and contourites (Belde et al., 2017). The lower relative topography of the leeward margin would have exacerbated exposure to suspended sediments and reduced light availability. These elements are reported as a possible factor in the failure of shallow reef communities to establish during MIS 1 elsewhere along the NWS, including Ashmore reef (Webster et al., 2022). Overall, the deep coral communities have been able to re-establish during each highstand,

indicating that both reefs have been resilient ecosystems during major eustatic and environmental perturbations.

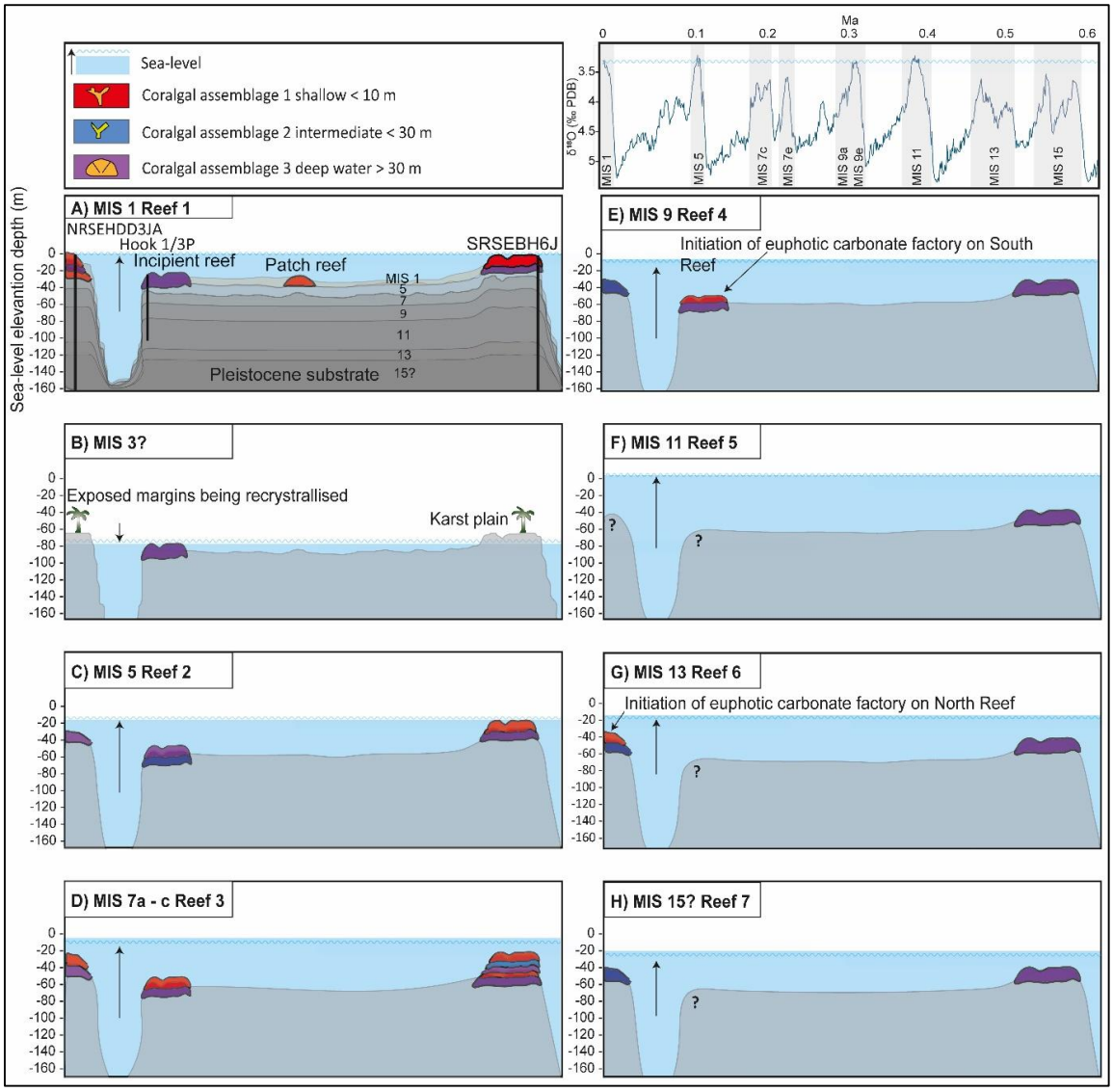


Figure 13. Conceptual sketch summarising the evolution of reef growth and coralgal assemblage development across Marine Isotope Stages 1–15 for North and South Scott Reef. Shallow reef assemblages establish during MIS 13 on the North Reef and MIS 9 on the South Reef submerged leeward margin, and MIS 7 on the South Reef SE margin. Schematic of relative sea-level curve from MIS 15 to present is shown in the top right with modern sea-level overlain for reference.

In combination with all available data, the defined coralgal assemblages and paleosol horizons indicate that seven distinct reef packages occur in the North Reef spanning MIS 1–15, and seven distinct reef packages occur in the South Reef Southeast margin spanning MIS 1–11 (Fig. 12 and 13). Four reef packages are interpreted at the leeward margin of the South Reef from MIS 1–9. These reef packages define separate growth phases bounded by paleosol horizons during sea-level rises and highstands of each MIS, including the MIS 7 and 9 substages. The coral and algal assemblages suggest that deeper water, low energy conditions existed in the South Reef during what is interpreted to be MIS 11–9, which may represent preservation bias, including diagenesis or removal of shallow reef tops by karstification during emersion (Mylroie and Carew, 1995). However, within MIS 7, distinct patterns in coral and algal species compositions emerge that indicate variations in paleodepositional environments, likely resulting from MIS 7 sea-level oscillations and associated environmental changes, such as sea surface temperature, and ocean current dynamics (Webster and Davies, 2003). This pattern is exemplified by coralgal assemblages in core SRSEBH6J, which record repeated shallowing-upwards successions within individual depositional packages spanning MIS 7–1. Each chronostratigraphic package initiates in a low energy reef slope setting during early sea-level highs, followed by vertical accretion and stabilisation near sea-level during highstands, before platform emergence during subsequent lowstands. The Hook 1/3P core records a shallowing upwards succession from MIS 9 to 7, followed by a transition to a submerged forereef slope that fails to keep pace with Holocene sea-level rise during MIS 1. The NRSEHDD3JA core in contrast is more complex and indicates a shallowing up sequence in MIS 13 and MIS 7, followed by an intermediate to deep setting during MIS 5. The MIS 1 succession initiates in a shallow reef crest environment, followed by relative deepening associated with rising sea-level and subsequent shallowing until present. Despite their

geographic proximity, the sedimentary packages defined do not correlate directly between the North and South Reef. These discrepancies are possibly a consequence of variable local accommodation (Collins et al., 2011), hydrodynamic energy, antecedent topography, and differences in accretion rates between the reef zones that were drilled, which are known to vary considerably within the same reef system (Davies and Montaggioni., 1985; Blanchon and Blakeway, 2003). Correlation of stratigraphic packages in carbonate systems in the absence of chronologic constraints is further complicated by the heterogeneous expression of pedogenic features, where exposure surfaces may be variably developed, discontinuous or cryptic. These limitations are discussed in Section 5.2.

5.2 *Diagenetic trends and implications for sea-level oscillations and associated climatic variability*

Hyperspectral carbonate mineral classifications were validated using XRD analyses from selected core intervals (Table 8). In all cores, the Holocene-Pleistocene boundary defined by U/Th ages and core observations corresponds to a clear transition in calcite-aragonite distributions (Figs. 6–8), with the exception of a calcitic grainstone interval above the boundary in NRSEHDD3JA. This grainstone interval is interpreted as reflecting either local hydrodynamic conditions associated with the large tidal range (ca. 4.1 m), or a minor exposure event accompanied by diagenetic alteration. In the NRSEHDD3JA core, dolomite is restricted to a single interval at 189 m (MIS 12 – see Fig. 14A), whereas gypsum is abundant throughout the core (Fig. 7H). In contrast, the other two cores show a closer spatial association between gypsum and dolomite, and overall higher abundance of dolomite. Although certain dolomite types do not necessarily co-occur with gypsum in restricted marine settings under concentrated brine or pore water solutions (Skeats, 1918), this spatial variability implies differences in

residence time and pore-water or sea water chemistry between the North and South Reef. The limited stratigraphic expression of dolomitization in the North Reef does not preclude its occurrence but might indicate that evaporative or sabkha-like environments existed but were not preserved or intersected by drilling. Instead, dolomitising fluids generated in these settings likely migrated to alter underlying or proximal carbonate strata (Fathi et al., 1997). Resolving the precise dolomitization mechanisms and dolomite type requires detailed elemental and isotopic analyses beyond the scope of this study.

Nevertheless, the occurrence of the single dolomite interval in NRSEHDD3JA is interpreted to coincide with the exceptionally long duration lowstand of MIS 12 (Fig. 14A) forming a major karst depression evident on seismic data (Williams et al., 2023) and reproduced in recent forward stratigraphic models by Williams et al. (2026). Subsequent interglacial conditions characterised by increased monsoonal activity and increased rainfall along the NWS (Gallagher et al., 2014; 2017; Petrick et al., 2019) likely increased dissolution, modification, and infilling of pre-existing karst features. The topographically variable karst surface likely facilitated mixing between marine and meteoric water in the upper vadose and phreatic zones during sea-level fall creating the environment required for mixing-zone dolomitization (Strasser and Strohmenger, 1997; Webster et al., 2022).

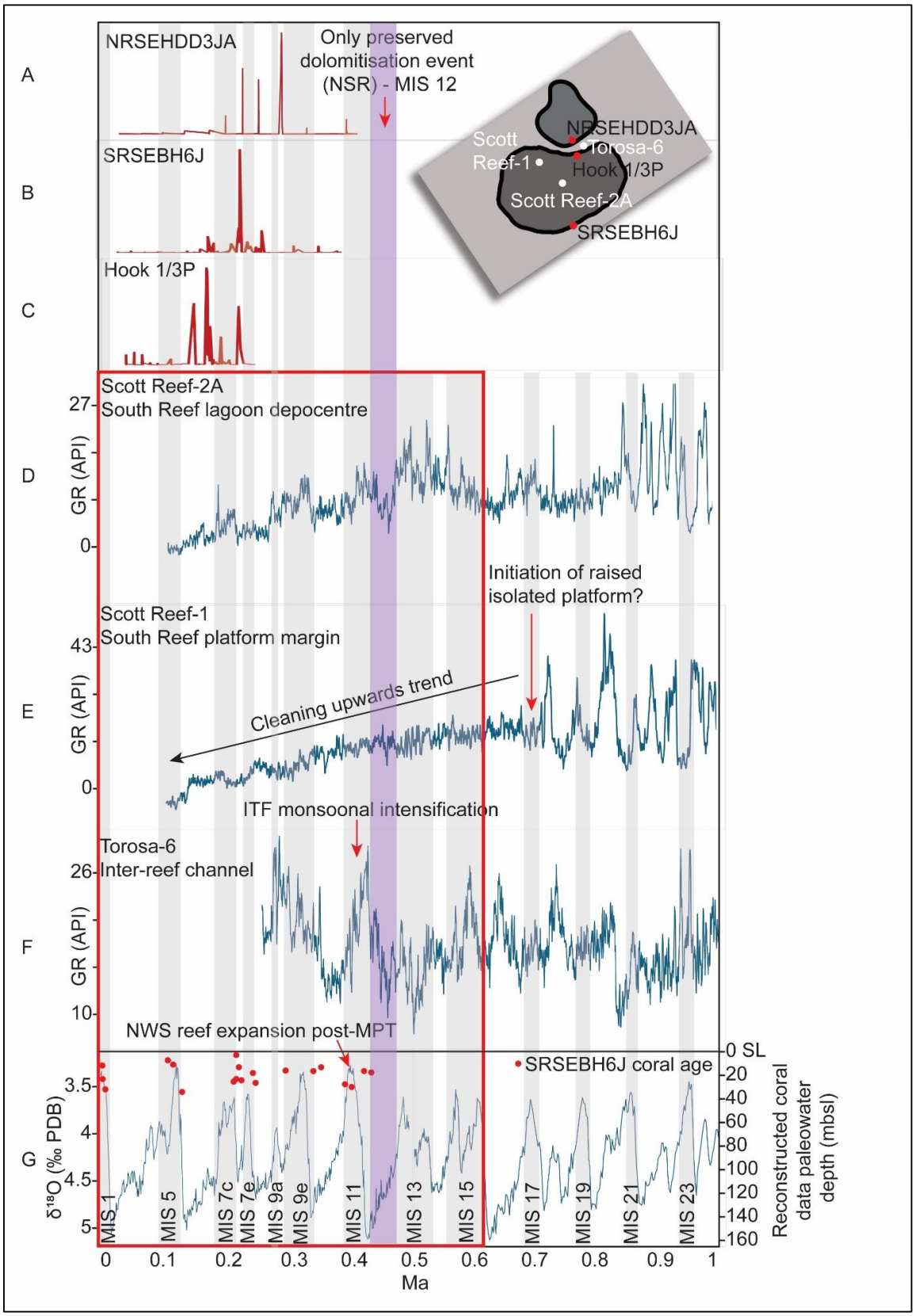


Figure 14. Long-term climate variability inferred from previously published Scott Reef GR logs (Williams et al., 2023) correlated with global sea-level change. (A–C) Iron oxide

abundance derived from hyperspectral data showing increased iron oxide deposition during glacial intervals. The purple vertical line indicates the only preserved dolomitization event in the NRSEHDD3JA core on NSR during the first long lowstand of MIS 12. (D-F) GR logs from Torosa-6, Scott Reef-2A, and Scott Reef-1 converted to time using age–depth models (Collins et al., 2009). Core locations are shown in the map inset. Elevated GR values are interpreted to reflect increased clay input associated with monsoonal intensification, showing strong correspondence in Torosa-6 (inter-reef channel) and Scott Reef-2A (lagoon depocentre), but weak correlation in Scott Reef-1. Scott Reef-1 shows a cleaning upwards trend associated with increasing carbonate content since MIS 17, interpreted as the initiation of a raised isolated platform void of terrigenous sediment influx. The red rectangle highlights the age interval of the cores used in this study. (G) Global sea-level stack derived from benthic $\delta^{18}O$ (Lisiecki and Raymo, 2005). Reconstructed coral age data are converted from core depth to paleo-depositional depths by adding cumulative subsidence, assuming a constant rate of 0.37 mm/yr, to sea level. Coral ages and reconstructed depths are plotted on a secondary (right) axis to illustrate reef growth relative to sea-level change and correspondence to MIS glacial-interglacial cycles.

Figure 14 compares gamma ray (GR) log records from three Scott Reef Industry wells (Scott Reef-1, Scott Reef-2A and Torosa-6) (Williams et al., 2023) with long term (1 Ma to present) orbital-scale climate variability to examine the relationship between monsoonal forcing, siliciclastic input, iron oxide deposits and carbonate platform development. In accordance with the interpretive framework by Gallagher et al. (2014; 2017) the GR logs provide useful proxies for terrigenous sediment influx, and therefore variations in Australian monsoonal intensity. Similarly, as per Webster et al. (2022), increased deposits of iron oxides occur during glacials. IODP Expedition 356 (Gallagher et al., 2017; Ishiwa et al., 2019) used

bathyal cores offshore NWS Australia to evaluate the history of the ITF (Gallagher et al., 2014; 2017). Increased siliciclastics during interglacials such as MIS 12 (gamma ray peaks) is related to increased monsoonal activity and ensuing terrestrial sediment runoff, and possibly increased autochthonous lagoonal sedimentation.

Superimposed on this monsoonal forcing was a fundamental reorganisation of the global climate system during the Brunhes Chron, beginning around MIS 19-17 (Jansen et al., 1986; Railsback et al., 2006; Barth et al., 2018). This interval marks the transition to more extreme glacial-interglacial cycles, characterised by warmer and longer interglacials, increased ice-volume variability, and strengthened ocean-atmosphere coupling (Jansen et al., 1986; Barth et al., 2018). Strengthening of the Leeuwin Current during interglacials delivered warm, nutrient-rich waters to the NWS, and increasing aridity after ca. 0.6 Ma. The oceanographic changes, including carbonate supersaturation, likely contributed to reef expansion during MIS 11 following the MPT (Fig. 14).

The GR logs from Torosa-6, which was drilled in the inter-reef channel on the seafloor below the North and South Scott Reef (Fig. 14F), shows strong correlation to sea-level variability, with GR peaks broadly correlating with interglacials. This trend is consistent with the more distal bathyal IODP cores (e.g., Angel-1; Gallagher et al., 2014). The Scott Reef-2A well, drilled in the South Reef lagoon depocentre at ca. 60 m water depth (Fig. 14D), also shows good correlation to MIS stages, but records lower GR amplitudes, indicating reduced terrigenous sediment relative to Torosa-6. Given that the platform is elevated above the surrounding seafloor and largely isolated from direct terrigenous input, this subdued signal is interpreted to reflect local processes, such as increased erosion, together with reworking and redeposition of autochthonous platform sediments during periods of monsoonal intensification.

Scott Reef 1-A (Fig. 14E), located on the raised South Reef margin, in contrast, shows little to no correlation between the GR logs and sea-level variability. Prior to MIS 17, GR values show little correspondence with orbital-scale climate variability derived from O-18 isotope values, and the record indicates a cleaning-upwards trend characterised by decreasing siliciclastic content and increasing carbonates. The significant change at MIS 17 corresponds with the development of the first thick (ca. 50 m) reef margin reproduced in forward stratigraphic models (Williams et al., 2026). Notably, this transition occurs during a relatively low amplitude interglacial in the global sea-level record (Fig. 14G; Lisiecki and Raymo, 2005), suggesting that local platform evolution was not solely controlled by eustatic amplitude and periodicity. The timing of this shift indicates a turning point or threshold in platform maturity and elevation during the early Brunhes. As global climate variability intensified, with more extreme glacials following warm interglacials (Ehlers et al., 2024), the elevated and well-established carbonate platforms became increasingly resilient to both siliciclastic stress and drowning.

These patterns demonstrate that Scott Reef persisted through periods of intensified monsoonal activity due to its elevated topography, while lower-lying inter-reef and lagoonal settings recorded increased terrigenous and reworked sediment input. This possibly contributed to the drowning of the South Reef leeward margin in combination with reef corals being outcompeted by more stress tolerant species (e.g., *Halimeda*). These sedimentary responses are consistent with observations from IODP Expedition 356, and thus in agreement with regional climate reconstructions. The data further support the interpretation that isolated and raised carbonate platforms were more resilient to drowning during interglacials than lower-relief systems, potentially explaining the contrasting evolutionary trajectories of Scott Reef relative to neighbouring platforms such as Ashmore Reef (Webster et al., 2022) and the Rowley atolls to the South (McCaffrey et al., 2025).

The Fe-stained, Al-phyllosilicate-rich intervals with stratified sediment infill and mud-coated bioclasts and coral framestone in the Hook cores (Fig. 4G, 4H) are interpreted as vadose-karst infill derived from terra rossa–like soil and atmospheric dust during subaerial exposure (Muhs et al., 1987; Taylor and Macquaker, 2011). However, consistent with the cautions of Carew and Mylroie (1991) and Kraus (1999), the presence of multiple paleosol-like horizons may reflect composite paleosol development, intrapaleosol bifurcation, or spatial variability in pedogenic expression rather than discrete sea-level oscillations and is a distinction that requires geochronological data to be resolved with the available spatio-temporal core resolution. The U/Th dates produced for core SRSEBH6J in this study suggest that the multiple paleosol horizons observed in core may correlate to glacio-eustatic sea-level fluctuations within sub-stages of MIS 7 and 9 (Figs. 11-13). The complex and continuous pedogenic events observed in Hook 3P (Table 7) and the shallow to deep to shallow trend in NRSEHDD3JA could represent sub-cycles of the saw-tooth MIS 7 sea-level oscillations. However, the poor preservation and contamination by detrital thorium preclude the opportunity to resolve these events within a robust chronostratigraphic framework.

According to interpretations of the hyperspectral and XRD data, the apparent exceptional preservation of aragonite within the SRSEBH6J core (Fig. 8C), relative to other Scott Reef cores and globally documented Pleistocene reef sequences (e.g., Tahiti, Hawaii, Ryukyus, RR5). This preservation coincides with comparatively low abundances of phyllosilicates (Fig. 8E), which may reflect reduced subaerial exposure, meteoric alteration, and associated weathering-related sediment input. Hyperspectral and XRD analyses indicate >99% aragonite at 71 m, 76% at 91 m, and 50% at 149 m (Table 8), suggesting substantial primary mineral preservation. However, integration of SEM observations demonstrates that mineralogical

screening alone is insufficient to guarantee closed-system U–Th behaviour. Even samples classified as dominantly aragonitic exhibit aragonite cementation and high-Mg calcite overgrowths (Fig. 6F), indicating microscale diagenetic modification that is not always detectable via bulk methods (i.e., resolution > 250 microns).

The observation that apparently well-preserved aragonite samples may still exhibit microscale diagenetic alteration is consistent with the findings of Chutcharavan et al. (2018), who demonstrate that $\delta^{234}U_i$ values in fossil corals can deviate from modern seawater values even after conventional mineralogical and detrital-Th screening (Chutcharavan et al., 2018). Their compilation shows that natural variability in seawater $\delta^{234}U$ through glacial–interglacial cycles (up to ca. 5–7‰ lower during the LGM) complicates strict screening thresholds, while subtle open-system behaviour can persist in apparently well-preserved aragonitic samples. Critically, diagenesis does not always manifest as detectable calcite replacement; uranium mobility and α-recoil redistribution can alter isotope ratios without major mineralogical transformation.

In this study, despite applying a multi-method screening protocol (hyperspectral imaging, XRD, SEM, $\delta^{234}U_i$ evaluation, and detrital-Th assessment), samples from MIS 9 and MIS 11 failed to yield closed-system ages. We therefore refrain from overinterpreting these intervals as precise sea-level markers. As noted by Chutcharavan et al. (2018), selection of entirely pristine (100% aragonite) early–middle Pleistocene corals is rarely achievable, and even minor diagenetic alteration can significantly affect U–Th ratios over these timescales. The challenge of obtaining robust closed-system ages beyond ca. 300 ka highlights the importance of (1) continued improvement of diagenetic screening at the microscale in combination with SEM

analyses, (2) cautious interpretation of $\delta^{234}U_i$ deviations, and (3) continued improvement of open-system correction models such as the Thompson et al. (2003) method used in this study.

Though there is little supporting evidence of why aragonite gets preserved over longer timeframes, higher subsidence rates (0.37 mm/yr; Fig. 10), which may have reduced residence time in the freshwater lens, could explain the apparently high preservation throughout the SRSEBH6J core. This core therefore provides an ongoing opportunity to reconstruct Holocene-Pleistocene evolution of the platform within a robust chronological framework (Fig. 11-12). The application of hyperspectral imaging enabled non-destructive identification of subtle diagenetic and depositional transitions, including thin clay horizons that improved recognition of high-frequency sea-level dynamics and improved stratigraphic resolution. In Figure 14G the coral ages likely correspond to sea-level rises and highstands with hiatuses between reef growth events during lowstands. The dense sampling of coral ages around MIS 7 (Fig. 10B) provides rare empirical constraints on a marine isotope stage associated with substantial uncertainty around the timing and magnitude of relative sea-level highstands (Medina-Elizalde, 2013; Woodroffe and Webster, 2014). In most global sea-level reconstructions, MIS 7 is interpreted as failing to reach present-day sea-level and is therefore associated with limited flooding of shallow-water environments (e.g., Waelbroeck et al., 2002). The coral ages presented herein therefore suggest that local accommodation and environmental conditions were sensitive to short-lived highstands or regional oceanographic conditions not previously recorded for the NWS and provide an opportunity for future work to better constrain the spatio-temporal variability of these events.

5.3 Comparisons with Ribbon Reef 5

5.3.1 Chronological framework

The revised chronological framework for Scott Reef described in this study extends from MIS 13 to present, providing one of the oldest and most continuous records of Quaternary fossil reefs drilled on a far-field site away from the effects of glacio-isostatic adjustment (Montaggioni and Braithwaite, 2009; Gallagher et al., 2014; Woodroffe and Webster, 2014). In comparison, the RR5 core, on the passive northeastern Australian margin contains a 210 m long succession of nine stacked reef growth sequences that record eight shallowing upwards reef cycles (Humblet and Webster, 2017). Although the available U-series and Sr-isotope ages are concentrated in the upper part of the core, paleomagnetic data constrain the entire succession to the Bruhnes chron (< 780 kyr), and integration with the independent age model of Montaggioni et al. (2011) suggests that true barrier reef style growth at RR5 likely initiated by MIS 15 and certainly predates MIS 11, which is in agreement with Dubois et al. (2008) and recent re-evaluation of coral community structure and chronostratigraphic framework by Humblet and Webster (2017). In any case, both Scott Reef and RR5 preserve mid to late Pleistocene reef growth histories that have evolved under contrasting accommodation regimes and climatic and oceanographic settings. Despite comparable total core lengths (ca. 200 – 210 m), the oldest reliable U-series age is markedly different between the two systems. At South Scott Reef, an age of ca. 428 kyr at 171 m depth suggests that relatively high long-term subsidence (ca. 0.37 mm/yr) produced thicker and therefore younger aggradational packages. In contrast, RR5 experiences much lower subsidence (ca. 0.1 mm/yr; Sandiford, 2007; Webster and Davies, 2003; Humblet and Webster, 2017; Rovere et al., 2023; Dutton et al., 2023), resulting in a condensed stratigraphic record in which older reef packages (ca. 780 kyr) are preserved at comparable depths. This interpretation is consistent with the North Scott Reef, where an age of ca. 515 kyr (MIS 13) occurs at 151 m depth under lower subsidence (0.29

mm/yr; Collins et al., 2011) compared to the South Reef and is therefore more analogous to RR5. These comparisons demonstrate how differing subsidence rates govern evolution of Quaternary reef systems during high amplitude sea-level oscillations (Webb et al., 2025) and emphasises how variable evolutionary histories can be within the same reef system.

5.3.2 Coralgal assemblages and paleoenvironmental evolution

The evolution of coralgal assemblages documented on the outer edge of the reef crests of North and South Scott Reef indicate a general shallowing trend from the base of the core and is comparable to the evolution of the Ribbon Reef 5 on the Great Barrier Reef (Webster and Davies, 2003; Humblet and Webster, 2017). The Holocene reef in South Scott is an overall shallowing upwards succession with the modern reef deposited in a shallow reef crest environment. Corals are characterised by the transition from Ca3 to Ca2 to Ca1 at about 20 m core depth corresponding to 6.6 kyr (Fig. 11). Based on the known distributions of the modern counterparts and associations with Aa1 and vermetid gastropods, this vertical pattern in reef evolution likely represents a shift from low to high energy environments as a consequence of vertical reef accretion in response to the rapid Holocene sea-level rise. The stacked saucer-shaped seismic architecture and raised-rim platform geometry reported by Williams et al. (2023) and Collins et al. (2011) are consistent with this interpretation, which is also characteristic of the RR5 Holocene reef on the margin (Webster and Davies, 2003). In contrast, the Holocene succession for North Scott is characterised by a shallow to deep to shallow reef community (Fig. 13A) succession with Aa3, composed of *Mesophyllum* and Peyssoneliales, marking the transition to low energy at 8.5 m with an age of 5.7 kyr. The establishment of shallow coral reef communities at the start of the Holocene sea-level rise could have been facilitated by the rate of sea-level rise when it passed the depositional surface, and the lower subsidence rates (ca. 0.29 mm/yr) as compared to the South Reef (0.37 mm/yr; Collins et al.,

2011), which then struggled to keep pace with rapid sea-level rise, possibly associated with the Meltwater Pulse 1B, (ca. 11.5 kyr; Collins et al., 2011) until eventually catching up to sea-level until present.

The base of the RR5 and Scott Reef cores transition from non-reefal (i.e., not a typical shallow high energy reef), deep successions to overlying coral frameworks, but important differences emerge between the paleodepositional environments that highlight distinct local environmental controls. The lower and middle RR5 sections (U1-4; minimum age 564 kyr) are dominated by grainstone-packstone facies and rhodoliths that accumulated in a mesophotic, open shelf setting prior to reef framework development at ca. 137 m (ca. 616 kyr: Humblet and Webster, 2017). In contrast, the base of Scott Reef accumulated in a deep forereef slope setting dominated by floatstones and rudstones, suggesting both platforms had quite different evolutionary histories. Neomorphosed *Halimeda*, coral and mollusc shells are comparable in both cores, although in RR5 a framework dominated interval in reef 2 (15–25 m ca. 125 kyr; MIS 5) is particularly distinctive due to the *Halimeda*-rich grainstone interval that marks a sharp lithologic change. A similar facies is observed in the LIG at One Tree Reef (OTR) on the southern GBR (Dechnik et al., 2017a). There is no clear counterpart in the long cores of Scott Reef; however, a 5 m *Halimeda*-rich grainstone package (e.g., Fig. 3H) is observed at 20 m (MIS 3/5?) in the Hook 1P core. The occurrence of a *Halimeda*-grainstone facies during the same MIS on the Northeast and Northwest margins of Australia likely results from short-lived phases when a green-algal carbonate factory became dominant as coral growth was suppressed under reduced light, increased nutrient upwelling and fluctuating hydrodynamic or turbidity regimes (Searle and Flood, 1988; Wilson, 2013). At South Scott Reef, the prevalence of modern *Halimeda* in the lagoon has been linked to episodic upwelling across the steep channel edge, which is likely modulated by steep local topography, monsoonal forcing and ITF strength

(Wilson, 2013). These conditions may have prevailed during MIS 3/5? when coral framework was stressed under similar conditions and possibly signals the onset of the leeward margin drowning. On the GBR, production of *Halimeda*-grainstone is possibly linked to inner-ramp or lagoonal circulation and nutrient conditions specific to the narrow, high energy shelf edge setting of the Northern GBR (Fig. 1C), as well as higher sea surface temperatures modulated by the East Australian Current (EAC) (Cortese et al., 2013; Dechnik et al., 2017a; McNeil et al., 2021; Szilagyi et al., 2023).

Scleractinian species are reportedly more diverse in RR5 with 58 species in 35 genera (Humblet and Webster, 2017), compared to 35 species in 24 genera at Scott Reef, although this difference may partly reflect lower taxonomic resolution at Scott Reef due to reliance on largely photographic identification of altered corals. The eight shallowing upwards cycles defined by Humblet and Webster, (2017) are characterised by initiation in deep low energy settings dominated by *Porites*-*Montipora*-merulinids coral communities that are succeeded by *Acropora*-*Isopora* communities during sea-level highs. The coral assemblages are consistent with the interpreted paleodepositional environments. For example, the shallow Ca1 defined for Scott Reef is dominated by massive *Porites* and associated branching *Acropora,* encrusting and massive *Montipora* and massive *Isopora,* however the deep reef assemblage identified at Scott Reef is composed of massive and encrusting forms of *Porites, Montipora,* and agaricids, but no identifiable merulinids communities. In both reef sites, there is an increase of *in situ* coral framework during the Holocene, that could be linked to either a shallowing or elevated SSTs across the tropics similar to today, and a weaker El Nino-Southern Oscillation (ENSO) (Gagan et al., 1998; Webster et al., 2009). Abundant shallow reef facies developed at RR5 by at least MIS 11 (ca. 400 kyr) and at North Scott Reef by MIS 13, whereas comparable shallow reef development in two cores at South Scott Reef did not occur until approximately MIS 7. This is

possibly a consequence of sampling location, since euphotic coral clasts are identified in the detrital sediments at the base of both reef cores (Humblet and Webster, 2017). The occurrence of *Cycloclypeus* foraminifera in Scott Reef is more biogeographically similar to Indonesian reefs and has only recently been discovered along the NWS at Ashmore reef (Webster et al., 2022). This indicates that the NWS reef systems are less isolated than previously thought and were likely influenced by the Indo-Pacific water masses and faunal exchange pathways associated with the ITF (Pandey et al., 2007), connecting the Indian Ocean and the Western Pacific.

5.3.3 Bathymetric and environmental controls on reef evolution on the NE and NW Australian margins

Sedimentary facies in the three Scott Reef cores interpreted in this study are broadly consistent with those described along the RR5 site during IODP 325 (Yokoyama et al., 2011; Gischler et al., 2013; Braga et al., 2019; Yagioka et al., 2019). However, there is a higher abundance of rudstone facies and more abundant *Porites*-dominated reef framework in the Scott Reef cores, which we attribute to higher hydrodynamic energy on the outer NWS and to differences in shelf width, wave fetch and along-slope currents relative to the much narrower northeastern shelf. These differences reflect fundamental bathymetric and oceanographic contrasts between the Northwest (Fig. 1B) and Northeast (Fig. 1C) margins. The NWS comprises a broad transition between the inner and outer shelf extending > 200 km offshore, with a gently sloping basinward profile and isolated carbonate platforms situated on the outer shelf in water depths of ca. 400 – 700 m. The Northeast shelf is comparatively narrow, with a sharp transition from the shallow inner shelf to the deep basin. Ribbon Reef 5 is located at 15 ^{o} S on the shelf edge of the Coral Sea, around 49 km offshore from the Northeast coast of Queensland, Australia (Webster and Davies, 2003; Humblet and Webster, 2017). The reef lies

in low turbidity water with high wave exposure facing the open ocean where modern SSTs average ca. 29 ^{o}C (Humblet and Webster, 2017; Petrick et al., 2024). However, both reefs sit above canyon systems that bypass sediment from the inner shelf to the deep basin inhibiting terrigenous sediment influx during periods of intensified monsoonal conditions. Differences in sedimentary facies between carbonate platforms on the NE and NW margins of Australia highlight the variations in precipitation, allochthonous and autochthonous sediments, and nutrient supply that likely influenced reef evolution. The ITF, which brings heat south from the Pacific and Eastern Indian Ocean (Pandey et al., 2007) and the Leeuwin current, which brings warm, low-salinity waters reduced terrigenous input during interglacials (Gotkas et al., 2016), coupled with arid conditions during glacial periods associated with increased aragonite production (Hallenberger et al., 2022), likely promoted carbonate production along the NWS during interglacials.

Along the NWS, the onset of monsoonal intensification occurred after ca. 0.5 Ma and 0.3 Ma (Gallagher et al., 2014), during MIS 13 and MIS 7. This climate change was driven by a weakened Leeuwin Current and a strengthened West Australian current (Gotkas et al., 2016; Palei et al., 2024), together with changes in ITF circulation (Clark et al., 2006; Petrick et al., 2019; Hallenberger et al., 2022) that facilitated the delivery of nutrient-rich cold-water via upwelling to the outer NWS. Increased monsoonal intensity has been correlated with reef demise in the Maldives during the Miocene, where increased sediment flux, turbidity, and nutrient delivery suppressed carbonate production (e.g., Alonso-Garcia et al., 2024 and Betzler et al., 2009; 2013). The distally positioned Scott and Ribbon Reefs were less directly affected by terrigenous input and instead experienced climate-driven increases in rainfall, sea-surface temperatures, primary productivity and episodic nutrient upwelling (Deniston et al., 2013; Auer et al., 2021; Sanborn et al., 2024). Under these conditions, monsoonal intensification was a

common regional forcing that likely had a profound impact on coral reef development in both regions, but its expression varied between both systems depending on local conditions. The onset of shallow reef development at Scott Reef during MIS 7, could be considered a consequence of these climate changes after ca. 0.3 Ma.

The Scott Reef and RR5 core records indicate that despite differences in early paleodepositional environments, subsidence rate and shelf geometry, both platforms - composed of similar coralgal communities - maintained long-term stable ecological and environmental conditions. They rapidly recovered following emersion events from at least MIS 15, highlighting their persistence and resilience as long-lived Quaternary reef systems.

6. Conclusions

Our detailed study of three cores from North and South Scott Reef allowed us to make the following conclusions:

1. Four coral assemblages and three algal assemblages are identified. Based on modern local and regional reef analogues, we interpret three distinct depositional environments: (1) reef crest to shallow upper reef slope (< 10 m), (2) intermediate forereef slope (< 30 m), and (3) deep forereef slope (> 20 m). An overall shallowing upwards trend is observed in all cores that initiates during MIS 9 on the South Reef and MIS 13 on the North Reef from a deep slope setting to a shallow water reef crest environment. Fewer but thicker chronostratigraphic packages are observed in the long core on the South Reef compared to the North Reef and is likely a result of higher subsidence rates.
2. Preservation of aragonitic material in the South Reef SE margin enabled new closed-system and Thompson-corrected open system U/Th ages and a detailed reconstruction of paleodepositional environments. Pervasive diagenesis in the Northern platform and higher

dolomitization on the South Reef leeward margin indicates more complex eustatic variations and fluid exchange with marine and meteoric waters, possibly due to variable subsidence across both reefs. A thick dolomite interval in the North Reef is temporally associated with the MIS 12 lowstand. The development of this dolomite is interpreted to reflect hydrographic and climatic conditions characteristic of the post-MPT climate regime, including increased rainfall driven by monsoonal intensification, a less restricted ITF, warmer conditions and a stronger Leeuwin Current. These interpretations are supported by the observed GR peaks in regional industry well logs that indicate increased terrigenous sediment influx. Iron oxides are most abundant during MIS 7 across all cores and indicates the platforms were repeatedly exposed during the saw-tooth oscillations of the MIS 7 sub-stages, which are characteristically shallow and thus poorly characterised. In the Scott Reef cores, it appears to have imposed variable redox and diagenetic conditions that produced iron rich carbonates across the platforms.

3. Despite differences in initial depositional environments – RR5 developing from mesophotic open-shelf grainstone-packstone and rhodolith facies, and Scott Reef from deeper forereef slope floatstones and rudstones – as well as differences in subsidence regime, shelf geometries and local oceanographic settings, both systems reveal similar long-term reef development from ca. MIS 15 to present. This includes broadly comparable coralgal assemblages, a distinct *Halimeda*-grainstone interval that occurs in the leeward margin of South Scott Reef possibly during MIS 5 and the R2 LIG unit in RR5, and evidence of persistent ecological resilience and recovery following repeated subaerial exposure events.

This study provides one of the most continuous far-field tropical fossil reef records and presents a major contribution to our understanding of Pleistocene reef sequences, Quaternary

sea-level and climate variability and the resilience of coralgal ecosystems to environmental change.

References

Adey, W.H. and Macintyre, I.G., 1973. Crustose coralline algae: a re-evaluation in the geological sciences. Geological Society of America Bulletin, 84(3), pp.883-904.

Adey, W.H., Townsend, R.A., Boykins, W.T., 1982. The crustose coralline algae (Rhodophyta: Corallinaceae) of the Hawaiian Islands. Smithsonian Contributions to the Marine Sciences 15, 1–74.

Abbey, E., Webster, J.M., Beaman, R.J., 2011. Geomorphology of submerged reefs on the shelf edge of the Great Barrier Reef: The influence of oscillating Pleistocene sea-levels. Marine Geology 288, 61–78.

Alonso-García, M., Reolid, J., Jiménez-Espejo, F.J., Bialik, O.M., Álvarez Zarikian, C.A., Laya, J.C., Carrasquiera, I., Jovane, L., Reijmer, J.J.G., Betzler, C., Eberli, G.P., 2024. Sea-level and monsoonal control on the Maldives carbonate platform (inguo (Indian Ocean) over the last 1.3 million years. Climate of the Past Discussions 2023, 1–44.

Auer, G., Petrick, B., Yoshimura, T., Mamo, B.L., Reuning, L., Takayanagi, H., De Vleeschouwer, D., Martínez-García, A., 2021. Intensified organic carbon burial on the Australian shelf after the Middle Pleistocene transition. Quaternary Science Reviews 262, 106965.

Bain, R.J., Foos, A.M., 1993. Carbonate microfabrics related to subaerial exposure and paleosol formation. In: Lavoie, D.L., Rezak, R., Bouma, A.H. (Eds.), Carbonate Microfabrics. Springer, New York, NY, pp. 19–27.

Barth, AM, Clark, PU, Bill, NS, He, F & Pisias, NG 2018, Climate evolution across the Mid-Brunhes Transition, Climate of the past, vol. 14, no. 12, pp. 2071–2087.

Belde, J., Back, S., Bourget, J. and Reuning, L., 2017. Oligocene and Miocene carbonate platform development in the Browse Basin, Australian northwest shelf. *Journal of Sedimentary Research*, *87*(8), pp.795-816.

Betzler, C., Hübscher, C., Lindhorst, S., Reijmer, J.J.G., Römer, M., Droxler, A.W., Lüdmann, T., 2009. Monsoon-induced partial carbonate platform drowning (Maldives, Indian Ocean). Geology 37, 867–870. https://doi.org/10.1130/G25702A.1

Betzler, C., Fürstenau, J., Lüdmann, T., Hübscher, C., Lindhorst, S., Paul, A., Reijmer, J.J.G., Droxler, A.W., 2013. Sea-level and ocean-current control on carbonate-platform growth, Maldives, Indian Ocean. Basin Research 25, 172–196.

Betzler, C., Hübscher, C., Lindhorst, S., Lüdmann, T., Hincke, C., Beaman, R.J., Webster, J.M., 2024. Seismic stratigraphic and sedimentary record of a partial carbonate platform drowning, Queensland Plateau, northeast Australia. Marine Geology 470, 107255. https://doi.org/10.1016/j.margeo.2024.107255

Bevitt, J.J., 2018. Discovering dinosaurs with neutrons. Nature Reviews Materials 3, 296–298. https://doi.org/10.1038/s41578-018-0049-0

Bishop, J.L., King, S.J., Lane, M.D., Brown, A.J., Lafuente, B., Hiroi, T., Roberts, R., Swayze, G.A., Lin, J.-F., Sánchez Román, M., 2021. Spectral properties of anhydrous carbonates and nitrates. Earth and Space Science 8, e2021EA001844.

Blanchon, P., Blakeway, D., 2003. Are catch-up reefs an artefact of coring? Sedimentology 50, 1271–1282.

Boardman, M.R., McCartney, R.F. and Eaton, M.R., 1995. Bahamian paleosols: origin, relation to paleoclimate, and stratigraphic significance. In Terrestrial and Shallow Marine Geology of the Bahamas and Bermuda, ed. H.A. Curran and B. White, 33-47. Boulder, Colorado: Geological Society of America Special Paper 300.

Boden-Hawes, K., 2025. The role of stratified tidal dynamics on coral reef resilience. Doctor of Philosophy thesis, Oceans Institute, School of Earth and Oceans, The University of Western Australia, Perth, Australia.

Braga, J.C., Aguirre, J., 2004. Coralline algae indicate Pleistocene evolution from deep, open platform to outer barrier reef environments in the northern Great Barrier Reef margin. Coral Reefs 23, 547–558. https://doi.org/10.1007/s00338-004-0414-x

Braga, J.C., Humblet, M., Ramos, D.A.E., Dechnik, B., Webster, J.M., 2022. Quaternary coral, coralline algal and vermetid assemblages as sea-level indicators: a review. In: IAS Special Publication: Coral Reefs and Sea-Level Change: Quaternary Records and Modelling. A Window Into the Future, 49, 1–38.

Braithwaite, C.J.R., Dalmasso, H., Gilmour, M.A., Harkness, D.D., Henderson, G.M., Kay, R.L.F., Kroon, D., Montaggioni, L.F., Wilson, P.A., 2004. The Great Barrier Reef: the chronological record from a new borehole. Journal of Sedimentary Research 74, 298–310. https://doi.org/10.1306/091603740298

Braithwaite, C.J.R., Montaggioni, L.F., 2009. Great Barrier Reef: a 700,000 year diagenetic history. Sedimentology 56, 1591–1622. https://doi.org/10.1111/j.1365-3091.2008.00982.x

Braithwaite, C.J.R., 2016. Coral-reef records of Quaternary changes in climate and sea-level. Earth-Science Reviews 156, 137–154.

Cabioch, G., Montaggioni, L.F., Faure, G., Ribaud-Laurenti, A., 1999. Reef coralgal assemblages as recorders of paleobathymetry and sea level changes in the Indo-Pacific province. Quaternary Science Reviews 18, 1681–1695. https://doi.org/10.1016/S0277-3791(99)00014-1

Cabioch, G., Montaggioni, L.F., Thouveny, N., Frank, N., Sato, T., Chazottes, V., Sémah, A.-M., 2008. The chronology and structure of the western New Caledonian barrier reef

tracts. Palaeogeography, Palaeoclimatology, Palaeoecology 268, 91–105. https://doi.org/10.1016/j.palaeo.2008.07.014

Camoin, G.F., Ebren, P., Eisenhauer, A., Bard, E., Faure, G., 2001. A 300,000-yr coral reef record of sea level changes, Mururoa atoll (Tuamotu archipelago, French Polynesia). Palaeogeography, Palaeoclimatology, Palaeoecology 175, 325–341.

Camoin, G.F., Iryu, Y., McInroy, D.B., 2007. IODP Expedition 310 reconstructs sea level, climatic, and environmental changes in the South Pacific during the last deglaciation. Scientific Drilling 5, 4–12.

Camoin, G.F., Webster, J.M., 2015. Coral reef response to Quaternary sea-level and environmental changes: State of the science. Sedimentology 62, 401–428. https://doi.org/10.1111/sed.12184

Caragnano, A., Foetisch, A., Maneveldt, G.W., Millet, L., Liu, L.-C., Lin, S.-M., Rodondi, G., Payri, C.E., 2018. Revision of Corallinaceae (Corallinales, Rhodophyta): recognizing Dawsoniolithon gen. nov., Parvicellularium gen. nov. and Chamberlainoideae subfam. nov. containing Chamberlainium gen. nov. and Pneophyllum. Journal of Phycology. https://doi.org/10.1111/jpy.12644

Carew, J.L., Mylroie, J.E., 1991. Some pitfalls in paleosol interpretation in carbonate sequences. Carbonates and Evaporites 6, 69–74.

Chappell, J., Omura, A., Esat, T., McCulloch, M., Pandolfi, J., Ota, Y., Pillans, B., 1995. Reconciliation of late Quaternary sea levels derived from coral terraces at Huon Peninsula with deep sea oxygen records. Journal of Geography (Chigaku Zasshi) 104, 777–784.

Cheng, H., Lawrence Edwards, R., Shen, C.-C., Polyak, V. J., Asmerom, Y., Woodhead, J., … Calvin Alexander, E., 2013. Improvements in 230Th dating, 230Th and 234U half-life values, and U–Th isotopic measurements by multi-collector inductively coupled plasma

mass spectrometry. Earth and Planetary Science Letters, 371–372, 82–91. https://doi.org/10.1016/j.epsl.2013.04.006.

Christe, P., Bernasconi, M., Vontobel, P., Turberg, P., Parriaux, A., 2007. Three-dimensional petrographical investigations on borehole rock samples: A comparison between X-ray computed and neutron tomography. Acta Geotechnica 2, 269–279. https://doi.org/10.1007/s11440-007-0045-9.

Chutcharavan, P. M., Dutton, A., & Ellwood, M. J., 2018. Seawater 234U/238U recorded by modern and fossil corals. Geochimica et Cosmochimica Acta, 224, 1–17. https://doi.org/10.1016/j.gca.2017.12.017

Clark, P.U., Archer, D., Pollard, D., Blum, J.D., Rial, J.A., Brovkin, V., Roy, M., 2006. The middle Pleistocene transition: Characteristics, mechanisms, and implications for long-term changes in atmospheric pCO2. Quaternary Science Reviews 25, 3150–3184. https://doi.org/10.1016/j.quascirev.2006.07.008

Clark, T.R., Roff, G., Zhao, J.-x., Feng, Y.x., Done, T.J. and Pandolfi, J.M., 2014. Testing the precision and accuracy of the U–Th chronometer for dating coral mortality events in the last 100 years. Quaternary Geochronology., 23, 35–45.

Collins, L.B., 2002. Tertiary foundations and Quaternary evolution of coral reef systems of Australia's northwest shelf. In: Keep, M., Moss, S. (Eds.), The Sedimentary Basins of Western Australia 3: Proceedings of the Petroleum Exploration Society of Australia Symposium, Perth, WA, pp. 129–152.

Collins, L.B., Testa, V., Zhao, J., Qu, D., 2009. Quaternary Growth History and Evolution of the Scott Reef Carbonate Platform and Coral Reef: Core Study. Final Report prepared for Woodside Energy Limited, Curtin University, March 2009 (unpublished; permission and access granted through WEL–UWA TIDE agreement).

Collins, L.B., 2010. Controls on morphology and growth history of coral reefs of Australia's western margin. In: Morgan, W.A., George, A.D., Harris, P.M., Kupecz, J.A., Sarg, J.F. (Eds.), Cenozoic Carbonate Systems of Australasia. SEPM Special Publication 95, Society for Sedimentary Geology, Tulsa, pp. 195–217. https://doi.org/10.2110/sepmsp.095.195.

Collins, L.B., Testa, V., 2010. Quaternary development of resilient reefs on the subsiding Kimberley continental margin, northwest Australia. Brazilian Journal of Oceanography 58, 67–77. https://doi.org/10.1590/S1679-87592010000500007

Collins, L.B., 2011. Geological setting, marine geomorphology, sediments and oceanic shoals growth history of the Kimberley region. Journal of the Royal Society of Western Australia 94, 89–105.

Collins, L.B., Testa, V., Zhao, J., Qu, D., 2011. Holocene growth history and evolution of the Scott Reef carbonate platform and coral reef. Journal of the Royal Society of Western Australia 94, 239.

Coral Trait Database, 2020. Coral Trait Database. Available at: https://coraltraits.org/

Cortese, G., Dunbar, G.B., Carter, L., Scott, G., Bostock, H., Bowen, M., Crundwell, M., Hayward, B.W., Howard, W., Martinez, J.I., Moy, A., 2013. Southwest Pacific Ocean response to a warmer world: insights from Marine Isotope Stage 5e. Paleoceanography 28, 585–598.

Courtney, T.A., Guest, J.R., Edwards, A.J., Dizon, R.M., 2021. Linear extension, skeletal density, and calcification rates of the blue coral Heliopora coerulea. Coral Reefs 40, 1631–1635.

Davies, P.J., Montaggioni, L.F., 1985. Reef growth and sea-level change: the environmental signature. Proceedings of the Fifth International Coral Reef Symposium 3, 477–515.

Dechnik, B., Webster, J.M., Davies, P.J., Braga, J.C., Reimer, P.J., 2015. Holocene "turn-on" and evolution of the Southern Great Barrier Reef: Revisiting reef cores from the Capricorn Bunker Group. Marine Geology 363, 174–190.

Dechnik, B., Webster, J.M., Webb, G.E., Nothdurft, L., Dutton, A., Braga, J.C., Zhao, J.-X., Duce, S., Sadler, J., 2017a. The evolution of the Great Barrier Reef during the last interglacial period. Global and Planetary Change 149, 53–71.

Dechnik, B., Webster, J.M., Webb, G.E., Nothdurft, L., Zhao, J.-X., 2017b. Successive phases of Holocene reef flat development: Evidence from the mid- to outer Great Barrier Reef. Palaeogeography, Palaeoclimatology, Palaeoecology 466, 221–230.

Denniston, R.F., Wyrwoll, K.-H., Asmerom, Y., Polyak, V.J., Humphreys, W.F., Cugley, J., Greaves, E., 2013. North Atlantic forcing of millennial-scale Indo-Australian monsoon dynamics during the Last Glacial period. Quaternary Science Reviews 72, 159–168. https://doi.org/10.1016/j.quascirev.2013.04.012

Deschamps, P., Durand, N., Bard, E., Hamelin, B., Camoin, G., Thomas, A.L., Henderson, G.M., Okuno, J., Yokoyama, Y., 2012. Ice-sheet collapse and sea-level rise at the Bølling warming 14,600 years ago. Nature 483, 559–564. https://doi.org/10.1038/nature10902

Done, T.J., 1982. Patterns in the distribution of coral communities across the central Great Barrier Reef. Coral Reefs 1, 95–107. https://doi.org/10.1007/BF00301691

Done, T.J., Williams, D.McB., Speare, P.J., Turak, E.I., Davidson, J., DeVantier, L.M., Newman, S.J., Hutchins, J.B., 1994. Surveys of coral and fish communities at Scott Reef and Rowley Shoals. Report produced under the Scott Reef Research Services Agreement between Woodside Offshore Petroleum Pty Ltd and the Australian Institute of Marine Science.

Drivet, E., Mountjoy, E.W., 1997. Dolomitization of the Leduc Formation (Upper Devonian), southern Rimbey-Meadowbrook reef trend, Alberta. Journal of Sedimentary Research 67, 411–423.

Dubois, N., Kindler, P., Spezzaferri, S., Coric, S., 2008. The initiation of the southern central Great Barrier Reef: New multiproxy data from Pleistocene distal sediments from the Marion Plateau (NE Australia). Marine Geology 250, 223–233.

Dutton, A., Dechnik, B., Webster, J., Kajan, M., Forte, A.M., Glisovic, P., 2023. Mantle-driven subsidence of Last Interglacial reef points to origins of the Great Barrier Reef. AGU Fall Meeting 2023, Abstract C11B-04.

Ehlers, J., Astakhov, V., Gibbard, P.L., Ingólfsson, Ó., Mangerud, J., & Svendsen, J.I., 2025. Early Pleistocene glaciations and precursors. In: Elias, S. (Ed.), *Encyclopedia of Quaternary Science*, 3rd ed. Elsevier, pp. 629–634. https://doi.org/10.1016/B978-0-323-99931-1.00192-6.

Eisenhauer, A., Wasserburg, G.J., Chen, J.H., Bonani, G., Collins, L.B., Zhu, Z.R., Wyrwoll, K.H., 1993. Holocene sea-level determination relative to the Australian continent: U/Th (TIMS) and 14C (AMS) dating of coral cores from the Abrolhos Islands. Earth and Planetary Science Letters 114, 529–547. https://doi.org/10.1016/0012-821X(93)90081-J.

Fathi, I., Hertelendi, E. and Haas, J., 1997. Geochemistry and dolomitization of Pleistocene coral reefs, in the Gulf of Aqaba region, South Sinai, Egypt. Acta Mineralogica-Petrographica, 38, pp.73-94.

Gagan, M.K., Ayliffe, L.K., Hopley, D., Cali, J.A., Mortimer, G.E., Chappell, J., McCulloch, M.T., Head, M.J., 1998. Temperature and surface-ocean water balance of the mid-Holocene tropical western Pacific. Science 279, 1014–1018.

Gallagher, S.J., Wallace, M.W., Hoiles, P.W., Southwood, J.M., 2014. Seismic and stratigraphic evidence for reef expansion and onset of aridity on the Northwest Shelf of Australia during the Pleistocene. Marine and Petroleum Geology 57, 470–481. https://doi.org/10.1016/j.marpetgeo.2014.06.011

Gallagher, S.J., Fulthorpe, C.S., Bogus, K., Auer, G., Baranwal, S., Castañeda, I.S., Christensen, B.A., De Vleeschouwer, D., Franco, D.R., Groeneveld, J., Gurnis, M., 2017. Expedition 356 summary. In: Proceedings of the International Ocean Discovery Program, Expedition Reports 356.

Gallagher, S.J., Auer, G., Brierley, C.M., Fulthorpe, C.S., Hall, R., 2024. Cenozoic history of the Indonesian Gateway. Annual Review of Earth and Planetary Sciences 52, 581–604. https://doi.org/10.1146/annurev-earth-040722-111322

Gilmour, J.P., Cook, K.L., Ryan, N.M., Puotinen, M.L., Green, R.H., Shedrawi, G., Oades, D., 2019. The state of Western Australia's coral reefs. Coral Reefs 38, 651–667. https://doi.org/10.1007/s00338-019-01795-8

Gilmour, J.P., Cook, K.L., Ryan, N.M., Puotinen, M.L., Green, R.H., Heyward, A.J., 2022. A tale of two reef systems: Local conditions, disturbances, coral life histories, and the climate catastrophe. Ecological Applications 32, e2509. https://doi.org/10.1002/eap.2509

Gischler, E., Ginsburg, R.N., Herrle, J.O., Prasad, S., 2010. Mixed carbonates and siliciclastics in the Quaternary of southern Belize: Pleistocene turning points in reef development controlled by sea-level change. Sedimentology 57, 1049–1068. https://doi.org/10.1111/j.1365-3091.2009.01133.x

Gischler, E., 2015. Quaternary reef response to sea-level and environmental change in the western Atlantic. Sedimentology 62, 429–465. https://doi.org/10.1111/sed.12184

Gischler, E., Thomas, A.L., Droxler, A.W., Webster, J.M., Yokoyama, Y., Schöne, B.R., 2013. Microfacies and diagenesis of older Pleistocene (pre-last glacial maximum) reef deposits, Great Barrier Reef, Australia (IODP Expedition 325): A quantitative approach. Sedimentology 60, 1432–1466.

Gischler, E., Hudson, J.H., 2019. Holocene tropical reef accretion and lagoon sedimentation: A quantitative approach to the influence of sea-level rise, climate and subsidence (Belize, Maldives, French Polynesia). The Depositional Record 5, 515–539. https://doi.org/10.1002/dep2.62

Goktas, P., Austin, J.A., Fulthorpe, C.S., Gallagher, S.J., 2016. Morphologies and depositional/erosional controls on evolution of Pliocene–Pleistocene carbonate platforms: Northern Carnarvon Basin, Northwest Shelf of Australia. Continental Shelf Research 124, 63–82. https://doi.org/10.1016/j.csr.2016.05.009

Gordon, A.L., 2005. The indonesian seas. *Oceanography*, *18*(4), p.14.

Gowan, E.J., Zhang, X., Khosravi, S., Rovere, A., Stocchi, P., Hughes, A.L.C., Gyllencreutz, R., Mangerud, J., Svendsen, J.-I., Lohmann, G., 2021. A new global ice sheet reconstruction for the past 80,000 years. Nature Communications 12, 1199. https://doi.org/10.1038/s41467-021-21469-w

Green, R.H., Lowe, R.J., Buckley, M.L., 2018. Hydrodynamics of a tidally forced coral reef atoll. Journal of Geophysical Research: Oceans 123, 7084–7101. https://doi.org/10.1029/2018JC013946

Grimaldi, C.M., Faubel, C., Thomas, L., Sahin, A.D., Ryan, N.M., Rayson, M., Green, R., Cuttler, M.W., Treml, E.A., Lowe, R.J., Gilmour, J.P., 2024. Local coral connections within an atoll reef system underlie reef resilience and persistence. Limnology and Oceanography 69, 3020–3032. https://doi.org/10.1002/lno.12720

Hallenberger, M., Reuning, L., Back, S., Gallagher, S.J., Iwatani, H., Lindhorst, K., 2022. Climate and sea-level controlling internal architecture of a Quaternary carbonate ramp (Northwest Shelf of Australia). Sedimentology 69, 1276–1300.

He, Y., Wang, H., Liu, Z., 2021. Development of the Leeuwin Current on the northwest shelf of Australia through the Pliocene–Pleistocene period. Earth and Planetary Science Letters 559, 116767. https://doi.org/10.1016/j.epsl.2021.116767

Heyward, A., Radford, B., 2019. Northwest Australia. In: Loya, Y., Puglise, K.A., Bridge, T.C.L. (Eds.), Mesophotic Coral Ecosystems. Springer, Cham, pp. 337–349.

Hibbert, F.D., Rohling, E.J., Dutton, A., Williams, F.H., Chutcharavan, P.M., Zhao, C., Tamisiea, M.E., 2016. Coral indicators of past sea-level change: A global repository of U-series dated benchmarks. Quaternary Science Reviews 145, 1–56. https://doi.org/10.1016/j.quascirev.2016.04.019

Huang, D., Benzoni, F., Fukami, H., Knowlton, N., Smith, N.D., Budd, A.F., 2014. Taxonomic classification of the reef coral families Merulinidae, Montastraeidae, and Diploastraeidae (Cnidaria: Anthozoa: Scleractinia). Zoological Journal of the Linnean Society 171, 277–355.

Huang, D., Arrigoni, R., Benzoni, F., Fukami, H., Knowlton, N., Smith, N.D., Stolarski, J., Chou, L.M., Budd, A.F., 2016. Taxonomic classification of the reef coral family Lobophylliidae (Cnidaria: Anthozoa: Scleractinia). Zoological Journal of the Linnean Society 178, 436–481.

Huang, W.-S., Jien, S.-H., Huang, S.-T., Tsai, H., Hseu, Z.-Y., 2017. Pedogenesis of red soils overlaid coral reef terraces in the Southern Taiwan. Quaternary International 441, 62–76.

Humblet, M., Hongo, C., Sugihara, K., 2015. An identification guide to some major Quaternary fossil reef-building coral genera (Acropora, Isopora, Montipora, and Porites). Island Arc 24, 16–30.

Humblet, M., Webster, J.M., 2017. Coral community changes in the Great Barrier Reef in response to major environmental changes over glacial–interglacial timescales. Palaeogeography, Palaeoclimatology, Palaeoecology 472, 216–235.

Humblet, M., Potts, D.C., Webster, J.M., Braga, J.C., Iryu, Y., Yokoyama, Y., Bourillot, R., Séard, C., Droxler, A., Fujita, K., Gischler, E., 2019. Late glacial to deglacial variation of coralgal assemblages in the Great Barrier Reef, Australia. Global and Planetary Change 174, 70–91.

Humphrey, J.D., Quinn, T.M., 1989. Coastal mixing zone dolomite, forward modeling, and massive dolomitization of platform-margin carbonates. Journal of Sedimentary Research 59, 438–454.

Huisman, J.M., Leliaert, F., Verbruggen, H., Townsend, R.A., 2009. Marine benthic plants of Western Australia's shelf-edge atolls. Records of the Western Australian Museum, Supplement 77, 50–87.

Huisman, J.M., Dixon, R.R., Townsend, R.A., Belton, G., 2021. Diversity and distribution of marine benthic algae and seagrasses in the tropical Kimberley, Western Australia. Records of the Western Australian Museum 36, 185–200.

Ishiwa, T., Yokoyama, Y., Reuning, L., McHugh, C.M., De Vleeschouwer, D., Gallagher, S.J., 2019. Australian Summer Monsoon variability in the past 14,000 years revealed by IODP Expedition 356 sediments. Progress in Earth and Planetary Science 6, 1–10.

Ivankina, T.I., Kichanov, S.E., Duliu, O.G., Abdo, S.Y., Sherif, M.M., 2020. The structure of scleractinian coral skeleton analyzed by neutron diffraction and neutron computed

tomography. Scientific Reports 10, 12869. https://doi.org/10.1038/s41598-020-69859-2.

Jansen, JHF, Kuijpers, A & Troelstra, SR 1986, 'A Mid-Brunhes Climatic Event: Long-Term Changes in Global Atmosphere and Ocean Circulation', Science (American Association for the Advancement of Science), vol. 232, no. 4750, pp. 619–622.

Jackson, J.B.C., 1992. Pleistocene perspectives on coral reef community structure. American Zoologist 32, 719–731.

Kaufman, J., 1994. Numerical models of fluid flow in carbonate platforms: implications for dolomitization. Journal of Sedimentary Research 64, 128–139.

Kraus, M.J., 1999. Paleosols in clastic sedimentary rocks: their geologic applications. Earth-Science Reviews 47, 41–70.

Lisiecki, L.E. and Raymo, M.E., 2005. A Pliocene-Pleistocene stack of 57 globally distributed benthic δ18O records. Paleoceanography, 20(1).

Littler, D.S., Littler, M.M., 2003. South Pacific Reef Plants: A Diver's Guide to the Plant Life of South Pacific Coral Reefs. Offshore Graphics, Washington, DC.

Mack, G.H., James, W.C., Monger, H.C., 1993. Classification of paleosols. Geological Society of America Bulletin 105, 129–136.

Machel, H.-G., Mountjoy, E.W., 1986. Chemistry and environments of dolomitization: A reappraisal. Earth-Science Reviews 23, 175–222.

Maneveldt, G.W., Keats, D.W., 2014. Taxonomic review based on new data of the reef-building alga Porolithon onkodes (Corallinaceae, Corallinales, Rhodophyta) along with other taxa found to be conspecific. Phytotaxa 190, 216–249.

Maneveldt, G.W., Van der Merwe, E. and Keats, D.W., 2016. Updated keys to the non-geniculate coralline red algae (Corallinophycidae, Rhodophyta) of South Africa. South African Journal of Botany, 106, pp.158-164.

McCaffrey, J.C., Wallace, M.W., Gallagher, S.J., 2020. A Cenozoic Great Barrier Reef on Australia's North West Shelf. Global and Planetary Change 184, 103048. https://doi.org/10.1016/j.gloplacha.2019.103048

McCaffrey, J.C., Gallagher, S.J., Wallace, M.W., Averes, T., Fabian, S.G., Lindhorst, K., Krastel, S., 2025. The Rowley Shoals atolls: Remnants of a Miocene great barrier reef on the north-west Australian margin. Global and Planetary Change 245, 104688. https://doi.org/10.1016/j.gloplacha.2024.104688

McGregor, H.V., Abram, N.J., 2008. Images of diagenetic textures in Porites corals from Papua New Guinea and Indonesia. Geochemistry, Geophysics, Geosystems 9, Q10013. https://doi.org/10.1029/2008GC002093

McKenzie, J.A., 1981. Holocene dolomitization of calcium carbonate sediments from the coastal sabkhas of Abu Dhabi, UAE: a stable isotope study. Journal of Geology 89, 185–198.

McNeil, M., Hua, Q., Erler, D.V., Nothdurft, L.D., Webster, J.M. and Moss, P., 2021. Evolution of the Great Barrier Reef *Halimeda* carbonate factory in response to Holocene environmental changes, determined from radiocarbon and nitrogen isotope measurements.

Medina-Elizalde, M., 2013. A global compilation of coral sea-level benchmarks: Implications and new challenges. Earth and Planetary Science Letters 362, 310–318. https://doi.org/10.1016/j.epsl.2012.12.001

Moberg, F., Nyström, M., Kautsky, N., Tedengren, M., Jarayabhand, P., 1997. Effects of reduced salinity on the rates of photosynthesis and respiration in the hermatypic corals Porites lutea and Pocillopora damicornis. Marine Ecology Progress Series 157, 53–59.

Montaggioni, L.F., Camoin, G.F., 1993. Stromatolites associated with coralgal communities in Holocene high-energy reefs. Geology 21, 149–152.

Montaggioni, L.F., 2005. History of Indo-Pacific coral reef systems since the last glaciation: Development patterns and controlling factors. Earth-Science Reviews 71, 1–75. https://doi.org/10.1016/j.earscirev.2005.01.002

Montaggioni, L.F., Braithwaite, C.J.R., 2009. Quaternary Coral Reef Systems: History, Development Processes and Controlling Factors. Elsevier.

Montaggioni, L.F., Cabioch, G., Thouveny, N., Frank, N., Sato, T., Sémah, A.-M., 2011. Revisiting the Quaternary development history of the western New Caledonian shelf system: from ramp to barrier reef. Marine Geology 280, 57–75. https://doi.org/10.1016/j.margeo.2010.12.001

Montaggioni, L.F., Borgomano, J., Fournier, F., Granjeon, D., 2015. Quaternary atoll development: new insights from the two-dimensional stratigraphic forward modelling of Mururoa Island (Central Pacific Ocean). Sedimentology 62, 466–500. https://doi.org/10.1111/sed.12175

Montaggioni, L.F., Martin-Garin, B., 2020. Quaternary development history of coral reefs from West Indian islands: A review. International Journal of Earth Sciences 109, 911–930. https://doi.org/10.1007/s00531-020-01839-3

Moustaka, M., Mohring, M.B., Holmes, T., Evans, R.D., Thomson, D., Nutt, C., Stoddart, J., Wilson, S.K., 2019. Cross-shelf heterogeneity of coral assemblages in Northwest Australia. Diversity 11, 15.

Müller, R.D., Zahirovic, S., Williams, S.E., Cannon, J., Seton, M., Bower, D.J., Tetley, M.G., Heine, C., Le Breton, E., Liu, S., Russell, S.H., 2019. A global plate model including lithospheric deformation along major rifts and orogens since the Triassic. Tectonics 38, 1884–1907.

Mylroie, J.E. and Carew, J.L., 1995. Karst development on carbonate islands. In: Budd, D.A., Saller, A.H. and Harris, P.M. (eds.) *Unconformities and porosity in carbonate strata*.

AAPG Memoir 63. Tulsa, OK: American Association of Petroleum Geologists, pp. 55–76.

Muhs, D.R. and Kyser, T.K., 1987. Stable isotope compositions of fossil mollusks from southern California: evidence for a cool last interglacial ocean. Geology, 15(2), pp.119-122.

Murray-Wallace, C.V., Woodroffe, C.D., 2014. Quaternary Sea-Level Changes: A Global Perspective. Cambridge University Press, Cambridge, UK.

Murphy, R.J., Webster, J.M., Nothdurft, L., Dechnik, B., McGregor, H.V., Patterson, M.A., Sanborn, K.L., Webb, G.E., Kearney, L.I., Rintoul, L., Erler, D.V., 2017. High-resolution hyperspectral imaging of diagenesis and clays in fossil coral reef material: a nondestructive tool for improving environmental and climate reconstructions. Geochemistry, Geophysics, Geosystems 18, 3209–3230.

Nettleton, W. D., Olson, C. G., & Wysocki, D. A., 2000. Paleosol classification: Problems and solutions. Catena (Giessen), 41(1), 61–92. https://doi.org/10.1016/S0341-8162(00)00109-0.

Nothdurft, L.D., Webb, G.E., 2009. Earliest diagenesis in scleractinian coral skeletons: Implications for palaeoclimate-sensitive geochemical archives. Facies 55, 161–201. https://doi.org/10.1007/s10347-008-0167-z

Nothdurft, L.D., Webb, G.E., Bostrom, T., Rintoul, L., 2007. Calcite-filled borings in the most recently deposited skeleton in live-collected Porites (Scleractinia): Implications for trace element archives. Geochimica et Cosmochimica Acta 71, 5423–5438. https://doi.org/10.1016/j.gca.2007.09.025

OBIS, 2020. Ocean Biodiversity Information System. Available at: https://obis.org/

Palei, R.R., Gupta, A.K., Sanyal, P., Jaiswal, M.K., 2024. Leeuwin Current dynamics in the SE Indian Ocean and implications for regional surface hydrography since the latest

Miocene: Results from ODP Site 763A. Global and Planetary Change 237, 104459. https://doi.org/10.1016/j.gloplacha.2024.104459

Pandey, V.K., Bhatt, V., Pandey, A.C., Das, I.M.L., 2007. Impact of Indonesian throughflow blockage on the Southern Indian Ocean. Current Science 93, 399–406.

Payri, C., N'Yeurt, A.D.R., Orempuller, J., 2000. Algae of French Polynesia. Au Vent des Îles, Tahiti.

Petrick, B., Martínez-García, A., Auer, G., Reuning, L., Auderset, A., Deik, H., Takayanagi, H., De Vleeschouwer, D., Iryu, Y., Haug, G.H., 2019. Glacial Indonesian Throughflow weakening across the Mid-Pleistocene Climatic Transition. Scientific Reports 9, 16995. https://doi.org/10.1038/s41598-019-53382-0

Petrick, B., Reuning, L., Auderset, A., Pfeiffer, M., Auer, G., Schwark, L., 2024. High sea surface temperatures were a prerequisite for the development and expansion of the Great Barrier Reef. Science Advances 10, eado2058.

Puotinen, M., Drost, E., Lowe, R., Depczynski, M., Radford, B., Heyward, A., Gilmour, J., 2020. Towards modelling the future risk of cyclone wave damage to the world's coral reefs. Global Change Biology 26, 4302–4315.

Quek, Z.B.R., Jain, S.S., Richards, Z.T., Arrigoni, R., Benzoni, F., Hoeksema, B.W., Carvajal, J.I., Wilson, N.G., Baird, A.H., Kitahara, M.V., Seiblitz, I.G., Vaga, C.F., Huang, D., 2023. A hybrid-capture approach to reconstruct the phylogeny of Scleractinia (Cnidaria: Hexacorallia). Molecular Phylogenetics and Evolution 186, 107867.

Railsback, L.B., 2006. Some fundamentals of mineralogy and geochemistry. On-line book, quoted from: www. gly. uga. edu/railsback, 387.

Rösler, A., Perfectti, F., Peña, V., Braga, J.C., 2016. Phylogenetic relationships of Corallinaceae (Corallinales, Rhodophyta): taxonomic implications for reef-building corallines. Journal of Phycology. https://doi.org/10.1111/jpy.12404

Rovere, A., Pico, T., Richards, F., O'Leary, M.J., Mitrovica, J.X., Goodwin, I.D., Austermann, J., Latychev, K., 2023. Influence of reef isostasy, dynamic topography, and glacial isostatic adjustment on sea-level records in Northeastern Australia. Communications Earth & Environment 4, 328.

Salas-Saavedra, M., Dechnik, B., Webb, G.E., Webster, J.M., Zhao, J.-X., Nothdurft, L.D., Clark, T.R., Graham, T., Duce, S., 2018. Holocene reef growth over irregular Pleistocene karst confirms major influence of hydrodynamic factors on Holocene reef development. Quaternary Science Reviews 180, 157–176.

Sanborn, K.L., Webster, J.M., Webb, G.E., Braga, J.C., Humblet, M., Nothdurft, L., Patterson, M.A., Dechnik, B., Warner, S., Graham, T., Murphy, R.J., Yokoyama, Y., Obrochta, S.P., Zhao, J., Salas-Saavedra, M., 2020. A new model of Holocene reef initiation and growth in response to sea-level rise on the Southern Great Barrier Reef. Sedimentary Geology 397, 105556. https://doi.org/10.1016/j.sedgeo.2019.105556

Sanborn, K.L., Webster, J.M., Erler, D., Webb, G.E., Salas-Saavedra, M., Yokoyama, Y., 2024. The impact of elevated nutrients on the Holocene evolution of the Great Barrier Reef. Quaternary Science Reviews 332, 108636. https://doi.org/10.1016/j.quascirev.2024.108636

Sandiford, M., 2007. The tilting continent: A new constraint on the dynamic topographic field from Australia. Earth and Planetary Science Letters 261, 152–163. https://doi.org/10.1016/j.epsl.2007.06.023

Saqab, M.M., Bourget, J., 2015. Controls on the distribution and growth of isolated carbonate build-ups in the Timor Sea (NW Australia) during the Quaternary. Marine and Petroleum Geology 62, 123–143. https://doi.org/10.1016/j.marpetgeo.2015.01.014

Saqab, M.M., Bourget, J., 2016. Seismic geomorphology and evolution of early–mid Miocene isolated carbonate build-ups in the Timor Sea, North West Shelf of Australia. Marine Geology 379, 224–245.

Schwarz, D., 2005. Neutron tomography of internal structures of vertebrate remains: A comparison with X-ray computed tomography. Palaeontologia Electronica 8, 1.

Scotese, C.R., Wright, N., 2018. PALEOMAP paleodigital elevation models (PaleoDEMS) for the Phanerozoic. PALEOMAP Project.

Searle, D.E., Flood, P.G., 1988. Halimeda bioherms of the Swain reefs—southern Great Barrier Reef. In: Proceedings of the 6th International Coral Reef Symposium, Vol. 3, pp. 139–144.

Siddall, M., Rohling, E.J., Thompson, W.G., Waelbroeck, C., 2008. Marine isotope stage 3 sea level fluctuations: Data synthesis and new outlook. Reviews of Geophysics 46, RG4003. https://doi.org/10.1029/2007RG000226

Skeats, E.W., 1918. The formation of dolomite and its bearing on the coral reef problem. American Journal of Science 46, 185–200.

Strasser, A., Strohmenger, C., 1997. Early diagenesis in Pleistocene coral reefs, southern Sinai, Egypt: response to tectonics, sea-level and climate. Sedimentology 44, 537–558.

Szilagyi, Z., Husdell, M., Chua, K., Behrens, B., Zeng, Y., Borghi, S., Clements, M. and Webb, M., 2023. Halo: Halimeda Bioherm origins, function, and fate in the Northern great barrier reef. Quaternary Australasia, 40(1), pp.12-16.

Tabor, N.J., Myers, T.S., Michel, L.A., 2017. Sedimentologist's guide for recognition, description, and classification of paleosols. In: Parker, W., Zeigler, K.E. (Eds.), Terrestrial Depositional Systems. Elsevier, pp. 165–208.

Taylor, K.G., Macquaker, J.H.S., 2011. Iron minerals in marine sediments record chemical environments. Elements 7, 113–118.

Thompson, W.G., Spiegelman, M.W., Goldstein, S.L., Speed, R.C., 2003. An open-system model for U-series age determinations of fossil corals. Earth and Planetary Science Letters 210, 365–381.

Toscano, M.A., Peltier, W.R., Drummond, R., 2011. ICE-5G and ICE-6G models of postglacial relative sea-level history applied to the Holocene coral reef record of northeastern St Croix, U.S.V.I.: investigating the influence of rotational feedback on GIA processes at tropical latitudes. Quaternary Science Reviews 30, 3032–3042. https://doi.org/10.1016/j.quascirev.2011.07.018

Twiggs, E.J., Collins, L.B., 2010. Development and demise of a fringing coral reef during Holocene environmental change, eastern Ningaloo Reef, Western Australia. Marine Geology 275, 20–36.

Van der Merwe, E., Maneveldt, G.W., 2016. A modern account of the South African non-geniculate Lithophylloideae (Corallinales, Corallinophycidae, Rhodophyta). South African Journal of Botany 103, 247–267.

Veron, J.J., 1986. Distribution of reef-building corals. Oceanus 29, 27–31.

Veron, J.E.N., Pichon, M., 1979. Scleractinia of Eastern Australia. Part III: Families Agariciidae, Siderastreidae, Fungiidae, Oculinidae, Merulinidae, Mussidae, Pectiniidae, Caryophylliidae, Dendrophylliidae. Australian Institute of Marine Science Monograph Series 4, 422 pp. https://doi.org/10.5962/bhl.title.60646

Veron, J.E.N., 2000. Reef evolution. Science 287, 811.

Veron, J.E.N., Stafford-Smith, M.G., Turak, E., DeVantier, L.M., 2016. Corals of the World, version 0.01. Available at: https://www.coralsoftheworld.org/

Waelbroeck, C., Labeyrie, L., Michel, E., Duplessy, J.C., McManus, J.F., Lambeck, K., Labracherie, M., 2002. Sea-level and deep water temperature changes derived from

benthic foraminifera isotopic records. Quaternary Science Reviews., 21 (1), 295–305. https://doi. org/10.1016/S0277-3791(01)00101-9.

Webb, G.E., Nothdurft, L.D., Kamber, B.S., Kloprogge, J.T., Zhao, J.-X., 2009. Rare earth element geochemistry of scleractinian coral skeleton during meteoric diagenesis: a sequence through neomorphism of aragonite to calcite. Sedimentology 56, 1433–1463.

Webb, G.E., Nothdurft, L.D., Zhao, J.-X., Opdyke, B., Price, G., Eberli, G., 2016. Significance of shallow core transects for reef models and sea-level curves, Heron Reef, Great Barrier Reef. Sedimentology 63, 1396–1424. https://doi.org/10.1111/sed.12266

Webb, G.E., 2024. Advances in understanding climate change on the Great Barrier Reef using coral-based proxies. Oceanographic Processes of Coral Reefs, pp.62-85.

Webb, G.E., 2025. Australia's two Great Barrier Reefs: What can ~360 million years of change teach us? Journal of Marine Science and Engineering 13, 1582. https://doi.org/10.3390/jmse13081582

Webster, J.M., Davies, P.J., 2003. Coral variation in two deep drill cores: Significance for the Pleistocene development of the Great Barrier Reef. Sedimentary Geology 159, 61–80. https://doi.org/10.1016/S0037-0738(03)00095-2

Webster, J.M., Clague, D.A., Riker-Coleman, K., Gallup, C., Braga, J.C., Potts, D., Paull, C.K., 2004. Drowning of the −150 m reef off Hawaii: A casualty of global meltwater pulse 1A? Geology 32, 249–252. https://doi.org/10.1130/G20170.1

Webster, J.M., Clague, D.A., Wallace, L.M., Braga, J.C., 2007. Numerical modeling of the growth and drowning of Hawaiian coral reefs during the last two glacial cycles (0–250 kyr). Geochemistry, Geophysics, Geosystems 8, Q03001.

Webster, J.M., Braga, J.C., Clague, D.A., Gallup, C., Hein, J.R., Potts, D.C., Wallace, L.M., 2009. Coral reef evolution on rapidly subsiding margins. Global and Planetary Change 66, 129–148. https://doi.org/10.1016/j.gloplacha.2008.07.010

Webster, J.M., Dechnik, B., Sanborn, K., Yokoyama, Y., Braga, J.C., Renema, W., Humblet, M., Beaman, R.J., Nothdurft, L.D., Webb, G.E., and Zhao, J.X., 2022, Coral reef development and sea-level changes over the past 50,000 years: New evidence from the North-West Shelf of Australia: in: Camoin, G.F., Hallmann, N. (Eds.), Coral Reefs and Sea-Level Change: Quaternary Records and Modelling, special Publication 49. International Association of Sedimentologists, pp. 215-273.

Webster, J.M., Yokoyama, Y., Humblet, M., Braga, J.C., Esat, T., Fallon, S., Bard, E., 2025. Constraints on sea-level rise during meltwater pulse 1B from the Great Barrier Reef. Nature Communications 16, 4698. https://doi.org/10.1038/s41467-025-59858-0

Weinstein, D.K., Maher, R.L., Correa, A.M., 2019. Bioerosion. In: Loya, Y., Puglise, K.A., Bridge, T.C.L. (Eds.), Mesophotic Coral Ecosystems. Springer, Cham, pp. 829–847.

Williams, J.N., Bevitt, J.J., Toy, V.G., 2017. A comparison of the use of X-ray and neutron tomographic core scanning techniques for drilling projects: Insights from scanning core recovered during the Alpine Fault Deep Fault Drilling Project. Scientific Drilling 22, 35–42. https://doi.org/10.5194/sd-22-35-2017

Williams, C., Paumard, V., Webster, J.M., Leonard, J., Salles, T., O'Leary, M., Lang, S., 2023. Environmental controls on the resilience of Scott Reef since the Miocene (North West Shelf, Australia): Insights from 3D seismic data. Marine and Petroleum Geology 151, 106188. https://doi.org/10.1016/j.marpetgeo.2023.106188

Williams, C., Webster, J.M., Bevitt, J.J., Webb, G.E., Nothdurft, L.D., Paumard, V., McGregor, H., Murphy, R.J., 2025. Neutron computed tomography: A novel high-resolution, non-destructive method for screening fossil coral for diagenetic alteration for geochronologic and paleoclimatic reconstructions. Geochemistry, Geophysics, Geosystems 26, e2025GC012439. https://doi.org/10.1029/2025GC012439

Williams, C., Webster, J. M., Salles, T., Paumard, V., Grimaldi, C., & Lejri, M., 2026. Carbonate platform evolution in response to the Mid - Pleistocene climate transition on the North-West Shelf of Australia: Insights from forward stratigraphic modelling. Marine Geology, 493. https://doi.org/10.1016/j.margeo.2026.107716.

Wilson, B., 2013. The Biogeography of the Australian North West Shelf: Environmental Change and Life's Response. Elsevier. https://doi.org/10.1016/C2012-0-00618-7

Woodroffe, C.D., Webster, J.M., 2014. Coral reefs and sea-level change. Marine Geology 352, 248–267. https://doi.org/10.1016/j.margeo.2013.12.006

Yagioka, N., Nakada, C., Fujita, K., Kan, H., Yokoyama, Y. and Webster, J.M., 2019. Depositional environments beneath the shelf-edge slopes of the Great Barrier Reef, inferred from foraminiferal assemblages: IODP Expedition 325. Palaeogeography, Palaeoclimatology, Palaeoecology, 514, pp.386-397.

Yamamoto, K., Iryu, Y., Sato, T., Chiyonobu, S., Sagae, K., Abe, E., 2006. Responses of coral reefs to increased amplitude of sea-level changes at the Mid-Pleistocene Climate Transition. Palaeogeography, Palaeoclimatology, Palaeoecology 241, 160–175.

Yokoyama, Y., Esat, T.M., Lambeck, K., 2001. Coupled climate and sea-level changes deduced from Huon Peninsula coral terraces of the last ice age. Earth and Planetary Science Letters 193, 579–587. https://doi.org/10.1016/S0012-821X(01)00515-5

Yokoyama, Y., Webster, J.M., Cotterill, C., Braga, J.C., Jovane, L., Mills, H., Suzuki, A., 2011. IODP Expedition 325: Great Barrier Reefs reveal past sea-level, climate and environmental changes since the last ice age. Scientific Drilling 12, 32–45. https://doi.org/10.2204/iodp.sd.12.04.2011

Yokoyama, Y., Esat, T.M., Thompson, W.G., Thomas, A.L., Webster, J.M., Miyairi, Y., Kan, H., 2018. Rapid glaciation and a two-step sea level plunge into the Last Glacial Maximum. Nature 559, 603–607. https://doi.org/10.1038/s41586-018-0335-4

Yu, K.-F., Zhao, J.-X., Shi, Q., Chen, T.-G., Wang, P.-X., Collerson, K.D., Liu, T.-S., 2006. U-series dating of dead Porites corals in the South China Sea: evidence for episodic coral mortality over the past two centuries. Quaternary Geochronology 1, 129–141.

Zhao, J.-X., Hu, K., Collerson, K.D., Xu, H.-K., 2001. Thermal ionization mass spectrometry U-series dating of a hominid site near Nanjing, China. Geology 29, 27–30.

Zhao, J.X., Yu, K.F. and Feng, Y.X., 2009. High-precision 238U–234U–230Th disequilibrium dating of the recent past: a review. Quaternary Geochronology, 4(5), pp.423-433.

Acknowledgments

Core data were provided with permission from the Perth Core Library and the Geocoastal Research Group, University of Sydney. We thank the reviewers for their constructive guidance on the manuscript. Additional support and workstation access were kindly provided by the School of Earth Sciences at The University of Western Australia. This paper reviews coral reef response since the Mid-Pleistocene Climate Transition on the Northwest Shelf, Australia, using fossil coral reef cores. It incorporates material that is © Australian Institute of Marine Science and © Woodside Energy Group Ltd. Neither organisation necessarily endorses any modifications made to that material. We thank Alexander Lowe and Richard Murphy for producing hyperspectral maps following Murphy et al. (2017), Corescan for generating additional hyperspectral datasets, the National Virtual Core Library (NVCL) for funding the hyperspectral acquisition, and CSIRO for hosting the dataset. We are also grateful to Woodside Energy Group Ltd for permission to publish previously unpublished U-series data (Collins et al., 2011) and acknowledge the original authors—Lindsey Collins, Viviane Testa, Jian-xin Zhao and Dingchuang Qu. The authors acknowledge the facilities and the scientific and technical support of Sydney Analytical at The University of

Sydney. We also thank Camille Grimaldi and Nicole Ryan (AIMS) for providing photographs of modern Scott Reef corals, and the University of Bremen for processing the thin sections.

Declaration of generative AI and AI-assisted technologies in the manuscript preparation process

During the preparation of this work the author(s) used CoPilot for the purposes of text enhancement. The use of this generative AI tool includes spelling corrections, minor sentence restructuring, and clarity enhancement. I confirm that where text was modified by generative AI, the content was reviewed for possible errors, inaccuracies, and bias. After using this tool/service, the author(s) reviewed and edited the content as needed and take(s) full responsibility for the content of the published article.

DATA AVAILABILITY

Data used in this study are available online. The hyperspectral data can be found on Coreshed at https://app.coreshed.com/cswebapp/login? with username: carra.williams and password: CompareRepeatedDoor. The supporting core datasets are publicly available upon request from the Perth Core Library. The core interpretations used in this manuscript can be accessed via Supplement 1.

Appendix

XRD detailed methodology

Each powder sample was loaded into the (0.2 or 0.5) mm deep cavity of a glass sample holder. X-ray powder diffraction data from the spinning samples were collected in Bragg-Brentano geometry on a Rigaku Smartlab SE powder diffractometer equipped with a Cu Kα X-ray source ($K\alpha_1$ = 1.540598 Å, $K\alpha_2$ = 1.544426 Å) operating at 40 kV and 40 mA, a 10 mm length-limiting

slit and 0.5° divergence slits. Diffraction data were collected using an XSPA-400 ER two-dimensional detector scanning continuously at 5 °/min over the 2θ angle range 5-90°. (XRD methods https://canvas.sydney.edu.au/courses/29144/pages/rigaku-smartlab-se?wrap=1)

Data curation

Cores NR SE HDD3-JA, SR SE BH6-J and Hook 3P are curated by Perth core store. Access was granted to view, log and sample for XRD, U/Th and thin section analysis. Core SR NE HDD1-J is curated by Fugro and owned by Woodside. Access was granted by Woodside to view, log and sample for XRD, U/Th and thin section analysis. High resolution hyperspectral reflectance spectra data were acquired through a research collaboration with NVCL (National Virtual Core Library), Corescan and CSIRO for Hook 1/3P and through the University of Sydney for SRSEBH6J and NRSEHDD3JA.

Supplemental Material

Supplements 1–10 correspond to Appendices I–Q of this thesis. Please contact the corresponding author with any questions.

[1] Supplement 1 (Appendix I) – Core Interpretation

[2] Supplement 2 (Appendix J) – Uranium-Series Data (Collins et al., 2009)

[3] Supplement 3 (Appendix K) – Uranium-Series Data (This study)

[4] Supplement 4 (Appendix L) – Raw XRD Data (This study)

[5] Supplement 5 (Appendix M) – Raw Neutron Computed Tomography Data (This study)

[6] Supplement 6 (Appendix N) – Hyperspectral Imaging Data (This study)

[7] Supplement 7 (Appendix O) – Quantitative Hyperspectral Data (This study)

[8] Supplement 8 (Appendix P) – Scott Reef Thin Sections (Collins et al., 2009)

[9] Supplement 9 (Appendix Q) – Scott Reef Thin Sections (This study)

[9] Supplement 10 (Appendix R) – Scott Reef SEM data (This study)

CHAPTER 6

General discussion and synthesis

"Science is mind applied to nature" – Alexander Von Humboldt

6.1 General Discussion and Synthesis

This chapter synthesises findings from all previous chapters, integrating interpretations of Scott Reef's geologic history to address the overarching research objective: "To advance understanding of the environmental and eustatic controls on carbonate platform evolution and coral reef development through Neogene-Quaternary climate transitions, using Scott Reef as a case study." A general discussion is presented to answer the research questions outlined in the introduction within the context of existing literature, drawing connections and correlations across the four core research themes outlined in the published or submitted scientific papers of chapters 2, 3, 4 and 5. The broader scientific implications are examined, limitations of this study are considered and recommendations for future research are provided.

6.1.1 Research question 1: What is the role and nature of eustacy and associated environmental perturbations in shaping carbonate platform development and coral reef evolution at Scott Reef during major Neogene-Quaternary climate transitions?

Chapter 2 and Chapter 4 demonstrate the usefulness of integrating seismic stratigraphic and geomorphologic interpretations with FSM to resolve platform-scale evolution and characterise the eustatic and environmental controls operating on isolated carbonate factories. Addressing

the first research question, this study demonstrates that the complex interplay between eustatic and environmental factors, driven by global climatic oscillations from the Miocene to present, can be resolved at the third-order through detailed analyses of seismic and well log data.

6.1.1.1 Miocene (18–5 Ma): Initiation of Carbonate Build-ups under Eustatic Control

During the early to middle Miocene, sea-level fluctuations associated with the Mid-Miocene Climatic Optimum (MMCO; 17–13.8 Ma) determined the initial transition from ramp-style sedimentation to the development of isolated carbonate build-ups (ICBs) on antecedent highs (Figure 9 of Chapter 2) (Rankey, 2020). Sea-level rise provided accommodation that enabled the nucleation of small reef structures, visible as prograding barrier reef systems in seismic units U1–U3 (see seismic movie in Appendix C). Lowstands during this time produced karstification and the development of exposure surfaces, particularly during the Serravallian, as recorded by collapse features and karst valleys (Figure 13 of Chapter 2), which are observed elsewhere along the NWS during this period (Rosleff-Soerensen et al., 2016). These transitions reflect alternating keep-up and catch-up growth modes directly paced by eustatic sea-level changes. These findings support the models of reef evolution along the NWS by Rankey (2020) and Riera et al. (2022), who propose that repeated eustatically-driven exposure of the NWS was a major factor in the origin of the Western Australian coral reef province.

6.1.1.2 Pliocene (5–2.5 Ma): Expansion of Isolated Carbonate Buildups

Following the Miocene - Pliocene boundary (ca. 5 Ma), a major sea-level rise during the Pliocene Climate Optimum (ca. 4.3 Ma; see Fig. 6.1) coincided with the widespread demise of ICB's across the Browse Basin (Van Tuyl et al., 2019; Belde et al., 2015), yet the characterisation of the Scott Reef platform evolution demonstrates that the precursor Scott Reef ICB's expanded and proliferated during this interval (Figure 9 of Chapter 2). This warm, highstand period also coincided with the onset of the Leeuwin current along the NWS. During carbonate factory phase 3, relatively stable, elevated sea-levels facilitated vertical aggradation and lateral progradation of the Scott reef precursor reefs. Although fluctuating monsoonal

conditions during the late Pliocene increased siliciclastic influx from the continent (Gallagher et al., 2014; Petrick et al., 2019; He et al., 2021), Scott Reef remained largely protected from current-driven siliciclastic sediment drifts (Figure 6.1) due to the inter-reef channel bypass, and their position on topographic highs above the Scott Reef fault trend. These unique local environmental settings allowed carbonate production to continue uninterrupted, while neighbouring platforms in lower-lying settings experienced drowning elsewhere along the NWS (Belde et al., 2017) and globally, such as in the Maldives (Alonso-Garcia et al., 2023) or the South China Sea (Chen et al., 2024). Eustasy and the unique environmental setting of the Scott Reef platforms were thus equally important factors in their resilience.

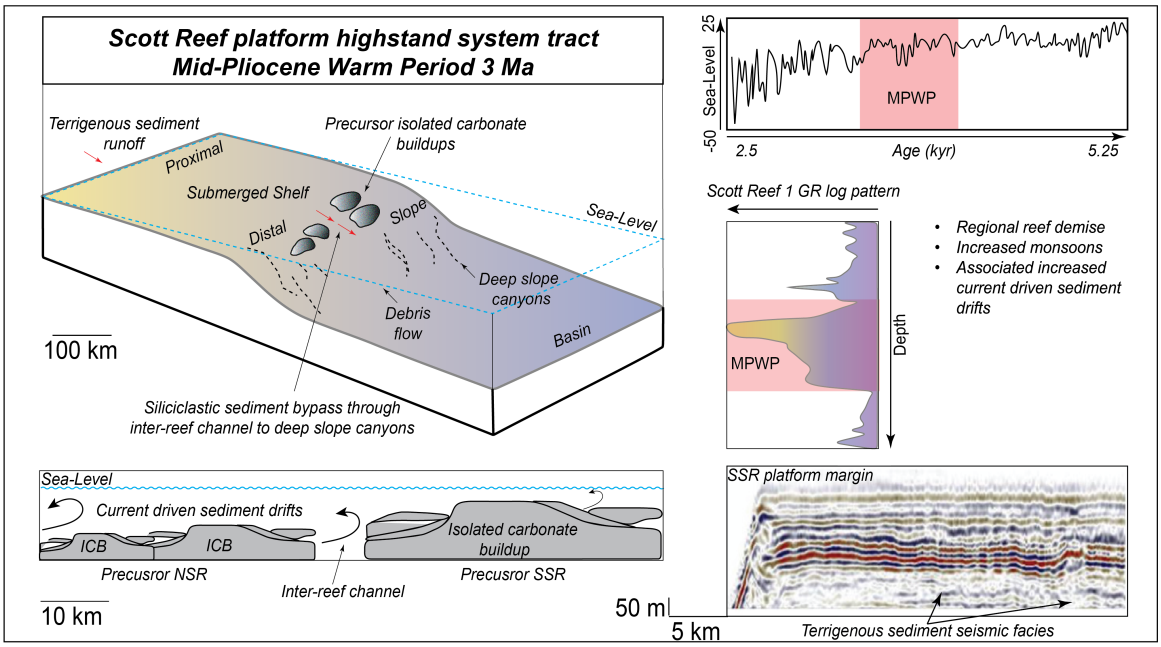


FIGURE 6.1: Conceptual sketch of Scott Reef during the MPWP from ca. 2.5 – 5.25 Ma, guided by observational data, including seismic facies and well log data.

6.1.1.3 Pleistocene (2.5 Ma–0 Ma): Increased Eustatic Sea-Level Variability and Platform Resilience

The onset of glacial–interglacial cycles after ca. 2.5 Ma, and particularly the Mid-Pleistocene Transition (MPT; ca. 1.2 - 0.7 Ma), fundamentally altered the style of platform development at

Scott Reef, which is consistent with the disruption to long-term patterns of carbonate factories around the world (Table 1 and Figure 2 of Chapter 5). Eustatic sea-level amplitude increased at around 1.2 Ma from ca. 60 - 70 m to ca. 120 m, and glacial cycles lengthened to ca. 100 kyr (Dwyer et al., 1995; Herbert, 2023). This eustatic transition correlates with sequence boundary H11 that also coincided with a decrease in siliciclastic influx observed on gamma ray well logs (Chapter 2 Figure 17) and supported by regional studies on the NWS that show comparable ages of reef initiation, for example, at Big Bank Shoals (Saqab and Bourget, 2015). FSM outputs in Chapter 4 elaborate on this third-fourth-order interpretation and indicate that this change resulted in an increase in sequence thickness and a transition from progradational/aggradational sequences to dominantly aggradational stacking with a bucket-shaped morphology on the South Reef and a more flat-topped 'filled' lagoon morphology on the North Reef (Chapter 4 Figure 14). The thickest reef succession (ca. 80 m) was produced during MIS 11 and correlates to periods of highstand stability and optimum climatic conditions (Husson et al., 2018). The model results broadly reproduce the seismic stratigraphic framework as well as providing a higher-resolution synthetic sequence stratigraphic model that exceeds the interpretability of the seismic data, which is compromised by data gaps, noise and quality. A GPM diagenetic model that characterised some of the key climatic changes associated with the MPT was also produced. For example, the first long duration lowstand of the MPT (MIS 12), correlates with the karst depression and subaerial exposure features observed on seismic data (Figure 7 and 8 of Chapter 2) and coincides with an increase in rainfall, due to monsoonal intensification along the NWS after ca. 0.3 Ma (Gallagher et al., 2014; Petrick et al., 2019). The Pleistocene development of Scott Reef was briefly described by Collins et al. (2009), Collins and Testa (2010) and Collins et al. (2011) based on shallow 2D seismic profiles and characterised by a conceptual model where sea level lowstand hiatuses separate distinct vertically stacked reef growth episodes during marine isotope stage highstands. However, their model did not resolve platform wide variations in reef growth sequences or provide details of coralgal assemblages and succession within each reef unit. Chapter 5 resolves higher-resolution exposure events not captured in the initial report. These interpretations were facilitated by the integration of new technological methods, including hyperspectral imaging, which revealed Al-rich and Fe-rich sediment intervals that

clearly demark periods of exposure above sea-level (Chapter 5, Figs. 7-9). The schematic of the LGM lowstand in Fig. 6.2 depicts platform exposure above sea level, in agreement with gamma-ray, thin-section, and seismic data that collectively indicate repeated emersion events and associated Fe and Al-rich sediment deposition.

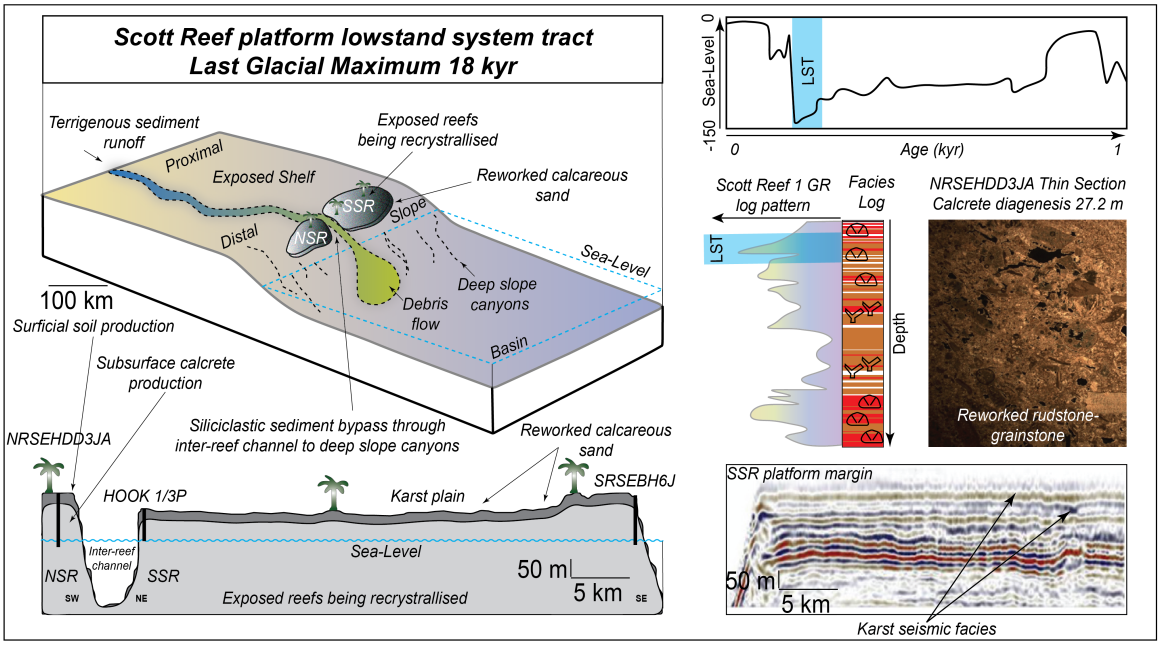


FIGURE 6.2: Conceptual sketch of Scott Reef during the LGM ca. 18 kyr, guided by observational data, including seismic facies, well log data, thin section data and lithologic interpretation.The thin section illustrates a high-energy depositional environment (rudstone–grainstone) that was subsequently overprinted by subaerial exposure diagenesis during relative sea-level lowstand. The Gamma Ray (GR) log response reflects variations in minor terrigenous input, sediment reworking, and karst-related infill during lowstand conditions, relative to highstand intervals which record elevated GR values due to increased terrigenous influx. This variability is interpreted as a conceptual proxy for reef growth phases and associated shifts in depositional and exposure conditions.

6.1.1.4 Holocene (11.7 kyr to present): Catch-up Growth during Rapid Sea-Level Rise

The a priori chronostratigraphic model defined in Chapter 2 is insufficient to precisely document the Holocene reef growth within carbonate factory phase 4. It may be apparent

from seismic that it is a thick vertically aggrading sequence (Chapter 2, Fig. 6), but it is not quantified. Chapter 4 utilises forward stratigraphic modelling to create new synthetic data for improving seismic interpretation and prediction. The FSM illustrates that deglacial sea-level rise during the Holocene produced a thick aggradational sequence (ca. 23 m for the North Reef, 40 m for the South Reef: Chapter 5, Fig. 5), which is supported by the literature (Collins et al., 2009). However, the sequences are dominated by intermediate to deeper reef assemblages and succeeded by a thin 1 m sequence of shallow reef assemblages. The higher resolution core analyses presented in Chapter 5 reveal greater complexity - a distinct shallowing upwards sequence along the South Reef SE margin, localised drowning of the NE margin, and a more complex deepening then shallowing to present sequence on the North Reef. Although Scott Reef largely kept pace with sea-level rise at the platform scale (keep-up mode), ecological assemblages showed a catch-up behaviour, lagging behind during the rapid early Holocene transgression (Collins et al., 2011; Camoin and Webster, 2015). While these results from different scales of analyses are broadly consistent, it demonstrates the usefulness of integrating datasets across different spatial and temporal resolutions. The combined application of seismic sequence stratigraphy, forward stratigraphic modelling and high resolution core analysis captured finer-scale details at higher spatio-temporal resolutions necessary to understand the complex and dynamic behaviour of the whole system.

6.1.2 Research question 2: How can neutron computed tomography and hyperspectral imaging be used to improve paleoclimatic and geochronologic reconstructions of coral reefs?

Chapter 2 introduces neutron computed tomography (NCT) to the coral reef science community as a novel high-resolution, non-destructive method for diagenetic screening of fossil corals for geochronologic and paleoclimatic reconstructions. NCT has been previously applied in coral reef science to investigate seasonal density variations in fossil skeletons (Ivankina et al., 2020), but its application to detect diagenetic changes in fossil corals remains unexplored. Many coral-based reconstructions are limited by the effects of post-depositional

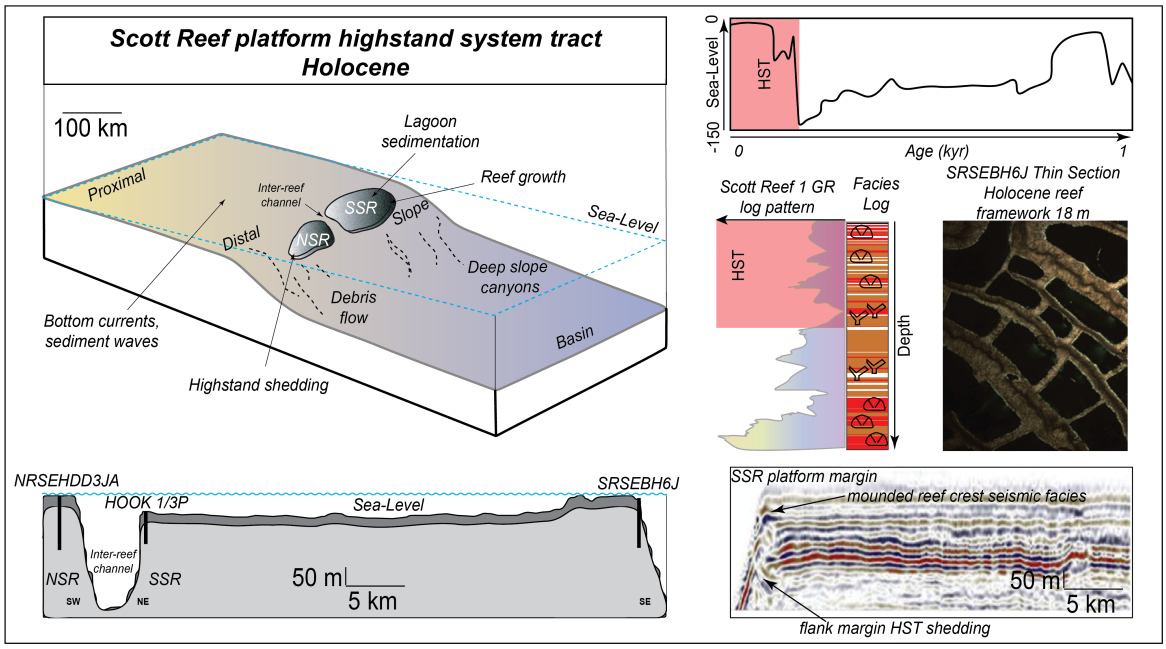


FIGURE 6.3: Conceptual model of Scott Reef during the Holocene highstand systems tract (HST), integrating seismic facies, GR well log data, and thin section data. The platform records overall aggradational growth during rapid post-glacial sea-level rise, with reef-margin development, lagoonal sedimentation, and highstand shedding to the basin. Spatial variability between the North and South Reefs are evident due to differential subsidence and platform morphologies.

alteration thus requiring extensive, usually destructive screening methods for the identification of primary aragonite, which preserves the isotopic and elemental tracers used in the reconstructions. Traditional methods such as XRD, SEM, and hyperspectral imaging are limited by their 2-D analyses or destructive sampling, and struggle to resolve mineral heterogeneity at depth or in 3-D (McGregor and Gagan, 2003; Murphy et al., 2017; Webster et al., 2022). In our study, it was demonstrated that NCT overcomes these limitations by mapping hydrogen content in 3-D, providing a reliable indicator for identifying regions of well-preserved skeletal aragonite, since aragonite typically retains more water organic-matter than calcite (Bevitt, 2018; Ivankina et al., 2020). The study also generated a new dataset of NCT scans of fossil corals that are publicly available for further research, and which were incorporated into the core analysis in Chapter 5. An unexpected finding of this study was the identification of previously undetected aragonitic zones within altered fossil coral frameworks

(Chapter 3, Fig. 7d). The *Acropora humilis* sample from Ribbon Reef 5 was previously deemed too diagenetically altered for reliable U-Th dating (Braithwaite et al., 2004). This discovery demonstrates the usefulness and potential of NCT to improve age control and refine paleochronologic and paleoclimatic reconstructions in previously investigated Quaternary reef cores. Chapter 3 provided recommendations to the coral reef science community for applying NCT in fossil coral screening. Building upon this foundation, Chapter 5 extends the application of NCT to the Scott Reef cores, generating a new high-resolution dataset and integrating these scans with hyperspectral, XRD, SEM, and petrographic analyses to produce a robust paleochronologic and paleodepositional reconstruction of the North and South Scott Reefs. The application of hyperspectral imaging of the Scott Reef cores resulted in identification of previously undescribed paleosols (Chapter 5, Table 7) and assisted in the sedimentological descriptions of the boreholes by highlighting key spectral features otherwise unidentified in hand specimen. For example, hyperspectral false colour imagery (Chapter 5, Figure 3) highlighted regions of coral framework (purple) that were difficult to distinguish from detrital components. This multi-proxy approach builds upon the methods of recent studies (Webster et al., 2022) and continues to develop this new investigative framework for fossil reef core studies.

6.1.3 Research question 3: Can we reconstruct the paleodepositional evolution and chronostratigraphic framework of Scott Reef by synthesising all available legacy data with new sedimentological analyses using innovative screening and dating techniques?

In Chapter 5, the Quaternary evolution of the Scott Reef carbonate platform was reconstrcted using detailed sedimentological, ecological, and chronological analyses of three long geotechnical cores from North and South Scott Reef. A new high-resolution hyperspectral dataset was produced that is hosted online by CSIRO (see Appendix N) and available for the public from the Perth Core Library, as well as NCT scans of select samples of the Scott Reef cores (see Appendix D). New populations of the Scott Reef cores were sampled as part of a stringent diagenetic screening process that resulted in the generation of new thin sections, SEM

images, XRD data (see Appendix L) and U-series ages (see Appendix K) that can be used in ongoing research in this area. With this rich dataset, it was possible to apply new methods and techniques to the analyses of the Scott Reef cores. The integration of hyperspectral mineralogical mapping, NCT, SEM, XRD, and petrography provided a robust framework for identifying sedimentary packages, coralgal assemblages, paleodepositional environments, and diagenetic histories. Using this multi-proxy approach, a revised chronological model constrained by new closed system and Thompson-corrected open system U-Th ages produced the first high-resolution reconstruction of reef growth cycles from MIS 15-1 in the region. Seven distinct sedimentary packages were resolved on the Southeast margin of North Scott Reef (MIS 15 to present), seven on the Southeast South Scott Reef margin (MIS 11-1), and four on the leeward South Scott Reef margin (MIS 7-1). Each reef growth unit is bounded by paleosols, representing alternating phases of reef accretion and subaerial exposure driven by glacio-eustatic sea-level oscillations. Three coralline algal assemblages and four coral assemblages corresponding to shallow (< 10 m), intermediate (< 15 m), and deep (> 20 m) reef environments were identified. The South Reef was shown to transition from deep, low-energy slope settings to shallow reef crest/upper reef slope environments during MIS 7. This coincides with changes in the orbital-scale sea-level reconstructions from MIS 9 to MIS 7, which differ in amplitude, duration, and pacing and likely had an impact on regional oceanography and climate. Specifically, MIS 7 (sedimentary package 3 in the North Reef and sedimentary package 3 and 4 in the South Reef) is characterised by complex saw-tooth shaped highstands composed of several sub-stages, with higher-frequency variability and lower overall amplitude. Two shallowing upwards successions within sedimentary package 3 and 4 on the South Reef, along with the complexity of pedogenic features is interpreted to reflect these oscillations and implies climate was modulated by increased instability. The FSM model in Chapter 4 more closely matches the North Reef, in which shallow reef communities developed from MIS 15. The extended MPT model simulates shallow reef during every highstand since model initiation at 1.2 Ma. This apparent contradiction with the findings from the South Reef core analysis could be a result of processes not captured in the model, such as tidal dynamics, wind and storm-driven currents, sea surface temperature variability and water pH. Alternatively, as indicated by evidence of shallow reef detrital material at the base

of both cores, the location of the boreholes may not have sampled the reef crest during each highstand. Consequently, the spatial resolution of the model was likely insufficient to resolve the lateral facies heterogeneity at the precise borehole locations. Addressing this limitation would require higher-resolution 2-D simulations capable of capturing small-scale and subtle reef margin progradation and backstepping while maintaining reasonable computational time. The research presented in Chapter 5 demonstrates the importance of re-evaluating legacy fossil reef datasets by integrating new analytical methods with the re-interpretation of three long boreholes (< 200 m), producing a high-resolution lithologic and chronostratigraphic framework that both corroborates and builds upon existing interpretations and theories (Collins et al., 2009).

6.1.4 Research question 4: What new insights into the main processes controlling reef and carbonate platform evolution emerge through the integration of observational data and synthetic reef growth models?

Synthesising quantitative forward stratigraphic modelling with fossil reef core observations provided a robust lithologic and chronostratigraphic framework for reconstructing the evolution of Scott Reef through successive glacial-interglacial cycles, and for understanding why the North and South platforms diverged.

In Chapter 4, FSM was applied to simulate the spatio-temporal evolution of Scott Reef from the mid to late Quaternary (1.2 Ma to present). First, FSM predicted a phase of reef growth at Hook 3P during MIS 3 - an interstadial characterised by low-amplitude, sea-level fluctuations and limited evidence along the NWS (Webster et al., 2022), and one that had not previously been conceptualized at Scott Reef. Model results indicate that this growth phase was facilitated by higher subsidence rates on the South Reef and deeper paleowater depths along the leeward margin, which combined, provided accommodation during lower sea-levels for reef backstepping. However, U-Th dating undertaken in Chapter 5, failed to yield reliable chronologies for the Pleistocene intervals of the Hook 3P core, despite rigorous diagenetic

screening. This is interpreted to reflect open-system behaviour associated with microbialite development, which is known to efficiently scavenge thorium and Fe-rich detrital material. These limitations highlight the need for alternative or complementary geochronological approaches in future work to independently test the synthetic MIS 3 reef-growth phase.

Second, FSM provided insights into the Holocene demise of the leeward margin, predicting a reduction in carbonate production driven by the inability of the reef to keep pace with rapid sea-level rise and to compete with taxa more tolerant of turbid, nutrient-rich conditions. These conditions are observed today and are hypothesised to have intensified following enhanced monsoonal activity after ca. 0.3 Ma. The occurrence of loose lagoonal sands observed in both core and bathymetric datasets (Chapter 5) supports this modelled outcome, demonstrating the value of quantitatively testing conceptual hypotheses against observational data.

Third, FSM proved particularly valuable in areas affected by data gaps. Seismic acquisition was unavailable across the shallow reef crest of South Scott Reef (SSR), and borehole coverage was spatially limited and incomplete. In these regions, FSM generated coherent and geologically realistic reconstructions of spatio-temporal facies distributions and platform architecture. This ability to synthetically bridge data gaps is especially important in reefal systems, where seismic imaging is often restricted by protected status (e.g., the Great Barrier Reef Marine Park) or technical limitations, and where dense drilling transects are logistically and financially impractical. FSM therefore provides a realistic means of interpreting reef evolution where observational data are sparse and can be used to guide future drilling strategies.

Fourth, while a sequence stratigraphic framework could be established from the 3-D seismic data presented in Chapter 2, FSM was essential for resolving the timing and mechanisms underlying changes in platform morphology. For example, the transition from a filled platform to an “empty-bucket” morphology coincided with the exceptionally prolonged MIS 11 highstand. Similarly, FSM results suggest that the major karst depression observed on seismic data (Fig. 12 of Chapter 4) developed during the MIS 12 lowstand. These temporal correlations link observed geomorphological features with known oceanographic and environmental transitions on the NWS, supporting the interpretation that these changes represent a response to the MPT.

This interpretation is consistent with global sedimentation shifts (Table 1 of Chapter 4) and regional changes documented along the NWS (Saqab and Bourget, 2016). Further support is provided by the occurrence of dolomite at 189 m depth in the North Scott Reef borehole, which coincides with both the seismically interpreted karst depression and the simulated MIS 12 exposure phase (Fig. 12C of Chapter 2).

Finally, iterative model calibration and sensitivity testing substantially improved geological understanding of the Scott Reef platform and provided quantitative validation for previous estimates of subsidence rates in the Browse Basin (Collins and Testa, 2010) and the new subsidence rate for the South Reef (0.37 mm/yr) determined from coral age data presented in Chapter 5. Systematic adjustment of input parameters enabled identification of key sensitivities and thresholds within the carbonate factory, fostering an intuitive understanding of reef system behaviour under varying environmental and eustatic conditions. Although FSM necessarily simplifies complex physical and ecological processes—many of which are explored in greater detail through core-based observations in Chapter 5—the integration of FSM with multi-proxy observational data offers a robust and transferable framework for investigating carbonate platform evolution in reef systems worldwide.

6.1.5 Research question 5: Are the observed differences in reef growth models on the GBR due to eustacy and environmental variances?

In Chapter 5, comparisons were made with the Ribbon Reef 5 borehole in the GBR, due to their similar latitudes and position on the shelf-edge to explore how regional oceanographic conditions and tectonic regimes determined sedimentation and coralgal assemblage communities over time. The 210 m RR5 borehole recorded eight reef growth sequences spanning ca. 700 kyr to present (MIS 17 – 1), whereas the 200 m borehole on the North Scott Reef platform recorded an age of 578 kyr at 171 m and 392 kyr at 190 m in the South Reef borehole. This implies that Scott Reef experienced higher long-term subsidence and consequent preservation of thicker but younger sedimentary packages. This is supported by subsidence rates reported for both reefs, estimated at ca. 0. 45 mm/yr for South Scott Reef (Collins et al., 2011) and 0.37 mm/yr from new coral age data presented in Chapter 5, and 0.1 mm/yr for RR5

(Dutton et al., 2023; Rovere et al., 2023). The lower and middle RR5 sections (Units U1–U4; minimum age 564 kyr) are dominated by grainstone–packstone facies and rhodolith-rich deposits that accumulated in a mesophotic, open-shelf setting prior to the initiation of reef framework development at 137 m depth. In contrast, the basal succession at Scott Reef comprises floatstones and rudstones deposited in a deeper fore-reef slope environment. This contrast indicates fundamentally different paleoenvironmental conditions and evolutionary trajectories for the two carbonate platforms. In RR5 a framework dominated interval in reef 2 (15–25 m ca. 125 kyr; MIS 5) is particularly distinctive due to the *Halimeda*-rich grainstone package. A similar lithology is observed in the drowned leeward margin of South Scott Reef at ca. 20 m (ca. MIS 3/5?). The occurrence of a *Halimeda*-dominated grainstone facies on the Northeast and Northwest Shelf of Australia during the Last Interglacial suggests a shift towards a green-algal carbonate factory under comparable climatic perturbations. This transition likely reflects suppression of coral growth due to reduced light availability, enhanced nutrient upwelling, and increased hydrodynamic or turbidity variability.

Despite these contrasts, both reef systems show resilient coralgal communities that re-established after subaerial exposure, demonstrating long-term ecological and environmental stability through multiple glacial-interglacial cycles. Thus, while eustasy acted as the primary control on reef growth at both sites, environmental variances, specifically differences in subsidence rates, terrigenous sediment supply, and shelf-edge morphology, modulated the expression of reef growth through time. These findings illustrate that although broad evolutionary patterns are consistent, different reef growth models emerge due to local environmental controls interacting with global sea-level forcing. This reinforces the need to consider both global and local processes when evaluating coral reef and carbonate platform systems.

6.2 Recommendations for future research

Each chapter in this study contributes to a growing body of knowledge on carbonate platform evolution and coral reef development in response to eustatic and environmental change, and raises a number of interesting scientific questions, for which ongoing research themes are

recommended. The strategies proposed below would substantially improve our understanding of Quaternary reef evolution and carbonate platform development in response to environmental and sea-level forcing along the NWS, by increasing the spatial and temporal resolution of data analyses.

6.2.1 Expanding and Refining Comparative Reef Datasets

Reef accretion patterns have been well documented at high spatial resolution from drilling transects in locations such as Tahiti (Camoin et al., 2012) and the GBR (Webster et al., 2018), including Heron Reef (Webb et al., 2016; Salas-Saavedra et al., 2018), capturing the fine-scale heterogeneity of reef development. In particular the drilling transects at One Tree Reef (Sanborn et al., 2020) showed high resolution and fine scale spatial variability compared with previous attempts probably anywhere around the world. Such studies at Scott Reef would clarify the higher-resolution mechanisms driving reef evolution, in response to relative sea-level and coeval environmental changes across multiple spatio-temporal scales (Camoin and Hallmann, 2022). While this study utilised three boreholes, 14 additional boreholes exist across Scott Reef (Collins et al., 2009), representing a valuable but underutilised resource for expanding the regional understanding of Quaternary reef evolution.

The three boreholes investigated in Chapter 4 and Chapter 5 (Hook 1P/3P, NRSEHDD3JA, SRSEBH6J) presented limitations in their complete reconstructions due to their missing sections of core. A logical extension of this research would involve acquiring deeper, more continuous core sections along spatially representative transects to reconstruct a more detailed reef framework. This approach could also yield better-preserved and more dateable sections of unaltered Pleistocene reef, particularly when combined with the non-destructive NCT method outlined in Chapter 3. Preliminary approval was granted during this study to access an uncut continuous long borehole (NR SE BH1 HDD-J) (200 m) from the leeward margin of North Scott Reef, owned by Woodside Energy and stored in the Perth Fugro Core facility. Future collaborations may allow for the application of non-destructive screening techniques, such as NCT and hyperspectral imaging, to identify sections suitable for destructive XRD

analysis and U-series dating while preserving valuable core material. This would facilitate the reconstruction of a much higher resolution sea-level curve than defined in this study.

To further constrain and compare chronostratigraphic resolution and add to the regional analogue database, future work should include developing directly comparable datasets from analogous reef systems along the North West Shelf, for example, Seringapatam Reef. Seringapatam Reef is located about 50 km to the North (Figure 1.12A), where no drilling has been done, and could offer continuous, dateable Quaternary reef sequences, comparable to Scott Reef, which would allow for a lateral extension of the chronostratigraphic framework outlined in this thesis.

In parallel, more advanced geophysical analysis is required. Seismic stratigraphic methods applied in Chapter 2 established a set of plausible and regionally useful carbonate factories for Scott Reef's evolution. However, these interpretations are inherently subjective. An intriguing future study could be to apply more detailed quantitative 3-D seismic stratigraphy (Paumard et al., 2019) to the existing seismic dataset and correlate it to the regionally available 3-D seismic datasets, such as the full depth-converted 3-D Torosa seismic survey. This approach would enable precise characterisation of reflection signals, reduce interpretive subjectivity, and improve understanding of stratigraphic complexity and spatio-temporal variability. Additionally, generating synthetic seismic data from the existing FSMs may improve resolution of higher-order sequences and help bridge current seismic data gaps, which could inform suitable sites for future drilling campaigns. A further avenue for future work is to extend the FSM beyond the Quaternary and into the Miocene, enabling direct comparison with the full tectono-stratigraphic and sequence stratigraphic framework established in Chapter 2. Expanding the model to encompass the entire evolutionary history of Scott Reef would allow a higher-resolution assessment of long-term controls on carbonate platform development and provide exploration of a unified reconstruction of platform architecture through both Neogene and Quaternary climate transitions.

6.2.2 Refining Paleowater Depth and Chronologic Reconstructions

Another exciting future study to pursue would be the interpretation of more precise paleowater depths from fossil reef cores using microendolithic trace fossils. While this thesis integrates stratigraphic and sedimentological evidence to reconstruct paleodepositional environments using coralgal assemblage interpretations, future studies might pursue more precise paleowater depth estimates using innovative biological indicators. One promising direction is the application of microendolithic trace fossil assemblages, which have shown potential as sensitive depth proxies (Chazottes et al., 2009; Remy et al., 2011). These microscopic borings, where calibrated with depositional context, may significantly improve paleowater depth constraints across reef successions.

There is potential to directly date the lower-amplitude MIS 3 interstadial simulated in Chapter 4 but unfortunately unconfirmed in the dating methods of Chapter 5. Age constraints on reef growth during MIS 3 remain debated (Siddall et al., 2008; Montaggioni, 2005; Gowan et al., 2021; Webster et al., 2022), and documenting this phase of reef development would provide critical insights into eustatic sea-level variability on the NWS, where continuous subsidence has been found to have preserved a record of this interval at Ashmore Reef (Webster et al., 2022). Botryoidal cements, which are observed in the Scott Reef cores, provide an additional chronological target. Recent studies demonstrate that such cements can yield robust U–Pb ages, even in the presence of significant diagenetic overprinting (Samankassou and West, 2002). Therefore, these cements offer an opportunity to generate independent age constraints that can test and support the synthetic stratigraphic MIS 3 reef growth phase in Chapter 4.

6.2.3 New Relative Sea Level, Modelling and Measuring Diagenesis

The SRSEBH6J borehole, recovered from the SE margin of South Scott Reef, was shown through hyperspectral imaging in Chapter 5 to preserve exceptional volumes of *in situ* aragonitic coral. This preservation provides a rare opportunity to reconstruct a regional high-resolution sea-level curve. Precisely dated submerged speleothems from Argentarola Cave (Italy) indicate three MIS 7 highstands (7.5, 7.3, 7.1), with MIS 7.3 peaking near

–18 m and displaying distinct phasing relative to insolation forcing (Dutton et al., 2009). Comparison with such independently constrained terrestrial sea-level markers would provide an important test of coral-derived chronologies in the Indo-Pacific. Such a record would represent a significant contribution to understanding Pleistocene reef evolution on the NWS, particularly for resolving sea-level variability during MIS 7 - an interval that remains poorly constrained in existing global and regional reconstructions.

The neutron computed tomography techniques explored in Chapter 3 of this thesis hold significant promise for broader application in coral reef research. The ANSTO funding for the DINGO beamtime also included data acquisition using the KOOKABURRA AND QUOKKA instruments, which produced Small Angle Neutron Scattering (SANS) and Ultra-SANS (USANS) data of fossil coral reef samples. Future studies should aim to expand these efforts by incorporating SANS and USANS to quantitatively assess porosity distribution (Bayrak et al., 2022), pore geometry, and diagenetic alteration in fossil reef cores, which has not been applied before. These methods provide ultra-high-resolution insights into the diagenetic history and microstructural evolution of carbonate platforms, enabling better characterisation of post-depositional changes that can inform on the possible relative sea-level histories (i.e., subsidence and sea-level change).

In addition, forward stratigraphic modelling should be extended to project the evolution of the Scott Reef system under future climate scenarios. Running the Scott Reef base case model from Chapter 4 forward in time under the three scenarios of sea-level rise of the IPCC would offer a predictive framework to assess the resilience of the reef and the morphological evolution under ongoing climate change.

CHAPTER 7

Conclusions and final remarks

This thesis has made significant contributions to advancing the understanding of carbonate platform evolution during Neogene - Quaternary climate transitions, using Scott Reef as a case study. New multi-scale datasets were generated, including the complete acquisition of hyperspectral imagery of all publicly available Scott Reef cores, NCT data from the Scott Reef, RR5, and PNG cores, and the digitization and archiving of existing XRD and thin section data. Notably, new Thompson-corrected open system ages and some new closed-system U-series dates were obtained from unaltered sections of Pleistocene reef, which is a rarely achieved outcome in Quaternary reef studies worldwide. It provides the most detailed and comprehensive investigation of Scott Reef across multiple spatial and temporal scales and identifies the relative complexity but resolvable interplay of environmental processes, relative sea-level change, and ecological thresholds that are determined by the constantly changing rhythms and perturbations of the Earth. Throughout this research, novel methods were systematically applied to both new and existing datasets. These included the integration of FSM workflows with seismic stratigraphy and the application of NCT to screen for unaltered reef material, representing a major advancement over traditional destructive screening techniques. Hyperspectral data not only facilitated core characterisation but also led to the discovery of unaltered coral framework allowing reliable chronologic reconstructions. These approaches enabled the development of new interpretations, including new sedimentological descriptions of three boreholes, and a revised chronostratigraphic framework for Scott Reef. A comprehensive FSM model of Scott Reef evolution, including a diagenesis model, provides a foundation for deeper exploration of marine and meteoric diagenetic alteration of Scott Reef. In addition, this research provided critical substantiation to existing evidence linking reef development during the MIS 11 highstand after the MPT. New discoveries included the

identification of synthetic MIS 3 reef growth at Hook 3P on South Scott Reef using FSM, and the finding of unaltered aragonite sections within Pleistocene reef sequences, validated through combined hyperspectral and NCT data. Further, this thesis developed a new solution to the long-standing challenge of non-destructive, three-dimensional screening of coral skeletons using NCT imaging, and established an integrated multi-scale framework linking borehole and seismic-scale stratigraphic interpretations. Although sampling of new core populations was outside the scope of this thesis, future work is recommended to target longer, more continuous core recovery at Scott and Seringapatam Reefs to further refine platform evolutionary models.

The FSM framework developed in this study can be utilised to characterise reef response to future relative sea-level and climate change. In doing so, this work offers a small yet meaningful contribution to the immense and ongoing scientific effort to understand the remarkable and wonderful intricacy of natural carbonate systems under anthropogenic stressors.

Bibliography of Chapters 1 and 6

Abbey, Elizabeth, Jody M Webster and Robin J Beaman (2011). 'Geomorphology of submerged reefs on the shelf edge of the Great Barrier Reef: the influence of oscillating Pleistocene sea-levels'. In: *Marine Geology* 288.1-4, pp. 61–78.

Alonso-Garcia, Montserrat et al. (2023). 'Sea-level and monsoonal control on the Maldives carbonate platform (Indian Ocean) over the last 1.3 million years'. In: *Climate of the Past Discussions* 2023, pp. 1–44.

Bard, Edouard et al. (2016). 'Comment on "Younger Dryas sea level and meltwater pulse 1B recorded in Barbados reefal crest coral Acropora palmata" by NA Abdul et al.' In: *Paleoceanography* 31.12, pp. 1603–1608.

Barrett, Samuel J and Jody M Webster (2012). 'Holocene evolution of the Great Barrier Reef: Insights from 3D numerical modelling'. In: *Sedimentary Geology* 265, pp. 56–71.

(2017). 'Reef Sedimentary Accretion Model (ReefSAM): Understanding coral reef evolution on Holocene time scales using 3D stratigraphic forward modelling'. In: *Marine Geology* 391, pp. 108–126.

Bassant, Phillip and Paul M Mitch Harris (2008). 'Analyzing reservoir architecture of isolated carbonate platforms'. In: *Search and Discovery Article* 40295.

Bates, Stephanie L, Mark Siddall and Claire Waelbroeck (2014). 'Hydrographic variations in deep ocean temperature over the mid-Pleistocene transition'. In: *Quaternary science reviews* 88, pp. 147–158.

Bayrak, Meltem et al. (2022). 'Physical disruption of gel particles on the macroscale does not affect the study of protein gel structure on the micro or nanoscale'. In: *Colloid and Interface Science Communications* 46, p. 100574.

Beaman, Robin J, Jody M Webster and Raphael AJ Wust (2008). 'New evidence for drowned shelf edge reefs in the Great Barrier Reef, Australia'. In: *Marine Geology* 247.1-2, pp. 17–34.

Belde, Johannes, Stefan Back and Lars Reuning (2015). 'Three-dimensional seismic analysis of sediment waves and related geomorphological features on a carbonate shelf exposed to large amplitude internal waves, B rowse B asin region, A ustralia'. In: *Sedimentology* 62.1, pp. 87–109.

Belde, Johannes et al. (2017). 'Oligocene and Miocene carbonate platform development in the Browse Basin, Australian northwest shelf'. In: *Journal of Sedimentary Research* 87.8, pp. 795–816.

Berggren, William A et al. (1985). 'Cenozoic geochronology'. In: *Geological Society of America Bulletin* 96.11, pp. 1407–1418.

Betzler, Christian and Yongsheng Ma (2024). 'Stratigraphic evolution and drowning steps of a submerged isolated carbonate platform in'. In: *Methods and Advances in Marine Geology and Hydrodynamics Environment*, p. 58.

Betzler, Christian et al. (2018). 'Refinement of Miocene sea level and monsoon events from the sedimentary archive of the Maldives (Indian Ocean)'. In: *Progress in Earth and Planetary Science* 5.1, pp. 1–18.

Bevitt, Joseph J (2018). 'Discovering dinosaurs with neutrons'. In: *Nature Reviews Materials* 3.9, pp. 296–298.

Bice, David M (1991). 'Computer simulation of carbonate platform and basin systems'. In: *Bulletin (Kansas Geological Survey)* 233, pp. 431–447.

Borgomano, Jean et al. (2020). 'Quantitative carbonate sequence stratigraphy: Insights from stratigraphic forward models'. In: *AAPG Bulletin* 104.5, pp. 1115–1142.

Bornholdt, Stefan, Ulf Nordlund and Hildegard Westphal (1999). 'Inverse stratigraphic modeling using genetic algorithms'. In: *Special Publications of SEPM*.

Bosence, Dan and Dave Waltham (1990). 'Computer modeling the internal architecture of carbonate platforms'. In: *Geology* 18.1, pp. 26–30.

Braga, Juan C. et al. (2022). 'Quaternary coral, coralline algal and vermetid assemblages as sea-level indicators: a review'. In: *SEPM Special Publication*.

Braithwaite, Colin JR et al. (2000). 'Origins and development of Holocene coral reefs: a revisited model based on reef boreholes in the Seychelles, Indian Ocean'. In: *International Journal of Earth Sciences* 89.2, pp. 431–445.

Braithwaite, Colin JR et al. (2004). 'The Great Barrier Reef: the chronological record from a new borehole'. In: *Journal of Sedimentary Research* 74.2, pp. 298–310.

Bruneau, Benjamin et al. (2017). '3D stratigraphic forward numerical modelling approach for prediction of organic-rich deposits and their heterogeneities'. In: *Marine and Petroleum Geology* 82, pp. 1–20.

Bubb, J. N. and W. G. Hatlelid (1978). 'Seismic stratigraphy and global changes of sea level, Part 10: Seismic recognition of carbonate buildups'. In: *AAPG Bulletin* 62.5, pp. 772–791.

Burgess, Peter M and Guy D Prince (2015). 'Non-unique stratal geometries: Implications for sequence stratigraphic interpretations'. In: *Basin Research* 27.3, pp. 351–365.

Burgess, Peter M, D Roberts and A Bally (2012). 'A brief review of developments in stratigraphic forward modelling, 2000–2009'. In: *Regional Geology and Tectonics: Principles of Geologic Analysis* 1, pp. 379–404.

Burgess, Peter M and V Paul Wright (2003). 'Numerical forward modeling of carbonate platform dynamics: An evaluation of complexity and completeness in carbonate strata'. In: *Journal of Sedimentary Research* 73.5, pp. 637–652.

Burgess, Peter M et al. (2006). 'Multivariate sequence stratigraphy: Tackling complexity and uncertainty with stratigraphic forward modeling, multiple scenarios, and conditional frequency maps'. In: *AAPG Bulletin* 90.12, pp. 1883–1901.

Burgess, Peter M et al. (2013). 'Methods for identification of isolated carbonate buildups from seismic reflection data'. In: *AAPG Bulletin* 97.7, pp. 1071–1098.

Busson, Jean et al. (2019). 'High-resolution stratigraphic forward modeling of a Quaternary carbonate margin: Controls and dynamic of the progradation'. In: *Sedimentary Geology* 379, pp. 77–96.

Cabioch, Guy et al. (1999). 'Reef coralgal assemblages as recorders of paleobathymetry and sea level changes in the Indo-Pacific province'. In: *Quaternary Science Reviews* 18.14, pp. 1681–1695.

Camoin, Gilbert and Nadine Hallmann (2022). 'Coral Reefs and Sea-Level Change: Quaternary Records and Modelling. A Window into the Future.' In: *Coral Reefs and Sea-Level Change: Quaternary Records and Modelling.* 49.

Camoin, Gilbert and Jody Webster (2014). 'Coral reefs and sea-level change'. In: *Developments in marine geology*. Vol. 7. Elsevier, pp. 395–441.

Camoin, Gilbert F, Yasufumi Iryu and Dave B McInroy (2007). 'IODP Expedition 310 reconstructs sea level, climatic, and environmental changes in the South Pacific during the last deglaciation'. In: *Scientific Drilling* 5, pp. 4–12.

Camoin, Gilbert F and Jody M Webster (2015). 'Coral reef response to Quaternary sea-level and environmental changes: State of the science'. In: *Sedimentology* 62.2, pp. 401–428.

Camoin, Gilbert F et al. (2012). 'Reef response to sea-level and environmental changes during the last deglaciation: Integrated Ocean Drilling Program Expedition 310, Tahiti Sea Level'. In: *Geology* 40.7, pp. 643–646.

Catuneanu, O et al. (2002). 'Foredeep submarine fans and forebulge deltas: orogenic off-loading in the underfilled Karoo Basin'. In: *Journal of African Earth Sciences* 35.4, pp. 489–502.

Cazenave, Anny and Frederique Remy (2011). 'Sea level and climate: measurements and causes of changes'. In: *Wiley Interdisciplinary Reviews: Climate Change* 2.5, pp. 647–662.

Chappell, John (1980). 'Coral morphology, diversity and reef growth'. In: *Nature* 286.5770, pp. 249–252.

Chauveau, Denovan et al. (2026). 'Unraveling the spatial variability of fossil coral reef morphology on Aruba and the implications for paleo sea level estimates'. In: *Journal of Geophysical Research: Earth Surface* 131.1.

Chazottes, Véronique et al. (2009). 'Bathymetric zonation of modern microborers in dead coral substrates from New Caledonia—implications for paleodepth reconstructions in Holocene corals'. In: *Palaeogeography, Palaeoclimatology, Palaeoecology* 280.3-4, pp. 456–468.

Chen, Jun-Yuan et al. (2002). 'Precambrian animal life: probable developmental and adult cnidarian forms from Southwest China'. In: *Developmental Biology* 248.1, pp. 182–196.

Chen, Weitao et al. (2024). 'Stratigraphic-sedimentary evolution of a mixed siliciclastic-carbonate system in the Huizhou Sag of the Pearl River Mouth Basin, Northern South China Sea'. In: *Frontiers in Earth Science* 11.

Cheng, Hai et al. (2013). ‘Improvements in 230Th dating, 230Th and 234U half-life values, and U–Th isotopic measurements by multi-collector inductively coupled plasma mass spectrometry’. In: *Earth and Planetary Science Letters* 371, pp. 82–91.

Cheng, Hai et al. (2016). ‘The Asian monsoon over the past 640,000 years and ice age terminations’. In: *Nature* 534.7609, pp. 640–646.

Christe, P et al. (2007). ‘Three-dimensional petrographical investigations on borehole rock samples: a comparison between X-ray computed-and neutron tomography’. In: *Acta Geotechnica* 2.4, pp. 269–279.

Christensen, Beth A et al. (2017). ‘Indonesian Throughflow drove Australian climate from humid Pliocene to arid Pleistocene’. In: *Geophysical Research Letters* 44.13, pp. 6914–6925.

Chutcharavan, Peter M and Andrea Dutton (2021). ‘A global compilation of U-series-dated fossil coral sea-level indicators for the Last Interglacial period (Marine Isotope Stage 5e)’. In: *Earth System Science Data* 13.7, pp. 3155–3178.

Chutcharavan, Peter M, Andrea Dutton and Michael J Ellwood (2018). ‘Seawater 234U/238U recorded by modern and fossil corals’. In: *Geochimica et Cosmochimica Acta* 224, pp. 1–17.

Clark, Peter U et al. (2006). ‘The middle Pleistocene transition: characteristics, mechanisms, and implications for long-term changes in atmospheric pCO2’. In: *Quaternary Science Reviews* 25.23-24, pp. 3150–3184.

Clavera-Gispert, Roger et al. (2017). ‘Process-based forward numerical ecological modeling for carbonate sedimentary basins’. In: *Computational Geosciences* 21.3, pp. 373–391.

Collins, LB et al. (2011). ‘Holocene growth history and evolution of the Scott Reef carbonate platform and coral reef’. In: *Journal of the Royal Society of Western Australia* 94.2, p. 239.

Collins, Lindsay B and Viviane Testa (2010). ‘Quaternary development of resilient reefs on the subsiding Kimberley continental margin, northwest Australia’. In: *Brazilian Journal of Oceanography* 58, pp. 67–77.

Collins, Lindsay B, Jian-Xin Zhao and Heather Freeman (2006). ‘A high-precision record of mid–late Holocene sea-level events from emergent coral pavements in the Houtman Abrolhos Islands, southwest Australia’. In: *Quaternary International* 145, pp. 78–85.

Collins, Lindsay B. et al. (2009). *Quaternary Growth History and Evolution of the Scott Reef Carbonate Platform and Coral Reef: Core Study*. Final report prepared for Woodside Energy Limited. Unpublished report; permission and access granted through WEL–UWA TIDE agreement. Curtin University.

Cross, TA and MA Lessenger (1998). 'Sediment volume partitioning: rationale for stratigraphic model evaluation and high-resolution stratigraphic correlation'. In: *Sequence Stratigraphy—Concepts and Application. Norwegian Petroleum Society Special Publication* 8, pp. 171–195.

Darwin, Charles (1842). *The Zoology of the Voyage of HMS Beagle, Under the Command of Captain Fitzroy, RN, During the Years 1832 to 1836: Published with the Approval of the Lords Commissioners of Her Majesty's Treasury.: Edited and Superintended by Charles Darwin, Esq....* Vol. 4. Smith, Elder and Company, 65, Cornhill.

(1859). *On the Origin of Species by Means of Natural Selection, or the Preservation of Favoured Races in the Struggle for Life*. London: John Murray.

Davies, Philip J. and Lucien F. Montaggioni (1985). 'Reef Zonation and Sea-Level Change: A Review of the Evidence'. In: *Proceedings of the Fifth International Coral Reef Congress*. Ed. by C. Gabrie and B. Salvat. Vol. 3. Tahiti, French Polynesia, pp. 477–487.

De Vleeschouwer, David et al. (2020). 'High-latitude biomes and rock weathering mediate climate–carbon cycle feedbacks on eccentricity timescales'. In: *Nature Communications* 11.1, p. 5013.

Deacon, Terrence W (2011). *Incomplete nature: How mind emerged from matter*. WW Norton & Company.

Dechnik, Belinda et al. (2017). 'Successive phases of Holocene reef flat development: Evidence from the mid-to outer Great Barrier Reef'. In: *Palaeogeography, Palaeoclimatology, Palaeoecology* 466, pp. 221–230.

Deschamps, Pierre et al. (2012). 'Ice-sheet collapse and sea-level rise at the Bølling warming 14,600 years ago'. In: *Nature* 483.7391, pp. 559–564.

Done, Terence, James Gilmour and Rebecca Fisher (2015). 'Distance decay among coral assemblages during a cycle of disturbance and recovery'. In: *Coral Reefs* 34.3, pp. 727–738.

Droxler, André W and Stéphan J Jorry (2021). 'The origin of modern atolls: challenging Darwin's deeply ingrained theory'. In: *Annual Review of Marine Science* 13.1, pp. 537–573.

Dumitru, Oana A et al. (2023). 'Last interglacial global mean sea level from high-precision U-series ages of Bahamian fossil coral reefs'. In: *Quaternary Science Reviews* 318, pp. 108–287.

Dutton, Andrea et al. (2009). 'Phasing and amplitude of sea-level and climate change during the penultimate interglacial'. In: *Nature Geoscience* 2.5, pp. 355–359.

Dutton, Andrea et al. (2023). 'Mantle-driven subsidence of Last Interglacial reef points to origins of the Great Barrier Reef'. In: *AGU Fall Meeting Abstracts*. Vol. 2023, C11B–04.

Dwyer, Gary S et al. (1995). 'North Atlantic deepwater temperature change during late Pliocene and late Quaternary climatic cycles'. In: *Science* 270.5240, pp. 1347–1351.

Eberli, Gregor P et al. (1994). 'Testing a seismic interpretation of Great Bahama Bank with a computer simulation'. In: *AAPG Bulletin* 78.6, pp. 981–1004.

Edinger, Evan N et al. (2007). 'Age accuracy and resolution of Quaternary corals used as proxies for sea level'. In: *Earth and Planetary Science Letters* 253.1-2, pp. 37–49.

Faichney, Iain DE et al. (2010). 'Unraveling the tilting history of the submerged reefs surrounding Oahu and the Maui-Nui Complex, Hawaii'. In: *Geochemistry, Geophysics, Geosystems* 11.7.

Faichney, Iain DE et al. (2011). 'The impact of the Mid-Pleistocene Transition on the composition of submerged reefs of the Maui Nui Complex, Hawaii'. In: *Palaeogeography, Palaeoclimatology, Palaeoecology* 299.3-4, pp. 493–506.

Finnegan, Seth et al. (2024). 'Using the fossil record to understand extinction risk and inform marine conservation in a changing world'. In: *Annual Review of Marine Science* 16.1, pp. 307–333.

Gallagher, Stephen J et al. (2014). 'Seismic and stratigraphic evidence for reef expansion and onset of aridity on the Northwest Shelf of Australia during the Pleistocene'. In: *Marine and Petroleum Geology* 57, pp. 470–481.

Gelder, Gino de et al. (2020). 'How do sea-level curves influence modeled marine terrace sequences?' In: *Quaternary Science Reviews* 229, pp. 106–132.

Gilmour, James P et al. (2022). 'A tale of two reef systems: Local conditions, disturbances, coral life histories, and the climate catastrophe'. In: *Ecological Applications* 32.3, pp. 2–509.

Gischler, Eberhard (2015). 'Quaternary reef response to sea-level and environmental change in the western Atlantic'. In: *Sedimentology* 62.2, pp. 429–465.

Gischler, Eberhard et al. (2013). 'Microfacies and diagenesis of older Pleistocene (pre-last glacial maximum) reef deposits, Great Barrier Reef, Australia (IODP Expedition 325): A quantitative approach'. In: *Sedimentology* 60.6, pp. 1432–1466.

Gischler, Eberhard et al. (2022). 'Neogene and Quaternary reef terraces of Mangaia, Rarotonga and Aitutaki (southern Cook Islands, South Pacific) revisited: gauges of sea-level change and island uplift?' In: *Coral Reefs and Sea-Level Change: Quaternary Records and Modelling*. Wiley, pp. 275–317.

Gowan, Evan J et al. (2021). 'A new global ice sheet reconstruction for the past 80 000 years'. In: *Nature Communications* 12.1, p. 1199.

Granjeon, D and Phillip Joseph (1999). 'Concepts and applications of a 3-D multiple lithology, diffusive model in stratigraphic modeling'. In: *Special Publications of SEPM*.

Granjeon, Didier (2014). '3D forward modelling of the impact of sediment transport and base level cycles on continental margins and incised valleys'. In: *From Depositional Systems to Sedimentary Successions on the Norwegian Continental Margin*, pp. 453–472.

Green, Rebecca H, Ryan J Lowe and Mark L Buckley (2018). 'Hydrodynamics of a tidally forced coral reef atoll'. In: *Journal of Geophysical Research: Oceans* 123.10, pp. 7084–7101.

Greenstein, Benjamin J and John M Pandolfi (2008). 'Escaping the heat: range shifts of reef coral taxa in coastal Western Australia'. In: *Global Change Biology* 14.3, pp. 513–528.

Grigg, Richard W (2006). 'Depth limit for reef building corals in the Au'au Channel, SE Hawaii'. In: *Coral Reefs* 25.1, pp. 77–84.

Grimaldi, Camille M et al. (2024). 'Local coral connections within an atoll reef system underlie reef resilience and persistence'. In: *Limnology and Oceanography* 69.12, pp. 3020–3032.

Groeneveld, J et al. (2021). 'Dating the northwest shelf of Australia since the Pliocene'. In: *Geochemistry, Geophysics, Geosystems* 22.3.

Hallock, Pamela and Wolfgang Schlager (1986). 'Nutrient Excess and the Demise of Coral Reefs and Carbonate Platforms'. In: *Palaios*, pp. 389–398.

Hawie, Nicolas et al. (2015). 'Forward stratigraphic modelling, deterministic approach to improve carbonate heterogeneity prediction; Lower Cretaceous, Abu Dhabi'. In: *Abu Dhabi International Petroleum Exhibition and Conference*. SPE, D041S077R005.

He, Yuxin, Huanye Wang and Zhonghui Liu (2021). 'Development of the Leeuwin Current on the northwest shelf of Australia through the Pliocene-Pleistocene period'. In: *Earth and Planetary Science Letters* 559, p. 116767.

Herbert, Timothy D (2023). 'The mid-Pleistocene climate transition'. In: *Annual Review of Earth and Planetary Sciences* 51.1, pp. 389–418.

Hibbert, FD et al. (2018). 'A database of biological and geomorphological sea-level markers from the Last Glacial Maximum to present'. In: *Scientific Data* 5.1, pp. 1–25.

Hill, Jon et al. (2009). 'Modeling shallow marine carbonate depositional systems'. In: *Computers & Geosciences* 35.9, pp. 1862–1874.

Hill, Jon et al. (2012). 'Preservation of forcing signals in shallow water carbonate sediments'. In: *Sedimentary Geology* 275, pp. 79–92.

Hongo, Chuki, Hideki Kawamata and Kazuhisa Goto (2012). 'Catastrophic impact of typhoon waves on coral communities in the Ryukyu Islands under global warming'. In: *Journal of Geophysical Research: Biogeosciences* 117.G2.

Hu, Hsun-Ming et al. (2025). 'Sub-epsilon natural 234U/238U measurements refine the 234U half-life and U-Th geochronology'. In: *Science Advances* 11.40, eadu8117.

Humblet, Marc and Jody M Webster (2017). 'Coral community changes in the Great Barrier Reef in response to major environmental changes over glacial-interglacial timescales'. In: *Palaeogeography, Palaeoclimatology, Palaeoecology* 472, pp. 216–235.

Husson, Laurent et al. (2018). 'Reef carbonate productivity during quaternary sea level oscillations'. In: *Geochemistry, Geophysics, Geosystems* 19.4, pp. 1148–1164.

Iryu, Yasufumi et al. (2010). 'Sealevel history recorded in the Pleistocene carbonate sequence in IODP Hole 310-M0005D, off Tahiti'. In: *Island Arc* 19.4, pp. 690–706.

Ivankina, Tatiana I et al. (2020). 'The structure of scleractinian coral skeleton analyzed by neutron diffraction and neutron computed tomography'. In: *Scientific Reports* 10.1, p. 12869.

James, Noel P et al. (2004). 'The importance of changing oceanography in controlling late Quaternary carbonate sedimentation on a high-energy, tropical, oceanic ramp: north-western Australia'. In: *Sedimentology* 51.6, pp. 1179–1205.

James, R Thomas et al. (1997). 'A sediment resuspension and water quality model of lake okeechobee 1'. In: *JAWRA Journal of the American Water Resources Association* 33.3, pp. 661–678.

Jiménez, Grisel et al. (2024). 'Effective application of geological process modeling for unravelling carbonate build-up complexity: A case study from the EX-Carbonate build-up in central Luconia Province, Malaysia'. In: *Marine and Petroleum Geology* 170, p. 107117.

John, Cédric M, Ilyas Kussanov and Nicolas Hawie (2021). 'Constraining stratal architecture and pressure barriers in the subsalt Karachaganak Carboniferous carbonate platforms using forward stratigraphic modelling'. In: *Marine and Petroleum Geology* 124, p. 104771.

Keep, Myra and Mathew Harrowfield (2008). 'Elastic flexure and distributed deformation along Australia's North West Shelf: Neogene tectonics of the Bonaparte and Browse basins'. In: *Geological Society special publication* 306, pp. 185–200.

Keep, Myra, Mathew Harrowfield and Warwick Crowe (2007). 'The neogene tectonic history of the North West Shelf, Australia'. In: *Exploration Geophysics* 38.3, pp. 151–174.

Kendall, CG St C et al. (1991). 'The simulation of the sedimentary fill of basins'. In: *Journal of Geophysical Research: Solid Earth* 96.B4, pp. 6911–6929.

Kennedy, DM and CD Woodroffe (2002). 'Fringing reef growth and morphology: a review'. In: *Earth-Science Reviews* 57.3-4, pp. 255–277.

Kirch, Patrick Vinton (2017). *On the road of the winds: an archaeological history of the Pacific Islands before European contact*. Univ of California Press.

Kolodka, Christophe et al. (2016). 'Stratigraphic modelling of platform architecture and carbonate production: a Messinian case study (Sorbas Basin, SE Spain)'. In: *Basin Research* 28.5, pp. 658–684.

Kruse, Kendra (2014). ‘Paleoenvrironmental Controls on Diagenesis of Organich-Rich Shales in the Eagle Ford Group; Texas AandM’. PhD thesis.

Kuhnt, Wolfgang et al. (2004). ‘Neogene history of the Indonesian throughflow’. In: *Continent-Ocean Interactions within East Asian Marginal Seas. Geophysical Monograph* 149, pp. 299–320.

Lambeck, Kurt et al. (2014). ‘Sea level and global ice volumes from the Last Glacial Maximum to the Holocene’. In: *Proceedings of the National Academy of Sciences* 111.43, pp. 15296–15303.

Lanteaume, Cyprien et al. (2018). ‘Testing geologic assumptions and scenarios in carbonate exploration: Insights from integrated stratigraphic, diagenetic, and seismic forward modeling’. In: *The Leading Edge* 37.9, pp. 672–680.

Liautaud, Parker and Peter Huybers (2022). ‘Uniformitarian Prediction of Early-Pleistocene Atmospheric CO2’. In: *Geophysical Research Letters* 49.20.

Liu, Jinlong et al. (2022). ‘The formation of atolls: New insights from numerical simulations’. In: *Journal of Geophysical Research: Earth Surface* 127.8.

Loucks, Robert G. and J. Frederick Sarg, eds. (1993). *Carbonate Sequence Stratigraphy: Recent Developments and Applications*. Vol. 57. AAPG Memoir. Tulsa, Oklahoma: American Association of Petroleum Geologists.

Mansour, Abbas M and Hashem A Madkour (2015). ‘Raised coral reefs and sediments in the coastal area of the Red Sea’. In: *The Red Sea: The formation, Morphology, Oceanography and Environment of a Young Ocean Basin*. Springer, pp. 379–393.

Marshall, NG and SC Lang (2013). ‘A new sequence stratigraphic framework for the North West Shelf, Australia’. In: *Petroleum Exploration Society of Australia (PESA)*.

Martin-Garin, Bertrand and Lucien F Montaggioni (2023). ‘The Modern Times’. In: *Corals and Reefs: From the Beginning to an Uncertain Future*. Springer, pp. 31–78.

McCaffrey, Jackson C et al. (2025). ‘The Rowley Shoals atolls: Remnants of a Miocene great barrier reef on the north-west Australian margin’. In: *Global and Planetary Change* 245, pp. 104–688.

McGregor, Helen V and Michael K Gagan (2003). 'Diagenesis and geochemistry of Porites corals from Papua New Guinea: Implications for paleoclimate reconstruction'. In: *Geochimica et Cosmochimica Acta* 67.12, pp. 2147–2156.

Medina-Elizalde, Martín (2013). 'A global compilation of coral sea-level benchmarks: implications and new challenges'. In: *Earth and Planetary Science Letters* 362, pp. 310–318.

Montaggioni, Lucien F (2005). 'History of Indo-Pacific coral reef systems since the last glaciation: development patterns and controlling factors'. In: *Earth-Science Reviews* 71.1-2, pp. 1–75.

Montaggioni, Lucien F and Colin JR Braithwaite (2009). *Quaternary coral reef systems: history, development processes and controlling factors*. Vol. 5. Elsevier.

Montaggioni, Lucien F et al. (2011). 'Revisiting the Quaternary development history of the western New Caledonian shelf system: from ramp to barrier reef'. In: *Marine Geology* 280.1-4, pp. 57–75.

Montaggioni, Lucien F et al. (2015). 'Quaternary atoll development: New insights from the two-dimensional stratigraphic forward modelling of Mururoa Island (Central Pacific Ocean)'. In: *Sedimentology* 62.2, pp. 466–500.

Moore, Clyde H and William J Wade (2013). *Carbonate reservoirs: Porosity and diagenesis in a sequence stratigraphic framework*. Vol. 67. Newnes.

Mortlock, Richard A et al. (2016). 'Reply to comment by E. Bard et al. on "Younger Dryas sea level and meltwater pulse 1B recorded in Barbados reef crest coral Acropora palmata" by NA Abdul et al.' In: *Paleoceanography* 31.12, pp. 1609–1616.

Müller, R Dietmar et al. (2022). 'Evolution of Earth's tectonic carbon conveyor belt'. In: *Nature* 605.7911, pp. 629–639.

Muñoz-López, Pablo et al. (2025). 'Numerical modeling of the influence of tidal flats on estuaries: the case of the Guadalquivir estuary, SW of the Iberian Peninsula'. In: *Frontiers in Marine Science* 12.

Murphy, RJ et al. (2017). 'High-resolution hyperspectral imaging of diagenesis and clays in fossil coral reef material: a nondestructive tool for improving environmental and climate reconstructions'. In: *Geochemistry, Geophysics, Geosystems* 18.8, pp. 3209–3230.

Murray-Wallace, Colin V and Colin D Woodroffe (2014). *Quaternary sea-level changes: a global perspective*. Cambridge University Press.

Mutti, Maria, André W Droxler and Andrew D Cunningham (2005). 'Evolution of the Northern Nicaragua Rise during the Oligocene–Miocene: drowning by environmental factors'. In: *Sedimentary Geology* 175.1-4, pp. 237–258.

Mutti, Maria and Pamela Hallock (2003). 'Carbonate systems along nutrient and temperature gradients: some sedimentological and geochemical constraints'. In: *International Journal of Earth Sciences* 92.4, pp. 465–475.

National Geographic Society (Nov. 2024). *New Discovery: Largest Coral in the World Found in the Solomon Islands*. https://news.nationalgeographic.org/new-discovery-largest-coral-in-the-world-found-in-the-solomon-islands/: Accessed 2025-11-12.

Nothdurft, Luke D and Gregory E Webb (2009). 'Earliest diagenesis in scleractinian coral skeletons: implications for palaeoclimate-sensitive geochemical archives'. In: *Facies* 55.2, pp. 161–201.

Palei, Rina Rani et al. (2024). 'Leeuwin current dynamics in the SE Indian Ocean and implications for regional surface hydrography since the latest Miocene: Results from ODP Site 763A'. In: *Global and Planetary Change* 237, p. 104459.

Paola, Chris (2000). 'Quantitative models of sedimentary basin filling'. In: *Sedimentology* 47, pp. 121–178.

Pastier, A-M et al. (2019). 'Genesis and architecture of sequences of Quaternary coral reef terraces: Insights from numerical models'. In: *Geochemistry, Geophysics, Geosystems* 20.8, pp. 4248–4272.

Paumard, Victorien (2018). 'Shelf-margin architecture, sediment partitioning and shallow-to deep-water reservoir distribution in the Barrow Group (Northern Carnarvon Basin, North West Shelf, Australia): Insights from quantitative 3D seismic stratigraphy'. In.

Paumard, Victorien et al. (2019). 'Full-volume 3D seismic interpretation methods: A new step towards high-resolution seismic stratigraphy'. In: *Interpretation* 7.3, B33–B47.

Petrick, Benjamin et al. (2019). 'Glacial indonesian throughflow weakening across the mid-pleistocene climatic transition'. In: *Scientific Reports* 9.1.

Pomar, L and Pamela Hallock (2008). 'Carbonate factories: a conundrum in sedimentary geology'. In: *Earth-Science Reviews* 87.3-4, pp. 134–169.

Pomar, Luis and Bilal U Haq (2016). 'Decoding depositional sequences in carbonate systems: Concepts vs experience'. In: *Global and Planetary Change* 146, pp. 190–225.

Posamentier, HW and GP Allen (1999). 'Siliciclastic sequence stratigraphy'. In: *Concepts and Applications: SEPM, Concepts in Sedimentology and Paleontology* 7, p. 210.

Rankey, Eugene C (2020). 'Eustatic, climatic, and oceanographic influences on geomorphology and architecture of isolated carbonate platforms: Miocene, Northwest Shelf, Australia'. In: *Lithosphere* 2020.1.

Raymo, Maureen E (1997). 'The timing of major climate terminations'. In: *Paleoceanography* 12.4, pp. 577–585.

Raymo, Maureen E and Jerry X Mitrovica (2012). 'Collapse of polar ice sheets during the stage 11 interglacial'. In: *Nature* 483.7390, pp. 453–456.

Rayson, Matthew D et al. (2011). 'Internal tide dynamics in a topographically complex region: Browse Basin, Australian North West Shelf'. In: *Journal of Geophysical Research: Oceans* 116.

Reeve, Matthew T et al. (2022). 'Stratigraphic record of continental breakup, offshore NW Australia'. In: *Basin Research* 34.3, pp. 1220–1243.

Reijmer, John JG (2021). 'Marine carbonate factories: review and update'. In: *Sedimentology* 68.5, pp. 1729–1796.

Rich, John Lyon (1951). 'Three critical environments of deposition, and criteria for recognition of rocks deposited in each of them'. In: *Geological Society of America Bulletin* 62.1, pp. 1–20.

Riera, Rosine et al. (2022). 'Early Miocene carbonate ramp development in a warm ocean, North West Shelf, Australia'. In: *Sedimentology* 69.1, pp. 219–253.

Rosenthal, Yair, Ann E Holbourn and Denise K Kulhanek (2018). 'Western Pacific warm pool'. In: *Proceedings of the International Ocean Discovery Program* 363.

Rosleff-Soerensen, Beke et al. (2012). 'Seismic geomorphology and growth architecture of a Miocene barrier reef, Browse Basin, NW-Australia'. In: *Marine and Petroleum Geology* 29.1, pp. 233–254.

Rosleff-Soerensen, Beke et al. (2016). ‘The response of a basin-scale Miocene barrier reef system to long-term, strong subsidence on a passive continental margin, Barcoo Sub-basin, Australian North West Shelf’. In: *Basin Research* 28.1, pp. 103–123.

Rovere, Alessio et al. (2023). ‘Influence of reef isostasy, dynamic topography, and glacial isostatic adjustment on sea-level records in Northeastern Australia’. In: *Communications Earth & Environment* 4.1, p. 328.

Ryan, Georgina et al. (2009). ‘A pre-cursor extensive Miocene reef system to the Rowley Shoals reefs, Western Australia: evidence for structural control of reef growth or natural hydrocarbon seepage?’ In: *The APPEA Journal* 49.1, pp. 337–364.

Salas-Saavedra, Marcos et al. (2018). ‘Holocene reef growth over irregular Pleistocene karst confirms major influence of hydrodynamic factors on Holocene reef development’. In: *Quaternary Science Reviews* 180, pp. 157–176.

Salles, Tristan et al. (2018). ‘A unified framework for modelling sediment fate from source to sink and its interactions with reef systems over geological times’. In: *Scientific reports* 8.1, p. 5252.

Salles, Tristan et al. (2025). ‘Carbonate burial regimes, the Meso-Cenozoic climate, and nannoplankton expansion’. In: *Proceedings of the National Academy of Sciences* 122.49, e2516468122.

Al-Salmi, Marya, Cédric M John and Nicolas Hawie (2019). ‘Quantitative controls on the regional geometries and heterogeneities of the Rayda to Shu’aiba formations (Northern Oman) using forward stratigraphic modelling’. In: *Marine and Petroleum Geology* 99, pp. 45–60.

Samankassou, Elias and Ronald R West (2002). ‘Construction versus accumulation in phylloid algal mounds: an example of a small constructed mound in the Pennsylvanian of Kansas, USA’. In: *Palaeogeography, Palaeoclimatology, Palaeoecology* 185.3-4, pp. 379–389.

Sanborn, Kelsey L et al. (2020). ‘A new model of Holocene reef initiation and growth in response to sea-level rise on the Southern Great Barrier Reef’. In: *Sedimentary Geology* 397, p. 105556.

Sanborn, Kelsey L et al. (2024). ‘The impact of elevated nutrients on the Holocene evolution of the Great Barrier Reef’. In: *Quaternary Science Reviews* 332, p. 108636.

Saqab, Muhammad M and Julien Bourget (2015). 'Controls on the distribution and growth of isolated carbonate build-ups in the Timor Sea (NW Australia) during the Quaternary'. In: *Marine and Petroleum Geology* 62, pp. 123–143.

Saqab, Muhammad Mudasar and Julien Bourget (2016). 'Seismic geomorphology and evolution of early–mid Miocene isolated carbonate build-ups in the Timor Sea, North West Shelf of Australia'. In: *Marine Geology* 379, pp. 224–245.

Sarg, JF (1988). 'Carbonate sequence stratigraphy'. In.

Schlager, Wolfgang (2000). 'Sedimentation rates and growth potential of tropical, cool-water and mud-mound carbonate systems'. In.

(2003). 'Benthic carbonate factories of the Phanerozoic'. In: *International Journal of Earth Sciences* 92.4, pp. 445–464.

(2005). *Carbonate sedimentology and sequence stratigraphy*. 8. SEPM Soc for Sed Geology.

Schlager, Wolfgang, John JG Reijmer and Andre Droxler (1994). 'Highstand shedding of carbonate platforms'. In: *Journal of Sedimentary Research* 64.3b, pp. 270–281.

Schmidt Ocean Institute (2020). *Australian scientists discover 500-meter-tall coral reef in the Great Barrier Reef – first to be discovered in over 120 years*. https://schmidtocean.org/australian-scientists-discover-500-meter-tall-coral-reef-in-the-great-barrier-reef-first-to-be-discovered-in-over-120-years/: Accessed 11 Dec 2025.

Scholz, Denis and Dirk Hoffmann (2008). '230Th/U-dating of fossil corals and speleothems'. In: *E&G Quaternary Science Journal* 57.1/2, pp. 52–76.

Scopélitis, J et al. (2011). 'Coral colonisation of a shallow reef flat in response to rising sea level: quantification from 35 years of remote sensing data at Heron Island, Australia'. In: *Coral Reefs* 30.4, pp. 951–965.

Seard, Claire et al. (2013). 'Impact of environmental parameters on coral reef development and drowning: Forward modelling of the last deglacial reefs from Tahiti (French Polynesia; IODP Expedition# 310)'. In: *Sedimentology* 60.6, pp. 1357–1388.

Siddall, Mark et al. (2008). 'Marine isotope stage 3 sea level fluctuations: Data synthesis and new outlook'. In: *Reviews of Geophysics* 46.4.

Spratt, Rachel M and Lorraine E Lisiecki (2016). 'A Late Pleistocene sea level stack'. In: *Climate of the Past* 12.4, pp. 1079–1092.

Steel, Ron J. and Torben Olsen (2002). 'Clinoforms, Clinoform Trajectories and Deepwater Sands'. In: *Sequence Stratigraphic Models for Exploration and Production: Evolving Methodology, Emerging Models and Application Histories*. Ed. by J. M. Armentrout and N. C. Rosen. Vol. 22. Gulf Coast Section SEPM Foundation Bob F. Perkins Research Conference. Houston, Texas: SEPM (Society for Sedimentary Geology), pp. 367–381.

Stuut, Jan-Berend W et al. (2019). 'A 5.3-million-year history of monsoonal precipitation in northwestern Australia'. In: *Geophysical Research Letters* 46.12, pp. 6946–6954.

Thompson, Schmitty B, Jessica R Creveling and Jerry X Mitrovica (2025). 'The sensitivity of tectonic uplift corrections to the penultimate deglacial ice volume and configuration'. In: *Quaternary Science Reviews* 353, p. 109210.

Thompson, William G et al. (2003). 'An open-system model for U-series age determinations of fossil corals'. In: *Earth and Planetary Science Letters* 210.1-2, pp. 365–381.

Toscano, Marguerite A, W Richard Peltier and Rosemarie Drummond (2011). 'ICE-5G and ICE-6G models of postglacial relative sea-level history applied to the Holocene coral reef record of northeastern St Croix, USVI: investigating the influence of rotational feedback on GIA processes at tropical latitudes'. In: *Quaternary Science Reviews* 30.21-22, pp. 3032–3042.

Vail, Peter R, Robert M Mitchum and SIII Thompson (1977). 'Seismic stratigraphy and global changes of sea level, part 4: global cycles of relative changes of sea level'. In: *Seismic Stratigraphy—Applications to Hydrocarbon Exploration*, pp. 83–97.

Van der Looven, Thomas et al. (2022). 'A biotic perspective on the Oligo-Miocene evolution of the Maldives carbonate platform from forward stratigraphic modelling (Indian Ocean)'. In: *Marine and Petroleum Geology* 145, p. 105907.

Van Tuyl, James et al. (2019). 'Geomorphological evidence of carbonate build-up demise on equatorial margins: A case study from offshore northwest Australia'. In: *Marine and Petroleum Geology* 104, pp. 125–149.

Veron, J. E. N. (2000). *Corals of the World. Vols. 1–3*. 3 volumes, 1382 pp. Townsville, Queensland, Australia: Australian Institute of Marine Science & CRR.

Veron, John Edward Norwood (1995). *Corals in space and time: the biogeography and evolution of the Scleractinia*. Cornell University Press.

Waelbroeck, Claire et al. (2002). 'Sea-level and deep water temperature changes derived from benthic foraminifera isotopic records'. In: *Quaternary Science Reviews* 21.1-3, pp. 295–305.

Warrlich, GMD, DA Waltham and DWJ Bosence (2002). 'Quantifying the sequence stratigraphy and drowning mechanisms of atolls using a new 3-D forward stratigraphic modelling program (CARBONATE 3D)'. In: *Basin Research* 14.3, pp. 379–400.

Watney, W Lynn, Eugene C Rankey and John Harbaugh (1999). 'Perspectives on stratigraphic simulation models: current approaches and future opportunities'. In: *Special Publications of SEPM*.

Webb, Gregory E et al. (2016). 'Significance of shallow core transects for reef models and sea-level curves, Heron Reef, Great Barrier Reef'. In: *Sedimentology* 63.6, pp. 1396–1424.

Webster, J. M. et al. (2022). 'Coral Reef Development and Sea-Level Changes over the Past 50,000 Years: New Evidence from the Northwest Shelf of Australia'. In: *Coral Reefs and Sea-Level Change: Quaternary Records and Modelling*. Ed. by G. F. Camoin and N. Hallmann. Vol. 49. International Association of Sedimentologists Special Publication. International Association of Sedimentologists, pp. 215–273.

Webster, Jody M et al. (2009). 'Coral reef evolution on rapidly subsiding margins'. In: *Global and Planetary Change* 66.1-2, pp. 129–148.

Webster, Jody M et al. (2018). 'Response of the Great Barrier Reef to sea-level and environmental changes over the past 30,000 years'. In: *Nature Geoscience* 11.6, pp. 426–432.

Webster, Jody M et al. (2025a). 'Constraints on sea-level rise during meltwater pulse 1B from the Great Barrier Reef'. In: *Nature Communications* 16.1, p. 4698.

Webster, Jody M. et al. (2025b). 'Expedition 389 Summary'. In: *Proceedings of the International Ocean Discovery Program* 389.

Whitney, Beau B, James V Hengesh and Dan Gillam (2016). 'Styles of neotectonic fault reactivation within a formerly extended continental margin, North West Shelf, Australia'. In: *Tectonophysics* 686, pp. 1–18.

Wilkins, Ian (2001). 'Scientists at sea: British seagoing naturalists in Australian waters in the nineteenth century'. In: *International Journal of Maritime History* 13.1, pp. 95–113.

Williams, Huw D et al. (2011). 'Investigating carbonate platform types: multiple controls and a continuum of geometries'. In: *Journal of Sedimentary Research* 81.1, pp. 18–37.

Wilson, Barry (2013). *The biogeography of the Australian North West Shelf: Environmental change and life's response*. Newnes.

Wilson, James L (1975). 'The stratigraphy of carbonate deposits'. In: *Carbonate facies in geologic history*. Springer, pp. 20–55.

Wilson, James Lee (2012). *Carbonate facies in geologic history*. Springer Science & Business Media.

Wilson, Moyra E. J. (2011). 'SE Asian carbonates: tools for evaluating environmental and climatic change in equatorial tropics over the last 50 million years'. In: *The SE Asian Gateway: History and Tectonics of the Australia–Asia Collision*. Ed. by Robert Hall, Margaret A. Cottam and Moyra E. J. Wilson. Vol. 355. Geological Society, London, Special Publications. Geological Society of London, pp. 347–369.

Wood, Rachel (1999). *Reef evolution*. Oxford University Press.

Woodroffe, Colin D and Jody M Webster (2014). 'Coral reefs and sea-level change'. In: *Marine Geology* 352, pp. 248–267.

(2025). 'Coral Records of Relative Sea-Level Changes'. In: *Encyclopedia of Quaternary Science*. Ed. by Scott Elias. UK: Elsevier, pp. 107–125.

Wulf, Andrea (2015). *The invention of nature: the adventures of Alexander von Humboldt, the lost hero of science: Costa & Royal Society Prize Winner*. Hachette UK.

Yamamoto, Kazuyuki et al. (2006). 'Responses of coral reefs to increased amplitude of sea-level changes at the Mid-Pleistocene Climate Transition'. In: *Palaeogeography, Palaeoclimatology, Palaeoecology* 241.1, pp. 160–175.

Yokoyama, Yusuke et al. (2001). 'Sea-level at the Last Glacial Maximum: evidence from northwestern Australia to constrain ice volumes for oxygen isotope stage 2'. In: *Palaeogeography, Palaeoclimatology, Palaeoecology* 165.3-4, pp. 281–297.

Yokoyama, Yusuke et al. (2011). 'IODP Expedition 325: Great Barrier Reefs reveals past sea-level, climate and environmental changes since the last ice age'. In: *Scientific Drilling* 12, pp. 32–45.

Yokoyama, Yusuke et al. (2018). ‘Rapid glaciation and a two-step sea level plunge into the Last Glacial Maximum’. In: *Nature* 559.7715, pp. 603–607.

Zhang, Yan et al. (2023). ‘Aridification of northwest Australia and nutrient decline in the Timor Sea during the 40 kyr world’. In: *Paleoceanography and Paleoclimatology* 38.10, e2023PA004683.

APPENDIX A

Chapter 2 Supplementary Data 1 - Results

Results supplementary data

Seismic unit 1 **(U1 Burdigalian – BMio)** Seismic unit U1 (ca. 18.3-15.6 Ma) is bounded by H1 at the base (1940 mbRT) and H2 at the top (1720 mbRT) (Fig. 5, Fig. 6). H1 is a regional high amplitude reflector associated with onlap and downlap reflection terminations above. It is continuous in the slope setting and less continuous on the inner platform. Strontium data gives an age of 18.3 Ma and on well data H1 is marked by a GR trough. A regional high amplitude age marker is identified within U1 (1830 mbRT) that is referred to elsewhere in the literature as BB1 (Van Tuyl et al, 2019) and is dated at 17.7 Ma.

Seismic unit 2 **(U2 Langhian – EMio)** Seismic unit U2 (ca. 15.6-12.9 Ma) is bounded by H2 at the base (1720 mbRT) and H3 at the top (1565 mbRT) (Fig. 5, Fig. 6). H2 is a very high amplitude continuous reflector, truncating underlying strata, with some apparent downlap from overlying strata. Biostratigraphic data from well NSR-1 suggests a Langhian age of 15.6 Ma and is referred to elsewhere in the literature as BB2 (Van Tuyl et al, 2019). Concave-upward V-shaped depressions are evident along H2 reflector and corresponds to a trough GR response.

Seismic unit 3 **(U3 Serravallian – MMio)** Seismic unit U3 (ca. 12.9-10.8 Ma) is bound by H3 at the base and H4 at the top (1305 mbRT) (Fig. 5, Fig. 6). H3 is a very high amplitude, continuous reflector throughout the area and is associated with onlap in the slope margin and occasional toplap in the inner slope. Strontium data from well NSR-1 suggests a Serravallian age of 12.9 Ma for H3. A trough reflector with onlap (ca. 11.63) at 1491 mbRT is identified above H3 as a sub-sequence within U3.

Seismic unit 4 **(U4 E-M. Tortonian – ETor)** H4 is very high amplitude, continuous reflector and constitutes a major downlap surface, though some onlaps are seen along the slope margin. Strontium ages from well NSR-1 gives a middle Tortonian age of 10.8 Ma at 1305 mbRT (Table 1), above H4, suggesting a slightly younger early to middle Tortonian age. A prominent high amplitude trough with downlap above and toplap below marks a major break in the mounded seismic character to the East of the survey. It can be tracked laterally beneath SSR with some confidence and continues as medium to high amplitude in this region. A high amplitude peak reflector (ca. 9.7 Ma) at 1228 mbRT is identified above H4, as a sub-sequence within U4. Toplap is observed in the East of the survey.

Seismic unit 5 **(U5 Late Tortonian – LTor)** Seismic unit U5 (ca. 980 mbRT) is bounded by H5 at the base and H6 at the top (910 mbRT) (Table 1, Fig. 5, Fig. 6). H5 is a high amplitude continuous reflector associated with downlapping sediments above and some apparent truncation of strata below, including draping over prograding sigmoidal clinoforms.

Seismic unit 6 **(U6 L. Messinian – LMio)** Seismic unit U6 (ca. 5.5-4.37 Ma) is bounded by seismic unconformity H6 at the base (ca. 940 mbRT), which marks the maximum lowstand of the Late Messinian and H7 at the top (ca. 790 mbRT). H6 is a very high amplitude reflector and constitutes a toplap surface of reflectors below. It is a major downlap surface to the North of SSR. Above H6, a regional, continuous low to

medium amplitude reflector characterises a major transition in seismic character. It is conformable with underlying sediments and overlying strata onlap where it is topographically higher. Data quality is too poor below NSR and SSR to support clear and consistent interpretations here. A biostratigraphic age marker (ca. 5.8 Ma) is taken from well data NSR-1 at 910 mbRT above H6, putting an estimated age of mid to Late Messinian for H6.

Seismic unit 7 **(U7 E.Pliocene – BPlio)** Seismic unit U7 is bound by H7 at the base (ca. 3.7-4.37 Ma) and H8 at the top (ca. 2.5 Ma). The seismic character between H6 and H7 is predominantly continuous, medium to low amplitude with parallel reflectors dipping basinward. H7 is a weak to medium amplitude, highly continuous, parallel reflector with onlapping sediments.

Seismic unit 8 **(U8 M. Pliocene – MPlio)** Seismic unit U8 (ca. 3.5 Ma) is bounded by H8 at the base and H9 at the top (ca. 1-0.8 Ma). H8 is a weak to medium amplitude, continuous reflector with onlapping sediments away from modern day Scott Reefs, and a low-medium, semi-continuous reflector beneath SSR and a very high amplitude, continuous reflector below NSR. Onlap above and toplap below is identified below NSR, while it is difficult to determine below SSR due to poor data quality.

Seismic unit 9 **(U9 L. Pliocene-E. Pleistocene – BQua)** Seismic unit 9 (ca. 1-0.8 Ma) is bound by H9 at the base and H10 at the top. H9 is a medium to high amplitude semi continuous reflector with some onlap above. Concave upward V-shaped features from 10's of m's across to 100's of m's are seen in section view. A larger U-shaped depression is evident to the North of SSR with vertical height difference being ca. 50 m and is conformable with underlying and overlying strata. A similar observation can be made below the South of NSR but is inconclusive due to the noisy, chaotic seismic reflections below modern reef crest.

Seismic unit 10 **(U10 Mid Pleistocene – MPl-1)** Seismic unit U10 (ca .0.8-0.6 Ma) is bound by H10 at the base and H11 at the top. H10 NSR is a high amplitude, continuous, reflector with onlap above and toplap below (Table 2). H10 SSR is a continuous weak to medium amplitude reflector with wavy undulating topography. It is an onlap surface and was correlated with NSR that sits topographically higher but with greater lateral variation in topography. H10 is parallel and conformable with the trend of two previous sequences, each ca. 100 m thick.

Seismic unit 11 **(U11 Mid Pleistocene – MPl-2)** Seismic unit U11 is bound by H11 at the base and H12 at the top. H11 NSR is a medium to high amplitude, continuous surface that sits topographically lower than H11 SSR. H11 has an overall gently dipping SE trend and the seismic reflection character is laterally and vertically variable with respect to thickness, topography and reflection strength. H11 SSR is a medium to high amplitude, wavy, semi-continuous surface with onlap above and toplap below. It is intermittently broken by positive mounded relief. A topographic concave-down depression ca. 50 m high by 1 km wide with associated onlapping strata is seen to the SE of SSR.

Seismic unit 12 **(U12 Late Pleistocene-2 – LPl-2)** Seismic unit 12 is bound by H12 at the base and H11 at the top. H12 is picked initially on SSR and tracked across to NSR. It is a medium to high amplitude semi-continuous reflector that varies laterally across NSR and is disturbed in the centre by high amplitude, wavy, discontinuous reflectors. H12 is more prominent over SSR and is identified by toplap below and onlap above (Table 2). It is variable, patchy and discontinuous to the West of SSR owing to poor data quality. Topographic variations exceeding up to 30 m are observed around the inner SSR platform and the topographic lows are commonly associated with onlap strata, whereas topographic highs are associated with toplap below and subsequent onlap.

Seismic unit 13 **(U13 Late Pleistocene-2 – LPl-2)** Seismic unit 13 is bound by H13 at the base and H14 at the top. H13 NSR is a high amplitude, moderately continuous reflector, characterised by a bucket shape morphology, including raised margins (Harris et al, 2015). H13 SSR is a very high amplitude reflector truncating toplap sediments below (Table 2). Amplitude strength becomes increasingly incoherent towards the centre of SSR and NSR platforms. H13 truncates underlying strata below the present-day central lagoon. It is more consistent and easy to correlate on the NSR margins where seismic character is more continuous. H13 NSR and SSR can be tracked to the platform margins where bursts of very high amplitude discontinuous chaotic reflectors are identified.

Seismic unit 14 **(U14 Late Pleistocene-3 – LPl-3)** Seismic unit U14 (ca. 115 mbRT) is bound by H13 at the base and water bottom at the top (present day seafloor, ca. 41 mbRT NSR and ca. 61 mbRT SSR). U14 is up to 80 m thick in the lagoon depocentre and is the first peak reflector below the water bottom trough for both NSR and SSR. H14 NSR is a very high amplitude, semi-continuous reflector, up to 20 m thick and occasionally disrupted by the above water bottom due to velocity pull-ups. H14 NSR truncates below strata. Towards the present-day reef margin and the centre of NSR, the reflector becomes chaotic and uncorrelatable with vertical offset apparent on the margins. H14 SSR is a high amplitude continuous reflector truncating below strata and lies parallel to the seabed. It sits topographically higher than SSR.

Seismic facies 1 (SF1): Clinoforms with sigmoidal (SF1.1) and parallel (SF1.2) configuration:

Seismic facies SF1 is composed of medium amplitude seismic reflectors, with mounded sigmoidal clinoform external geometries, and high-angle inclined prograding strata reflectors downlapping underlying strata. SF1.1 displays sigmoidal internal configurations of lower amplitude and transition to SF3 or SF5 towards the platform interior, and SF1.2 shows parallel clinoform patterns that develop basinward into SF6, SF8 or SF9. SF1.1 seismic reflectors extend for up to 10 km basinward, whereas the lateral extension of SF1.2 is predominantly less than 1 km. Recognition of SF1.2 is often heavily affected by noise/multiples from overlying modern reef. SF1 is observed on the outer flanks of the carbonate platform margins. High amplitude

continuous reflectors are identified but uninterpreted as seismic unconformities or sub-sequences within SF1 that usually signals a transition from aggradational to progradational geometries.

Seismic facies 2 (SF2): Mounded seismic reflectors (platform margin)

Seismic facies SF2 represents mounded seismic reflectors that occur specifically along a platform margin. They display a range of weak to high amplitude, semi-continuous and parallel to chaotic seismic reflectors. Adjacent seismic facies associations are mainly SF1.2, SF3 and SF9. SF2 is commonly surrounded by reflector geometries that indicate the presence of onlap and depositional wings (forereef facies, i.e., SF1.2), significant local thickening and a common antecedent topography. The seismic facies commonly display a continuous high amplitude reflector cap at the top, and velocity pull-ups below.

Seismic facies 3 (SF3): Horizontal parallel seismic reflectors (platform interior)

Seismic facies SF3 constitutes sub-parallel to parallel, continuous, and high amplitude seismic reflectors that occur in the platform interior in common association with SF4. External geometries range from sheet to wavy with vertical thickness varying laterally between 10 and 20 m. Other common associations are SF1.1, SF2, SF4, SF5 and SF7 (vertically).

Seismic facies 4 (SF4): Mounded seismic reflectors (platform interior)

Seismic facies SF4 corresponds to mounded seismic reflectors observed in the platform interior. They are commonly located with SF4 and are commonly successive in section view. These mounded features are 10-20 m high and <400 m wide high with downlapping strata. Internally, they are convex up and often medium to high amplitude with good continuity. They transition laterally to SF5 and occasionally vertically to SF7.

Seismic facies 5 (SF5): Chaotic seismic reflectors (platform interior)

Seismic facies SF5 is a semi-discontinuous chaotic, wavy, medium to low amplitude facies that is regarded here as transitional. Sharp lateral transitions can occur with SF3 in the platform interior and with SF2 and SF9 in a platform margin setting. Beneath SSR, SF5 is particularly chaotic and wavy, extending vertically ca. 500 m with occasional concave-down V-shape depressions (not to be confused with SF7 out of context).

Seismic facies 6 (SF6): Chaotic seismic reflectors (platform slope)

Seismic facies SF6 is a very chaotic, seismic facies that is seen occasionally on both the proximal and distal platform slope. They are characterised by moderate to high amplitude strength, high angle reflectors with instances of sigmoidal downlapping strata, but more commonly – sharp truncations and low continuity. The chaotic nature puts them in association with SF1, SF8 and SF9. With increasing distance from the platform margin, higher amplitude, irregular, semi-continuous bursts extending up to 1 km in length are observed and commonly disrupts the modern seafloor reflector.

Seismic facies 7 (SF7): Concave-up seismic reflector

Seismic facies SF7 are sub-circular concave-down seismic reflectors that are easily identified by negative V-shaped depressions and occasionally chimney-like features. The internal configurations are chaotic to patchy with medium amplitude, semi-continuous reflectors, occurring in lateral proximity to SF3 and SF4, otherwise, always occurring in a platform interior.

Seismic facies 8 (SF8): Double dipping seismic reflector

Seismic facies SF8 is composed of weak reflectors that are identified by double onlapping terminations. They are highly continuous and parallel occurring next to SF6 and SF1.2. They extend across the entire eastern section of the survey at times and are characterised by typically thin vertical thicknesses, less than ca. 30 m.

Seismic facies 9 (SF9): Parallel seismic reflectors surrounding platform

Seismic facies SF9 includes parallel seismic reflectors surrounding the platforms in a deep-sea setting. They are parallel, or occasionally forming toplap and onlap surfaces for the overlying and underlying strata, respectively. Strata packages vary in thickness between 20 and 60 m and are occasionally slightly wavy and extend for 10's of km's dipping basinward. They are horizontal, parallel to sub-parallel and can display lenticular, convex-up external geometries between the smaller platforms, often associated with onlap onto SF2. Internal configurations display sheet structures with very high amplitude and high continuity, occurring in proximity to SF1.1, and are frequently bound by SF2 or SF5. In some instances, e.g., below SSR, a thick unit of SF9 presents an overall concave shape over about 5 km, with the base of the unit being an erosional (toplap) unconformity.

Geomorphologic Pattern 1 (GP1.1 and GP1.2) – medium to steep gradient feature

Geomorphologic pattern GP1.1 occurs basinward along a continuous margin identified on variance attribute. It is characterised by a medium amplitude and low to medium frequency. In plan view, a linear, sinuous edge can often be detected. GP1.2 in map view is similar to GP1 but with steeper gradients in the Plio-Quaternary sequences.

Geomorphologic Pattern 2 (GP2) – curvi-linear feature (platform margin)

Geomorphologic pattern GP2 is observed along the platform margin as a continuous sinuous to linear pattern or as a curved, stepped morphology with occasional concentric growth rings. A gradual, stepped gradient is observed in high pass frequency filter and exhibits low amplitude and low frequency.

Geomorphologic Pattern 3 (GP3) – sub-circular to elongate feature (platform interior)

Geomorphologic pattern GP3 displays a very high amplitude and frequency and no character in variance attribute. The plan view feature displays little character variation and is associated with a sinuous, irregular

circumference with only a gentle change in gradient on high pass filters. It is associated with SF3 on section view, which is a high amplitude, parallel, continuous reflectors located on the inner platform.

Geomorphologic Pattern 4 (GP4) – circular to sub-circular feature (platform interior)

Geomorphologic pattern GP4 is identified by general circular to sub-circular features with locally steep gradients and sub-circular discrete features on variance attribute plan view, with low to medium amplitude and low frequency.

Geomorphologic Pattern 5 (GP5) – discrete, patchy, grouped features (platform interior)

Geomorphologic pattern GP5 displays low to medium amplitude and frequency and occasional significant gradient variation with a plan view configuration of collective patchy small sub-circular patterns confined to the inner platform and in front of leeward prograding margins.

Geomorphologic Pattern 6 (GP6) – chaotic feature (platform margin)

Geomorphologic pattern GP6 is characterised by irregular low to high amplitude and frequency, identified in plan view by chaotic disturbed regions encompassing both linear to sub-circular patterns.

Geomorphologic Pattern 7 (GP7) – sub-circular to linear features (platform interior)

Geomorphologic pattern GP7 is identifiable by sub-circular discontinuities, medium amplitude and medium to high frequency and sub-circular to sub-linear, occasional sinuous features in plan view. Observed gradient can be locally steep to variable.

Geomorphologic Pattern 8 (GP8) – uniform, sinuous feature

Geomorphologic pattern GP8 occurs as a weak to medium amplitude and low frequency, uniform geomorphologic pattern, with an unidentifiable gradient in plan view. It is regularly characterised by prominent sinuous waves and occurs in association with GP2.

Geomorphologic Pattern 9 (GP9) – uniform feature surrounding platform

Geomorphologic pattern GP9 is a high amplitude, low frequency feature with uniform, homogeneous geometry in plan view surrounding the carbonate platforms, often identified basinward of GP2 and is interpreted on variance as continuous facies.

APPENDIX B

Chapter 2 Supplementary Data 2 - Interpretation

Interpretation supplementary data

Paleogeographic evolution of Scott Reefs

Six interpretative maps were designed (Fig. 9) to describe the evolution of Scott Reefs from the Burdigalian to the Middle Pleistocene.

Figure 9 Paleogeographic maps of carbonate factory evolution

Miocene (U1-U6)

The Miocene seismic sequence consists of U1-U6 and is characterised by a prograding barrier reef system. There is an apparent inner platform reef evolution from; small patch reefs, to small ICB's, and to larger ICB's that eventually coalesce in the mid to late Miocene, and finally to larger carbonate platforms. This is consistent with Browse Basin literature (Rosleff-Soerensen et al, 2012; Van Tuyl et al 2019, McCaffrey et al, 2020; Riera et al, 2022,). Preceding the Miocene (not investigated in this study) is the development from a ramp-type to a rimmed platform, which has prepared the shelf for tropical reef growth by stabilization and formation of hardgrounds. This is regarded as a common pattern for carbonate shelf evolution (Schlager, 2005; Rosleff-Sorensen et al, 2012; Saqab and Bourget, 2015; Paumard et al, 2019, Riera et al, 2019).

Figure 10 Evolution of Miocene ICB's

Figure 11 Cross-section profile and 3D map showing vertical evolution of Miocene ICB's

Carbonate factory Phase I

Seismic unit U1: Burdigalian (B. Mio). H1 is interpreted as a sequence boundary that marks a regional transition from a carbonate ramp setting to an aggradational phase associated with coralgal community growth and isolated carbonate build-up development on the inner platform (Saqab, 2015). Seismic Unit U1 (Tile 1, Fig. 9) represents a range of carbonate depositional environments, including a barrier reef >25 km in length. In plan view, the seismic geomorphology of H1 represents a barrier reef crest (GP2) trending NE-SW parallel to the platform margin. Channels are seen on the outer slope, and small patch reefs (SF4 and GP4) associated with lagoon facies (SF3 and GP3) in the inner carbonate platform. Shoals (GP5) border the outer shelf, as seen on variance attribute (Fig. 10A). A high pass frequency filter shows evidence of small ICB's forming on the shelf margin and a large ICB below the NE crest of modern day SSR oriented perpendicular to the platform edge (Tile 1, Fig. 9), and patch reefs (SF4 and GP4) confined to a narrow belt parallel to the barrier reef crest (e.g., Tile 1, Fig. 9). To the south of the survey, a ca. 5 km elongated carbonate platform sits on the outer barrier reef crest and is separated by a 2 km wide seaway from a smaller carbonate platform. H2 divides U1 and U2 and is characterised by increasing numbers of isolated patch reefs in the platform interior. Isopach data from U1 shows high sediment thickness (ca. 200 m) on the inner platform shelf and thinning gradually basinward.

Seismic unit U2: Langhian (E. Mio) (ca. 15.9 Ma, correlated to *T35.0 SB TM2*, Fig. 20). H2 is regional sequence boundary marking the base Langhian. It is conformable to the overlying strata and is part of a series of basinward (West) prograding, dipping packages. Seismic Unit U2 continues as a basinward prograding barrier reef system, leaving a stepped pattern of reef crest migration (Fig. 8, GP2; Table 4). Shoal deposits are interpreted ca. 1-2 km landward of the reef crest, in patches (Fig. 8, GP5; Table 4) and are more abundant to the NE along H2. Two small (<1km) E-W oriented faults are visible to the West on the outer slope, and is consistent with fault reactivation at this time interpreted in the Poseidon 3D survey to the NE (Van Tuyl et al, 2019). A lagoonal environment is interpreted with sparser patch reefs, but several larger distinct circular isolated carbonate buildups appear to the South-East, ranging in size from 600-1800 m in width. The increase in lagoonal sediments as evidenced by high amplitudes in plan view attribute maps (Fig. 8, GP3, Table 5) and section view (SF3, Table 6), suggests that the barrier reef crest is sufficiently linear and consolidated at this time to create a more closed marine environment in the platform interior. Rosleff-Soerensen et al (2012) also find a distinct relationship between the demise of the barrier reef and subsequent control on the patch reef distribution. Patch reefs are limited to areas exposed to open marine conditions where the reef crest is broken or discontinuous along BR1, which corresponds in depth to H2. Along H2, SF4, corresponding to GP4, exists in a range of scales from <100 m to >1 km and is apparent on the inner, middle and outer platform areas, including the very edge of the carbonate platform margin. Basin sediments (GP9 and SF9) are interpreted in section view (Fig. 6) along H2 onlapping onto the platform margin.

Seismic unit U3: Serravallian (M. Mio) (ca. 12.9 Ma *SB*). Sequence boundary H3 corresponds to an exposure event during a RSL fall. A resulting karst sequence (SF7 and GP7, Fig. 2) is interpreted with collapsed dolines (sinkholes), infilled karst valleys/streams and vertically continuous karst caves that are directly above smaller ICB's in seismic unit 2, (Tile 2 of Fig. 9). An onlap stratigraphic event within U3 (see H3a in Fig. 20) is interpreted as a sequence boundary but not described in this study. This SB corresponds to the regional pick T37.0 SB (TM1) (Gradstein et al, 2012; Powell, 2020). Karst is interpreted in the inner carbonate platform and is identified as densely distributed low amplitude (white) circular patches <50 m in circumference in plan view (Fig. 8, GP7; Table 4). Apparent gradient change is visible in high pass filters, with a low topographic centre and raised margins. GP7 corresponds to SF7 in section view, which is identified as sub-circular, negative V-shaped depressions. The sinuous carbonate platform margin trending E-W across the survey is also interpreted here as a karstified platform edge (Fig. 12; Fig. 13). This feature was initially identified as a large channel; however, section view (SF7) showed no evidence of onlap (Fig. 13). Instead, a trough collapse (concave-down) feature is identified (Fig. 9, Tile 2; Fig. 13) and the geomorphology elsewhere along unconformity H3 provides further evidence of an exposure surface, and as such is interpreted as a non-depositional surface. For example, a doline is interpreted in the SE of the survey and is supported by interpretations of high amplitudes in high pass frequency attribute map view (Fig. 12A), that is probably caused by cementation of the reflector H3 during subaerial exposure of the proximal regions of the survey. This karst horizon coincides with a global (eustatic) RSL fall recorded in the Browse basin before the

Serravallian-Tortonian boundary by Rosleff-Soerensen et al, (2012). They also observe similar karst trough and doline features during two phases of barrier reef exposure in the Miocene.

Figure 12 Attribute maps showing evidence of subaerial exposure in the East of the survey during the Miocene

Figure 13 Cross-sections from Fig.12 showing section view of karst features

Carbonate factory Phase II

Seismic unit U4: Middle Tortonian (M. Tor) U4 is a period of continued reef expansion with larger isolated carbonate platforms interpreted on the inner shelf to the centre and north of the survey and to the south west (Tile 3, Fig. 9). H4 is a prominent downlap surface and marks the maximum transgression and is thus interpreted as a maximum flooding surface marking reflooding of the shelf and the re-establishment of reef growth after U3. Seismic attribute maps suggest there is no more evidence of the barrier reef along H4. It is interpreted that the H3 karst event preceded the demise of the barrier reef, or at least is not visible in the survey at this time. Rosleff-Soerensen et al (2012) also interpret the demise of the barrier reef after this karst event, as well as a eustatic RSL rise. A toplap stratigraphic event within U4 (see H4a in Fig. 20) is interpreted as a sequence boundary but not described in this study.

Plan view geomorphologic patterns and section view stratal relationships (Fig. 10C) agree with the Van Tuyl et al (2019) interpretation of ICB leeward progradation and windward shedding from westerly winds in the Poseidon 3D survey to the NE. This contrasts the Rankey (2020) interpretation in Torosa field to the south, which shows the opposite, with windward progradation directed by easterly trade winds. Similar interpretations by Rosleff-Soerensen et al (2012) lead to the conclusion of reef detritus on the leeward side of the ICB's due to unidirectional currents. So, at this time, (U4, ca. 10.8 Ma) evidence of increasing current strength is interpreted in the Torosa field, however, this is usually associated with drift deposits (SF8) (Betzler et al, 2009). No evidence of SF8 or GP8 is interpreted in the area. Instead, IPSW sediments (SF9) are interpreted as onlapping the ICB's.

To the south and west of the survey, small patch reefs are identified in plan and section view on the platform margin and evidence of a larger platform/topographic high is seen to the SW, below present SSR (Tile 3, Fig. 9). A gradient change is seen in map view trending N-S moving from topographic platform high to the east and sloping down basinward to the west, with the exception of the isolated platform to the SW, which is separated by an IPSW. High pass attributes show evidence of sediment flows (tidal outlets/channels?) basinward to the NW of the survey. Sub-sequences are identified by rapid aggradational geometries locally within the ICB's in U4, as reefs keep up with sea level rise. They are interrupted as high level (4th/5th order) exposure events seen as high amplitude reflectors that are confined to the East of the area and do not extend laterally throughout the survey (Fig. 8).

Seismic unit U5: Early Messinian (E. Mes). Seismic unit U5 demonstrates a sharp transition from large isolated carbonate buildups ca. 10 km in length with well-established inter-platform seaways, to coalescing

carbonate platforms with double reef crests in H5 and a North-South oriented sinuous carbonate platform margin. H5 is interpreted as a sequence boundary associated with increasing outer shelf subsidence >150 m/Ma (McCaffrey et al, 2020). This resulted in increasing sediment influx and basinward prograding clinoforms. The modern day SSR is an example in scale and morphology for the double reef crest (Fig. 11) seen to the SE of the survey, and is an indication of both margins being exposed to open ocean currents. Both crests prograde outward leading to an increase in carbonate platform extent. Noise surrounding the NSR crest distorts much of the plan view geomorphologic character, nevertheless, three smaller ICB's can be seen in a triangle below modern day NSR along the edge of the platform margin (Tile 4, Fig. 9), identified by high amplitude sub-circular geomorphologic patterns on RMS attribute maps. This elevated platform is interpreted as the foundations for the first stage of the modern-day isolated carbonate platform. Gravity slumps are interpreted to the NW of NSR that suggests high volumes of carbonate material is being shed off the platform during this highstand (highstand shedding) and is interpreted as early contouring of the platforms with moats identified around the margin (e.g., Fig. 14) (*sensu* Betzler et al, 2019). Small patch reefs (SF4) can be seen behind the double reef crest in the SE in a lagoon setting (Tile 4, Fig. 9), suggesting that there is continued reef growth on topographic highs during this sea level rise.

Fluid escape features are seen to the NE of NSR crest throughout U5 and into U6. They are identified as vertical negative displacements of the horizontal seismic reflectors in section view and circular features ca. 50 m in plan view can in some instances be traced to below the Miocene. Studies (Van Tuyl et al, 2019) interpret similar features in the Poseidon survey to the NE as possible hydrothermal vents or hydrocarbon migration pathways ongoing due to Tertiary fault reactivation. These geomorphologic features lie to the NE of the Jurassic Scott Reef fault block, and their ongoing presence suggests continued sub-seismic resolution faulting persisted throughout the Cenozoic.

Seismic unit U6: Late Messinian (L. Mes) (ca. 5.9 Ma, correlated to *T40.0 SB TM1*, Fig. 20) H6 corresponds to the late Miocene and is interpreted as a major regional sequence boundary that marks the top of an aggradational package. The isolated buildups identified in U5 show complex episodes of aggradation, progradation and backstepping (e.g., Fig. 10C) and subsequently merge with adjacent platforms in U6 to form composite systems (Tile 4, Fig. 9; Table 5; Rankey, 2020). This composite system is a vertically aggrading, elongated platform that extends to an elbow shape platform into the adjoining Poseidon 3D survey.

Three key geomorphologic patterns and seismic facies associations are evident; (1) GP1.1 occurs along the platform margin in plan view as a linear, sinuous (S-shaped) edge trending N-S with a steep gradient to the north and a more stepped plan view profile to the south (Tile 4, Fig. 9 and Fig. 14C). It is perpendicular to GP2 (reef crest) along H6. GP1.1 corresponds to SF1.1 in section view, which are identified along H6 as high angle, sigmoidal, mounded clinoforms prograding basinward (West) (Fig. 14). (2) An IPSW (SF9), ca. 7 km wide and 20 km long is interpreted, trending parallel to GP1.1 and confined to a narrow belt between the platform margin (GP1.1) and another topographic high to the SW (Tile 4, Fig. 9). This feature is identified by onlap onto the ICB margins as GP9 in plan view. (3) The geomorphologic pattern GP5 (shoal) is interpreted

along H6 to the SW of SSR. On section view SF5 is deposited adjacent to SF1.2 on the inner platform and SF6 along the platform margin SW of SSR. SF6 (MTD's) are identified by short bursts of high amplitude chaotic facies in section view and low to high amplitude, discrete low frequency patterns in plan view, corresponding to GP6 (Fig. 8, GP6).

Figure 14 shows the stepped platform profile transitioning from the eastern topographic high to the western low where the N-S trending IPSW (SF9) separates the eastern platform from a large ICB or isolated carbonate platform in the South-West, extending 7-10 km in length (that is not fully resolvable on seismic due to a data gap) (Tile 4, Fig. 9). These two platforms subsequently expand and merge (from U6 to U14), with transitional shoal facies (SF5) and downlapping reef apron deposits indicating leeward progradation, interfingered by deposition of IPSW (SF9) sediments. Thus, it is interpreted that SSR initiates on the offbank prograding clinoforms of the platform margin during a marine transgression.

Pliocene (U7-U8)

The Pliocene sequence is bound by H7 and H8 and is characterised by a significant reduction in the size of the carbonate factory. The Pliocene sequence is homogeneous with respect to seismic facies diversity. Thick, high amplitude conformable and continuous reflectors consistent with lagoon facies characterise the inner platform with basin sediments on the basinward outer platform margin. Despite a eustatic highstands in the Pliocene, evidence of karst is interpreted throughout U7 and U8 on the Eastern half of the survey as well as on the NSR and SSR platforms. This is evidence of higher order sequences and possibly lower sea level on the inner shelf than previously described for the Pliocene (Qin et al, 2022), however, the resolution of the seismic is insufficient to interpret them in this study. Nevertheless, this seismic unit defines the key shift from ICB's drowning on the inner platform – where suspended sediment reduced light penetration and thus inhibiting carbonate growth (Van Tuyl et al, 2018) - to the onset of the pre-cursor Scott Reef ICB's on the outer shelf margins.

Figure 14 Seismic attribute maps showing initiation of SSR

Carbonate factory Phase III

Seismic unit U7: Early Pliocene (E. Plio). H7 is interpreted as the base Pliocene 'drowning' unconformity and is the most recent horizon (ca. 4.8 Ma) constrained by biostratigraphic data (Table 1) in the Megator seismic dataset. Unconformity H7 follows an aggradational sequence (U6, Fig. 16) and is consistently documented (Van Tuyl et al, 2019, Belde et al, 2015) as the demise of the carbonate factory in the Browse basin. However, several characteristics, including a major conversion between seismic facies, suggest this reflector is, instead, a transition to a reduced carbonate production factory localised to topographic highs (Fig. 16).

Downlap and mound shaped, positive relief features (SF4 – patch reef) continue above H7 below North SSR and is interpreted as continuation of *in situ* carbonate reef growth despite a highstand/flooding event. Concave

down V-shaped depressions, interpreted as karst (SF7) are identified on the South-West isolated high - suggesting the platform was periodically exposed during U7. MTD's (SF6 and GP6) are identified along the platform margins (e.g., Tile 5, Fig. 9).

The platform margin to the North of NSR remains a topographic high and sediments, including gravity slumps downlap onto the slope and basinward where erosion has transported large volumes of sediment off the platform (highstand shedding) (Fig. 8, GP6; Table 4). It is noted that this topographic high is directly above the Tertiary rifted Scott Reef trend, implying that tectonic reactivation may have controlled the continuous development of this reef sequence. Similarly, the continuation of reef building below SSR occurs directly above a precursor Miocene ICB (Tile 1, Fig. 9) on the continental margin, but which likely remained a topographic high for later stage reef establishment or could indicate reactivation of basement faults that were originally responsible for confining carbonate accumulation to this isolated high (Burgess et al 2013). H7 is interpreted across SSR with uncertainty due to significant chaotic reflectors (Shoal facies), however, the consistency of interpretation comes from context of facies associations tracked vertically and laterally throughout the seismic survey.

Most notably, there is no evidence along this reflector of *in situ* carbonate production in the East of the survey, (i.e., GP1 and SF1 or GP2 and SF2). Elongate sediment drift bodies (SF8) downlap onto the H7 reflector along the eastern half of the survey, blanketing the preceding carbonate platforms (Tile 5, Fig. 9; Fig. 8, GP8; Table 4). This is consistent with a partial drowning interpreted elsewhere in the Browse basin (Rosleff-Soerensen et al, 2012; Rankey, 2020). There is also evidence of early formation of current controlled moats (Tile 5, Fig. 9). The depression to the east of SSR (Fig. 19) is described as a moat and not a velocity pull-up. The feature does not sit directly below the modern-day moat (hence not a reflection artefact), and evidence on seismic shows a lateral transition of this facies (Fig. 19). This suggests it migrates with the platform slope with increasing ICB size. Large areas of shoals (GP5) (Fig. 15B) are also identified by a series of migrating channel belts (plan view) and a U-shaped depression (section view) deposited between NSR and SSR, similar to ooid shoals in the modern Great Bahama Banks (e.g., Harris et al, 2015).

Seismic unit U8: Middle Pliocene (M. Plio) H8 (ca. 3.5 Ma, correlated to *T45.2 MFS TPL*, Fig. 20) truncates underlying strata and is interpreted to be a maximum flooding surface across the entire survey (U7). Carbonate drift sedimentation, characterised by double downlap (Fig. 8, GP8 and Fig. 7, SF8; Table 3; Table 4) continues to be deposited in the eastern half of the survey. However, negative depressions indicative of karst (SF7) below both NSR and SSR suggest topographic highs remained periodically exposed during this maximum marine transgression.

H8 is characterised by two main isolated topographic highs and a steep descent basinward with canyons and a well-established inter-reef channel. A reef crest (SF2) is apparent to the North and South of NSR identified by mounded positive topographic relief, prograding leeward and windward (Fig. 15 and Tile 5, Fig. 9). Established lagoon facies (SF3) and associated patch reefs and shoal are identified on the inner NSR platform

(Fig. 15). The reef slope (SF1.2) of both NSR and SSR is steep with respect to the surrounding seafloor, becoming raised isolated carbonate platforms. Overall, the gradient across H8 is highly variable. The eastern half of the survey and inter-reef channels are between 600-700 m depth and descends rapidly basinward to ca. 1500 m.

Quaternary (U9-WB)

The Quaternary sequence is bounded by H9 and WB. No biostratigraphic markers are available for the Pliocene-Pleistocene boundary and are inferred from seismic and well log data, and regional Quaternary literature (Table 1). The Quaternary geomorphology is dominated by episodic, aggradational reef turn on events and variable lateral facies distributions. Poor seismic quality beneath NSR makes it difficult to trace unconformities across the steep flanks and thus between both reefs. It is inferred that major unconformities H10-H14 correlate; however, it is possible that higher order unconformities are locally specific to each reef system. A change in seismic facies from chaotic, mound shape to more continuous, parallel to sub-parallel seismic facies implies a change in depositional processes. A regional transgression marking the Plio-Pleistocene boundary (H9) suggests a change from ICB and reef crest aggradation on topographic highs in 'catch up' phase, to larger isolated carbonate platforms in 'keep up' phase, with consistent and established lateral facies hierarchy. This also suggests a transition to a more stable tectonic setting, (reduced or steady subsidence) and a decrease in the supply of allogenic clastic detritus. This resulted in a shift from siliciclastic and carbonate hemipelagic deposition to a more restricted and protected shallow marine environment, with local uninterrupted carbonate production.

Seismic unit U9 (L. Pliocene - E. Pleistocene) *and* ***seismic unit 10 (Middle Pleistocene MPl-1).*** U9 is interpreted to be Late Pliocene – Early Pleistocene and is inferred as the base Quaternary (B. Qua), ca. 1-0.8 Ma. Seismic unit U9 and U10 represent a change in seismic facies from chaotic, high amplitude reflectors to conformable and aggradational, repetitive, cyclic sequences. Several reflectors throughout U9 and U10 are interpreted as subaerially exposed due to evidence of karst features, (i.e., V-shaped depressions on section view (SF7) and high amplitude sparse, small circular patterns on plan view (GP7)). This suggests, it is a lagoonal environment below SSR with periods of RSL fall and exposure. Significant gravity slope deposits to the east of NSR seen in cross section (chaotic high amplitude reflectors – SF6) and plan view (high amplitude, chaotic reflectors on RMS amplitude and variance attribute maps – GP6) (Fig. 15), suggests the raised reef rims are exposed to high wave energy and offbank transport. GR log data shows moderate amplitude cycles throughout this unit, but overall low GR values (Fig. 17, Fig. 18), indicative of carbonate deposits (sensu Gallagher et al, 2014 and Saqab and Bourget, 2019). Mounded, chaotic reflectors are seen downlapping onto H9 over NSR and suggests there may have been continued carbonate production on regional highs. The cross-sectional geomorphology of SSR draws comparisons to the 'unbalanced aggrading/onlapping' reef anatomy model proposed by Kennedy and Woodroffe (2002) and described for Indo-Pacific reefs by Montaggioni (2005). This model suggested vertical accretion rates of coral frameworks was highly variable. This could therefore suggest that there is higher variability of coral framework facies in SSR than NSR. This concurs

with the present-day facies' distribution and diversity across NSR and SSR (Green, 2018; Collins, 2002; Collins & Testa, 2009).

Figure 15 Seismic attribute maps showing initiation of NSR

Figure 16 Uninterpreted seismic section and concept sketch of NSR initiation and development

Carbonate factory Phase IV

Seismic unit U11: Middle Pleistocene (MPl-2). The geomorphology of seismic unit U11 reflects a key change in seismic facies. Mounded seismic features (patch reefs) on section view (SF4) and high amplitude sub-circular features ca. 20^{+}m in plan view (GP4) in variance and spectral decomposition seismic attributes (Fig. 15) are evident along H11. Larger patch reefs are interpreted below SSR, whilst reef crest (GP2) is widest and more complete around NSR. High pass attribute maps reflect the steep slope that descends to the basin and canyons traversing ca. 150 m on the Western flank of NSR (Tile 6, Fig. 9). Drift sedimentation persists along the eastern section of the survey and is interrupted by a large debris fan (ca. 10 km in length) between NSR and SSR flowing landward (Tile 6, Fig. 9).

H11 is interpreted as the mid-Pleistocene climate transition, where sea level amplitudes changed to high amplitude, low frequency with rapid deglacial RSL rise and slow falls. It is apparent that this triggered reef growth on both NSR and SSR during a general eustatic sea level fall. This is contrary to general thought that reefs grow preferentially during a marine transgression (Burgess et al, 2013). By this time, NSR and SSR are developed as isolated platforms on the distal carbonate ramp margin (i.e., Tile 6, Fig. 9).

Figure 17 Seismic section profile with GR logs showing key events of siliclastic influx and MPT 'turn on'

Figure 18 Zoomed in seismic section showing H11 (MPT) initiation/reef 'turn-on' and seismic attribute maps of NSR and SSR with GR log profiles and interpreted lithologic columns

Seismic unit U12 (Late Pleistocene (LPl-1) *and* ***seismic unit 13 (Late Pleistocene LPl-2).*** H13 truncates underlying strata that aggraded in a previous depression over present day central lagoon, and so it is determined to be a truncation unconformity with onlapping strata. Seismic units 12 and 13 are interpreted to be a continuation of phases of rapid reef crest growth (GP2 and SF2) separated by thin weak chaotic reflections of SF5 (i.e., shoal), representing sediment reworking and lagoon infilling and onlapping the reef crest during periods of slow RSL fall. The mounded highs are consistent with patch reef geomorphology in plan view (GP4) and section view (SF4). It is apparent that SF4 occurs above SF4 in previous units (e.g., Fig. 18), indicating they are either reflection artefacts or genetically related patch reefs persisting throughout the Late Pleistocene, i.e., continuing growth on established topographic highs within the lagoon. The latter is interpreted based on variation in the succeeding onlapping sediments. Enhanced subsidence and recurring sea level highstands (Collins et al, 2014) clearly results in a pattern of repetitive reef stacking that is aggradational on seismic data. GR log data shows high amplitude cycles throughout U12 and U13, and overall decreasing GR values that are interpreted as more homogeneous, cleaner carbonate deposits towards the top of the unit

(Fig. 17). Some peaks may correlate to fluctuating sea levels of the late Quaternary (e.g., Saqab and Bourget, 2019).

Seismic unit U14: Late Pleistocene (LPl-3). H14 SSR and H14 NSR are identified as erosional unconformities. Seismic unit U14 constitutes an isolated, raised carbonate platform environment, with a significant expanse of lagoonal facies, patch reefs, reef crest, shoals and sand aprons (and channels?) on the inner platform (Fig. 2). The lateral facies distribution is similar to the modern benthic environment, e.g., Fig. 1C. Collins & Testa, (2009) provide U/Th ages from core samples, which can be correlated to U14 NSR. This provides an estimated age of ca. 0.098 Ma, which pre-dates the onset of the Last Glacial Maximum. This suggests that seismic unit 14 extends from ca. MIS 5 to MIS 1. Post glacial sea level rise (ca. 0.019 to 0.007 Ma, Webster et al, 2022; O'Leary et al, 2020) inundated the shelf and some evidence of this can be seen above SSR U14 with sediments onlapping the reef crests. Isopach data shows high sediment thickness toward the centre of both NSR and SSR, representing the lagoon environment. This high sedimentation rate, a flattening of the seismic reflectors, (i.e., fewer patch reefs) and sediments onlapping the reef crests suggests a rise in RSL and continued 'keep up' mode of sedimentation. Mounded drift sedimentation remains apparent on the reef slope flanks, suggesting continued strong currents.

APPENDIX C

Chapter 2 Supplementary Data 3 - Movie of Megator 3-D seismic data

---

A supplementary video illustrating the 3-D Megator seismic volume with the spectral decomposition attribute described in Chapter 2 is available online at: https://youtu.be/aAnWMbAcJx4

APPENDIX D

Chapter 3 Supplementary Information - Raw NCT data and movie of NCT scans of fossil reef cores

---

The NCT scan data used for imaging fossil coral reef cores to reveal 3-D diagenetic alteration in the study are available via Morphosource DOI's (Williams, 2024a, 2024b, 2024c, 2024d). Data include the reprocessed data that were reconstructed with Octopus Reconstruction version 8.9.4.9© (Heidelberg Engineering GmbH) software. Reconstructed neutron tomographic scans are 16-bit .tiff files that can be visualized in 2-D and 3-D visualization software. This study used public domain software for 2-D (ImageJ™ (Schneider et al., 2012)) and 3-D (Slicer 5.2.2 (Fedorov et al., 2012)). No registration, permission, or licenses are required.

Williams, C. (2024a). Neutron computed tomography: A novel high-resolution, non-destructive method for screening fossil coral for diagenetic alteration for geochronologic and paleoclimate reconstructions [Dataset 1: Media 000646660: Holocene Porites Fossil Coral]. Morphosource. https://doi.org/10.17602/M2/M646660

Williams, C. (2024b). Neutron computed tomography: A novel high-resolution, non-destructive method for screening fossil coral for diagenetic alteration for geochronologic and paleoclimate reconstructions [Dataset 2: Media 000645633: Modern Porites Coral Slab]. Morphosource. https://doi.org/10.17602/M2/M645633

Williams, C. (2024c). Neutron computed tomography: A novel high-resolution, non-destructive method for screening fossil coral for diagenetic alteration for geochronologic and paleoclimate reconstructions [Dataset 3: Media 000645639: Acropora Fossil Coral]. Morphosource. https://doi.org/10.17602/M2/M645639

Williams, C. (2024d). Neutron computed tomography: A novel high-resolution, non-destructive method for screening fossil coral for diagenetic alteration for geochronologic and paleoclimate reconstructions [Dataset 4: Media 000647218: Isopora Palifera Fossil Coral]. Morphosource. https://doi.org/10.17602/M2/M647218

Supplementary Movies

Movies S1 to S6 described in the Supporting Information below can be found in the links below or in the online version of this article: https://doi.org/10.1029/2025GC012439

Movie S1. Supplementary Movie S1 (2.3 MB). Available at: Supplementary Movie S01

Movie S2. Supplementary Movie S2 (2.1 MB). Available at: Supplementary Movie S02

Movie S3. Supplementary Movie S3 (3.5 MB). Available at: Supplementary Movie S03

Movie S4. Supplementary Movie S4 (3.3 MB). Available at: Supplementary Movie S04

Movie S5. Supplementary Movie S5 (1.5 MB). Available at: Supplementary Movie S05

Movie S6. Supplementary Movie S6 (9.9 MB). Available at: Supplementary Movie S06

Journal of Geophysics, Geochemistry, Geosystems

Supporting Information for

Neutron Computed Tomography: A novel high-resolution, non-destructive method for screening fossil coral for diagenetic alteration for geochronologic and paleoclimatic reconstructions

Carra Williams[1, 5], Jody M. Webster[1], Joseph J. Bevitt[2], Gregory E. Webb[3], Luke D. Nothdurft[4], Victorien Paumard[1, 5], Helen McGregor[6, 7], Richard J. Murphy[9]

[1] Geocoastal Research Group, School of Geosciences, Madsen Building F09, University of Sydney, NSW, 2006, Australia. [2] Australian Nuclear Science and Technology Organisation, New Illawarra Rd, Lucas Heights, NSW, 2234, Australia. [3] The University of Queensland, School of the Environment, 4072 Brisbane, Australia. [4] Queensland University of Technology, School of Earth and Atmospheric Sciences, 4000 Brisbane, Australia. [5] Centre for Energy and Climate Geoscience, School of Earth and Oceans, The University of Western Australia, Stirling Highway, Perth WA 6009, Australia. [6] Securing Antarctica's Environmental Future, University of Wollongong, Australia. [7] School of Earth, Atmospheric and Life Sciences, University of Wollongong, Australia. [9] School of Geosciences, Madsen Building F09, University of Sydney, NSW, 2006, Australia.

Contents of this file

Additional Supporting Information (Files uploaded separately)

Captions for Movies S1 to S6

Introduction

Video .mp4 files show animations of the 3-D structure of fossil coral cores described in this study (Sample 1, sample 2, sample 4). Filters of the neutron counts are applied to reveal the identified mineral phases calcite or aragonite and the porous matrix. The samples are displayed with colour bars to describe the filter values applied. A slider bar was used to pan through the sample in 3-D. The full view of the 3-D face of the samples is obscured in places by other samples due to the loading and orientation of the sample in an aluminum tube as described in the methods.

Data Set S1: CarraWilliams-ds01 Sample 1 **-** FM19: a filter of 35,000 – 56,000 neutron counts are applied with rainbow colour attribute to describe sections of aragonite in 3-D.

Data Set S2: CarraWilliams-ds02 Sample 1 **-** FM19: a filter of 10,000 - 35,000 neutron counts are applied with rainbow colour attribute to describe sections of calcite in 3-D.

Data Set S3: CarraWilliams-ds03 Sample 3 – RR5-70-1: a filter of 35,000 – 56,000 neutron counts are applied with rainbow colour attribute to describe sections of aragonite in 3-D.

Data Set S4: CarraWilliams-ds04 Sample 3 – RR5-70-1: a filter of 10,000 - 35,000 neutron counts are applied with rainbow colour attribute to describe sections of calcite in 3-D.

Data Set S5: CarraWilliams-ds05 Sample 3 – RR5-70-1: no filter of neutron counts is applied to describe the full neutron count range in 3-D.

Data Set S6: CarraWilliams-ds06 Sample 1 – modern *Porites* coral: video showing the full neutron count range in rainbow colour attribute then a filter of 35,000 – 56,000 neutron counts is applied to describe sections of aragonite, below which, only the porous matrix remains in black.

APPENDIX E

Chapter 4 Supplement 1 - Details of seismic and well data

LIST AND DETAILS OF OBSERVED DATA USED IN THIS STUDY INCLUDING GEOGRAPHIC LOCATION OF ALL MATERIALS

Data type		Location			Data source
Seismic survey	Coordinate Reference System Projection	X Coordinate	Y Coordinate	Description	
Megator 3-D Repro 2014	UTM Zone 51S on GDA94	35479292	845186880	Depth migrated reprocessed seismic data	Woodside Energy LTD
Lithologic data		Location			
Geotechnical borehole	Depth (MD)	Lat (°N)	Long (°W)	Lithologic and facies interpretation	
SR SE BH6- J	180	-15.147	122.150	This study	Geotechnical PROD drill core conducted by Worley Parsons for Woodside Energy LTD, 2006
NR SE HDD3-JA	200	-14.996	122.164	This study	Geotechnical PROD drill core conducted by Worley Parsons for Woodside Energy LTD, 2006
Hook 1/3P	100	-15.042	122.174	This study	Geotechnical PROD drill core conducted by Worley Parsons for Woodside Energy LTD, 2006
Age data					

Stratigraphic event*	Period	Dating method	Age (Ma) *	Depth (mbRT)	Borehole	Data source
H13	L. Pleistocene-2	U/Th	0.392 MIS11(?)	-171.9	SR SE BH6- J	Williams et al. (2023)

APPENDIX F

Chapter 4 Supplement 2 - Core interpretation

Hole ID	From	To	RECOVERY	SAMPLE LOCATION	REEF UNIT	LITHOLOGY	PALEO SOIL	VERMETIDS 0, 1=1-5, 2=5-10, 3=10-15, 4=>15	CORAL ID	CORALLINE ALGAE ID	DEPOSITIONAL ENVIRONMENT	LOGGING/COMMENTS
Hook 1P	0	4	MISSING		1	PACKSTONE						Loose sand in bag
Hook 1P	4.08	4.13	RECOVERED	Perth core library	1	FRAMESTONE			(1) *Montipora* /*Porites* , (2) Merulinidae, (3) Agaricid? (4) *Pavona* ?, (5) Agaricid?		typical deep water?	Encrusting coral complex with thin algae in between. Corals are bored and infilled
Hook 1P	4.13	4.19	MISSING		1	FRAMESTONE						
Hook 1P	4.19	4.65	RECOVERED	Perth core library	1	FRAMESTONE			(1) ?, (2) *Porites* ?, (3)?		typical deep water?	platy/encrusting and massive corals with intervals of carbonate gravel fine to coarse with some burrows.
Hook 1P	4.65	6.7	CORE LOSS		1							
Hook 1P	6.7	6.93	MISSING		1	FRAMESTONE						Encrusting corals with algal laminations up to 50mm thick, with some uncemented sand grains and bivalve borings.
Hook 1P	6.936	7.05	RECOVERED	Perth core library	1	FRAMESTONE			Merulinidae?	*Peyssonneliales* , CCA indet (male conceptacles). Between coral. No matrix.	Consistent with being deep, CAA do not indicate any paleodepth	
Hook 1P	7.05	7.21	RECOVERED	Perth core library	1	FRAMESTONE			(1-3) *Porites* /*Montipora* ?, (4) M *Porites*			x4 seqeunces of thin interlaminated algae/coral on top of M/SM Porites
Hook 1P	7.21	7.31	MISSING		1	FRAMESTONE						
Hook 1P	7.31	7.38	RECOVERED	Perth core library	1	FRAMESTONE			(1)? *Montipora* ? (2)? (3) *Montipora* ? Agaricid? Merulinidae? Agaricid?		consistent with being deep	Encrusting thin algal laminations bounding thin encrusting corals
Hook 1P	7.38	7.6	MISSING		1	FRAMESTONE						
Hook 1P	7.6	9.4	CORE LOSS		1							
Hook 1P	9.4	9.9	MISSING		1	FRAMESTONE						highly fractured
Hook 1P	9.9	11.02	CORE LOSS		1							
Hook 1P	11.02	11.24	RECOVERED	Perth core library	1	FRAMESTONE			Merulinidae (corallites)			
Hook 1P	11.24	12.08	MISSING		1	FRAMESTONE						Transition from laminar/encrusting and some sub massive corals to massive. Massive coral intervals bounded by encrusting corallined algae, white- to pale grey. Trace burrows and shell vodis/dissolved.
Hook 1P	12.08	12.18	RECOVERED	Perth core library	1	BINDSTONE			*Porites*			Interstitial carbonate sand - bound in place by encrusting algae (bindstone)
Hook 1P	12.18	12.3	MISSING		1	FRAMESTONE						
Hook 1P	12.3	13.5	CORE LOSS		1							
Hook 1P	13.5	13.94	MISSING		1	CARBONATE SAND						carbonate sand, fine to coarse grained, angular to subangular, sarbonate shell frags, pale grey, some fine gravel sized coral frags.
Hook 1P	13.94	14.18	RECOVERED	Perth core library	1	FRAMESTONE	P?		*Porites*			
Hook 1P	14.18	14.22	RECOVERED	Perth core library	1	FRAMESTONE			*Porites*			
Hook 1P	14.22	14.58	MISSING		1	FRAMESTONE						massive to encrusting corals, white, intercalated intervals of encrusting coralline algae up to 70mm thick (!? Collins interp), borings up to 12mm diameter, bivalves embedded in coral, some calcrete infill of boring clasts, massive coral intervals up to 400mm thick (14-15m).
Hook 1P	14.58	14.67	RECOVERED	Perth core library	1	FRAMESTONE			*Porites* ?			
Hook 1P	14.67	14.9	MISSING		1	FRAMESTONE						
Hook 1P	14.9	15.22	CORE LOSS		1							
Hook 1P	15.22	15.29	RECOVERED	Perth core library	1	FRAMESTONE			*Porites*			
Hook 1P	15.29	15.7	MISSING		1	FRAMESTONE						
Hook 1P	15.7	15.815	RECOVERED	Perth core library	1	FRAMESTONE			*Porites*			
Hook 1P	15.815	16.02	MISSING		1	FRAMESTONE						100mm thick algal laminated interval
Hook 1P	16.02	16.23	RECOVERED	Perth core library	1	FRAMESTONE			Merulinidae-*Goniastrea* ? (corallites)			
Hook 1P	16.23	16.3	MISSING		1	FRAMESTONE						highly bored interval, borings open and to 20mm diameter
Hook 1P	16.3	17.95	CORE LOSS		1							
Hook 1P	17.95	17.97	RECOVERED	Perth core library	1	RUDSTONE						
Hook 1P	17.97	17.99	RECOVERED	Perth core library	1	FRAMESTONE			Merulinidae?			
Hook 1P	17.99	18.05	RECOVERED	Perth core library	1	FRAMESTONE			?			
Hook 1P	18.05	18.28	MISSING		1	FRAMESTONE			*Porites* ?			50 mm interval of platy coral, recrystallised fabric … abundant borings to 10 mm diameter, with some dissolution of massive coralline limestone intervals, grey discolouration of coralline limestone on encrusted and dissolution surfaces.
Hook 1P	18.28	18.45	RECOVERED	Perth core library	1	MICROBIAL FRAMESTONE			*Porites* ?			microbialite scavenging clay and iron
Hook 1P	18.45	18.75	MISSING		1	FRAMESTONE						
Hook 1P	18.75	18.959	RECOVERED	Perth core library	1	MICROBIAL FRAMESTONE			Agaricid/Merulinidae?			clay present (as expected in microbrialite - scavanges detritus material!) Back reef/reef flat/shallow lagoon environment?
Hook 1P	18.959	19.1	MISSING		1	FRAMESTONE						200 mm interval of encrusting coralline algae, fine algal laminations (<3 mm thick), variably cemented and porous, grey staining along algal laminations.
Hook 1P	19.1	20.1	CORE LOSS		1							
Hook 1P	20.1	20.46	MISSING		1	FRAMESTONE						
Hook 1P	20.46	20.55	RECOVERED	Perth core library	1	BINDSTONE			*Porites* ?	No CCA. Frgaments of bivalves, bryozoans. Larger benthic foraminifera and a few small ones		Altered and recrystallised coral
Hook 1P	20.55	20.58	MISSING		1	FRAMESTONE	MIS 1					… 100 mm interval with fibrous coral fabric
Hook 1P	20.58	20.73	RECOVERED	Perth core library	2	HALIMEDA FRAMESTONE	Holocene-Pleistocene boundary		?			
Hook 1P	20.73	20.98	MISSING		2	RUDSTONE	MIS 5					
Hook 1P	20.98	21.09	RECOVERED	Perth core library	2	HALIMEDA FRAMESTONE						
Hook 1P	21.09	21.73	MISSING		2	RUDSTONE						partially leached with thick coralgal crusts
Hook 1P	21.73	21.89	RECOVERED	Perth core library	2	HALIMEDA FRAMESTONE						
Hook 1P	21.89	22.2	MISSING		2	RUDSTONE						
Hook 1P	22.2	22.7	CORE LOSS		2							
Hook 1P	22.7	23	MISSING		2	RUDSTONE						subhorizontal open voids 4-15 mm common (shell and boring voids)
Hook 1P	23	23.3	RECOVERED	Perth core library	2	HALIMEDA FRAMESTONE						
Hook 1P	23.3	24	MISSING		2	RUDSTONE						fine algal lamination <2mm…highly voided horizon ca. 150mm thick
Hook 1P	24	24.2	CORE LOSS		2							
Hook 1P	24.2	24.43	MISSING		2	RUDSTONE						… open voids up to 10 mm, with some fine algal interlaminations, with some calcarenite infill of algal laminated horizons.
Hook 1P	24.43	24.48	RECOVERED	Perth core library	2	HALIMEDA FRAMESTONE						branching coral clasts.
Hook 1P	24.48	25.56	MISSING		2	RUDSTONE						
Hook 1P	25.56	25.62	RECOVERED	Perth core library	2	HALIMEDA FRAMESTONE						black calcite crystls, iron/manganese staining. Similar facies to Dechnik 2017 for GBR Halimeda/laminar facies LIG GBR
Hook 1P	25.62	25.8	MISSING		2	FRAMESTONE						
Hook 1P	25.8	26.3	CORE LOSS		2							
Hook 1P	26.3	26.81	MISSING		2	FRAMESTONE						…some algal laminations, strong alteration/diagenesis. Large bivalve boring up to 20mm diameter
Hook 1P	26.81	26.95	RECOVERED	Perth core library	2	FRAMESTONE			coral?			Iron stained coral, iron rich on coral.
Hook 1P	26.95	27.12	MISSING		2							
Hook 1P	27.12	27.22	RECOVERED	Perth core library	2	FRAMESTONE			Merulinidae? (corallites)			
Hook 1P	27.22	27.4	MISSING		2	FRAMESTONE						… 26.75 – 27.15 m: intercalated intervals of encrusting algal laminations, porous, with some interstitial calcarenite… tabulate fabric with thin (<3 mm) algal interlaminations, small borings <4 mm
Hook 1P	27.4	28.8	CORE LOSS		2							
Hook 1P	28.8	28.95	MISSING		2	RUDSTONE						
Hook 1P	28.95	29.09	RECOVERED	Perth core library	2	RUDSTONE				No CCA. MATRIX: Coral fragment?		fine sediment at top, iron dark staining, some algae?, remnant iron stained coral, cements.
Hook 1P	29.09	30.88	MISSING		2	RUDSTONE						
Hook 1P	30.88	30.99	RECOVERED	Perth core library	2	FRAMESTONE			coral?			Platy coral. Sediment? Bivalve/gastropod - lagoonal?
Hook 1P	30.99	31.4	MISSING		2	RUDSTONE						
Hook 1P	31.4	31.5	CORE LOSS		2							
Hook 1P	31.5	31.78	MISSING		2	RUDSTONE						… abundant open voids to 30 mm diameter, voids associated with dissolution of branching coral fragments, from 31.785 – 32.856 m.
Hook 1P	31.78	31.85	RECOVERED	Perth core library	2	FRAMESTONE			Coral?			
Hook 1P	31.85	32.3	MISSING		2	RUDSTONE						
Hook 1P	32.3	32.7	CORE LOSS		2							
Hook 1P	32.7	33	MISSING		2	RUDSTONE						
Hook 1P	33	33.1	CORE LOSS		2							
Hook 1P	33.1	33.4	MISSING		2	RUDSTONE						thin subhorizontal algal laminae, borings 5x20mm
Hook 1P	33.4	33.5	CORE LOSS		2							
Hook 1P	33.5	33.97	MISSING		2	RUDSTONE						…encrusting algal interlaminations at ca. 100mm intervals. Platy coral
Hook 1P	33.97	34.04	RECOVERED	Perth core library	2	FRAMESTONE			Coral? Some structure			

Hook 1P	34.04	34.3	MISSING		2	RUDSTONE					…open voids to 15mm, calcrete cementation not pervasive, within algal lamination, few bioclasts.
Hook 1P	34.3	34.5	CORE LOSS		2						
Hook 1P	34.5	34.91	MISSING		2	RUDSTONE					… porous with coarse sand-sized voids, inclined fractures, some zones fractured to medium gravel-sized fragments. Platy coral
Hook 1P	34.91	35.01	RECOVERED	Perth core library	2	FRAMESTONE		Merulinidae? Mussidae?			iron staining
Hook 1P	35.01	35.55	MISSING		2	RUDSTONE		coral?			
Hook 1P	35.55	35.69	RECOVERED	Perth core library	2	FRAMESTONE					Iron staining
Hook 1P	35.69	37.1	MISSING		2	RUDSTONE					…with occasional pale yellow staining. Branching corals, molluscs/bivalves, borings, porous fabric, irregular white algal laminations.
Hook 1P	37.1	37.25	CORE LOSS		2						
Hook 1P	37.25	37.4	MISSING		2	FLOATSTONE					
Hook 3P	37.4	37.6	RECOVERED	Perth core library	2	FLOATSTONE		Merulinidae/Mussidae coral clast			chalky white framestone or rudstone with grains (RUDSTONE?), strong dissolution, cavities, rusty iron staining
	37.6	38.27	MISSING		2						
Hook 3P	38.27	38.46	RECOVERED	Perth core library	2	FLOATSTONE					grey tinge, laminar, very bioeroded and altered
Hook 3P	38.46	38.88	MISSING		2	FLOATSTONE					thin intervals of coralline limestone 50-100mm thick
Hook 3P	38.88	39.13	RECOVERED	Perth core library	2	FLOATSTONE		coral			
Hook 3P	39.13	39.8	MISSING		2	FLOATSTONE					
Hook 3P	39.8	40	CORE LOSS	Perth core library	2						dolomotised (?) framestone with slight brown staining
Hook 3P	40	41.23	MISSING		2	FLOATSTONE					
Hook 3P	41.23	41.35	RECOVERED	Perth core library	2	RUDSTONE					
	41.35	42.24	MISSING		2	RUDSTONE					void spoace becoming pervasively infilled with secondary cement
Hook 3P	42.24	42.54	RECOVERED	GRG lab	2	FRAMESTONE		Coral			halimeda? Biolcasts more micro-facies, domal and laminar CCA coral pieces? Dissolution - diagenesis? Cementation
Hook 3P	42.54	42.67	MISSING		2	RUDSTONE					
Hook 3P	42.67	43.13	RECOVERED	Perth core library	2	FLOATSTONE		*Porites* ?			thick ca. 50 cm domal framestone (porites?) encrusting algae on top? Not in situ, mixed in with finer detrital sediment.
Hook 3P	43.13	43.6	MISSING		2	FLOATSTONE					… with needle-shaped brown-white calcite crystals infilling void space 10 mm diameter.
Hook 3P	43.6	44	MISSING		2	FRAMESTONE					
Hook 3P	44	45.95	MISSING		2	RUDSTONE					
Hook 3P	45.95	46.24	RECOVERED	Perth core library	2	FRAMESTONE		*Porites*			
Hook 3P	46.24	46.365	MISSING		2	FRAMESTONE					
Hook 3P	46.365	46.53	RECOVERED	Perth core library	2	FRAMESTONE		*Porites*			
Hook 3P	46.53	46.96	MISSING		2	RUDSTONE					
Hook 3P	46.96	47.22	RECOVERED	Perth core library	2	RUDSTONE					Sediments between fragments, more rudstone
Hook 3P	47.22	48.38	MISSING		2	RUDSTONE					… 47.6 to 47.7m: interval of massive coralline limestone, tabulate fabric, white. …….. large gastropod shell to 35mm diameter, becoming coarse grained with abundant branching coral fragments. …. 47.24 - 48.44m: pale grey-brown staining in voids with pink coral algae fragments
Hook 3P	48.38	48.66	RECOVERED	Perth core library	2	RHODOLITH RUDSTONE					buff white CCA? Small vertical corralites - nodules - big rhodoliths? Width of core tray. Reworked deposit - more rudstone to floatstone detrital facies - can be sharp transition…
Hook 3P	48.66	50	MISSING		2	RUDSTONE					. with shell fragments to coarse gravel size. branching coral fragments to 25mm diameter
Hook 3P	50	50.9	CORE LOSS		2						
Hook 3P	50.9	51.89	MISSING		2	RUDSTONE					
Hook 3P	51.89	52.01	RECOVERED	Perth core library	2	RHODOLITH RUDSTONE	MIS3?				increasing grains in matrix between coral clasts - bafflestone if in situ or grainstone if detrital? Rhodolith facies - algae. There is some evidence of phyloosilicates on the 2200nm hyperspectral feature, but no evidence of soil/calcrete horizon in the core. There is missing core, however, so this is possible that this could indicate MIS3?
Hook 3P	52.01	53.2	MISSING		2	RUDSTONE					
Hook 3P	53.2	53.6	CORE LOSS	Perth core library	2						
Hook 3P	53.6	53.66	MISSING		2	FLOATSTONE					… porous fabric with abundant voids to 10 mm diameter, voids associated with dissolution of branching coral fragments.
Hook 3P	53.66	54	RECOVERED	GRG lab	2	FLOATSTONE					IS coral, CCA, bottom section sent for TS (Jody georeef notes). Rhodoliths with algal coating, 1mm thick binding laminations. Clear detrital facies mixed spectral colours with clear bnoundaries between sediment and clasts.
Hook 3P	54	54.66	RECOVERED	Perth core library	2	FRAMESTONE		(1) *Porites* (corallites), (2) different coral?			Porites in amongst detrital material
Hook 3P	54.66	54.76	RECOVERED	Perth core library	2	FRAMESTONE		*Porites*		deep?	domal and branching coral pieces - framestone or rudstone - x2 colonies separated by encrusting surface? Top of section smaller coral branches with CCA?
Hook 3P	54.76	55.2	RECOVERED	Perth core library	2	RUDSTONE					orange staining iron/clays? Algae, nodules/rhodoliths
Hook 3P	55.2	55.66	RECOVERED	Perth core library	2	FRAMESTONE		*Porites*		reef flat? (detrital and corals that are microatolls?) e.g., nodules on OTR reef flat	Shallow reef crest with individual coral colonies amonsgt high energy rudstone facies? Detrital at base. Porites IS with corallite orientation and encrustation base.
Hook 3P	55.66	56.35	MISSING		2	RUDSTONE					
Hook 3P	56.35	56.778	RECOVERED	GRG lab	2	FRAMESTONE					
Hook 3P	56.778	57.042	RECOVERED	Perth core library	2	FRAMESTONE		*Porites*			Porites ca. 40-45 years old? Counted growth rings which are partially obscured. Ca. 400mm long. Growth rate= 8.9-10mm/yr.
Hook 3P	57.042	57.22	RECOVERED	Perth core library	2	FRAMESTONE					
Hook 3P	57.22	57.26	MISSING		2	FRAMESTONE					
Hook 3P	57.26	58	RECOVERED	Perth core library	2	BINDSTONE				Shallowing? Increasing CCA thickness	increasingly thick crusts of algae binging coral and sediment - bindstone
Hook 3P	58	58.23	RECOVERED	Perth core library	2	FLOATSTONE		*Pocillopora* (mold), *Porites* /*Montipora* ?			dissolved branches (molds) not in situ
Hook 3P	58.23	58.6	MISSING		2	FLOATSTONE					
Hook 3P	58.6	59.1	MISSING		2	FRAMESTONE					
Hook 3P	59.1	59.3	MISSING		2	FLOATSTONE					
Hook 3P	59.3	59.8	MISSING		2	FRAMESTONE					
Hook 3P	59.8	60.13	CORE LOSS		2						
Hook 3P	60.13	60.28	RECOVERED	Perth core library	2	FRAMESTONE		thin laminar coral?			
Hook 3P	60.28	60.59	MISSING		2	RUDSTONE					
Hook 3P	60.59	60.9	RECOVERED	GRG lab	2	FRAMESTONE		*Porites* ? Branching frags at base.			Porites has basal attachment - possibly in situ.
Hook 3P	60.9	61.4	MISSING		2	FRAMESTONE					
	61.4	61.89	MISSING		2	FLOATSTONE	MIS 5				
Hook 3P	61.89	62.07	RECOVERED	GRG lab	2	FLOATSTONE	U/C				IS Coral , CCA, crust, bottom section sent for TS & U/Th (Jody georeef notes). Becoming slightly stained dark grey-brown. Branching coral frags with algal coating.
Hook 3P	62.07	62.42	MISSING		3	FLOATSTONE	MIS 7a?				
Hook 3P	62.42	62.54	RECOVERED	Perth core library	3	RUDSTONE	P	*Acropora* B frags?		BR robust frags come from a shallow reef environment?	
Hook 3P	62.54	62.81	MISSING		3	FLOATSTONE					62.8m…. massive coralline limestone interval bound by algal laminated interval up to 300mm thick, most void space infilled by secondary cement, trace voids remain,
Hook 3P	62.81	63	RECOVERED	Perth core library	3	FLOATSTONE	P	*Acropora* B frags? (coenosteum interbranch)		BR robust frags come from a shallow reef environment?	Facies transition, robust branching coral clasts in fine grained bioclastic matrix
Hook 3P	63	63.5	RECOVERED	Perth core library	3	FRAMESTONE	P	*Porites*			calcite infill, of dissolution cracks, geopetal, calcite crystals
Hook 3P	63.5	63.81	RECOVERED	Perth core library	3	FLOATSTONE		*Acropora* frags			Robust branching coral clasts in fine grained bioclastic matrix
Hook 3P	63.81	63.96	MISSING								
Hook 3P	63.96	64.81	RECOVERED	Perth core library	3	FLOATSTONE	P	*Porites* , *Acropora* and *Pocillopora* branches.		Pocillopera higher energy?	red-brown sediment staining/infill, coating acropora and pocillopera branches floating in finer grained matrix. Some nodules?
Hook 3P	64.81	66	MISSING		3	RUDSTONE					…. with open voids up to ~150mm, voids associated with branching coral dissolution
Hook 3P	66	66.48	RECOVERED	Perth core library	3	FLOATSTONE	P	*Acropora* ?	*Lithothamnion* sp., *Lithophyllum* gr. *pustulatum* , fragments of *Lithophyllum* sp. and Amphiroa. Coral in the rudstone, encrusting foraminifers (Acervulinids and Homotrema-like). MATRIX: Bryozoans, bivalve fragments	higher energy branching corals	red-brown sediment staining/infill, coating acropora and pocillopera branches floating in finer grained matrix. Some nodules? Heavily bored and infilled. Dissolved coral frags and calcite cements and nodules. Bioclastic. Mix of fine and robust branches heavily bioeroded and infilled.
Hook 3P	66.48	66.85	RECOVERED	Perth core library	3	FLOATSTONE	P				small rhodoliths?
Hook 3P	66.85	66.95	MISSING		3	RUDSTONE	P				
Hook 3P	66.95	67.08	RECOVERED	Perth core library	3	FRAMESTONE	P	*Porites*			Calcrete surface, , paleosol unconformity surface
Hook 3P	67.08	67.19	RECOVERED	Perth core library	3	FRAMESTONE	P	*Porites* (same colony as above)			Calcrete surface, , paleosol unconformity surface
Hook 3P	67.19	67.35	MISSING		3	FRAMESTONE	MIS 7a?				
Hook 3P	67.35	67.48	RECOVERED	Perth core library	3	FRAMESTONE	U/C, Paleosol	*Porites* (same colony as above)			Calcrete surface, , paleosol unconformity surface, very thick dark brown stain on Porites colony
Hook 3P	67.48	68.04	MISSING		4	FRAMESTONE	MIS 7c?				67.4-67.8 laminated coral, no septa preserved, corallite 0.7mm, probably lamelar coral.
Hook 3P	68.04	68.31	RECOVERED	Perth core library	4	FRAMESTONE	P	*Porites* (base of colony - insitu?)			
Hook 3P	68.31	68.61	RECOVERED	Perth core library	4	RUDSTONE	P				IS Acropora? Altered? Bottom section sent for U/Th (jody georeef notes). …. with some cobble-sized fragments of massive coralline limestone and bored. Smooth calcite nodules, fine grained matrix. Coral clasts touching >3mm = rudstone
Hook 3P	68.61	68.9	RECOVERED	GRG lab	4	RUDSTONE	P	large coral BR frag			large robust branching coral clasts in fine grained matrix. Larger corals touching >3mm rudstone

Hook 3P	68.9	69.04	RECOVERED	Perth core library	4	FRAMESTONE		*Porites* ? (growth lines visible on hyperspectral false colour)			
Hook 3P	69.04	69.13	RECOVERED	Perth core library	4	FLOATSTONE	P	Base of *Porites* colony above			calcite linings
Hook 3P	69.13	69.24	RECOVERED	Perth core library	4	FLOATSTONE	P				sediment, diagenetic fronts, branching and massive coral clasts heavily altered in fine-grained bioclastic matrix. Heterogeneous diagenetic alteration because of lithologic control. Karst/cavities, secondary calcite rinds.
Hook 3P	69.24	69.385	RECOVERED	Perth core library	4	FLOATSTONE					
Hook 3P	69.385	69.515	RECOVERED	Perth core library	4	FLOATSTONE	P				
Hook 3P	69.515	69.54	MISSING		4	FLOATSTONE					
Hook 3P	69.54	70.03	RECOVERED	Perth core library	4	FLOATSTONE	P				
Hook 3P	70.03	70.29	RECOVERED	Perth core library	4	RUDSTONE	P				
Hook 3P	70.29	70.61	RECOVERED	GRG lab	4	FLOATSTONE	P				with pockets of coarse grained shell fragments, interstitial to coarse coral fragments, geopetal infill?
Hook 3P	70.61	70.75	RECOVERED	Perth core library	4	FLOATSTONE	P				subvertical seam - 60mm length, partially infilled with green carbonate cement - different phase of sedimentation - layered - exposure...?
Hook 3P	70.75	71.75	RECOVERED	Perth core library	4	PACKSTONE	P				. becoming grey-brown in colour ....several generations of vug infilling cement, becoming red-brown in colour. thin pocket of crystalline calcarenite, red-brown in colour. Layered sediment infill at top.
Hook 3P	71.75	71.808	RECOVERED	Perth core library	4	PACKSTONE	MIS 7c?				.. red-brown calcarenite matrix occurring interstitial to coralline limestone fragments
Hook 3P	71.808	72.054	RECOVERED	Perth core library	4	FRAMESTONE	U/C				.... irregular mottled fabric, red-brown calcarenite matrix with calcite vug-infilling cement
Hook 3P	72.054	72.426	RECOVERED	GRG lab	5	FRAMESTONE	MIS 7c?	*Porites*	*Mesophyllum* gr. *funafutiense* , *Lithoporella* sp., *Lithophyllum* gr. *pustulatum* , Amphiroa sp., thin CCA indeterminable. encrusting foraminifera, most probably acervulinids. Other encrusting foramifera. They seem to be part, together with the CCA, of a nodule that can be called macroid or foralgalith. Fragments of mollusks and echinoids, planktonic foraminifera.		stratified layering - paleosol dark brown sediment infill coating growth rings of porites, thick algal crust on porites. Borings and infill. Exposed with red soil infill. Karst/cement linings of cavities
Hook 3P	72.426	72.75	RECOVERED	Perth core library	5	RUDSTONE					becoming white, coarse branching coral fragments in a calcarenite matrix
Hook 3P	72.75	73.467	RECOVERED	Perth core library	5	RUDSTONE					
Hook 3P	73.467	73.87	MISSING		5	RUDSTONE					branching coral framework without calcarenite matrix, open voids to 20mm. Coralline branches and coralline thin crusts. Calcite infilled fracture.
Hook 3P	73.87	73.97	RECOVERED	Perth core library	5	FLOATSTONE		*Pavona* ?/Agaricid?			more pavona but heavily altered with thin algal crust
Hook 3P	73.97	74.168	RECOVERED	Perth core library	5	RUDSTONE					
Hook 3P	74.168	74.47	RECOVERED	Perth core library	5	FRAMESTONE		*Pavona* ?/Agaricid?		Pavona suggests possibly shallow?	check columnar pavona similar to Ashmore? Possibly coral assemblage of massive porites with columnar pavona?
Hook 3P	74.47	74.536	MISSING		5	FRAMESTONE					
Hook 3P	74.536	74.912	RECOVERED	GRG lab	5	FRAMESTONE		*Porites*			Massive Porites growth rate ca. 60-70 years old? Counted growth rings which are partially obscured. Ca. 80-90cm/1m long. Growth rate=4.3–16.7mm/year. Each growth band around 1cm...
Hook 3P	74.912	75.27	RECOVERED	Perth core library	5	FRAMESTONE		*Porites*			masive porites colony with growth banding visible and cavities on edge of colony filled with sediment.
Hook 3P	75.27	75.47	MISSING		5	PACKSTONE				Lower energy lagoonal?	Lagoonal gastropod facies!
Hook 3P	75.47	75.63	RECOVERED	Perth core library	5	PACKSTONE					coral frags and finer detrital sediment/matrix
Hook 3P	75.63	76.03	RECOVERED	Perth core library	5	PACKSTONE					coral frags and finer detrital sediment/matrix
Hook 3P	76.03	76.18	MISSING		5	FLOATSTONE					
Hook 3P	76.18	76.42	RECOVERED	Perth core library	5	FRAMESTONE		*Pavona* ?/Agaricid?		possibly shallow?	Interval of coralline limestone to 80mm thickness with algal crust
Hook 3P	76.42	76.93	RECOVERED	Perth core library	5	RUDSTONE					Leached Halimeda plates
Hook 3P	76.93	77.18	RECOVERED	Perth core library	5	RUDSTONE		*Acropora* mold?			nodules, branches, possibly acropora, matrix, algae, cements
Hook 3P	77.18	77.426	RECOVERED	Perth core library	5	FLOATSTONE					
Hook 3P	77.426	77.628	RECOVERED	Perth core library	5	RUDSTONE					
Hook 3P	77.628	77.678	RECOVERED	Perth core library	5	RUDSTONE					
Hook 3P	77.678	77.816	RECOVERED	Perth core library	5	RUDSTONE					
Hook 3P	77.816	77.865	RECOVERED	Perth core library	5	RUDSTONE					
Hook 3P	77.865	77.906	RECOVERED	Perth core library	5	RUDSTONE					
Hook 3P	77.906	78.19	RECOVERED	GRG lab	5	RUDSTONE			Thin encrusting thalli of CCA indet. Intergrown with encrusting forams in nodules? MATRIX: Halimeda, CCA fragments, bivalves, echinoids, encrusting foraminifera, small benthic foraminifera, bryozoans.	CCA do not indicate any paleodepth but nodules of CCA with encrusting forams comonly occur in depths of sveral tens of metres	small branching coral clasts, nodules, dissolved, matrix, SM coral?
Hook 3P	78.19	78.354	RECOVERED	Perth core library	5	FLOATSTONE					
Hook 3P	78.354	78.818	RECOVERED	Perth core library	5	RUDSTONE				possibly shallow?	Secondary calcite infill along subhorizontal joint. Branching fabric possibly platy corals. Two encrusting coral colonies with thin algal crusts possibly in place?
Hook 3P	78.818	78.88	RECOVERED	Perth core library	5	RUDSTONE		*Lobophyllia* ?			branching coral clasts, bored and infilled, cements, more algae
Hook 3P	78.88	79.168	RECOVERED	Perth core library	5	RUDSTONE					
Hook 3P	79.168	79.288	RECOVERED	Perth core library	5	RUDSTONE					mostly rudstone with pockets of floatstone...
Hook 3P	79.288	79.564	RECOVERED	Perth core library	5	RUDSTONE					Secondary calcite infill along subhorizontal joint.
Hook 3P	79.564	79.88	RECOVERED	Perth core library	5	RUDSTONE					branching coral clasts, acropora bored and infilled, nodules
Hook 3P	79.88	80.176	RECOVERED	Perth core library	5	GRAINSTONE		*Acropora*			more abundant smaller coral frags, more densely spaced in grainstone matrix -with occasional large coral frags > 3mm. Some nodules/rhodoliths
Hook 3P	80.176	80.308	RECOVERED	Perth core library	5	GRAINSTONE		*Acropora*			
Hook 3P	80.308	80.338	RECOVERED	Perth core library	5	FRAMESTONE					
Hook 3P	80.338	80.838	RECOVERED	Perth core library	5	FRAMESTONE		Seriatopora molds? *Porites* in place			coral frags including encrustiong, massive in place porites, more matrix with branching frags, gastropod. Molds of branches. Algal crusts.
Hook 3P	80.838	81.12	RECOVERED	Perth core library	5	FLOATSTONE					coral frags in matrix, heavy diagenetic alteration, mostly floatstone with some rudstone pockets...
Hook 3P	81.12	81.444	RECOVERED	Perth core library	5	FLOATSTONE					
Hook 3P	81.444	81.57	RECOVERED	Perth core library	5	FRAMESTONE					geopetal. Porites colony with algal crust.
Hook 3P	81.57	81.88	RECOVERED	Perth core library	5	RUDSTONE		*Porites* ?			pervasive secondary cement, remnant algal laminated fabric. SM, B coral frags in detrital bioclastic matrix, pale brown colour...
Hook 3P	81.88	82.13	RECOVERED	Perth core library	5	RUDSTONE					massive coralline limestone intervals 300mm thick, bound by algal laminated intervals to 200mm thick, white, pervasive calcite cement infill of void space
Hook 3P	82.13	82.36	RECOVERED	Perth core library	5	RUDSTONE		*Seratopora* ?			branching coral molds?
Hook 3P	82.36	82.59	RECOVERED	Perth core library	5	FRAMESTONE		*Porites*			coral, algae, matrix, porites? Same colony as below? With encrusting coral on top?
Hook 3P	82.59	82.83	RECOVERED	Perth core library	5	FRAMESTONE		*Porites*			Possibly the edge of an insitu massive Porites colony with detrital material infilling cavities?
Hook 3P	82.83	83.1	RECOVERED	Perth core library	5	FRAMESTONE		*Porites*			borings infilled with secondary cement. Large massive coral clasts.
Hook 3P	83.1	83.59	RECOVERED	GRG lab	5	FRAMESTONE		*Porites* , Merulinidae?			coral and algae, matrix with finer coral frags, Porites? On side of porites colony transitions to Merulinidae?
Hook 3P	83.59	83.72	RECOVERED	Perth core library	5	RUDSTONE					large >40mm coral clasts, BR? In cream to pale brown bioclastic grainstone matrix
Hook 3P	83.72	83.782	MISSING		5	FRAMESTONE					10cm large coral clasts of massive coral
Hook 3P	83.782	84.214	RECOVERED	Perth core library	5	FRAMESTONE		Mussidae? *Symphyllia* /*lobophyllia* ?			
Hook 3P	84.214	84.27	MISSING		5	FRAMESTONE					Rhodoliths and algal laminations.
Hook 3P	84.27	84.47	RECOVERED	Perth core library	5	RUDSTONE					nodules/rhodoliths, larger corals >30mm diameter, SM? Higher proportion of coral frags relative to bioclastic grainstone matrix - rudstone. Not in place.
Hook 3P	84.47	84.509	RECOVERED	Perth core library	5	RUDSTONE					
Hook 3P	84.509	84.899	RECOVERED	Perth core library	5	RUDSTONE					higher proportion of coral fragments and thicker algal crusts...higher energy.
Hook 3P	84.899	85.044	RECOVERED	Perth core library	5	RUDSTONE		*Galaxea* ? *Acropora*			algal crusts around branching corals, possibly binding, coral material stabilised and bound by in place algae but not in place coral? Galaxea
Hook 3P	85.044	85.27	RECOVERED	Perth core library	5	RUDSTONE					IS enc coral, CCA, PWS, top section sent for TS & U/Th (Jody georeef notes)
Hook 3P	85.27	85.5	RECOVERED	GRG lab	5	BINDSTONE	P?	Pocilloporid? *Acropora* ?		changing branch composition and increasing algal thickness indicate higher energy...?	BR coral frags indicate higher energy/shallow? More algae, paleosol material in borings...
Hook 3P	85.5	85.91	RECOVERED	Perth core library	5	RUDSTONE					
Hook 3P	85.91	86.27	RECOVERED	Perth core library	5	RUDSTONE	P?	Merulinidae?			brown sediment infill of cracks - possibly another paleosol? Coral and algae, can see coralites -Merulinidae? In place? Another encrusting coral on top..
Hook 3P	86.27	86.43	MISSING		5	RUDSTONE					
Hook 3P	86.43	87.83	RECOVERED	Perth core library	5	RUDSTONE		coral frags, *Porites* ?			encrusting algal fabric - 350mm thick
Hook 3P	87.83	87.93	MISSING		5	RUDSTONE					
Hook 3P	87.93	88.262	RECOVERED	GRG lab	5	FRAMESTONE		*Porites*			darker brown sediment still coats the bioclasts and lines cracks with calcite cements infilling.
Hook 3P	88.262	88.44	RECOVERED	Perth core library	5	PACKSTONE		Branching coral frags dissolved			bioclastic matrix with sections of in place porites and ISX floating dissolved branches
Hook 3P	88.44	88.756	RECOVERED	Perth core library	5	PACKSTONE		Branching coral frags dissolved			
Hook 3P	88.756	88.88	RECOVERED	Perth core library	5	PACKSTONE	P	*Porites*			>80mm section of in situ massive porites continues to section below. Coral with algal crusts, detrital matrix. Some framework - bindstone? Some branching coral frags. Some in situ porites at top?

Hook 3P	88.88	88.98	MISSING		5	FLOATSTONE					.... large boring - 15mm diameter in massive coralline limestone interval, bound by encrusting algal laminations
Hook 3P	88.98	89.63	RECOVERED	Perth core library	5	PACKSTONE	P	coral frags, massive *Porites* in place? Base of *Porites* above...			massive porites on top of encrusting coral. darker brown sediment still coats the bioclasts and lines cracks with calcite cements infilling.
Hook 3P	89.63	90.006	RECOVERED	Perth core library	5	PACKSTONE	P	*Porites* and branching coral frags?			coral frags in matrix, porites? Branching coral. Calcite linings, diagenetic features ongoing...
Hook 3P	90.006	90.35	RECOVERED	Perth core library	5	PACKSTONE	P				dissolved coral frags floating in matrix (floatstone) - some frags touching (rudstone?)
Hook 3P	90.35	90.63	RECOVERED	Perth core library	5	PACKSTONE	P				evidence of mud coated coral clasts and grains - packstone rather than grainstone...one isolated coral branch with thick algal crust -transported not necessarily indicative of shallower/higher energy.
Hook 3P	90.63	91.23	MISSING		5	FLOATSTONE					
Hook 3P	91.23	91.81	RECOVERED	Perth core library	5	PACKSTONE					
Hook 3P	91.81	91.99	RECOVERED	Perth core library	5	PACKSTONE	P				
Hook 3P	91.99	92.39	RECOVERED	Perth core library	5	PACKSTONE					
Hook 3P	92.39	92.85	RECOVERED	Perth core library	5	PACKSTONE					
Hook 3P	92.85	93	RECOVERED	Perth core library	5	PACKSTONE		coral frags		deep if forams?	Either long thin cyclocylpeus forams (deep) or super thin agaricid corals...packstone-grainstone>?
Hook 3P	93	93.238	RECOVERED	Perth core library	5	RUDSTONE		Fungidae?			nodules? Detrital facies, larger coral frags ISN? Fungidae?
Hook 3P	93.238	93.39	RECOVERED	GRG lab	5	FRAMESTONE		*Porites*		still deep?	coral frags still coated in light brown sediment. Remnant of below paleosol. Porites coral frag? With encrusting coral on top.
Hook 3P	93.39	93.71	RECOVERED	Perth core library	5	RUDSTONE	P				Halimeda? Different facies to below paleosol - detrital, slightly hiigher energy, halimeda, coral frags. Extends to the next paleosol for a long while.
Hook 3P	93.71	93.95	RECOVERED	Perth core library	5	RUDSTONE	P				
Hook 3P	93.95	94.39	RECOVERED	Perth core library	5	RUDSTONE	P	coral, Agaricid?		lower energy, deep?	Agaricid coral, lower energy, deeper? Coenosteum of Acropora?
Hook 3P	94.39	94.47	RECOVERED	Perth core library	5	BINDSTONE	P				Coral, sediment, algae, algae binding it in place? Bindstone?
Hook 3P	94.47	94.87	MISSING		5	RUDSTONE	MIS 7c?				encrusting coralline algal interval. ... 94.65 m: thin (5 mm) bands of planar laminated, red-brown siltstone and calcrete, with brown and black manganese surfaces
Hook 3P	94.87	94.97	RECOVERED	GRG lab	5	RUDSTONE	U/C, Paleosol				First sharp unfonformable surface for MIS 9? IS massive coral - Goniopora? Top sention sent for TS & U/Th (Jody georeef notes)
Hook 3P	94.97	95.08	RECOVERED	Perth core library	6	RUDSTONE	MIS 9c?				... 94.98 m: 50 mm interval of fine grained calcarenite
Hook 3P	95.08	95.3	RECOVERED	Perth core library	6	RUDSTONE		*Goniopora* ?			95.03m: planar laminated red-brown siltstone, pale brown calcrete and black manganese surfaces
Hook 3P	95.3	95.61	RECOVERED	GRG lab	6	RUDSTONE		*Galaxea* ?		more Turbid environment?	... 95.15 - 95.70m: void space between branching coral fragments is infilled with planar laminated pale brown calcrete, red-brown siltstone and black_ manganese laminations. Lots of thin encrusting corals transitioning into SM Galaxea, which can be turbid...
Hook 3P	95.61	95.96	RECOVERED	Perth core library	6	RUDSTONE	MIS 9c?	*Acropora* ?			Acropora branches? Bored and infilled (light blue onf false colour)
Hook 3P	95.96	96.13	RECOVERED	GRG lab	6	RUDSTONE	U/C, Paleosol	coral frags	*Lithophyllum* gr. *pustulatum* , CCA indet. On heavely bored coral and intergrown with encrusting forams. MATRIX: Echinoid spine, dissolved bivalve fragments	CAA do not indicate any paleodepth	Second sharp unfonformable surface for MIS 9? Soil horizon, exposure surface, stratified brown sediment infill, black manganese? Nodules?coral clasts and coarse sand sediment matrix. Amazing textures.
Hook 3P	96.13	96.76	MISSING		7	RUDSTONE	MIS 9e?				
Hook 3P	96.76	97.12	RECOVERED	Perth core library	7	RUDSTONE		coral frags - *Montipora/Porites* ? Thin and encrusting.		lowere energy deeper fore-reef slope setting?	Transition to completely different reef unit below paleosol. Into fine-sediment matrix, lowere energy deeper fore-reef slope setting? Rhodoliths
Hook 3P	97.12	97.27	RECOVERED	Perth core library	7	FLOATSTONE		foliaceous, encrusting Agaricid?		deep	some stratification of sediment layers and maybe really thin encrusting corals? Multiple phases of sediments. Branching coral frags, thickened algal crusts on bottom surfaces, so not in place. Nodules, fine sediment. Remnant of coral - structure infilled. foliaceous, encrusting agaricid?
Hook 3P	97.27	97.7	RECOVERED	GRG lab	7	FLOATSTONE			*Lithophyllum* gr. *pustulatum* , thin coaxial CCA indet. On coral, intergrown with encrusting forams. MATRIX: CCA fragments, bivalves, echinoid, soft coral spicule, encrusting foraminifera	CAA do not indicate any paleodepth	dissolution cracks and sediment infill, slight darker brown staining.
Hook 3P	97.7	97.82	RECOVERED	Perth core library	7	FLOATSTONE		Merulinidae?			largeer SM coral clasts floating in same fine sediment matrix as below. Some cement infill of cracks - minor dissolution surface remnant from paleosol above?
Hook 3P	97.82	97.88	RECOVERED	Perth core library	7	FLOATSTONE					small nodules?
Hook 3P	97.88	97.94	RECOVERED	Perth core library	7	FLOATSTONE					Branching and/or encrusting corals in fine, dense matrix - floatstone/foreef slope sands?
Hook 3P	97.94	98.18	RECOVERED	Perth core library	7	FLOATSTONE					.... 200mm interval of massive coralline limestone. Encrusting bioeroded coral infilled with fine sediment. Thin algae
Hook 3P	98.18	98.59	RECOVERED	Perth core library	7	FRAMESTONE				deep, forereef slope? Foreef slope sands?	.... 200mm interval of massive coralline limestone
Hook 3P	98.59	98.64	RECOVERED	Perth core library	7	FLOATSTONE				deep, forereef slope?	
Hook 3P	98.64	98.82	RECOVERED	Perth core library	7	FLOATSTONE				deep, forereef slope?	some dissolution of branching coral fragments
Hook 3P	98.82	98.91	MISSING		7	FLOATSTONE				deep, forereef slope?	
Hook 3P	98.91	99.2	RECOVERED	Perth core library	7	FLOATSTONE				deep, forereef slope?	Very fine buff homogenous white chalky sediment with floating branch coral pieces > 10mm
Hook 3P	99.2	99.69	RECOVERED	GRG lab	7	FLOATSTONE		*Porites /Montipora* ?		deep, forereef slope?	Very fine buff homogenous white chalky sediment with floating dissolved branch coral pieces > 10mm
Hook 3P	99.69	99.82	RECOVERED	Perth core library	7	FLOATSTONE		coral frags		deep, forereef slope?	interval of weakly cemented coralline limestone. Very small rhodoliths on grainstone fabric!?
Hook 3P	99.82	100.45	RECOVERED	GRG lab	7	FLOATSTONE		coral frags - *Porites/Montipora* ?		deep, forereef slope?	Very fine chalky sediment with floating branch coral pieces > 10mm

Hole ID	From	To	RECOVERY	SAMPLE LOCATION	REEF UNIT	LITHOLOGY	PALEOSOIL	VERMETIDS 0, 1=1-5, 2=5-10, 3=10-15, 4=>15	CORAL ID	CORALLINE ALGAE ID	DEPOSITIONAL ENVIRONMENT	LOGGING/COMMENTS
SRSEBH6J	0.000	1.500	MISSING	Perth core library	1	RUDSTONE						
SRSEBH6J	1.500	1.500	MISSING		1	FRAMESTONE				*Porolithon onkodes* (section is very thick but can see heterocyst rows	Shallow	
SRSEBH6J	1.500	1.900	MISSING		1	FRAMESTONE						
SRSEBH6J	1.900	2.000	RECOVERED	Perth core library	1	FRAMESTONE		1	*Porites*			
SRSEBH6J	2.000	2.300	MISSING		1	FRAMESTONE						
SRSEBH6J	2.300	2.400	RECOVERED	Perth core library	1	FRAMESTONE		1	*Porites*			borings
SRSEBH6J	2.400	2.600	CORE LOSS	Perth core library	1							
SRSEBH6J	2.600	3.000	MISSING		1	RUDSTONE						
SRSEBH6J	3.000	3.200	MISSING		1	FRAMESTONE						cobble of domal coral
SRSEBH6J	3.200	3.600	CORE LOSS	Perth core library	1							
SRSEBH6J	3.600	4.000	MISSING		1	RUDSTONE						
SRSEBH6J	4.000	4.350	MISSING		1	FRAMESTONE						
SRSEBH6J	4.350	4.450	RECOVERED	Perth core library	1	FRAMESTONE		2	*Montipora* x 4 colonies		abundant vermetids = shallow	
SRSEBH6J	4.450	4.650	MISSING		1	RUDSTONE						
SRSEBH6J	4.650	4.750	MISSING		1	FRAMESTONE						
SRSEBH6J	4.750	5.000	MISSING		1	RUDSTONE						
SRSEBH6J	5.000	5.100	CORE LOSS		1							
SRSEBH6J	5.100	5.250	MISSING		1	RUDSTONE						
SRSEBH6J	5.250	5.750	RECOVERED	GRG Lab	1	FRAMESTONE		4	*Porites* /*Montipora*			Domal coral framestone, white, some encrusting coralline red algal laminations, bores and moulds in places 10-20mm (10%). .... with a 60mm interval of porous coralline red algal laminations with uncemented sand interstitial to laminae
SRSEBH6J	5.750	6.000	MISSING		1	FRAMESTONE						
SRSEBH6J	6.000	6.200	MISSING		1	RUDSTONE						
SRSEBH6J	6.200	6.500	CORE LOSS		1							
SRSEBH6J	6.500	7.400	MISSING		1	RUDSTONE						
SRSEBH6J	7.400	8.000	CORE LOSS		1							
SRSEBH6J	8.000	9.300	MISSING		1	FRAMESTONE						
SRSEBH6J	9.300	9.450	RECOVERED	Perth core library	1	FRAMESTONE		1?	*Porites* ?			
SRSEBH6J	9.450	10.000	MISSING		1	FRAMESTONE						
SRSEBH6J	10.000	10.750	MISSING		1	RUDSTONE						
SRSEBH6J	10.750	12.000	MISSING		1	FRAMESTONE						
SRSEBH6J	12.000	12.100	MISSING		1	RUDSTONE						
SRSEBH6J	12.100	12.500	CORE LOSS		1							
SRSEBH6J	12.500	13.500	MISSING		1	RUDSTONE						
SRSEBH6J	13.500	13.650	MISSING		1	FRAMESTONE						
SRSEBH6J	13.650	14.000	CORE LOSS		1							
SRSEBH6J	14.000	15.000	MISSING		1	RUDSTONE						
SRSEBH6J	15.000	15.500	CORE LOSS		1							
SRSEBH6J	15.500	15.600	MISSING		1	RUDSTONE						
SRSEBH6J	15.600	15.900	MISSING		1	FRAMESTONE						
SRSEBH6J	15.900	16.050	MISSING		1	RUDSTONE						
SRSEBH6J	16.050	16.150	MISSING		1	FRAMESTONE						
SRSEBH6J	16.150	16.700	MISSING		1	RUDSTONE						
SRSEBH6J	16.700	17.000	CORE LOSS		1							
SRSEBH6J	17.000	17.300	MISSING		1	RUDSTONE						
SRSEBH6J	17.300	17.530	MISSING		1	FRAMESTONE						
SRSEBH6J	17.530	18.120	RECOVERED	Perth core library	1	FRAMESTONE			Mussidae? (*Lobophyllia* ?)			
SRSEBH6J	18.120	18.500	MISSING		1	RUDSTONE						
SRSEBH6J	18.500	18.600	MISSING		1	FRAMESTONE						
SRSEBH6J	18.600	18.700	RECOVERED	Perth core library	1	FRAMESTONE		1	*Porites*		vermetids = shallow	
SRSEBH6J	18.700	19.150	MISSING		1	RUDSTONE						
SRSEBH6J	19.150	19.400	MISSING		1	FRAMESTONE						
SRSEBH6J	19.400	19.700	MISSING		1	RUDSTONE						
SRSEBH6J	19.700	19.900	MISSING		1	FRAMESTONE						
SRSEBH6J	19.900	20.000	CORE LOSS		1							
SRSEBH6J	20.000	20.500	MISSING		1	RUDSTONE						
SRSEBH6J	20.500	20.600	RECOVERED	Perth core library	1	FRAMESTONE		1?	*Porites*		vermetids = shallow	20.55 - 20.75m: cobble of coral framestone 60-100mm separated by sand and fine to medium gravel
SRSEBH6J	20.600	20.750	MISSING		1	FRAMESTONE						
SRSEBH6J	20.750	21.000	MISSING		1	RUDSTONE						
SRSEBH6J	21.000	21.150	MISSING		1	FRAMESTONE						
SRSEBH6J	21.150	21.250	MISSING		1	RUDSTONE						
SRSEBH6J	21.250	21.500	CORE LOSS		1							
SRSEBH6J	21.500	22.300	MISSING		1	FRAMESTONE						
SRSEBH6J	22.300	22.400	RECOVERED	Perth core library	1	FRAMESTONE		1	*Porites*		vermetids = shallow	Domal coral framestone: crystalline, white to pale brown-white, predominantly Porites, with some fine to medium gravel and sand between cobbles and along algal encrusted defect surfaces, sand and gravel comprises coral rubble, algal platelets and shell fragments.
SRSEBH6J	22.400	22.550	MISSING		1	FRAMESTONE						
SRSEBH6J	22.550	22.650	MISSING		1	RUDSTONE						
SRSEBH6J	22.650	23.000	CORE LOSS		1							
SRSEBH6J	23.000	23.250	MISSING		1	RUDSTONE						
SRSEBH6J	23.250	23.850	MISSING		1	FRAMESTONE						
SRSEBH6J	23.850	24.500	CORE LOSS		1							
SRSEBH6J	24.500	24.850	MISSING		1	RUDSTONE						
SRSEBH6J	24.850	25.750	MISSING		1	FRAMESTONE						
SRSEBH6J	25.750	26.000	CORE LOSS		1							
SRSEBH6J	26.000	26.300	MISSING		1	FRAMESTONE						
SRSEBH6J	26.300	26.500	RECOVERED	GRG Lab	1	FRAMESTONE		1?	3 x colonies, *Montipora* ?, *Acropora* (basal coenosteum, *Porites*)			Domal coral Porites framestone with disrrupted intervals with cavities filled with sandy gravels and cobbles, angular, pale grey-white. Coarse fraction consists of coral fragments and sand comprises of coral rubble, *Halimeda* plates, shell fragments
SRSEBH6J	26.500	26.650	MISSING		1	FRAMESTONE						
SRSEBH6J	26.650	27.100	MISSING		1	RUDSTONE						
SRSEBH6J	27.100	27.200	MISSING		1	FRAMESTONE						

SRSEBH6J	27.200	27.500	CORE LOSS		1							
SRSEBH6J	27.500	29.500	MISSING		1	FRAMESTONE						
SRSEBH6J	29.500	29.610	RECOVERED	GRG Lab	1	BINDSTONE			*Galaxea* ??, *Turbinaria* ?? multiple colonies enc coral, and *Tubipora*			
SRSEBH6J	29.610	30.000	MISSING		1	FLOATSTONE						
SRSEBH6J	30.000	30.200	RECOVERED	Perth core library	1	FRAMESTONE		1?	*Porites*			
SRSEBH6J	30.200	30.500	CORE LOSS		1							
SRSEBH6J	30.500	31.400	MISSING		1	RUDSTONE						
SRSEBH6J	31.400	31.600	MISSING		1	FRAMESTONE						
SRSEBH6J	31.600	32.000	CORE LOSS		1							
SRSEBH6J	32.000	32.200	MISSING		1	FRAMESTONE						
SRSEBH6J	32.200	32.470	RECOVERED	Perth core library	1	FRAMESTONE		1?	*Porites*			
SRSEBH6J	32.470	33.000	MISSING		1	FRAMESTONE						some subvertical encrusting coralline red algal laminations domal coral framestone, grey, brown. ... with a pocket of calcirudite, comprising coarse subangular to subrounded gravel and cobble sized fragments of coral, trace of shells in variably cemented matrix. ... abundant cavities and borings on domal coral framestone
SRSEBH6J	33.000	33.150	RECOVERED	Perth core library	1	FRAMESTONE			*Porites*			
SRSEBH6J	33.150	34.700	MISSING		1	FRAMESTONE					Deep?	
SRSEBH6J	34.700	34.850	RECOVERED	Perth core library	1	FRAMESTONE		1	*Porites*			
SRSEBH6J	34.850	35.500	MISSING		1	FRAMESTONE				Coaxial core of unknown algae ID (*Mesophyllum*? Maybe) algae is highly micritised so difficult to ID		
SRSEBH6J	35.500	35.750	MISSING		1	FLOATSTONE						
SRSEBH6J	35.750	35.800	RECOVERED	Perth core library	1	FLOATSTONE	MIS 1	1	Ukn coral fragments			
SRSEBH6J	35.800	36.300	MISSING		2	FLOATSTONE	P					
SRSEBH6J	36.300	36.500	RECOVERED	Perth core library	2	RUDSTONE	MIS 5		Ukn corals			
SRSEBH6J	36.500	36.850	MISSING		2	FLOATSTONE						
SRSEBH6J	36.850	37.000	RECOVERED	Perth core library	2	BINDSTONE			2 x colonies, Merulinidae?, *Montipora* ?			
SRSEBH6J	37.000	37.170	RECOVERED	Perth core library	2	BINDSTONE			*Acropora* 2x colonies			
SRSEBH6J	37.170	37.330	RECOVERED	Perth core library	2	BINDSTONE		1	Acroporidae??			
SRSEBH6J	37.330	37.585	RECOVERED	Perth core library	2	BINDSTONE			Ukn *Porites* /*Montipora* ?			
SRSEBH6J	37.585	38.000	RECOVERED	Perth core library	2	BINDSTONE						Bindstone - maybe algae and corals. Sediment.
SRSEBH6J	38.000	38.050	MISSING		2	FLOATSTONE						
SRSEBH6J	38.050	38.130	RECOVERED	Perth core library	2	BINDSTONE		1	*Pocillopora* ???			
SRSEBH6J	38.130	38.660	MISSING		2	FLOATSTONE				*Porolithon onkodes* (heterocyst rows) and something coaxial below unknown ll	Shallow	
SRSEBH6J	38.660	38.900	RECOVERED	GRG Lab	2	BINDSTONE		1?	2 x colonies, Merulinidae, *Montipora* ?	CCA indet (male conceptacle). Looks like *Neogoniolithon* . On coral and overgrown by coral, abundant vermetids, encrusting forams. Matrix: nothing	CAA plus vermetids indicate < 6 m	sub massive circular corallites merulinidae - framestone to bindstone. If sm more likely bindstone
SRSEBH6J	38.900	40.500	MISSING		2	FLOATSTONE				*Porolithon onkodes*, thin layer of either *Mesophyllum* (coaxial core)or "*Pneophyllum*" conicum possibly a cavity assemblage. Fragment of *Lithophyllum* gr *pustulatum* (fanning surface cut oblique)	Shallow	
SRSEBH6J	40.500	40.690	RECOVERED	Perth core library	2	BINDSTONE		1	mutiple colonies, *Montipora* ???, lots of interlayered CCA			
SRSEBH6J	40.690	41.000	MISSING		2	FLOATSTONE						
SRSEBH6J	41.000	41.400	RECOVERED	Perth core library	2	FRAMESTONE			*Porites* ?, Merulinidae, *Montipora* ?			
SRSEBH6J	41.400	43.150	MISSING		2	FLOATSTONE						
SRSEBH6J	43.150	43.350	RECOVERED	Perth core library	2	GRAINSTONE						
SRSEBH6J	43.350	43.750	MISSING		2	FLOATSTONE						
SRSEBH6J	43.750	43.800	RECOVERED	Perth core library	2	GRAINSTONE				coaxial thali (*Mesophyllum*? Or "*Pneophyllum*" *conicum*?) covering a dimerous unknown ID algae (too thick to ID)		
SRSEBH6J	43.800	44.000	CORE LOSS		2							
SRSEBH6J	44.000	44.120	MISSING		2	RUDSTONE						
SRSEBH6J	44.120	44.354	RECOVERED	Perth core library	2	PACKSTONE-RUDSTONE						
SRSEBH6J	44.354	44.369	MISSING		2	RUDSTONE						
SRSEBH6J	44.369	44.504	RECOVERED	Perth core library	2	PACKSTONE-RUDSTONE						
SRSEBH6J	44.504	44.510	MISSING		2	RUDSTONE						
SRSEBH6J	44.510	44.600	RECOVERED	Perth core library	2	PACKSTONE-RUDSTONE						
SRSEBH6J	44.600	45.640	MISSING		2	RUDSTONE						
SRSEBH6J	45.640	45.810	RECOVERED	Perth core library	2	FRAMESTONE			Merulinidae (*Goniastrea* ?), *Gonipora* ??			
SRSEBH6J	45.810	46.800	MISSING		2	RUDSTONE						
SRSEBH6J	46.800	47.000	CORE LOSS		2							
SRSEBH6J	47.000	48.300	MISSING		2	RUDSTONE						
SRSEBH6J	48.300	48.600	RECOVERED	Perth core library	2	FRAMESTONE		1?	*Gonipora* ??			
SRSEBH6J	48.600	48.800	RECOVERED	Perth core library	2	FRAMESTONE			*Porites* , Ukn encrusting corals			... domal Porites framestone ... domal coral framestone and coralline red algal laminations with encrusting Homotrema rubrum
SRSEBH6J	48.800	49.200	MISSING		2	RUDSTONE						
SRSEBH6J	49.200	49.240	RECOVERED	Perth core library	2	GRAINSTONE				soft coral or octocoral spicules making up most of sediment. No algae		
SRSEBH6J	49.240	49.700	MISSING		2	RUDSTONE						
SRSEBH6J	49.700	50.000	RECOVERED	Perth core library	2	RUDSTONE		2	*Montipora* ?, *Porites* ?, & *Pocillopora* branches			
SRSEBH6J	50.000	50.300	RECOVERED	Perth core library	2	RUDSTONE						
SRSEBH6J	50.300	50.335	MISSING		2	RUDSTONE						
SRSEBH6J	50.335	50.720	RECOVERED	GRG Lab	2	RUDSTONE			*Acropora* ???? *Acropora* . Important!	Coaxial CCA indet (possibly *Dawsoniolithon*), unconformable thick *Porolithon* gr. *onkodes* . On coral and overgrown by coral, bivalves, serpulids, encrusting forams. NO MATRIX	CCA indicate < 10 m	. Homotrema rubrum encrusting abraded coralgal framestone porous and leached
SRSEBH6J	50.720	51.000	RECOVERED	Perth core library	2	FLOATSTONE			*Porites* ?, Merulinidae?			
SRSEBH6J	51.000	51.250	MISSING		2	FLOATSTONE						
SRSEBH6J	51.250	51.350	RECOVERED	Perth core library	2	FRAMESTONE			*Porites*			BASAL ENCRUSTATION SURFACE

SRSEBH6J	51.350	51.980	MISSING		2	FLOATSTONE					
SRSEBH6J	51.980	52.000	RECOVERED	Perth core library	2	FRAMESTONE		*Porites*			
SRSEBH6J	52.000	52.200	MISSING		2	RUDSTONE					
SRSEBH6J	52.200	55.850	MISSING		2	RUDSTONE					
SRSEBH6J	55.850	56.000	CORE LOSS		2						
SRSEBH6J	56.000	56.950	MISSING		2	RUDSTONE					
SRSEBH6J	56.950	57.050	RECOVERED	Perth core library	2	GRAINSTONE			Only fragments of algae and section is too thick to ID		
SRSEBH6J	57.050	58.300	MISSING		2	RUDSTONE					
SRSEBH6J	58.300	58.400	RECOVERED	Perth core library	2	FRAMESTONE		*Montipora* x 2 colonies			
SRSEBH6J	58.400	60.600	MISSING		2	RUDSTONE					
SRSEBH6J	60.600	61.350	MISSING		2	RUDSTONE					
SRSEBH6J	61.350	61.550	RECOVERED	GRG Lab	2	RUDSTONE					
SRSEBH6J	61.550	61.900	MISSING		2	RUDSTONE					
SRSEBH6J	61.900	62.400	CORE LOSS		2						
SRSEBH6J	62.400	62.600	MISSING		2	RUDSTONE					
SRSEBH6J	62.600	62.900	RECOVERED	Perth core library	2	FRAMESTONE		*Porites*			
SRSEBH6J	62.900	63.250	MISSING		2	RUDSTONE					
SRSEBH6J	63.250	63.550	RECOVERED	Perth core library	2	RUDSTONE		several enc/laminar? corals(*Montipora* /*Porites* , thin CCA crust			not in place - rudstone or floatstone, ... becoming pervasively cemented
SRSEBH6J	63.550	64.500	MISSING		2	RUDSTONE					
SRSEBH6J	64.500	64.600	RECOVERED	Perth core library	2	GRAINSTONE-RUDSTONE		small branches,			small shells 1-2mm, rhodoliths?
SRSEBH6J	64.600	65.000	MISSING		2	RUDSTONE					
SRSEBH6J	65.000	65.200	RECOVERED	Perth core library	2	GRAINSTONE					
SRSEBH6J	65.200	65.750	RECOVERED	Perth core library	2	FLOATSTONE					Brown sediment or algal staining?
SRSEBH6J	65.750	67.650	MISSING		2	FLOATSTONE					
SRSEBH6J	67.650	68.000	RECOVERED	Perth core library	2	FLOATSTONE	soils	*Galaxea* ?, BF unk branches, almost nodules, thin CCA			Brown–orange sediment – siliciclastics? Exposure. floatstone with nodules - rhodoliths - nodules more generic, branching corals with encrusting algae. Galaxea? Marc ID. not sure if in situ. Algal crust good photo.
SRSEBH6J	68.000	68.300	MISSING		2	FLOATSTONE					
SRSEBH6J	68.300	68.500	RECOVERED	Perth core library	2	WACKESTONE	soils				maybe coral? Dragged finer sediment. Wackestone.
SRSEBH6J	68.500	69.250	MISSING		2	FLOATSTONE	MIS 5				
SRSEB+K17+169:179	69.250	69.450	RECOVERED	GRG Lab	3	PACKSTONE-RUDSTONE	P	Acroporidae, Merlinidae fragment at the top		Cyclocypeus and what looks like Operculinella (uncertain): grainstone, deep facies >50m (Willem Renema)	Unconformity/paleosol, stratified sediment infill
SRSEBH6J	69.450	69.800	MISSING		3	FLOATSTONE	MIS 7c?		Fragment of highly dissolved algae*Lithophyllum* gr *kotschyanum* (bulbous branches), surrounded by an unknown algae ID		
SRSEBH6J	69.800	70.000	RECOVERED	Perth core library	3	FLOATSTONE	soils	*Acropora* branches?			not framestone. Branching things more like floatstone altered floating acropora.
SRSEBH6J	70.000	70.200	RECOVERED	Perth core library	3	RUDSTONE	soils	Unknown			
SRSEBH6J	70.200	70.730	MISSING		3	RUDSTONE					
SRSEBH6J	70.730	70.880	RECOVERED	Perth core library	3	BINDSTONE		several enccorals(*Montipora* ?, Agaricid? thin CCA crust			
SRSEBH6J	70.880	71.310	MISSING		3	RUDSTONE					
SRSEBH6J	71.310	71.580	RECOVERED	GRG Lab	3	FRAMESTONE	soils	Important! big changes, Columnar (*Helipora*) and defintiely BR.*Acropora* above with well developed CCA.	Thin section too thick in the CCA sector. On coral, some encrusting forams. MATRIX: Fragments of encrusting foraminifera, molluscs, other aragonitic skeletons	Shallow? CAA do not indicate any paleodepth	noT bafflestone. Framestone. Branching acropora right way up. Heliopora - blue coral. Classic photo - use this as example image for framestone.
SRSEBH6J	71.580	71.900	MISSING		3	RUDSTONE					
SRSEBH6J	71.900	72.190	RECOVERED	Perth core library	3	FRAMESTONE		Same *Helipora* continues	Possibly algae here but too thick to see any structure here.		
SRSEBH6J	72.190	72.310	RECOVERED	Perth core library	3	RUDSTONE	MIS 7a?	*Acropora* branches?			
SRSEBH6J	72.700	73.400	RECOVERED	Perth core library	3	RUDSTONE	P	*Isopora* ??	*Lithoporella* under *Sporolithon* (like *Lithophyllum* but has a dimerous core).*Lithophyllum* gr *pustulatum*?? *Peyssonellia* (highly dissolved)	Intermediate to deep??	Karst/cavities infilled with terrigenous sediment?
SRSEBH6J	73.400	74.300	MISSING		3	RUDSTONE	MIS 7c?				
SRSEBH6J	74.300	74.550	RECOVERED	Perth core library	3	RUDSTONE		*Acropora* branches?			Geopetal horizon with calcrete/soils
SRSEBH6J	74.550	76.410	MISSING		3	RUDSTONE					
SRSEBH6J	76.410	76.710	RECOVERED	Perth core library	3	HALIMEDA RUDSTONE		branching and laminar *Porites* ?			
SRSEBH6J	76.710	76.950	RECOVERED	Perth core library	3	HALIMEDA RUDSTONE		branching and laminar *Porites* ?			
SRSEBH6J	76.950	77.000	MISSING		3	RUDSTONE			frag of *Lithophyllum* gr *pustulatum* (plumose core dimerous periphery and a branch?)*Lithoporella* crust on top of *Acervulina* on top of coral. Need to check context if it is a rudstone if these are fragments of coral or framework!		
SRSEBH6J	77.000	77.200	RECOVERED	Perth core library	3	HALIMEDA RUDSTONE	P	*Porites* ?			
SRSEBH6J	77.200	77.900	MISSING		3	RUDSTONE					
SRSEBH6J	77.900	78.000	CORE LOSS	Perth core library	3						
SRSEBH6J	78.000	78.200	RECOVERED	GRG Lab	3	PACKSTONE-RUDSTONE	P	*Acropora* branches?	CCA fragments (*Harveylithon* or *Porolithon*), thin encrusting CCA around coral, possibly *Lithophyllum* sp. MATRIX: *Halimeda* , gastropods, bivalves, CCA fragments, encrusting foraminifera, larger benthic foraminifer, small benthic foraminifera, sponge spicules	CAA do not indicate any paleodepth	Geopetal surface boundary – exposure surface? Thin calcrete, coral fragments, CCA, *Halimeda*
SRSEBH6J	78.200	78.730	MISSING		3	RUDSTONE					
SRSEBH6J	78.730	78.850	RECOVERED	Perth core library	3	GRAINSTONDE-RUDSTONE		*Acropora* branches?			
SRSEBH6J	78.850	78.900	CORE LOSS		3						
SRSEBH6J	78.900	79.700	MISSING		3	RUDSTONE					
SRSEBH6J	79.700	80.000	RECOVERED	Perth core library	3	HALIMEDA-RUDSTONE					
SRSEBH6J	80.000	80.350	RECOVERED	Perth core library	3	HALIMEDA-RUDSTONE	P	*Acropora* and other genera			Cements
SRSEBH6J	80.350	80.600	RECOVERED	Perth core library	3	HALIMEDA-RUDSTONE	P	Merulinidae fragment, 2x EN corals	2 generations of cements: 1)? 2)Aragonite (submarine cement)		Lots of orange cements around cavities/karst and *Halimeda*
SRSEBH6J	80.600	81.000	MISSING		3	RUDSTONE					
SRSEBH6J	81.000	81.250	RECOVERED	Perth core library	3	FRAMESTONE		Merulinidae (*Diploastrea* ??)			
SRSEBH6J	81.250	81.264	MISSING		3	FRAMESTONE					
SRSEBH6J	81.264	81.590	RECOVERED	Perth core library	3	RUDSTONE		Poritidae ??			
SRSEBH6J	81.590	81.880	RECOVERED	Perth core library	3	GRAINSTONE-RUDSTONE		*Acropora* ??			
SRSEBH6J	81.590	81.880	RECOVERED	Perth core library	3	GRAINSTONE-RUDSTONE		unkn coral, Acroporiidae?			
SRSEBH6J	81.590	81.880	RECOVERED	Perth core library	3	GRAINSTONE-RUDSTONE		X3 EN corals			

SRSEBH6J	81.880	81.980	MISSING		3	RUDSTONE						
SRSEBH6J	81.980	82.000	RECOVERED	Perth core library	3	FRAMESTONE						
SRSEBH6J	82.000	82.230	RECOVERED	Perth core library	3	GRAINSTONE-RUDSTONE						
SRSEBH6J	82.230	83.450	MISSING		3	RUDSTONE						
SRSEBH6J	83.450	83.870	RECOVERED	Perth core library	3	GRAINSTONE-RUDSTONE			*Acropora* branches?			Karst, cements
SRSEBH6J	83.870	84.500	MISSING		3	RUDSTONE						
SRSEBH6J	84.500	84.700	RECOVERED	Perth core library	3	HALIMEDA-GRAINSTONE			*Acropora* branches?			
SRSEBH6J	84.700	85.100	RECOVERED	Perth core library	3	FRAMESTONE			*Porites*	Frag of *Porolithon onkodes* (dimerous, heterocysts?). The fact that there are frags of shallow water reefs might indicate that is a shallow water reef coeval at the time of deposition acting as the sediment source to this location.	shallow?	
SRSEBH6J	85.100	85.150	MISSING		3	FRAMESTONE					shallow?	
SRSEBH6J	85.150	85.200	RECOVERED	Perth core library	3	FRAMESTONE			*Porites*			Crystalline domal coral framestone, Porites colony
SRSEBH6J	85.200	85.300	MISSING		3	FRAMESTONE						
SRSEBH6J	85.300	85.340	RECOVERED	Perth core library	3	FRAMESTONE			*Porites*			
SRSEBH6J	85.340	87.550	MISSING		3	RUDSTONE		1				
SRSEBH6J	87.550	87.750	RECOVERED	Perth core library	3	FRAMESTONE			Merlinidae, 2x EN corals, with CCA			
SRSEBH6J	87.750	87.950	MISSING		3	RUDSTONE						
SRSEBH6J	87.950	88.000	RECOVERED	Perth core library	3	RUDSTONE				Fragments of *Porolithon onkodes*, frags of plumose and dimerous algaes unknown ID and some coaxial thali unknown algal II		
SRSEBH6J	88.000	88.050	MISSING		3	RUDSTONE						
SRSEBH6J	88.050	88.530	RECOVERED	Perth core library	3	GRAINSTONE-RUDSTONE			branch coral fragments (*Acropora* , *Pocilloproa*)		higher energy reef flat/upper reef slope?	Very coarse-grained grainstone–rudstone – high energy
SRSEBH6J	88.050	88.530	RECOVERED	Perth core library	3	GRAINSTONE-RUDSTONE			large coral fragments, mixed.		higher energy reef flat/upper reef slope?	Very coarse-grained grainstone–rudstone – high energy
SRSEBH6J	88.050	88.530	RECOVERED	Perth core library	3	GRAINSTONE-RUDSTONE					higher energy reef flat/upper reef slope?	Very coarse-grained grainstone–rudstone – high energy
SRSEBH6J	88.530	89.000	MISSING		3	RUDSTONE						
SRSEBH6J	89.000	89.100	RECOVERED	Perth core library	3	GRAINSTONE-RUDSTONE			*Acropora* fragments			
SRSEBH6J	89.100	89.450	MISSING		3	CRYSTALLINE CALCIRUDITE						
SRSEBH6J	89.450	89.790	RECOVERED	Perth core library	3	GRAINSTONE-RUDSTONE			mainly *Acropora* fragments		higher energy reef flat/upper reef slope?	Very coarse-grained grainstone–rudstone – high energy
SRSEBH6J	89.790	90.950	MISSING		3	RUDSTONE						
SRSEBH6J	90.950	90.900	RECOVERED	GRG Lab	3	GRAINSTONE-RUDSTONE			mainly *Acropora* fragments, with CCA coating			
SRSEBH6J	90.900	91.150	MISSING		3	RUDSTONE						
SRSEBH6J	91.150	91.300	RECOVERED	Perth core library	3	GRAINSTONE-RUDSTONE			mainly *Acropora* fragments, with CCA coating, plus unk coral (Fungidae?)		black coating - manganese - redox? Deep?	black coating - manganese - redox? Deep?
SRSEBH6J	91.300	92.450	MISSING		3	RUDSTONE						
SRSEBH6J	92.450	92.470	RECOVERED	Perth core library	4	GRAINSTONE-RUDSTONE	P					
SRSEBH6J	92.470	93.200	MISSING		4	RUDSTONE						
SRSEBH6J	93.200	93.400	RECOVERED	Perth core library	4	GRAINSTONE-RUDSTONE			mainly *Acropora* fragments, some *Pocillipora* , with CCA coating			
SRSEBH6J	93.400	94.700	MISSING		4	RUDSTONE						
SRSEBH6J	94.700	94.940	RECOVERED	Perth core library	4	FRAMESTONE			complex, lots of EN coral			
SRSEBH6J	94.940	95.670	MISSING		4	RUDSTONE						
SRSEBH6J	95.670	96.000	RECOVERED	Perth core library	4	FRAMESTONE						
SRSEBH6J	96.000	96.350	RECOVERED	Perth core library	4	RUDSTONE			mainly robust *Acropora* fragments, some *Pocillipora* ,, EN at the top			
SRSEBH6J	96.350	97.200	MISSING		4	RUDSTONE						
SRSEBH6J	97.200	97.350	RECOVERED	GRG Lab	4	FRAMESTONE			*Porites*	*Porolithon* gr. *onkodes* , small fragment of *Lithophyllum* sp. On coral, abundant encrusting forams, serpulids. MATRIX: Serpulids, larger benthic foraminifera, geniculate CA, CCA, encrusting foraminifera, bivalves	CCA indicate < 10 m	
SRSEBH6J	97.350	97.550	RECOVERED	Perth core library	4	FRAMESTONE	soils? Or cements/manganese		*Porites*	Fragments of algae not able to ID, that have filled in hole inside cavity of coral - so probably not useful anyways		
SRSEBH6J	97.550	99.350	MISSING		4	RUDSTONE						
SRSEBH6J	99.350	99.410	RECOVERED	Perth core library	4	GRAINSTONE-RUDSTONE	soils?		*Acropora* and *Porites* ?	Several fragments of*Porolithon onkodes* , fragments of *Lithophyllum* gr *prototypum* (looks like *pustulatum*), frags of coaxial thalli unknown ID, frags of geniculate algae (not*Amphiroa*), frag of *Lithoohvllum*: so?	larger, thicker branch clasts indicates higher energy?	larger, thicker branch clasts indicates higher energy?
SRSEBH6J	99.410	100.000	MISSING		4	RUDSTONE						
SRSEBH6J	100.000	100.196	RECOVERED	GRG Lab	4	BINDSTONE			numerous EN corals, EN Merulinidea at the bottom			
SRSEBH6J	100.196	100.326	RECOVERED	Perth core library	4	BINDSTONE						
SRSEBH6J	100.326	100.506	RECOVERED	Perth core library	4	BINDSTONE						
SRSEBH6J	100.506	100.588	MISSING		4	RUDSTONE						
SRSEBH6J	100.588	100.648	RECOVERED	Perth core library	4	BINDSTONE						
SRSEBH6J	100.648	101.000	RECOVERED	Perth core library	4	BINDSTONE			*Pocillopora*			
SRSEBH6J	100.648	101.000	RECOVERED	Perth core library	4	BINDSTONE			numerous EN corals, EN Merulinidea at the bottom			
SRSEBH6J	100.648	101.000	RECOVERED	Perth core library	4	BINDSTONE						
SRSEBH6J	101.000	101.200	RECOVERED	Perth core library	4	BINDSTONE						
SRSEBH6J	101.200	101.188	MISSING		4	RUDSTONE						
SRSEBH6J	101.188	101.526	RECOVERED	Perth core library	4	BINDSTONE						... small (7mm) corallite domal coral
												... small (7mm) corallite domal coral
SRSEBH6J	101.526	101.626	RECOVERED	Perth core library	4	BINDSTONE						cements
SRSEBH6J	101.626	101.750	RECOVERED	Perth core library	4	BINDSTONE						
SRSEBH6J	101.750	102.000	RECOVERED	Perth core library	4	BINDSTONE						
SRSEBH6J	102.000	102.168	RECOVERED	Perth core library	4	FRAMESTONE	MIS 7c?					
SRSEBH6J	102.168	102.333	RECOVERED	Perth core library	4	PACKSTONE	P		merulinidae massive, SM/M, *Favia* /*Montastria* ?			packstone? Grainstone, bivalve, sediment, coralites circular, merulinidae massive, SM/M, favia/montastria? Marc ID? not shared walls.
SRSEBH6J	102.333	102.588	RECOVERED	Perth core library	4	PACKSTONE	MIS 7e?			Fragments of *Porolithon* gr. *onkodes* , frags of *Hydrolithon boergesenii* (cell fusions visible), frags of *Lithophyllum* gr. *prototypum* (tall cells, not pustulatum), encrusting foraminifera, Peyssonneliaceans, unknown algae ID of very thi algae		
SRSEBH6J	102.588	102.660	RECOVERED	Perth core library	4	FRAMESTONE						

SRSEBH6J	102.660	102.720	RECOVERED	Perth core library	4	BINDSTONE						
SRSEBH6J	102.720	103.000	RECOVERED	Perth core library	4	BINDSTONE						
SRSEBH6J	103.000	103.200	RECOVERED	Perth core library	4	BINDSTONE						
SRSEBH6J	103.200	103.510	MISSING		4	RUDSTONE						
SRSEBH6J	103.510	103.670	RECOVERED	Perth core library	4	BINDSTONE						20mm open cavity, dark brown-black staining 103.3m: sandy matrix interval
SRSEBH6J	103.670	104.000	MISSING		4	RUDSTONE						
SRSEBH6J	104.000	104.138	RECOVERED	Perth core library	4	FRAMESTONE						
SRSEBH6J	104.138	104.294	RECOVERED	Perth core library	4	FRAMESTONE						
SRSEBH6J	104.294	104.642	RECOVERED	Perth core library	4	FRAMESTONE						
SRSEBH6J	104.294	104.642	RECOVERED	Perth core library	4	FRAMESTONE						
SRSEBH6J	104.294	104.642	RECOVERED	Perth core library	4	FRAMESTONE						
SRSEBH6J	104.642	104.929	RECOVERED	Perth core library	4	FRAMESTONE						
SRSEBH6J	104.929	105.000	RECOVERED	Perth core library	4	FLOATSTONE						branching frags not in situ - rudstone/floatstone mostly sediment frags of corals, floatstone
SRSEBH6J	105.000	106.000	MISSING		4	RUDSTONE						
SRSEBH6J	106.000	106.242	RECOVERED	Perth core library	4	FRAMESTONE					Shallowing, higher energy?	
SRSEBH6J	106.200	106.450	RECOVERED	Perth core library	4	FRAMESTONE	P?		*Goniastrea* /Merulinidae?			framestone, massive and small corallites - goniastrea, alagal crust - in situ not baffflestone, majority is not sediment. More circular so maybe not goniastrea meulinidae for sure.
SRSEBH6J	106.242	106.607	RECOVERED	Perth core library	4	PACKSTONE-RUDSTONE			*Acropora* , *Millepora*			rudstone, still quite bit of matrix, acropora and porites branches, so massive and branching, big branch of acropora, packstone matric, millepora axial branch, crust sitting matrix, use this figure as example of rudstone
SRSEBH6J	106.242	106.607	RECOVERED	Perth core library	4	RUDSTONE						
SRSEBH6J	106.242	106.607	RECOVERED	Perth core library	4	RUDSTONE						
SRSEBH6J	106.607	106.887	RECOVERED	Perth core library	4	RUDSTONE						
SRSEBH6J	106.887	107.000	RECOVERED	Perth core library	4	FLOATSTONE						
SRSEBH6J	107.000	107.188	MISSING		4	RUDSTONE						
SRSEBH6J	107.188	107.388	RECOVERED	Perth core library	4	RUDSTONE			*Acropora*			one algal crust, forams in sdiment, still rudstone, not bindstone. Context of algae is nodule. Large mix brsanching corals of diff sizes. Acropora?
SRSEBH6J	107.388	107.548	RECOVERED	Perth core library	4	FRAMESTONE						
SRSEBH6J	107.390	107.420	RECOVERED	Perth core library	4	FRAMESTONE						
SRSEBH6J	107.548	107.678	RECOVERED	Perth core library	4	FRAMESTONE						
SRSEBH6J	107.678	107.728	RECOVERED	Perth core library	4	GRAINSTONE						
SRSEBH6J	107.728	107.784	RECOVERED	Perth core library	4	FLOATSTONE	layered soils?		*Porites*		Deep?	possibly porites? Transitions into floatstone and back to porites - possibly collectively bindstone? Noting sediment in between. Geopetals. Porites looks similar (homogeneous, sandy texture) to deep fine sediment in these cores..interpeted here as deep fine sediment.
SRSEBH6J	107.784	108.400	MISSING		4	RUDSTONE						
SRSEBH6J	108.400	108.650	RECOVERED	Perth core library	4	PACKSTONE	layered soils?				Deep?	packstone reasonable with larger fragments, large geopetal, some stratified layers of pale brown to black mud, some fractures and cavities.
SRSEBH6J	108.650	108.660	MISSING		4	RUDSTONE						
SRSEBH6J	108.660	109.000	RECOVERED	Perth core library	4	PACKSTONE-RUDSTONE						rudstone with larger corals some *Halimeda* and packstone matrix
SRSEBH6J	109.000	109.300	RECOVERED	Perth core library	4	PACKSTONE-RUDSTONE						
SRSEBH6J	109.620	109.950	RECOVERED	Perth core library	4	GRAINSTONE-RUDSTONE						
SRSEBH6J	109.950	110.500	MISSING		4	RUDSTONE						
SRSEBH6J	110.500	110.800	RECOVERED	Perth core library	4	PACKSTONE-RUDSTONE	layered soils?				deep? Hemipelagic	cyclocly peus = deep?
SRSEBH6J	111.000	111.254	RECOVERED	Perth core library	4	BINDSTONE						bindstone at least part of it - top is more difficult, coral with algae at base with encrusting corals.
SRSEBH6J	111.254	111.344	RECOVERED	Perth core library	4	PACKSTONE						
SRSEBH6J	111.344	111.400	MISSING		4	RUDSTONE						
SRSEBH6J	111.400	111.450	RECOVERED	Perth core library	4	FLOATSTONE						
SRSEBH6J	111.408	111.458	RECOVERED	Perth core library	4	FLOATSTONE						
SRSEBH6J	111.458	111.524	RECOVERED	Perth core library	4	FLOATSTONE						
SRSEBH6J	111.524	111.770	RECOVERED	Perth core library	4	FLOATSTONE						
SRSEBH6J	111.770	112.000	RECOVERED	Perth core library	4	GRAINSTONE-RUDSTONE						grainstone-rudstone, coral at base? With algal crust? Hard to know
SRSEBH6J	112.000	112.250	MISSING		4	RUDSTONE						
SRSEBH6J	112.250	112.500	RECOVERED	Perth core library	4	GRAINSTONE-RUDSTONE	P					
SRSEBH6J	112.500	112.600	RECOVERED	Perth core library	4	FRAMESTONE					Deep?	
SRSEBH6J	112.600	114.250	MISSING		4	RUDSTONE						
SRSEBH6J	114.250	114.400	RECOVERED	Perth core library	4	HALIMEDA RUDSTONE						
SRSEBH6J	114.400	115.650	MISSING		4	RUDSTONE						
SRSEBH6J	115.650	115.800	RECOVERED	Perth core library	4	RUDSTONE						
SRSEBH6J	116.100	116.200	RECOVERED	Perth core library	4	PACKSTONE						*Halimeda* floating in matrix - grainstone-packstone - still fine grained material in there - wackestone? Stick with packstone?
SRSEBH6J	116.200	116.996	MISSING		4	RUDSTONE				planktonic foraminifera	Pelagic deepwater?	
SRSEBH6J	116.996	117.276	RECOVERED	Perth core library	4	GRAINSTONE-PACKSTONE						grainstone -packstone not convinced framework. Large
SRSEBH6J	117.276	117.460	RECOVERED	Perth core library	4	GRAINSTONE						From ca. 116-130m is a very distinct facies with encrusting or laminated thin corals with some thin algal interlaminations and detrital bioclastic matrix
SRSEBH6J	117.460	117.455	MISSING		4	RUDSTONE						
SRSEBH6J	117.455	117.480	RECOVERED	Perth core library	4	FRAMESTONE						
SRSEBH6J	117.480	119.050	MISSING		4	CARBONATE SAND						
SRSEBH6J	119.050	119.250	RECOVERED	Perth core library	4	FRAMESTONE						
SRSEBH6J	119.250	119.260	MISSING		4	CALCIRUDITE						
SRSEBH6J	119.260	119.400	RECOVERED	Perth core library	4	FLOATSTONE						
SRSEBH6J	119.400	120.450	MISSING		4	CALCIRUDITE						
SRSEBH6J	120.450	120.800	RECOVERED	Perth core library	4	FLOATSTONE						Floatstone matrix
SRSEBH6J	120.800	121.200	MISSING		4	RUDSTONE						
SRSEBH6J	121.200	121.550	RECOVERED	Perth core library	4	GRAINSTONE						
SRSEBH6J	121.550	122.520	MISSING		4	RUDSTONE						
SRSEBH6J	122.520	123.000	RECOVERED	Perth core library	4	PACKSTONE-RUDSTONE		1				
SRSEBH6J	122.520	123.000	RECOVERED	Perth core library	4	PACKSTONE-RUDSTONE						
SRSEBH6J	122.520	123.000	RECOVERED	Perth core library	4	PACKSTONE-RUDSTONE						
SRSEBH6J	122.520	123.000	RECOVERED	Perth core library	4	PACKSTONE-RUDSTONE						
SRSEBH6J	123.000	123.550	RECOVERED	Perth core library	4	FRAMESTONE						
SRSEBH6J	123.550	124.000	MISSING		4	RUDSTONE						
SRSEBH6J	124.000	124.300	RECOVERED	Perth core library	4	GRAINSTONE-RUDSTONE						Accumulation of *Halimeda* plates
SRSEBH6J	124.300	124.610	RECOVERED	GRG Lab	4	RUDSTONE			*Acropora*	Thin thallus of *Lithophyllum* gr. *pustulatum* around *Halimeda* plate, fragments of thin laminar CCA and geniculate corallines. Rudstone, lots of *Halimeda* . MATRIX: *Halimeda* , CCA, geniculate CA, bivalves, gastropods, encrusting foraminifera, larger bethic foraminifera, coral fragments	CAA do not indicate any paleodepth	branching not in place, rudstone/floatstone probably rudstone, acropora sitting in sediment facing wrong way

SRSEBH6J	124.610	124.955	RECOVERED	Perth core library	4	FRAMESTONE						
SRSEBH6J	124.955	125.010	MISSING		4	RUDSTONE						
SRSEBH6J	125.010	125.030	RECOVERED	Perth core library	4	FRAMESTONE						
SRSEBH6J	125.000	125.318	RECOVERED	Perth core library	4	RUDSTONE						
SRSEBH6J	125.318	125.636	RECOVERED	Perth core library	4	FRAMESTONE	2				vermetids indicate shallow	
SRSEBH6J	125.636	125.880	MISSING		4	RUDSTONE						
SRSEBH6J	125.880	125.995	RECOVERED	Perth core library	4	PACKSTONE-RUDSTONE						
SRSEBH6J	125.995	126.000	RECOVERED	Perth core library	4	PACKSTONE-RUDSTONE						... domal coral fragment in fine to coarse skeletal grainstone in a cemented matrix
SRSEBH6J	126.000	126.300	MISSING		4	RUDSTONE						
SRSEBH6J	126.300	126.400	RECOVERED	Perth core library	4	FRAMESTONE				coaxial (no visible concepticles) thali too thick too ID, *Mesophyllum* (what looks like a multiporate concepticle, looks like the*mesophyllum* is binding the substrate and providing substrate for the coral (above?)pretty sure is*Mesophyllum* but would be good to thin this section)	deep? Dark?	
SRSEBH6J	126.400	127.300	MISSING		4	RUDSTONE						
SRSEBH6J	127.300	127.400	RECOVERED	Perth core library	4	GRAINSTONE						
SRSEBH6J	127.400	128.000	MISSING		4	CALCIRUDITE						
SRSEBH6J	128.000	128.150	RECOVERED	Perth core library	4	GRAINSTONE						
SRSEBH6J	128.150	130.000	MISSING		4	CALCIRUDITE						
SRSEBH6J	130.000	130.400	RECOVERED	Perth core library	4	PACKSTONE						some coral frages with some algae, rest is sediment grainstone packstone. Sediment with forams, some dissolved corals with algae,
SRSEBH6J	130.400	131.150	MISSING		4	RUDSTONE						
SRSEBH6J	131.150	133.000	MISSING		4	PACKSTONE						
SRSEBH6J	133.000	133.200	RECOVERED	Perth core library	4	WACKESTONE						
SRSEBH6J	133.200	133.800	MISSING		4	PACKSTONE						... large benthic foraminifera
SRSEBH6J	133.800	133.900	RECOVERED	Perth core library	4	FRAMESTONE						
SRSEBH6J	133.900	135.100	MISSING		4	PACKSTONE						
SRSEBH6J	135.100	135.300	RECOVERED	Perth core library	4	GRAINSTONE						
SRSEBH6J	135.300	135.600	RECOVERED	Perth core library	4	WACKESTONE					Deeper forereef slope	sections of really larfge forams, wacksetone, rhodoliths? Cycoplethids? Smaller forams in sediment - deeper forereef slope algae could be useful - send photo to willem. Mudstone/wackestone? Or possibly thin foliaceous corals? In deep water environments. major distinct facies change.
SRSEBH6J	135.600	137.000	MISSING		4	RUDSTONE						
SRSEBH6J	137.000	137.100	RECOVERED	Perth core library	4	GRAINSTONE						
SRSEBH6J	137.100	137.200	MISSING		4	RUDSTONE						
SRSEBH6J	137.200	137.400	RECOVERED	Perth core library	4	HALIMEDA-RUDSTONE						
SRSEBH6J	137.400	138.000	MISSING		4	RUDSTONE						
SRSEBH6J	138.000	139.700	MISSING		4	RUDSTONE						
SRSEBH6J	139.700	139.900	RECOVERED	Perth core library	4	GRAINSTONE						
SRSEBH6J	139.900	140.300	MISSING		4	RUDSTONE	MIS 7e?					.... Carbonate gravel: interval 30-40mm thick
SRSEBH6J	140.300	140.430	RECOVERED	Perth core library	5	GRAINSTONE	P					
SRSEBH6J	140.430	142.200	MISSING		5	RUDSTONE	MIS 9					
SRSEBH6J	142.200	142.400	RECOVERED	Perth core library	5	PACKSTONE-RUDSTONE					Forereef slope?	not framestone - *Halimeda* some mud grainstone/packstone, finer material on outside. Cca at base, lithoclasts, sediment to right, geopetals. Rudstone with finer material, boundary, cavity. Not sure if coral - massive? Sediment at base wackestone/packstone. forereef slope environment?
SRSEBH6J	142.400	142.950	MISSING		5	RUDSTONE						
SRSEBH6J	142.950	143.000	CORE LOSS		5							
SRSEBH6J	143.000	143.350	MISSING		5	RUDSTONE						
SRSEBH6J	143.350	144.000	MISSING		5	RUDSTONE						
SRSEBH6J	144.000	144.400	RECOVERED	Perth core library	5	FRAMESTONE						
SRSEBH6J	144.000	144.400	RECOVERED	Perth core library	5	FRAMESTONE						
SRSEBH6J	144.000	144.400	RECOVERED	Perth core library	5	FRAMESTONE						
SRSEBH6J	144.400	144.800	RECOVERED	Perth core library	5	FRAMESTONE				Intermixed algaes including: Polystrata (type of *Peyssonellia* but it has plumose core or is fan-like), *Spongites*, *Mesophyllum*	Deep?	
SRSEBH6J	144.500	144.900	RECOVERED	Perth core library	5	FRAMESTONE	P					
SRSEBH6J	144.900	145.050	MISSING		5	FLOATSTONE				*Halimeda*. mostly *Neogoniolithon* (fanning concepticle), *spongites*, polystrata (*peyssonellia*), articulate (geniculate algae), frags of coaxial thali, frag of *Sporolithon* (looks like*Lithophyllum* gr *pustulatum*)	Deep?? (but also could be shallower)	
SRSEBH6J	145.050	145.250	RECOVERED	Perth core library	5	FLOATSTONE						Packstone matrix, floatstone
SRSEBH6J	145.250	146.080	MISSING		5	FLOATSTONE						
SRSEBH6J	146.080	146.220	RECOVERED	Perth core library	5	FRAMESTONE						
SRSEBH6J	146.220	147.300	MISSING		5	RUDSTONE						
SRSEBH6J	147.300	147.550	RECOVERED	Perth core library	5	RUDSTONE						
SRSEBH6J	147.550	149.000	MISSING		5	RUDSTONE						
SRSEBH6J	149.000	149.550	RECOVERED	GRG Lab	5	RUDSTONE	P?			Coaxial CCA indet, *Spongites* sp., *Lithophyllum* gr. *pustulatum* . On coral, intergrown with encrusting forams. MATRIX: *Halimeda* , CCA, soft coral spicules, bryozoans, bivalves, gastropods, encrusting foraminifera, serpulids, coral fragments	CAA do not indicate any paleodepth	148.0-148.65m *Halimeda* plates 148.65-149.0m domal coral framestone
SRSEBH6J	149.000	149.550	RECOVERED	Perth core library	5	RUDSTONE	P?					
SRSEBH6J	149.000	149.550	RECOVERED	Perth core library	5	RUDSTONE	P?					
SRSEBH6J	149.550	150.400	MISSING		5	FRAMESTONE						
SRSEBH6J	150.400	150.700	RECOVERED	Perth core library	5	RUDSTONE	P?					
SRSEBH6J	150.700	151.550	MISSING		5	FRAMESTONE						
SRSEBH6J	151.550	151.850	RECOVERED	Perth core library	5	HALIMEDA-RUDSTONE			Milleporid coral? (fine branched coral)	*Peyssonellia* fragment, thin algae of unknown ID around coral branches (can see cells), frag *Porolithon onkodes* , frag *Lithophyllum* gr *pustulatum*/*prototypum*		
SRSEBH6J	151.850	153.000	MISSING		5	RUDSTONE						
SRSEBH6J	153.000	153.200	RECOVERED	Perth core library	5	RUDSTONE						
SRSEBH6J	153.200	153.400	MISSING		5	RUDSTONE						
SRSEBH6J	153.400	153.750	RECOVERED	Perth core library	5	RUDSTONE						
SRSEBH6J	153.750	154.100	MISSING		5	RUDSTONE						
SRSEBH6J	154.100	154.350	RECOVERED	GRG Lab	5	RUDSTONE						
SRSEBH6J	154.350	155.310	MISSING		5	RUDSTONE						

SRSEBH6J	155.310	155.620	RECOVERED	Perth core library	5	FLOATSTONE				
SRSEBH6J	155.620	156.000	MISSING		5	RUDSTONE				
SRSEBH6J	156.000	156.200	RECOVERED	Perth core library	5	GRAINSTONE				
SRSEBH6J	156.200	156.530	MISSING		5	RUDSTONE				
SRSEBH6J	156.530	156.770	RECOVERED	Perth core library	5	FRAMESTONE				
SRSEBH6J	156.770	157.550	RECOVERED	Perth core library	6	HALIMEDA-RUDSTONE	P?/UNC?			
SRSEBH6J	157.550	157.700	MISSING		6	RUDSTONE		Frags of coaxial thali, crust too thick to ID but part of crust is *Lithophyllum* gr *pustulatum*		
SRSEBH6J	157.700	157.930	RECOVERED	Perth core library	6	GRAINSTONE	P?			
SRSEBH6J	157.930	158.000	MISSING		6	RUDSTONE				
SRSEBH6J	158.000	158.200	RECOVERED	Perth core library	6	GRAINSTONE-RUDSTONE			Deep water slope.	large forams again or foliaceous corals deep water. Deep water slope.
SRSEBH6J	158.200	158.460	MISSING		6	RUDSTONE				
SRSEBH6J	158.460	158.680	RECOVERED	Perth core library	6	GRAINSTONE-RUDSTONE			Deep	... blackening throughout core along linear vuggs, small concentric rhodoliths and foraminifera (?)
SRSEBH6J	158.680	159.000	MISSING		6	RUDSTONE				
SRSEBH6J	159.000	159.370	RECOVERED	Perth core library	6	RUDSTONE				
SRSEBH6J	159.370	159.800	MISSING		6	RUDSTONE				
SRSEBH6J	159.800	160.100	RECOVERED	Perth core library	6	FRAMESTONE		*Sporolithon* in crust, *Lithophyllum* gr *pustulaum*, *Lithoporella* (cell fusions so isnt pustulatum), *Peyssonellia*, thin crust of unknown algae ID intermingled in *Peyssonellia*	Typical deep water	... large rhodoliths
SRSEBH6J	160.100	163.000	MISSING		6	FLOATSTONE				
SRSEBH6J	163.000	163.400	RECOVERED	Perth core library	6	FLOATSTONE				
SRSEBH6J	163.000	163.400	RECOVERED	Perth core library	6	FLOATSTONE				
SRSEBH6J	163.000	163.400	RECOVERED	Perth core library	6	FLOATSTONE				
SRSEBH6J	163.400	165.200	MISSING		6	FLOATSTONE				
SRSEBH6J	165.200	165.400	RECOVERED	Perth core library	6	FLOATSTONE				
SRSEBH6J	165.400	168.000	MISSING		6	FLOATSTONE	MIS 9	*Lithophyllum* gr *pustulatum*, *Mesophyllum* (coaxial thali, multiporatre concepticles), *Spongites*?, *Lithothamnion* (big multiporate concepticles without a plumose core so not *Mesophyllum*), Big fragment of *Porolithon onkodes* covered by acervulinid and a small laminar crust (but ignore this in env. interpretation). need to check if the algae crust is around a fragment	Deep water?	
SRSEBH6J	168.000	168.300	RECOVERED	Perth core library	7	FLOATSTONE	P			stratified sediments in bands
SRSEBH6J	168.300	171.000	MISSING		7	FLOATSTONE	MIS 11?			
SRSEBH6J	171.000	171.250	RECOVERED	GRG Lab	7	FLOATSTONE	P			
SRSEBH6J	171.000	171.250	RECOVERED	GRG Lab	7	FLOATSTONE				
SRSEBH6J	171.250	171.900	MISSING		7					
SRSEBH6J	171.900	172.000	RECOVERED	Perth core library	7	FRAMESTONE				
SRSEBH6J	172.000	173.250	MISSING		7	FLOATSTONE				
SRSEBH6J	173.250	173.550	RECOVERED	Perth core library	7	FLOATSTONE				not framestone possible floatstone *Halimeda* ?
SRSEBH6J	173.250	173.550	RECOVERED	Perth core library	7	FLOATSTONE				
SRSEBH6J	173.250	173.550	RECOVERED	Perth core library	7	FLOATSTONE				
SRSEBH6J	173.550	175.000	MISSING		7	FLOATSTONE				
SRSEBH6J	175.000	175.300	RECOVERED	Perth core library	7	GRAINSTONE				
SRSEBH6J	175.000	175.300	RECOVERED	Perth core library	7	GRAINSTONE				
SRSEBH6J	175.300	177.100	MISSING		7	FLOATSTONE				
SRSEBH6J	177.100	177.200	RECOVERED	Perth core library	7	FRAMESTONE		Frags of coaxial thali, a small Lithophyllum gr pustulatum	Deep water - never terrestrially exposed?	
SRSEBH6J	177.200	179.000	MISSING		7	FLOATSTONE				
SRSEBH6J	179.000	179.200	RECOVERED	GRG Lab	7	FLOATSTONE				branching medium coral clasts in floatstone matrix?

APPENDIX G

Chapter 4 Supplement 3 - Detailed methodology and modelling workflow

---

1. SUPPLEMENT 3 – DETAILED METHODOLOGY

1.1 Modelling workflow and design

Model scenario 1 (Fig. 4A) is the base case 3-D forward model. It was constrained using multiple observational datasets and interpretation, including seismic sequence thickness and architecture, U/Th ages, modern bathymetry, and facies distributions. The U-Th ages depend on open-system behaviour, and are not robust constraints, but provide a useful reference framework to guide model calibration. Key parameters with greater associated uncertainty, for example carbonate production rates through time, were tested through sensitivity experiments to evaluate their effect on model outputs and minimise misfit to hard data, such as the modern multibeam bathymetry. The full modelling workflow, including data inputs, sensitivity testing, and calibration steps, is summarised in Figure 3. A seismic transect intersecting the three boreholes used in this study (Fig. 1B) served as the primary calibration reference. The model initiated at 392 kyr, and input parameters were iteratively adjusted until the final timestep reproduced the modern sea-level position, seismic sediment thickness and facies distribution (i.e., shallow reef framework on the platform margin and lagoonal facies in the platform interior). Highstand intervals that simulated shallow reef facies were qualitatively compared with borehole data. The modern seabed (Figs. 2 and 4D) and facies maps (Allen Coral Atlas, 2022) served as an empirical data constraint on the final timestep. Due to the seismic data gap over the South Scott Reef crest, this helped identify instances where for example, leeward margins were overly progradational, reef growth was too slow to fill accommodation, or subsidence rates were unrealistically high relative to sediment production and accumulation. In practice, this meant directly matching the elevation of stratigraphic horizons in the model to those observed in the seismic cross-sections and bathymetry, ensuring that both thickness trends and facies transitions were geologically consistent.

Calibration was achieved using an iterative trial-and-error approach, whereby input parameters were manually adjusted until the model reproduced the key observed elements of stratigraphy and platform geometry. While this qualitative approach lacks the quantitative rigour of inverse stratigraphic modelling methods that employ formal objective functions to calculate errors (e.g., Cross and Lessenger, 1999; Burgess et al., 2012; Ducros et al., 2023; Lottin Boing et al., 2025), it remains a widely used and effective strategy in

forward stratigraphic modelling. As noted by Lottin Boing et al. (2025), trial-and-error calibration provides flexibility, transparency and sufficient geological plausibility when the primary aim is to capture third-order stratigraphic controls rather than achieve statistically optimised fits. Objective function approaches can introduce computational expense, rely on incomplete data and risk biasing calibration towards parameter sets that minimise misfit but reduce geological realism. For the purpose of this study, reproducing third-order controls on Scott Reef platform evolution, the trial-and-error approach was therefore both sufficient and appropriate, while also enabling exploration of parameter sensitivity constrained by hypothesised environmental change.

1.1.1 Paleobathymetry and paleowater depth

Regional sequence stratigraphic horizons interpreted from Megator 3-D (Williams et al., 2023) are used in this study to constrain model paleobathymetry inputs and simulated sequence thicknesses (Supplement 1 and 2). Initial topography was derived from the H13 interpreted sequence boundary on seismic data (Fig. 8 and Table 1; Williams et al., 2023), identified using standard seismic stratigraphic criteria (Mitchum et al., 1977; Posamentier et al., 2022) as regionally continuous unconformities marked by characteristic stratal terminations, including truncation and offlap below, and onlap and downlap above (Paumard et al., 2017). Interpretation was based on seismic reflection continuity, geometry, amplitude and frequency. The mapped unconformity was converted to a depth grid to reconstruct the paleo-topography that was used as the base topography for model initiation. Seismic architecture reveals a bucket-shaped platform characterized by margin reefs that border steep marginal slopes mirroring the present-day surface environments (Williams et al., 2023). There are distinct cycles of upward platform growth forming "stacked saucer" shapes, with each stratigraphic layer closely resembling the previous one (Collins et al., 2011). As such, a multibeam map of the modern water bottom (Beaman, 2017) is deemed appropriate to use for the initial paleobathymetry to fill seismic data gaps. Four mapped sequence boundaries (Williams et al., 2023) provided vertical and lateral geometric constraints on platform morphology, margin position, and internal aggradational and progradational patterns. These were applied as constraints to guide and qualitatively validate the model platform architecture by assessing whether equivalent stratigraphic horizons in the model reproduced the general seismic trends.

1.1.2 Accommodation

In GPM, accommodation is calculated as the sum of vertical space created at every timestep in the model by a user-defined tectonic map and geotime curve, and a user-defined eustatic sea-level curve with an option to add a high-resolution secondary sine curve.

In our model, subsidence rates were derived from Holocene radiometric ages (Table 2; Collins et al., 2002; Collins et al., 2011; Hengesh and Whitney, 2016), which are generally reliable given the high preservation of Holocene reef material and thus behave as closed system. In contrast, U/Th ages from older Pleistocene sections are more diagenetically altered and prone to open system behaviour and associated uncertainties. The subsidence experiments, inspired by De Gelder et al., (2020), who examined the influence of sea-level curves on modelled marine terraces, and Husson et al., (2018), who explored the changing pace of reef productivity to the changing pace of sea-level cycles during the MPT, were refined through a trial-and-error approach.

1.1.3 Carbonate factory

Detrital sediments are produced in GPM through a user-defined time-controlled decay of *in situ* lithologies, which are then subjected to downslope diffusion, with transport distance and volume governed by the diffusion coefficient and additional user-defined erodibility and transportability factors for each sediment (*See Table 2 for parameters*). While terrigenous siliciclastics accumulated on the seafloor around Scott Reef during the Plio-Quaternary (Williams et al., 2023), they are absent from the platform interior, which was higher compared to the surrounding seafloor, and thus excluded from the model. Sedimentological interpretations from three boreholes (this study - *See Supplement 2 for further details*) across North and South Scott Reef informed sediment inputs and facies patterns.

1.1.7 Carbonate sediment transport properties

In GPM, multiple carbonate sediments are modelled *in situ*, whereby growth rates are scaled by user-defined environmental functions that represent ecological thresholds and environmental limiting factors. Production rates are defined as:

$$P\ (z,\ W,\ SSC) = P_{max} \cdot f(z) \cdot g(W) \cdot h(SSC)$$

where P_{max} is the maximum potential growth rate for a given facies, $f(z)$ is a depth-dependent scaling function, $g(W)$ is a wave-exposure scaling function, and $h(SSC)$ is a suspended sediment reduction function.

The depth function *(f(z))* uses facies-specific Gaussian or parabolic curves and/or facies maps to describe growth as a function of paleo-water depth, with optimal growth at shallow depths and declining production below the photic zone (Schlager, 2000). The wave-energy function *(g(W))* controls growth, which is scaled by relative wave exposure, and parameterised as a depth-dependent multiplier that increases production on exposed reef crests and reduces it in sheltered settings. The suspended sediment function *(h(SSC))* determines that growth decreases exponentially with increasing suspended sediment concentration, consistent with empirical relationships for light attenuation and sediment stress on coral/algal communities. These functions can be combined or applied independently depending on data availability. The explicit equations, parameter values, and references for each scaling function are provided in Hill et al. (2009; 2012) and Table 2, ensuring reproducibility. Despite its importance, FSM's often fail to capture or underrepresent wave-induced sediment suspension as a carbonate growth-dependent function (Harris et al., 2014; 2015; Blanchon et al., 2014). This flexible formulation allows GPM to simulate spatial and temporal variability in reef growth as a response to key environmental controls, which we regard as a key strength of the GPM tool. In our model design, we incorporate all three carbonate growth rules.

The choice of how GPM combines growth factors (wave-power, depth, and suspended sediment-dependant growth) additively or multiplicatively, influences facies patterns and sediment volume. When combined additively, the effective growth is the sum of the user-defined contributions of wave-power, water depth and suspended sediment, so a low value in one factor can be offset by a high value in another. When combined multiplicatively, any limiting factor can inhibit the overall growth. For example, a facies with a depth-production curve from 10 – 30 m, with a multiplicative combination of wave-energy and depth confines

growth to the platform margins where both depth and wave power are optimal. When applied additively, the facies are distributed platform-wide because model cells with sufficient depth, but low wave power still attain growth from the depth control. Other than the occurrence of coralgal assemblages on patch reefs, which is observed in the modern Scott Reef environment (Gilmour et al., 2024), the GBR (Hopley et al., 2007) and the Indo-Pacific (Montaggioni, 2005) it is not realistic to observe coralgal facies develop uniformly throughout the lagoon (Barrett and Webster, 2017). However, reef growth constrained by either multiplicative or additive controls of water depth, wave energy and suspended sediment, can still develop throughout the lagoon, as well as the reef crest and slope, unless additional growth rules are applied. Warrlich et al. (2002) and Liu et al. (2022) use a horizontal restriction function to limit carbonate production with increasing distance from open marine waters. Similarly, the ReefSAM forward stratigraphic model implemented a substrate-dependant coralgal growth rule to reproduce the Holocene development of coralgal facies confined to patch reefs in the One Tree Reef lagoon (Barrett and Webster, 2017), which was implemented based on evidence that substrate composition is an important control reef establishment (Babcock and Davies, 1991). In GPM, a similar rule can be applied by incorporating an area growth scaling map detailing the spatial zones in which a user-defined carbonate sediment can grow as a fraction of the defined production rate (Fig. 4A). In our model, we restrict coralgal production in the lagoon gradually away from the platform margin avoiding the problem of platform-wide growth. We apply a reduction of 90% growth, while considering that the deepest part of the South Reef lagoon is a bare limestone pavement with patches of dense communities of branching and foliose corals unique to the NWS, as reported by Wilson, (2013) and the ongoing AIMS Scot Reef monitoring project. Given the isolated setting of Scott Reef, coral community recruitment during transgressions would have had to rely on deeper reef communities (Wilson, 2013). We therefore permit some coralgal facies to establish in the platform interior as well as allowing backstepping into the interior when relative sea-level rise exceeds accretion potential or when reduced wave energy at a landward position favours the survival of the rim, or when elevated topography of differential subsidence make interior settings more stable (Schlager, 2005). We also permit all coralgal facies to establish on topographic highs within the lagoon that correspond to modern day patch reefs to maintain realism (Fig. 4A).

The development of karstification within a carbonate platform can occur during subaerial exposure whereby processes of chemical erosion dissolves carbonate grains and can result in significant changes in platform morphologies (Liu et al., 2022). Rainfall intensity and duration of exposure can significantly increase potential karst formation. The forward stratigraphic model Badlands (Salles, 2016) is capable of developing topographic variations of stratigraphic sequences that occur due to differential dissolution of a carbonate platform due to rainfall intensity (Liu et al., 2022). This is not possible in GPM, however, a calculation of the residence time of strata within a user-defined defined water depth, i.e., the vadose, mixing or phreatic zones, can be used as a proxy to identify periods of possible karstification, cementation or dissolution. However, structural changes incurred due to processes of differential dissolution and fracture karst cannot be implemented. We run the diagenetic GPM model to simulate duration of subaerial exposure in the vadose zone with a surface coefficient of 0.8 which approximates the position of the surface as a fraction of the distance between the topography and the sea-level.

1.1.8 Carbonate facies and production-depth profiles

In the model, the three coralgal assemblages were defined as *in situ* facies - Coralgal 1 (shallow reef, <10 m), Coralgal 2 (intermediate reef, 10 - 30 m), and Coralgal 3 (deep reef, 30 - 60 m) that grow as a function of water depth, wave energy and suspended sediment. These assemblages were modelled using the production-depth curves shown in Figures 4 and 7, with their productivity values defined in Table 2. Coralgal 1 occurs only in the Holocene section of both cores and MIS 5 in SRSEBH6J (Fig. 3). These interpretations are guided by vertical accretion rates (Table 2; Collins et al., 2011) and regional Indo-Pacific coralgal assemblages (Webster et al., 2022) and other sites globally. The drowned carbonate platforms in the Huon Gulf, Papua New Guinea (Webster et al., 2004) provide a comparison for interpreting paleowater depths in regions experiencing rapid subsidence (2-6 m/kyr; Webster et al., 2009). In this setting, shallow, high energy reef communities, characteristic of windward margins were found ca. 10 mbsl. The occurrence of colonies of robust branching corals and calcareous red algae are interpreted to represent high energy environments on the reef crest. Associations of domal, tabular-branching and arborescent corals indicate moderate hydrodynamic

conditions, and sheltered areas are characterised by the association of arborescent, foliaceous and encrusting corals (Collins et al., 2011).

1.2 Wave energy

1.2.1 Wave energy rules

In GPM, wave energy is not directly responsible for transporting coarse sediment, instead the model uses wave dissipation to estimate wave-induced velocities, which are then incorporated into the broader sediment transport algorithm that includes advective flow, diffusion, and Shields criteria for erosion and entrainment (Tetzlaff and Harbaugh, 1989). Thus, sediment transport in the model reflects the combined effects of wave-modulated currents, such as longshore drift and bottom current orbital flows (Hill et al., 2009).

Trade winds significantly influence near-surface currents, driving nutrient transport and modulating primary productivity through seasonal variability (Deniston et al., 2013; Deckker et al., 2020). FSM's have reproduced facies successions observed in 1-D cores, which are interpreted as responses to oceanographic conditions such as pH, temperature, salinity (Salles et al., 2018) and nutrient availability (Clavera-Gispert et al., 2012). Several other carbonate forward stratigraphic models also incorporate platform-top currents and wind-driven waves (e.g., CarboCAT, CarboKitten, Carb3D; Burgess et al., 2013; Masiero et al., 2020). GPM does not explicitly simulate time-varying tides, winds, or currents. GPM parameterises wave exposure as a user-defined, depth and temporal dependent scaling factor that modifies carbonate production and transport, with higher wave energy increasing sediment redistribution. As such, it imposes ecological constraints on the defined facies (Jiminez et al., 2024). In our model, wave propagation is generated from source points defined on a map with wave energy decreasing upon breaking with the platform margin towards the platform interior. However, wave energy that initially breaks on the reef crest can accumulate more energy with sufficient lagoon space and fetch to be conducive to patch reef formation (Hill et al., 2009). Wave energy is therefore an important component in simulating facies patterns across the carbonate platform.

1.2.2 Wave energy data

For the base case model calibration, mean significant wave height (H_s = 1.25 m) was set to 1.25 m based on data from Scott Reef monitoring projects (Gilmour et al., 2019) and the WaveWatch III global hindcast dataset (ca. 50 km resolution) (Tolman 2009). Additional data-driven scenarios incorporated downscaled wave field data (Grimaldi et al., 2024), computed using the third generation Simulating WAves Nearshore (SWAN) model, which computes wave propagation, wave generation by wind, nonlinear wave-wave interactions and dissipation (Booij et al., 1999). Wave input conditions were based on modern conditions, including (1) daily averages from 1980 to 2020 from the Centre for Australian Weather and Climate Research (CAWCR) Wave Hindcast (Smith et al., 2021), where the significant wave height (1.4 m), period (13 sec), and direction (217°N, SW) were used; and (2, 3 and 4) additional scenarios where similar conditions but varying wave directions (SE, NW and NE) were used.

APPENDIX H

Chapter 4 Supplement 4 - Petrel GPM model parameter files

The input data and parameters used to produce the forward stratigraphic models in Chapter 4 can be downloaded from the following GitHub repository: Scott Reef GPM base-case forward stratigraphic model repository. A Schlumberger Petrel GPM license is required to run the model.

Details: Forward stratigraphic model of the Scott Reef carbonate platform on the Northwest Shelf of Australia, using Petrel carbonate Geologic Process Modelling.

Description: This dataset contains results from forward stratigraphic modelling (FSM) of the North and South Scott Reef carbonate platforms on the Northwest Shelf of Australia. The model explores environmental and eustatic controls on reef development during the mid-Pleistocene climate transition (1.2 Ma to present), evaluating the relative influence between eustacy (sea-level and tectonics), carbonate sediment production, wave energy and proxies for oceanographic controls (i.e., sediment suspension and tides).

Contents: JSON files: Contain model parameters, input configurations, and boundary conditions, including carbonate production rates, subsidence, and the Miller et al, (2020) sea-level curve. HDF5 files: Store 2-D and 3-D simulation outputs, including spatial and temporal facies distributions, carbonate accumulation rates, platform evolution through time, and reef initiation and drowning events.

Usage: This dataset can be used as a reference for setting up similar carbonate platform and coral reef FSM studies, testing parameter sensitivity, or conducting comparative analyses in carbonate platform evolution and reef response to climate-driven sea-level fluctuations.

APPENDIX I

Chapter 5 Supplement 1 - Core Interpretation

APPENDIX J

Chapter 5 Supplement 2 - Uranium Series Data (Collins et al., 2009)

Cells highlighted blue indicate values used to calculate open-system ages and uncertainty error bars. Cells highlighted yellow indicate the three boreholes used in this study.

Sample Name	Sample wt.(g)	Spike wt.(g)	meas. 238/233	SE%	meas. 238/234	SE%	meas. 232/229	SE%	meas. 229/230	SE%	U^{238} (nm/g)	Th^{230} (nm/g)	Th^{232} (nm/g)	U (ppm)
BH1-HDD-J-0.5	1.071	0.286	3139.60	0.047	15509.31	0.048	2.417	0.231	1357.728	0.942	11.603	2.6093E-07	0.00092	2.7821
BH1-HDD-J-8.7	1.085	0.289	3686.15	0.034	15582.73	0.044	2.293	0.334	56.696	0.084	12.558	6.1433E-06	0.00080	3.0110
BH1-HDD-J-15.25~15.45	0.995	0.292	2779.97	0.047	15526.14	0.061	0.892	0.328	32.955	0.093	9.461	1.057E-05	0.00031	2.2685
BH1-HDD-J-21.85~22.0	1.036	0.300	2833.55	0.049	15497.82	0.066	0.937	0.261	23.557	0.050	10.616	1.6287E-05	0.00036	2.5455
BH1-HDD-J-23.1	1.019	0.305	3349.30	0.049	15600.34	0.057	2.216	0.227	18.941	0.087	12.381	1.9989E-05	0.00084	2.9686
BH1-HDD-J-25.45	1.085	0.276	3758.59	0.044	15621.86	0.055	5.255	0.270	16.567	0.060	14.560	2.3953E-05	0.00209	3.4913
BH1-HDD-J-25.75	1.042	0.271	3253.87	0.044	15574.98	0.050	5.373	0.180	19.028	0.051	10.580	1.7502E-05	0.00179	2.5368
BH6-J-1.50	1.039	0.296	3038.58	0.051	15532.71	0.057	14.676	0.190	249.401	0.189	11.592	1.5494E-06	0.00574	2.7794
BH6-J-1.80	1.007	0.279	3339.78	0.047	15555.25	0.054	4.321	0.219	211.465	0.264	10.871	1.5621E-06	0.00144	2.6066
BH6-J-5.25	1.016	0.291	4085.10	0.048	15618.94	0.056	1.772	0.208	104.364	0.203	14.463	3.4605E-06	0.00064	3.4680
BH6-J-9.45	1.044	0.331	3205.61	0.043	15589.02	0.048	3.510	0.236	78.826	0.110	11.723	4.7383E-06	0.00132	2.8110
BH6-J-11.65	1.016	0.267	3218.82	0.046	15554.60	0.061	1.111	0.340	69.618	0.302	13.012	5.933E-06	0.00046	3.1200
BH6-J-15.85	1.037	0.306	3544.32	0.044	15585.88	0.055	1.281	0.279	48.999	0.087	14.328	8.438E-06	0.00053	3.4355
BH6-J-17.55	1.008	0.291	3405.90	0.042	15556.17	0.048	37.433	0.170	45.001	0.120	11.410	7.6158E-06	0.01286	2.7360
BH6-J-18.65	0.998	0.291	3137.69	0.052	15557.61	0.058	2.428	0.182	46.237	0.126	11.815	8.3304E-06	0.00094	2.8330
BH6-J-23.40	1.002	0.281	3107.94	0.048	15576.43	0.058	7.917	0.298	33.045	0.104	11.562	1.1523E-05	0.00302	2.7723
BH6-J-26.60	1.001	0.279	2961.68	0.036	15496.69	0.044	7.938	0.514	27.856	0.128	10.682	1.3256E-05	0.00294	2.5614
BH6-J-27.90	0.993	0.281	2681.02	0.039	15513.23	0.045	4.569	0.285	27.873	0.072	9.592	1.3141E-05	0.00168	2.2999
BH6-J-32.20	1.029	0.343	2501.56	0.047	15479.77	0.063	1.697	0.348	26.394	0.085	8.889	1.3784E-05	0.00062	2.1313
BH6-J-32.45	1.008	0.290	2765.08	0.037	15532.68	0.050	8.580	0.208	23.561	0.062	9.976	1.568E-05	0.00317	2.3919
BH6-J-32.95	1.015	0.294	2865.03	0.042	15548.24	0.054	1.057	0.211	22.292	0.082	10.525	1.6876E-05	0.00040	2.5236
BH6-J-34.60	1.022	0.296	2617.64	0.045	15506.76	0.056	4.865	0.229	23.039	0.087	9.687	1.6449E-05	0.00185	2.3228
BH6-J-51.25	1.013	0.285	3072.98	0.049	16039.83	0.058	1.663	0.336	2.617	0.029	11.172	0.00014238	0.00062	2.6788
BH6-J-85.10	1.011	0.304	2461.77	0.039	16252.05	0.056	2.082	0.226	2.558	0.022	8.842	0.00014393	0.00077	2.1202
BH6-J-177.20	0.964	0.272	2664.56	0.045	16715.96	0.059	8.001	0.167	2.170	0.036	9.814	0.00017401	0.00302	2.3531
BH7-J-7.35	1.082	0.306	2820.42	0.047	15489.20	0.054	1.361	0.459	84.494	0.148	9.292	3.9811E-06	0.00046	2.2280
BH7-J-16.65~16.85	1.010	0.297	2600.62	0.045	15436.67	0.051	1.481	0.300	41.131	0.156	11.058	1.0577E-05	0.00065	2.6515
BH7-J-18.85~19.1	1.090	0.293	3509.48	0.047	15600.51	0.050	1.154	0.205	26.704	0.097	13.171	1.4389E-05	0.00044	3.1581
BH7-J-20.85	1.034	0.305	3667.15	0.062	15589.13	0.069	8.256	0.354	22.841	0.111	12.567	1.5364E-05	0.00290	3.0132
BH7-J-21.95~22.1	1.047	0.270	3060.06	0.047	15507.76	0.049	0.751	0.206	25.475	0.084	11.524	1.5136E-05	0.00029	2.7631

±2s	(^{230}Th/^{232}Th)	(^{232}Th/^{238}U)	±2s	(^{230}Th/^{238}U)	±2s	(^{234}U/^{238}U)	±2s	Uncorr. ^{230}Th Age (ka)	±2s	Uncorr. Initial (^{234}U/^{238}U)	±2s		Detrital (^{232}Th/^{238}U)	±2s	Detrital (^{230}Th/^{238}U)	±2s
0.00098	52.962	2.517E-05		0.0013	2.6E-05	1.150	0.0011	0.126	0.0025	1.150	0.0011	-0.047	1.21	0.606	1	0
0.00124	1425.686	2.034E-05		0.0290	6.8E-05	1.149	0.0010	2.779	0.0071	1.150	0.0010	-0.351	1.21	0.606	1	0
0.00047	6316.657	1.048E-05		0.0662	0.00018	1.145	0.0014	6.470	0.0203	1.148	0.0014	-0.398	1.21	0.606	1	0
0.00044	8410.065	1.081E-05		0.0909	0.00018	1.148	0.0015	8.959	0.0222	1.152	0.0015	-0.553	1.21	0.606	1	0
0.00089	4423.688	2.163E-05		0.0957	0.00026	1.145	0.0013	9.474	0.0290	1.149	0.0013	-0.383	1.21	0.606	1	0
0.00262	2132.959	4.572E-05		0.0975	0.0002	1.146	0.0013	9.650	0.0238	1.150	0.0013	-0.464	1.21	0.606	1	0
0.00150	1816.232	5.399E-05		0.0981	0.00019	1.146	0.0011	9.708	0.0218	1.150	0.0012	-0.462	1.21	0.606	1	0
0.00505	50.173	0.0002		0.0079	3.8E-05	1.148	0.0013	0.753	0.0037	1.148	0.0013	-0.230	1.21	0.606	1	0
0.00147	201.329	4.231E-05		0.0085	5.3E-05	1.148	0.0012	0.809	0.0051	1.149	0.0012	-0.170	1.21	0.606	1	0
0.00062	1000.246	1.418E-05		0.0142	7.1E-05	1.148	0.0013	1.351	0.0070	1.149	0.0013	-0.217	1.21	0.606	1	0
0.00144	669.143	3.58E-05		0.0240	7.3E-05	1.145	0.0011	2.299	0.0075	1.146	0.0011	-0.299	1.21	0.606	1	0
0.00073	2394.052	1.129E-05		0.0270	0.00019	1.147	0.0014	2.591	0.0185	1.149	0.0014	-0.169	1.21	0.606	1	0
0.00069	2954.003	1.182E-05		0.0349	9.1E-05	1.148	0.0013	3.357	0.0096	1.149	0.0013	-0.385	1.21	0.606	1	0
0.01014	110.093	0.0004		0.0396	0.00013	1.149	0.0011	3.808	0.0132	1.150	0.0011	-0.282	1.21	0.606	1	0
0.00079	1652.136	2.53E-05		0.0418	0.00015	1.147	0.0013	4.035	0.0154	1.148	0.0013	-0.304	1.21	0.606	1	0
0.00418	709.252	8.329E-05		0.0591	0.00018	1.145	0.0013	5.755	0.0192	1.147	0.0013	-0.352	1.21	0.606	1	0
0.00700	839.381	8.763E-05		0.0736	0.00024	1.149	0.0010	7.182	0.0251	1.153	0.0010	-0.254	1.21	0.606	1	0
0.00222	1457.548	5.572E-05		0.0812	0.00018	1.145	0.0010	7.988	0.0199	1.148	0.0010	-0.368	1.21	0.606	1	0
0.00100	4144.208	2.218E-05		0.0919	0.00024	1.145	0.0014	9.083	0.0278	1.149	0.0015	-0.429	1.21	0.606	1	0
0.00306	918.326	0.0001		0.0932	0.00018	1.145	0.0011	9.218	0.0213	1.148	0.0012	-0.448	1.21	0.606	1	0
0.00039	7879.106	1.206E-05		0.0950	0.00024	1.145	0.0012	9.411	0.0265	1.148	0.0013	-0.395	1.21	0.606	1	0
0.00196	1656.321	6.077E-05		0.1007	0.00027	1.145	0.0013	9.989	0.0300	1.149	0.0013	-0.386	1.21	0.606	1	0
0.00096	42707.145	1.769E-05		0.7554	0.00118	1.111	0.0013	120.497	0.4396	1.156	0.0017	-0.579	1.21	0.606	1	0
0.00080	34887.642	2.766E-05		0.9649	0.00117	1.089	0.0012	220.461	1.2566	1.166	0.0019	-0.600	1.21	0.606	1	0
0.00233	10704.452	9.818E-05		1.0510	0.00168	1.060	0.0012	386.851	7.6016	1.180	0.0030	0.434	1.21	0.606	1	0
0.00098	1609.990	1.577E-05		0.0254	9.9E-05	1.149	0.0012	2.431	0.0100	1.150	0.0012	-0.264	1.21	0.606	1	0
0.00090	3044.686	1.862E-05		0.0567	0.00023	1.150	0.0012	5.493	0.0233	1.152	0.0012	-0.238	1.21	0.606	1	0
0.00042	6025.995	1.075E-05		0.0648	0.00019	1.146	0.0011	6.317	0.0198	1.149	0.0012	-0.321	1.21	0.606	1	0
0.00476	984.481	7.361E-05		0.0725	0.00025	1.148	0.0016	7.080	0.0272	1.151	0.0016	-0.370	1.21	0.606	1	0
0.00028	9701.373	8.025E-06		0.0779	0.0002	1.150	0.0011	7.616	0.0220	1.153	0.0012	-0.348	1.21	0.606	1	0

±2s	corr. (^{234}U/^{238}U)	±2s		corr. ^{230}Th Age (ka)	±2s	corr. Initial (^{234}U/^{238}U)	±2s	
0.00003	1.150	0.0011	-0.000518	0.124	0.003	1.150	0.0011	-0.04
0.00007	1.149	0.0010	-0.000146	2.777	0.007	1.150	0.0010	-0.35
0.00018	1.145	0.0014	-9.85E-06	6.469	0.020	1.148	0.0014	-0.40
0.00018	1.148	0.0015	-9.92E-06	8.958	0.022	1.152	0.0015	-0.55
0.00026	1.145	0.0013	-3.11E-05	9.473	0.029	1.149	0.0013	-0.38
0.00020	1.146	0.0013	-0.000183	9.647	0.024	1.150	0.0013	-0.46
0.00019	1.146	0.0011	-0.000305	9.704	0.022	1.150	0.0012	-0.46
0.00007	1.148	0.0013	-0.00637	0.741	0.007	1.148	0.0013	-0.11
0.00006	1.148	0.0012	-0.000645	0.806	0.005	1.149	0.0012	-0.16
0.00007	1.148	0.0013	-5.42E-05	1.350	0.007	1.149	0.0013	-0.22
0.00007	1.145	0.0011	-0.000373	2.296	0.008	1.146	0.0011	-0.29
0.00019	1.147	0.0014	-1.18E-05	2.590	0.019	1.149	0.0014	-0.17
0.00009	1.148	0.0013	-2.97E-05	3.356	0.010	1.149	0.0013	-0.38
0.00019	1.149	0.0011	-0.014725	3.780	0.019	1.151	0.0011	-0.19
0.00015	1.147	0.0013	-7.76E-05	4.033	0.015	1.148	0.0013	-0.30
0.00018	1.145	0.0013	-0.000669	5.749	0.019	1.147	0.0013	-0.35
0.00024	1.150	0.0010	-0.000735	7.175	0.025	1.153	0.0010	-0.25
0.00018	1.145	0.0010	-0.00038	7.983	0.020	1.148	0.0010	-0.37
0.00024	1.145	0.0014	-3.13E-05	9.081	0.028	1.149	0.0015	-0.43
0.00019	1.145	0.0011	-0.001074	9.210	0.022	1.148	0.0012	-0.44
0.00024	1.145	0.0012	-1.12E-05	9.410	0.027	1.148	0.0013	-0.39
0.00027	1.145	0.0013	-0.000239	9.985	0.030	1.149	0.0013	-0.38
0.00118	1.111	0.0013	-9.5E-07	120.496	0.440	1.156	0.0017	-0.58
0.00117	1.089	0.0012	-2.83E-07	220.459	1.257	1.166	0.0019	-0.60
0.00168	1.060	0.0012	2.41E-06	386.844	7.602	1.180	0.0030	0.43
0.00010	1.149	0.0012	-4.98E-05	2.429	0.010	1.150	0.0012	-0.26
0.00023	1.150	0.0012	-3.14E-05	5.492	0.023	1.152	0.0012	-0.24
0.00019	1.146	0.0011	-1.27E-05	6.316	0.020	1.149	0.0012	-0.32
0.00025	1.148	0.0016	-0.000316	7.075	0.027	1.151	0.0016	-0.37
0.00020	1.150	0.0011	-6.6E-06	7.615	0.022	1.153	0.0012	-0.35

Sample Name	Sample wt.(g)	Spike wt.(g)	meas. 238/233	SE%	meas. 238/234	SE%	meas. 232/229	SE%	meas. 229/230	SE%	U^{238} (nm/g)	Th^{230} (nm/g)	Th^{232} (nm/g)	U (ppm)
HDD3-JA-1.10	1.038	0.279	3018.79	0.045	15499.59	0.055	1.584	0.167	71.360	0.107	11.571	5.4877E-06	0.00062	2.7744
HDD3-JA-8.60	1.041	0.269	3478.84	0.046	15606.41	0.052	1.705	0.121	29.334	0.099	11.943	1.1981E-05	0.00060	2.8637
HDD3-JA-23.25 final	1.015	0.291	2973.81	0.033	15564.17	0.036	2.869	0.212	23.350	0.087	11.971	1.7654E-05	0.00118	2.8703
HDD3-JA-23.80 final	1.009	0.265	4174.33	0.037	15656.79	0.036	7.862	0.184	16.797	0.036	15.300	2.2353E-05	0.00295	3.6686
HDD3-JA-27.20 final	1.016	0.304	3100.00	0.059	16078.31	0.081	14.849	0.160	2.506	0.031	10.395	0.00013714	0.00510	2.4926
HDD3-JA-31.60	1.029	0.284	2302.03	0.051	15919.39	0.057	0.710	0.228	3.281	0.044	8.800	0.00011942	0.00028	2.1101
HDD3-JA-58.00	1.036	0.283	3291.30	0.049	16430.17	0.051	2.904	0.829	1.944	0.125	12.063	0.00019325	0.00109	2.8925
HDD3-JA-91.40	1.043	0.295	2334.74	0.043	16498.71	0.055	1.608	0.184	2.496	0.044	8.149	0.00014333	0.00058	1.9539
HDD3-JA-151.10	1.060	0.290	1397.97	0.038	16707.60	0.059	17.028	0.166	4.204	0.065	5.051	8.8103E-05	0.00631	1.2112
1P-02	0.891	0.170	4146.24	0.068	15660.39	0.070	2.962	0.329	14.065	0.126	10.107	1.78E-05	0.00074	2.4235
HOOK 1P-03	0.826	0.157	4007.63	0.071	15677.22	0.078	1.841	0.265	13.565	0.167	9.704	1.83E-05	0.00046	2.3267
SR SE BH4B-P-01	0.851	0.163	4443.55	0.074	15699.13	0.068	17.167	0.242	12.024	0.141	10.830	2.08E-05	0.00429	2.5967
SR SE BH6-J-01	0.848	0.155	4535.14	0.082	15589.32	0.077	4.624	0.125	112.447	0.412	10.590	2.12E-06	0.00111	2.5393
SR SE BH6-J-02	0.792	0.210	3129.02	0.057	15532.80	0.072	0.983	0.573	74.512	0.146	10.569	4.63E-06	0.00034	2.5343
SR SE BH6-J-08	0.945	0.160	5619.30	0.082	15736.88	0.080	4.097	0.214	15.936	0.087	12.170	1.39E-05	0.00091	2.9181
SR SE BH6-J-09	1.068	0.166	5445.45	0.074	15713.13	0.061	3.581	0.166	15.516	0.103	10.801	1.31E-05	0.00073	2.5900
SR SE BH6-J-11	0.829	0.158	3858.36	0.057	15662.63	0.066	4.121	0.076	19.313	0.111	9.411	1.29E-05	0.00103	2.2565
SR SE BH6-J-12	0.940	0.140	5488.94	0.088	15713.23	0.078	2.577	0.195	13.120	0.096	10.467	1.49E-05	0.00050	2.5099
SR SE BH6-J-15	0.807	0.152	4695.29	0.077	15699.70	0.066	2.917	0.214	12.760	0.116	11.294	1.93E-05	0.00072	2.7081
SR SE BH6-J-16	0.817	0.158	5281.81	0.064	16253.82	0.064	5.231	0.136	1.521	0.109	13.067	1.67E-04	0.00133	3.1332
SR SE BH6-J-18	0.854	0.162	3654.56	0.072	16545.88	0.074	0.514	0.348	1.770	0.070	8.865	1.40E-04	0.00013	2.1256
SR SE BH6-J-19	0.888	0.159	4705.84	0.072	16630.83	0.083	6.380	0.373	1.274	0.096	10.741	1.84E-04	0.00149	2.5755
SR SE BH6-J-20	0.911	0.174	2768.42	0.057	16519.96	0.085	3.244	0.349	1.892	0.081	6.737	1.32E-04	0.00081	1.6154
SR SE BH6-J-21	0.864	0.154	3751.12	0.064	16645.11	0.080	2.540	0.541	1.493	0.102	8.526	1.56E-04	0.00059	2.0444
SR SE BH6-J-22	0.808	0.142	4355.83	0.065	16681.02	0.073	2.822	0.222	1.339	0.100	9.746	1.71E-04	0.00065	2.3369
SR SE BH6-J-23	0.860	0.162	4443.57	0.071	16931.97	0.069	1.841	0.178	1.290	0.099	10.666	1.91E-04	0.00045	2.5576
SR SE BH6-J-24	0.948	0.165	4756.40	0.072	17042.73	0.092	10.036	0.158	1.222	0.070	10.592	1.87E-04	0.00229	2.5397
SR SE BH6-J-27	0.809	0.137	4659.87	0.072	16515.32	0.062	3.597	0.238	1.333	0.084	10.094	1.67E-04	0.00080	2.4204
SR SE BH6-J-29	0.847	0.135	6289.84	0.075	17090.17	0.069	6.370	0.284	0.902	0.120	12.806	2.31E-04	0.00133	3.0707

±2s	(^{230}Th/^{232}Th)	(^{232}Th/^{238}U)	±2s	(^{230}Th$^{/2}$^{38}U)	±2s	(^{234}U/^{238}U)	±2s	Uncorr. ^{230}Th Age (ka)	±2s	Initial (^{234}U/^{238}U)	±2s		Detrital (^{232}Th/^{238}U)	±2s	Detrital (^{230}Th/^{238}U)	±2s
0.00048	1638.323	1.716E-05		0.0281	8.6E-05	1.150	0.0013	2.691	0.0088	1.151	0.0013	-0.337	1.21	0.606	1	0
0.00034	3710.233	1.603E-05		0.0595	0.00017	1.146	0.0012	5.790	0.0183	1.148	0.0012	-0.333	1.21	0.606	1	0
0.00117	2771.088	3.155E-05		0.0874	0.00021	1.145	0.0008	8.627	0.0225	1.148	0.0008	-0.279	1.21	0.606	1	0
0.00252	1406.241	6.158E-05		0.0866	0.00013	1.146	0.0008	8.531	0.0145	1.150	0.0009	-0.444	1.21	0.606	1	0
0.00379	4992.932	0.0002		0.7820	0.00142	1.108	0.0018	128.951	0.6267	1.156	0.0024	-0.658	1.21	0.606	1	0
0.00029	79753.924	1.009E-05		0.8043	0.00153	1.110	0.0013	135.652	0.6069	1.161	0.0017	-0.459	1.21	0.606	1	0
0.00419	32918.623	2.885E-05		0.9496	0.00331	1.085	0.0011	212.285	2.3285	1.156	0.0019	0.180	1.21	0.606	1	0
0.00049	46295.264	2.252E-05		1.0426	0.00182	1.070	0.0012	334.057	4.6851	1.180	0.0024	0.194	1.21	0.606	1	0
0.00487	2595.922	0.0004		1.0339	0.00214	1.031	0.0012	515.008	29.8636	1.132	0.0089	0.887	1.21	0.606	1	0
0.00113	4458.145	0		0.1041	0.00040	1.146	0.0016	10.343	0.0448	1.150	0.0016	-0.334	1.21	0.606	1	0
0.00056	7439.281	0	0	0.1117	0.00053	1.144	0.0018	11.154	0.0588	1.148	0.0018	-0.303	1.21	0.606	1	0
0.00483	899.822	0	0	0.1137	0.00049	1.144	0.0016	11.354	0.0538	1.149	0.0016	-0.295	1.21	0.606	1	0
0.00064	355.553	0	0	0.0119	0.00012	1.153	0.0018	1.124	0.0113	1.153	0.0018	-0.152	1.21	0.606	1	0
0.00090	2528.060	0	0	0.0260	0.00011	1.148	0.0016	2.487	0.0108	1.149	0.0017	-0.332	1.21	0.606	1	0
0.00090	2844.476	0	0	0.0678	0.00023	1.146	0.0018	6.627	0.0255	1.148	0.0019	-0.425	1.21	0.606	1	0
0.00056	3342.462	0	0	0.0719	0.00025	1.147	0.0014	7.029	0.0271	1.150	0.0014	-0.323	1.21	0.606	1	0
0.00036	2333.346	0	0	0.0815	0.00027	1.144	0.0015	8.023	0.0300	1.147	0.0015	-0.364	1.21	0.606	1	0
0.00046	5494.662	0	0	0.0843	0.00031	1.147	0.0018	8.292	0.0344	1.150	0.0018	-0.385	1.21	0.606	1	0
0.00071	4989.903	0	0	0.1014	0.00039	1.145	0.0015	10.060	0.0429	1.149	0.0016	-0.318	1.21	0.606	1	0
0.00084	23363.322	0	0	0.7565	0.00263	1.108	0.0014	121.467	0.8223	1.152	0.0019	-0.225	1.21	0.606	1	0
0.00021	204401.585	0	0	0.9394	0.00267	1.080	0.0016	209.202	2.0522	1.145	0.0025	-0.275	1.21	0.606	1	0
0.00259	22860.997	0	0	1.0134	0.00341	1.080	0.0018	272.090	4.5496	1.173	0.0033	0.054	1.21	0.606	1	0
0.00131	30271.857	0	0	1.1598	0.00321	1.074	0.0018	0.000	0.0000	0.000	0.0000	0.000	1.21	0.606	1	0
0.00149	49009.252	0	0	1.0850	0.00361	1.074	0.0017	447.716	22.6653	1.265	0.0146	0.937	1.21	0.606	1	0
0.00067	49162.164	0	0	1.0415	0.00343	1.075	0.0016	319.282	6.8258	1.186	0.0038	0.451	1.21	0.606	1	0
0.00037	78270.051	0	0	1.0599	0.00362	1.059	0.0015	424.069	18.4616	1.198	0.0091	0.884	1.21	0.606	1	0
0.00168	15155.991	0	0	1.0456	0.00296	1.054	0.0019	397.191	14.1012	1.166	0.0053	0.516	1.21	0.606	1	0
0.00088	38759.548	0	0	0.9782	0.00306	1.088	0.0014	231.161	2.6573	1.169	0.0023	0.051	1.21	0.606	1	0
0.00175	32357.756	0	0	1.0715	0.00418	1.055	0.0015	554.266	65.2592	1.266	0.0466	0.991	1.21	0.606	1	0

±2s	corr. (^{234}U/^{238}U)	±2s		corr. ^{230}Th Age (ka)	±2s	Initial (^{234}U/^{238}U)	±2s	
0.00009	1.150	0.0013	-6.76E-05	2.689	0.009	1.151	0.0013	-0.34
0.00017	1.146	0.0012	-2.92E-05	5.789	0.018	1.148	0.0012	-0.33
0.00021	1.145	0.0008	-0.000129	8.624	0.023	1.148	0.0008	-0.28
0.00013	1.146	0.0008	-0.000801	8.526	0.015	1.150	0.0009	-0.44
0.00142	1.108	0.0018	-3.85E-05	128.939	0.627	1.156	0.0024	-0.66
0.00153	1.110	0.0013	-1.91E-07	135.651	0.607	1.161	0.0017	-0.46
0.00331	1.085	0.0011	-1.67E-07	212.283	2.328	1.156	0.0019	0.18
0.00182	1.070	0.0012	1.2E-07	334.055	4.685	1.180	0.0024	0.19
0.00214	1.031	0.0012	1.08E-05	514.977	29.864	1.132	0.0089	0.89
0.00040	1.146	0.0016	-1.86E-05	10.341	0.045	1.150	0.0016	-0.33
0.00053	1.144	0.0018	-5.15E-06	11.153	0.059	1.148	0.0018	-0.30
0.00049	1.144	0.0016	-0.000453	11.344	0.054	1.149	0.0016	-0.29
0.00012	1.153	0.0018	-0.000136	1.121	0.011	1.153	0.0018	-0.15
0.00011	1.148	0.0016	-1.49E-05	2.486	0.011	1.149	0.0017	-0.33
0.00023	1.146	0.0018	-3.15E-05	6.626	0.025	1.148	0.0019	-0.42
0.00025	1.147	0.0014	-3E-05	7.027	0.027	1.150	0.0014	-0.32
0.00027	1.144	0.0015	-6.62E-05	8.021	0.030	1.147	0.0015	-0.36
0.00031	1.147	0.0018	-9.75E-06	8.291	0.034	1.150	0.0018	-0.39
0.00039	1.145	0.0015	-1.55E-05	10.058	0.043	1.149	0.0016	-0.32
0.00263	1.108	0.0014	-1.25E-06	121.465	0.822	1.152	0.0019	-0.22
0.00267	1.080	0.0016	-4.13E-09	209.202	2.052	1.145	0.0025	-0.28
0.00341	1.080	0.0018	5.87E-08	272.087	4.550	1.173	0.0033	0.05
0.00321	1.074	0.0018	5.09E-07	0.000	0.000	0.000	0.0000	0.00
0.00361	1.074	0.0017	8.54E-08	447.715	22.665	1.265	0.0146	0.94
0.00343	1.075	0.0016	4.46E-08	319.280	6.826	1.186	0.0038	0.45
0.00362	1.059	0.0015	2.11E-08	424.068	18.462	1.198	0.0091	0.88
0.00296	1.054	0.0019	3.47E-07	397.186	14.101	1.166	0.0053	0.52
0.00306	1.088	0.0014	-5.01E-08	231.159	2.657	1.169	0.0023	0.05
0.00418	1.055	0.0015	1.22E-07	554.264	65.259	1.266	0.0466	0.99

APPENDIX K

Chapter 5 Supplement 3 - Uranium Series Data (This study)

Lab code	Sample Name	Date & Time	Sample wt.(g)	Spike wt.(g)	U (ppm)	±2s	^{232}Th (ppb)	±2s	(^{230}Th/^{232}Th)	±2s	(^{230}Th/^{238}U)	±2s	(^{234}U/^{238}U)	±2s	uncorr. ^{230}Th Age (ka)	±2s	corr. ^{230}Th Age (ka)	±2s	corr. Initial (^{234}U/^{238}U)	±2s	
ERH55-12_628889	628889	run on 20 December 2025 at 19:3	0.01105	0.02982	3.1260	0.0029	1.322	0.004	169.86	2.96	0.0237	0.0004	1.1472	0.0013	2.276	0.040	2.265	0.040	1.1481	0.0013	
ERH55-13_628890	628890	run on 20 December 2025 at 20:5	0.00966	0.02995	2.5410	0.0026	0.112	0.002	3842.99	79.87	0.0556	0.0006	1.1478	0.0016	5.417	0.058	5.416	0.058	1.1500	0.0016	
ERH55-14_628891	628891	run on 20 December 2025 at 21:1	0.01022	0.02996	2.3954	0.0024	0.047	0.002	14703.29	644.42	0.0951	0.0007	1.1451	0.0014	9.456	0.071	9.455	0.071	1.1490	0.0014	
ERH55-15_628892	628892	run on 20 December 2025 at 21:4	0.00915	0.02974	2.7207	0.0025	0.146	0.003	40768.43	885.63	0.7188	0.0029	1.1114	0.0014	110.8	0.8	110.8	0.8	1.1523	0.0019	
ERH55-16_628893	628893	run on 20 December 2025 at 22:1	0.01092	0.02983	2.3313	0.0014	1.978	0.005	2647.83	12.06	0.7404	0.0028	1.1096	0.0015	117.0	0.9	117.0	0.9	1.1526	0.0020	
ERH55-17_628895	628895	run on 20 December 2025 at 22:4	0.01004	0.02997	0.4905	0.0009	1.901	0.005	626.06	3.69	0.7997	0.0045	1.1151	0.0020	133.2	1.5	133.1	1.5	1.1678	0.0028	
ERH55-18_628894	628894	run on 20 December 2025 at 23:5	0.01269	0.02860	1.9520	0.0017	4.428	0.013	1286.29	7.00	0.9617	0.0045	1.0828	0.0015	223.6	3.5	223.6	3.5	1.1559	0.0027	
ERH55-19_628896	628896	run on 21 December 2025 at 00:2	0.01008	0.02996	3.0713	0.0019	0.317	0.004	28141.59	341.95	0.9562	0.0023	1.0826	0.0016	219.8	2.0	219.8	2.0	1.1538	0.0025	
ERH55-20_628897	628897	run on 21 December 2025 at 00:5	0.01188	0.02986	2.3018	0.0019	0.416	0.003	16153.03	140.42	0.9630	0.0033	1.0797	0.0013	227.1	2.7	227.1	2.7	1.1515	0.0023	
ERH55-21_628898	628898	run on 21 December 2025 at 01:2	0.01018	0.02985	1.7827	0.0017	4.410	0.011	1175.25	4.61	0.9583	0.0031	1.0827	0.0015	221.3	2.5	221.2	2.5	1.1546	0.0025	
ERH55-22_628899	628899	run on 21 December 2025 at 01:5	0.01177	0.03009	3.1232	0.0022	0.139	0.003	66878.44	1385.27	0.9822	0.0031	1.1096	0.0009	217.6	2.1	217.6	2.1	1.2027	0.0018	
ERH55-23_628900	628900	run on 21 December 2025 at 03:0	0.00990	0.02991	2.5833	0.0024	0.451	0.004	17093.08	143.34	0.9833	0.0027	1.0758	0.0012	247.6	2.8	247.6	2.8	1.1527	0.0022	
ERH55-24_628901	628901	run on 21 December 2025 at 03:3	0.01036	0.03010	2.5667	0.0026	0.501	0.004	15365.47	130.73	0.9890	0.0042	1.0767	0.0014	252.0	4.2	252.0	4.2	1.1564	0.0028	
ERH55-25_928902	928902	run on 21 December 2025 at 04:0	0.01105	0.02985	1.7531	0.0014	1.417	0.004	3865.47	14.14	1.0294	0.0029	1.0758	0.0016	300.3	5.1	300.3	5.1	1.1772	0.0031	
ERH55-26_628903	628903	run on 21 December 2025 at 04:3	0.00908	0.02988	1.9495	0.0020	-0.023	-0.002	-266205.53	-23161.69	1.0347	0.0038	1.0600	0.0018	345	10	345	10	1.1593	0.0046	
ERH55-26_628903	628903	run on 22 December 2025 at 15:5	0.00908	0.02988	1.9499	0.0018	0.00	0.000	2044183.58	204614.58	1.0396	0.0022	1.0598	0.0021	357	9	357	9	1.1642	0.0036	
ERH55-27_628904	628904	run on 21 December 2025 at 05:0	0.01049	0.02955	2.1723	0.0014	0.079	0.002	88256.62	2677.39	1.0525	0.0047	1.0596	0.0019	396	19	396	19	1.1825	0.0085	
ERH55-27_628904	628904	run on 22 December 2025 at 16:2	0.00975	0.03003	2.3750	0.0022	0.11	0.004	70862.35	2380.58	1.0609	0.0037	1.0598	0.0018	428	21	428	21	1.2005	0.0097	
ERH55-28_628905	628905	run on 21 December 2025 at 06:1	0.00975	0.03003	2.4294	0.0026	0.737	0.004	10578.62	73.54	1.0578	0.0046	1.0557	0.0012	440	25	440	25	1.1931	0.0130	
ERH55-28_628905	628905	run on 22 December 2025 at 18:0	0.01203	0.29610	19.4041	0.0152	6.52	0.038	9502.01	58.38	1.0530	0.0022	1.0578	0.0017	406	12	406	12	1.1824	0.0044	
ERH55-29_609964	609964	run on 21 December 2025 at 06:4	0.01203	0.02961	3.2914	0.0026	0.148	0.002	3612.38	64.74	0.0536	0.0005	1.1459	0.0014	5.224	0.048	5.223	0.048	1.1480	0.0014	
ERH55-30_609971	609971	run on 21 December 2025 at 07:1	0.01106	0.02876	1.0064	0.0011	64.616	0.103	55.12	0.21	1.1663	0.0041	1.0756	0.0016	***Significant U loss, fall into Forbidden Zone***						
ERH55-30_609971	609971	run on 22 December 2025 at 19:1	0.01106	0.02876	1.0067	0.0012	64.45	0.093	54.85	0.19	1.1573	0.0040	1.0775	0.0017	***Significant U loss, fall into Forbidden Zone***						
ERH55-31_609983	609983	run on 21 December 2025 at 07:4	0.01165	0.03138	1.4891	0.0014	11.933	0.031	414.14	2.10	1.0938	0.0049	1.0384	0.0020	***Significant U loss, fall into Forbidden Zone***						
ERH55-31_609983	609983	run on 22 December 2025 at 19:4	0.01165	0.03138	1.4874	0.0017	11.97	0.014	413.49	0.97	1.0964	0.0026	1.0405	0.0020	***Significant U loss, fall into Forbidden Zone***						
Lab standards																					
ERH55-32_HU-1	HU-1	run on 21 December 2025 at 08:1	0.04635	0.03210	2.9372	0.0063	0.249	0.002	35940.62	380.84	1.0050	0.0053	0.9998	0.0007	0.00	0.00	0.00	0.00	0.0000	0.0000	Close to secular equilibrium, unable to calculate, age >500ka
ERH55-32_HU-1	HU-1	run on 22 December 2025 at 20:1	0.04635	0.03210	2.9500	0.0020	0.251	0.002	35825.24	372.97	1.0038	0.0031	1.0001	0.0014	0.00	0.00	0.00	0.00	0.0000	0.0000	Close to secular equilibrium, unable to calculate, age >500ka
ERH55-33_YB-1	YB-1	run on 21 December 2025 at 09:2	0.10205	0.03009	0.1273	0.0001	0.498	0.001	337.04	1.86	0.4345	0.0022	1.7459	0.0020	30.60	0.18	30.54	0.18	1.8140	0.0022	
ERH55-35_U-metal	U-metal	run on 21 December 2025 at 10:2	0.08097	0.03075	5.2831	0.0089	0.004	0.000	3807.96	185.76	0.0009	0.0000	0.9634	0.0018	0.098	0.001	0.098	0.001	0.9634	0.0018	

Note: Data in blue indicate repeated measurements acquired using a two-cycle acquisition mode, whereas data in black were obtained using static acquisition mode. The results from both modes demonstrate good reproducibility.

APPENDIX L

Chapter 5 Supplement 4 - Raw XRD Data (This study)

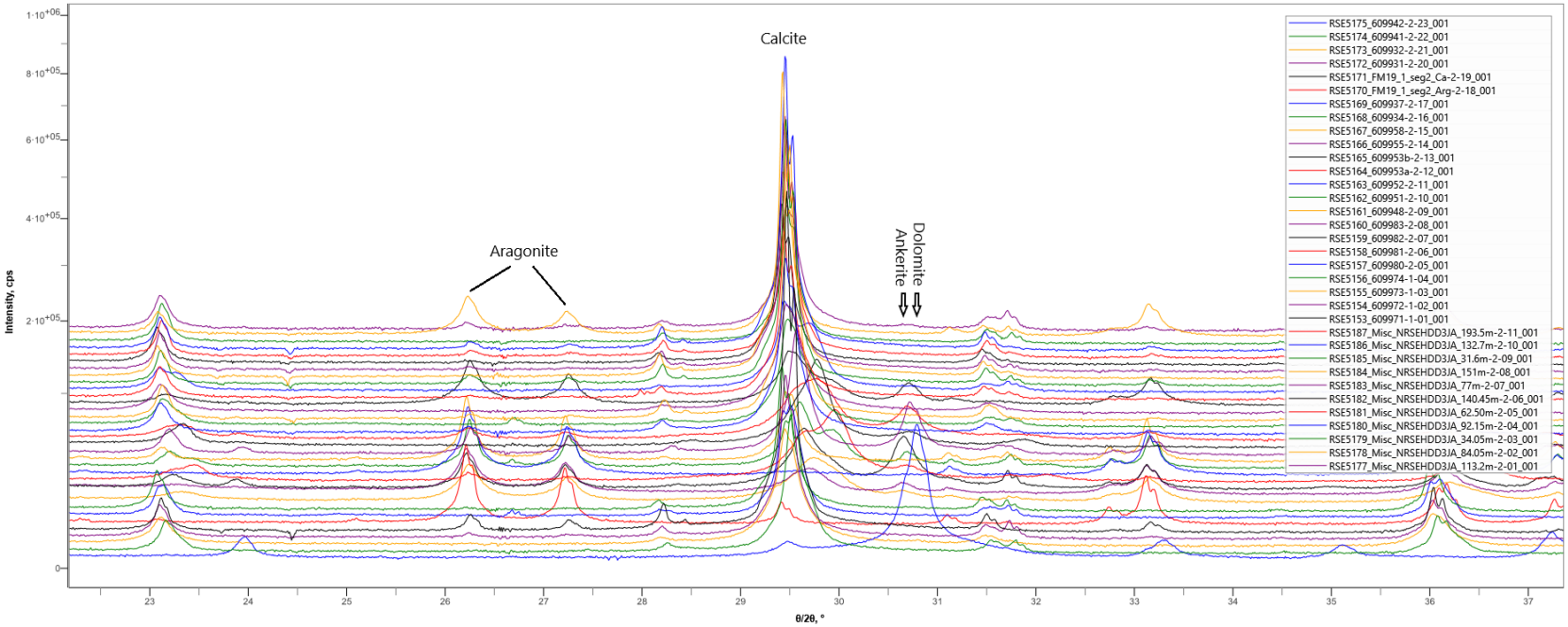


FIGURE L.1: Stacked powder X-ray diffraction (XRD) diffractograms of selected carbonate core samples. Major reflections of calcite (∼29.4° 2θ), aragonite (∼26–27° 2θ), and dolomite/ankerite (∼30–31° 2θ) are indicated. Individual samples are vertically offset for clarity. Variations in peak intensity and relative phase abundance reflect differences in primary carbonate mineralogy and degrees of diagenetic alteration across the analysed intervals.

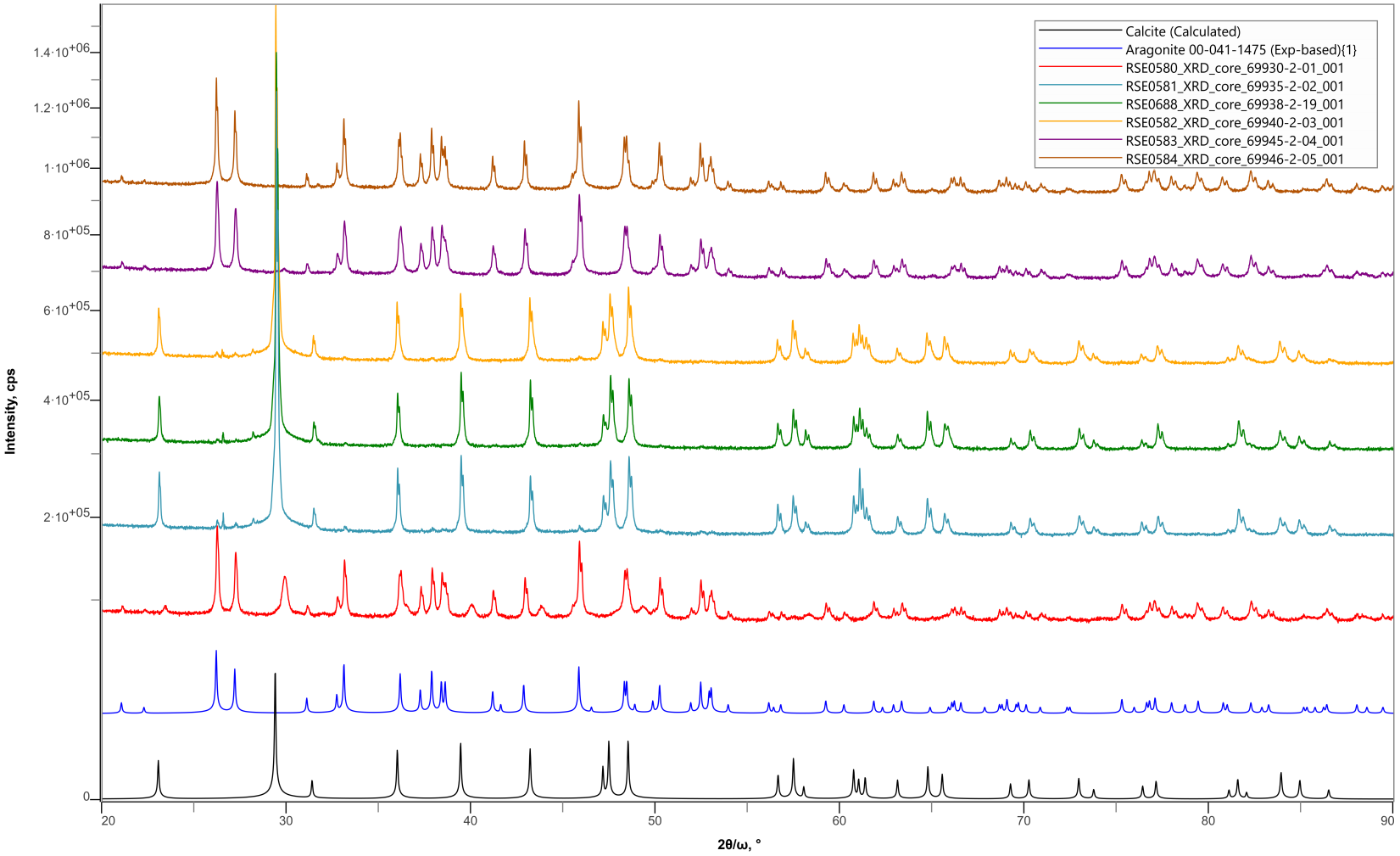
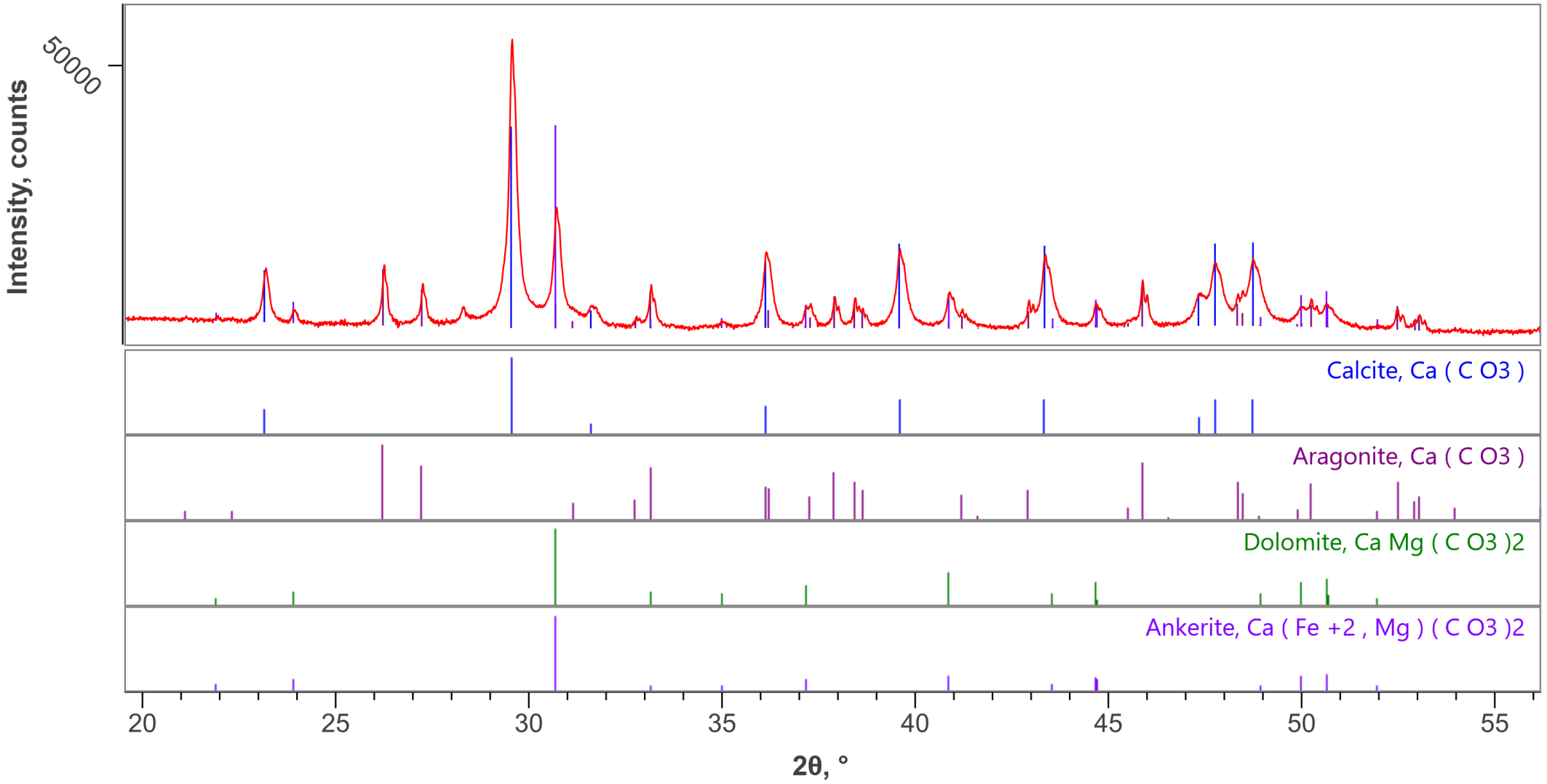


FIGURE L.2: Stacked powder X-ray diffraction (XRD) diffractograms of representative carbonate core samples compared with reference patterns for calcite and aragonite. Major diffraction peaks correspond predominantly to calcite, with variable aragonite contributions evident in selected samples. Individual diffractograms are vertically offset for clarity. Differences in peak intensity and phase distribution reflect variability in primary mineralogy and diagenetic alteration across the analysed intervals.


Intensity, counts
50000
Calcite, Ca (C O3)
Aragonite, Ca (C O3)
Dolomite, Ca Mg (C O3)2
Ankerite, Ca (Fe +2 , Mg) (C O3)2
20
25
30
35
40
45
50
55
2θ, °

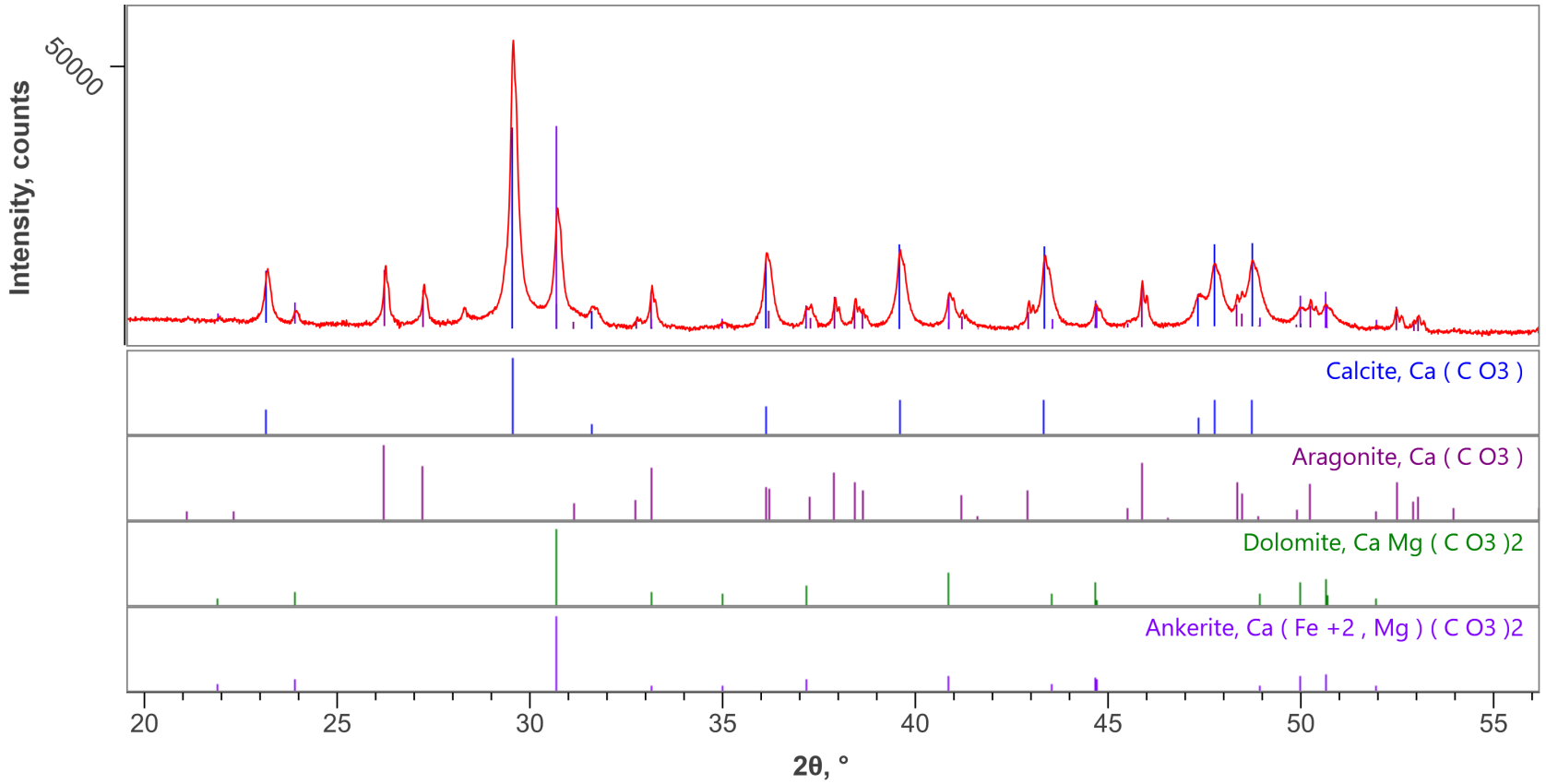


FIGURE L.3: X-ray diffraction (XRD) pattern of a representative carbonate core sample (red trace) with reference peak positions for calcite ($CaCO_3$), aragonite ($CaCO_3$), dolomite ($CaMg(CO_3)_2$), and ankerite ($Ca(Fe^{2+},Mg)(CO_3)_2$) shown below. Vertical bars indicate characteristic diffraction peak positions for each mineral phase. The dominant peak at $\sim$29.4° 2θ corresponds to calcite, with aragonite and minor dolomite/ankerite reflections indicating variable diagenetic overprinting within the sample.

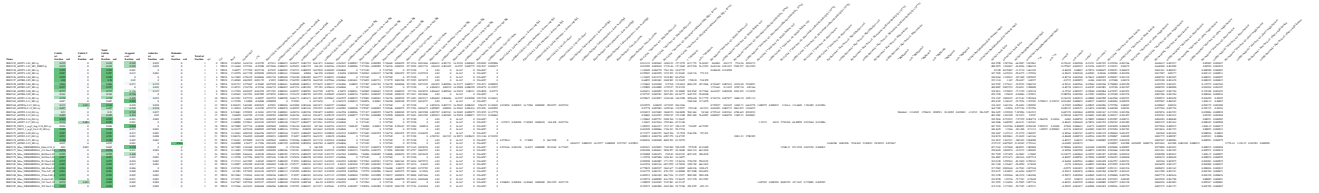


FIGURE L.4: Raw XRD data

APPENDIX M

Chapter 5 Supplement 5 - Raw Neutron Computed Tomography Data (This study)

A 75 GB dataset of the raw NCT data are archived at the Geocoastal Research Group, University of Sydney and available to be sent on hard drive by request. Email: Carra.Williams@sydney.edu.au or jody.webster@sydney.edu.au

APPENDIX N

Chapter 5 Supplement 6 - Hyperspectral Imaging Data (This study)

Hyperspectral imaging data of the boreholes listed in Table N.1 were scanned with the hyperspectral core imager (HCI) by Corescan pty ltd, funded by the National Virtual Core Library and hosted on Coreshed at (https://app.coreshed.com/). Colour scale ranges of the global spectral parameters are shown in the Corescan mineral key below.

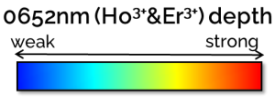
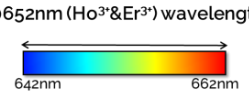
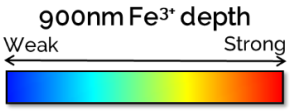
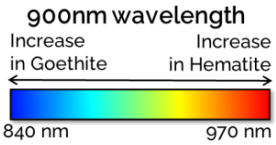
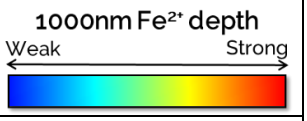
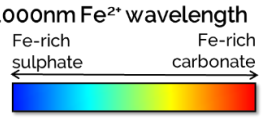
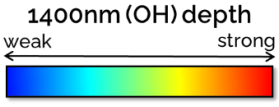
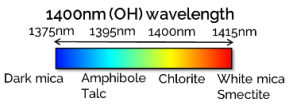
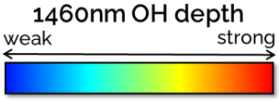
Website username: **Carra.Williams** and password: **CompareRepeatedDoor**

The dataset consists of the following:

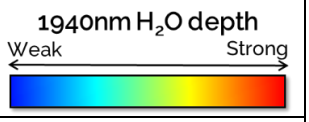
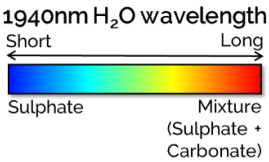
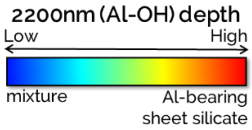
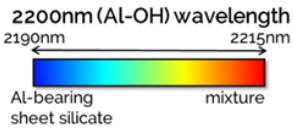
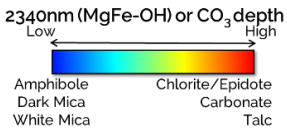
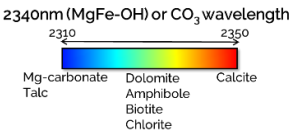
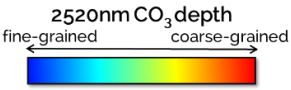
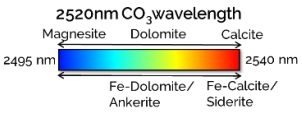
- Core imagery at 250 μm resolution
- Global spectral parameters (parameter ranges shown in the Corescan mineral key below)
- Mineralogical classification maps, including: Aragonite, Calcite, Dolomite, Gypsum, Kaolinite, Iron oxides and Chlorophyll.

Hyperspectral imaging data of select samples of Scott Reef cores described in Chapter 5 were scanned using the equipment and modified code of (Murphy et al., 2017) by Alexander Lowe at the Australian Centre for Field Robotics at Sydney Robotics Institute. The code is open source and available at https://github.com/acfr/hyperspec$_a fe_c arbonate$.

GLOBAL SPECTRAL PARAMETER IMAGERY

Image Product	Measurement*	Description	Notes
650nm (Ho^{3+} & Er^{3+}) depth	650D	Depth variation of the 0650nm feature in the REE's	
650nm (Ho^{3+} & Er^{3+}) wavelength	650L	Wavelength variation of the 0650nm feature in the REE's	
900nm Fe^{3+} depth	900D	Depth variation of the 900nm feature in iron oxides, related to ferric iron. Approximately correlates to abundance of material present	
900nm Fe^{3+} wavelength	900L	Wavelength variation of the position of the 900nm feature in iron oxides, related to ferric iron	
1000nm Fe^{2+} depth	1000D	Depth variation of the 1000nm feature related to ferrous iron in iron-rich sulphates and iron-rich carbonates	
1000nm Fe^{2+} wavelength	1000L	Wavelength variation of the position of the 1000nm feature related to ferrous iron in iron-rich sulphates and iron-rich carbonates	
1400nm (OH) depth	1400D	Depth variation of the 1400nm feature in the OH-bearing silicates	
1400nm (OH) wavelength	1400L	Wavelength variation of the position of the 1400nm features in OH-bearing silicates	
1460nm OH depth	1460D	Depth variation of the 1460nm feature related to the OH bond	

1/127 Grandstand Road
Ascot, WA, 6104
Australia
T +61 8 9277 2355
ABN 65 139 606 867
corescan.com.au

Image Product	Measurement*	Description	Notes
1940nm H_2O depth	1940D	Depth variation of the 1940nm feature related to H_2O in sulphates	
1940nm H_2O wavelength	1940L	Wavelength variation of the 1940nm feature related to H_2O. Pure sulphates are related to shorter wavelengths whereas longer wavelengths are related to mixture with carbonates	
2200nm (Al-OH) depth	2200D	Depth variation of the 2200nm feature in Al-rich phyllosilicates	
2200nm (Al-OH) wavelength	2200L	Wavelength variation of the 2200nm feature in Al-rich phyllosilicates	
2340nm (MgFe-OH) or CO_3 depth	2340D	Depth variation of the 2340nm feature in ferromagnesian silicates and/or carbonates	
2340nm (MgFe-OH) or CO_3 wavelength	2340L	Wavelength variation of the 2340nm in ferromagnesian silicates and/or carbonates	
2520nm CO_3 depth	2520D	Depth variation of the 2520nm feature in carbonates	
2520nm CO_3 wavelength	2520L	Wavelength variation of the 2520nm feature in carbonates	

* *L = wavelength (nm) at the absorption minima,*
D = depth of the absorption minima

1/127 Grandstand Road
Ascot, WA, 6104
Australia

T +61 8 9277 2355
ABN 65 139 606 867
corescan.com.au

TABLE N.1: Drill hole depth intervals scanned with the hyperspectral core imager

Drill Hole	Start (m)	End (m)
HOOK-1-P	4	35
HOOK-3-P	36	100
NRCH1J	13	18
NRSEHDD3-JA	1	200
SR-SEBH6J	2	179
SRSEBH1-J	1	28
SRSEBH2PA	11	36
SRSEBH3C	34	38
SRSEBH3D-P	13	47
SRSEBH3J	3	69
SRSEBH4-P	4	18
SRSEBH7J	6	35
SRSEBH8-J	0	50

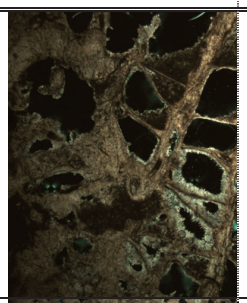
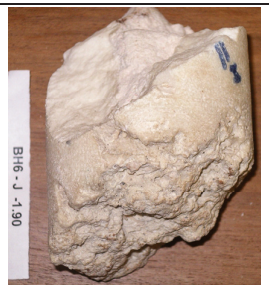
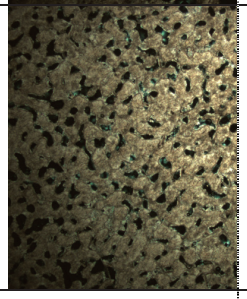
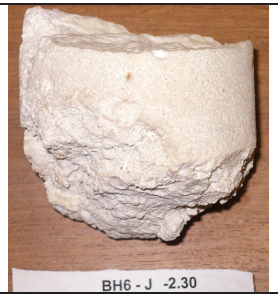
APPENDIX O

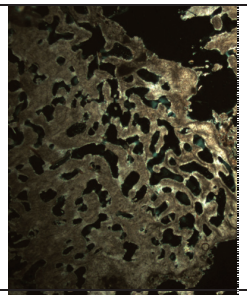
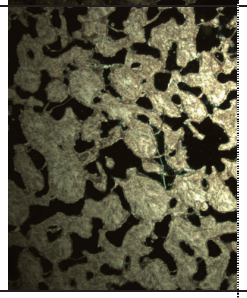
Chapter 5 Supplement 7 - Quantitative Hyperspectral Data (This study)

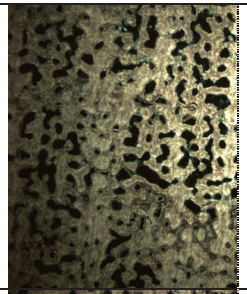
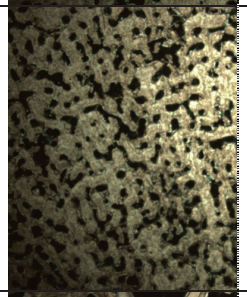
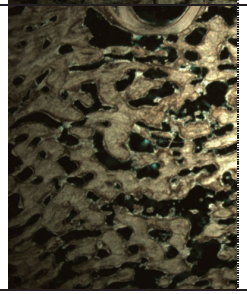
The quantitative hyperspectral mineral logs produced in this study can be downloaded from the following GitHub repository: Quantitative hyperspectral mineral log dataset.

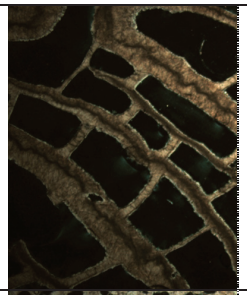
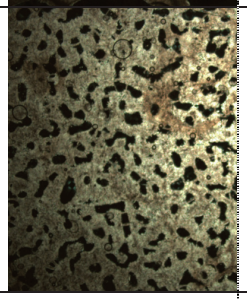
APPENDIX P

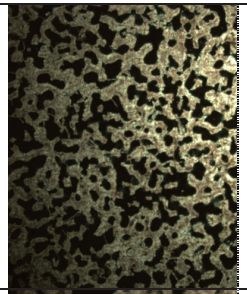
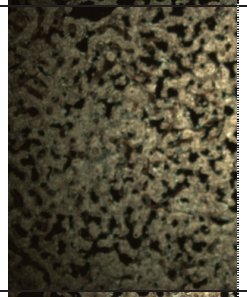
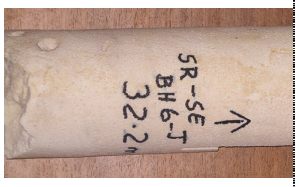
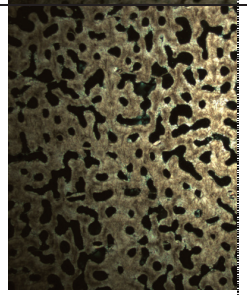
Chapter 5 Supplement 8 - Thin sections (Collins et al., 2009)

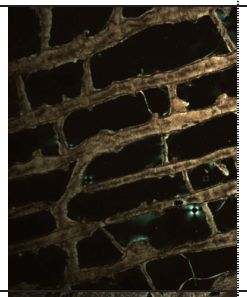
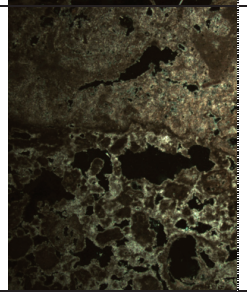
Area	Borehole	Depth (m)	Polished section	Thin section (Width 4.64mm)	Core Log	Core slab	Lithology	Diagenesis	Environment
SR-SE	BH 6-J	1.50			Coral Framestone, porous		Coral framestone, branching and massive corals, open chambers predominate.	Coral skeleton has micritized microborings , fibrous aragonite linings in 25% of chambers, and 5% peloidal marine micrite infills	Holocene reef facies
SR-SE	BH 6-J	1.80			Coral Framestone, porous		Coral framestone, thick walled massive corals, open chambers predominate.	Coral skeleton has micritized microborings , fibrous aragonite linings in 2% of chambers, and no peloidal marine micrite infills	Holocene reef facies
SR-SE	BH 6-J	2.32							

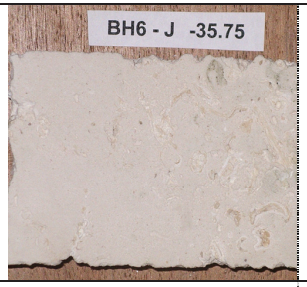
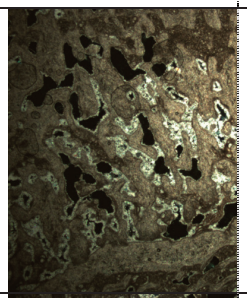
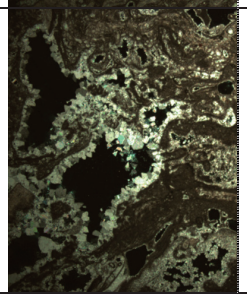
SR-SE	BH 6-J	4.35							
SR-SE	BH 6-J	5.25							
SR-SE	BH 6-J	9.30							

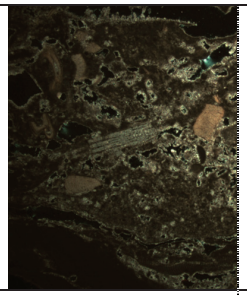
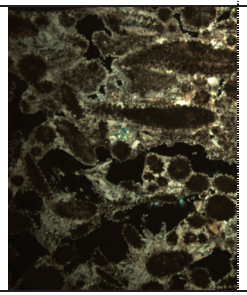
SR-SE	BH 6-J	9.45			Coral Framestone, porous		Coral framestone, thick walled massive corals, open chambers predominate	Coral skeleton has few micritized microborings , fibrous aragonite linings absent, and no peloidal marine micrite infills	Holocene reef facies
SR-SE	BH 6-J	11.65			Coral Framestone, porous		Coral framestone, thick walled massive corals, open chambers predominate	Coral skeleton has few micritized microborings , fibrous aragonite linings minor, and no peloidal marine micrite infills	Holocene reef facies
SR-SE	BH 6-J	15.85			Coral Framestone, porous		Coral framestone, thick walled massive corals, open chambers predominate	Coral skeleton has few micritized microborings , fibrous aragonite linings minor, and no peloidal marine micrite infills	Holocene reef facies

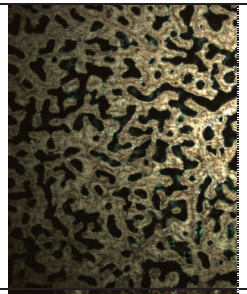
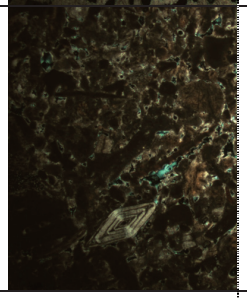
SR-SE	BH 6-J	17.55			Coral Framestone, porous, rubbly, branching and plate corals		Coral framestone, thick walled massive corals, open chambers predominate, fibrous aragonite lines 5% of frame voids; peloidal micrite fills 5% of frame voids	Coral skeleton has few micritized microborings , fibrous aragonite linings minor, and peloidal marine micrite infills	Holocene reef facies
SR-SE	BH 6-J	18.65			Coral Framestone, porous		Coral framestone, thick walled massive corals, open chambers predominate	Coral skeleton has few micritized microborings , fibrous aragonite linings minor, and minor peloidal marine micrite infills	Holocene reef facies
SR-SE	BH 6-J	20.5							
SR-SE	BH 6-J	23.40							

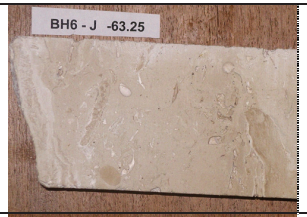
SR-SE	BH 6-J	26.60			Coral Framestone, porous, massive corals		Coral framestone, thick walled massive corals, open chambers predominate, fibrous aragonite lines 20% of frame voids; peloidal micrite fills 1% of frame voids	Coral skeleton has few micritized microborings , fibrous aragonite linings minor, and peloidal marine micrite infills; no subaerial diagenesis (therefore Holocene coral).	Holocene reef facies
SR-SE	BH 6-J	27.90			Coral Framestone, porous		Coral framestone, thick walled massive corals, open chambers predominate	Coral skeleton has common micritized walls and microborings , fibrous aragonite linings in 5% of frame voids, and minor peloidal marine micrite infills	Holocene reef facies
SR-SE	BH 6-J	32.20			Coral Framestone, porous		Coral framestone, thick walled massive corals, open chambers predominate	Coral skeleton has common micritized walls and microborings , fibrous aragonite linings in 1% of frame voids, and minor peloidal marine micrite infills. Not subaerially exposed (therefore Holocene coral)	Holocene reef facies
SR-SE	BH 6-J	32.45			Coral Framestone, porous		Coral framestone, thick walled massive corals, open chambers predominate	Coral skeleton has common(65%) micritized walls and microborings , fibrous aragonite linings in 5% of	Holocene reef facies

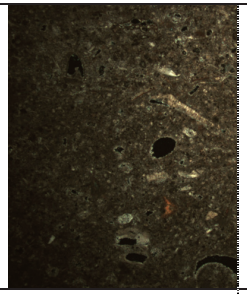
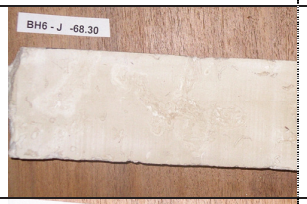
								frame voids, and minor peloidal marine micrite infills	
SR-SE	BH 6-J	32.95							
SR-SE	BH 6-J	33.00							
SR-SE	BH 6-J	34.60			Coral Framestone, porous		Coral framestone, thick walled massive corals, open chambers predominat	Coral skeleton has common micritized walls and microborings , fibrous aragonite linings in 2% of frame voids, and minor peloidal marine micrite infills	Holocene reef facies, just above base of Holocene at 35.0m
SR-SE	BH 6-J	35.25			Coral Framestone, dense; infilled		Coral framestone, dense; 20% of skeletal voids infilled by brown micrite, with microspar linings to common linear (root tube?) voids	Subaerial diagenesis, vadose micrite and microspar introduced. Sample is below unconformity at 35 m; probable MIS Stage 5 reef.	Pre-Holcene (Stage 5) reef facies, just below base of Holocene at 35.0m

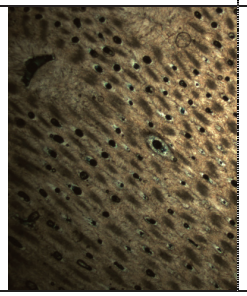
SR-SE	BH 6-J	35.75							
SR-SE	BH 6-J	38.40							
SR-SE	BH 6-J	39.70			Coral Framestone, dense; infilled		Coral framestone, branching corals, coralline algal bindstone, and minor skeletal grainstone; coral framework recrystallized to blocky calcite spar; pervasive micrite with tubular secondary voids, some with spar linings, patches of blocky spar recrystallization	Subaerial diagenesis, vadose micrite and microspar introduced; minor phreatic alteration.. Sample is below unconformity at 35 m	Pre-Holcene (Stage 5) reef facies, below base of Holocene at 35.0m.

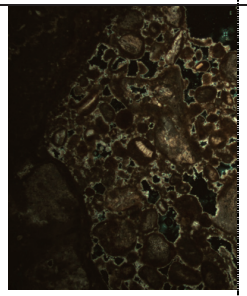
SR-SE	BH 6-J	43.75							
SR-SE	BH 6-J	48.30							
SR-SE	BH 6-J	49.20			Coral Framestone, chalky, leached, minor skeletal grainstone		Skeletal grainstone, composed of elongate skeletal grains (one variety only) , set in botryoidal to fibrous marine aragonite cement	Marine cementation is dominant	Marine cemented grainstone facies within coral reef framework; skeletal grains indeterminate

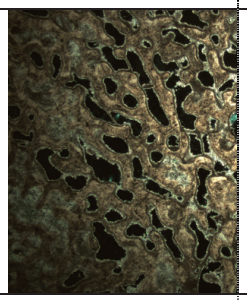
SR-SE	BH 6-J	51.35			Coral Framestone, massive, calcretized, with skeletal grainstone		Coral framestone, massive Porites, chambers empty, walls have micritic borings , few marine cements, minor micrite and fibrous aragonite	Subaerial diagenesis is minor; probable MIS Stage 5 reef; possible dating sample	Pre-Holcene (Stage 5) reef facies, massive Porites
SR-SE	BH 6-J	56.95			Limestone, calcretized, white, chalky, fabric destroyed		Skeletal grainstone, minor coral framestone; skeletal grains are coralline algae, forams, echinoids, molluscs; heavily micritized throughout, but lacks calcite spar; traces of aragonite marine cemen	Subaerial diagenesis is srong; development of vadose micrite	Reef associated grainstone facies
SR-SE	BH 6-J	56.95							
SR-SE	BH 6-J	62.90							

SR-SE	BH 6-J	63.25							
SR-SE	BH 6-J	64.50							
SR-SE	BH 6-J	65.00							

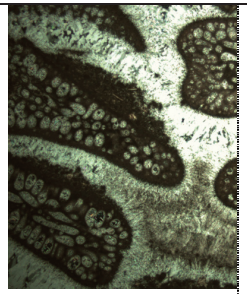
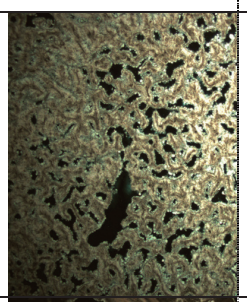
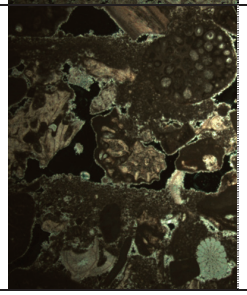
SR-SE	BH 6-J	65.75							
SR-SE	BH 6-J	68.3							
SR-SE	BH 6-J	65.25							
SR-SE	BH 6-J	69.30			Limestone, pink stained, calcretized, mottled, well lithified		Skeletal grainstone, with sparse coral framework. Skeletal grainstone has abundant fine skeletal debris, chiefly coralline algal segments, also benthic forams, echinoid plates, bryozoans. Skeletal grains micritized; weak calcrete overprint.	Subaerial diagenesis is weak in the form of vadose micritization. development of vadose micrite.	Sediment interval is possible fine grained lagoonal facies; surface at 69 m identified as possible unconformity. (Further investigation required, eg. the sediment could represent a possible

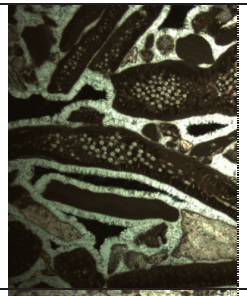
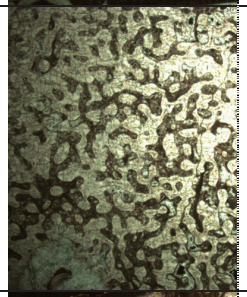
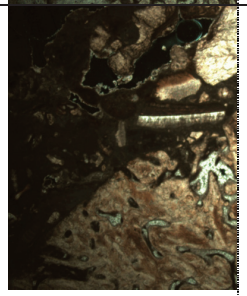
									drowning surface).
SR-SE	BH 6-J	70.00							
SR-SE	BH 6-J	71.90			Coral Framestone, massive, well cemented zone		Coral framestone, massive corals, with encrusting forams, minor skeletal grainstone. Pervasive micrite throughout the grainstone and porous corals, with peloidal fabric; contains tubular voids with sparry linings.	Subaerial diagenesis is strong, mainly in vadose environment	Reef facies and grainstone, strongly calcretized

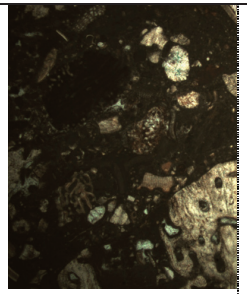
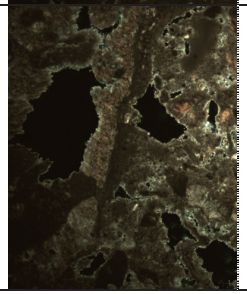
									
SR-SE	BH 6-J	72.70			Limestone, coral framestone, calcrete mottles, leached Halimeda?		Coral framestone, massive corals with encrusting forams and coralline algae; pervasive peloidal micrite with tubular voids which are spar filled; linear zones of dark brown calcrete composed of calcrete ooids and peloids, producing local pellet packstone diagenetic fabric. minor skeletal grainstone	Subaerial diagenesis is strong, forming distinct calcrete stringers which cut the rock fabric.	Reef facies and grainstone, strongly calcretized and overprinted by subaerial diagenesis
SR-SE	BH 6-J	74.30							

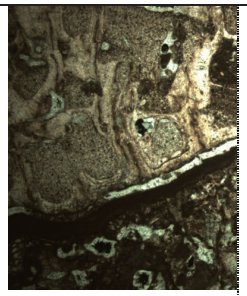
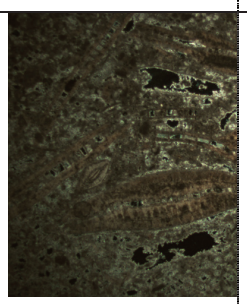
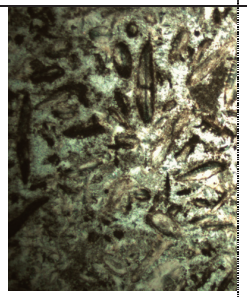
			 						
SR-SE	BH 6-J	76.95			Limestone, with leached Halimeda plates common		Coral framestone, and Halimeda rudstone/grainstone; Halimeda plates are leached, micritized, and recrystallized, with sparry secondary void linings. Pervasive micrite development	Subaerial diagenesis is strong, with a heavy vadose overprint	Reef facies and Halimeda rudstone/grainstone, strongly calcretized and overprinted by subaerial diagenesis
SR-SE	BH 6-J	77.00							

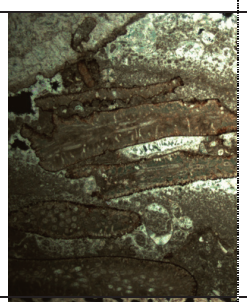
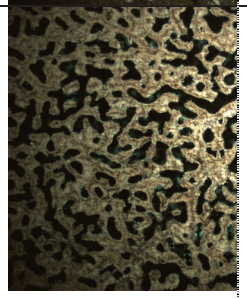
SR-SE	BH 6-J	78.00							
SR-SE	BH 6-J	80.35							

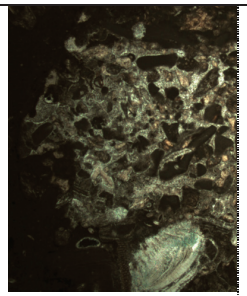
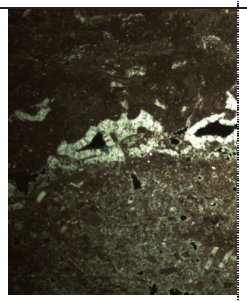
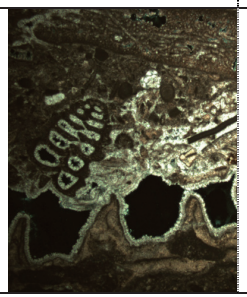
SR-SE	BH 6-J	80.60			Limestone, coral framestone, Halimeda plates common		: Halimeda rudstone/grainstone; Halimeda plates are subhorizontally oriented and set in radiaxial fibrous aragonite marine cement which occupies 30% of the rock. Halimeda internal chambers filled by fibrous aragonite with micritized walls. Aragonite cement in larger voids coarsens towards void centre to become bladed spar.	Cementation occurred originally in marine phreatic environment, filling much pore space; later subaerial leaching and recrystallization followed.	Reef related Halimeda rudstone/grain stone, initially marine cemented, later leached
SR-SE	BH 6-J	85.10			Limestone, coral framestone, interbedded skeletal grainstone		Coral framestone, Porites, massive, chambers empty but lined by blocky spar crystals; 10% of voids have remnant marine fibrous aragonite cement, recrystallized to blocky spar; 2% brown calcrete micrite present	Cementation occurred originally in marine phreatic environment, filling minor pore space; later subaerial alteration was probably in a meteoric phreatic environment.	Reef, Porites head
SR-SE	BH 6-J	87.95			Limestone, coral framestone, interbedded skeletal grainstone		Coral framestone, and skeletal grainstone, dominated by Halimeda skeletons. Fibrous aragonite marine cement is common within coral skeletons. Overprint of peloidal micrite, with secondary voids filled by block calcite in tubular arrangement (root hairs).	Initial minor early marine cements; subsequent strong subarial vadose diagenesis.	Reef facies and Halimeda grainstone

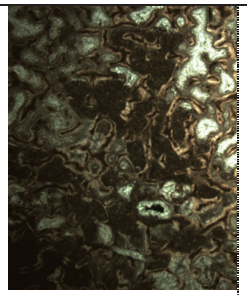
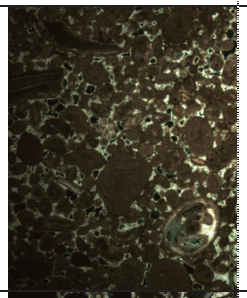
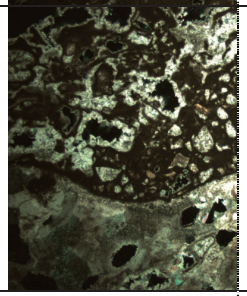
SR-SE	BH 6-J	90.90			Limestone, coral framestone, well lithified; branching and plate corals; Halimeda rudstone/grainstone intervals		Halimeda –skeletal rudstone/grainstone, composed of halimeda plates, forams, encrusting and benthic, molluscs; isopachous fibrous aragonite marine cement rims interskeletal voids and fills intraskeletal Halimeda pores	Well developed marine phreatic cement	Reef facies and Halimeda grainstone
SR-SE	BH 6-J	97.35			Limestone, coral framestone, well lithified; Porites head		Coral framestone, massive, void space filled by fibrous aragonite marine cement throughout. Minor blocky spar overprint present in 2% of rock	Incipient marine phreatic cement, with light overprint of meteoric phreatic alteration..	Reef facies. **NOTE: VUGS AND CALCRETE AT 97.5 TO 99.3 INDICATE POSSIBLE UNCONFORMITY**
SR-SE	BH 6-J	99.35			Limestone, coral framestone, calcretized		Coral framestone, and skeletal grainstone; coral has internal voids lined and filled by blocky spar; skeletal grainstone has Halimeda plates, molluscs, forams, coralline algae; with early marine void-fill cement penetrated by tubular voids lined by blocky calcite spar.. Minor blocky spar overprint present in 2% of rock	Incipient marine phreatic cement, with light overprint of vadose calcrete alteration	Reef facies and related skeletal grainstone

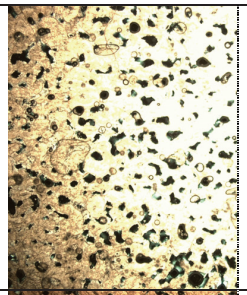
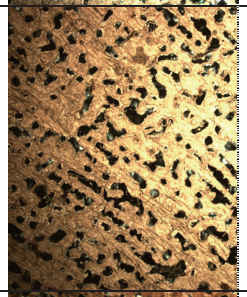
SR-SE	BH 6-J	102.30			Limestone, coral framestone, branching corals, encrusting forams (Homotrema), serpulids and skeletal grainstone		Coral framestone, and interbedded skeletal grainstone; latter has coralline algae, forams (encrusting and benthic), mollusc debris, with peloidal micrite cement. Initial fibrous aragonite marine cement in both framestone and grainstone is common but later partially recrystallized to blocky spar; skeletal grainstone peloidal cements have secondary voids with localised blocky spar fills	Initial marine phreatic cement, with light overprint of vadose calcrete alteration	Reef facies and related skeletal grainstone
SR-SE	BH 6-J	110.50			Limestone, skeletal grainstone, white, leached, minor corals		Skeletal packstone, fine skeletal debris of benthic forams, pelecypod fragments, thin walled bivalves, ostracods? , set in peloidal micrite marine cement. Skeletal grains leached ; secondary void space 5%, lined by microspar	Initial marine phreatic cement, with light overprint of vadose leaching and calcrete development	Skeletal grainstone interval, low energy cf. lagoonal environment, within reef facies
SR-SE	BH 6-J	116.20			Limestone, skeletal grainstone, small coral plates common		Skeletal grainstone to packstone, fine grained, with benthic forams, thin walled bivalves, and rare echinoid fragments; dense peloidal micrite marine cement, leached skeletal grains and 15% secondary porosity	Initial marine phreatic cement, with light overprint of vadose leaching and calcrete development	Skeletal grainstone interval, low energy cf lagoonal environment (similar interval 115-120.7 m) within reef facies

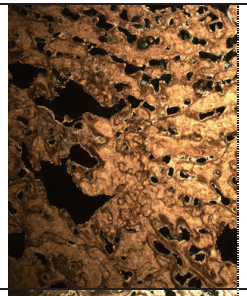
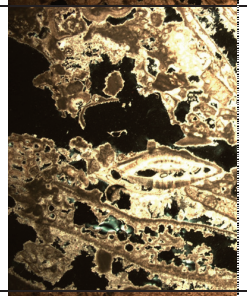
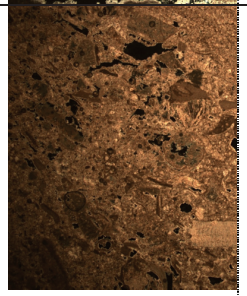
SR-SE	BH 6-J	126.30			Limestone, skeletal grainstone, white, leached, porous, unit underlying coral framestone facies		Coral framestone and interbedded skeletal grainstone; coral framestone has chambers lined by isopachous fibrous aragonite cement; partly recrystallized to blocky spar. Skeletal grainstone is biofragmental with pelecypods, forams, set in marine cements-fibrous aragonite and marine micrite, the former recrystallized to blocky spar	Initial marine phreatic cements, recrystallized in meteoric phreatic environment.	Skeletal grainstone interval, minor corals, from 126.3-at least 134 m; possible shelf facies; possible unconformity at 126 m ?.
SR-SE	BH 6-J	133.90			Limestone, skeletal grainstone, white, leached, chalky		Skeletal grainstone/rudstone, micritic, Tertiary? larger forams abundant (first occurrence in borehole), other benthic forams cf Amphistegina, planktic forams, fine skeletal debris abundant. Micritized; 5% secondary pores present, after leached fossils	Little obvious diagenesis other than micritization	Shelf facies sediment, moderate depth, near wave base. **NOTE: POSSIBLE TERTIARY LIMESTONE; SIMILAR FACIES FROM 126.3 M; POSSIBLE UNCONFORMITY**
SR-SE	BH 6-J	144.80			Limestone, grey sediment filled vug 144.8- 145 m in reef		Coralline algal bindstone host rock, marine cements, overlain by vug-fill (grey sediment)-skeletal grainstone, fine grained, with skeletal grains (circular cross-section; elongate, lateral canal system; wavy extinction; appear to be recrystallized Tertiary larger forams) cemented by fibrous aragonite and peloidal micrite marine	Marine cementation ,phreatic, is dominant	Hardground (coralline algal) with vug filled by marine shelf sediment containing larger forams similar to 133.9 m. **NOTE: POSSIBLE BASAL CYCLE**

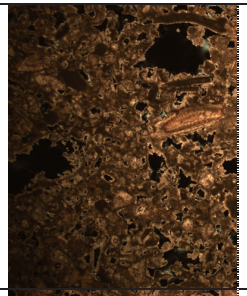
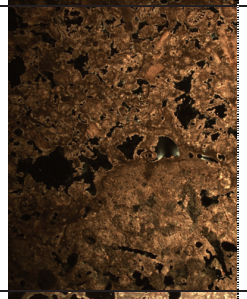
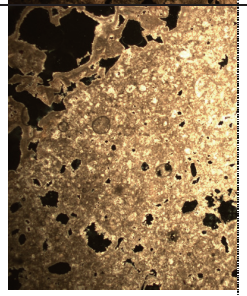
							cements		**BOUNDARY FOR SHELF SEDIMENT PACKAGE, 144M TO 126.3 M**
SR-SE	BH 6-J	144.90							
SR-SE	BH 6-J	151.85			Limestone, coral framestone, Halimeda plates common		Halimeda rudstone and coral framestone, Halimeda plates, coralline algae and benthic and encrusting forams set in fibrous isopachous aragonite marine cement; interspersed with peloidal micrite cement. Corals are strongly recrystallized. DIAGENESIS: Well developed marine phreatic cement	Well developed marine phreatic cement	Reef facies, coral-Halimeda

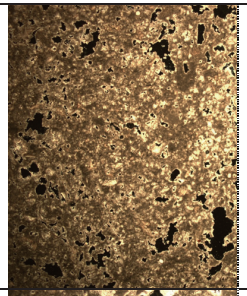
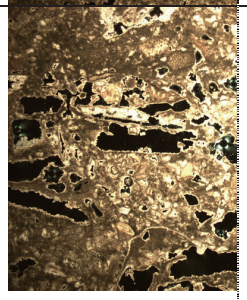
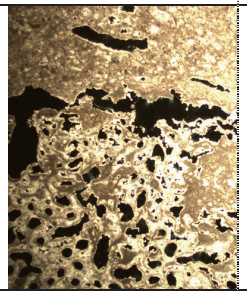
SR-SE	BH 6-J	157.55			Limestone, coral framestone, with vug filled by grey lithified sediment.		Halimeda rudstone and skeletal grainstone; abundant Halimeda plates and skeletal debris; including benthic forams and bivalve fragments; skeletal grains micritized; set in blocky spar/microspar cement- probably originally fibrous aragonite marine cement.	Well developed marine phreatic cement; recrystallized during meteoric phreatic diagenesis	Reef facies, vug infill, Halimeda.and skeletal debris
SR-SE	BH 6-J	160.10			Limestone, coral framestone, branching and plate corals		Coralline algal bindstone, heavily micritized; contains skeletal debris, also rare larger forams (Tertiary?); micritic and fibrous aragonite marine cements; and skeletal grainstone, biofragmental, encrusting and benthic foram fragments abundant; fibrous aragonite marine cements throughout	Well developed marine phreatic cement	Reef facies, and vug infill of skeletal debris
SR-SE	BH 6-J	165.40			Limestone, coral framestone, branching and plate coral, also Halimeda.		Skeletal rudstone/grainstone, contains Tertiary larger forams, Halimeda (abundant) and sand size skeletal grains, set in fibrous aragonite and marine micrite cements. No corals visible	Well developed marine phreatic cement	Reef associated algal-foram sediment

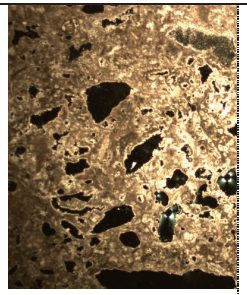
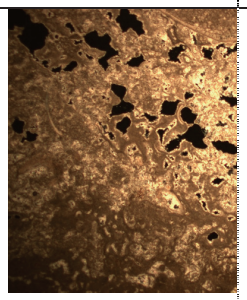
SR-SE	BH 6-J	177.20			Limestone, coral framestone, branching and massive corals, also Halimeda.		Coral framestone, micritized walls, pores filled by fibrous aragonite cement, partly recrystallized to blocky calcite; and skeletal rudstone/grainstone, contains Tertiary larger forams, Halimeda (abundant) and sand size skeletal grains, set in fibrous aragonite and marine micrite cements	Well developed marine phreatic cement, weak recrystallization overprint, probably subaerial diagenesis	Reef facies and associated algal-foram sediment
SR-SE	BH7-J	22.9							
SR-SE	BH7-J	26.75							

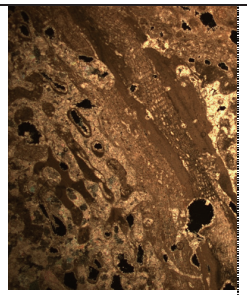
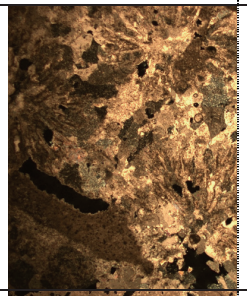
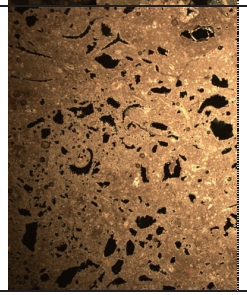
NR-SE	HDD3-JA	1.10			Coral framestone, porous	massive coral framestone	Coral framestone; massive coral, thick walled; porous, with open void system, well preserved. Void space is ca 30%.	5% of original frame voids filled with marine micrite cement; otherwise unaltered.	Coral reef; part of massive coral dominated Holocene reef buildup.
NR-SE	HDD3-JA	8.60 or 6.6m ?			Coral framestone; massive coral, thick walled; porous, with open void system, well preserved. Void space is ca 30%.	Massive coral framestone.	Coral framestone; massive coral, thick walled; porous, with open void system, well preserved, with encrusting coralline algae. Void space is ca 30%.	Little alteration; minor marine micrite cements	Coral reef; part of massive coral dominated Holocene reef buildup.
NR-SE	HDD3-JA	23.25			Coral framestone; massive coral, thick walled; porous, with open void system, well preserved. Void space is ca 30%.:	Massive coral framestone.	Coral framestone; massive coral, thick walled; porous, with open void system, well preserved, with encrusting coralline algae. Void space is ca 30%. Porites coral head.	Little alteration: minor marine micrite cement.	Coral reef frame rock; massive Holocene buildup.

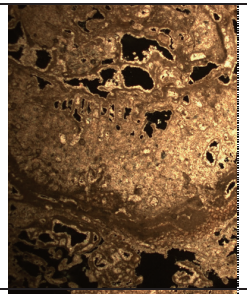
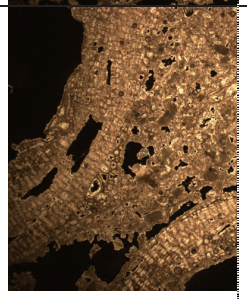
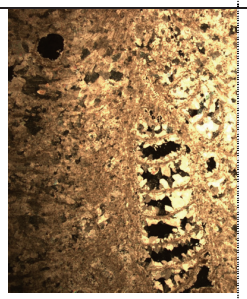
NR-SE	HDD3-JA	23.80			Coral framestone; massive coral, thick walled; porous, with open void system, well preserved. Void space is ca 30%.	Massive coral framestone, porous	Massive coral framestone, small voids, no marine cements; marginal encrustation by Homotrema and encrusting coralline algae.	Little diagenetic alteration.	Massive coral reef buildup; Holocene
NR-SE	HDD3-JA	26.80			Massive coral framestone.	massive coral framestone, porous; minor grey skeletal sand.	Coral framestone; cylindrical coral colonies; with interstitial skeletal grainstone, with benthic and encrusting forams, halimeda plates, coralline algal fragments.	Micritization of skeletal grains, and leaching; minor bladed marine cements in 1% of voids (MgCalcite or aragonite).	Coral reef buildup; Holocene.
NR-SE	HDD3-JA	27.20			Limestone; skeletal rudstone/grainstone.	Limestone, skeletal rudstone/ grainstone, well lithified.	Skeletal grainstone, well lithified, fine-medium grained, poorly sorted, composed of benthic forams, coralline algae, serpulids, halimeda, skeletal debris	Minor marine fibrous aragonite cement in serpulid chambers; micritization of skeletal grains is common, as part of calcrete diagenesis; blocky calcite spar cement lines leached voids and fills leached skeletal grains.	Shallow water, open marine depositional setting; lacks coral reef framework.

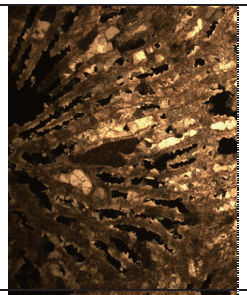
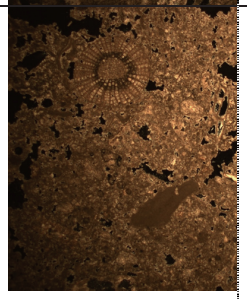
NR-SE	HDD3-JA	28.90			Coral framestone, leached.	Coral framestone and interbedded skeletal grainstone.	Skeletal grainstone, fine-medium grained, moderately well lithified, micritized; skeletal grains are benthic forams, coralline algae, micritized grains.	Micritization of skeletal grains; leaching of skeletal grains, generation of secondary pores which are lined by spar/microspar, alteration by vadose diagenesis in a calcrete profile.	Shallow marine biofragmental sediment associated with coral reef buildup.
NR-SE	HDD3-JA	31.60			Coral framestone, mixed massive, branching corals.	Coral framestone and associated skeletal limestone.	Skeletal grainstone, micritized; composed of benthic forams, echinoids, molluscs, altered skeletal grains.	Skeletal grains micritized, recrystallized and also leached, with root structure secondary voids throughout; vadose diagenesis in calcrete profile.	Shallow marine skeletal sandy substrate associated with reef framework development.
NR-SE	HDD3-JA	34.05			Coral framestone.	Coral framestone, and associated sediment; massive corals; leached.	Skeletal grainstone, medium grained, micritized, recrystallized; composed of forams and micritized grains, with minor corals.	Heavily micritized. Secondary voids are lined with microspar cement which is pervasive in the rock; corals are recrystallized to blocky calcite. Spar/microspar contains “dog-tooth” crystals. Probably both vadose and phreatic diagenetic events, superimposed, occurred.	Shallow marine deposition associated with coral ref buildup.

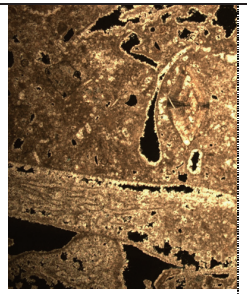
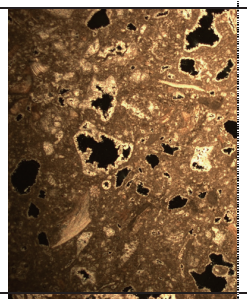
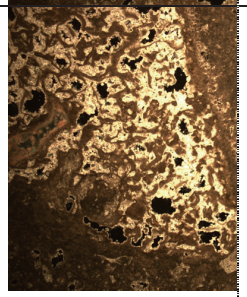
NR-SE	HDD3-JA	36.10			Coral framestone, massive corals, and skeletal grainstone; leached.	Coral framestone with skeletal grainstone.	Skeletal grainstone, heavily micritized, benthic forams, chiefly Amphistegina, and remnant micritized skeletal grains. .	Heavily micritized; strong root structuring with blocky calcite cements lining some rootlet voids. Strong calcrete overprint developed in vadose conditions.	Shallow marine, reef associated sediment.
NR-SE	HDD3-JA	41.40			Limestone, friable, leached corals, leached bioclasts.	As for core log..	Skeletal grainstone, micritized and leached, altered skeletal grains, mainly benthic forams, set in micritic limestone. Large voids after root structuring are abundant, usually solution enlarged, open, with minor microspar linings. Calcrete-related vadose soil diagenesis is a strong overprint.		Shallow marine reef associated sediment.
NR-SE	HDD3-JA	49.10			Limestone, coral framestone, with leached bioclastic molds as secondary pores.	As for core log.	Coral framestone, massive corals, bored, chambers infilled by homogeneous blocky calcite; coarsely crystalline; overlain by skeletal grainstone, micritized, leached, voids empty or lined with calcite microspar.	Strong leaching during subaerial diagenesis, with 30% secondary moldic pore space after leached skeletal grains.	Reef facies with interstitial shallow marine sediment.

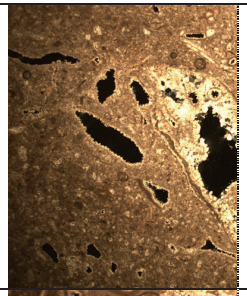
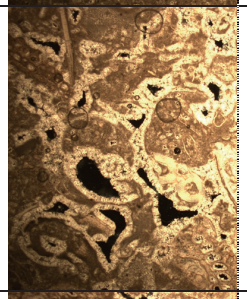
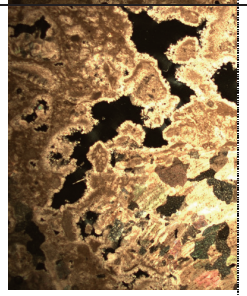
NR-SE	HDD3-JA	49.50			Limestone, leached, bioclastic molds; interspersed with coral framestone.	As for core log.	Skeletal grainstone, micritized, leached, rare fresh skeletons are forams and echinoids; leached platy microfossils and angular skeletons are abundant. Bivalves recrystallized to calcite, then leached.	Micritic limestone; with network of secondary voids, either empty or filled with blocky spar which has also replaced skeletal grains; leached microfossils contribute 25% secondary pore space; strong vadose diagenetic overprint, subsequently leached.	Shallow marine reef facies and interbedded skeletal grainstone; fabric obscured by heavy diagenetic overprint.
NR-SE	HDD3-JA	51.90			Limestone, leached coral framestone; dense calcrete zone, at R2 surface.	Coral framestone, heavily altered, leached bioclasts. .	Limestone, heavily altered; skeletal grainstone with coral remnants; micritized throughout; much of primary fabric destroyed..	Heavy diagenetic overprint with root structuring and micritization throughout, micritization generating pellet packstone fabric. Blocky calcite recrystallization in 20% of rock probably represents original coral framestone host. Apparent strong calcrete diagenesis associated with R2 surface.	Shallow marine reef facies and associated sediment..

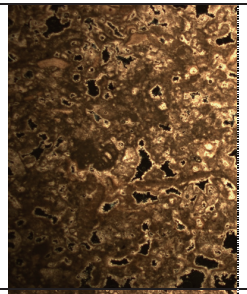
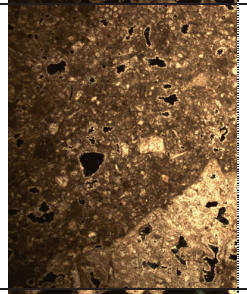
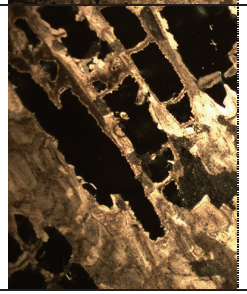
NR-SE	HDD3-JA	53.60			Limestone, coral framestone, massive corals, thin calcrete horizons	Limestone, as for core log.	Limestone, coral framestone, with recrystallized branching corals; void fills of micrite and blocky spar, overlain by skeletal grainstone,hevily micritized and leached, with echinoid and foram fragments; secondary leached skeletal voids lined or filled by blocky spar cement, often with dog-tooth morpoology;lacy calcite and pelloidal micrite fabrics are typical of root structured calcrete; moldic pore space is 25% of rock.	Calcretization of coral framestone and skeletal grainstone; mainly soil-related vadose diagenesis.	Marine, reef framework, with sandy infill.
NR-SE	HDD3-JA	58.00			Coral framestone, massive corals. :	Coral framestone, massive and branching corals.	Coral framestone, branching corals abundant; heavily recrystallized, blocky calcite cement fills or lines coral framework voids.	Borings in coral framestone filled by marine micrite cement-up to 10% of rock. Patched of coarse blocky calcite recrystallization, probably developed during phreatic zone alteration.	Reef and skeletal sand facies; recrystallized.
NR-SE	HDD3-JA	65.25			Limestone, coral framestone, leached, branching corals abundant; rubbly.	As above.	Limestone, micritic, fine grained, 20% irregular voids after leached skeletal grains; some infilled by blocky calcite. Minor calcified root filaments present.	Heavily calcretized with micritic alteration in vadose soil profile	Coral reef framestone, shallow marine.

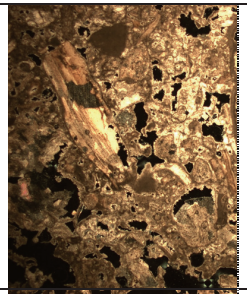
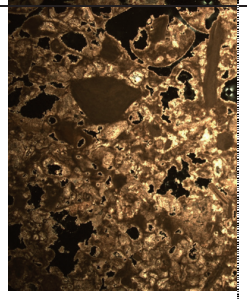
NR-SE	HDD3-JA	70.35			Limestone, leached coral framestone, with cemented zones.	As above.	Coral framestone and skeletal grainstone, recrystallized, with micritic overprint, calcified micritic filaments and ovoid voids lined or filled by microspar cement, large skeletal grains recrystallized to blocky spar; secondary voids comprise 20% of rock.	Strongly calcretized, also leached.	Coral reef framestone and associated sediment.
NR-SE	HDD3-JA	77.00			Limestone, coral framestone, leached, chalky, mainly branching corals, with head corals and bioclastic intervals.	As above.	Coral framestone, predominantly branching corals, and interspersed skeletal grainstone; micritized, recrystallized, leached. Skeletal grainstone has lacy diagenetic fabric with micritic remnants, spar lined and filled voids, and occasional calcified root filaments.Blocky calcite partly infills voids in coral framestone.	Strong calcretization; mainly vadose diagenes but also leached.	Coral framestone reef and associated grainstone.
NR-SE	HDD3-JA	84.05			Limestone, white, chalky, leached, vuggy.	As above.	Coral framestone, predominantly branching corals, recrystallized, block calcite fills frame voids, with interstitial skeletal grainstone, micritized, leached, with lacy to peloidal fabric; skeletal grains- echinoids, forams, pelecypods, coralline algae- rarely preserved; sparite fills leached skeletal voids.	Strong calcrete overprint, vadose diagenetic environment..	Shallow water reef and associated skeletal sediment.

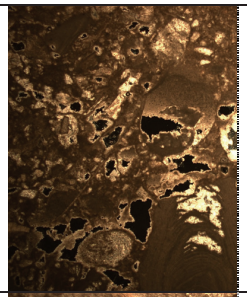
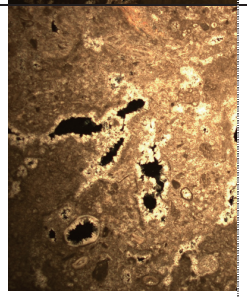
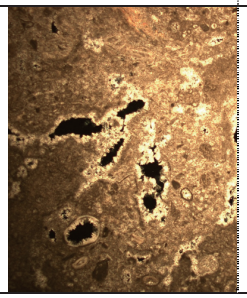
NR-SE	HDD3-JA	91.40			Limestone, coral framestone, leached, vuggy; friable intervals.	Coral framestone, leached, vuggy..	Coral framestone, massive corals, recrystallized coral frame partly filled by coarse calcite blocky spar cement; calcite crystals tend to be poikilitic.	Recrystallization in a phreatic diagenetic environment.	Coral reef, shallow water.
NR-SE	HDD3-JA	92.15			Limestone, coral framestone, leached, vuggy, with friable intervals.	Limestone, coral framestone, leached, vuggy.	Limestone, fine grained, micritic, leached, recrystallized; remnant skeletal grains are forams, echinoids, pelecypods, rare coralline algal nodules; leached voids, empty or filled by microspar, comprise 15% of rock. Root structured, with micrite lined root hairs common; coarse blocky calcite patches throughout the micritic limestone.	Calcretized; mainly vadose alteration, probably soil-associated.	Shallow marine..
NR-SE	HDD3-JA	111.5 m			Limestone, well lithified, yellow stained, leached, vuggy (note: sample from below possible calcrete zone; core loss).				

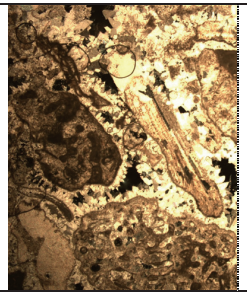
NR-SE	HDD3-JA	113.20			Limestone, well lithified, leached, vuggy.	: As above.	Skeletal grainstone, heavily micritized; remnant skeletal grains –forams (Amphistegina), echinoid fragments, coralline algae; network of voids after leached skeletal grains, lined to filled by calcite microspar; secondary voids comprise 30% of rock; remnant coral framestone patches.	Strong vadose calcrete overprint.	Shallow marine, reef associated sediment and reef facies.
NR-SE	HDD3-JA	115.45			Limestone, well lithified, leached.	As above.	Limestone, skeletal, heavily micritized, leached, with pores filled by blocky calcite spar, contains forams, coralline algae, other skeletal debris. Secondary void system provided by calcified root tubes (rhizocretions) in 10% of rock.	Strong calcrete overprint in vadose diagenetic environment..	Shallow open marine sand.
NR-SE	HDD3-JA	119.20			Limestone, well lithified, recrystallized, with calcrete mottles (possible unconformity)	: As above.	Branching coral framestone (30%), recrystallized, and skeletal grainstone (70%), micritized, recrystallized. Coral framestone is recrystallized to sparry calcite, with thin micritic wall remnants. Micritized skeletal grainstone of bivalves, forams, echinoids, skeletal debris, with secondary tubular voidslined by blocky calcite spar/microspar.	Calcrete overprint is strongly developed; vadose diagenesis..	Shallow water reef and associated sediment.

NR-SE	HDD3-JA	127.10			Limestone, white, recrystallized, leached, moldic porosity.	: As above.	Limestone, fine grained, leached, heavily micritized; composed of fragmented skeletal debris; elongate leached voids up to 1 cm long are probably after foram or algal constituents; 30% secondary pores; recrystallization of micrite to microspar is pervasive.	Strongly calcretized	Marine skeletal sand of shallow water aspect.
NR-SE	HDD3-JA	132.70			Limestone, leached, with orange stained vugs.	As above.	Limestone, skeletal, with forams-benthic and encrusting, echinoids, thin walled pelecypods, micritized throughout. Leached fossil fragments (10% of rock) have void walls lined by calcite spar/microspar.	Calcretized limestone, vadose diagenesis.	Shallow marine sand..
NR-SE	HDD3-JA	135.40			Limestone, massive, recrystallized, calcrete mottles fill vugs.	As above.	Skeletal grainstone, micritized (80%) and coral framestone, recrystallized, (20%). Skeletal debris of echinoids, encrusting forams, encrusting coralline algae, is set in dense micrite cement; an irregular secondary void system is lined with calcite microspar (probably root structuring); coral frame is completely recrystallized to calcite; 20% secondary voids.	Strong vadose calcrete overprint.	Shallow marine, reef associated..

NR-SE	HDD3-JA	136.00			Limestone, recrystallized, dense, calcrete mottles.	As above.	Limestone, skeletal; fragments of forams, coralline algae, Halimeda, pelecypods;micritized; dense micritic overprint obscures primary fabric; tends to develop pelletal fabric. Small tubular voids throughout, with microspar linings.	Calcretization of shallow water sand; also root structuring; vadose diagenesis.	Shallow water marine sand, calcretized.
NR-SE	HDD3-JA	140.45			Limestone, Massive, Recrystalised, very few vugs, low porosity. Calcrete mottles fill voids.	As Above	Limestone, Skeletal Debris, minor hole skeletons of echinoids, benthic forams are common; heavily micritised with dense pervasive calcite micrite. Secondary voids are small, minor, with linings of calcite microspar.	Strong calcrete development in vadose zone.	Shallow marine, bioclastic limestone
NR-SE	HDD3-JA	151.10			Limestone, white, well lithified, occasionally vuggy, with corals and bioclasts.	As above	Coral Framestone, massive, porous; both coral fabric and pores retained but substantially recrystallised to blocky calcite. (Not suitable for dating)	Recrystallisation in Phreatic zone.	Shallow marine coral reef facies

NR-SE	HDD3-JA	154.45			Limestone, yellow-brown, well lithified, low pore space, possible calcrete horizon.	As above	Limestone, skeletal grainstone (benthic forams, small coralline algal nodules, echinoid plate fragments) with dense micritisation throughout. Leached skeletal grains are common and secondary voids comprise 20% of rock.	Strong calcrete development and leaching.	Shallow marine, bioclastic.
NR-SE	HDD3-JA	156.25			Limestone, white, dense, voids filled by brown calcrete, well lithified.	: As above	Limestone, skeletal, heavily micritised and calcretised with original fabric obscured, probably laminar calcrete zones present. Polloidal micrite zones with lacy voids lined by microspar are abundant.	Strong calcretisation in vadose zone.	Shallow marine bioclastic.
NR-SE	HDD3-JA	158.50			Limestone, recrystallised, coral framestone, brown calcrete mottles abundant.	As Above	Limestone, biofragmental, with fragments of forams, coralline algae and molluscs. All heavily micritized with pervasive micrite, leaching and development of secondary voids filled by blocky calcite spar.	Strong calcretization of skeletal limestone in vadose zone.	Shallow marine, biofragmental

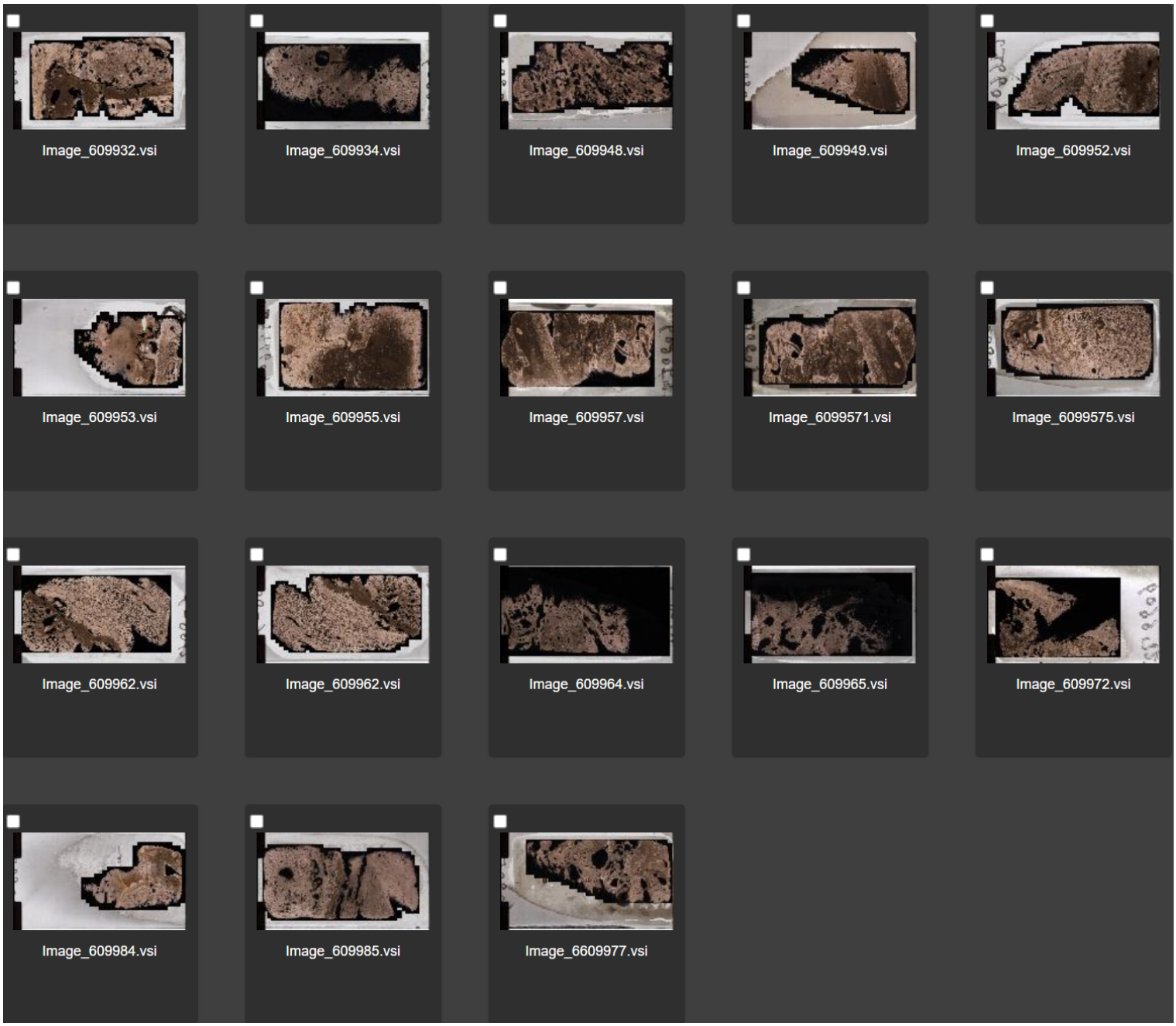
NR-SE	HDD3-JA	170.40			Limestone, coralline algal framestone, with intervals of coralline algal boundstone.	As Above	Limestone, coralline algal boundstone, with coralline algal thallae throughout, filled by skeletal sediment composed of skeletal grainstone, micritized. Sparry recrystallisation is present along root structured secondary voids within the grainstone.	Calcretization of boundstone and skeletal grainstone in vadose zone.	Shallow water, reframeworked facies and skeletal grainstone
NR-SE	HDD3-JA	184.90			Bioclastic grainstone/rudstone and coral framestone, occasionally vuggy with calcrete infills. Below possible calcrete zone at 191 metres.	As Above	Limestone/skeletal grainstone, biofragmental (benthic forams, bivalves, echinoids) all recrystallised and leached with pervasive blocky calcite cement throughout a leached pore system (10% secondary void space is retained). Spar lines and partially fills secondary pore space with blocky, dog tooth and radiating fabrics.	Leached limestone with heavily altered skeletal grains due to phreatic diagnesis.	Shallow marine.
NR-SE	HDD3-JA	189.40 189.9 ?							

NR-SE	HDD3-JA	193.05			Limestone, recrystallized, dense, calcrete mottles.	As above.	Limestone, skeletal; fragments of forams, coralline algae, Halimeda, pelecypods;micritized; dense micritic overprint obscures primary fabric; tends to develop pelletal fabric. Small tubular voids throughout, with microspar linings.	Calcretization of shallow water sand; also root structuring; vadose diagenesis.	Shallow water marine sand, calcretized.

APPENDIX Q

Chapter 5 Supplement 9 - Thin sections (This study)

Thin sections produced in this study and presented in Chapter 5 are archived at the School of Earth and Atmospheric Sciences, Faculty of Science, Queensland University of Technology and are available to be sent on hard drive by request. Email: Carra.Williams@sydney.edu.au, l.northdurft@qut.edu.au or jody.webster@sydney.edu.au.

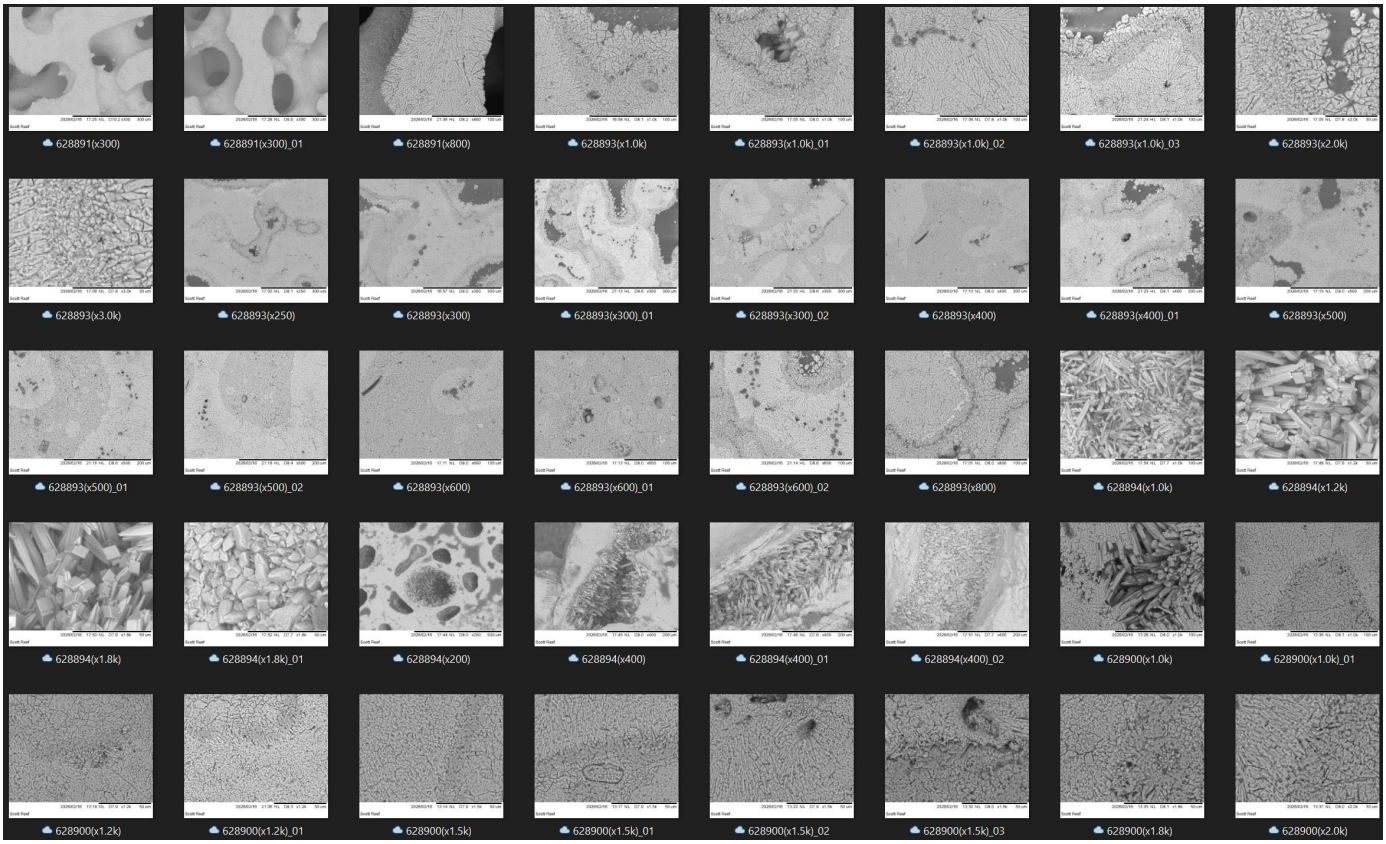

Image_609932.vsi
Image_609934.vsi
Image_609948.vsi
Image_609949.vsi
Image_609952.vsi
Image_609953.vsi
Image_609955.vsi
Image_609957.vsi
Image_6099571.vsi
Image_6099575.vsi
Image_609962.vsi
Image_609962.vsi
Image_609964.vsi
Image_609965.vsi
Image_609972.vsi
Image_609984.vsi
Image_609985.vsi
Image_6609977.vsi

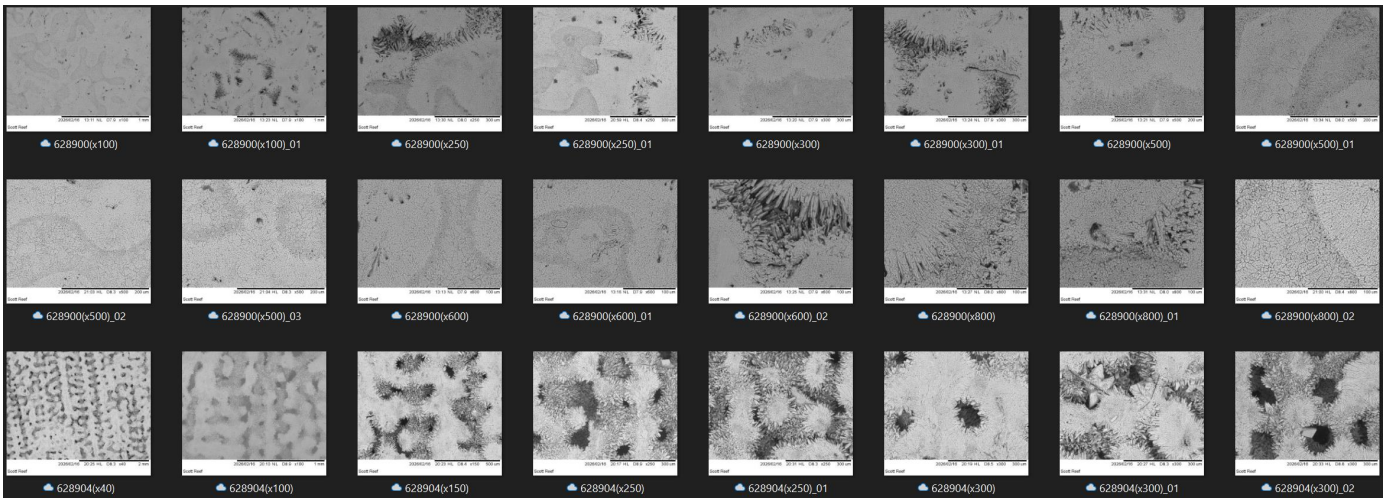
APPENDIX R

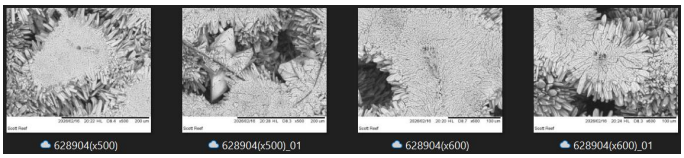
Chapter 5 Supplement 10 - SEM data (This study)

The raw SEM micrographs shown below that were produced in this study and presented in Chapter 5 are archived at the Geocoastal Research Group, University of Sydney and are available to be sent on hard drive by request. Email: Carra.Williams@sydney.edu.au or jody.webster@sydney.edu.au.


628889(x1.0k)
628889(x1.0k)_01
628889(x1.2k)
628889(x1.2k)_01
628889(x1.5k)
628889(x2.5k)
628889(x60)
628889(x100)
628889(x100)_01
628889(x120)
628889(x150)
628889(x150)_01
628889(x180)
628889(x200)
628889(x250)
628889(x250)_01
628889(x250)_02
628889(x300)
628889(x300)_01
628889(x300)_02
628889(x300)_03
628889(x400)
628889(x400)_01
628889(x400)_02
628889(x500)
628889(x500)_01
628889(x500)_02
628889(x600)
628889(x600)_01
628889(x600)_02
628889(x600)_03
628889(x600)_04
628891(x1.0k)
628891(x1.0k)_01
628891(x1.0k)_02
628891(x1.5k)
628891(x2.0k)
628891(x30)
628891(x100)
628891(x100)_01


628891(x300)
628891(x300)_01
628891(x800)
628893(x1.0k)
628893(x1.0k)_01
628893(x1.0k)_02
628893(x1.0k)_03
628893(x2.0k)
628893(x3.0k)
628893(x250)
628893(x300)
628893(x300)_01
628893(x300)_02
628893(x400)
628893(x400)_01
628893(x500)
628893(x500)_01
628893(x500)_02
628893(x600)
628893(x600)_01
628893(x600)_02
628893(x800)
628894(x1.0k)
628894(x1.2k)
628894(x1.8k)
628894(x1.8k)_01
628894(x200)
628894(x400)
628894(x400)_01
628894(x400)_02
628900(x1.0k)
628900(x1.0k)_01
628900(x1.2k)
628900(x1.2k)_01
628900(x1.5k)
628900(x1.5k)_01
628900(x1.5k)_02
628900(x1.5k)_03
628900(x1.8k)
628900(x2.0k)


628900(x100)
628900(x100)_01
628900(x250)
628900(x250)_01
628900(x300)
628900(x300)_01
628900(x500)
628900(x500)_01
628900(x500)_02
628900(x500)_03
628900(x600)
628900(x600)_01
628900(x600)_02
628900(x800)
628900(x800)_01
628900(x800)_02
628904(x40)
628904(x100)
628904(x150)
628904(x250)
628904(x250)_01
628904(x300)
628904(x300)_01
628904(x300)_02


628904(x500)
628904(x500)_01
628904(x600)
628904(x600)_01

APPENDIX S

Academic conference presentations and awards

Conference presentations undertaken during candidature (presenting author in **bold**).

2021

Williams, C., Courtade, S., Dutra, H.P.L., Lejri, M., Habel, W.B., Salomonsen, P. (2021). Reproducing carbonate sedimentary processes and architectures with stratigraphic forward modelling. **AAPG/SEG Annual Convention and Exhibition (ACE)**, **San Francisco, USA — *Oral presentation***.

Williams, C., Courtade, S., Dutra, H.P.L., Lejri, M., Habel, W.B., Salomonsen, P. (2021). Reproducing carbonate sedimentary processes and architectures with stratigraphic forward modelling. **Geological Society of America (GSA) GESSS Meeting — *Oral presentation***.

2022

Williams, C., Paumard, V., Webster, J.M., Leonard, J., Salles, T., O'Leary, M., Lang, S. (2022). Environmental controls on the resilience of Scott Reef since the Miocene (North West Shelf, Australia): Insights from 3D seismic data. **International Coral Reef Symposium (ICRS) — *Oral presentation***. *University of Sydney, School of Geosciences Award of Excellence*.

Williams, C. (2022). Neutron scattering technology to date fossil coral reefs from the North West Shelf, Australia. **Geological Society of America (GSA) GESSS Meeting — *Oral presentation***.

Williams, C., Paumard, V., Webster, J.M., Leonard, J., Salles, T., O'Leary, M., Lang, S. (2022). Environmental controls on the resilience of Scott Reef since the Miocene (North West Shelf, Australia): Insights from 3D seismic data. **Browse Team, Woodside Energy — *Oral presentation***.

2023

Williams, C., Paumard, V., Webster, J.M., Leonard, J., Salles, T., O'Leary, M., Lang, S. (2022). Environmental controls on the resilience of Scott Reef since the Miocene (North West Shelf, Australia): Insights from 3D seismic data. **Australian Exploration Geoscience Conference (AEGC)**, **Brisbane, Australia — *Poster presentation***.

Williams, C. (2023). PhD overview. **AEGC GeoPitch — *Three-minute lightning talk***.

Williams, C. (2023). Difficulties with diagenesis in fossil coral reef archives. **IAS SedSon-Line Seminar Series — *Invited online presentation***.

Williams, C, **Webster, JM**, Bevitt, JJ, Webb, GE, Nothdurft, LD, Paumard, V, McGregor, H and Murphy, RJ 2023, Neutron Computed Tomography: A Novel High-Resolution, Non-Destructive Method for Screening Fossil Coral for Diagenetic Alteration for Geochronologic and Paleoclimatic Reconstructions **International Association of Sedimentologists (IAS) Conference**, **Dubrovnik, Croatia — *Oral presentation***. *Presented by Prof. J.M. Webster*.

2024

Williams, C. (2024), Webster, JM, Salles, T, Paumard, V, Grimaldi, C and Lejri, M 2026, Carbonate platform evolution in response to the Mid - Pleistocene climate transition on the North-West Shelf of Australia: Insights from forward stratigraphic modelling **European Geosciences Union (EGU) General Assembly**, **Vienna, Austria — *Oral presentation***.

2025

Williams, C. (2024), Webster, JM, Salles, T, Paumard, V, Grimaldi, C and Lejri, M 2026, Carbonate platform evolution in response to the Mid - Pleistocene climate transition on the North-West Shelf of Australia: Insights from forward stratigraphic modelling **International Association of Sedimentologists (IAS) Conference**, **Huelva, Spain** — ***Poster presentation***. *Best Poster Award. Associated publication: Marine Geology (2026), Article 107716.*

2026

Williams, C. (2024), Webster, JM, Salles, T, Paumard, V, Grimaldi, C and Lejri, M 2026, Carbonate platform evolution in response to the Mid - Pleistocene climate transition on the North-West Shelf of Australia: Insights from forward stratigraphic modelling. **International Sedimentological Congress (ISC)**, **Wellington, New Zealand** — ***Oral presentation***.

Williams, C., Paumard, V., Webster, J. M., Leonard, J., Salles, T., O'Leary, M., and Lang, S. (2023). Environmental controls on the resilience of Scott Reefs since the Miocene (North West Shelf, Australia): Insights from 3D seismic data. Marine and Petroleum Geology, 151. https://doi.org/10.1016/j.marpetgeo.2023.106188 **Browse Team, Woodside Energy** — ***Oral presentation***.